

ISBN 978-2-87355-031-8

**Proceedings of the  
International Meteor Conference  
Petnica, Serbia  
21–24 September, 2017**



Published by the International Meteor Organization 2018  
Edited by Marc Gyssens and Jean-Louis Rault



ISBN 978-2-87355-031-8

**Proceedings of the  
International Meteor Conference  
Petnica, Serbia  
21–24 September, 2017**



Published by the International Meteor Organization 2018  
Edited by Marc Gyssens and Jean-Louis Rault

Proceedings of the International Meteor Conference  
Petnica, Serbia, 21–24 September, 2017  
International Meteor Organization  
ISBN 978-2-87355-031-8

### **Copyright notices**

© 2018 The International Meteor Organization

The copyright of papers in this publication remains with the authors.

It is the aim of the IMO to increase the spread of scientific information, not to restrict it. When material is submitted to the IMO for publication, this is taken as indicating that the author(s) grant(s) permission for the IMO to publish this material any number of times, in any format(s), without payment. This permission is taken as covering rights to reproduce both the content of the material and its form and appearance, including images and typesetting. Formats may include paper and electronically readable storage media. Other than these conditions, all rights remain with the author(s). When material is submitted for publication, this is also taken as indicating that the author(s) claim(s) the right to grant the permissions described above. The reader is granted permission to make unaltered copies of any part of the document for personal use, as well as for non-commercial and unpaid sharing of the information with third parties, provided the source and publisher are mentioned. For any other type of copying or distribution, prior written permission from the publisher is mandatory.

### **Editing team and Organization**

Publisher: The International Meteor Organization

Editors: Marc Gyssens and Jean-Louis Rault

Typesetting: L<sup>A</sup>T<sub>E</sub>X 2<sub>ε</sub> (with styles from Imolate 2.4 by Chris Trayner)

Printed in Germany

Legal address: International Meteor Organization, Jozef Mattheessensstraat 60, 2540 Hove, Belgium

### **Distribution**

Further copies may be ordered from the Treasurer of the International Meteor Organization, Marc Gyssens, Jozef Mattheessensstraat 60, 2540 Hove, Belgium, or through the IMO website (<http://www.imo.net>).

# Contents

Contents . . . . .	1
Marc Gyssens and Jean-Louis Rault: Editors' notes . . . . .	5
<b>Workshops reports</b>	
Jean-Louis Rault (compiler): IMC 2017 Questions and Answers Session . . . . .	6
Cis Verbeeck, Vincent Perlerin, and Jürgen Rendtel: Summary of the Visual Workshop . . . . .	7
Jürgen Rendtel: Analysis of visual meteor observations . . . . .	8
<b>Lecture presentations</b>	
Detlef Koschny, Andrea Toni, Regina Rudawska, Joe Zender, François Colas, and Jérémie Vaubaillon: FRIPON-NL—The first FRIPON camera in the Netherlands . . . . .	10
Stijn Calders, Hervé Lamy, Antonio Martínez Picar, Cédric Tétard, Cis Verbeeck, and Emmanuel Gamby: The Radio Meteor Zoo: Involving citizen scientists in radio meteor research networks . . . . .	13
Juraj Tóth, Leonard Kornoš, František Ďuriš, Pavol Zigo, Dušan Kalmančok, Jozef Világi, Jaroslav Šimon, Štefan Gajdoš, Pavol Matlovič, Alžbeta Kubirtová, and Martin Baláz: AMOS from Slovakia, Canary Islands, and Chile . . . . .	16
Denis Vida, Peter Brown, Margaret Campbell-Brown, and Sean Huggins: Canadian Automated Meteor Observatory: Cometary meteoroid strengths derived from a highly frag- menting event observed on July 21, 2017 . . . . .	18
Stefan Beriša, Tina Dufke, Åse Marie Erklev, Igor Smolić, and Nemanja Vojvodić: Nomon Project . . . . .	25
Mariusz Wiśniewski, Przemysław Żołądek, Arkadiusz Olech, Zbigniew Tymiński, Maciej Maciejewski, Arka- diusz Raj, Karol Fietkiewicz, Mariusz Gozdalski, Marcin Przemysław Gawroński, Tomasz Su- chodolski, Maciej Myszkiewicz, Marcin Stolarz, and Krzysztof Polakowski: Current status of Polish Fireball Network . . . . .	29
Regina Rudawska, Joe Zender, Detlef Koschny, Stefan Loehle, Imanol Uriarte Latorre: The CILBO spectral observation program . . . . .	32
Nagatoshi Nogami: Meter-sized meteorite impacts . . . . .	34
Ayyub S. Guliyev: About one possible mechanism of comet splitting . . . . .	35
Esther Drolshagen, Theresa Ott, Detlef Koschny, Gerhard Drolshagen, and Björn Poppe: NEMO—Near Real-Time Monitoring System . . . . .	38
François Colas, Sylvain Bouley, David Baratoux, Salma MBaye, Marc Delcroix, and Jean Luc Dauvergne: Detection of impacts on giant planets: Another way to determine meter-sized object flux in our Solar System . . . . .	42
Kristina Veljkovic: Description of the R package METFNS for analysis of visual meteor data . . . . .	43
Leonard Kornoš, František Ďuriš, and Juraj Tóth: AMOS orbit software, EDMOND database . . . . .	46

Antal Igaz, Gergely Csépany, Nándor Opitz, Krisztián Sárnecky, and László L. Kiss: The Konkoly Meteor Observing Network (KoMON) . . . . .	50
Jérémie Vaubaillon, Auriane Egal, Min-Kyung Kwon, Chiara Marmo, Mirel Birlan, Simon Jeanne, Jean-Louis Rault, Cyril Blanpain, Julien Lecubin, Adrien Malgoyre, François Colas, Sylvain Bouley, Stéphane Caminade, Pierre Vernazza, Jérôme Gattacceca, and Brigitte Zanda: FRIPIPE: the FRIPON pipeline . . . . .	53
Peter S. Gural: New developments in meteor processing algorithms . . . . .	56
Marcelo De Cicco, Susana Zoghbi, Andres P. Stapper, Antonio J. Ordoñez, Jack Collison, Peter S. Gural, Siddha Ganju, José-Luis Galache, and Peter Jenniskens: Artificial intelligence techniques for automating the CAMS processing pipeline to direct the search for long-period comets . . . . .	65
Peter C. Slansky: Meteor film recording with digital film cameras with large CMOS sensors . . . . .	71
Pavel Zigo: Kolonica-Modra: the new system for forward-scatter radio meteor observations . . . . .	76
William Ward, Paul Reynolds, Rachel Love, and Nikolaž Gadegaard: Novel injection moulded gratings for video meteor spectroscopy. . . . .	79
Tom Roelandts: How the received radio meteor signal determines the final spectrogram . . . . .	82
Antonio Martínez Picar and Christophe Marqué: Using a small phased array for meteor observations . . . . .	85
Sirko Molau: Twenty years of IMO Video Commission: a retrospective . . . . .	88
Daniel Kastinen and Johan Kero: Orbital uncertainties in radar meteor head echoes . . . . .	92
Pavol Matlovič, Juraj Tóth, Regina Rudawska, and Leonard Kornoš: Study of distinct meteor spectra populations . . . . .	99
Jean-Louis Rault, Mirel Birlan, Cyril Blanpain, Sylvain Bouley, Stéphane Caminade, François Colas, Jérôme Gattacceca, Simon Jeanne, Julien Lecubin, Adrien Malgoyre, Chiara Marmo, Jérémie Vaubaillon, Pierre Vernazza, and Brigitte Zanda: Fine-scale observations of Doppler frequency shifts affecting meteor head radio echoes . . . . .	103
Damir Šegon, Maria Vukić, Marko Šegon, Željko Andreić, and Peter S. Gural: Meteors in the near-infrared as seen in the Ondřejov catalogue of representative meteor spectra . . . . .	107
Vlastimil Vojáček and Jiří Borovička: Properties of faint meteors derived from video observations . . . . .	109
Jürgen Rendtel: Detectability of minor features in meteor shower activity profiles . . . . .	115
Giancarlo T. Tomezzoli: Radio observations of the 2016 daytime meteor showers . . . . .	118
Przemysław Źołądek and Mariusz Wiśniewski: Zeta Cassiopeids—Twelve years of observations . . . . .	125
Christian Steyaert and Jeffrey Brower: The 2016 Gamma Draconids outburst . . . . .	128
Hervé Lamy, Cédric Tétard, Michel Anciaux, Sylvain Ranvier, Antonio Martínez Picar, Stijn Calders, and Cis Verbeeck: First observations with the BRAMS radio interferometer . . . . .	132

Cis Verbeeck, Hervé Lamy, Stijn Calders, Cédric Tétard, and Antonio Martínez Picar: Overview of major shower observations 2016–2017 by the BRAMS network . . . . .	138
Joe Zender, Regina Rudawska, Detlef Koschny, Gerhard Drolshagen, Gert-Jan Netjes, Mirko Bosch, Rik Bijl, Rob Crevecoeur, and Felix Bettonvil: Meteorite detection with airborne support—a study case . . . . .	145
Auriane Egal, Jérémie Vaubaillon, Min-Kyung Kwon, Vincent Perlerin, Mike Hankey, François Colas, and William Thuillot: Time perception of a meteorite fall: first results . . . . .	153
Ana Vodopivec and Hakan Kayal: Autonomous sensor network for detection and observation of meteors . . . . .	156
Marcelo De Cicco, Daniela Lazzaro, Eduardo P. Santiago, and EXOSS team: Brazilian video monitoring meteors network EXOSS: Status and first results—a citizen science project	162
F. Colas, M. Birlan, J.-L. Rault, B. Zanda, S. Bouley, J. Gattacceca, J. Vaubaillon, P. Vernazza, S. Jeanne, L. Jorda, C. Marmo, A. Steinhauser, K. Baillie, A. Egal, C. Blanpain, J. Lecubin, A. Malgoyre, S. Caminade, M. Marsset, D. Gardiol, A. Cellino, M. Di Martino, D. Koschny, A. Toni, R. Rudawska, H. Lamy, E. Jehin, B. Poppe, E. Drolshagen, T. Ott, G. Drolshagen, S. Molau, L. Ferrière, A. Nedelcu, and S. Ribas: FRIPON—Status of radio and optical network . . . . .	165
Timothy W. Beck, Martin Bradley, Daniel Hunchard, Crystal Morataya, Jeremy Ronco, and Chatnaree Upton: Installation of the Mendocino College-Ukiah International Latitude Observatory meteor project . . . .	169
Leonardo S. Amaral, Lauriston S. Trindade, Carlos A. P. B. Bella, Marcelo L. P. V. Zurita, Renato C. Poltronieri, Gabriel G. Silva, Cristóvão J. L. Faria, Carlos F. Jung, and Jakub A. Koukal: Brazilian Meteor Observation Network: History of creation and first developments . . . . .	171
Damir Šegon, Korado Korlević, Željko Andreić, Denis Vida, Filip Novoselnik, and Ivica Skokić: Ten years of the Croatian Meteor Network . . . . .	176
Mike Hankey and Vincent Perlerin: American Meteor Society fireball camera . . . . .	177
 <b>Poster presentations</b>	
Mert Acar, Alper K. Ateş, and Cenk Kayhan: Observation of lunar impact flashes . . . . .	181
Roman Dvořák, Jan Štrobl, and Jakub Kákona: Data management system of the Bolidozor network . . . . .	184
Ivanka Getsova-Momcheva, Ivaylo Belchev, Katerina Ruseva, and Kalina Georgieva: Visual and photographic observations of meteors carried out by students of the Astronomical Observatory and Planetarium “Nicolaus Copernicus” . . . . .	187
Abderrahmane Ibhi, Fouad Khiri, and Lahcen Ouknine: New meteorite fall in the region of Igdí (Tata, Morocco) . . . . .	189
Antal Igaz, Gergely Csépany, Nándor Opitz, Krisztián Sárneczky, and László L. Kiss: Evaluation of cosmic effects and risks of small bodies in the Solar System at Konkoly Observatory . .	192
Jakub Kákona, Roman Dvořák, Martin Kákona, and Jan Mikeš: Atmospheric phenomena radio localization system . . . . .	194
Anna Levin, Tamira Tchenak, Ella Ratz, Shlomi Eini, Yaron Eini, and Shy Halatzi: Nineteen years of meteor astronomy in Israel . . . . .	197
Alexandra Terentjeva and Sergey Barabanov: Meteorite-producing fireball streams . . . . .	199
Filip Fabris, Marija Kosić, Snježana Štefanić Hoefel, Damir Šegon, and Mateja Dumbović: Calendar of meteor activity based on IMO video observations 2006–2015 . . . . .	203

Tibor Hegedüs, Zoltán Jäger, Zoltán Jäger, Jr., Szilárd Csizmadia, Zsolt Kereszty, and Zoltán Zelkó: Dark flight integrator in action: 2015 Easter bolide recalculated . . . . .	206
Jim Rowe: SCAMP, a new UK bolide network . . . . .	210
Elizabeth A. Silber, Wayne K. Hocking, and Reynold E. Silber: Shock waves generated by overdense meteors in the mesosphere-lower thermosphere . . . . .	212
Kimio Maegawa and Sumio Nakane: Past, present, and future of beacon signal transmissions for meteor radio observations in Japan . . . . .	216
Przemysław Żołądek, Arkadiusz Olech, Mariusz Wiśniewski, Zbigniew Tymiński, and Marcin Stolarz: Large Taurids detected by U.S. Government sensors . . . . .	218
Pei-Ying Wu, I-Ching Yang, and Chun-Nan Lin: Statistical analysis of height and velocity distribution of the Perseids . . . . .	220
Diana Sekulić, David Buzgo, and Sara Knežević: Some aspects of team visual observation analysis . . . . .	223
Milica Rakić and Ana Nikolić: Meteor video observations, F and T factor . . . . .	225
Vladimir Nikolić, Leander Schröder, and Aleksa Tešić: Cloudiness estimation for video meteor observations . . . . .	228
Author index . . . . .	231

## Editors' notes

Marc Gyssens and Jean-Louis Rault

The 36th International Meteor Conference (IMC) took place from September 21 to 24, 2017, in Serbia, in the Petnica Science Center, Petnica, Valjevo. It was organized by the Petnica Meteor Group, exactly 20 years after the previous IMC took place at this location.

The conference brought together 132 participants from 25 countries (Azerbaijan, Belgium, Bosnia and Herzegovina, Brazil, Bulgaria, Canada, Croatia, Czech Republic, France, Germany, Hungary, Ireland, Israel, Japan, the Netherlands, Norway, Poland, Serbia, Slovakia, Slovenia, Spain, Sweden, Turkey, United Kingdom, and United States). The varied schedule of events comprised 62 presentations (43 lectures and 19 posters), an excursion to the Valjevo city surroundings, and several long-lasting socializing evenings.

All these dry facts and figures do not reflect the very nice atmosphere and the exciting discussions that took place for four days between the participants aged from 2 to 77. Those who were lucky to attend both Petnica events, twenty years ago and now, could witness the incredible transformation the Center had undergone from a fairly primitive facility to a state-of-the art science center, but this was luckily not at the expense of the enthusiasm and the atmosphere that characterized the previous event and that was still present today. For this, we must thank the drive and enthusiasm of the Local Organization Committee and their many collaborators, in particular Dušan Pavlović and the Center's Program Director, Nikola Božić.

The annual IMCs are a unique opportunity for amateurs and professionals interested in meteors to meet each other. However, the publication and distribution of the IMC Proceedings that bring together all the papers prepared by the contributors is also an important aspect, to make sure that results of the Conference are documented and can be relied on for future meteor work.

After this IMC 2017, the IMO failed in preparing the Proceedings in a reasonable time. Producing quickly the conference book depends mainly on the ability of the lecturers to deliver their paper in time, and of the editors to carry out quickly the publication tasks. This year, most of the lecturers forwarded their papers within the desired period, so the cause of the delay must be sought in the difficulties experienced by the editors' team. Preparing the Proceedings consists of exchanges with the authors, checking the science contents, preparing the layout, checking the bibliography references, correcting typos and language mistakes, printing the document, etc. Three volunteers came forward for editing the 2017 Proceedings, but one of them could not honor the commitments made for personal reasons. As a consequence, the remaining editors were seriously handicapped. Marc now had to do almost all of the LaTeX editing, while scientific content, bibliography checks, corrections of typos, and safe electronic archiving were managed by Jean-Louis. Despite the delay caused by this, we still had good hopes to finish this volume before the IMC 2018 until some health concerns of Marc interfered. Thanks to the help of David J. Asher, Edith Leblanc, Antonio Martínez Picar, Francisco Ocaña González, Javor Kac, Charles Powell, and Cis Verbeeck, whose support is acknowledged here, the IMC 2017 Proceedings finally came to light.

The main lessons to be learnt are that a reliable team of volunteers has to be chosen for any future IMC Proceedings editions, and that a sufficient number of them must be proficient with the text editor chosen. Our most sincere apologies for the delay in publishing these long-awaited IMC 2017 Proceedings!

Happy reading!

# IMC 2017 Questions and Answers Session

compiled by Jean-Louis Rault

International Meteor Organization, Radio Commission, 91360 Épinay-sur-Orge, France  
f6agr@orange.fr

The Questions and Answers Session took place on Thursday evening. It was chaired by Jean-Louis Rault and had many participants. A selection of Questions and Answers are sketched below.

## Selection of questions and answers

- **Q:** I would like to know about triboelectric effects and how we can calculate them in case of a meteor, if it is possible at all. (*Matija Dodović*)

**A:** Jiří Borivička suggested triboelectric effects to explain strange wobbles in light curves. Also the FRIPON fireball network has observed Doppler curves that oscillate near the end.

- **Q:** Which projects might be accomplished by students in the field of meteor sciences at middle school (ages 12–13)? What kind of research might be done by middle-school children in this field (or are they too young for this)? (*Ella Ratz*)

**A:** Here are a few examples:

- Visual observations;
- Building an all-sky camera, write the software, put it on internet (as Chris Peterson is doing);
- Use a slingshot to sling little marble spheres into sand and compare the images with images of craters on the Moon and on Mars;
- Make a comet (dry ice, water, sand);
- Google for “project astro” and you will find a lot of inspiration.

- **Q:** Are visual observations still useful in the era of video observations? (*Ella Ratz*)

**A:** These are a few important considerations in this respect:

- In order to know the temporal evolution of a meteor shower, we need to continue the same observing techniques for a long time. We have got a much longer record of visual observations than video observations;
- The limiting magnitude of visual observations is typically a lot higher than that of video observations;
- If we ever stop with visual observations, they need to be intercalibrated with video observations in order to be able to track the video observations of the pre-video period;

- The pleasant quietness of visual observations in the middle of the night can be an important incentive to perform visual meteor observations;
- For many more years, we will need both visual and video observations.

- **Q:** Which spectral resolution would you recommend for spectroscopic observations? (*Marcello de Cicco*)

**A:** It is best to take a low resolution so you collect more photons. One to four nanometers per pixel is recommended if you want to identify spectral lines. If you want to go more into detail for checking models, you need sub-nanometer resolution.

- **Q:** Is there a Virtual Meteor Observatory? (*Roman Dvořák*)

**A:** There is a database, which is presently located at ESTEC (maintained by Detlef Koschny), and which adheres to the Virtual Meteor Observatory format (Barentsen et al., 2010). This database contains all video observations performed with the METREC software.

- **Q:** How can you track parent bodies back in time? (*Filip Matković*)

**A:** Use planetary ephemerides to see where all the planets were 1 minute ago. Use a software (e.g., REBOUND) to get the ephemeris of the planets (e.g., CALCEPH or JPG ones), calculate the sum of the gravitational attractions of the planets on the parent body to find out where the body as a function of time. Daniel Kastinen is working on PYTHON code that traces back bodies in time and visualizes them.

## Reference

Barentsen G., Arlt R., Koschny D., Atreya P., Flohrer J., Jopek T., Knöfel A., Koten P., McAuliffe J., Oberst J., Tóth J., Vaubaillon J., Weryk R., Wiśniewski M., and Żołądek P. (2010). “The VMO file format. I. Reduced camera meteor and orbit data”. *WGN, Journal of the IMO*, **38**, 10–24.

# Summary of the Visual Workshop

Cis Verbeeck<sup>1,4</sup>, Vincent Perlerin<sup>2,4</sup>, and Jürgen Rendtel<sup>3,4</sup>

<sup>1</sup> Royal Observatory of Belgium, Ringlaan 3, 1180 Brussels, Belgium  
cis.verbeeck@oma.be

<sup>2</sup> American Meteor Society  
vperlerin@gmail.com

<sup>3</sup> Leibniz Institut für Astrophysik, 14482 Potsdam, Germany  
jrendtel@aip.de

<sup>4</sup> International Meteor Organization

A summary is given of the activities during the Visual Meteor Workshop which took place at the International Meteor Conference 2017 in Petnica, Serbia.

## Summary

The Visual Workshop took place on the Friday evening. It was chaired by Cis Verbeeck and had many participants. In his introduction, Cis pointed out that visual observations are still very relevant. The incentives for having the Visual Workshop are the following:

- providing tips and tricks regarding the new online visual form on the IMO website;
- communication of two recently fixed bugs in the online visual form: both the “past midnight” and “input data gone” bugs have now been solved;
- interaction with visual meteor observers to improve the online visual form where possible; and
- encouraging meteor workers to perform global meteor shower analyses employing the Visual Meteor DataBase (VMDB) and discussing tools that can aid this purpose.

First, Vincent Perlerin talked about “How to use the new IMO form to minimize the time for submitting a visual observation session?”. This presentation was very interactive, several suggestions by the participants will be incorporated in the form in the near future:

1. check whether the radiant is above the horizon;
2. ten observing sites per observer ranked by usage;
3. put the sporadics at the last row of the magnitude distribution;
4. Since at least 90% of observations use counting (“C”), “C” will become the default;
5. option to express the field center in  $(A, h)$  or  $(\alpha, \delta)$  (with automatic conversion between both); and
6. option to provide observations via an EXCEL file or similar (useful for experienced groups with a lot of observations and poor internet connection).

Next, Vincent presented “Towards an open API for the VMDB”. The VMDB Open API ([http://www.imo.net/members/vmdb\\_open\\_api](http://www.imo.net/members/vmdb_open_api)) allows the user to query the VMDB, either by calling the right API function with your API Key directly (URL) or from a script written in whatever language. The results can be provided in many formats, including JSON, XML, CSV, and text files. Meteor workers are kindly invited to employ the VMDB Open API.

As last speaker of the workshop, Jürgen Rendtel (2018) presented “Analysis of visual meteor observations” in which he focused on the Perseids 2017. From his presentation, it was obvious that selecting the right binning parameters for a given shower return is not straightforward. Binning parameters include the minimal and maximal bin size (time interval), the minimal number of meteors in a bin, the maximal correction, maximal error and minimal limiting magnitude.

Proper binning parameters ensure that real features stand out while no artifacts are introduced. It is clear that the selection of proper binning parameters is an iterative process.

Since the live ZHR plots of past shower returns on the IMO website ([http://www.imo.net/members/imo\\_live\\_shower](http://www.imo.net/members/imo_live_shower)) employ default binning parameters, they should be treated with care.

For upcoming meteor showers, IMO officers will carefully select binning parameters such that the live ZHR plots are reliable. Over time, the binning parameters of old shower returns will also be optimized.

## Reference

Rendtel J. (2018). “Analysis of visual meteor observations”. In Gyssens M. and Rault J.-L., editors, Proceedings of the International Meteor Conference, Petnica, Serbia, 21–24 September 2017. IMO, pages 8–9.

# Analysis of visual meteor observations

Jürgen Rendtel<sup>1,2</sup>

<sup>1</sup> Leibniz Institut für Astrophysik, An der Sternwarte 16, 14482 Potsdam, Germany  
jrendtel@aip.de

<sup>2</sup> International Meteor Organization, Eschenweg 16, 14476 Potsdam

The Visual Meteor DataBase (VMDB) contains numerous data covering the activity of all major and most minor showers. Each analysis of activity requires a careful data selection and several iteration steps to adjust interval lengths (bins) and required sample size. Here we show a basic approach using data of the 2017 Perseid return.

## 1 Introduction

One major aim of visual meteor observations is the calculation of flux or number density along the Earth's path through the meteoroid stream. For this purpose we obtain two measures: the number of meteors per shower and the magnitudes of the shower meteors. An essential step of the calculation of physical parameters is a correction to standard conditions which are an unlimited field of view, a reference limiting magnitude, and the position of the shower radiant in the zenith (vertical incidence). The effective field of view of a visual observer has a radius of roughly  $50^\circ$  (Koschack and Rendtel, 1990)—hence also the recommendation to choose a field center at least  $50^\circ$  above the horizon. The standard limiting magnitude (lm) is  $+6.5$ . The corrected rate, called Zenithal Hourly Rate (ZHR), is calculated using

$$\text{ZHR} = \frac{Nr^{6.5-\text{lm}}c_F}{T_{\text{eff}} \sin^\gamma h_R},$$

with  $N$  the number of shower meteors,  $r$  the population index,  $c_F$  the field correction (for sky obstruction),  $T_{\text{eff}}$  the effective observing time,  $h_R$  the radiant elevation, and  $\gamma$  the zenith exponent which is set to 1.0 for visual work. The latter conversion into flux or number density is described by Koschack and Rendtel (1990).

## 2 Population index

It is obvious that the correction  $r^{6.5-\text{lm}}$  for the observing condition is crucial. We know that the meteor magnitude distribution is different for various showers but may also vary during the activity of one shower. Peculiar changes may occur close to the maximum (center) or during dust trail encounters. Hence we need to know the value of  $r$  during the activity period. The parameter  $r$  describes the increase of meteor numbers towards fainter magnitudes (which needs to be corrected to the reference value). Procedures to analyse the magnitude data are available and also in preparation—so we just emphasize this fact here.

## 3 ZHR profile: successive approximation

Our aim is to find the general activity profile as well as significant short variations. As a first step, we want to get an overview of the temporal distribution of the data and a first impression which parts of the profile are most interesting. For this purpose, we run the ZHR calculation with a relatively relaxed parameter set. As an example, we choose the 2017 Perseid maximum which occurred under moonlit skies. From stream modelling, there was only one enhancement expected—a possible filament encounter on August 12 around 13<sup>h</sup> UT (Jenniskens, 2006; p. 662).

*Table 1* – Perseid 2017 peak analysis: selection parameters. The interval length was between 900 s (minimum) and 86400 s (maximum), and the population index was set as  $r = 2.2$  for all profiles shown.

Parameter	Figure 1	Figure 2	Figure 3
Min. lm	3.50	5.00	4.80
Max. correction	20	10	10
Min. meteors/bin	10	50	80

For the first calculation, we allow (almost) all intervals, including those obtained under poor conditions (see Table 1). Some observers give limiting magnitudes of just  $+3$ , which means an enormous correction and thus large error margins. Including all data, however, implies a larger sample and reduces the risk of missing any period of interest (Figure 1).

This first ZHR profile in Figure 1 shows that:

1. the values for the maximum period are not evenly distributed, namely there is a large gap between August 12, 4<sup>h</sup> UT and 20<sup>h</sup> UT; and
2. there occur several apparent peaks and dips for which we need to find out whether they are artifacts or not.

If we are too strict and use longer intervals—which might be useful if we just want to obtain a rough idea about the period under study—we would just smear out all features and would just learn that the maximum occurred in the night of August 12/13.

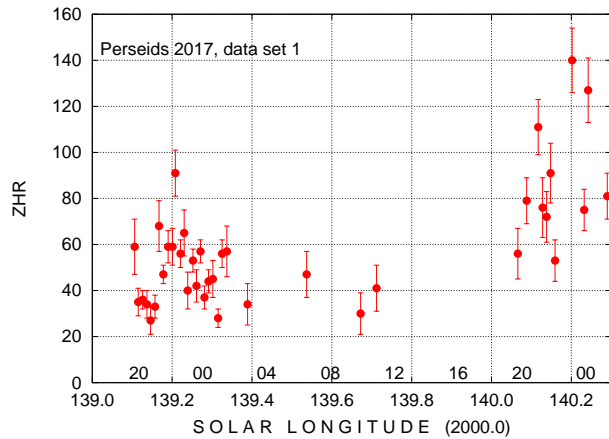


Figure 1 – ZHR profile of the Perseid maximum period in 2017 including the possible filament crossing time, obtained from visual data using the data set 1 given in Table 1. The plot is shown like the live graphs on the IMO webpage.

As a next step, however, we use less relaxed parameters, i.e., only observations obtained under good skies, resulting in smaller error margins but also a smaller sample (column 2 in Table 1). The result (Figure 2) is a smoother profile, but we lose both data points for the middle of August 12 obviously because of the  $1m$  limit (we cannot resolve any detail here anyway). We see that a first peak at August 11, around 23<sup>h</sup> UT, is better defined and the high ZHR > 80 on August 12 immediately after 2<sup>h</sup> UT disappears. It was based on few data obtained under poor conditions only. Furthermore, the single peak value on August 12 before 22<sup>h</sup> UT remains. The composition of the sample needs to be checked since it is a single value only. Instead, we find a better defined dip on August 12 after 22<sup>h</sup> UT as in the first profile.

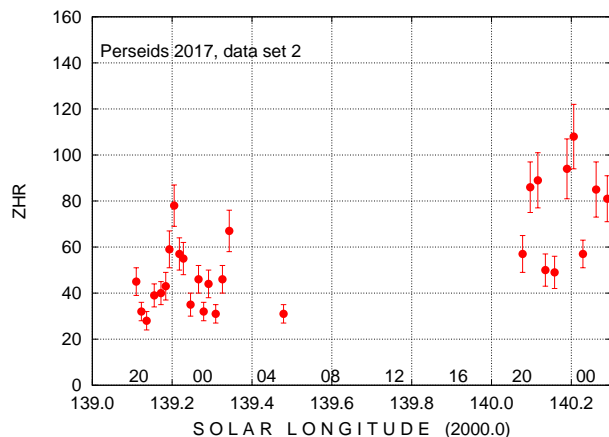


Figure 2 – ZHR profile of the 2017 Perseid maximum for the same period as shown in Figure 1. For this profile, we applied the selection parameter set 2 given in Table 1.

For the third approach we allow a slightly poorer limit for the limiting magnitude, but require a larger sample per bin (column 3 in Table 1). This obviously helps (Figure 3) and brings even back the mid-day data as just one point. The profile indicates that there was a higher ZHR around 18<sup>h</sup> UT on August 12. This is very likely the descent from the main peak which usually

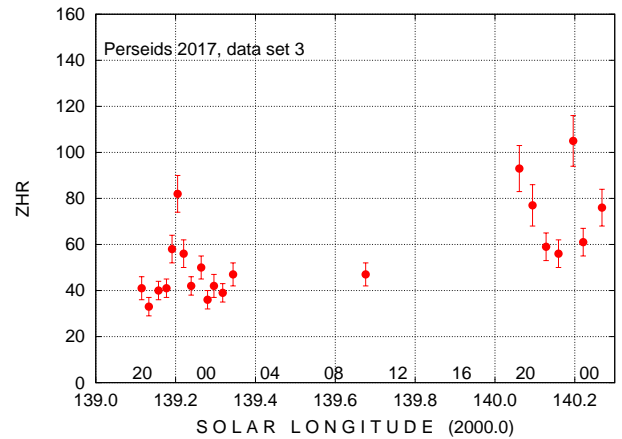


Figure 3 – ZHR profile of the 2017 Perseid maximum for the same period as shown in Figure 1, applying the selection parameter given in column 3 of Table 1.

occurs near  $\lambda_{\odot} = 140^{\circ}$ . Obviously, this portion of the profile is not covered at all. After that, the already mentioned dip occurs, followed by another one-data-point maximum—based on 9 count intervals. Before we start any interpretation, we have to inspect all tables to find outliers or reasons for distinct values.

## 4 Conclusions

Apart from the omitted question of determining a population index profile first, we showed the effects of the data and parameter selection to obtain a reliable ZHR profile. The procedure requires several approximations. The three examples above are just a first attempt and also demonstrate the uncertainties which may occur when using the live graphs shown at the IMO website. For a final analysis, the interval lengths need to be adapted throughout the investigated period, taking into account the uneven temporal distribution of the submitted reports. This simple demonstration also emphasizes the need of reports for all intervals, even if some may have been obtained under poor observing conditions. It is also obvious, however, that an insufficient sample does not allow us to extract information about the passage of the Earth through a given meteoroid stream.

## Acknowledgements

Thanks to all observers submitting their reports to the VMDB. We can produce live graphs as well as detailed analyses only with your help which is very much appreciated.

## References

- Jenniskens P. (2006). *Meteor streams and their parent comets*. Cambridge Univ. Press.
- Koschack R. and Rendtel, J. (1990). “Determination of spatial number density and mass index from visual meteor observations (I)”. *WGN, Journal of the IMO*, **18**, 44–58.

# FRIPON-NL—The first FRIPON camera in the Netherlands

Detlef Koschny<sup>1,3</sup>, Andrea Toni<sup>1</sup>, Regina Rudawska<sup>2</sup>,  
Joe Zender<sup>1</sup>, François Colas<sup>2</sup>, and Jérémie Vaubaillon<sup>2</sup>

<sup>1</sup> ESA-ESTEC, Keplerlaan 1, 22001 AZ Noordwijk, the Netherlands  
detlef.koschny@esa.int

<sup>2</sup> Observatoire de Paris, IMCCE, 77 Av. Denfert Rochereau, 75014 Paris, France

<sup>3</sup> Chair of Astronautics, TU Munich, Boltzmannstr. 17, 85748 Garching, Germany

Since 1 March 2017, we operate one of the FRIPON all-sky fireball cameras on the roof of the ESA/ESTEC building in Noordwijk, the Netherlands. We have had a total of four fireball detections since then. Three additional cameras are ready for installation within the Netherlands, and we expect an increase of the detections once we have the new stations operational.

## 1 Introduction

The Meteor Research Group (MRG) of the European Space Agency is operating a FRIPON camera (Colas et al., 2015b) on top of the building of ESA/ESTEC in the Netherlands since 1 March 2017. Our main research interest is the determination of meteoroid flux densities (e.g., Koschny et al., 2017), but also constraining the luminous efficiency from looking at deceleration data (e.g., Gritsevich and Koschny, 2011). We are working on setting up a network of cameras that would fill the gap between France/Belgium and Northern Germany. Here, we briefly describe the camera setup, our first detections, and then give an outlook into the future.



Figure 1 – FRIPON camera installed at the European Space Agency’s center ESTEC, in Noordwijk, the Netherlands.



Figure 2 – Computer and network switch located in the first author’s office, 10 m below the camera.

## 2 The FRIPON camera

Figure 1 shows a photograph of the camera on the roof of the ESA/ESTEC building. The system comes ready to be plugged in. It uses a video-rate CMOS camera with a fish-eye lens covering the complete sky. For technical details, see Colas et al. (2015a). Figure 2 shows the computer and network switch in the office of the first author. The system was installed in February 2017 and has been operational since 1 March 2017. One of the first images shows a flock of birds (Figure 3).



Figure 3 – Almost first light—one of the first images of the camera, showing a flock of birds flying over ESTEC.

Table 1 – Recorded fireball events (i.e., those which were also seen by at least one other station) since 1 March 2017.

Time of event (UT)	Other stations
2017-07-14 23 <sup>h</sup> 17 <sup>m</sup> 46 <sup>s</sup>	Arras, Cappelle-la-Grande, Lille, Maubeuge, Wimereux
2017-08-14 01 <sup>h</sup> 41 <sup>m</sup> 24 <sup>s</sup>	Brussels
2017-08-15 22 <sup>h</sup> 25 <sup>m</sup> 01 <sup>s</sup>	Brussels
2017-09-21 21 <sup>h</sup> 00 <sup>m</sup> 00 <sup>s</sup>	Brussels, Lille

we only rarely had recorded events until now. This is expected to change once additional cameras will be commissioned closer to the ESTEC camera.

Table 1 shows all recorded events to date. Just the night before presenting this paper at the International Meteor Conference, the largest event observed so far took place (Figure 4).

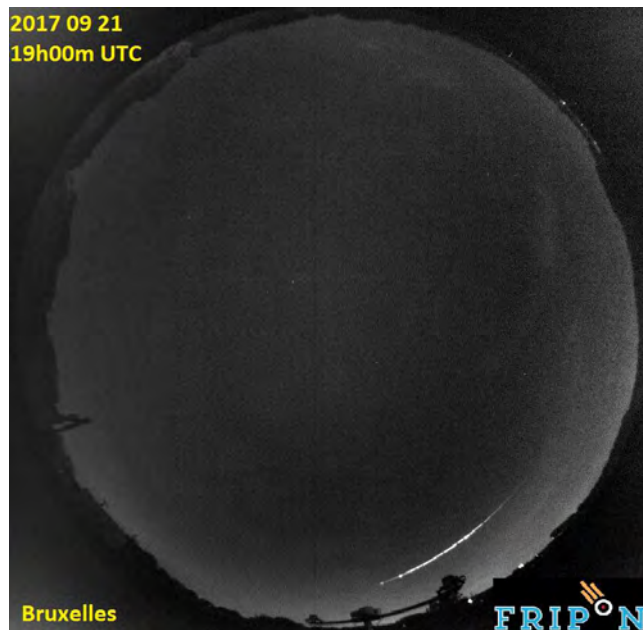
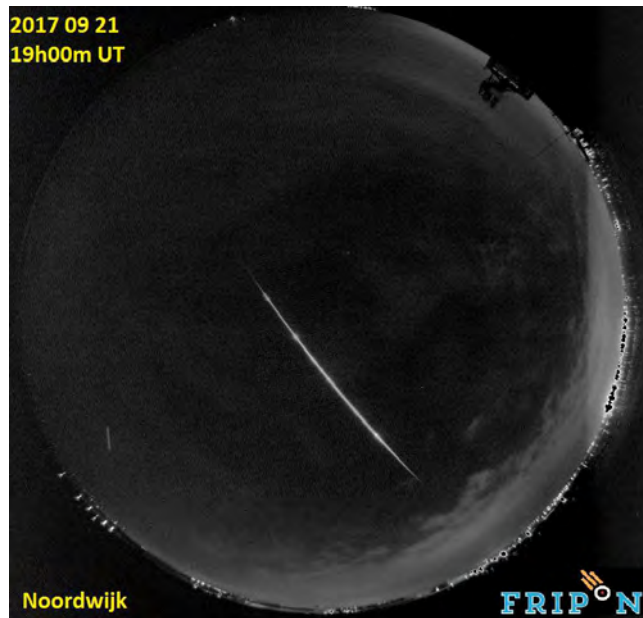


Figure 4 – Large fireball over the Netherlands on 21 September 2017. The top image shows the view from ESTEC is on top; the bottom image shows the fireball close to the horizon as seen from Brussels.

### 3 First detections

The way the system works is the following: A personal computer is continuously grabbing images. When a potential fireball is detected, it sends the data to a central server at the Paris Observatory. If other cameras have recorded a matching fireball, an event is generated. Since our camera is fairly far from other stations,

### 4 The next cameras

Completely covering the Netherlands would require 8–10 cameras if the distance between them should be less than 100 km. Figure 5 shows a view of the setup with the new cameras in their planned locations.

### 5 Summary

We have started to expand the FRIPON network into the Netherlands. We aim at “connecting” also with the network in Germany, where we collaborate closely with the group in Oldenburg. In addition to the camera at ESA/ESTEC, we have already identified three additional locations with identified hosts.

### Acknowledgments

The Faculty of ESA’s Scientific Support Office of ESA provided funding for purchasing several FRIPON cameras. One system was kindly provided by the Paris Observatory. The hard work of the French team over several years to develop the system, including the server environment at Paris Observatory, is highly appreciated. Günther Thörner from our office’s IT group helped us with sorting out all internet permission issues. Finally, Felix Bettonvil, Klaas Jobse, and Jos Nijland offered to host additional stations in the future.



Figure 5 – Location of future cameras in the Netherlands where a host has already been found.

## References

- Colas F., Zanda B., Bouley S., Vaubaillon J., Vernazza P., Gattacceca J., Marmo C., Audureau Y., Kyung Kwon M., Maquet L., Rault J.-L., Birlan M., Egal A., Rotaru M., Birnbaum C., Cochard F., Thizy O. (2015a). “The FRIPON and Vigie-Ciel networks”. In Rault J.-L. and Roggemans P., editors, *Proceedings of the International Meteor Conference*, Giron, France, 18–21 September 2014. IMO, pages 34–38.
- Colas F., Zanda B., Vaubaillon J., Bouley S., Marmo C., Audureau Y., Kyung Kwon M., Rault J.-L., Caminade S., Vernazza P., Gattacceca J., Birlan M., Maquet L., Egal A., Rotaru M., Birnbaum C., Cochard F., Thizy O. (2015). “French fireball network FRIPON”. In Rault J.-L. and Roggemans P., editors, *Proceedings of the International Meteor Conference*, Mistelbach, Austria, 27–30 August 2015. IMO, pages 37–40.
- Gritsevich M. and Koschny, D. (2011). “Constraining the luminous efficiency of meteors”. *Icarus*, **212**, 877–884.
- Koschny D., Drolshagen E., Drolshagen S., Kretschmer J., Ott T., Drolshagen G., Poppe B. (2017). “Flux densities of meteoroids derived from optical double-station observations”. *Planet. Space Sci.*, **143**, 230–237.

# The Radio Meteor Zoo: Involving citizen scientists in radio meteor research

Stijn Calders<sup>1</sup>, Hervé Lamy<sup>1</sup>, Antonio Martínez Picar<sup>2</sup>,  
Cédric Tétard<sup>1</sup>, Cis Verbeeck<sup>2</sup>, and Emmanuel Gamby<sup>1</sup>

<sup>1</sup>Royal Belgian Institute for Space Aeronomy, Brussels, Belgium  
stijn.calders@aeronomy.be

<sup>2</sup>Royal Observatory of Belgium

The BRAMS (Belgian Radio Meteor Stations) Network, consisting of one beacon and about 25 receiving stations, generates a huge amount of data with thousands of meteor echoes detected every day. With such large amount of data, it is difficult to process it all ourselves. Several attempts were made to develop an automatic detection algorithm, but up-to-now none of these algorithms can perfectly mimic the human eye which stays the best detector. Therefore, the BRAMS researchers, in collaboration with the Zooniverse team (<http://www.zooniverse.org/>), have launched a citizen science project called the Radio Meteor Zoo (RMZ, <http://www.radiometeorzoo.org/>) in August 2016. With the RMZ, thousands of citizen scientist eyes are manually identifying meteor echoes during meteor showers. Hitherto more than 5000 registered volunteers have identified meteors in almost 30 000 spectrograms. In 2016 the Perseids and the Geminids meteor showers were processed. In 2017 the volunteers helped us with processing the Quadrantids, Lyrids, and Perseids meteor showers. In this paper the results obtained during the first year of the Radio Meteor Zoo are discussed. We will also look into the future: how can we improve the RMZ and what will be done with these results?

## 1 Introduction

BRAMS (Belgian Radio Meteor Stations) is a radio network located in Belgium using forward scatter measurements to detect and characterize meteoroids. It consists of one dedicated transmitter located in Dourbes, in the south of Belgium, and approximately 25 receiving stations spread all over the Belgian territory. The transmitter emits a circularly polarized continuous wave (CW) at a frequency of 49.97 MHz and with a power of 150W. All receiving stations use the same equipment (including a 3-elements Yagi antenna) and are synchronized using GPS clocks. More details can be found in, e.g., Lamy et al. (2015).

Each BRAMS receiving station is recording continuously, producing each day 288 WAV files and detecting circa 1500-2000 meteors. This huge amount of data requires the use of automatic detection algorithms. Several attempts were made to identify meteor reflections either in raw data or in spectrograms by using automatic detection algorithms, with varying degrees of success (Calders and Lamy, 2014). The automatic detection of overdense radio meteor echoes in particular remains a difficult task due to the various and complex shapes they produce in spectrograms (see Figure 1). This problem is particularly striking during meteor showers where these types of meteor echoes are observed abundantly.

On 12 August 2016, the BRAMS researchers launched the Radio Meteor Zoo (<http://www.radiometeorzoo.org/>), a citizen science project hosted on the Zooniverse platform (<http://www.zooniverse.org/>; see also Lintott, 2008). So, instead of detecting meteor reflections

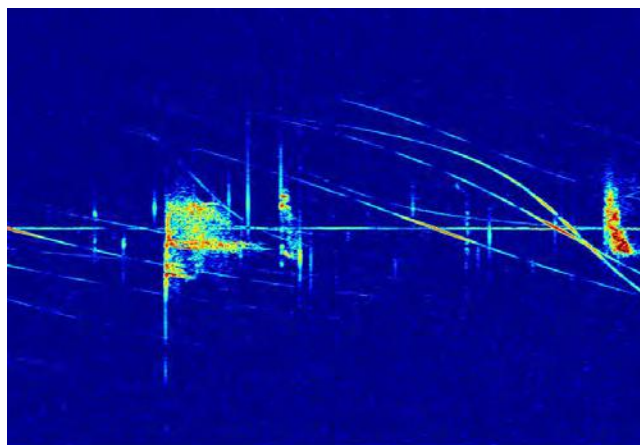


Figure 1 – An example of a spectrogram with complex meteor reflection shapes, closely interwoven with airplane reflections (oblique lines). Here, the human eye remains the best detector to identify the meteor reflections.

automatically by means of software, we rely on the best detector which is the (trained) human eye for classifying radio meteors during certain campaigns. Volunteers are asked to draw rectangles around what they consider to be a meteor. The first campaign was focused on generating a plot of the Perseids 2016 activity.

## 2 Method description

The objectives of the Radio Meteor Zoo are twofold:

1. to calibrate and to validate existing and future automatic detection algorithms; and
2. to detect the complex shapes of overdense radio meteor reflections. These reflections are more abundant during meteor showers.

New volunteers are asked to first read a tutorial. This tutorial explains what a spectrogram looks like and provides examples of typical signatures of meteor reflections and common distortions (like reflections on airplanes or broad-band interferences). Finally, the tutorial explains what is expected from the volunteer: drawing rectangles around potential meteor echoes and how to do it correctly.

Each spectrogram is shown to ten different volunteers to improve the quality of the classifications. A region in the spectrogram is considered to be a real meteor if at least four volunteers selected it. So, when one volunteer makes a mistake (either forgetting a meteor echo or classifying incorrectly another signal as a meteor), the risk of a false detection is minimal. An extensive discussion of the classification algorithm applied in the Radio Meteor Zoo can be found in Calders et al. (2016).

Finally a forum has been installed to allow interaction among the volunteers and between the volunteers and the researchers. Four topics are available: notes (for questions and comments about individual spectrograms); science (a place to talk about the science behind the Radio Meteor Zoo and related research); chat (“everything you want to know about meteors but were afraid to ask”); and help (questions about the classification interface, bug reporting, and general help).

### 3 Results

A press release was sent to Belgian newspapers and radio stations to announce the launch of the Radio Meteor Zoo on 12 August 2016.<sup>1</sup> The Zooniverse team has also sent an e-mail to all volunteers that contributed in the past to one of the other projects hosted on their citizen science platform. In total more than 2000 volunteers registered during the first days after the launch. The very first day, more than 12 500 spectrograms were processed. Motivated by this huge success, the authors made available spectrograms observed during the Perseids shower from eight different receiving stations.

Later on in 2016, also the Geminids (5 stations) meteor showers were processed. In 2017, a successful campaign has been launched to obtain an activity plot of the Quadrantids (2 stations), Lyrids (1 station), and Perseids (3 stations) meteor showers. For the Perseids 2017, all registered volunteers were contacted by e-mail to ask their support for this campaign. More than 10 000 spectrograms were processed in only two days, which gave the authors the opportunity to produce a preliminary activity plot quickly after the Perseids peak (see Figure 2).

In October 2017, more than 5000 registered volunteers had produced aggregated classifications of meteors in almost 29 500 spectrograms (i.e., each of these spectro-

<sup>1</sup>E.g., <https://www.imo.net/the-brams-team-needs-your-help-to-detect-perseid-echoes-in-the-radio-meteor-zoo-project/>.

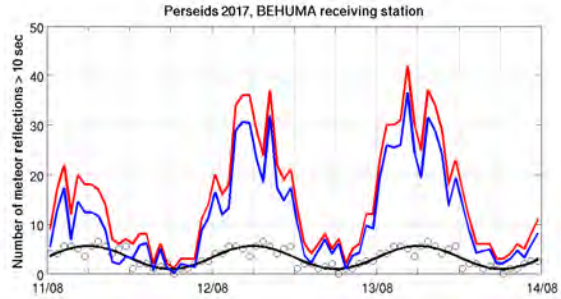


Figure 2 – The Perseids 2017 activity curve (reflections lasting at least 10 seconds) for the Humain receiving station, based on the results obtained from the Radio Meteor Zoo. The red curve is the total activity, the blue curve only the Perseids. (All times are in UT.)

grams is processed by ten different volunteers). This result is above and beyond all expectations.

### 4 Future plans

As a first step, the aggregated classification of meteors in a spectrogram is calculated as described in Calders et al. (2016). However, when comparing each individual classification with the aggregated result, the authors notice sometimes major deviations. Therefore, we are testing if the data quality can be improved by automatically removing classifications that are obviously wrong (see, e.g., Figure 3). The following formula will be used:

$$\alpha = \frac{|S_{\text{agg}} \cap S_i|}{|S_{\text{agg}} \cup S_i|}$$

with  $S_{\text{agg}}$  the surface of the aggregated rectangles and  $S_i$  the surface of the rectangles drawn by one volunteer. If  $\alpha$  is small, the rectangles drawn by this volunteer are excluded from the dataset.

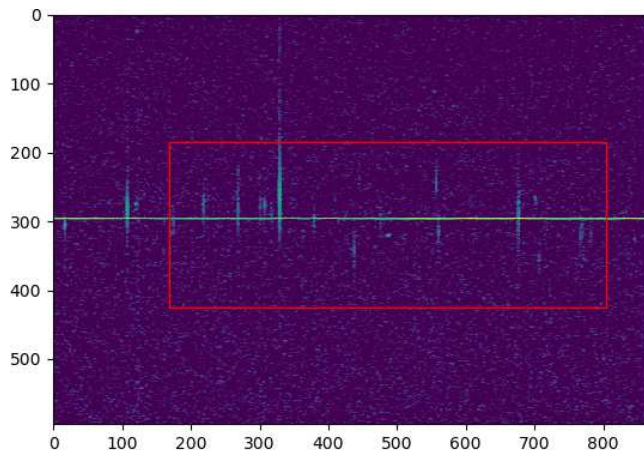


Figure 3 – Here, a volunteer has drawn a rectangle around all meteors together instead of each meteor individually. This result should be excluded from the aggregated classification set.

A new aggregated classification is then calculated on a smaller but more accurate set of classifications. It should however be noticed that we still adhere to the egalitarian principle: all volunteers are considered as equal; only classifications that are too far off the aggregated classification are removed from the dataset. It

does not make any difference if the classification has been made by a registered or an unregistered volunteer.

The next step is to correct the activity curve for parameters such as the radiant height and the sensitivity of the receiver. The Observability Function (OF, Verbeeck, 1997) represents the sensitivity of a particular forward scatter setup to detect underdense meteors of a given shower at a given time  $t$ . If the OF at time  $t_1$  is twice as big as the OF at time  $t_2$ , and the meteor activity is constant, then the set-up will observe twice as many shower meteors at  $t_1$  than at  $t_2$ . The OF is a number that varies with each configuration of the transmitter and receiver (each receiving station in the case of BRAMS) and with the position of the radiant of the meteor shower (hence with time).

The aggregated results of the Radio Meteor Zoo will be also used as the ground truth for the calibration and validation of the automatic detection algorithms (cf. the first objective mentioned before).

## 5 Conclusions

Thanks to the Radio Meteor Zoo, the BRAMS project can analyze for the first time several meteor showers per year.

However, this citizen science project depends on the motivation of volunteers to classify the spectrogram. Therefore, a continuous effort is needed to make publicity for this project to the general public, to give feedback to the volunteers, and to explain what has been done with their work. People who would like to contribute to this effort are invited to contact the article's first author ([stijn.calders@aeronomy.be](mailto:stijn.calders@aeronomy.be)).

## Acknowledgements

The BRAMS Network is a project from the Royal Belgian Institute for Space Aeronomy<sup>2</sup>, funded by STCE, the Solar-Terrestrial Center of Excellence<sup>3</sup>.

The authors thank all volunteers who helped us with the classification of the spectrograms. These volunteers

make the success of the Radio Meteor Zoo. They also thank the Zooniverse team, who is hosting the Radio Meteor Zoo and who is always very enthusiastic in supporting us. Last but not least, there would be no observations without volunteers hosting the BRAMS receiving stations. The authors are grateful for their constant support.

## References

- Calders S. and Lamy H. (2014). "Automatic detection of meteors in the BRAMS data". In Rault J.-L. and Roggemans P., editors, *Proceedings of the International Meteor Conference*, Giron, France, 18–21 September 2014. IMO, pages 194–196.
- Calders S., Verbeeck C., Lamy H., and Martinez Picar A. (2016). "The Radio Meteor Zoo: a citizen science project". In Roggemans A. and Roggemans P., editors, *Proceedings of the International Meteor Conference*, Egmond, the Netherlands, 2–5 June 2016. IMO, pages 46–49.
- Lamy H., Anciaux M., Ranvier S., Caldere S., Gamby E., Martinez Picar A., and Verbeeck C. (2015). "Recent advances in the BRAMS Network". In Rault J.-L. and Roggemans P., editors, *Proceedings of the International Meteor Conference*, Mistelbach, Austria, 27–30 August 2015. IMO, pages 171–175.
- Lintott C. J., Schawinski K., Slosar A., Land K., Bamford S., Thomas D., Raddick M. J., Nichol R. C., Szalay A., Andreescu D., Murray P. and Vandenberg J. (2008). "Galaxy Zoo: Morphologies derived from visual inspection of galaxies from the Sloan Digital Sky Survey". *Mon. Not. Roy. Astron. Soc.*, **389**, 1179–1189.
- Verbeeck C. (1997). "Calculating the sensitivity of a forward scatter setup for underdense shower meteors". In Knöfel A. and Roggemans P., editors, *Proceedings of the International Meteor Conference*, Apeldoorn, the Netherlands, 19–22 September 1996. IMO, pages 122–132.

<sup>2</sup><http://www.aeronomie.be/>.

<sup>3</sup><http://www.stce.be/>.

# AMOS from Slovakia, Canary Islands, and Chile

Juraj Tóth, Leonard Kornoš, František Ďuriš, Pavol Zigo,  
Dušan Kalmančok, Jozef Világi, Jaroslav Šimon, Štefan Gajdoš,  
Pavol Matlovič, Alžbeta Kubirtová, and Martin Baláž

Dept. of Astronomy, Physics of the Earth and Meteorology, Faculty of Mathematics, Physics and Informatics, Comenius University in Bratislava, Slovakia  
toth@fmph.uniba.sk

AMOS (All-Sky Meteor Orbit System) is an autonomous meteor intensified video system observing from Slovakia, the Canary Islands, and Chile. A short overview of the development, installations, observations, and results of trajectory and orbital data are presented.

## 1 Introduction

The details about the setup of the AMOS (All-Sky Meteor Orbit System) cameras and software development can be found in previous papers (Tóth et al., 2011; Zigo et al., 2013; Tóth et al., 2015) or current papers (Kornoš et al., 2018). All together, 8 AMOS cameras are working from both hemispheres in autonomous mode with light, temperature, humidity, and rain sensors. Also, a test in an artificial wind tunnel confirmed safe and stable operation of the AMOS camera up to wind speeds of 115 km/h in open, observing mode and up to wind speeds of 190 km/h in close, non-observing mode. Moreover, one station in Slovakia, two stations on the Canary Islands, and one station in Chile are also equipped by a video meteor spectral camera (Matlovič et al., 2018).

## 2 Detection efficiency of AMOS

We have conducted simultaneous visual and video observation during the Perseids 2016 peak activity on August 11–13 in a dark-sky location, Tepličné, in the center of Slovakia. Visual observations were conducted by 6–7 skilled observers. They recorded time of appearance, stream identification, and visual magnitude estimation using convenient electronic recorders feeding

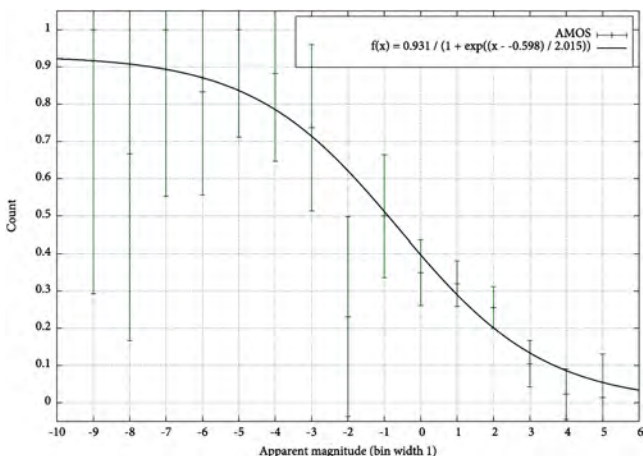


Figure 1 – Detection efficiency curve of AMOS (UFOCAPTURE).

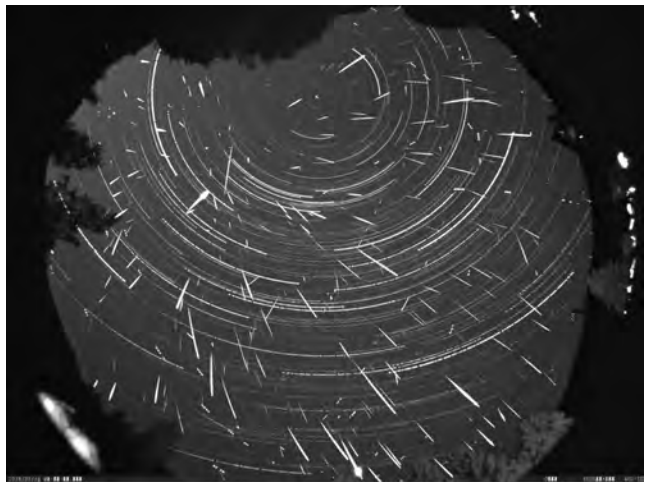


Figure 2 – Composition picture of individual meteor detections during the Perseids 2016, August 12–13, in Tepličné.

the individual observations directly into computer. Simultaneously, two AMOS cameras were running UFOCAPTURE detection software just 15 m away from the group of visual observers, and hence sharing the same conditions and all-sky view. We compared the numbers of simultaneously observed meteors in magnitude bins. The result is shown in Figure 2.

Because of insufficient numbers of meteors brighter than magnitude  $-2$ , we extended the data coverage with all-sky photographic observations from the AGO Modra Observatory from 2011–2013, where simultaneous observations by photographic and AMOS observations were carried out. We plan to evaluate the final detection efficiency of the AMOS cameras by UFOCAPTURE software and to compare the results with the newly developed detection software AMOS in the near future.

## 3 Interesting observations from the Canary Islands and Chile

During regular meteor observation, the AMOS cameras from the Canary Islands registered a fireball on July 12, 2017 at 22<sup>h</sup>05<sup>m</sup>58<sup>s</sup>.8 UT, low over the northeastern horizon from the Tenerife Station, which is in the direction of the meteorite-dropping fireball recently an-

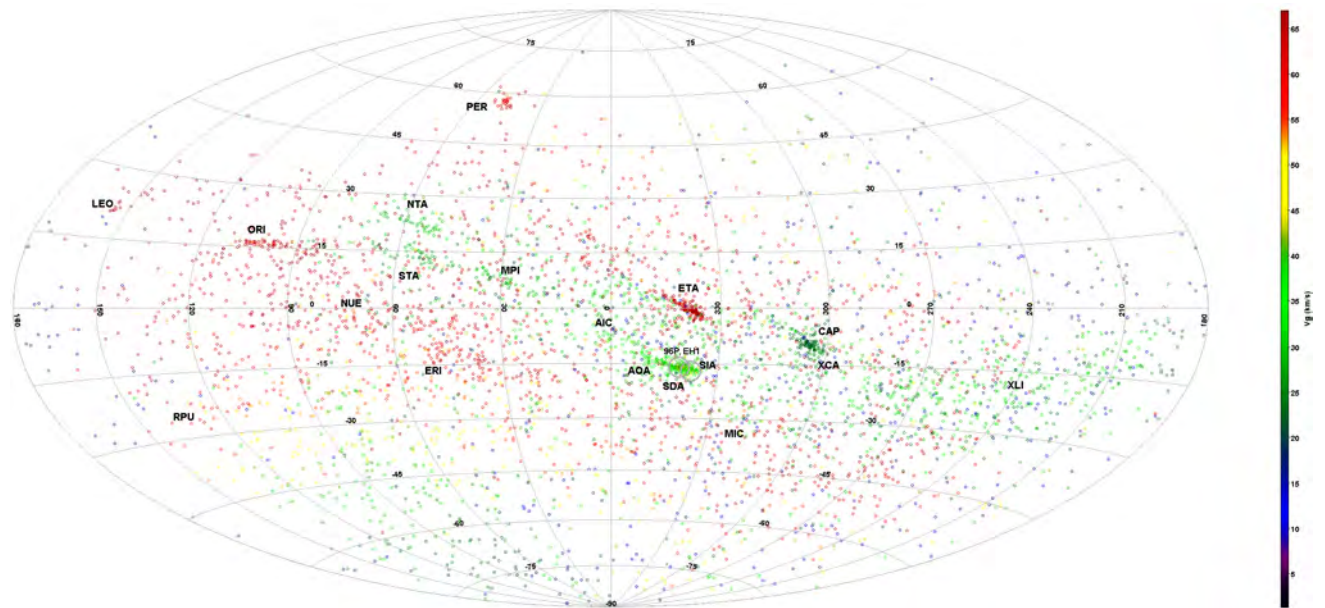


Figure 3 – Radiant distribution in the southern hemisphere from AMOS-Chile.

nounced by Abderrahmane Ibhi under the name Igdi II (Ibhi et al., 2018).

The pair of AMOS cameras in the Atacama Desert in Chile simultaneously observed 4463 meteors during the first 9 months of operations (March–November 2016), resulting in the radiant distribution shown in Figure 3. At least ten 10 meteor showers (CAP, STA, SDA, PER, ORI, LEO, NTA, ETA, ERI, and NUE) from the IAU established list and 7 meteor showers (SIA, XLI, MIC, AIC, XCA, MPI, and AOA) from the working list were clearly identified. Detailed analyses will be published in future papers.

## 4 Conclusions

We have successfully developed, tested, and installed AMOS cameras in Slovakia, on the Canary Islands, and in the Atacama Desert in Chile. Cameras require occasional cleaning, regular maintenance, data archiving, and processing.

Newly developed software for higher-precision analyses will be launched soon along with published data.

## Acknowledgements

We would like to thank the meteor observers of the 2016 Tepličné expedition for their visual observations (J. Gerboš, J. Kučerka, M. Izák, M. Škrekla, J. Plavúchová, E. Gabrišová, and S. Kaniansky).

We are also grateful to the IAC Canary Islands and their staff, the SpaceObs team led by A. Maury, and the Paniri Caur Observatory in Chile led by S. Lisoni.

This work was supported by the Slovak Research and Development Agency under contract nos. APVV-16-0148 and APVV-0517-12, and by the Slovak Grant Agency for Science under grant no. VEGA 1/0225/14.

## References

- Ibhi A., Khiri F., and Ouknine L. (2018) “A new meteor fell in the region of Igdi (Tata, Morocco), ‘sowing panic among the inhabitants’”. In Gyssens M. and Rault J.-L., editors, *Proceedings of the International Meteor Conference*, Petnica, Serbia, 21–24 September 2017. IMO, pages 189–191.
- Kornoš L., Ďuriš F., and Tóth J. (2018). “AMOS orbit software, EDMOND database”. In Gyssens M. and Rault J.-L., editors, *Proceedings of the International Meteor Conference*, Petnica, Serbia, 21–24 September 2017. IMO, pages 46–49.
- Matlovič P., Tóth J., Rudawska R., and Kornoš L. (2018). “Study of distinct meteor spectra populations”. In Gyssens M. and Rault J.-L., editors, *Proceedings of the International Meteor Conference*, Petnica, Serbia, 21–24 September 2017. IMO, pages 99–102.
- Tóth J., Kornoš L., Vereš P., Šilha J., Kalmančok D., Zigo P., and Világi J. (2011). “All-sky video orbits of Lyrids 2009”. *Publ. Astron. Soc. Japan*, **63**, 331–334.
- Tóth J., Zigo P., Kalmančok D., Simon J., Kornoš L., Világi J. Rudawska R., Serra-Ricart M., Perez J. C., and Licandro J. (2015). “Five months of AMOS on the Canary Islands”. In Rault J.-L. and Roggemans P., editors, *Proceedings of the International Meteor Conference*, Mistelbach, Austria, 27–30 August 2015. IMO, pages 63–65.
- Zigo P., Tóth J., and Kalmančok D. (2013). “All-Sky Meteor Orbit System (AMOS)”. In Gyssens M. and Roggemans P., editors, *Proceedings of the International Meteor Conference*, La Palma, Canary Islands, Spain, 20–23 September 2012. IMO, pages 18–20.

# Canadian Automated Meteor Observatory: Cometary meteoroid strengths derived from a highly fragmenting event observed on July 21, 2017

Denis Vida<sup>1,2</sup>, Peter Brown<sup>2</sup>, Margaret Campbell-Brown<sup>2</sup>, and Sean Huggins<sup>2</sup>

<sup>1</sup> Dept. of Earth Sciences, Univ. of Western Ontario, London, Ontario, N6A 5B7, Canada  
dvida@uwo.ca

<sup>2</sup> Dept. of Physics and Astronomy, Univ. of Western Ontario, London, Ontario, N6A 3K7, Canada  
pbrown@uwo.ca, margaret.campbell@uwo.ca, shuggins@uwo.ca

On July 21, 2017, at 7<sup>h</sup>04<sup>m</sup>20<sup>s</sup> UTC, a shallow-entry meteor lasting more than 3.9 seconds was observed with the Canadian Automated Meteor Observatory (CAMO). The narrow-field camera (4 m per pixel at 100 km resolution) recorded a dozen discrete fragmentation events. Here, we present an initial analysis of the high-precision flight dynamics of the fragments and the implications for the strength of cometary meteoroids.

## 1 Introduction

The Canadian Automated Meteor Observatory (CAMO) is a multi-instrument optical observatory which consists of two subsystems: the influx and the mirror system (Weryk et al., 2013). For this study, we use data from the mirror system, which is designed for high temporal and spatial two-station measurements of millimeter-sized meteors.

The mirror system performs real-time tracking of meteors through an 80 mm telescope. The system rapidly detects a meteor using a wide-field camera (640 × 480 resolution, 12 bits, 80 frames per second, 25 mm  $f/0.85$  lens) with a field of view of 28° and uses this information to dynamically steer two mirrors. These redirect the light of the meteor through the telescope, where the image is recorded in a narrow-field camera (640 × 480 resolution, 12 bits, 110 frames per second) which has a field of view of 1°5, giving it a precision of 4 m per pixel at 100 km. Both cameras are equipped with 18 mm GaAs Gen-III image intensifiers, which give the wide-field camera a limiting magnitude of +7.5 for stars, and +5.5 for meteors.

Figure 1 shows the physical layout of the CAMO system at the Elginfield site. There are two identical CAMO systems, one at Elginfield, and the other one at the Tavistock site, with a baseline of about 45 km. The stations were built in 2007 and the system has been fully automated since 2009 (Weryk et al., 2013). Data from CAMO has been used for high-resolution modeling of meteor ablation (Campbell-Brown et al., 2013), measuring trail widths of faint meteors (Stokan et al., 2013) and transverse motion meteor fragments (Stokan and Campbell-Brown, 2014), discovering a population of low-velocity asteroidal meteoroids outside sporadic sources (Campbell-Brown, 2015), and estimating the luminous efficiencies of faint meteors (Subasinghe, Campbell-Brown, and Stokan, 2017); among other research topics.

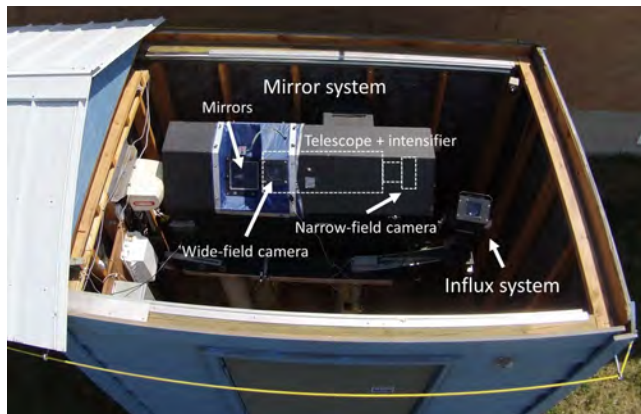


Figure 1 – CAMO system layout. Both the influx and the mirror system are located in a shed with a roll-off roof. The roof is opened only in ideal observing conditions. The mirror system is shown with its protective cover on, but the outlines of narrow-field optics are drawn on with dashed lines.

## 2 The event of July 21, 2017

We describe an unusual event observed on wide-field cameras of the mirror system from both sites. The beginning of the event was recorded from Tavistock (Figure 2) and the last part from Elginfield (Figure 3), although the meteor probably did continue to ablate after exiting the wide field of view. The meteor was tracked through the narrow-field camera only from Tavistock—the tracking algorithm at Elginfield did not estimate the tracking parameters well and the meteor disappeared from the field of view after a couple of frames, making data from that narrow-field camera unusable.

The narrow-field tracking at Tavistock began 0.45 s after the appearance in the wide field video, having started below the detection threshold of the real-time meteor detection algorithm during that time. (For the complete narrow-field video, see [http://meteor.uwo.ca/~dvida/IMC2017/20170721\\_tavis\\_narrow.gif](http://meteor.uwo.ca/~dvida/IMC2017/20170721_tavis_narrow.gif).) Figure 4 shows 18 individual video frames from the narrow-field video, with the individual fragments numbered by



Figure 2 – Co-added video frames from the Tavistock wide-field camera. The beginning of the meteor is visible.

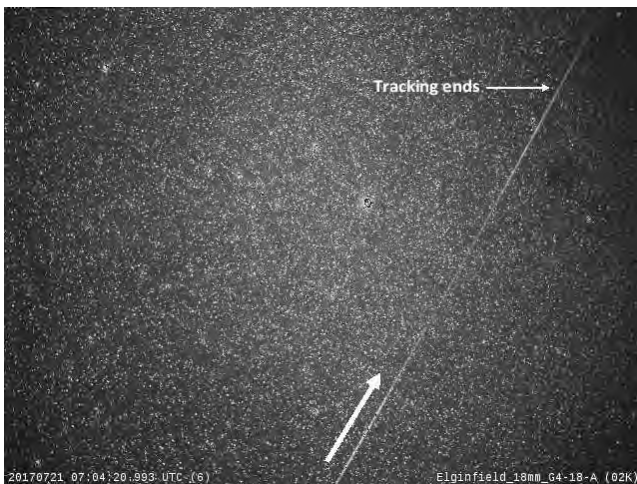


Figure 3 – Co-added video frames from Elginfield. Notice that the meteor spans the entire field of view, disappearing at the end.

their order of appearance. When the narrow-field tracking started, an extended wake could be seen in the wide field video. The narrow-field video shows that the wake is caused by dust being blown away from discrete fragments. After 1.4 s, this wake was completely gone, leaving several individual fragments with stellar point-spread functions and no wake recorded for another 1 s. Shortly after the wake disappeared, the fragments themselves disintegrated further, creating a total of 12 discrete fragments. During the following 1 s, the fragments noticeably decelerated, and some showed transverse motion. All showed different rates of deceleration which caused an increase in the along-track distance between them over the period of their flight. Several fragments with lower deceleration, which were always brighter and presumably more massive, overtook fainter fragments. Furthermore, the wide-field video at this period shows a significant decrease in the brightness of the meteor as a whole. Near the end, the fragments started to disintegrate themselves, first showing short trails behind them and finally turning into elongated collections of dust, which caused the increase in the intensity of the meteor’s light curve recorded by the wide-field camera.

### 3 Data calibration and reduction

Even though the system has been operational for almost 10 years, it was only recently that the methods of calibration of narrow-field data have been fully developed, allowing estimates of high-precision meteor trajectories from narrow-field imagery limited only by instrumentation (and not software) possible. Complete calibration procedures for obtaining high-precision trajectories using narrow-field imagery will be described in detail in a future paper. Here, we describe this process only briefly. The mirror system is equipped with 16-bit encoders, thus every mirror position (of the  $X$  and  $Y$  mirror axes) has a unique value between 0 and 65 535. To obtain celestial coordinates from narrow-field imagery, one has to first convert the image coordinates to mirror encoder coordinates, then the mirror encoder coordinates are transformed into celestial coordinates. The calibration is performed by roughly pointing the mirrors to known positions of stars—the star is then centered in the middle of the narrow field of view and a unique pair of mirror encoder versus celestial coordinates is obtained for every star. An astrometric plate is then fitted enabling direct transformation of image coordinates to celestial coordinates. Essential information here is the time and position of the mirrors at every video frame, as the image plane is not fixed—this info is written to a file during real-time meteor tracking.

Although it is possible to get high-precision trajectories using two-station narrow-field observation, there was in this case only one narrow-field video which was then “paired” with the wide-field data from the Elginfield site. To explore the dynamics of individual fragments, their narrow-field observations were projected to the trajectory estimated from the wide field solution.

The astrometric and photometric data reduction was done manually, following existing procedures used for CAMO (Weryk et al., 2013). The position of the meteor on wide field video frames was manually centroided by appropriately adjusting the size of the annulus, and the photometry was done by “coloring in” the pixels which belong to the meteor. The manual procedure was needed due to the noise in image intensified data and the complex morphology of the meteor, as it exhibited a wake which may confuse an automatic meteor detection algorithm. During the manual reduction, we aimed to select the head of the meteor, as it is the only consistent feature over the whole duration of the meteor. Furthermore, the narrow-field reduction was done manually as well—every individual fragment was tracked separately when it could be distinguished from the background and from other fragments.

## 4 Results

### Wide-field trajectory solution and photometry

The meteor had a very shallow entry angle of only  $8^\circ 054$  and a low initial velocity of  $(16.425 \pm 0.074)$  km/s, which translated into a long duration and a small range

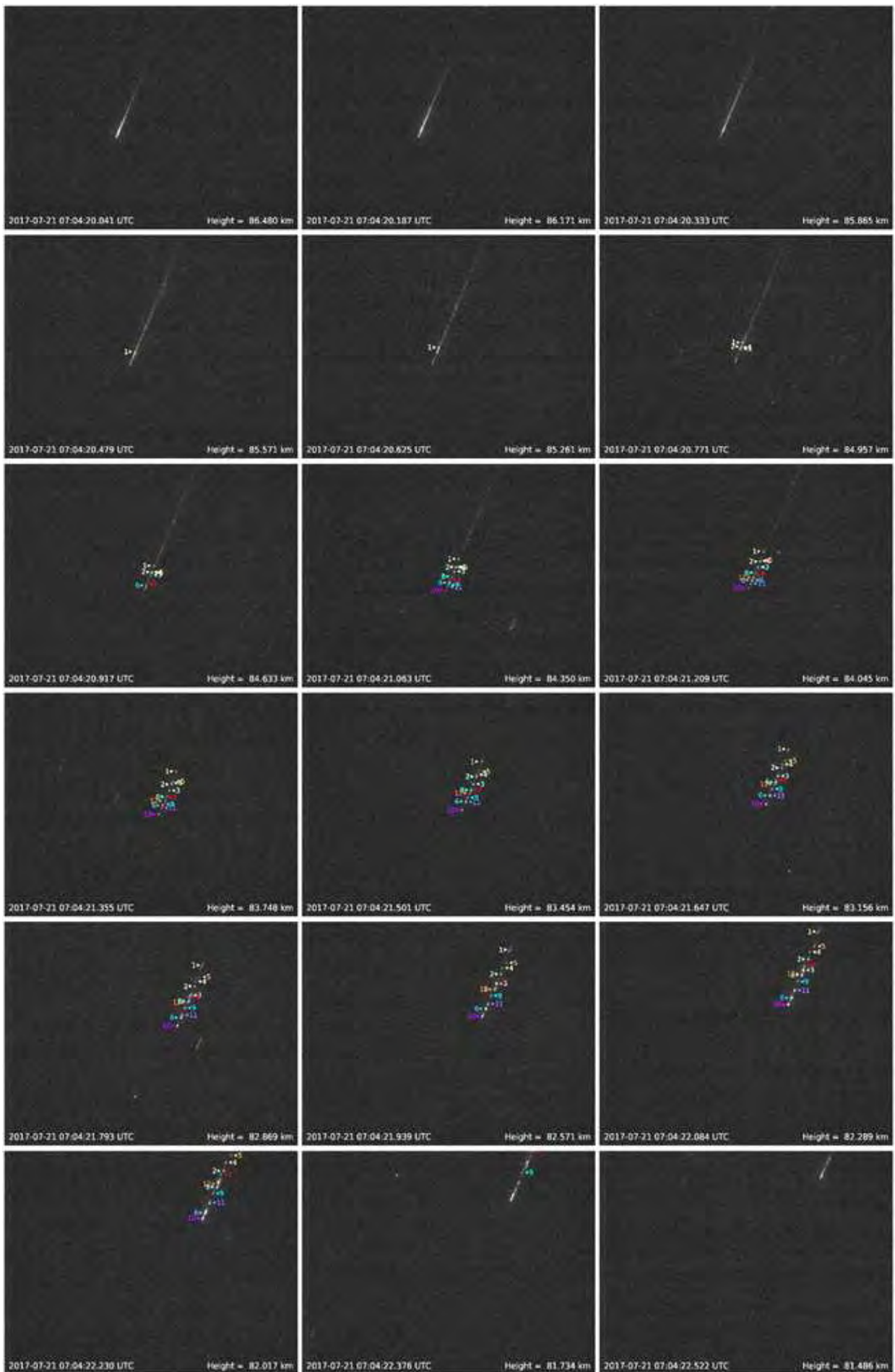


Figure 4 – Eighttteen chosen video frames of the narrow-field video. Fragments are numbered by order of appearance.

of covered heights—the meteor began at 87.641 km and the last observed point was at 80.017 km above sea level. The terminal velocity was about 11 km/s. The meteor covered about 60 km of distance above ground. The trajectory was estimated using a modified lines of sight method of Borovička (1990); details will be given in a future paper. The spatial residuals between the lines of sight and the estimated trajectory from wide-field data averaged to about 20 meters. Nevertheless, due to the very large number of data points (476), the precision of the trajectory is high, based on the consistency of the lag. The meteor showed substantial deceleration—Figure 5 shows the lag of the meteor, i.e., the difference in the along-track distance between a hypothetical meteor moving constantly with the meteor’s initial velocity and the observed meteor itself, following the procedure first described by Borovička, Spurný, and Koten (2007). The lag was obtained in two steps: first, by fitting a line to time versus length along the track of the first part of the meteor’s trajectory, where it was assumed there was no significant deceleration, and, second, by subtracting the values obtained from the line from the length along the track, thus leaving only the deceleration component. It can be noticed that the cumulative length difference at the end of the record is about 4 km, which gives an average deceleration of about  $500 \text{ m/s}^2$  for the complete trajectory.

The photometric light curve is given in Figure 6. A photometric mass of 0.269 g was calculated using as bolometric power of a zero-agnitude meteor  $P_{m=0} = 840 \text{ W}$  (Weryk and Brown, 2013) and a luminous efficiency  $\tau = 0.7\%$  (Campbell-Brown et al., 2013) in the R pass-band. Assuming a bulk density of  $1000 \text{ kg/m}^3$  and spherical geometry, the meteoroid had a diameter of approximately 8 mm. As the complete light curve was not recorded, we consider this mass to be a lower limit. Due the uncertainly of the luminous efficiently, we consider this value to be accurate to no better than a factor of 2. The meteor exhibits an interesting light curve—after an initial period of brightening, which coincides

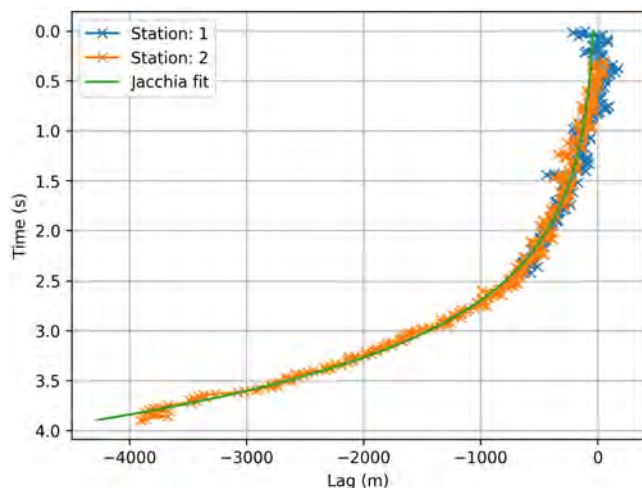


Figure 5 – Meteor lags showing significant deceleration. Observations from both stations are plotted: Station 1 is Tavistock and Station 2 is Elginfield. “Jacchia fit” stands for an exponential function fit to the lag; see Equation (1).

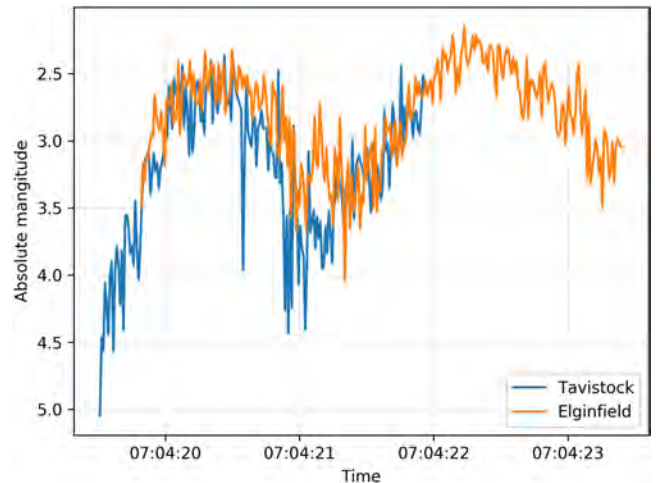


Figure 6 – Photometric light curve. The absolute magnitudes (i.e., visual magnitude at 100 km) from both sites are matching well, except during the part when the meteor dimmed, where it was close to the noise floor.

with the appearance of the large-scale wake, the meteor dims suddenly when the dust is completely gone and only the fragments are left. When the fragments start to disintegrate themselves, the meteor brightens again. Multiple maxima meteor light curves were also described by Roberts et al. (2014), who discuss the possible mechanism producing such light curves. The behavior we have observed does not match any of the proposed meteoroid fragmentation models.

#### Radiant and orbit

The geocentric radiant of the event is  $\alpha = 254^\circ 068 \pm 0^\circ 162$ ,  $\delta = -30^\circ 330 \pm 0^\circ 264$ , and  $V_{\text{geo}} = (12.095 \pm 0.101) \text{ km/s}$ . There were no active meteor showers at the given coordinates, thus the meteoroid was a sporadic originating in the antihelion source.

The orbital parameters are given in Table 1. According to the Tisserand’s parameter of the meteoroid, it may be of the Jupiter-family comet (JFC) origin. A parent body search returned a best match to the orbit of asteroid 2016 LX48: the Southworth and Hawkins  $D$ -criterion (Southworth and Hawkins, 1963) between the two orbits is 0.083. As the meteoroid was on a Jupiter-crossing orbit, we believe this might be a spurious connection, as JFCs with such orbits have short dynamical lifetimes. Thus, the ejection probably happened very recently as Jupiter-crossing orbits are very unstable.

Table 1 – Orbital parameters of the event.

Parameter	Value	Uncertainty
$a$	3.282 AU	0.065 AU
$q$	0.949 AU	0.001 AU
$e$	0.711	0.006
$i$	$2^\circ 462$	$0^\circ 072$
$\omega$	$31^\circ 980$	$0^\circ 116$
$\Omega$	$298^\circ 845$	$0^\circ 003$
$Q$	5.616 AU	0.130 AU
$T_j$	2.701	0.032

Although the formal precision of the initial velocity solution is high—the uncertainty being only  $\pm 74$  m/s—we were not confident in the true accuracy of the result as the event entered the atmosphere with such a low entry angle. That is, we believe the meteoroid decelerated significantly before it became instrumentally visible.

To explore this possibility, we simulated the meteor using the model of Campbell-Brown and Koschny (2004) to compare the velocities at the top of the atmosphere (180 km) and at the height of detection. We have found that assuming a mass  $m = 0.17$  g, bulk density  $\rho = 700$  kg/m<sup>3</sup>, heat of ablation  $Q = 4.6 \times 10^6$  J/kg, a luminous efficiency of 1.4%, and a beginning entry angle of  $15^\circ$  reproduces the observed conditions at the point of meteor’s detection, though we emphasize this is a non-unique solution.

Note that the entry angle here is the angle at the beginning of the meteoroid trajectory at 180 km relative to the surface of the Earth at that point, which differs significantly from the entry angle at the first point of detection, due to the curvature of the Earth—the meteoroid was about 800 km away from the point of detection when it was at the height of 180 km. To obtain the same velocity at the height of detection (87.641 km) as the observed one, we had to assume a velocity at 180 km that is about 400 m/s higher than the observed initial velocity. This emphasizes that the real orbit of the meteoroid was likely much different than our calculated value. After adding 400 m/s to the initial velocity, the recalculated orbital parameters are:  $a = 3.691$  AU,  $e = 0.744$ ,  $i = 2^\circ 30' 2''$ ,  $\omega = 32^\circ 55' 57''$ ,  $\Omega = 298^\circ 85' 1''$ ,  $Q = 6.437$  AU, and  $T_j = 2.534$ .

#### Deceleration of fragments and meteoroid strength

Using the one narrow field video we performed a high-resolution analysis of the flight dynamics of all dozen discernable fragments. After determining the celestial coordinates of each fragment on every narrow field video frame, they were projected on the trajectory line determined from the wide field observations. Nevertheless, as we were lacking two station high-resolution data, we were only able to determine the along-track position of every fragment, thus losing the information about their transverse position. For example, fragments 4 and 7 show a perpendicular offset from the main trajectory, obtained at the moment of their formation, but the uncertainties in the trajectory would make any conclusions about their transverse positions unreliable. Moreover, the bending of the trajectory due to the Earth’s gravity was not taken into account, although its influence was not negligible.

Figure 7 shows the lags of individual fragments—the graph was normalized to the first visible fragment, which starts at 0 s and at a lag of 0 m. As the first visible fragment (Fragment 1) was the furthest behind the leading edge of the meteor, all other fragments, which are in front of it, have positive lag. Fragment 10 was at the head of the “fragment train” in the meteor. The fragments did not have uniform deceleration, which caused

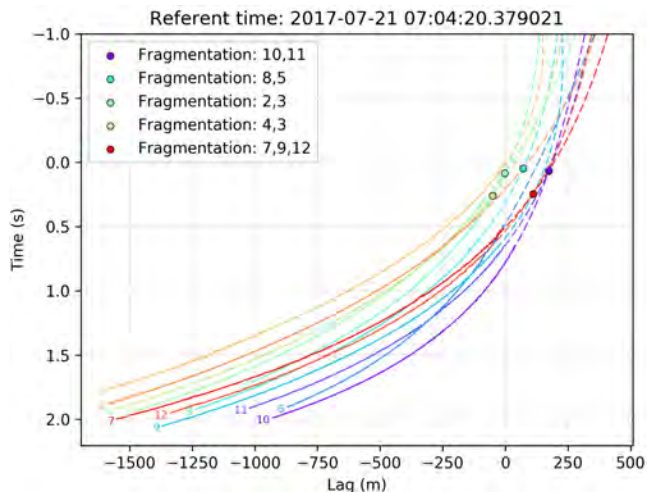


Figure 7 – Lags of individual fragments. Solid lines show the observed lag, while the dashed lines show an extrapolation using an exponential function fit; see Equation (1). Solid circles are showing the point of fragmentation of individual fragments.

some of them to overtake one another. This behavior is visible as the moments when the lags of individual fragments cross each other. For example, Fragment 6 had the smallest deceleration, which caused it to overtake Fragments 7, 12, 9, and 11. Obviously, all fragments were transversally sufficiently distant from one another not to collide. The case of Fragment 7, which shows a larger transversal offset at the moment of fragmentation, suggests that the rotation of the fragments may be one of the explanations.

To determine an approximate time of fragmentation of individual fragments, we fit an exponential function of length versus time of every fragment (Jacchia and Whipple, 1961):

$$D(t) = k + vt + a_1 e^{a_2 t}, \quad (1)$$

where  $t$  is the time,  $v$  is the initial velocity of every fragment,  $a_1$  and  $a_2$  are deceleration coefficients, and  $D(t)$  is the along-track distance of every fragment from the beginning of the meteor. Next, we propagated the positions of the fragments back in time and looked for the moments when they intersect. The plausibility of each intersection/fragmentation was confirmed by looking at the video as well. It was found that all fragments except Fragments 1 and 6 emerged from larger fragments. For Fragments 1 and 6, the possible points of fragmentation could not be visually confirmed.

Furthermore, we have computed dynamic pressures for every fragment, as shown in Figure 8. When computing dynamic pressure, we assumed that the drag coefficient is  $\Gamma = 1$ , and the atmosphere densities were taken from the NRLMSISE-00 atmosphere model (Picone et al., 2002) for the time and location of the meteor. Although the statistics are small, two clusters of dynamic pressures at the moment of fragmentation can be seen, one at about 2 kPa and the other at about 2.1 kPa.

The fragments themselves start to disintegrate to dust at a height of about 82.5 km, which corresponds to a

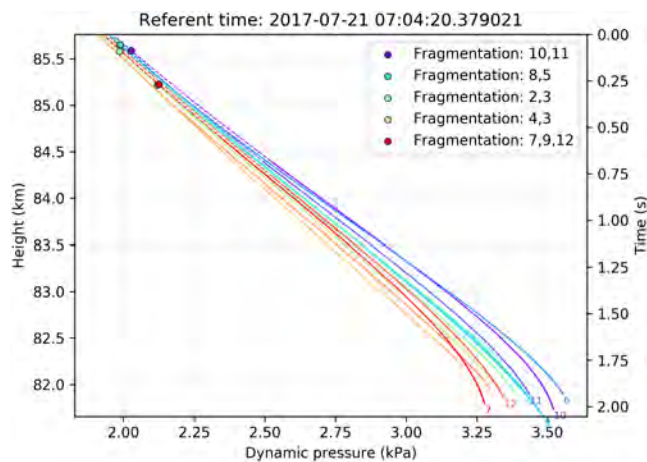


Figure 8 – Dynamic pressures of individual numbered fragments. Solid circles represent moments of fragmentation for individual fragments.

dynamic pressure of about 3.25 kPa. This suggests on the one hand that the compressive strength of the more compact parts of fresh JFC material ranges from 2.0 to 3.5 kPa. On the other hand, presuming that the dust seen in the narrow field video which was blown away early on is the matrix in which these fragments resided indicates that its strength is sub-kilopascal, possibly on the order of several hundreds of pascals for large (cm-sized) JFC meteoroids.

Trigo-Rodríguez and Llorca (2006) determined compressive strengths at the moment of fragmentation to range from 400 Pa for Draconids to 340 kPa for Taurids, assuming that the moment of meteoroid fragmentation coincides with the point of maximum brightness. In contrast, Borovička, Spurný, and Koten (2007) show that the fragmentation does not coincide with the brightest point on the meteor’s light curve, except for photographic fireballs. They found that the compressive strengths of more compact parts of Draconid meteoroids are in the range of 5–20 kPa. Furthermore, they argue that the erosion of meteoroids may start earlier and not due to mechanical forces, while only a fireball’s flair is caused by mechanical brake-up. We find that these values are in good agreement with our findings for this particularly unusual case of a long duration, shallow entry JFC meteoroids. The reason may be that both the Draconids and our meteoroid originate from a Jupiter-family comet. Finally, Biele et al. (2015) used measurements from the ESA Philae lander and reported that the upper limit of the compressive strength of the top 10-cm layer of the Jupiter-family comet 67P/Churyumov-Gerasimenko is in the range from 1 to 3 kPa, which is also in agreement with our observations.

## 5 Conclusions

A highly fragmenting meteor observed on July 21, 2017, with the Canadian Automated Meteor Observatory enabled high-precision measurements on a train of discrete fragments produced during ablation. The meteoroid orbit is probably of Jupiter-family comet origin,

probably ejected recently as the meteoroid was on a Jupiter-crossing orbit. We find that the initial velocity of the meteoroid might have been as much as 400 m/s larger than the measured one due to deceleration during the non-luminous part of the trajectory. This is particularly acute in this case as the meteoroid had a very low entry angle of only  $8^\circ$ .

We measured the apparent compressive strength of the meteoroid and its daughter fragments with high precision largely due to its shallow entry angle. This unique geometry, combined with the low speed of the meteoroid resulted in a very gradual change with time in the dynamic pressure allowing unusual precision in the estimated fragmentation points.

The flight dynamics and fragmentation locations of 12 fragments was determined from narrow field observations. The fragments showed non-uniform deceleration, which caused them to overtake one another. The estimated compressive strength of the entire meteoroid was ca. 2.0 kPa, while the strength of the daughter fragments was ca. 3.25 kPa. The appearance of the wake even earlier in flight suggests that the outer matrix of material has very low strength (less than 1 kPa).

Future work includes calculating the mass ratio between the fragments and the dust, as well as determining the size distribution of individual fragments through photometric and dynamical mass calculations.

## Acknowledgements

We thank Jason Gill for data management and format conversion, and Zbigniew Krzeminski for hardware support.

## References

- Biele J., Ulamec S., Maibaum M., Roll R., Witte L., Jurado E., Muöz P., Arnold W., Auster H. U., Casas C., Faber C., Fantinati C., Finke F., Fischer H. H., Geurts K., Güttler C., Heinisch P., Herique A., Hviid S., Kargl G., Knapmeyer M., Knollenberg J., Kofman W., Kömle N., Kührt E., Lommatsch V., Mottola S., Pardo de Santayana R., Remetean E., Scholten F., Seidensticker K. J., Sierks H., and Spohn T. (2015). “The landing(s) of Philae and inferences about comet surface mechanical properties”. *Science*, **349** (6247), aaa9816.
- Borovička J. (1990). “The comparison of two methods of determining meteor trajectories from photographs”. *Bulletin of the Astronomical Institutes of Czechoslovakia*, **41**, 391-396.
- Borovička J., Spurný P., and Koten P. (2007). “Atmospheric deceleration and light curves of Draconid meteors and implications for the structure of cometary dust”. *Astronomy & Astrophysics*, **473** (2), 661–672.

- Campbell-Brown M. D. and Koschny D. (2004). “Model of the ablation of faint meteors”. *Astronomy & Astrophysics*, **418** (2), 751–758.
- Campbell-Brown, M. D., Borovička J., Brown P. G., and Stokan E. (2013). “High-resolution modelling of meteoroid ablation”. *Astronomy & Astrophysics*, **557**, A41.
- Campbell-Brown M. (2015). “A population of small refractory meteoroids in asteroidal orbits”. *Planetary and Space Science*, **118**, 8–13.
- Jacchia L. G. and Whipple F. L. (1961). “Precision orbits of 413 photographic meteors”. *Smithsonian Contributions to Astrophysics*, **4**, 97–129.
- Picone J. M., Hedin A. E., Drob D. P., and Aikin A. C. (2002). “NRLMSISE-00 empirical model of the atmosphere: Statistical comparisons and scientific issues”. *Journal of Geophysical Research: Space Physics*, **107** (A12), SIA 15-1–SIA 15-16.
- Roberts I. D., Hawkes R. L., Weryk R. J., Campbell-Brown M. D., Brown P. G., Stokan E., and Subasinghe D. (2014). “Meteoroid structure and ablation implications from multiple maxima meteor light curves”. In Jopek T. J., Rietmeijer F. J. M., Watanabe J., and Williams I. P., editors, *Proceedings of Meteoroids*, Poznań, Poland, 26–30 August 2013. A. M. Univ. Press, Poznań, pages 155–162.
- Stokan E., Campbell-Brown M. D., Brown P. G., Hawkes R. L., Doubova M., and Weryk R. J. (2013). “Optical trail widths of faint meteors observed with the Canadian Automated Meteor Observatory”. *Monthly Notices of the Royal Astronomical Society*, **433** (2), 962–975.
- Stokan E. and Campbell-Brown M. D. (2014). “Transverse motion of fragmenting faint meteors observed with the Canadian Automated Meteor Observatory”. *Icarus*, **232**, 1–12.
- Southworth R. B. and Hawkins G. S. (1963). “Statistics of meteor streams”. *Smithsonian Contributions to Astrophysics*, **7**, 261–285.
- Subasinghe D., Campbell-Brown M., and Stokan E. (2017). “Luminous efficiency estimates of meteors. I. Uncertainty analysis”. *Planetary and Space Science*, **143** (Supplement C), 71–77.
- Trigo-Rodríguez J. M. and Llorca J. (2006). “The strength of cometary meteoroids: Clues to the structure and evolution of comets”. *Monthly Notices of the Royal Astronomical Society*, **372**(2), 655–660.
- Weryk R. J. and Brown P. G. (2013). “Simultaneous radar and video meteors. II. Photometry and ionisation”. *Planetary and Space Science*, **81**, 32–47.
- Weryk R. J., Campbell-Brown M. D., Wiegert P. A., Brown P. G., Krzeminski Z., and Musci R. (2013). “The Canadian Automated Meteor Observatory (CAMO): System overview”. *Icarus*, **225** (1), 614–622.

# Nomon Project

Stefan Beriša, Tina Dufke, Åse Marie Erklev, Igor Smolić, and Nemanja Vojvodić

Norwegian Meteor Network

stefan@ntgruppen.no, tina.dufke@kristiansand.kommune.no, aase.marie.erklev@ntgruppen.no,  
igor.smolic@ntgruppe.no, nemanja.vojvodic@ntgruppe.no

The Nomon Project consisted of deploying a small network of high-sensitivity video cameras for automatic detection of simultaneously observed meteors. While mainly of educational interest at this time, there are plans of extending this project in the future.

## 1 Introduction

The Nomon Network of high-sensitivity video cameras was deployed for automatic and simultaneous monitoring of approximately 40 000 km<sup>2</sup> of the atmosphere at 100 km height over southern Norway. Analysis of recorded data during the maximum of the Geminid meteor shower on December 13-14, 2016 (over 700 meteor detections on 4 cameras) indicates that it is possible to classify detected meteors to parent meteor showers. For particular meteors, the statistical error is a few angular degrees for radiant determination and 5 km/s for meteor velocities. Because of the small ground distances of video cameras (around 6 km), obtained data are good enough for educational purposes.

In order to get data with scientific value for meteor astronomy, it is necessary to spread the camera network to larger distances (50–150 km).

A web application based on rating was developed for classifying meteors from non-meteor videos/data. This process will be automatized in the future by implementing a machine-learning algorithm.

## 2 System

Each observation spot consisted of two high-sensitivity video cameras equipped with appropriate lenses. This equipment was protected by a waterproof casing with heaters. It was connected to a PC via USB video capture cards. Each computer is equipped with UFOCAPTURE, the automatic meteor detection application.

## 3 Network

Cameras are located in three different schools. Their exact locations are shown in Table 1. The distance between each two schools is around 6 km.

## 4 Geminid observations

Maximum activity for the Geminid meteor shower in 2016 was expected on the night of December 13-14. During the entire night, four cameras were recording.

Table 1 – School locations.

School	$\lambda$ (E)	$\varphi$ (N)	$h$
Grim	7°9697	58°1484	22 m
Havlimyra	8°0337	58°1914	34 m
Torrival	7°9256	58°2014	41 m

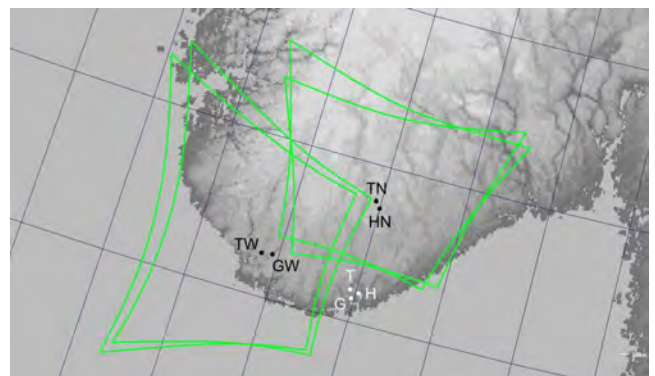


Figure 1 – Observing locations (H—Havlimyra, G—Grim, T—Torrival) and observed areas of skies for each of the four cameras that were operational (HN, GW, TN, and TW, where N—North and W—West indicate the orientation of the cameras).

They were oriented so that each observed part of the sky was covered by two cameras from different locations. Figure 1 shows the observing locations (H—Havlimyra, G—Grim, T—Torrival) as well as the observed areas by each of the four cameras at this locations (N—North and W—West are used for the orientation of the cameras).

During the observation, each camera recorded over 150 meteors. It is worth mentioning in this regard that it was Full Moon, and, consequently, that the Moon was above the horizon for the larger part of the night. Using UFOANALYZER, trajectory and motion parameters were determined (coordinates, direction, trail, and apparent speed). The meteors detected by each of the cameras are shown in Figure 2.

The celestial projections of all detected meteors are shown in Figure 3. Red lines represent the observed meteor trails and green represent the extrapolated trajectories. In each instance, the radiant of the Geminid meteor shower is easy to spot, as most of the trajectories cross each other there.

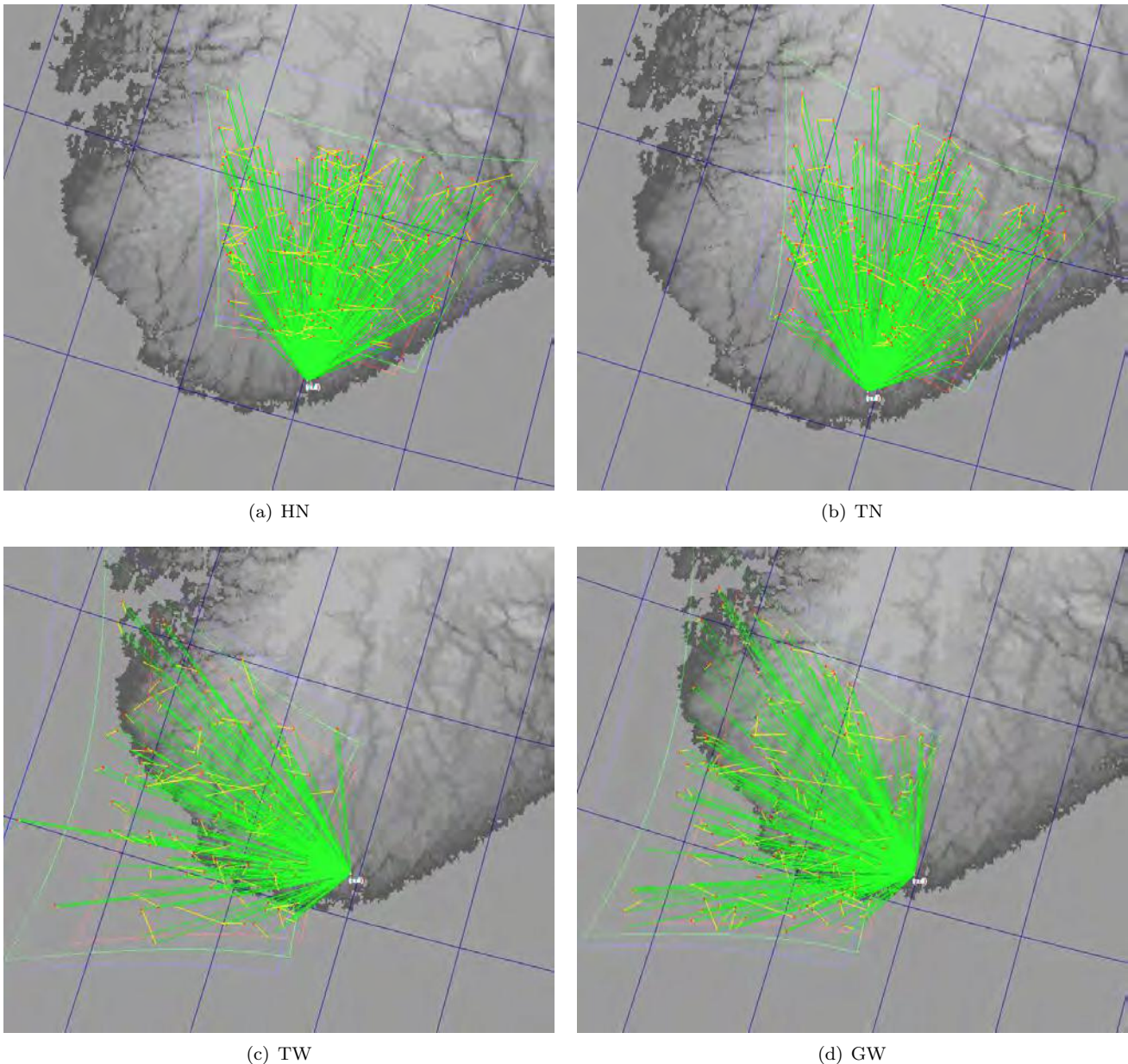


Figure 2 – Meteors detected by each of the cameras. For the abbreviations used, see the caption of Figure 1.

During the night of December 13-14, 2016, the four cameras that were operational detected a total of 714 meteors. Using UFOORBIT and metrics from UFOANALYZER, the orbital elements of each meteor that was observed by at least two cameras were determined. As a result, the radiant point was determined for 204 meteors.

Figure 4 shows the radiants and the geocentric velocities of all the particles that caused the observed meteors.

As can be seen, most of them were, as is to be expected, part of the Geminid meteor shower. The error margin for determining the coordinates of individual radiants was around  $5^\circ$ . It is also worth mentioning that the average calculated geocentric speed for the Geminids is 35 km/s with an error margin of 5 km/s.

Prior orbits in the Solar System for all the particles responsible for observed meteors during the aforementioned night can be seen in Figure 5.

## 5 Conclusion

The network was set up so that the distance between each two of the three camera locations was only around 6 km, far less of course than the optimal distance of around 100 kilometers. In order to obtain scientifically—as opposed to educationally—valuable results, the network should be expanded so that this condition is met.

Despite this limitation, the data obtained from this small video camera network were sufficiently accurate to classify meteors to their corresponding meteor showers. The error margins for determining meteoroid orbit parameters, however, were significantly greater than what is expected for a network with optimal distances.

As mentioned in the Introduction, a web application based on rating was developed for classifying meteors from non-meteor videos/data. We intend to automatize this process using a machine-learning algorithm.

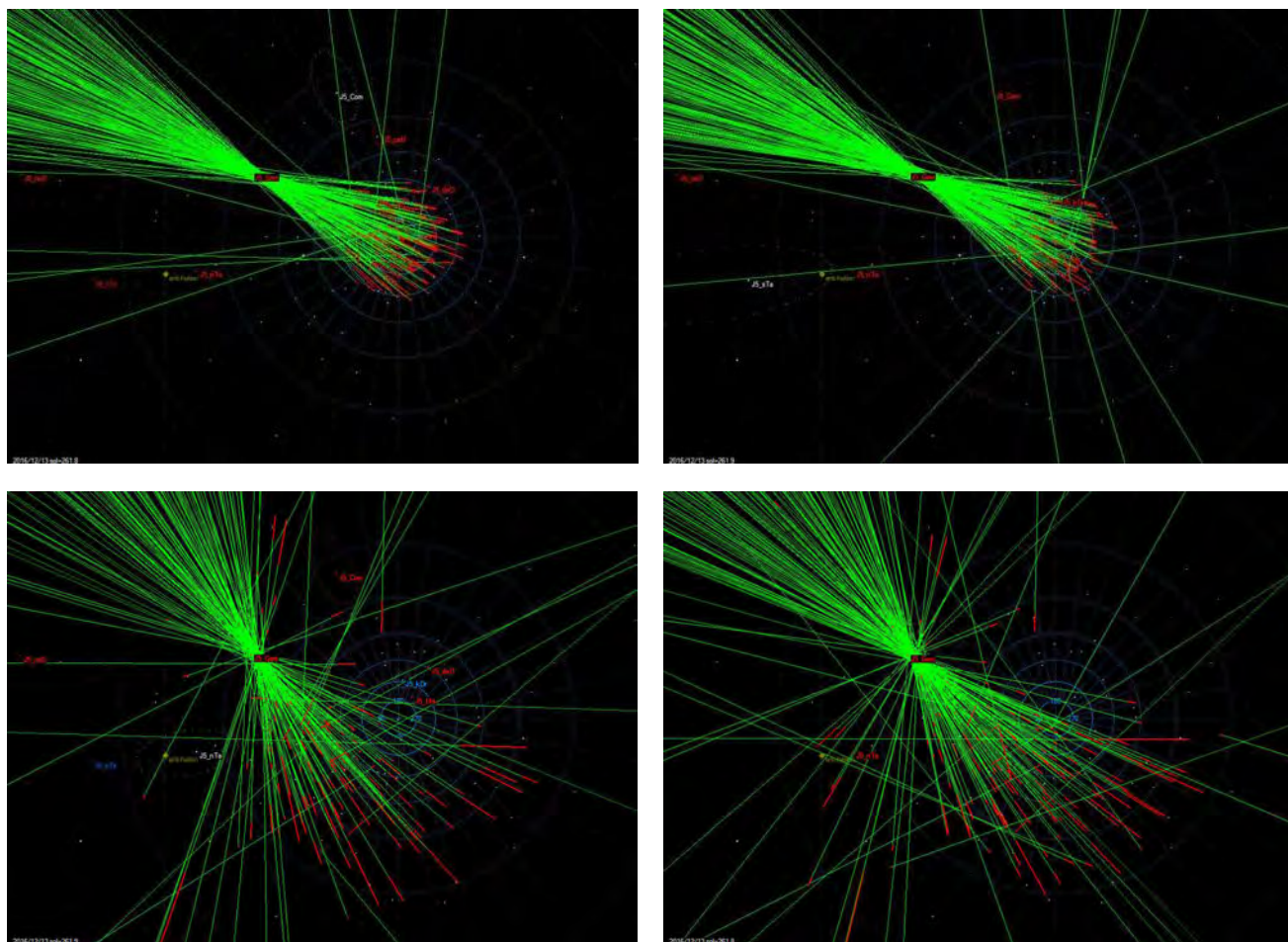


Figure 3 – Detected meteors projected on the celestial sphere. The actual meteors are in red, and their extended trajectories in green. The Geminid radiant is clearly visible in each instance.

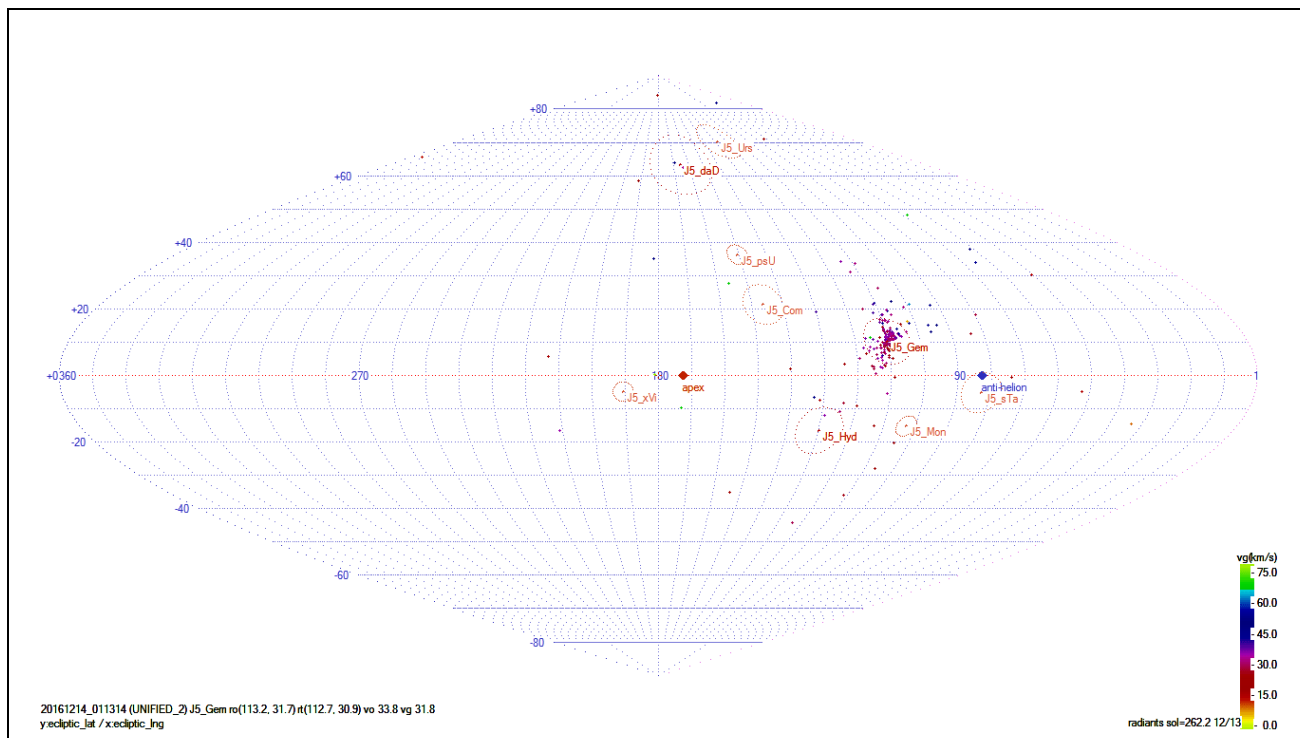
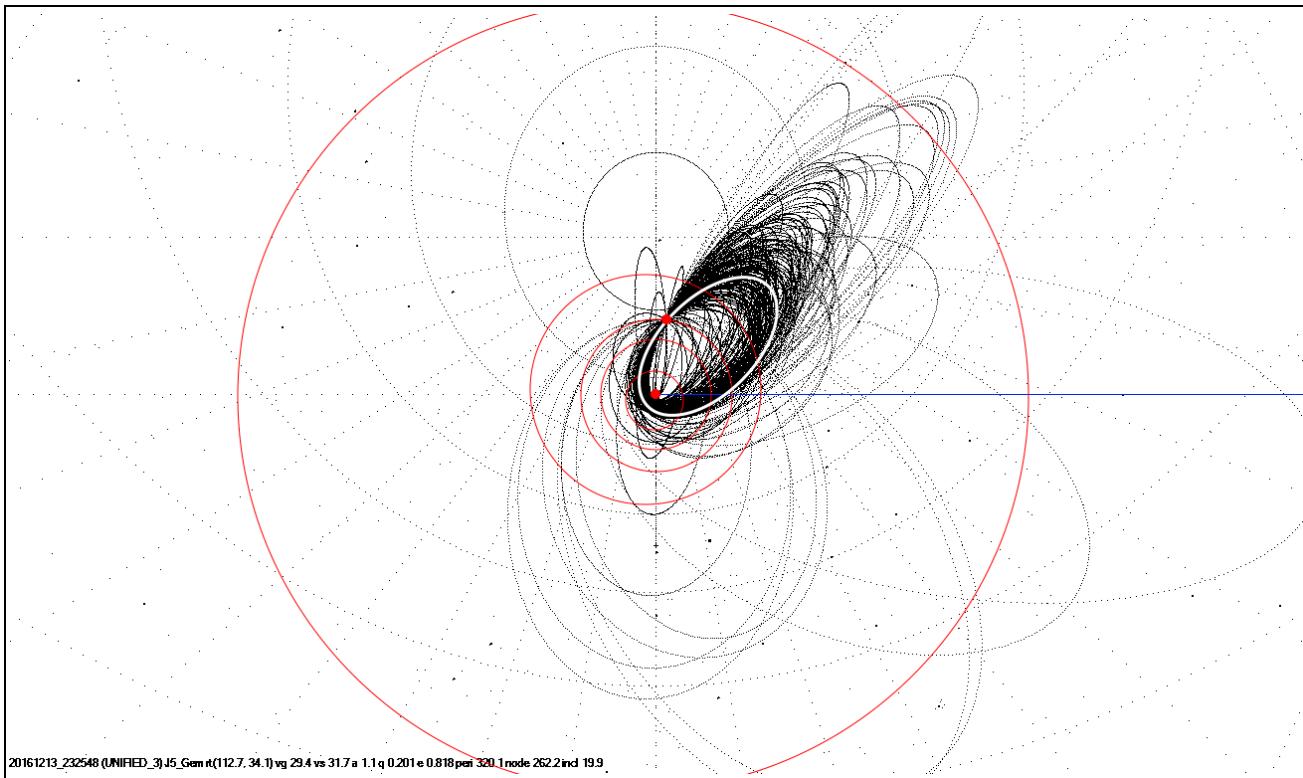


Figure 4 – Radiants and geometric velocities of all the particles that caused the observed meteors.



*Figure 5* – Orbits of the particles responsible for the observed meteors. The Sun, the orbits of the planets up to Jupiter, the position of the Earth, the orbit of the parent body, and the direction of the equinox is also indicated.

# Current status of Polish Fireball Network

Mariusz Wiśniewski<sup>1,2</sup>, Przemysław Żołądek<sup>1</sup>, Arkadiusz Olech<sup>1,3</sup>,  
Zbigniew Tyimiński<sup>1,4</sup>, Maciej Maciejewski<sup>1</sup>, Arkadiusz Raj<sup>1</sup>, Karol Fietkiewicz<sup>1</sup>,  
Mariusz Gozdalski<sup>1</sup>, Marcin Przemysław Gawroński<sup>1,5</sup>, Tomasz Suchodolski<sup>1,6</sup>,  
Maciej Myszkiewicz<sup>1</sup>, Marcin Stolarz<sup>1</sup>, and Krzysztof Polakowski

<sup>1</sup> Polish Fireball Network, Comets and Meteors Workshop, ul. Bartycka 18, 00-716 Warsaw, Poland  
brahi@op.pl, mazziiek@gmail.com, arek.raj@gmail.com, parmo.pfn@gmail.com,  
ma.gozdalski@gmail.com, spammer.m@gmail.com, marcin.stolarz@gmail.com, krzysiek-pol20@o2.pl

<sup>2</sup> Central Office of Measures, ul. Elektoralna 2, 00-139 Warsaw, Poland  
marand.w@gmail.com

<sup>3</sup> Nicolaus Copernicus Astronomical Center, ul. Bartycka 18, 00-716 Warsaw, Poland  
a.olech@camk.edu.pl

<sup>4</sup> National Center of Nuclear Research RC POLATOM, Soltan 7, Otwock-Świerk, Poland  
zbyszek.tyminski@gmail.com

<sup>5</sup> Fac. of Phys., Astron., and Inform., N. Copernicus Univ., Grudziądzka 5, 87-100 Toruń, Poland  
motylek@astro.uni.torun.pl

<sup>6</sup> Space Research Centre, Polish Academy of Sciences, ul. Bartycka 18A, 00-716 Warsaw, Poland  
tomasz.suchodolski@ptma.pl

The Polish Fireball Network (PFN) started in March 2004. Most of its observers are amateurs, members of the *Comets and Meteors Workshop*. The Network consists of 38 continuously working stations, where nearly 71 sensitive CCTV video and digital cameras operate. In 2016, PFN cameras recorded 100389 single events. Using these data, 19087 trajectories and orbits was calculated.

## 1 Introduction

Since 2004, the Polish sky has been patrolled by cameras of Polish Fireball Network (PFN). Most of the PFN observers are amateurs, members of the *Comets and Meteors Workshop* and perform observations from their homes. Some stations are located in astronomical clubs and schools. The Network consists of 38 continuously working stations, where nearly 71 sensitive CCTV video and digital cameras operate (Olech et al., 2006, Wiśniewski et al., 2017).

## 2 Cameras of PFN

The cameras of the PFN were able to cover the entire sky above Poland, but south-eastern Poland was particularly well-covered because the majority of cameras are located in that area. This part of the country also enjoys the largest number of clear nights, statistically speaking (see Figure 1). In most stations, we use low-cost sensitive CCTV analog video cameras equipped with lenses with a  $65^\circ 6' \times 49^\circ 2'$  field of view. Currently there are 36 cameras of this type. We use METREC (Molau, 1999) and UFOCAPTURE (SonotaCo, 2005) software for meteor detection. UFOANALYZER is used for astrometric reduction of video recordings. Some stations were equipped with 16 high-sensitive Mintron 12v6 cameras with fast lenses. These cameras detected up to four times more meteors than low-cost cameras. Due to higher sensitivity and smaller fields of view, we can record larger numbers of fainter meteors.

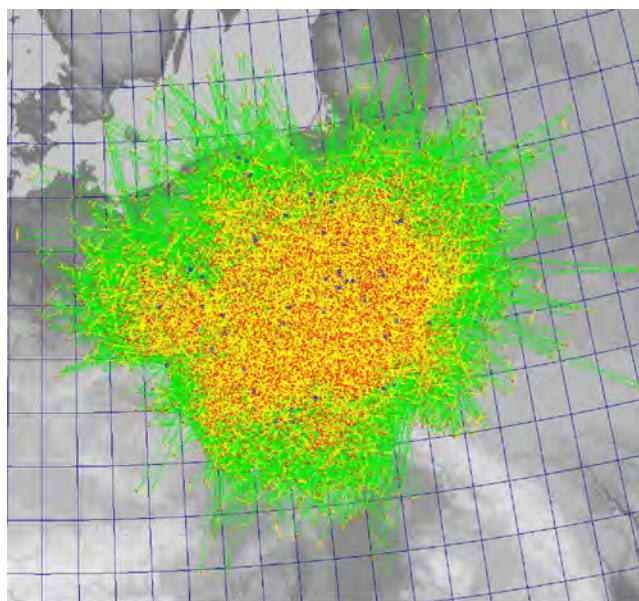


Figure 1 – Calculated trajectories of meteoroids in 2016.

Set-ups with digital cameras are based on the sensitive DMK 33GX236. This camera has a resolution of  $1920 \times 1200$  pixels. The new cameras are operated with lenses with a focal length of 2.4 mm, which gives a  $130^\circ \times 80^\circ$  field of view. New cameras offer images with much better quality compared to analog cameras.

A comparison of the various parameters of the low-cost set-up, the sensitive set-up and the new digital HD set-up is presented in Table 1.

Table 1 – Types of camera working in PFN.

Parameter	Low-cost set-up	Sensitive set-up	HD digital set-up
Camera type	Tayama C3102-01A1	Mintron 12v6	DMK 33GX 236
Image resolution	480 × 576 pixels	768 × 576 pixels	1920 × 1200 pixels
	Interlaced	Interlaced	Progressive
Time resolution	25/50 fps 8 bit	25/50 fps 8 bit	50/25 fps 8/12 bit
Lens	1.2/4 mm	0.8/6 mm–0.8/12 mm	1.2/2.4 mm
Field of view	66° × 50°	< 66° × 50°	130° × 80°
Pixel size	5/pixel	< 5'/pixel	4/pixel

The detections from all PFN cameras are automatically transmitted via Internet to the central server, where double-station events are identified and analyzed, and, then, trajectories and orbits for these double-station events are determined. In addition, all calculations are checked by manual inspection.

### 3 Results of PFN in 2016

In 2016, PFN cameras recorded 100 389 single events. The collected data were preliminary analyzed using the UFOORBIT software. The calculations were performed in a fully automatic way. The quality of the final results was controlled by UFOORBIT's multiple parameter settings. Detailed information about the limiting parameters can be found in the software documentation (SonotaCo, 2007). Results with high uncertainty were rejected, and the criterion for this was based on the set of limit values.

We also created the PYFN software for trajectory and orbit calculation. PYFN (Żołądek, 2012) utilizes the Celpcha method (Ceplecha, 1987).

Using these data, 19 087 trajectories and orbits were calculated for meteors detected in 2016. Detailed numbers of meteors for the period 2011–2016 are presented in Table 2.

As one can see, 2016 is the second year in a row for which a very rapid increase in the number of detected meteors occurs. On the one hand, this was due to the introduction of new sets of sensitive cameras. On the other hand, a large number of cloudless nights in September 2016 as contributed favorably to the number of recorded meteors (see Figure 2).

During the first half of the year the PFN cameras typically record only 20% of all detections of a given year (see Figure 3).

Table 2 – Results of PFN during 2011–2016.

Year	Detections	Orbits
2011	24 099	3 430
2012	28 471	4 186
2013	36 347	6 114
2014	46 936	7 351
2015	79 083	13 528
2016	100 389	19 087

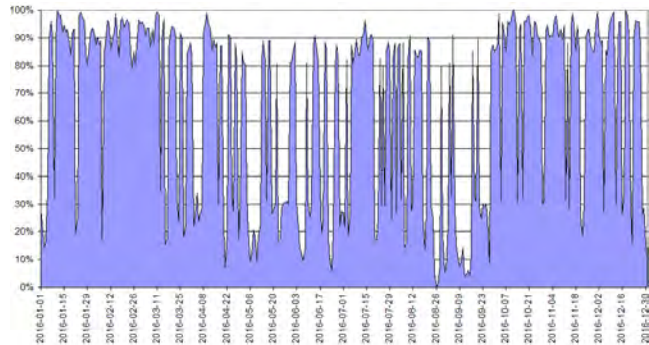


Figure 2 – Cloud coverage for PFN stations in 2016.

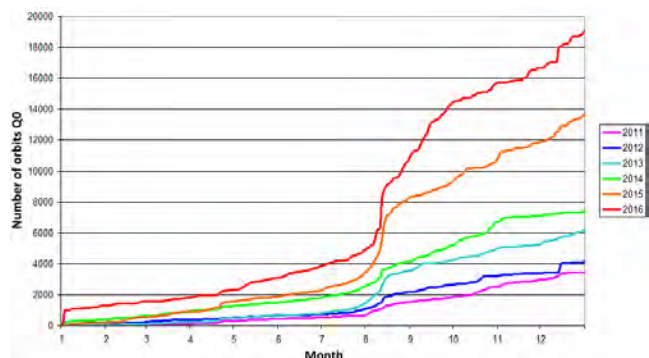


Figure 3 – Cumulative distribution of multi-station detections in 2011–2016

### Acknowledgement

We would like to thank to all station owners, operators, and observers for long-term and precise work for Polish Fireball Network (see Table 2).

This work was supported by the National Science Center (decision No. DEC-2013/09/B/ST9/02168).

### References

- Ceplecha Z. (1987). “Geometric, dynamic, orbital, and photometric data on meteoroids from photographic fireball networks”. *Bulletin of the Astronomical Institutes of Czechoslovakia*, **38**, 222–234.
- Molau S.,(1999). “The meteor detection software MetRec”. In Baggaley W. J. and Porubčan V., editors, *Proceedings of Meteoroids*, Tatranská Lomnica, Slovakia, 17–21 August 1998, pages 131–134.
- Olech A., Żołądek P., Wiśniewski M., Kransowski M., Kwinta M., Fajfer T., Fietkiewicz K., Dorosz D.,

Table 3 – Stations and observers of the Polish Fireball Network.

ID	Name	Observer	Equipment
PFN01	Ostrowik	Maciej Myszkiewicz	PAVO1
PFN03	Złotokłos	Karol Fietkiewicz	PAVO3
PFN06	Kraków	Maciej Kwinta	PAVO6, PAVO7, PAV79, MDC14
PFN13	Toruń	Tomasz Fajfer	PAV14
PFN19	Kobiernice	Mariusz Szlagor	PAVO8
PFN20	Urzędów	Mariusz Gozdalski	PAV25, PAV26, PAV38, PAV99
PFN24	Gniewowo	Krzysztof Polakowski	PAV40, MDC09
PFN32	Chełm	Maciej Maciejewski	PAV35, PAV36, PAV43, PAV60, MDC09
PFN37	Nowe Miasto Lubawskie	Janusz Laskowski	PAV41
PFN38	Podgórzyn	Tomasz Krzyżanowski	PAV44, PAV49, PAV50, MDC15
PFN39	Rosocha	Andrzej Dobrychłop	PAV42
PFN40	Otwock	Zbigniew Tyimiński	PAVO1, PAVO9, PAV52
PFN41	Twardogóra	Henryk Krygiel	PAV45, PAV53
PFN43	Siedlce	Maciej Myszkiewicz	PAV27, PAV61, PAV67, MDC07
PFN45	Łañcut	Łukasz Woźniak	PAV37
PFN46	Grabniak	Tomasz Łojek	PAV57, MDC06
PFN47	Jeziorko	Tomasz Lewandowski	PAV13, PAV62, PAV63, PAV65
PFN48	Rzeszów	Marcin Bęben	PAV59, PAV64, PAV77
PFN49	Helenów	Paweł Woźniak	PAV23
PFN51	Zelów	Jarosław Twardowski	PAV22
PFN52	Stary Sielc	Marcin Stolarz	PAV66, PAV75, MDC04, MDC12
PFN53	Bełecin	Michał Kałużny	PAV68
PFN54	Lęgowo	Grzegorz Tisler	PAV69
PFN55	Ursynów	Przemysław Żoładek	MDC01, MDC02
PFN56	Kolbudy	Cezary Wierucki	PAV71
PFN57	Krotoszyn	Tomasz Suchodolski	PAV70
PFN58	Opole	Filip Kucharski	PAV72
PFN59	Drawsko Pomorskie	Mirek Krasnowski	MDC10
PFN60	Bystra	Piotr Nowak	PAV74, PAV80
PFN61	Piwnice	Marcin Gawroński	PAV10
PFN62	Szczecin	Zbigniew Laskowski	MDC05
PFN63	Starowa Góra	Arkadiusz Raj	MDC11, MDC20
PFN64	Grudziądz	Sebastian Soberski	MDC18
PFN65	Wadowice	Mariusz Szlagor	MDC13
PFN67	Nieznaszyn	Walburga Węgrzyk	PAV78
PFN69	Lamkówko	Jacek Kapcia	PAV69
PFN70	Kodeń	Piotr Onyszczyk	PAV67
PFN71	Radomsko	Hubert Drózdź	PAVO1
PFN72	Koźmin Wielkopolski	Krzysztof Polak	PAVO1, PAVO2
PFN74	Brwinów	Paweł Zaręba	PAVO1, PAVO2

Kowalski L., Olejnik J., Mularczyk K., Złoczewski K. (2006). “Polish Fireball Network”. In Bastianes L., Verbert J., Wislez J.-M., and Verbeeck C., editors, *Proceedings of the International Meteor Conference*, Oostmalle, Belgium, 15–18 September 2005. IMO, pages 53–62.

SonotaCo (2005). “UFCaptureV2 Users Manual”. <http://sonotaco.com/soft/UF02/help/english/index.html>.

SonotaCo (2007). “UFOOrbitV2 Users Manual”. [http://sonotaco.com/soft/U02/U021Manual\\_EN.pdf](http://sonotaco.com/soft/U02/U021Manual_EN.pdf).

Wiśniewski M., Żoładek P., Olech A., Tyimiński Z., Maciejewski M., Fietkiewicz K., Rudawska R., Gozdalski M., Gawroński M. P., Suchodolski T., Myszkiewicz M., Stolarz M., Polakowski K. (2017) “Current status of Polish Fireball Network”. *Planetary and Space Science*, **143**, 12–20.

Żoładek P. (2012). “PyFN - multipurpose meteor software”. In Gyssens M. and Roggemans P., editors, *Proceedings of the International Meteor Conference*, Sibiu, Romania, 15–18 September 2011. IMO, pages 53–55.

# The CILBO spectral observation program

Regina Rudawska<sup>1</sup>, Joe Zender<sup>1</sup>, Detlef Koschny<sup>1,3</sup>,  
Stefan Loehle<sup>2</sup>, Imanol Uriarte Latorre<sup>4</sup>

<sup>1</sup>ESA European Space Research and Technology Center, Noordwijk, the Netherlands  
Regina.Rudawska@esa.int, Joe.Zender@esa.int, and Detlef.Koschny@esa.int

<sup>2</sup>High Enthalpy Flow Diagnostics Group, Inst. f. Raumfahrtsysteme, Univ. Stuttgart, Germany

<sup>3</sup>Lehrstuhl für Raumfahrttechnik, TU Munich, Garching, Germany

<sup>4</sup>Technical University of Berlin, Berlin, Germany

In recent years, spectroscopic observations of meteors have become quite popular. The Meteor Research Group (MRG) of the European Space Agency (ESA) has been working on upgrading the analysis of meteor spectra as well (Koschny et al., 2013). Our system works on image-intensified cameras with objective grating (ICC8) adopted to this purpose. Its current status is presented.

## 1 CILBO spectral pipeline

The sketch of the CILBO spectroscopic pipeline is presented in Figure 1. ICC7 and ICC8 cameras are located at the Tenerife station of the double-station camera set-up CILBO (Canary Island Long-Baseline Observatory). At the same time when ICC8 records the first order of a meteor spectrum, the zero order (meteor) is recorded by ICC7 camera mounted next to it.

This allows MESS (MEteor Spectra Selector) to scan records of ICC8 along expected positions in images and find spectra.

The same procedure is used by ViDAS (Video Data Archiving System), to compute the first-order spectrum as a function of wavelength. Following the procedures described by Zender et al. (2014), the pipeline software processes data with the standard calibration procedure (dark current, flat field, lens distortion correc-

tions). The extracted meteor spectrum is then further analyzed.

A synthetic spectrum is fitted to the observed one using the PARADE database (Liebhart et al., 2012), a tool that was developed for ESA for the calculation of the radiation of emission lines of atoms and molecules. At the moment PARADE has implemented only four of meteoritic origin species, i.e., Mg I, Fe I, Ca I and Na I. Moreover, it includes atmospheric elements (OI, NI, N<sub>2</sub>).

## 2 Example: Geminids

The double-station meteor observations carried out by ICC7 (Tenerife) and ICC9 (La Palma) allow the determination of the trajectory of a meteor and its orbit.

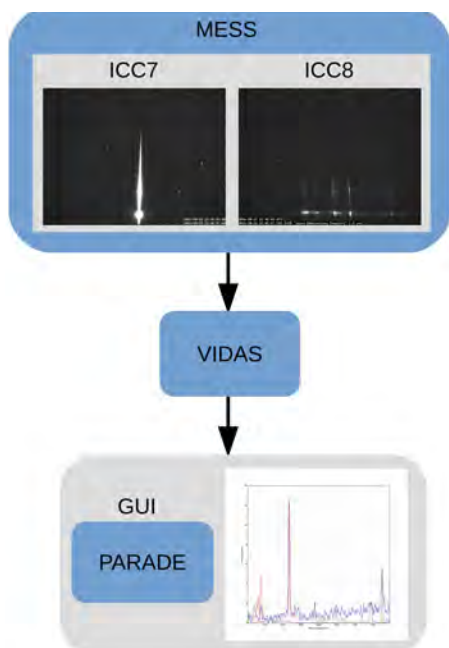


Figure 1 – CILBO spectral pipeline.

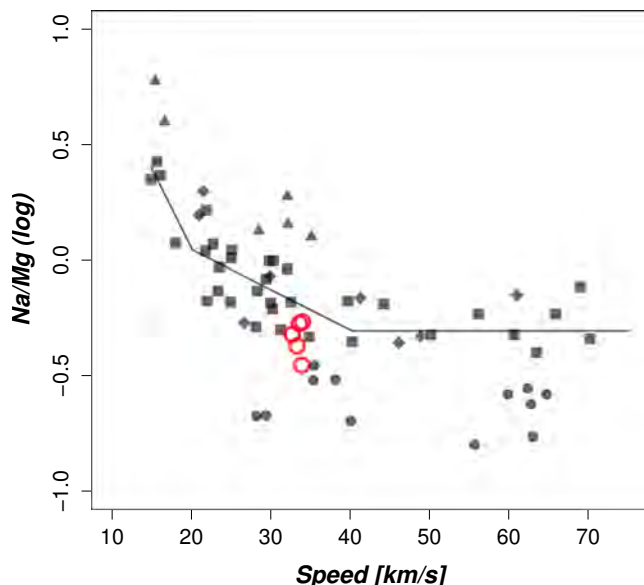


Figure 2 – The observed Mg/Na line intensity ratio in Cilbo meteors (red open circles) as a function of meteor speed compared to those derived by Borovička et al. (2005), defining several classes of meteors (symbols represents: ■ normal, ● Na-poor, ◆ Fe-poor, ▲ enhanced Na, × irons, ○ Na-free, and △ Na-rich).

The data is stored in the Virtual Meteor Observatory (VMO) (Koschny et al., 2014), which is the long-term archive of the IMO video meteor camera network. In particular, it contains a record of precise measurements of Geminid meteors that we merged with simultaneous measurements of meteor spectra obtained from ICC8.

Figure 2 shows the observed Mg/Na line intensity ratio in our example of Geminid meteors as a function of meteor speed.

## Acknowledgement

We acknowledge funding support from the faculty of ESA's Science Support Office.

## References

- Borovička J., Koten P., Spurný P., Boček J., and Štork R. (2005). “A survey of meteor spectra and orbits: evidence for three populations of Na-free meteoroids”. *Icarus*, **174**, 15–30.
- Koschny D., Bettonvil F., Licandro J., v. d. Lijdt C., Mc Auliffe J., Smit H., Svedhem H., de Wit F., Witasse O., and Zender J. (2013). “A double-station meteor camera set-up in the Canary Islands —CILBO”. *Geoscientific Instrumentation, Methods, and Data Systems*, **2**, 339–348.
- Koschny D., Smit H., and Barentsen G. (2014). “The Virtual Meteor Observatory (VMO)”. In Gyssens M., Roggemans P., and Żołądek P., editors, *Proceedings of the International Meteor Conference*, Poznań, Poland, 22–25 August 2013. IMO, pages 133–135.
- Liebhart H., Herdrich G., and Merrifield J. A. (2012). In *XLIII AIAA Thermophysics Conf.*, Reston, VA, USA. AIAA.
- Zender J., Koschny D., and Ravensberg K. (2014). “Calibration of spectral video observations in the visual: theoretical overview of the ViDAS calibration pipeline”. In Gyssens M., Roggemans P., and Żołądek P., editors, *Proceedings of the International Meteor Conference*, Poznań, Poland, 22–25 August 2013. IMO, pages 126–129.

# Meter-sized meteorite impacts

**Nagatoshi Nogami**

**Sakamoto, Ohtsu, Shiga 520-0113, Japan**  
nogamin@sc.sumitomo-chem.co.jp

Meter-sized meteorites are supposed to hit the Earth with a frequency in the order of once per one hundred years. While they may not cause fatal damage, they could potentially have serious impact on citizens' lives and modern industry. We discuss the risk of these meteorites and a couple of ideas for measures to prevent damage.

# About one possible mechanism of comet splitting

Ayyub S. Guliyev

Shamakhy Astrophysical Observatory, SHAO, National Academy of Sciences of Azerbaijan  
S. Rustam, 11c 7, AZ1014, Baku, Azerbaijan  
guliyevayyub@gmail.com

Some aspects of the hypothesis on the role of meteoroid impacts on splitting a comet's nucleus are considered. We compare the inclinations of the orbits of splitted comets relative to the mean orbital planes of the known meteor streams. Calculations are based on the assumption that the impacts occur at angles exceeding the studied inclinations. Inclinations of the orbits of 114 comets relative to the plane of 100 meteor streams are calculated and are analyzed statistically. Then, distributions of inclinations were obtained for splitted long- and short-period comets. This analysis concerns the cases where the nodes of the comet's orbit are within 0.1 AU of the meteoroids' orbit. In the case of long-period comets, appreciable irregularity of the distribution of the inclinations has been found. One reason for this irregularity is the maximum near  $180^\circ$ . This peculiarity means that head-on collisions are responsible for most of the studied processes, in agreement with the discussed hypothesis. In the case of short-period comets, a local maximum has been found too for high inclinations. In conclusion, the distribution of the inclinations of cometary orbits agrees well with the hypothesis that meteoroids play a partial role in the splitting of cometary nuclei.

## 1 Introduction

The present work is a further development of ideas proposed in earlier work of the present author (Guliyev, 2016a; 2016b). According to these ideas, one of the possible causes of the disintegration of comets is their collision with large meteoroids. In the cited papers, the data of 114 comets which underwent splitting have been analyzed relative to mean orbital planes of orbits of 125 known meteoroid streams. For some of the considered comets, the number of expected collisions of the meteoroids streams exceed background values.

In this paper, we analyze the distribution of possible angles of comet-meteoroid collisions. If these angles are very large, the chances of the comets disintegrating increase—the limiting case of this process is a head-on collision. If the angles are small, however, the collisions will lead mainly to less destructive processes, such as the formation of craters on the surface of comet nucleus or the appearance of outbursts.

Our calculations are based on the assumption that the collision angle is at least the inclination of the comet's orbit relatively to the plane of motion of the selected meteoroid stream. Starting from this assumption, we analyze the values of the inclinations  $i'$  of the orbits of 114 comets relatively to 112 meteoroid streams, from the list approved by the IAU<sup>1</sup>.

## 2 Method of calculation

The values  $i'$  for the inclination of the comets' orbits relative to the considered meteoroid streams is obtained from spherical astronomy:

$$i' = \arccos(\cos i_C \cos i_S + \sin i_C \sin i_S \cos(\Omega_C - \Omega_S)),$$

<sup>1</sup><https://www.ta3.sk/IAUC22DB/MDC2007>.

where  $i_C$  and  $\Omega_C$  are inclination and longitude of the ascending node of the comet's orbit, and  $i_S$  and  $\Omega_S$  are the corresponding elements of the orbit of the considered meteoroid stream. Taking into account considerations from previous work (Guliyev, 2016a; 2016b), the values of  $i'$  will be calculated for comets having

$$\Delta = |r_C - r_S| \leq 0.1 \text{ AU.}$$

Here,  $r_C$  is the heliocentric distances from a node of the comet's orbit and  $r_S$  the heliocentric distance to the orbit of the considered meteoroid stream in the direction of the corresponding node of the comet's orbit. After calculating all the values of  $i'$  we can deal with the statistics of the obtained sample. To start with, we can determine  $\min i'$  and  $\max i'$  and divide this range into intervals to compute the frequency of the inclination corresponding to each interval. In this process, we can use Sturges rule, whereby the number of intervals is determined by

$$h = 1 + 3.322 \log_{10} N$$

with  $N$  the number of  $i'$  values. However, the calculations showed that  $\min i'$  and  $\max i'$  differ only slightly from  $0^\circ$  and  $180^\circ$ , respectively, so the entire range  $0^\circ - 180^\circ$  was divided into intervals. In determining the intervals for the parameter  $i'$  we will use the rule of equal distance of the cometary orbits poles on the celestial sphere. This means that, to determine the frequency intervals,  $\cos i'$  must be divided into equal parts.

## 3 Results for long-period comets

Because the orbit inclinations of long-period comets orbits have an almost random distribution, their analysis within this project is most important. Of the comets investigated, 73 have a period of more than 200 years.

The number of values for  $i'$  obtained under the condition  $\Delta \leq 0.1$  AU is 573, implying that, for the statistics,  $\cos i'$  must be divided into 10 equal parts. The upper bounds of these intervals are shown in Table 1.

As can be seen from the data in Table 1, the number of inclinations in the interval  $143.1^\circ$ – $180^\circ$  is higher than in the other intervals. The significance of this can be checked using the one-sided Student  $t$ -test (Gmurman, 1968). The mid-range values of the standard deviation for the number of inclinations for 9 intervals are equal:  $n = 57.8$  and  $\sigma = 7.69$ , respectively. We find for the normalized difference

$$t = (N - n)/\sigma = (71 - 57.8)/7.69 = 1.98,$$

yielding a probability  $\alpha$  that the higher frequencies in the last interval are significant of more than 0.95.

If we limit the value of  $\Delta$  to 0.08, 0.06, and 0.05 AU, respectively, then we obtain the following statistical values, accordingly:

$$\begin{aligned} N = 61, n = 45.9, \sigma = 5.84, t = 2.58, \alpha > 0.99; \\ N = 49, n = 35.9, \sigma = 6.31, t = 2.07, \alpha > 0.95; \\ N = 34, n = 25.5, \sigma = 4.61, t = 1.83, \alpha > 0.95. \end{aligned}$$

This means that in all these cases the interval  $143.1^\circ$ – $180^\circ$  has a significantly higher frequency, which also means that frontal collisions have a significant advantage over other ones. This feature might be considered in satisfactory agreement with our proposed mechanism of comet nucleus splitting.

## 4 Results for short-period comets

Applying the above analysis to short-period comets involves some difficulties. It is known that such comets have small orbital inclinations. This feature will of course influence the distribution of  $i'$ . It can be predicted that the maximum of such distribution will correspond to small values of this parameter. Therefore, the detection of the second maximum in the region of the larger values of  $i'$  requires a special approach. In addition, the inclinations of the orbits of the used meteor streams also have a maximum near small values (Table 2,  $N(\text{MS})$ ).

Nevertheless, we managed to do the calculations and build the distribution of  $i'$  for 42 short-period comets subject to disintegration of the nucleus. (The comets P/2010 V1 and P/2016 J1 were added to our list later.) After the calculations, we have identified 250 cases where  $\Delta$  is not greater than 0.1 AU (Table 2,  $N(\text{PC})$ ).

As expected, the number  $N$  in the first interval ( $0^\circ$ – $38.9^\circ$ ) clearly dominate over the other ones. However, in the range  $70.5^\circ$ – $180^\circ$ , there is significant local maximum in the interval  $141.1^\circ$ – $180^\circ$  ( $N = 21$ ).

The distribution of inclinations for D class comets is given in Table 2 ( $N(\text{DC})$ ). It is very similar to the distribution of  $N$  in the previous case. It should also be mentioned that while this class of short-period comets contributes 114 from the 250 values of  $i'$  (46%), their number is considerably less (36%).

## 5 Conclusion

In this work, we started from the precondition that the impact of a meteoroid on a comet nucleus can occur at angles exceeding the inclination  $i'$ . Based on this precondition, we carried out an analysis of  $i'$  for comets subject to disintegration of the nucleus. A significant maximum of the distribution of  $i'$  for long-period comets was found, corresponding to high values of this parameter. This agrees qualitatively with the proposed mechanism of comet splitting. The mutual velocity of a comet and meteoroid body in such nearly head-on collisions can reach up to 60–70 km/s. The collision energy in such events can be very large, so that even a small meteoroid may thoroughly destroy the comet's nucleus.

Generally speaking, we can state again that the distribution of  $i'$  is in good agreement with the hypothesis that the splitting of comets may be explained in part by the possibility of collisions with large meteoroids. Hence, we have found one more argument in favor of the ideas developed in our earlier work (Guliyev, 2016; 2016b).

## Acknowledgements

We thank the International Meteor Organization and the Organizing Committee of the IMC 2017 for their assistance.

## References

- Gmurman V. E. (1968). *Fundamentals of Probability Theory and Mathematical Statistics*. American Elsevier Publishing Co., 249 pages.
- Guliyev A. (2016a). “Meteoroid streams and comet disintegration”. In Roggemans A. and Roggemans P., editors, *Proceedings of the International Meteor Conference*, Egmond, the Netherlands, 2–5 June 2016. IMO, pages 94–95.
- Guliyev A. (2016b). “Collision with meteoroids as one of possible causes of cometary nucleus splitting”. *Planetary and Space Science*. **143**, 2017, 40–42.
- Sturges H. A. (1926). “The choice of a class interval”. *Journal of the American Statistical Association*, **21** (153), 65–66.

Table 1 – Frequencies of  $i'$  for long-period comets. The intervals considered are identified by their upperbound.

Upperbound of $i'$	36°9	53°1	66°4	78°5	90°0	101°5	113°6	126°9	143°1	180°
$N(\Delta \leq 0.10 \text{ AU})$	59	63	44	57	64	57	42	57	59	71
$N(\Delta \leq 0.08 \text{ AU})$	50	47	36	52	51	44	37	47	49	61
$N(\Delta \leq 0.06 \text{ AU})$	35	36	29	40	47	33	29	31	43	49
$N(\Delta \leq 0.05 \text{ AU})$	28	22	31	31	18	20	26	27	27	34

Table 2 – Frequencies of  $i'$  for periodic comets. The intervals considered are identified by their upperbound.

Upperbound of $i'$	38°9	56°3	70°5	83°6	96°4	109°5	123°7	141°1	180°
$N(\text{MS})$	41	5	9	10	6	1	5	7	6
$N(\text{PC})$	132	24	16	18	14	5	9	11	21
$N(\text{DC})$	56	11	15	12	7	2	4	2	5

# NEMO—Near Real-Time Monitoring System

Esther Drolshagen<sup>1\*</sup>, Theresa Ott<sup>1\*</sup>,  
Detlef Koschny<sup>2,3</sup>, Gerhard Drolshagen<sup>1</sup>, and Björn Poppe<sup>1</sup>

<sup>1</sup> University of Oldenburg, Germany

esther.drolshagen@uni-oldenburg.de, theresa.ott@uni-oldenburg.de

<sup>2</sup> ESA/ESTEC, Noordwijk, the Netherlands

<sup>3</sup> Chair of Astronautics, TU Munich, Germany

Several ground-based stations and networks exist to monitor meteors and fireballs optically or by radar. At present, there is no monitoring system for small near-Earth objects that systematically analyses the available data and combines the individual pieces of available information. The aim of this project is to develop such a system to monitor the impact of fireballs on a global scale. This can only be achieved by combining data from different types of observations. There are very few meteor detection methods as well as different types of data which can offer information on fireballs. We are preparing to combine diverse data sources, as, e.g., the CTBTO (Comprehensive Nuclear Test Ban Treaty Organization) infrasound data which monitors most of the Earth atmosphere and contains world-wide information on atmospheric explosions. Fireball sensors from space as well as lightning sensors are also being tested as a possible data source. Furthermore, social media is proposed to be a source for global information. Debris re-entry data will be taken into consideration, also. A significant part of data is already present in the different fireball networks. These data contain a large amount of scientific information. A network unifying this information can multiply the scientific output. There are already various cooperation being prepared. The overall goal of this project is to develop a method to combine all available fireball data in a more automated manner. Therefore, a global near real-time fireball monitoring might be achieved with NEMO (NEar real-time MOonitoring system). The final aim is a better understanding of the fluxes and characteristics of impacting objects in the size range of some tens of centimeters to a few meters.

## 1 Introduction

Roughly 54 tons of extra-terrestrial material is statistically accumulated by the Earth each day. Most of this material can be classified as either interplanetary dust, meteoroids, or asteroids (Drolshagen et al., 2017). The larger objects are called near-Earth objects or NEOs. If the objects are larger than a few millimeters, they produce a light phenomenon when entering the Earth’s atmosphere called a meteor. If the object is large enough, it can cause a bright fireball which can be quite spectacular. Several ground-based networks exist to monitor meteors and fireballs optically or by radar.

At present, there is no monitoring system for small NEOs that systematically analyzes the available data and combines the individual pieces of information. The aim of this project is to develop such a system to monitor the impact of fireballs on a global scale. This can only be achieved by combining data from different types of observations, because most of them are locally confined. All these observations could be combined to one “mosaic”, allowing a global coverage. This is a goal we are working towards with NEMO, the NEar real-time MOonitoring system for fireballs.

The final aim of this project is a better understanding of the fluxes and characteristics of impacting objects in the size range of some tens of centimeters to a few meters. Objects in this size range are too big and therefore

too infrequent to be regularly seen in regional meteor monitors and too small to be detected in space by ongoing NEO surveys (where the lower threshold is typically some tens of meters).

The NEMO system will combine data from sources like social media, which give very fast alerts for events (Section 3.1). It will have more detailed information obtained by various meteor networks, providing in most cases fast scientific information for the events, e.g., the brightness of the fireball and the velocity of the corresponding meteoroid or asteroid. This is described more closely in Section 3.2. Moreover, different sources not directly related to fireball research can and will be used for this system, like infrasound data and data from weather satellites. This will be used to supplement earlier information on events (Sections 3.3 and 3.4, respectively). An additional point of interest is the origin of the object which caused an event. Different sources will be used to differentiate between objects of natural origin and re-entries of man-made objects. This will be described more detailed in Section 3.5.

## 2 Motivation

The current situation is as follows. There is a fireball event which causes public attention. People, who are spread over a sometimes very large area, have seen this

\*These authors contributed equally to this work.

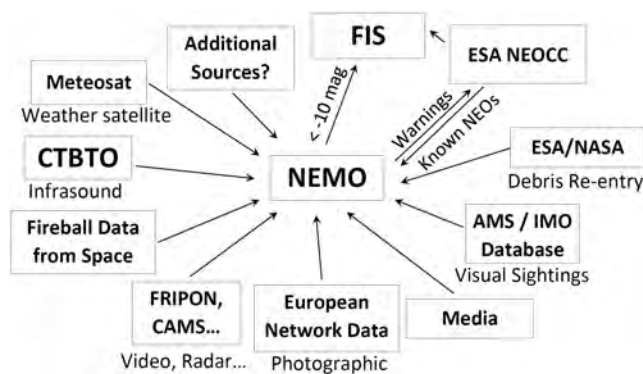


Figure 1 – Architectural diagram of NEMO: FIS—Fireball Information System of SSA-NEO (Space Situational Awareness-NEO); NEOCC—NEO Coordination Center, at ESRIN (European Space Research Institute) in Frascati, Italy; AMS/IMO—American Meteor Society/International Meteor Organization; CTBTO—Comprehensive Nuclear Test Ban Treaty Organization; FRIPON—Fireball Recovery and InterPlanetary Observation Network; CAMS—Cameras for All-sky Meteor Surveillance.

event and it is trending in social media. Those bright events are usually observed and analyzed by fireball and meteor networks. The output is a lot of scientific data. However, since there are different networks covering all areas of Europe or even around the world it is not clear which networks have detected the event. That is why, in the moment, it is difficult for officials, e.g., for ESA, to react to queries from the public or journalists regarding such a fireball event.

To change this is the goal of NEMO. The system should include information about the events which cause public attention in near real-time from all possible sources. It will give a short summary, referring to all networks that have seen the fireball and citing their scientific information. There will be a coordination with FIS—the SSA-NEO (Space Situational Awareness-NEO) Fireball Information System, which is in preparation at NEOCC, the NEO Coordination Center, at ESRIN (European Space Research Institute) in Frascati, Italy. FIS should in turn include all events with a magnitude brighter than  $-10$ . An architectural diagram of NEMO including potential contributors is shown in Figure 1.

### 3 Planned data sources

The goal of NEMO is to combine all available information of fireball events. To do so, a large amount of different data sources will be used, from social media to fireball networks, up to weather satellites. Social media offer very fast and, depending on the population density, world-wide information. Output from meteor and fireball networks gives scientific details about the event. More unconventional sources like weather satellites or the CTBTO network (Comprehensive Nuclear Test Ban Treaty Organization) can provide additional information. Moreover, those fireball data and detection methods will be studied in more detail.

### 3.1 Social media

Nowadays, social media are some of the most important sources of information. They are fast, world-wide, and, in most cases, open to the public. This applies for nearly all topics of our lives and hence also for fireball events. Shooting stars are a phenomenon known by most members of the public. Very bright fireballs cause public attention. They scare, frighten, astound, surprise, or amaze people. That is why, for fireballs, social media are a particularly good source of information. In some cases, there are photographs or even videos from an event online. Platforms like Twitter, Facebook, Instagram, and YouTube contain a lot of posts if there was a fireball event.

Moreover, witness reports are numerous after a fireball appearance over a densely populated area. These witness reports are mainly collected by the AMS/IMO (American Meteor Society/International Meteor Organization) and provide information very fast regarding the time, location, and direction of an event. For more information in this regard see, e.g., Hankey and Perlerin (2014).

NEMO is not limited to reports by the general public; news coverage and journals are an additional source. DLR Berlin (Deutsches Zentrum für Luft- und Raumfahrt), under contract with ESA, will be a data source for ESA’s Fireball Information System and can also provide input to NEMO.

To conclude, social media and witness reports are very fast. Using this will make it possible to have near world-wide and near real-time information on events. Nevertheless, we would like to point out that the output is dependent on the observing public. The sightings are highly correlated to the location of the event as well as to the time it appeared.

### 3.2 Meteor and fireball networks

A significant part of data is already present in the different fireball networks. These data contain a large amount of scientific details. A network unifying this information can multiply the scientific output. There are already various cooperations being prepared, e.g. of NEMO with the fireball-detecting FRIPON (Fireball Recovery and InterPlanetary Observation Network), covering the sky of France, extending into different countries in Europe. For more information about FRIPON see, e.g., Colas et al. (2014).

One interesting example of a European fireball is the fireball over France on September 10, 2017, at about 19<sup>h</sup>29<sup>m</sup> UTC. It was observed by people in the east-west region of France as well as near the French borders of Germany and Switzerland. Unfortunately, there were no eyewitness videos. However, the FRIPON cameras caught this fireball and the team was able to analyze it. This way, its magnitude is known as well as the velocity and trajectory of the corresponding meteoroid.

### 3.3 Infrasound data

The CTBTO (Comprehensive Nuclear Test Ban Treaty Organization) operates infrasound stations all over the world with the aim to monitor most of the Earth's atmosphere. Infrasound data have no spatial limitations and contain world-wide information on fireballs during day and night.

It has already been shown that it is possible to detect fireballs using this infrasound data. The Chelyabinsk superbolide, for example, was detected by 20 infrasonic stations, enabling the determination of its location and explosive energy (Le Pichon et al., 2013; Brown et al., 2013; Pilger et al., 2015). Furthermore, the CTBTO infrasound data recorded multiple bright fireballs all over the world, e.g., the Bangkok fireball in 2015 (Caudron et al., 2016) or the Indonesian fireball in 2009 (Silber et al., 2011). Additionally, there have already been more than 70 NEO impacts identified from infrasound data until the year 2017 (Gi and Brown, 2018).

The CTBTO measurements of fireball events can be combined with results from other fireball sources, to enhance the amount of knowledge of the event as well as of the detection method itself.

### 3.4 Weather satellites

It has been demonstrated that it is possible to detect fireballs with meteorological satellites. The 2008 TC<sub>3</sub> entry was recorded by the Meteosat satellites operated by EUMETSAT (the European Organization for the Exploration of Meteorological Satellites) (Borovička and Charvát, 2009). From the data, Borovička and Charvát could confirm the trajectory of the asteroid in the atmosphere. In 2013, the Chelyabinsk superbolide was recorded by different satellites, geostationary and low-Earth-orbiting (Miller et al., 2013). Miller et al. were able to combine different observations of the fireball from the Meteosat satellites, from the DMSP F-16 (Defense Meteorological Satellite Program), as well as from the MTSAT (Multifunctional Transport Satellites). By using the parallax effect, they were able to determine the trajectory of the impacting asteroid.

The idea is to use Meteosat data for the NEMO system if an event was already observed. This way ground-based observations and their results can be confirmed and the knowledge about detecting fireballs using meteorological data can be enhanced.

### 3.5 Re-entries

For every bright fireball, it will be investigated if it was caused by a natural or a man-made object. This will be done in cooperation with the Aerospace database of upcoming and recent re-entries and ESAs re-entry predictions. Moreover, NEMO will keep an eye on upcoming close approaches of known NEOs from the NEOCC.

## 4 Conclusions

In this work, we introduce NEMO, the NEar real-time MOonitoring system. It will systematically analyse all available data of bright fireball events in near-real time on a global scale. To do so, NEMO will collect the data from different data sources combining all information yielding the most amount of knowledge.

The near-real time information can be achieved by using social media as well as the witness report database AMS/IMO. The scientific information about a fireball and corresponding meteoroid or asteroid will be obtained from various meteor networks, which are spread all over the world.

Furthermore, different unconventional sources will be used for this system, like the CTBTO infrasound data or the Meteosat weather satellites. On the one hand, these data will be used to get more, respectively, confirmed information about single events. On the other hand, these techniques will be investigated more systematically. There are more possible unconventional data sources under investigation at the moment, like lightning sensors or rain radars. Their potential to detect fireballs remains to be seen.

Additionally, for every event the question will be answered if the object was a meteoroid or asteroid of natural origin or if it was a re-entering piece of debris of a man-made object.

By combination of all known information, the largest amount of knowledge can be reached.

The goal of this system is to provide information on objects which regularly impact the Earth's atmosphere, are too small to be detected by NEO surveys, but still cause bright fireballs. This will enhance the knowledge about the fluxes and characteristics of objects in space which have a size of some tens of centimeters to a few meters. Hence, the aim is to close the gap between large meteoroids and small asteroids.

## Acknowledgements

We thank the European Space Agency and the University of Oldenburg for funding this project.

We also thank all networks and projects that have already agreed to cooperate with this endeavor.

## References

- Borovička J. and Charvát Z. (2009). "Meteosat observation of the atmospheric entry of 2008 TC<sub>3</sub> over Sudan and the associated dust cloud". *Astronomy & Astrophysics*, **507**, 1015–1022.
- Brown P. G., Assink J. D., Astiz L., Blaauw R., Boslough M. B., Borovička J., Brachet N., Brown

- D., Campbell-Brown M., Ceranna L., Cooke, de Groot-Hedlin C., Drob D. P., Edwards W., Evers L. G., Garces M., Gill J., Hedlin M., Kingery A., Laske G., Le Pichon A., Mialle P., Moser D. E., Saffer A., Silber E., Smets P., Spalding R. E., Spurný P., Tagliaferri E., Uren D., Weryk R. J., Whitaker R., and Krzeminski Z. (2013). “A 500-kiloton airburst over Chelyabinsk and an enhanced hazard from small impactors”. *Nature*, **503**, 238–241.
- Caudron C., Taisne B., Perttu A., Garcés M., Silber E. A., and Mialle P. (2016). “Infrasound and seismic detections associated with the 7 September 2015 Bangkok fireball”. *Geoscience Letters*, **3**, 26.
- Colas F., Zanda B., Bouley S., Vaubaillon J., Vernazza P., Gattacceca J., Marmo C., Audureau Y., Kwon M. K., Maquet L., Rault J.-L., Birlan M., Egal A., Rotaru M., Birnbaum C., Cochard F., and Thizy O. (2014). “The FRIPON and Vigie-Ciel networks”. In Rault J.-L. and Roggemans P., editors, *Proceedings of the International Meteor Conference*, Giron, France, 18-21 September 2014. IMO, pages 34–38.
- Drolshagen G., Koschny D., Drolshagen S., Kretschmer J., and Poppe B. (2017) “Mass accumulation of Earth from interplanetary dust, meteoroids, asteroids, and comets”. *Planetary and Space Science*, **143**, 21–27.
- Gi N. and Brown P. (2018) “Refinement of bolide characteristics from infrasound measurements”. *Planetary and Space Science*, **143**, 169–181.
- Hankey M. and Perlerin V. (2014). “IMO Fireball Reports”. In Rault J.-L. and Roggemans P., editors, *Proceedings of the International Meteor Conference*, Giron, France, 18-21 September 2014. IMO, pages 160–161.
- Le Pichon A., Ceranna L., Pilger C., Mialle P., Brown D., Herry P., and Brachet N. (2013). “The 2013 Russian fireball largest ever detected by CTBTO infrasound sensors”. *Geophysical Research Letters*, **40**, 3732–3737.
- Miller S. D., Straka W. C., Bachmeier A. S., Schmit T. J., Partain P. T., Noh Y.-J. (2013). “Earth-viewing satellite perspectives on the Chelyabinsk meteor event”. *PNAS*, **110** (45), 18092–18097.
- Pilger C., Ceranna L., Ross J. O., Le Pichon A., Mialle P., Garcés M. A. (2013). “CTBT infrasound network performance to detect the 2013 Russian fireball event”. *Geophysical Research Letters*, **42**, 2523–2531.
- Silber E. A., Le Pichon A., and Brown P. G. (2011). “Infrasonic detection of a near-Earth object impact over Indonesia on 8 October 2009”. *Geophysical Research Letters*, **38**, L12201.

# Detection of impacts on giant planets: Another way to determine meter-sized object flux in our Solar System

François Colas, Sylvain Bouley, David Baratoux, Salma MBaye, Marc Delcroix,  
and Jean Luc Dauvergne

IMCCE-Observatoire de Paris, 77 avenue Denfert Rochereau, 75014 Paris, France  
colas@imcce.fr

We know since the impact of Comet D/1993 F2 Shoemaker-Levy 9 on Jupiter that it is possible to view these kind of events on giant planets. The continuous amateur monitoring of Jupiter has led to the discovery of fireballs in Jupiter's atmosphere, providing information not only on Jupiter's gravitational influence but also on the properties and populations of the impactors. We also got data from observations of impacts on the Moon. We explain how it is possible to connect these data with those of fireball networks in order to get a better picture on metric objects. We focus in particular on one of our key observational program at Pic du Midi Observatory.

# Description of the R package MetFns for analysis of visual meteor data

Kristina Veljkovic

Petnica Meteor Group, Serbia  
mackikac@gmail.com

The latest version of the R package METFNS for analysis of visual meteor data is discussed, along with its contents and major improvements. Also, R's SHINY application that complements the package and facilitates its use, is described.

## 1 Introduction

Since its first version in 2014 (Veljkovic and Ivanović, 2014), many improvements and updates were made on the software METFNS for analysis of visual meteor data (Veljkovic and Ivanović, 2015; Veljkovic, 2016). The goal is to make a package containing all functions necessary for the selection of rate and magnitude data, calculation and graphical representation of the population index and the zenithal hourly rate (ZHR). Also, it is intended to optimize population index and ZHR algorithms.

The package METFNS is written in the programming language R. Its main advantages are that it is free and open-source. On the other hand, its main disadvantage is that the user has to have at least basic knowledge of R. To facilitate its use, a simple SHINY application was made which uses the most important functions from the METFNS package.

In Section 2, the contents of the latest version of the package METFNS and major recent improvements are discussed. R's SHINY application is described in Section 3. Conclusions are made in Section 4.

## 2 Latest version of MetFns

The latest version, 3.0.1, of the package METFNS can be downloaded from the R site<sup>1</sup>. There, one can also find the pdf manual of the package, with description of the various functions and examples of their use.

In its present form, the package METFNS contains the following functions and data:

- filter functions for selecting data (by shower code, dates, limiting magnitude, percentage of field-of-view obstruction, radiant elevation, solar longitudes, latitude and longitude, country, ZHR total correction factor, observing site, and observer's name);
- functions for calculating the population index (linear regression method and method of average distance from the limiting magnitude);

- function for calculating the Zenithal Hourly Rate (ZHR);
- plot functions for making graphs of the magnitude distribution, population index, and ZHR;
- functions for calculating the solar longitude corresponding to a given date and the date corresponding to a given solar longitude; and
- the 2015 rate and magnitude data, coordinates of radiant of meteor showers, list of meteor showers, tables for calculation of population index and its standard error.

The latest version of the package is adapted to use rate and magnitude data published on the new IMO site.

An optimal bin size algorithm is used in the calculation of population index and ZHR. A major improvement to the efficiency of the algorithm was implemented in the latest version of the METFNS package. The algorithm can be described in the following way:

1. The optimal bin size algorithm searches for an optimal bin size between minimum bin size and maximum bin size with total number of meteors per bin.
2. If there are not enough meteors, a maximum bin size is used.
3. Only data for which the length of the observing interval is smaller than or equal to the optimal bin are used.

The optimal bin size algorithm, integrated in the population index (method of the average distance from the limiting magnitude) and ZHR calculations, first sorts magnitude and rate data corresponding to the specified shower by solar longitudes, in increasing order, and takes the first block of data of maximum bin size (the so called "block period"). Then, it calculates the cumulative number of meteors in the block period and gradually searches for the data subset that has enough meteors with observing lengths smaller than or equal to the bin size of the block. After finding the optimal

<sup>1</sup><https://CRAN.R-project.org/package=MetFns>.

block period (with optimal bin size), it continues the same procedure with the next block period.

Also in the latest version of the package, the mean solar longitude appearing in the result tables for population index and ZHR is calculated as the weighted mean of the observers' solar longitudes in each bin as follows:

- In the population index table, the mean solar longitude is the mean of the observers' solar longitudes weighted by  $N_{\text{obs}}/C_{\text{obs}}$ , the numbers of meteors seen in each observing interval divided by the total correction factor, which is given by  $C_{\text{obs}} = F_{\text{obs}} r^{6.5 - \text{lm}_{\text{obs}}} / \sin h_{\text{obs}}$ .
- In the ZHR table, the mean solar longitude is the mean of the observers' solar longitudes weighted by  $T_{\text{eff, obs}}/C_{\text{obs}}$ , the effective time of each observing interval divided by the total correction factor.

### 3 Shiny application

The SHINY application of R for analyzing visual meteor data complements the R package METFNS. It calls functions for selecting rate and magnitude data, and calculating and graphically representing the population index and zenithal hourly rate (ZHR). The application facilitates the use of the package. It consists of 6 tabs: **About**, **Data**, **Filter**, **Population index**, **ZHR** and **References**. Currently, the application exists only locally. In the near future, after some more further testing, it will be made publicly available, after publishing it on the `shinyapps.io` site.

The description of the tabs and how to use application are given in the **About** tab.

In the **Data** tab, the user can select rate or magnitude data for the year 2015 and see their structure. This step is important if the user wants to use some other visual meteor data for further calculations. Minimal functional rate data consist of the columns named *Latitude*, *Longitude*, *Start.Date*, *End.Date*, *Sollong*, *Teff*, *P*, *F*, *Lmg*, *Shower*, and *Number*. Minimal magnitude data consist of the columns named *Latitude*, *Longitude*, *Start.Date*, *End.Date*, *Sollong*, *Teff*, *P*, *F*, *Lmg*, *Shower*, *Mag.N6*, *Mag.N5*, *Mag.N4*, *Mag.N3*, *Mag.N2*, *Mag.N1*, *Mag.0*, *Mag.1*, *Mag.2*, *Mag.3*, *Mag.4*, *Mag.5*, *Mag.6*, *Mag.7*, and *Number*.

In the **Filter** tab, the user can select rate or magnitude data using various filters. First, rate and magnitude data must be uploaded. Then, data can be selected by date (providing start and end dates for the selection), shower code, limiting magnitude, percentage of obstruction of field-of-view, and radiant elevation (Figure 1). All the above-mentioned filters are optional, except for the filter by shower, which must be selected.

In the **Population index** tab, the user can calculate the population index on selected magnitude data. The application calls the method of the average distance

The image shows a sidebar panel with the following sections:

- Filter by date (optional)**: Two input fields. The first is labeled "Enter start date in format YYYY-mm-dd HH:MM (e.g. 2015-08-01 23:00)". The second is labeled "Enter end date in format YYYY-mm-dd HH:MM (e.g. 2015-08-20 07:00)".
- Filter by shower (obligatory)**: A dropdown menu labeled "Select the shower code".
- Filter by limiting magnitude (optional)**: A slider labeled "Select the lower and upper magnitude values". The scale ranges from 1 to 8 with tick marks at 1, 1.7, 2.4, 3.1, 3.8, 4.5, 5.2, 5.9, 6.8, 7.3, and 8. The current selection is from 1 to 8.
- Filter by percentage of obstruction of field of view (optional)**: A slider labeled "Select the lower and upper percentage values". The scale ranges from 0 to 90 with tick marks at 0, 9, 18, 27, 36, 45, 54, 63, 72, 81, and 90. The current selection is from 0 to 90.
- Filter by radiant elevation (optional)**: A slider labeled "Select the lower and upper radiant elevation values". The scale ranges from 0 to 90 with tick marks at 0, 9, 18, 27, 36, 45, 54, 63, 72, 81, and 90. The current selection is from 0 to 90. Below the slider is a "Select" button.

Figure 1 – Part of the sidebar panel in the **Filter** tab of the SHINY application for the selection of rate or magnitude data by date, shower code, limiting magnitude, percentage of field-of-view obstruction, and radiant elevation.

from the limiting magnitude. Calculations are performed on magnitude data that were previously filtered in the **Filter** tab. The user specifies dates, shower code, minimum and maximum bin size, and total number of meteors (Figure 2). After computing the table with the values of the population index in each bin, the user can plot the table by choosing the limits and increments on the  $x$  and  $y$  axes (Figure 3). The parameters of the plot function change dynamically after the computation of the population index table.

**Calculate population index**

Enter start date in format YYYY-mm-dd HH:MM (e.g. 2015-08-01 23:00)

Enter end date in format YYYY-mm-dd HH:MM (e.g. 2015-08-20 07:00)

Select the shower code

ACE

Select the minimum and maximum bin size

0.01 1 3

Select number of meteors

1000

Compute

Figure 2 – Part of the sidebar panel in the Population index tab of the SHINY application in which the user specifies dates, shower code, minimum and maximum bin size, and number of meteors for calculating the population index on the filtered magnitude data.

In the ZHR tab, the user can calculate Zenithal Hourly Rates on selected rate data. Calculations are performed on rate data that were previously filtered in the Filter tab. The user specifies dates, shower code, minimum and maximum bin size, and total number of meteors (as in the Population index tab). Also, the user can choose between the options of a constant population index value versus population index values calculated from the data. The value from the shower list table is used as the constant population index value. To select the option of calculating the population index from the data, the population index table must first be calculated in the Population index tab. After computing the table with ZHR values, the user can plot the table by choosing the parameters for the plot function (as in the Population index tab). The limits and increments on the  $x$  and  $y$  axes change dynamically after the computation of the ZHR table. Via the References tab, users can access the pdf manual of the R package METFNS.

## 4 Conclusions

The contents and major improvements of the latest version of the R package METFNS for the analysis of visual meteor data are discussed. The code of the optimal bin

**Plot population index**

First calculate population index, then select the parameters for the plot.

Select the limits on x-axis

0 360

Select increment on x-axis

1

Select the limits on y-axis

1.5 3.5

Select increment on y-axis

0.1

Plot

Figure 3 – Part of the sidebar panel in the Population index tab of the SHINY application in which the user specifies limits and increments on the  $x$  and  $y$  axes of the population index plot.

size algorithm, integrated in the calculation of population index and ZHR, is made much more efficient. In order to facilitate the use of the package, a R SHINY application was created. In the near future, this application will be made publicly available. Hopefully, new users will provide insights how to further improve the package and the application.

## References

Veljkovic K. (2016). “Software for analysis of visual meteor data: R package MetFns—Workshop report”. In Roggemans A. and Roggemans P., editors, *Proceedings of the International Meteor Conference*, Egmond, the Netherlands, 2–5 June 2016. IMO, page 304.

Veljkovic K. and Ivanović I. (2014). “Software for analysis of visual meteor data”. In Rault J.-L. and Roggemans P., editors, *Proceedings of the International Meteor Conference*, Giron, France, 18–21 September 2014. IMO, pages 104–108.

Veljkovic K. and Ivanović I. (2015). “Improvement of software for analysis of visual meteor data”. In Rault J.-L. and Roggemans P., editors, *Proceedings of the International Meteor Conference*, Mistelbach, Austria, 27–30 August 2015. IMO, pages 27–29.

# AMOS orbit software, EDMOND database

Leonard Kornoš, František Ďuriš, and Juraj Tóth

Faculty of Mathematics, Physics and Informatics, Comenius University in Bratislava, Slovakia  
kornos@fmph.uniba.sk

A new version of the program for meteor orbit determination is presented. The parameters of 10 Taurids, recorded and computed by European Fireball Network and independently by AMOS systems, are compared. Also, a perspective of the EDMOND meteor orbit database is outlined.

## 1 Introduction

AMOS is the all-sky system for meteor observation and orbit determination. It has been developed and constructed at the Astronomical and Geophysical Observatory (AGO) of Comenius University in Modra, Slovakia. The AMOS system operates at four stations in Slovakia, two on the Canary Islands, and two in the Atacama Desert in Chile (Tóth et al., 2018; Matlovič et al., 2018). At present, UFO software (SonotaCo, 2009) is used. However, we are developing our own program for astrometric reduction and orbit computation. The program will also be helpful for computations of the meteor database EDMOND (Kornoš et al., 2014).

## 2 Astrometric reduction

At the IMC 2015 in Mistelbach, Austria (Kornoš et al., 2015), the present authors showed that, in comparison to UFOANALYZER (SonotaCo, 2009), for AMOS (All-sky Meteor Orbit System) records, the all-sky astrometric reduction according to Borovička et al. (1995) is more suitable. In their procedure, an exponential formula for zenithal distance is used, and, by an iterative process, 13 reduction constants are searched for. At present, we have developed an algorithm for identifying the reference stars in the field of view (FOV) by iteratively searching the best solution of the procedure of Borovička et al., appropriately changing the  $(x, y)$  scale in the image, and removing the worst-fitted stars. In Figure 1, FOV of AMOS record is depicted with catalogued and measured reference stars. The differences in positions are multiplied by a factor of 50 to make error distribution better visible.

## 3 Meteor trajectory and velocity

In Kornoš et al. (2015), the present authors introduced a new program for meteor orbit computation (MT—Meteor Trajectory). We have developed a new version of the program since then, v3.21, in which additional functions are implemented. The program at present calculates

- meteor atmospheric trajectory;
- heliocentric orbital elements;
- dark flight, if possible (a drag coefficient  $\Gamma$  had been derived by numerical simulation of real frag-

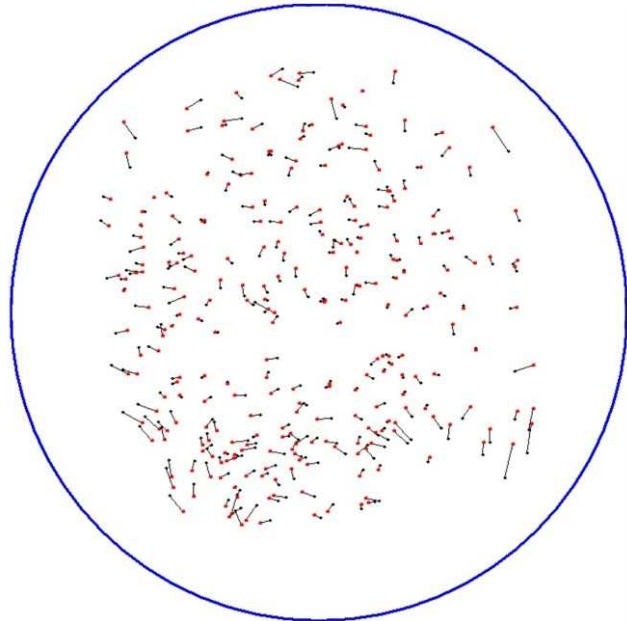


Figure 1 – FOV of AMOS—catalogued and measured reference stars. The differences in the positions are multiplied by a factor of 50 to make the error distribution better visible.

ments of the meteorite Košice. They were performed by our diploma student P. Hrábek);

- impact points;
- error estimation;
- visualization of results.

The program is written in LAZARUS/OBJECT PASCAL and R (The R Project for Statistical Computing) which is used for fitting and minimization processes. The program has various types of output files, e.g., `txt`, `csv`, `kml`, and various plots. It can run in single mode—to compute individual meteors, and in batch/folder mode (currently under testing). It has a graphical interface.

In the program, we have implemented three methods for radiant and atmospheric trajectory calculation.

### 3.1 Ceplecha

The first one is the method described by Ceplecha (1987) which is based on computing a meteor trajectory as the intersection of two planes. Each of these two planes contains one station with the supposed meteor trajectory. The plane is an averaged plane across all the measured

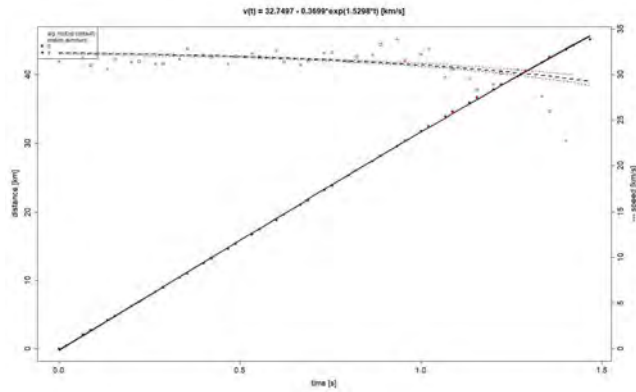


Figure 2 – Atmospheric velocity solution as distance along the trajectory as a function of time,  $s = s(t)$  (solid curve). Its derivation is the velocity,  $v = v(t)$  (dashed curve).

points, where the points do not lie exactly on the line of meteor track. In case of multi-station observation, a weighted mean intersection is computed from all pairs.

### 3.2 Borovička

The method of Borovička (1990), named also straight least squares method, is based on a line of sight from a station. Every measured point on the meteor trajectory is connected to the station by the line of sight and is processed separately. Next,  $D_i$  is defined as the spatial distance of  $i$ -th line of sight from the supposed line of meteor trajectory. Then all the distances  $D_i$  along the meteor track from all stations are minimized by the least squares method.

### 3.3 Velocity solution

Using the two methods mentioned above, the atmospheric velocity is derived after the radiant is known. For a velocity solution along the meteor flight, we use the distance along the trajectory as a function of time,  $s = s(t)$ , according to Jacchia and Whipple (1961), Pecina and Ceplecha (1983), and others. In case of a sufficient number of measured points, we use the exponential formula

$$s = at - be^{ct} \tag{1}$$

to fit the measurement, where the unknown parameters  $a$ ,  $b$ , and  $c$  are searched for by a nonlinear least squares method. If the exponential fit is not found, a linear fit is computed instead (specifically, the median-based linear model is used).

An example of the atmospheric velocity solution is shown in Figure 2. The solid curve represents the fit of the function  $s = s(t)$  according to (1), and its derivative is the velocity,  $v = v(t)$  (dashed curve).

### 3.4 Gural

The third method for meteor atmospheric trajectory calculation was proposed by Gural (2012). Basing himself on the idea of Borovička (1990), Gural suggested to derive the atmospheric trajectory solution together with

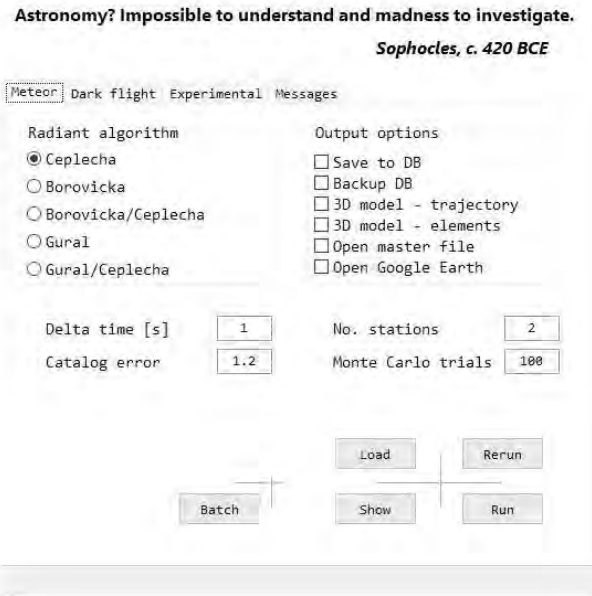


Figure 3 – Graphical interface of the program MT—Meteor Trajectory.

the velocity solution. This means that all unknown parameters are estimated simultaneously. The method iteratively solves the meteor trajectory, time shift among stations, and velocity of the meteor, so that the model fits the measured data best.

### 3.5 Error estimation

After the mean atmospheric trajectory is calculated, instead of the spatial distance of Borovička (1990), the angular distance of every measured point from the mean trajectory is derived. Then, the Gaussian distribution around each measured point in azimuth and zenithal distance ( $A, z$ ) is generated.

### 3.6 Program

The graphical interface of the program is shown in Figure 3. The methods of radiant computations are on the left. *Borovicka* and *Gural* mean that the calculation begins with the starting conditions according to Borovička (1990), and both *Borovicka/Ceplecha* and *Gural/Ceplecha* mean that starting values are computed by the Ceplecha method.

Figure 4 shows the distribution of entry speed as an example of the Monte Carlo simulation. The dispersions of all parameters, as showed in this plot, help us to assess how compact the solution is.

## 4 Results

Finally, we have compared orbital parameters of 10 Taurids observed in 2015 by stations of European Fireball Network (EFN) and independently by AMOS stations. The records of EFN were mostly obtained by the new digital cameras with resolution better than 1' per pixel. These data show high reliability of astrometric solution,

Table 1 – Comparison of the orbits of two Taurids from November 5, 2015, recorded independently by EFN (Spurný et al. 2017) and by AMOS and computed by MT (this work) and UFOORBIT (SonotaCo, 2009).

Stations	$\alpha$	$\delta$	$V_g$ (km/s)	$a$ (AU)	$q$ (AU)	$e$	$i$	$\omega$	$\omega + \Omega$
EFN (23 <sup>h</sup> 12 <sup>m</sup> 01 <sup>s</sup> UT)	54°25	+15°06	29.15	2.260	0.3400	0.8495	5°15	115°48	158°49
	± 0°01	0°00	0.04	0.010	0.0004	0.0009	0°01	0°02	0°02
AGO-KNM (MT)	54°1	+15°1	29.2	2.30	0.342	0.851	4°9	115°2	158°2
	± 0°5	0°2	0.5	0.20	0.005	0.014	0°3	0°8	0°4
AGO-KNM (UFO)	53°7	+14°6	27.10	1.95	0.339	0.805	4°7	114°1	157°1
EFN (20 <sup>h</sup> 53 <sup>m</sup> 04 <sup>s</sup> UT)	53°87	+21°71	29.26	2.076	0.3195	0.8461	2°98	298°63	161°50
	± 0°02	0°01	0.02	0.005	0.0003	0.0004	0°01	0°04	0°04
AGO-KNM-VAZ (MT)	54°3	+21°4	30.9	2.45	0.296	0.879	2°7	299°9	162°8
	± 0°5	0°3	0.6	0.20	0.004	0.013	0°5	0°7	0°4
Reduced	54°2	+21°7	29.9	2.19	0.309	0.859	2°9	299°3	162°2
AGO-KNM-VAZ (UFO)	54°4	+21°2	28.5	1.89	0.323	0.829	2°3	299°2	162°1

Table 2 – Mean differences and their standard deviations of 10 Taurids between records of EFN (Spurný et al., 2017) and AMOS data (this work).

$d\alpha$	$d\delta$ (km/s)	$dV_g$ (AU)	$da$ (AU)	$dq$	$de$	$di$	$d\omega$	$d(\omega + \Omega)$	$dD_{SH}$
0°30	0°50	0.66	0.174	0.009	0.014	0°55	0°61	0°64	0.017
± 0°15	0°50	0.57	0.128	0.006	0.012	0°62	0°39	0°37	0.005

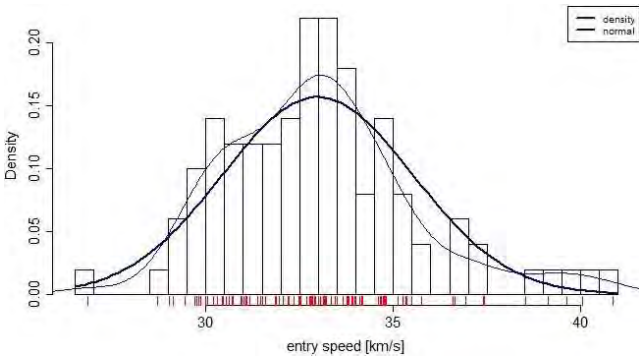


Figure 4 – The distribution of entry speed as an example of the Monte Carlo simulation.

e.g., standard deviation (SD) of lateral deviations of all measured points from the resulting atmospheric trajectory is only 7 m (Spurný et al., 2017), while for AMOS data it is usually several tens of meters. So, the resulting heliocentric orbits of EFN are of high precision and we can consider them as a reference.

In Table 1, the first meteor EN051115\_205304 is an example where the data from EFN (Spurný et al., 2017) and from AMOS stations in Slovakia computed by MT are in good agreement. The atmospheric velocity from AMOS could be derived by the exponential function (1), so the geocentric velocity  $V_g$  is well determined. In case of the second meteor EN051115\_205304, the data from AMOS and from EFN do not agree so well; especially the difference in  $V_g$  is quite large. However, if only the first part of the meteor is considered (without flares), the solution of the geocentric velocity is closer to the EFN solution (in Table 1 labeled as “Reduced”).

A summary of comparison of the all 10 Taurids is in Table 2, where the mean differences in all parameters

with their SD are shown. Also, the value of  $D$ -criterion of Southworth and Hawkins (1963) is presented. The low value of  $D_{SH}$  displays a quite close similarity of orbits obtained independently in EFN and by AMOS. The difference, for example in right ascension, is defined as  $d\alpha = |\alpha_S - \alpha_A|$  for all meteors, where the index “S” means “Spurný” and “A” “AMOS”.

## 5 EDMOND database

The European viDeo Meteor Observation Network is freely accessible at <http://www.daa.fmph.uniba.sk/edmond>. The latest version, 5.03, contains 252 425 meteor orbits till the end of 2015. At present, the orbits are computed by UFOORBIT (SonotaCo, 2009) using \*.csv files and filtered according to Kornoš et al. (2014). However, we would like to compute the next version of the database by our own MT program. The METREC data (Molau, 1999), in principle, could be used, after a conversion program is developed. We will need input files containing positions of the meteor in spherical coordinates frame by frame.

## 6 Conclusions

We have developed an algorithm for identifying the reference stars in the all-sky field of view of AMOS by iteratively finding the best solution of the procedure of Borovička et al. (1995), appropriately changing the  $(x, y)$  scale in the image, and removing the worst fitted stars.

We have introduced a new version of the program (MT 3.21) for meteor orbit determination, in which also new functions are implemented. Main advantages of the program are an exponential velocity solution (for longer

meteors), so a deceleration could be detected, and the computation of uncertainty of parameters by a Monte Carlo simulation. MT could be an independent tool for orbit determination. In future, we plan to calculate a new version of the EDMOND database using the new version of the MT program.

## Acknowledgments

This work was supported by the Slovak Research and Development Agency under the Contract Nos. APVV-0516-10 and APVV-0517-12, and by the Slovak Grant Agency for Science, Grant No. VEGA 1/0225/14.

## References

- Borovička J. (1990). “The comparison of two methods of determining meteor trajectories from photographs”. *Bull. Astron. Inst. Czechosl.*, **41**, 391–396.
- Borovička J., Spurný P., and Keclíková J. (1995). “A new positional astrometric method for all-sky cameras”. *Astron. Astrophys. Suppl. Ser.*, **112**, 173–178.
- Ceplecha Z. (1987). “Geometric, dynamic, orbital and photometric data on meteoroids from photographic fireball networks”. *Bull. Astron. Inst. Czechosl.*, **38**, 222–234.
- Gural P. S. (2012). “A new method of meteor trajectory determination applied to multiple unsynchronized video cameras”. *Meteorit. Planet. Sci.*, **47**, 1405–1418.
- Jacchia L. G. and Whipple F. L. (1961) “Precision orbits of 413 photographic meteors”. *Smithson. Contrib. Astrophys.*, **4**, 97–129.
- Kornoš L., Koukal J., Piffi R., and Tóth J. (2014). “EDMOND meteor database”. In Gyssens M., Roggemans P., and Žołądek P., editors, *Proceedings of the International Meteor Conference*, Poznań, Poland, 22–25 August 2013. IMO, pages 23–25.
- Kornoš L., Ďuriš F., and Tóth J. (2015). “Astrometric precision and orbit determination by AMOS”. In Rault J.-L. and Roggemans P., editors, *Proceedings of the International Meteor Conference*, Mistelbach, Austria, 27–30 August 2015. IMO, pages 105–108.
- Matlovič P., Tóth J., Rudawska R., and Kornoš L. (2018). “Study of distinct meteor spectra populations”. In Gyssens M. and Rault J.-L., editors, *Proceedings of the International Meteor Conference*, Petnica, Serbia, 21–24 September 2017. IMO, pages 99–102.
- Molau S. (1999). “The meteor detection software Me-tRec”. In Baggaley W. J. and Porubčan V., editors, *Proceedings of Meteoroids*, Tatranská Lomnica, Slovakia, 17–21 August 1998, pages 131–134.
- Pecina P. and Ceplecha Z. (1983). “New aspects in single-body meteor physics”. *Bull. Astron. Inst. Czechosl.*, **34**, 102–121.
- SonotaCo (2009). “A meteor shower catalog based on video observations in 2007–2008”. *WGN, Journal of the IMO*, **37**, 55–62.
- Southworth R. B. and Hawkins G. S. (1963). “Statistics of meteor streams”. *Smithson. Contrib. Astrophys.*, **7**, 261–285.
- Spurný P., Borovička J., Mucke H., Svoreň J. (2017). “Discovery of a new branch of the Taurid meteoroid stream as a real source of potentially hazardous bodies”. *Astron. Astrophys.*, **605**, A68.
- Tóth J., Kornoš L., Ďuriš F., Zigo P., Kalmančok D., Világi J., Šimon J., Gajdoš Š., Matlovič P., Kubirtová A., and Baláž M. (2018). “AMOS from Slovakia, Canary Islands, and Chile”. In Gyssens M. and Rault J.-L., editors, *Proceedings of the International Meteor Conference*, Petnica, Serbia, 21–24 September 2017. IMO, pages 16–17.

# The Konkoly Meteor Observing Network (KoMON)

Antal Igaz, Gergely Csépany,  
Nándor Opitz, Krisztián Sárnecky, and László L. Kiss

Konkoly Observatory, Research Center for Astronomy and Earth Sciences,  
Hungarian Academy of Sciences, 1121 Budapest, Konkoly Thege Miklós út 15-17  
igaz.antal@csfk.mta.hu and csepany.gergely@csfk.mta.hu

The Konkoly Meteor Observing Network (KoMON) is a meteor camera system being developed at the Konkoly Observatory in Hungary. KoMON aims at recording the brightest fireballs, while having high spatial resolution and high temporal resolution at the same time and operating also at night as a regular meteor observing system. Using this system, we aim at observing the fragmentation processes in high resolution to support meteorite recovery and give insights to the fragmentation process itself. The system is currently in the prototyping phase and we expect to enter engineering mode by 2018.

## 1 Introduction

The Konkoly Observatory of Budapest have received a 3.1 million EUR grant from the Hungarian National Research, Development, and Innovation Office for the four-year project “GINOP-2.3.2-15-2016-00003 Kozmikus hatások és kockázatok” — “Cosmic effects and risks”. This project focuses on the observational study of small bodies in the Solar System that approach the Earth and have the potential of impacting our planet. The planned observational techniques cover a range of astronomical and geophysical approaches, including a network of dedicated digital meteor cameras, an advanced digital ionosonde to complement the optical meteor observations with radar measurements, and a sensitive system for detecting lunar impacts to characterize the impactor population.

Operation of an amateur network started in 2009 based on analogue cameras and the METREC<sup>1</sup> software. Observers got used to the comfort of automatic recording and trajectory measurement but at the same time were faced with difficulties such as oversaturated fireball images and low resolution compared to new digital megapixel cameras. We describe a newly designed automatic hybrid camera solution in this paper. The concept itself actually does not have very new elements. It is rather a combination of ideas and design principles from other meteor camera builders (and recent IMC participants) from all over the world. State of the art electronics and modern software solutions provide a solid base for a separate high-speed and long-exposure camera. The project is currently in the prototyping phase and we expect to be able to report regular observation results soon.

## 2 Goal of KoMON

The usual meteor camera systems are mostly tailored to observe meteors at night and record the path of meteors and meteorites. These systems tend to have problems

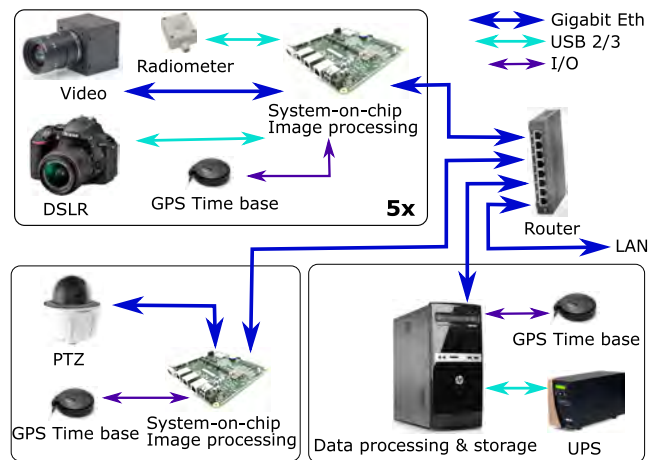


Figure 1 – System diagram: five optical units (video + DSLR), one fast-reaction camera, and a data processing and storage unit.

with bright fireballs at night and most of them are unable to observe fireballs at daylight. The KoMON system aims to overcome the problem of observing bright fireballs by employing a camera and a video camera that is capable of both night- and day-time observations.

## 3 KoMON

The KoMON network will consist of four stations scattered along Hungary. One station will consist of five optical units that cover about 90° of the sky (four looking at the horizon and one to the zenith), which will use Nikon D5500 cameras and a Gigabit Ethernet video cameras as optical devices, controlled by a single-board computer (SBC). The boxes will be connected to each other over Ethernet and the data will be locally stored for each station on dedicated a data storage server, which will processes the video and image data before uploading it to the central data storage. (See also Figure 1.)

Both the camera and the video camera will be equipped with wide field lenses to achieve the 90° field of view. Each station will also have a fast-reaction pan-tilt secu-

<sup>1</sup><http://metrec.org/>.

rity camera oriented upwards that we will observe the fragmentation of the meteors by tracking them after the video cameras have detected the presence of a meteor.

### 3.1 Camera

We use the Nikon D5500 DSLR camera which is equipped with a  $23.5 \times 15.6$  mm CMOS sensor producing 24 Megapixel images. The D5500 will be controlled by the gPhoto library<sup>2</sup>. The lens is a Tokina AT-X 11–20 mm  $f/2.8$  PRO DX.

The DSLR camera will start acquisition as soon as the continuously running video cameras detect a meteor on the sky and signal the DSLR(s) to start the exposure. The long exposure enables us to modulate the meteor track with an LC-shutter that helps to precisely measure the speed of the meteor in the captured image (Bettonvil, 2009).

### 3.2 Video camera

The video cameras in the optical units will detect the meteors by running a modified version of METREC on the continuous video feed. The METREC software may be customized later to match the needs of a meteor observing network where the stations can interoperate with each other.

We plan to use a Gigabit Ethernet video camera that has been tested over the summer of 2017. From these tests we have concluded that it is indeed capable of day- and night-time observation using the built-in gain function of the CMOS sensor.

### 3.3 Fast-reaction unit

The fast-reaction unit will consist of a weather resistant security camera with low light capabilities turned upside down to watch the sky. The video camera is capable of very fast repositioning with up to  $400^\circ/\text{s}$  rotating speed. With the  $32\times$  optical zoom it can narrow the field of view down to approximately  $3^\circ$ , which is small enough to capture a meteor on the sky and follow with it with continuous repositioning.

### 3.4 Radiometer

We plan to record the light curve of the fireballs by using a dual channel radiometer. All KoMON optical units will be equipped with a dual-channel radiometer, which monitors the light levels at a speed of 100–1000 Hz in the low-light and day-light regime. The latter is made possible by adding a sheet of solar filter to one of the light sensors.

## 3.5 Housekeeping

Most of the delicate optical instruments require a stable temperature and humidity to function properly, usually within the  $0\text{--}40^\circ\text{C}$  temperature and  $0\text{--}80\%$  relative humidity regime. We intend to install the KoMON stations in open sites on plains and mountains, thus we have to take care of stabilizing the environmental parameters of the boxes. All boxes will have heat insulation, heating, and liquid CPU coolers refitted to cool the inside of the boxes. In addition to the general heating and cooling, we also need to heat the outlook windows on the boxes to prevent fogging and take care of the excess humidity in the boxes. The humidity will be controlled by heating the air inside, supplemented with silica gel desiccants. The heating and cooling will be operated by a separate embedded micro-controller that takes reading from temperature and humidity sensors in- and outside of each box.

The KoMON network will start operating at four sites: Piskésetető Mountain Station, national parks with dark skies, and geodesic or GSM towers in rural areas, far from the light pollution of the cities.

## 4 Results

We have partial results from the various subsystems of the prospective KoMON network that show the feasibility of this project. Figure 2 shows the photograph of the prototype of the optical unit as of 2017 summer.



Figure 2 – Inner view of the prototype of the planned optical unit, including a video and DSLR camera, cooling, sensors and an SBC.

### 4.1 DSLR camera

We tested the Nikon camera with the Tokina lens in various set-ups. Figure 3 shows one of the early tests when the camera was operated without the LC-shutter at Piskésetető. The cutout shows the details in the center, and hence also the camera's astrophotographic capabilities.

<sup>2</sup><http://www.gphoto.org>.

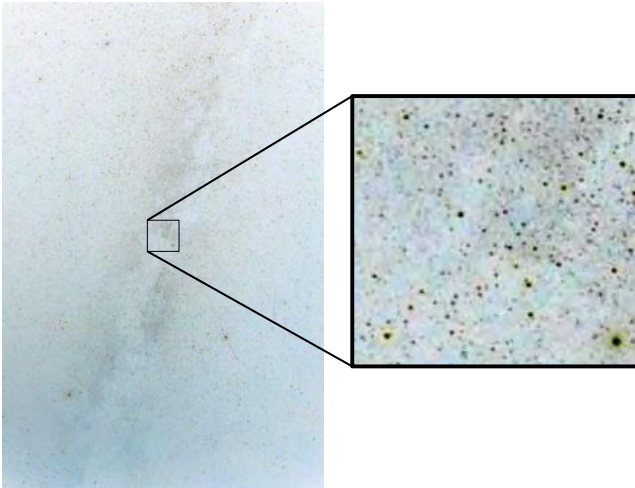


Figure 3 – Field of view and the details in the picture of the Nikon D5500 camera with a Tokina AT-X 11–20 mm  $f/2.8$  PRO DX lens. The image was taken at the Piskésető Mountain Station with 15 seconds of exposure time. The colors are inverted to make it suitable for printing.

## 4.2 Video camera

We have tested the video camera thoroughly over the summer and have also captured a few meteors with it.

Figure 4 shows a meteor captured by the video camera and an analog camera at the same time. We use an analog video camera with the original METREC software to benchmark and calibrate our new system.

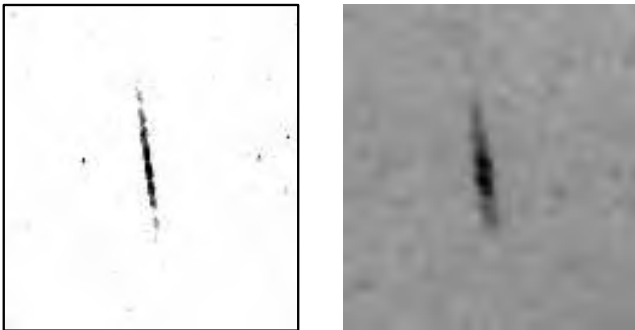


Figure 4 – The same meteor captured by the video camera (left) and an analog video camera (right). The images are not scaled to each other; they are purely for demonstration. The colors are inverted to make them suitable for printing.

## 4.3 Fast-reaction unit

We have tested the fast-reaction video camera to see whether it is indeed capable for astronomical imaging.

Figure 5 shows a frame taken from the video feed of the camera pointed at the north-eastern part of the Pleiads, clearly showing the bright stars. The image covers  $64.9 \times 36.5$  and has a spatial resolution of  $2.03$  per pixel<sup>3</sup>.

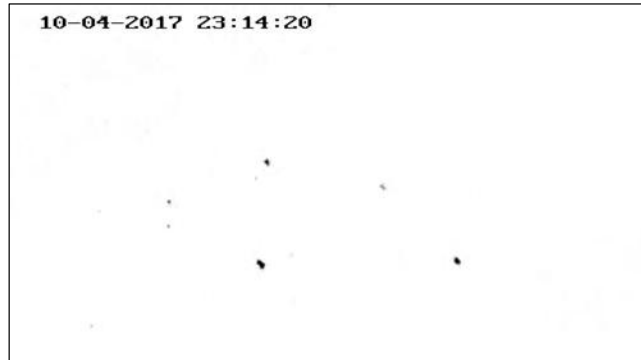


Figure 5 – Field of view of the fast-reaction camera with maximum zoom, pointed at the NE part of Pleiads. The image is a single frame from the video feed with exposure time of approximately 40 ms. The colors are inverted to be suitable for printing.

## 5 Outlook

The assembly of the first optical unit in the final box will take place in late 2017, including a heating system along the optical devices. We plan to benchmark and tune the software to detect meteorites in the coming months with this first optical unit.

The first station will be built at Piskésető in 2018, after the benchmark has succeeded with the first optical unit. We will concentrate on interconnecting the five optical units and the fast-reaction unit into one system in early 2018. Once one station works adequately, we will move on to build and install the three other stations by the end of 2018. The integrated operation of all stations is planned to start in early 2019.

## 6 Conclusions

The Konkoly Meteor Observing Network is in the development phase at Konkoly Observatory. The individual devices that we intend to use for meteor and fireball observation are being successfully evaluated in different scenarios and the prototype optical unit has shown the feasibility of the project. The development continues and we expect to enter into engineering mode by 2018 and scientific mode by 2019.

## Acknowledgements

This project has been supported by Grant GINOP-2.3.2-15-2016-00003 of the National Research, Development and Innovation Office (NKFIH, Hungary) and by the Hungarian Academy of Sciences.

## Reference

- Bettonvil F. (2009). “Digital all-sky cameras V: Liquid crystal optical shutters”. In Andreić Ž. and Kac J., editors, *Proceedings of the International Meteor Conference*, Poreč, Croatia, 24–27 September 2009. IMO, pages 14–18.

<sup>3</sup>The image can be looked up on [astrometry.net](http://nova.astrometry.net) at [http://nova.astrometry.net/user\\_images/1841406](http://nova.astrometry.net/user_images/1841406).

# FRIPIPE: the FRIPON pipeline

J r mie Vaubaillon<sup>1</sup>, Auriane Egal<sup>1</sup>, Min-Kyung Kwon<sup>1</sup>, Chiara Marmo<sup>2</sup>,  
Mirel Birlan<sup>1</sup>, Simon Jeanne<sup>1</sup>, Jean-Louis Rault<sup>3</sup>, Cyril Blanpain<sup>4</sup>,  
Julien Lecubin<sup>4</sup>, Adrien Malgoyre<sup>4</sup>, Fran ois Colas<sup>1</sup>, Sylvain Bouley<sup>2</sup>,  
St phane Caminade<sup>2</sup>, Pierre Vernazza<sup>5</sup>, J r me Gattacceca<sup>6</sup>, and Brigitte Zanda<sup>7</sup>

<sup>1</sup> Institut de M canique C leste et de Calcul des Eph m rides (IMCCE), Observatoire de Paris,  
75014 Paris, France

jeremie.vaubaillon@obspm.fr, auriane.egal@obspm.fr, mirel.birlan@obspm.fr,  
francois.colas@obspm.fr, simon.jeanne@obspm.fr,

<sup>2</sup> G osciences Paris Sud (GEOPS), Universit  Paris Sud, CNRS, Universit  Paris-Saclay,  
91405 Orsay, France

chiara.marmo@u-psud.fr, stephane.caminade@ias.u-psud.fr, sylvain.bouley@gmail.com

<sup>3</sup> International Meteor Organization (IMO), Radio Commission, 91360 Epinay sur Orge, France  
f6agr@orange.fr

<sup>4</sup> OSU Pyth as, CNRS, Universit  dAix-Marseille, 13007 Marseille, France

blanpain@osupytheas.fr, julien.lecubin@osupytheas.fr, adrien.malgoyre@osupytheas.fr

<sup>5</sup> Laboratoire dAstrophysique de Marseille, Universit  dAix-Marseille, 13007 Marseille, France  
pierre.vernazza@lam.fr

<sup>6</sup> Centre Europ en de Recherche et dEnseignement des Gosciences de lEnvironnement  
(CEREGE), CNRS, Aix-en-Provence, France

gattacceca@cerge.fr

<sup>7</sup> Mus um National dHistoire Naturelle, 75005 Paris, France

brigitte.zanda@mnhn.fr

The Fireball Recovery and Interplanetary Observation Network (FRIPON) Project aims to observe fireball and meteorite falls. The goal of the data reduction pipeline is to automatically compute trajectory, orbit, dark flight, and strewn field. Preliminary results are shown, remembering that the Achilles' heel of any such pipeline is ultimately the astrometry and the method used to compute the trajectory. The OpenMeteor Project aims at sharing meteor reduction codes in order to compare the results and save lots of development time in the future. The part of FRIPIPE dealing with the computation of trajectory will be released in early 2018 at the latest.

## 1 Introduction

The FRIPON (Fireball Recovery and Interplanetary Observation Network) project aims to observe fireballs and recover meteorite falls (Colas et al., 2014). For this, 100 cameras are currently being deployed in France. To this day, more than 80 of those are running.

The FRIPON data processing pipeline is called FRIPIPE (FRIPon PipeLine) and aims at automatically ingesting all the scientific data as well as to compute trajectory, orbit, dark flight and strewn field of the possible meteorite fall.

In this paper, we introduce several features of FRIPIPE.

## 2 Why yet another meteor data reduction pipeline?

Several pipeline already exist in the meteor community. They are developed in several languages and are focused on several different aspects of meteor science.

For example, the well known METREC program (Molau, 1999) is widely used to record meteors and performs astrometric reduction. The SonotaCo software suite (UFOCAPTURE, UFOANALYZER, and UFOORBIT) is also more and more widely used to detect meteors and to compute their trajectory and orbit. The Polish Fireball Network is using a custom PYFN PYTHON code. Veljkovic (2016) proposed powerful R code to perform statistical analysis of the IMO VMDB. Atreya and Christou (2007) and Egal et al. (2014) are using the IDL language. Gural (2016) and Brown et al. (2010) are using C, whereas Ceplecha and Spurn y (1987) use FORTRAN. Of course, this short list is not exhaustive.

Although there is open pipeline software, it might be extremely hard (or impossible) to have access to them. Hence, it is very difficult to compare codes and methods. The idea of developing yet another meteor observation reduction software is coming from the need to

- compare;
- test the pipeline with artificial meteors (fakeors; Barentsen, 2009); and

- add and/or contribute to the improvement of meteor pipelines in general.

In order to address these needs, FRIPIPE was designed to be open source and to clearly state the methods used. In particular, so far it implements the Borovička (1990) as well as the Egal et al. (2017) methods.

### 3 FRIPIPE structure, ongoing and future work

In this paper, we describe FRIPIPE in general terms. FRIPIPE is written in PYTHON and makes extensive use of `astropy` and `spiceypy` libraries. It can ingest FRIPON data as well as UFOANALYZER data. In a near future, capabilities to ingest METREC data are foreseen. FRIPIPE creates SPICE frame and instrument kernels for each observation station, and creates *Event*, *Station*, *Observation*, *TrajectorySolver*, and *Trajectory* objects. It outputs 3D trajectory in both text and kml files. The dark flight is computed using the French MeteoFrance data, but capabilities to use public data in either text or grub2 format are foreseen.

FRIPIPE also includes a section that creates artificial meteors (fakeors) in order to test the accuracy reached by the method and the software. The simulation of the disintegration of a meteoroid in the atmosphere is an independent program written in FORTRAN. In the future, ideally, a PYTHON wrapper would be needed to include this feature in the public version of FRIPIPE.

In addition, FRIPIPE include routines to process radio forward scatter observations. This part is still under development, and is so far written in C.

### 4 Some preliminary results

Below are some examples of preliminary results provided by FRIPIPE. It is worth mentioning that the astrometry part still needs to be greatly improved, which is a challenge for any all-sky meteor record. As a consequence, we know that these results will change in the near future, once the astrometry is improved. However, we also know it will not drastically change.

### 5 OpenMeteor project

The need to share methods, codes, and results is very high today. FRIPIPE is of course not the only meteor pipeline software under development. In collaboration with some other meteor enthusiasts (among whom are Daniel Kastinen (IRF), Denis Vida (CMN/UWO), Hadrien Devillepoix, to mention but a few), we intend to release many other meteor-related codes. The goal we aim for with this project is that

- data, methods, and software performances can be directly compared;



Figure 1 – A few examples of trajectory computation with FRIPIPE, visualised with GoogleEarth software.

- any newcomer in the field can save a lot of development time by using, or by being inspired by, already existing code; and
- the future meteor-related pipeline will only be better.

Therefore, in late 2017 or early 2018, some codes will be made publicly available.

### 6 Conclusions

The FRIPIPE FRIPON data reduction software is written in PYTHON and will be released in 2018 at the latest. Any contribution to the OpenMeteor project aiming to improve the software and advancing the science of meteor will of course be most welcome.

### Acknowledgements

FRIPON is funded by ANR grant N.13-BS05-0009-03. FRIPON data are hosted at IDOV+C (Integrated Data and Operation Center). Support for IDOC is provided by CNRS and CNES.

### References

- Atreya P. and Christou A. (2007). “Software for photometric and astrometric reduction of video meteors”. In Bettonvil F. and Kac J., editors, *Proceedings of the International Meteor Conference*, Roden, the Netherlands, 14–17 September 2006. IMO, pages 18–23.
- Barentsen G. (2009). “Astrometric precision requirements for orbit determinations” *Lecture at the International Meteor Conference*, Poreč, Croatia, 24–27 September 2009. <https://www.imo.net/imcs/imc2009/pdf/barentsen-imc2009.pdf>.
- Borovička J. (1990). “The comparison of two methods of determining meteor trajectories from photographs”. *Bull. Astron. Inst. Czechosl.*, **41**, 391–396.

- Brown P., Weryk R. J., Kohut S., Edwards W. N., Krzeminski Z. (2010) “Development of an all-sky video meteor network in Southern Ontario, Canada: the ASGARD System.” *WGN, Journal of the IMO*, **38**, 25–30.
- Cepelcha Z. and Spurný P. (1987). “The Valec fireball and predicted meteorite fall.” In *International Council of Scientific Unions, Middle Atmosphere Program. Handbook for MAP*, volume 25, pages 321–328.
- Colas F., Zanda B., Bouley S., Vaubaillon J., Vernazza P., Gattacceca J., Marmo C., Audureau Y., Kwon M.-K., Maquet L., Rault J.-L., Birlan M., Egal A., Rotaru M., Birnbaum C., Cochard F., and Thizy O. (2014). “The FRIPON and Vigie-Ciel networks”. In Rault J.-L. and Roggemans P., editors, *Proceedings of the International Meteor Conference*, Giron, France, 18–21 September 2014. IMO, pages 34–38.
- Egal A., Vaubaillon J., Colas F., and Atreya P. (2014). “Low dispersion meteor velocity measurements with CABERNET”. In Rault J.-L. and Roggemans P., editors, *Proceedings of the International Meteor Conference*, Giron, France, 18–21 September 2014. IMO, pages 49–51.
- Egal A., Gural P. S., Vaubaillon J., Colas, F., Thuillot W. (2017). “The challenge associated with the robust computation of meteor velocities from video and photographic records”. *Icarus*, **294**, 43–57.
- Gural P. (2016). “A fast meteor detection algorithm”. In Roggemans A. and Roggemans P., editors, *Proceedings of the International Meteor Conference*, Egmond, the Netherlands, 2–5 June 2016. IMO, pages 96–104.
- Molau S.,(1999). “The meteor detection software Met-Rec”. In Baggaley W. J. and Porubčan V., editors, *Proceedings of Meteoroids*, Tatranská Lomnica, Slovakia, 17–21 August 1998, pages 131–134.
- Veljkovic K. (2016). “Software for analysis of visual meteor data: R package MetFns—Workshop report”. In Roggemans A. and Roggemans P., editors, *Proceedings of the International Meteor Conference*, Egmond, the Netherlands, 2–5 June 2016. IMO, page 304.

# New developments in meteor processing algorithms

Peter S. Gural

Gural Software Development, Sterling, Virginia, USA  
pgural@gmail.com

Several new algorithms in meteor image processing and post-detection analysis have been recently developed supporting both the Cameras for All-sky Meteor Surveillance (CAMS) version 2.2 software upgrades and a University of Western Ontario (UWO) faint meteor detection project. These include robust automated meteor track aggregation, velocity estimation improvements, multi-parameter fit trajectory upgrades using the particle swarm optimizer, multi-frame flat field estimation, and a matched filter refinement technique for estimating leading edge points in propagating meteor tracks.

## 1 Introduction

Meteor astronomy continues to dramatically expand in the deployment of electro-optical sensors for visible and near-IR wavelengths, along with the addition of larger focal plane arrays and more sensitive imaging chips. Computer technology has also improved dramatically with faster processing power, multiple cores, graphical processing units (GPUs), and smaller form factors. The added processing capacity has opened up new possibilities for alternative image processing approaches, while at the same time new innovations in algorithms have also recently come online. The focus of this paper is specifically on algorithms, some of which have been enabled by the advances in available processing. The two major areas of the meteor image processing pipeline to be addressed herein are trajectory estimation and faint meteor detection.

The first concerns the formation of trajectories and orbits from multiple cameras positioned at multiple sites. The CAMS system and software (Jenniskens et al., 2011) has been in operation for seven years and was in need of greater automation of those steps requiring a human-in-the-loop to process data, namely confirmation of meteors and space-time coincidence of tracks. The automation was required to maintain efficiency in the face of greater expansion of the CAMS camera networks around the world, provide a centralized processing site and clearinghouse of products, and allow faster dissemination/visualization of results to the contributing users. Most aspects of this automation effort were developed under the auspices of NASA's Frontier Development Lab (FDL) and are reported on separately in the 2017 IMC Proceedings (De Cicco et al., 2018). Herein the focus will be strictly on the algorithm development associated with trajectory aggregation of tracks, more robust velocity estimation via least mean squares, the application of the particle swarm optimizer for improved orbits, along with thoughts on handling deceleration during trajectory estimation.

The second piece of the processing pipeline concerns pushing the detection limits to fainter meteors. The University of Western Ontario (UWO) has recently deployed two pairs of electron-multiplying charge-coupled

devices (EMCCDs), which are very low-light imaging systems, as part of an effort to detect meteors of mass down to that detected by radar. The challenge was to apply the latest image processing techniques to see how faint one could go in optical meteor detection. This requires a more careful application of background clutter suppression and sensitive detection techniques than are normally employed by typical meteor collection system software. Thus, this paper will include a discussion of flat field estimation, equalization, covariance based clutter suppression, matched filter detection, and the refinement of track measurements. The latter are of particular interest for obtaining better track positions by moving away from centroid estimation to a propagating line segment fit via matched filtering.

Section 2 covers the trajectory algorithm improvements made and implemented as part of the CAMS software upgrades and UWO trajectory estimator, while Section 3 covers the faint meteor detection image processing developed for the UWO. Summarization of results and future work are covered in Section 4.

## 2 Trajectory estimation

### 2.1 Aggregation of tracks

To perform trajectory estimation between combinations of two or more cameras or sites, one needs to associate multiple camera tracks together that represent the same meteor. In the case of two stations with one camera track contributing from each site, the pairing association is pretty straightforward using temporal coincidence, basic geometry, and the expected height ranges of meteors. The problem gets more complex when multiple cameras from the same site and two or more sites are contributing, along with the potential for the inclusion of false tracks such as clouds and aircraft. This latter situation is what has been experienced in the CAMS system where for example in one network, 20 cameras have been deployed at each of three sites (CAMS, California, USA). The mix of same and different site tracks sometimes spanning several cameras at one site, plus false alarm contamination and lack of camera timing synchronization on the order of seconds, makes

the space-time combinatorics and logic very challenging. So, until recently, CAMS employed a coordinator analyst to visually review each trajectory triangulation, and try to cull outlier tracks from the desired single-meteor trajectory solution. This was painfully slow during major showers with large numbers of meteor events to examine by hand, but that process did provide a high level of quality control. Note that prior to this point in the pipeline, it was essentially an automated process (except for human confirmation of meteors which was an optional step for smaller networks).

Thus in the past, the CAMS coincidence application combined track “aggregation”, user interactive culling, and trajectory and/or orbit estimation. The software looked for timing coincidence between available tracks from a network of cameras that fell within a user specified timing tolerance. It then applied pairing constraints in convergence angle, begin height, and end height, which were based on simple intersecting planes (IP) geometry (Davidson, 1936; Porter, 1942; Whipple and Jacchia, 1957; Wray, 1967; Ceplecha 1987). If the paired solution failed any of the constraints (one of the pair being the primary track), the secondary track was returned to the pool of potential contributory tracks for later use. Once all potential pairs were examined, the app then visually presented the analyst with the multiple-camera trajectory solution and the analyst had the option to accept, reject, or remove a contributing camera track from the solution. At this stage, the analyst would look for co-linearity between all the contributing tracks in 3D and a similarity in light curve response versus height between cameras. Unfortunately, it was the aggregation step that was presenting too many erroneous solutions to the analyst, usually when contaminating tracks were not culled out in a prior confirmation step.

It was thought that machine learning could automate the meteor or not-a-meteor confirmation step and also help with the aggregation issue, so both areas were investigated under the FDL program. For the latter, it was found, however, that adding some additional geometric constraints was all that was needed to make the coincidence app more robust and eliminate virtually all false trajectories from incorrect track aggregation (see De Cicco, 2017, for confirmation automation via machine learning).

The additional constraints focused on two areas. The first was in the aggregation step itself where the IP pairs that formed a radiant had a velocity estimate calculated along the 3D radiant line, and then constrained by a user selectable minimum velocity, maximum velocity, and consistent (relative) velocity between the independent measurements of the track pair. Next each IP pair’s radiant that passed the first set of constraints, was looked at for consistency in overall radiant direction between all the contributing pairs. Once the secondary track outliers were removed and all valid tracks aggregated, they formed up a trajectory solution as in the past, but via an updated solver (see Section 2.2 for more details).

The second area of constraints came after the formation of an aggregated trajectory solution. That is, rejecting solutions automatically in a fashion similar to how the CAMS human operators made a decision. For example, a rising trajectory was considered not acceptable. Also, the multiple contributing tracks had to be co-linearly aligned in 3D space. This was tested by using a least mean squares line fit and calculating the total root mean square (RMS) deviation of the measurement projections from the trajectory solution path. If outside the RMS constraint, the secondary tracks were all returned to the pool of potential contributors, the primary track tossed, and the process started again on the next primary track in increasing temporal order.

This proved to be a very robust procedure and has allowed the coincidence step of the CAMS pipeline to move towards a fully automated process from photon capture to orbits. False estimation in the automated coincidence version is now operating below 1% and considered an acceptable false alarm rate given the prospect of full hands-off automation. Adding a machine-learning-based meteor confirmation step upstream should help further lower the false alarm rate as fewer contaminating tracks would feed the coincidence aggregator. The CAMS coordinator still has the option to visually review each trajectory solution in lieu of automated coincidence processing.

## 2.2 Trajectory solvers

In version 2.2 of the CAMS software, the trajectory solver has been improved with a number of algorithmic enhancements that underwent development for the UWO. Traditional meteor trajectory solutions are often based on either the intersecting planes method or least mean squares (LMS) line fit solution. The IP takes a given camera’s fan of measurement rays along the meteor track and forms the normal to the best fitting plane of those rays. A second camera’s view provides a second normal, whose cross product with the first yields the radiant direction. In the LMS approach (Borovička 1990), a 3D line is adjusted in position and orientation until the closest point of approach (CPA) distances or angles are minimized for all the measurement rays to the line. In either approach after the radiant is found, a velocity estimate is made along the 3D line as an independent second step.

CAMS had employed a more robust approach based on the multi-parameter fit or MPF (Gural 2012). In this approach, a propagation model is used that is defined by at least 9 unknowns: starting position vector, starting velocity vector, deceleration terms, and timing offsets between all contributing cameras. All the parameters are solved for simultaneously in a coupled sense using a cost function that tries to minimize the angles between the measurement rays and model positions along-track.

The minimization algorithm used in the past had been the amoeba/simplex technique (Nelder and Mead, 1965). This algorithm is a local minimizer and thus requires a

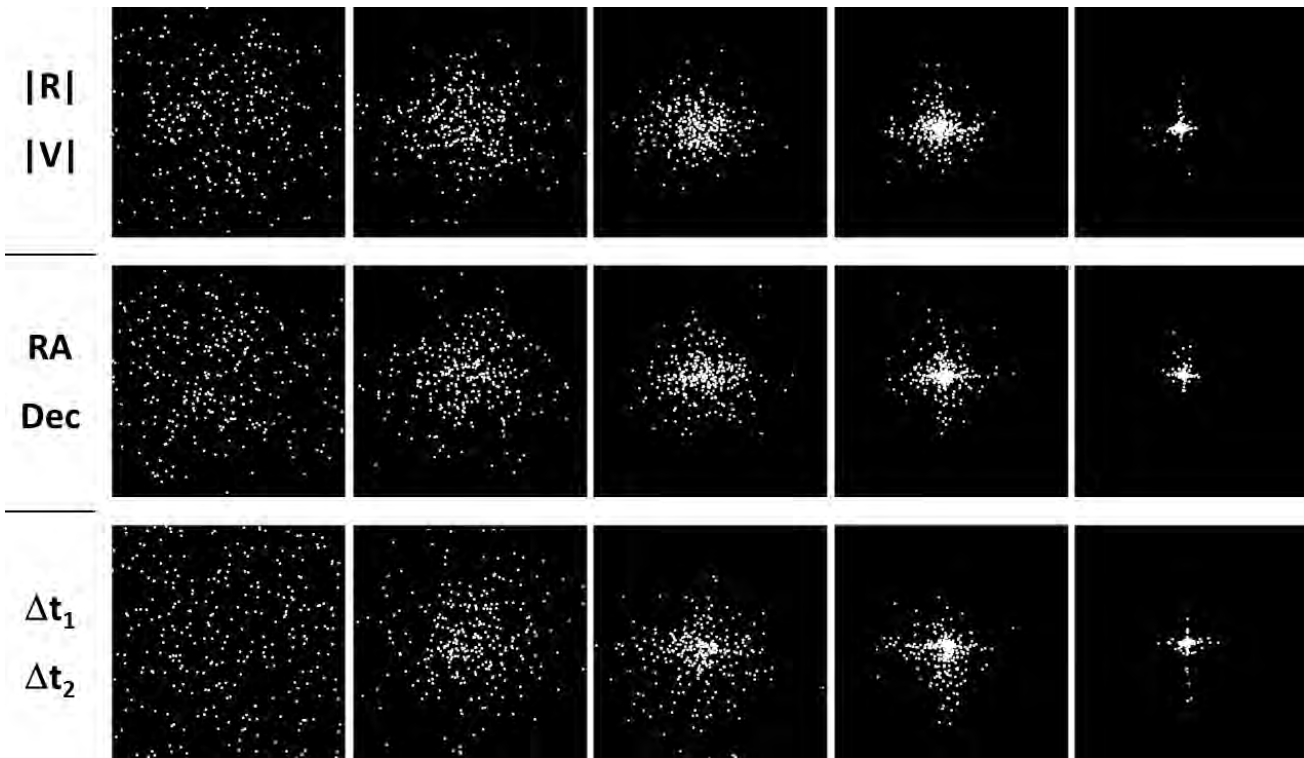


Figure 1 – Particle Swarm Optimizer particle distribution at various iteration stages for range versus speed, radiant right ascension versus declination, and timing offsets  $\Delta t_1$  versus  $\Delta t_2$ .

good first guess on all the parameters to ensure one will find the global minima in the cost function. To accomplish that, a bootstrapping technique was employed as follows:

- line of sight angles' measurements are converted to ECI coordinates;
- IP is applied on all camera pairs and a starting radiant direction is selected based on largest convergence angle;
- LMS 3D line fit algorithm is applied to all measurements to refine the radiant direction;
- an along-track fit is performed to find the velocity magnitude and inter-camera timing offsets;
- a minimizer is run to refine the velocity and deceleration terms (other parameters fixed);
- a minimizer is run to refine position, velocity and timing offset terms (other parameters fixed);
- a minimizer is run to estimate *all* the parameters simultaneously;
- Monte Carlo trials are run with added measurement noise for Keplerian elements' error estimates;
- output products of latitude, longitude, altitude, and velocity versus time for both measurements and model are generated.

Despite the attempt at a good initial guess, it was found on occasion that the simplex could still get caught in a

local minimum, missing the true global minimum solution. Thus, alternative minimizer functions were investigated in a recently published paper associated with meteor velocity estimation (Egal et al., 2017). The authors examined other “local” methods such as Powell’s, conjugate gradients, and quasi-Newton, as well as “global” minimization techniques such as Particle Swarm Optimization (PSO), simulated annealing, and genetic algorithms. The conclusion drawn was that the PSO was the most robust at finding global solutions for trajectories and thus has been recently incorporated into the trajectory estimation modules used by the UWO and CAMS.

The PSO follows the concept of the flocking behavior of birds (Shi and Eberhart, 1998; Tsoulos and Stavrakoudis, 2010; Eslami et al., 2012).

In summary, it is a means by which the multi-dimensional search space is filled with lots of particles possessing the 9+ meteor trajectory parameters with random starting values (particle positions) and random motion vectors associated with each parameter (particle velocities). The particles are allowed to follow complex paths through the multi-dimensional space. They have a tendency to regroup themselves and gravitate towards regions where favorable conditions are met based on a user-provided cost function. But their individual motion is governed by weights that control inertia (reluctance to move), stubbornness (reluctance to change direction of motion), and group pressure (attraction towards the best solution known at any point in the iterative process). As the particles wander around, they pass through many points in the multi-dimensional space and could “fly near” a very favorable minimum while

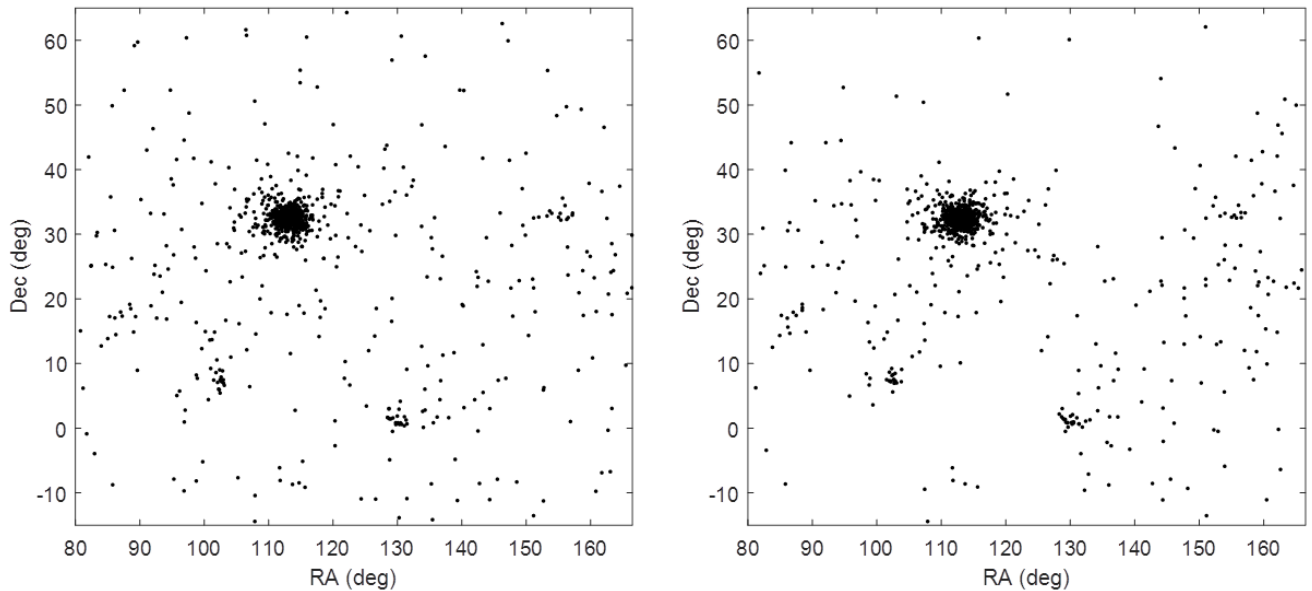


Figure 2 – Radiant results showing improvement due to the trajectory algorithm upgrades of the velocity initial guess, bootstrapping parameter reordering, and the PSO. The radiant spread of the 2012 Geminids has dropped from  $0^\circ.76$  (left) to  $0^\circ.71$  (right) along with fewer outliers. Note the clusters for MON, COM, and HYD as well.

being drawn towards another minimum. The probability of finding a global minimum is still not guaranteed, but is far, far higher than a local minimum search technique. An example of 6 parameter values and how they change as the particles move about towards a convergence stopping criteria of a sample meteor trajectory is shown in Figure 1.

### 2.3 LMS velocity estimate

In the bootstrapping operation of the previous subsection, there is a need for an initial velocity estimate to be calculated after the IP and LMS radiant solutions are found. Given the radiant line, the most common way the velocity is computed is to difference adjacent-in-time measurements along track, and compute an average velocity from the pairings of the short distances over each frame’s time step. This approach tends to add  $\sqrt{2}$  measurement noise when differencing and thus makes for a less robust mean. Instead, a new approach is suggested where (i) the difference is taken with a fixed reference position upstream on the radiant line to avoid the  $\sqrt{2}$  additive noise, and (ii) use an LMS solution of combining multiple camera measurements to get a single velocity fit. To perform this, a constant velocity propagation model is assumed and if desired, can be restricted to apply only to the early portion of the tracks. Note that we are just trying to get a good first guess at the velocity, so deceleration could be ignored at this stage. Since all cameras should witness the same absolute velocity, the problem is overdetermined in the number of equations versus unknowns. The LMS solution for the velocity  $V$  and timing offsets  $\Delta T_k$  ( $k = 1, \dots, N$ ,  $N$  being the number of cameras, is the “camera index” running over all cameras) are as follows:

Define along-track (CPA) distance as  $L_{ik} = |\mathbf{X}_{ik} - \mathbf{X}_{\text{ref}}|$ , where  $\mathbf{X}_{ik}$  is the cartesian vector of 3D position mea-

surement  $i$  for camera  $k$  along the radiant line ( $i = 1, \dots, M_k$ ,  $M_k$  being the number of measurements for camera  $k$ , is the “measurement index” running over all measurements for camera  $k$ ), and  $\mathbf{X}_{\text{ref}}$  is an arbitrary reference 3D position along the radiant line (usually taken near the first measurement point). Fit to the model  $L_{ok} - VT_{ik}$ , where  $L_{ok}$  represents a position offset from the reference position for each camera  $k$ , associated with an unsynchronized timing offset between cameras, and  $T_{ik}$  is the time along-track for measurement  $i$  for camera  $k$ . Then, if  $W_{ik}$  is the weight applied to measurement  $i$  for camera  $k$ ,

$$a = \sum_{k=1}^N \sum_{i=1}^{M_k} W_{ik} L_{ik} T_{ik} - \sum_{k=1}^N \frac{\left( \sum_{i=1}^{M_k} W_{ik} L_{ik} \right) \left( \sum_{i=1}^{M_k} W_{ik} T_{ik} \right)}{\sum_{i=1}^{M_k} W_{ik}}; \quad (1)$$

$$b = \sum_{k=1}^N \sum_{i=1}^{M_k} W_{ik} T_{ik} T_{ik} - \sum_{k=1}^N \frac{\left( \sum_{i=1}^{M_k} W_{ik} T_{ik} \right) \left( \sum_{i=1}^{M_k} W_{ik} T_{ik} \right)}{\sum_{i=1}^{M_k} W_{ik}}; \quad (2)$$

$$V = \frac{a}{b}; \quad (3)$$

$$L_{ok} = \frac{\left( \sum_{i=1}^{M_k} W_{ik} L_{ik} \right) - V \left( \sum_{i=1}^{M_k} W_{ik} T_{ik} \right)}{\sum_{i=1}^{M_k} W_{ik}}; \quad (4)$$

$$\Delta T_k = \frac{L_{ok} - L_{o1}}{V}. \quad (5)$$

To the author’s knowledge, this LMS solution for velocity has not been published before. Combining these improved velocity guesses, rearranging the bootstrapping sequence from the original CAMS implementation in 2010, and adding the PSO minimizer, has resulted in approximately a 7% tightening of stream radiants and less radiant outliers contributing to the sporadic background as seen in Figure 2.

## 2.4 Deceleration

The MPF trajectory solver requires there be defined a propagation model which may or may not include a deceleration component. The original MPF trajectory module (Gural, 2012) had options for a constant velocity, linearly decreasing velocity, quadratic velocity, and an exponential decay model (Whipple and Jacchia, 1957; Jacchia et al., 1967). It has been found that none of these models match very well with the actual measurements of decelerating meteors.

In addition, the exponential model is ill-conditioned in its coefficients, since you can rewrite the position model expression and show there is a linear-in-time term repeating twice when the exponential is Taylor-series expanded—see Equation (7). This flattens the bowl of the minimization cost function and effectively trades value between  $V$  and  $a\kappa$ , making the entry velocity accuracy susceptible to small measurement errors:

$$L = L_o + Vt + ae^{\kappa t}; \quad (6)$$

$$L \approx L_o + Vt + a(1 + \kappa t + \frac{\kappa^2}{2} t^2 + \dots), \quad (7)$$

where  $L$  is the distance along the radiant line (along the fit straight line track),  $L_o$  the distance along the radiant line associated with the timing offset of the camera under consideration, and  $\kappa$  a deceleration term.

Thus, ongoing work concerning trajectory estimation is focused on finding a better conditioned deceleration model or alternative solution approach.

In particular, the following three methods are currently being investigated:

- Use a mathematical model that is consistent with a simplified set of a meteor’s equations of motion (Gritsevich, 2009) relying on a single parameter  $\beta$  to be fit by the MPF. The model will be based on a genetic algorithm solution to many meteor trajectory curves derived from solving the equations of motion. The model will need to demonstrate that it more closely matches actual measurements than the exponential deceleration model.
- Use Denis Vida’s two-stage Monte Carlo approach based on actual measurements, which is currently under development at the UWO.
- Obtain a smooth fit of the estimated along-track positions and use that as the motion model in the MPF. As the MPF solution proceeds, the smooth model fit would need to be updated. This approach utilizes a motion model based on actual measurement behavior rather than forced into a restrictive mathematical model. But is it a stable solution when changing the motion model during the MPF iterations? Should the smooth model be monotonic? And what is the best smoothing algorithm to employ?

## 3 Faint meteor detection

To detect the faintest meteors possible with a visible light sensor, the University of Western Ontario (UWO) obtained four EMCCD cameras with high gain, flat response and low noise. To take advantage of the superb image quality and attempt to see meteors of masses typically seen only by radar, one needs to apply more sophisticated image processing algorithms to process the data close to the noise floor. The next two subsections will discuss the front-end clutter suppression phase of imagery prep followed by a discussion on streak detection with a matched filter.

### 3.1 Clutter suppression

Clutter suppression is a catch-all phrase that encompasses pre-processing the data into a uniform response across the focal plane along with removal of stationary objects as we are looking for propagating streaks. It is comprised of several processing steps:

- *Dark removal*: Generally of no consequence in frame rate video.
- *Flatten*: Equalizes the individual pixel responses via a flat field.
- *Equalize*: Equalizes the global background level between frames.
- *Mean removal*: Subtracts an estimate of the stationary background.
- *Whiten*: Suppresses noisier pixels via second-order noise statistics (covariance).

For the work involving the UWO’s EMCCD, an attempt was made to generate a flat field from multiple frames collected over the course of the night. Originally, a collection was done with the sensor randomly pointed around the sky. This “random”-based flat, generated from star-free background regions, was used as a comparison to a “staring” fixed-mount sensor collection. For the staring sensor, the assumption was made that the stars drift sufficiently so every pixel at some point during the night sees a background sky with no star contamination. To locate star positions quickly, a linked-list gray-level histogram was formulated and implemented so contributing gray levels could be tied back to pixel locations. Gray levels below 5% and above 50% cumulative probability were declared unusable within a given frame (either a pixel was too low in value or was part of a star or the PSF tail of a star). These were removed from further processing for that frame. The remaining pixels had their collective global mean estimated and all pixels scaled (equalized) to a reference frame. These designated background pixels were added to a per-pixel cumulative sum and the corresponding pixel running counter incremented. This was to be used for an average background calculation per pixel

at the end. The resultant average was the flat field and compared very closely with the flat generated from the random-pointing sensor collection.

After the image sequence is flattened, the next step is to estimate a mean. Blocks of 32 frames of imagery are temporally summed and the top four values in time per pixel removed from the sum before the mean is calculated. This eliminated any meteor ghost contamination in the mean that would have suppressed the meteor signal upon the mean's removal. At the same time, a running temporal sum of squared pixel values was also computed, so that a variance per pixel could be estimated. In the same way as the mean, the top four temporal values were removed from the variance calculation. The variance was then used to create a diagonal covariance matrix by assuming the pixel noise was uncorrelated between adjacent pixels. The inverse of the covariance was then applied to the mean removed image, which resulted in a "whitened" image where high variance pixels are effectively suppressed and all pixels have a uniform responsiveness to light. The mean and covariance of a given block of imagery is only applied to the 32 frames in that block.

### 3.2 Matched filter detector

Once the clutter suppression step is completed, the next stage of processing is to perform detection of a meteor across multiple frames. The optimal detector in Gaussian noise is the matched filter (MF) detector (Mohanthy, 1981; Dawson et al., 2016). The MF concept can be simply described as finding an image template that propagates in space and time that would reproduce the actual meteor image. That is, postulate a line segment of some length, orientation, and starting position, convolve it with the imaging system's point spread function (PSF), and try to match that to the actual whitened imagery streak moving across multiple frames.

The advantage of this approach is that it does not require taking the centroid of long line segments to get the measurement positions of the meteor on the focal plane. The PSF convolved line segments align approximately with the leading/trailing edges of each frame's meteor track when the detection metric is high. The disadvantage to matched filtering is a CPU loading issue. It is totally unknown where, when and how fast (starting position, frame, apparent angular speed respectively) a meteor will appear, and thus one has to hypothesize *all* possible motion vectors to find the best match to the propagating meteor track and get the highest maximum-likelihood estimate (MLE). This is often impractical for meteor detection unless the hypothesis set can be reduced in size significantly. For the problem at hand, the options are:

1. Create a brute force hypothesis set of all motion vectors to examine the faint magnitude limit.
2. Use a fixed short vector length that spans multiple velocity ranges for suboptimal detection.

3. Employ a less sensitive detector up front and "cue" the MF with final validation using the MLE.

Another advantage to the MF is that if there is a potential detection from either a brute force search or a cued detection, then the application of an iterative MF refinement algorithm can very closely align the leading edges of the hypothesized track to the imagery and obtain far better measurement pick points per frame than standard centroid calculations. This is what was implemented during the first phase of development and was found to be highly successful at finding leading edge positions as seen in Figure 3.

Options 1 and 2 above for the brute force MF is currently a work in progress, and will require distributing the processing load across a large cluster of processors and breaking up the hypothesis set into manageable chunks. Working within the existing application parameter interface, the plan is to select subsets of the large hypothesis set by defining restricted annuli of motion and eventually fill out the full motion space with many processors running at different inner/outer radii of motion. To further make the processing manageable, each processor will be devoted to only one triplet of frames at a time. This will still be prohibitive in exploring the entire search space of motion vectors for an entire night's worth of imagery, but it will be tried on a limited frame set to determine the faint detection limit for the EMCCD system.

Option 3 has been more compelling as it was the first attempt at cueing the MF refinement by using a CAMS-like detection algorithm up front. To meet a near real-time processing requirement to demonstrate end-to-end capability of video capture to orbit estimation with the EMCCDs, a less computationally intense meteor detection process was applied after the imagery was whitened. The maximum temporal pixel compression (Gural and Segon, 2009; Gural, 2016) was used over blocks of 32 frames to obtain the mean, standard deviation, maxi-

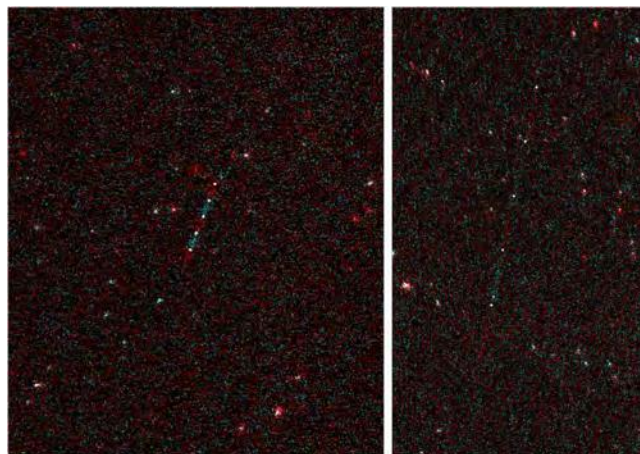


Figure 3 – Faint meteor detection examples from the UWO EMCCD image processing pipeline for short, and medium length meteors showing the leading edge pick points (white plus fiducials). The display uses red and cyan applied to alternating frames.

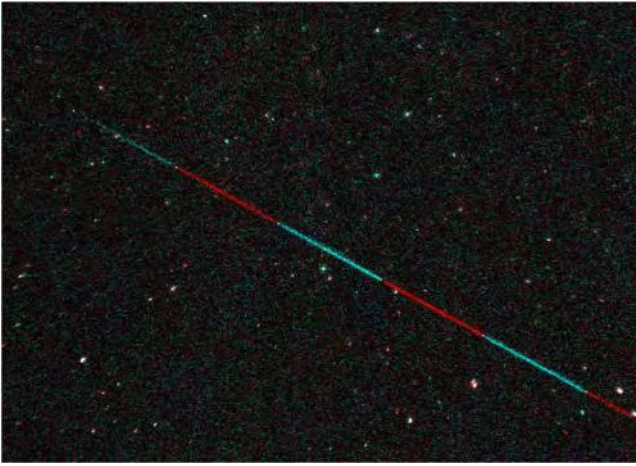


Figure 4 – Meteor detection example for a long length meteor.

mum pixel, and frame number of maximum pixel. This compression technique naturally generates an imagery threshold at approximately two times the standard deviation above the mean (for 32 frames), and operates about four times faster than a standard if statement threshold scheme. The resultant exceedance pixels per frame are fed into a very fast cluster detector and multi-frame tracker (Gural, 2016). To address the fact that the cluster detector is more of a blob detector than a line detector, the imagery is decimated at 2 $\times$ , 4 $\times$ , and 8 $\times$  levels to handle up to the maximum motion of 300 pixels/frame expected in the UWO EMCCD imagery. This processing approach met the initial baseline goal of near real-time pacing of collection and processing with the existing computer hardware on site.

The resultant sequence of measurement centroids from the cluster/tracker cued detection was found to have a very low false alarm rate. Thus the four parameters of 2D position and velocity for every cued event are fed into the MF refinement module. This produces the best fit of the propagating streak immediately after detection is declared. The refinement is an iterative algorithm and utilizes the PSO once again to maximize the MLE metric (cost function) as defined by Equation 8. The algorithm effectively modifies the two position and two velocity coefficients until a best match to the image is obtained. The controlling features that define goodness of fit are the alignment of the endpoints of the line segments as well as the line orientation

$$\text{MLE} = \log \frac{\sum_j [(S_j - \langle S \rangle) R^{-1} T^\tau]^2}{2 \sum_j T R^{-1} T^\tau}, \quad (8)$$

where  $S_j$  is the raw imagery (with  $j$  the frame number),  $\langle S \rangle$  the mean imagery,  $T_j$  the template of streak for frame  $j$ , and  $R$  the covariance matrix. The symbol “ $\tau$ ” indicates transposition, and the summations over  $j$  run over all frames.

This cued approach was found to be very reliable and detect much fainter meteors than expected. See examples in Figures 3 and 4. Meteors also show nice positioning of the leading edge pick points. In rare cases,

there has been a problem where either the optical system warping bends long streaks across the focal plane or there is evidence of deceleration. Both of these types of cases cause the current constant-velocity straight-line-segment propagation assumption to break down. A better motion model for the MF refinement step will be explored in the future.

How faint can one go with a matched filter detector is still under investigation. The trade-off will be whether the timing and processing load requirements justify any further gains in limiting magnitude over what has been achieved thus far, which has already exceeded expectations. There are other cued options that are between the computational load of a brute force MF and the highly efficient cluster detector. One algorithm would be to threshold each pixel above its mean plus a fixed factor times its standard deviation (known from the block compression products) rather than use the compression’s segmentation into max pixels per frame. The threshold could thus be run at a level below the current compression’s effective factor of two. The resultant exceedances would be fed into a Hough transform line detector variant, whose most promising options are the following:

- the phase-coded disk to estimate line orientation of binary pixels around each exceedance pixel (Claude et al., 2004);
- the Hueckel transform to estimate line orientation of gray pixels around each exceedance pixel (Hueckel, 1973);
- spatially localized pixel pair estimate of slope as has been done in the METEORSCAN application (Gural, 1999); and
- a kernel-based Hough transform (Fernandes and Oliveira 2008).

## 4 Conclusions

New algorithms have been developed for meteor trajectory estimation with success in the areas of track aggregation, velocity estimation, and multi-parameter fitting using a global PSO based minimizer. Meteor detection has also moved towards fainter tracks and improved leading-edge position measurements by using clutter suppression with a matched filtering approach for image processing the video frames. Next steps involve focusing on a way to handle deceleration in trajectory estimation more robustly, determining the faint detection limit of the matched filter compared to more standard techniques, and performance of cued detection alternatives feeding the iterative MF refinement.

Several algorithms that can be applied to the meteor processing pipeline have been presented. These have been utilized either at the UWO or embedded into the CAMS processing stream. CAMS version 2.2 is now

available as exportable applications with a continued push towards more automation and a centralized collection and dissemination of data products. With a planned rapid one-day turnaround of results available in the very near future, CAMS image collection sites and their users should quickly see their submission feedback from combined contributors' collective results. Also available are the particle swarm optimizer and trajectory estimation software modules as stand-alone C callable functions.

## 5 Acknowledgement

Support for the CAMS coincidence automation development was made possible by NASA's Frontier Development Lab through a grant with the SETI Institute.

The trajectory estimation improvements and EMCCD detector module development was supported in part by NASA Marshall in partnership with the University of Western Ontario.

The author would like to thank the FDL Long-Period Comets team of Dr. Peter Jenniskens, Andres Plata Stapper, Antonio Ordoñez, Marcelo De Cicco, Susana Zoghbi, Jack Collison, and Siddha Ganju for stimulating discussions on the application of machine learning to CAMS processing.

Also, thanks go out to Dr. Peter Brown and his team at the UWO Meteor Physics Group for mutually beneficial conversations and support on their EMCCD project.

## References

- Borovička J. (1990). "The comparison of two methods of determining meteor trajectories from photographs". *Bull. Astron. Inst. Czechosl.*, **41**, 391–396.
- Ceplecha Z. (1987). "Geometric, dynamic, orbital and photometric data on meteoroids from photographic fireball networks". *Bull. Astron. Inst. Czechosl.*, **38**, 222–234.
- Clode S. P., Zelniker, E. E., Kootsookos P. J., and Clarkson I. V. L. (2004). "A phase coded disk approach to thick curvilinear line detection". In *12th European Signal Processing Conference*, Vienna, Austria, 6–10 September 2004. IEEE, pages 1147–1150.
- Davidson M. (1936). "The computation of the real paths of meteors". *Journal of the British Astronomical Association*, **46**, 292–300.
- Dawson W., Schneider M., and Kamath C. (2016). "Blind detection of ultra-faint streaks with a maximum-likelihood method." In S. Ryan, editor, *Proc. Advanced Maui Optical and Space Surveillance Technologies Conference*, Wailea, Maui, Hawaii, 20–23 September 2016.
- De Cicco M., Zoghbi S., Stapper A. P., Ordonez A. J., Collison J., Gural P. S., Ganju S., Galache J.-L., and Jenniskens P. (2018). "Artificial intelligence techniques applied to automating meteor validation and trajectory quality control to direct the search for long-period comets". In Gyssens M. and Rault J.-L., editors, *Proceedings of the International Meteor Conference*, Petnica, Serbia, 21–24 September 2017. IMO, pages 65–70.
- Egal A., Gural P. S., Vaubaillon J., Colas, F., Thuillot W. (2017). "The challenge associated with the robust computation of meteor velocities from video and photographic records". *Icarus*, **294**, 43–57.
- Eslami M., Shareef H., Khajehzadeh M., and Mohamed A. (2012). "A survey of the state of the art in Particle Swarm Optimization". *Research Journal of Applied Sciences, Engineering, and Technology*, **4** (9), 1181–1197.
- Fernandes L. A. F. and Oliveira M. M. (2008). "Real-time line detection through an improved Hough transform voting scheme". *Pattern Recognition*, **41**, 299–314.
- Gritsevich M. (2009) "Determination of parameters of meteor bodies on flight observational data". *Advances in Space Research*, **44**, 323–334.
- Gural P. (1999). *METEORSCAN Documentation and Users Guide*, version 2.2. Sterling, VA, USA.
- Gural P. S. (2012). "A new method of meteor trajectory determination applied to multiple unsynchronized video cameras". *Meteoritics & Planet. Sci.*, **47**, 1405–1418.
- Gural P. (2016). "A fast meteor detection algorithm". In Roggemans A. and Roggemans P., editors, *Proceedings of the International Meteor Conference*, Egmond, the Netherlands, 2–5 June 2016. IMO, pages 96–104
- Gural P. and Šegon D. (2009). "A new meteor detection processing approach for observations collected by the Croatia Meteor Network (CMN)". *WGN, Journal of the International Meteor Organization*, **37**, 28–32.
- Hueckel M. (1973). "A local visual edge operator which recognizes edges and lines". *Journal of the ACM*, **20**, 634–647.
- Jacchia L., Verniani F., and Briggs R. (1967). "An analysis of the atmospheric trajectories of 413 precisely reduced photographic meteors". *Smithsonian Contributions to Astrophysics*, **10**, 1–139.
- Jenniskens P., Gural P., Dynneson L., Grigsby B., Newman K., Borden M., Koop M., and Holman D. (2011). "CAMS: Cameras for Allsky Meteor-Surveillance to establish minor meteor showers". *Icarus*, **216**, 40–61.

- Mohanty N. C. (1981). “Computer tracking of moving point targets in space”. *IEEE Trans. Pattern Anal. Mach. Intell.*, **3**, 606–611.
- Nelder J. and Mead R. (1965). “A simplex method for function minimization”. *Comput. J.*, **7**, 308–313.
- Porter J. (1942). “The reduction of meteor observations”. *Memoirs Br. Astron. Assoc.*, **34**, 37–64.
- Shi Y. and Eberhart R. (1998). “A modified Particle Swarm Optimizer”. In *Proceedings of the International Conference on Evolutionary Computation*, Anchorage, AK, USA, 4–9 May 1998. IEEE, pages 69–73.
- Tsoulos I. and Stavrakoudis A. (2010). “Enhancing PSO methods for global optimization”. *Applied Mathematical Compututation*, **216**, 2988–3001.
- Whipple F. and Jacchia L. (1957). “Reduction methods for photographic meteor trails”. *Smithsonian Contributions to Astrophysics*, **1**, 183–206.
- Wray J. (1967). *The Computation of Orbits of Doubly Photographed Meteors*. The University of New Mexico Press, pages 5–18.

# Artificial intelligence techniques for automating the CAMS processing pipeline to direct the search for long-period comets

Marcelo De Cicco<sup>1,2,3,4</sup>, Susana Zoghbi<sup>1,8</sup>, Andres P. Stapper<sup>1</sup>, Antonio J. Ordoñez<sup>1</sup>, Jack Collison<sup>1,6</sup>, Peter S. Gural<sup>5</sup>, Siddha Ganju<sup>1,7</sup>, José-Luis Galache<sup>1</sup>, and Peter Jenniskens<sup>1</sup>

<sup>1</sup> SETI Institute, 189 Bernardo Ave, Mountain View, CA 94043, USA  
decicco10@gmail.com, susana.zoghbi@cs.kuleuven.be, andresplatastapper@gmail.com,  
jack10@stanford.edu, siddhaganju@gmail.com,  
jlgalache@gmail.com, and petrus.m.jenniskens@nasa.gov

<sup>2</sup> INMETRO, Divisão de Metrologia em Telecomunicações,  
Av. Nossa Senhora das Graças 50, Duque de Caxias, 25250-020, Brazil

<sup>3</sup> Observatório Nacional, Rua Gal. José Cristino 77, 20921-400, Brazil

<sup>4</sup> Exoss.org, Brazil

<sup>5</sup> Gural Software Development, 351 Samantha Drive, Sterling, VA 20164, USA  
pgural@gmail.com

<sup>6</sup> Stanford University, 450 Serra Mall, Stanford, CA 94305, USA

<sup>7</sup> Deep Vision Inc, 2627 Hanover Street, Palo Alto, CA 94304

<sup>8</sup> Computer Science Department, KU Leuven, Belgium

We describe an effort to automate the CAMS (Cameras for All-sky Meteor Surveillance) data reduction pipeline using artificial intelligence techniques to discriminate meteors from other types of detections and to determine correct solutions during triangulation. The effort will make it possible to have the results from a night of low-light video observations available to the observers the following day. As part of the data reduction pipeline, meteors are classified as real and assigned to showers. Results are presented in such a way that each shower can be identified, and new showers from the occasional encounter with the dust trails of long-period comets can be recognized. The detection of such rare showers will allow to direct the search for long-period comets in dedicated deep surveys.

## 1 Introduction

Long-period comets (abbreviated LPC), due to their potentially large size and fast impact speeds of up to 72 km/s, contribute to the impact hazard on planet Earth along with short-period comets and asteroids. These impacts can severely disrupt the ecosphere and entire human populations. Evidence indicates that the impact of a comet or asteroid with a diameter of about 10 km was responsible for the mass extinction of most species of dinosaurs. Impacts of future threatening asteroids could be mitigated if given sufficient warning time. However, any new long-period comet type on an impact trajectory with the Earth would likely be discovered only 6–12 months before impact, when it becomes visible as the Sun's heat and wind start sublimating its icy surface and ejecting rocky debris.

To provide extra warning time, the orbits of the comets debris could be used by researchers to guide the search for comets while they are still far out, providing us years of extra warning time in case they can be detected along that orbit. Most suitable is debris ejected during the previous return of the comet to the inner Solar System,

which will cause rare aperiodic meteor showers (outbursts). Therefore, detecting those showers requires a continuous and global search (Jenniskens, 1997).

Figure 1 shows how the debris evolve from a meteoroid coma into a meteoroid stream in one revolution as a result of differences in orbital period between grains. The intersection point at the Earth's orbit (the node) of those orbits is not constant. As described by Jenniskens (1997), LPC outbursts are due to gravitational perturbations on the individual meteoroid orbits, causing a periodic displacement of the stream relative to the Earth's orbit, which follows the Sun's reflex motion around the barycenter, with dominating contributions by Jupiter (12-year period) and Saturn (30-year).

Given that the long term hazard posed by long-period comets is statistically comparable to other naturally occurring events (Chapman and Morrison, 1994), it is important to design detection and prevention strategies in order to mitigate potential impacts.

To do so, the night sky needs to be monitored for an extended period of time (approximately 60 years) and from various locations around the globe (Jenniskens et

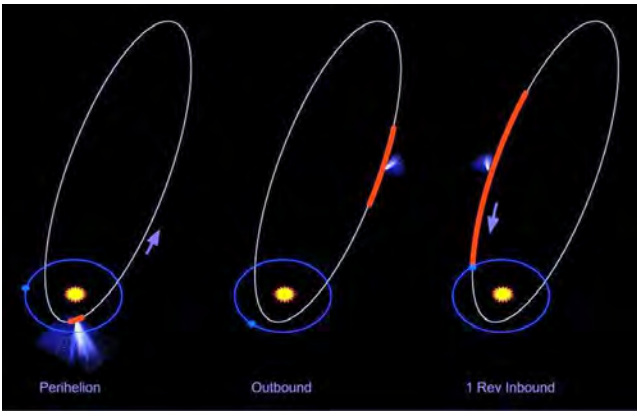


Figure 1 – A diagram showing debris trails formed during LPC travel to the inner Solar System. An LPC outburst happens when the Earth (the blue point) crosses that debris. Created by Peter S. Gural.

al., 1997; Lyytinen and Jenniskens, 2003). Low-light video camera surveillance of the night skies aimed at detecting previously observed and unobserved meteor showers has been demonstrated to produce meteoroid orbits that can be used to identify where in the sky a parent long-period comet may reside when it still many years out.

In this study, we improved the data reduction pipeline for CAMS, the Cameras for All-sky Meteor Surveillance project (Jenniskens et al., 2016), to make it possible to operate this network into the future and create more of such networks globally. To achieve this goal, we set out to improve and automate the classification of meteors from non-meteors using machine learning and deep learning approaches and to improve the data visualization tools to recognize new meteor showers.

## 2 CAMS pipeline automation

The ability of CAMS to successfully identify meteor showers associated with potentially hazardous, long-period comets relies heavily on its time coverage, cadence, and total field-of-view. Meteoroids associated with these comets will appear sporadically in time, creating non-annual showers that last only between one and a few hours. When such showers have not been previously detected, they cannot be predicted. Observing these unpredictable meteor showers thus requires a coordinated, global effort amongst the meteor observing community.

For this effort to proceed efficiently, it is imperative that the data reduction involved be performed in an automated, systematic fashion. The overarching goal of this work is to automate the reduction pipeline for the CAMS network in order to perform the systematic identification and characterization of previously unknown meteor showers. Before this project, the CAMS reduction pipeline required an inordinate amount of human effort to calibrate, confirm, and triangulate meteor orbits. Thus, the major goal with this automation is to provide software tools that completely remove the hu-

man element from the CAMS data reduction from end to end. Ideally, we intend to proceed from image capture to orbit calculation without any human intervention without loss of fidelity for the results.

For this goal, a pipeline was implemented performing the following steps on CAMS data automatically: (1) meteor confirmation on operator end (i.e., on the local machines capturing the data at observing sites); (2) data retrieval; (3) data processing; (4) coincidence; and (5) data visualization.

The proposed automation involves the development of a series of software tools which perform these processes efficiently and cross-platform. Specifically, we developed PYTHON scripts which implement this procedure from end to end. Step 1 provides code that will implement the automated confirmation learned on the observing machines. Step 2 requires automated FTP of detected object data from a server holding incoming data from CAMS sites around the world. Steps 3 and 4 interface with the existing CAMS software to process the incoming data automatically. Step 5 will combine the trajectory solution classifier trained on coincidence data (see Section 4) with the existing CAMS coincidence software to automatically find the best orbital solution for each incoming meteor. Finally, we provide tools for the public to visualize the CAMS meteor shower data on the web in an effort to ensure continued amateur engagement in the project.

## 3 Confirmation automation using Deep Learning

Current practice is for observers to visually inspect the CAMS detections to determine whether or not a detection is a meteor, or a non-meteor. This is a time consuming task that can be automated.

As a proof of concept for confirming meteor candidates using machine learning, we trained a random forest classifier (Breiman, 2001) on a training set of approximately 200 000 CAMS object detection data. This dataset consisted of time-series information for meteors, aircraft, clouds, and other objects identified in CAMS data (see Figure 2). For this classifier, we focused on the time-series of spatial and photometric data for each object (see Figure 2). Given the heterogeneity of the data (i.e., disparate numbers of data points), we opted to mine metrics from these time-series data that describe

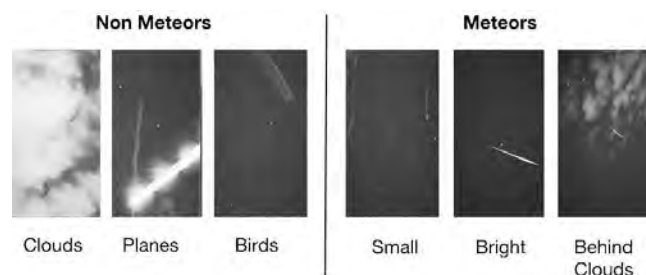


Figure 2 – Non-meteor and meteors images from CAMS.

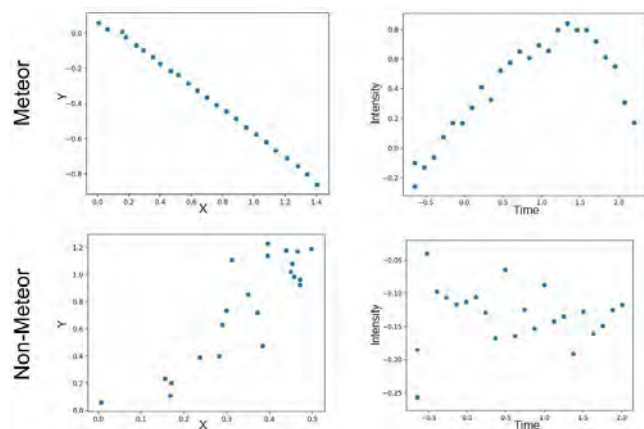


Figure 3 – Mining tracklets for features. In the trajectory graphs, distances are measured in pixels of images (left); light curves show intensity versus time (right).

the trajectories and light curves of each object. For the trajectories, we calculated the coefficient of determination ( $R^2$ ) and residual standard deviation of a best-fit line to the  $XY$  paths in the images, as well as the total distance traveled. Regarding the photometric variations, we extracted several statistical measures of the shape of their light curves including the mean intensity, median absolute deviation (MAD), skew, and kurtosis. We also included in this model two measures of the timescale of the event: the total time observed and the optimal period from a fast Fourier transform on the light curves.

In order to verify that these selected features do provide useful information for an object classifier, we examined the relationship of each feature to the object class. Figure 4 displays an example of such an investigation. This illustration shows that the light curve mean and MAD do seem to correlate with the different object classes.

Following this verification, we trained a Random Forest classifier to perform a binary classification of meteor vs. non-meteor. To account for the class imbalance in this

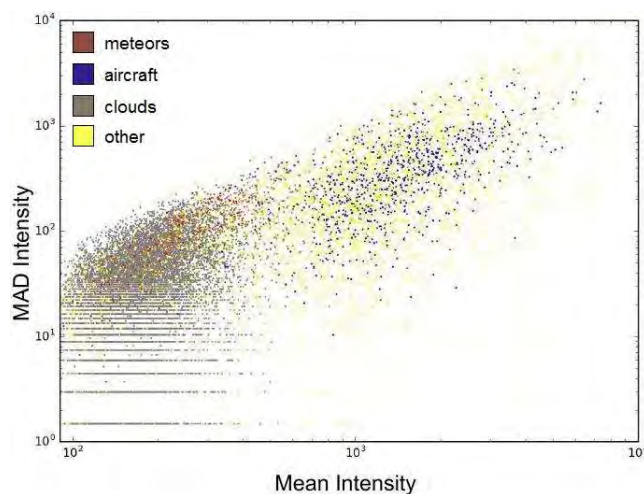


Figure 4 – An example distribution of light curve features (light curve mean and MAD) that appear to display correlations with different objects (maroon, meteor; blue, aircraft; grey, clouds; yellow, other).

training set (i.e., only 3% of the data are true meteors), we employed a class weighting scheme that accounts for the different class frequencies. Without any hyperparameter tuning, we achieved a meteor classification precision and recall on a test set of 90% and 81%, respectively.

Also, a classifier was implemented that takes as input a set of image frames and returns as output a probability score indicating whether or not the frames contain a meteor. Convolutional Neural Networks (CNNs) (Krizhevsky et al., 2012) provide an ideal architecture to tackle this effort since they are responsible for state-of-the-art performance in computer vision tasks such as object classification. Three main functional layers are used in their architecture: the convolutional, pooling (subsampling), and fully-connected layers (see Figure 4).

The convolutional layer consists of small, learnable filters. Each filter corresponds to a set of weights. During the forward pass, we convolve each filter with the input by successively computing dot products between small windows (also known as local receptive fields) of the input and the filter. As we slide the filter across the input, we produce an activation map that gives the responses of that filter at every spatial position. During backpropagation, we learn how to update the weights to minimize the errors the network makes on a given task. Intuitively, each filter learns to detect specific patterns, e.g., edges and color patches. The activation maps are then stacked together and become the input of the next layer.

The pooling layer down-samples the results from the previous layer by using a simple operation (e.g., the maximum or L2 norm) over a small window. The purpose of this pooling operation is to sort or summarize the findings of the activation map. It reveals whether a given feature is found anywhere in a region of the image and it discards the exact positional information. The rationale is that once a feature has been found, its exact location is not as important as its rough location relative to other features. The advantage is that it reduces the number of parameters needed in subsequent layers.

In a fully connected layer, neurons have full connections to all activations in the previous layer. The output is simply computed by a matrix multiplication between the input and the weights, followed by a bias offset. The weights and the biases are learned through the backpropagation algorithm. In a classification task, the output of the last fully connected layer is usually passed through a softmax function to compute the probability of each class, which comprises the network predictions.

A typical CNN architecture is composed of a series of convolutional layers each followed by a pooling layer. Then a couple of fully-connected layers follows which feed into the final output. An example architecture is shown in Figure 5.

The network used in our study used five convolutional layers followed two fully connected layers and a binary

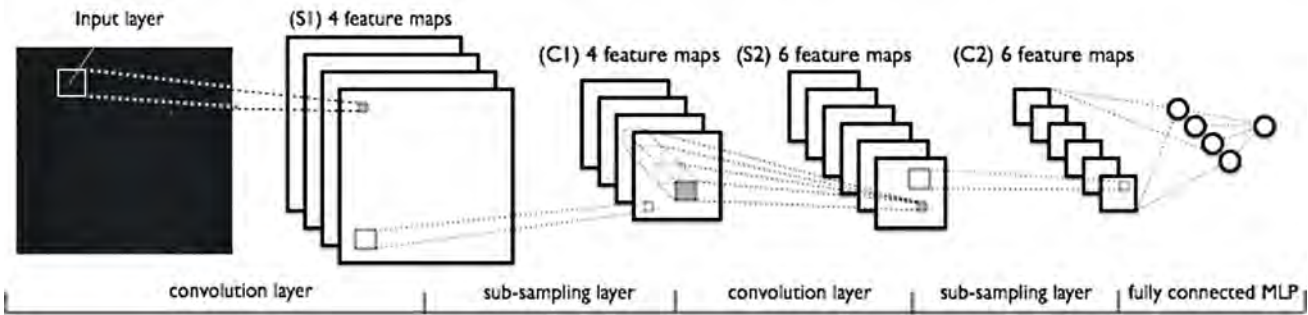


Figure 5 – Schematic diagram of a deep neural network.

softmax classifier. The network needs a large dataset to give reliable results. We performed standard data augmentation techniques on instances of the positive class, such as rotation and flipping.

Our CNN achieves precision and recall scores are 88.3% and 90.3%, respectively. Precision describes the percentage of objects assigned as “meteors” to be actual meteors in a pre-classified data set. The recall describes the percentage of actual meteors in that dataset that were detected as such. That means that a CNN would let about 12% of false detections through, while losing about 10% of all meteors in the data.

In addition, we trained a Long-Short Term Memory (LSTM) network that encodes the light curve tracklets into a latent space, and that learns to predict whether or not the tracklet corresponds to a meteor. The LSTM achieves a precision of 90.0% and a recall of 89.1%. One key advantage of using Deep Learning is that we did not have to hand-engineer the meaningful features from both images and light curves. The models learned these on their own.

The advantage of using a machine learning approach is that it generally requires less training data and computation time when compared with deep learning. On the other hand, manually extracting and engineering features from the data will require more human time pre-training. In the end, we will explore combining this approach with the deep learning results in an ensemble classifying scheme.

## 4 Coincidence

Once a meteor has been confirmed the information from different cameras is used to generate a trajectory for each meteor. Deviations in the video capture can lead to erroneous solutions and improper trajectories and orbits. These deviations can be identified from the light curves, the latitude and longitude and the velocity of the observed meteor measured by each camera.

Current practice is for a data analyst to inspect each meteor trajectory calculated from meteor detections at two or more sites. The data are presented in the form of a light curve, a geographic projection of the trajectory and a side-view of the trajectory. The effort is labor intensive and time consuming and can be automated.

Considering the heterogeneity of the data, using the raw coincidence data in a machine learning classifier presents a significant challenge. As an alternative to this, we propose to proceed similarly as with the machine-learning-based approach for the meteor confirmation.

To summarize the method, we plan to extract singular metrics describing the goodness-of-fit for an individual coincidence solution. The two feature sets most important to this coincidence is the trajectory and light curve resulting from a solution. Thus, we propose to extract some descriptive features from these feature spaces for each object in an effort to define a parameter space conducive to discriminating between good and poor solutions. One example of such a metric is the co linearity of the combined, three-dimensional trajectory of a solution, incorporating data from all cameras that observed the object.

An optimal solution produces high co linearity between the trajectories from different cameras. Another example is the unit-lag autocorrelation of the light curve differences with respect to some reference light curve. A mismatching light curve should exhibit an anomalously high autocorrelation, indicating different light curve structures.

Choosing these methods, we hope to train a machine learning classifier to distinguish good solutions from poor ones. The goal with this project is to implement this classifier in the automated CAMS pipeline. For this, it may be necessary to search through much of the camera combinatorial space when coinciding new datasets. We plan to use a hierarchical method which first scores the goodness of the initial solution using all  $N$  cameras for an object. If this solution is poor, we will then search through the next series combinations using  $N - 1$  cameras to search for an optimal solution. This iterative procedure will be repeated until an optimal solution is reached.

At the time of writing, we only implemented relatively simple classifiers in Coincidence based on the light curve shape (i.e., needing to have an  $F_{\text{skew}}$  shape between 0.05 and 0.95) and maximum errors in geographic positions. Plotting up such data as in Figure 4 showed meteors and non-meteors to separate to better than circa 70%.

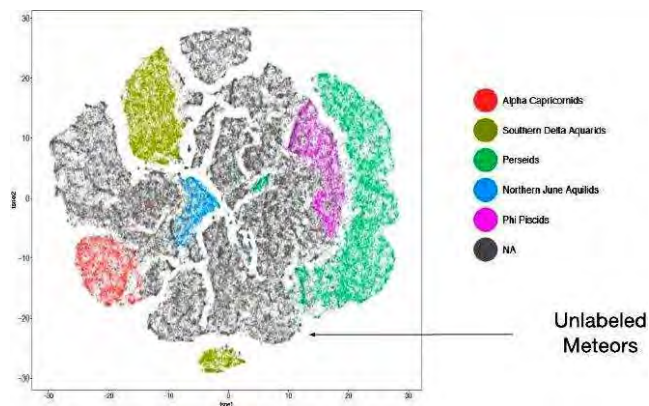


Figure 6 – Graphic showing groupings identified by t-SNE among meteor orbital parameters, compared to groupings (meteor showers) previously identified by visual inspection.

### 5 Data clustering: searching for outbursts and new meteor showers

Once the meteoroid orbits are calculated, the final step is to identify outbursts and new showers. Using a dataset of 122 295 CAMS meteoroid orbits preliminarily classified as showers, we tested the use of unsupervised machine learning (Hodeghatta Rao and Nayak, 2017) to identify newly recognized meteor showers and outbursts.

First, all parameters related to a meteoroid orbit were separated, then clustering methods were tested in order to identify the most effective ones for recognizing showers. The following methods were applied: dimension reduction via PCA and t-Stochastic Neighbor Embedding (t-SNE). We found that the IAU list shower classification was correctly clustered only by t-SNE, as shown in Figure 6.

A number of clusters are readily seen in Figure 6 that might also be as of yet unidentified meteor showers. In the next step, unsupervised machine learning with DBSCAN (density-based spatial clustering of applications with noise) was used to identify these groupings. Figure 7 shows some of the groups identified by DBSCAN. Some previously unidentified groups are indicated. They may represent previously unrecognized meteor showers. Apart from the diffuse groups associated with the main showers and with sporadic sources, there are also some compact clusters in these data. Those are potential meteor outbursts. DBSCAN can be used to identify such outbursts in an automated way.

### 6 Visualization

It is current practise to collect the meteoroid orbits over a period of time, then analyze for the presence of meteor showers. This provides insufficient feed-back to the observers. To keep up efficiency, it is important to present the results in near-real time.

To do so, we developed Java scripts to display the meteor radiant positions of each network. We chose to

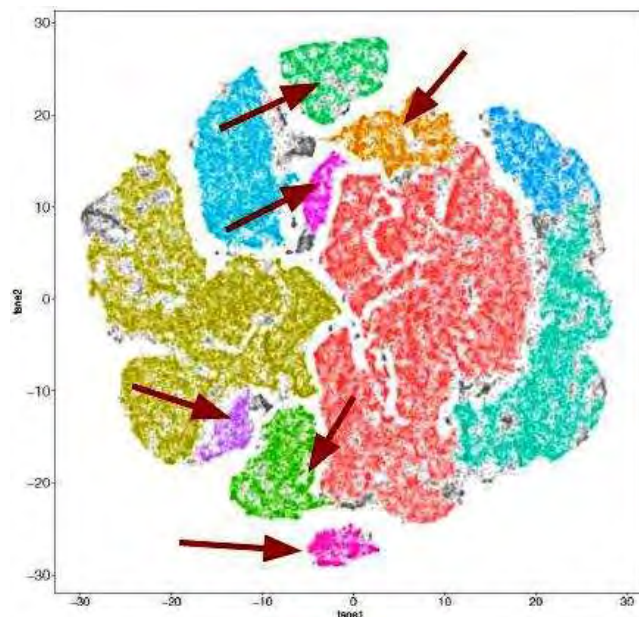


Figure 7 – In addition to established meteor showers, the Unsupervised Machine Learning with DBSCAN method yielded clusters corresponding to possible meteor showers not described before. These clusters are indicated by maroon arrows.

present the data on a sphere<sup>1</sup> that can be rotated so that at each point in time the whole sky can be examined and radiants near the poles are not spread out. The results are presented in Sun-centered ecliptic coordinates in order to provide a constant perspective (direction of Earth motion center of the graph when first displayed). The meteor showers are identified by comparing the new orbits to a look-up table of previously assigned meteor showers. The current look-up table is based on over 900 000 meteoroid orbits detected in all major video-based meteoroid orbit surveys (CAMS, SonotaCo, Edmond, and CMN).

The final display makes it possible to see the active meteor showers in any given night (Figure 8). Results from current data can be compared to past data (2010–2016) of shower-assigned CAMS data. That makes it possible to see unusual meteor shower activity and new showers. Hovering over a point produces the IAU meteor number and clicking on a point brings up that shower in a planetarium program. This new method for visualizing meteor radiants will improve public interest in meteor science, as well as allowing a novel approach to studies of new meteor showers.

### 7 Conclusions

In order to fully automate meteor shower detection and classification from video observations, we applied Artificial Intelligence (AI) methods of Deep Learning and Machine Learning. Deep learning enabled a simple meteor/non-meteor classifier that took as input a set of max-pixel image frames and outputs a probability score that indicated whether or not the frames contained a

<sup>1</sup><http://cams.seti.org/FDL>.

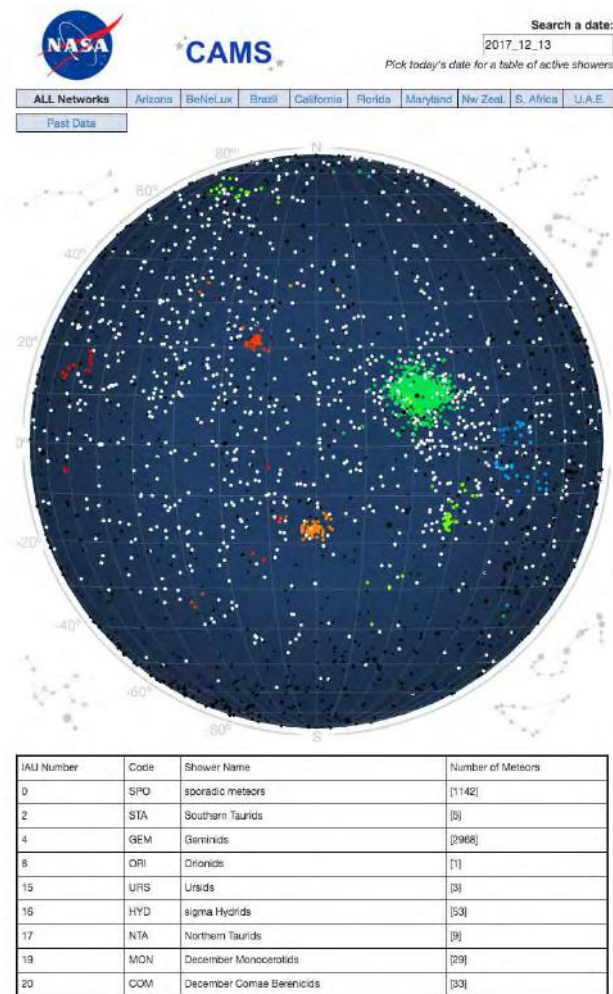


Figure 8 – A web-based interactive graphic showing meteor radiants plotted on the celestial sphere.

meteor. Machine Learning techniques were used to evaluate the triangulated trajectories to determine whether a solution was correct/incorrect. Machine Learning was also used to identify known and previously uncharacterized showers.

In doing so, we are able to identify meteoroid orbits potentially associated with long-period comets that pass close to Earth's orbit. When they were ejected in the previous return, the orbits of the meteoroids should directly trace that of their parent comet. Taking into consideration uncertainties in the orbital parameters of these meteoroids, the search space for these hazardous comets can be narrowed down. These regions can be then probed with dedicated, deep-sky surveys searches to attempt to locate these long-period comets.

And, finally, the interactive web-based tool enables an increase public commitment in meteor shower observations, which will hopefully result in expanded night sky

surveillance coverage. The goal is to identify new, rare and non-episodic meteor showers and their potentially hazardous long-period comets.

## Acknowledgements

This effort was executed as part of NASA's Frontier Development Lab, a research accelerator led by James Parr and Jason Kessler and by the SETI Institute's Bill Diamond. We acknowledge support of the NASA Portal (Robert B. Pittman and Daniel J. Rasky). The effort was sponsored by NASA (Victoria Friedensen and Darlene Weidemann) and by private parties, in particular IBM (Troy Hernandez and Graham Mackintosh) and NVIDIA (Alison Lowndes).

## References

- Breiman L. (2001). "Random forests". *Machine Learning*, **45**, 5–32.
- Chapman C. R. and Morisson D. (1994) "Impacts on the Earth by asteroids and comets: assessing the hazard". *Nature*, **367**, 33–40.
- Hodeghatta Rado U. and Nayak U. (2012). *Business Analytics Using R—A Practical Approach*. Apress, Chapter 7, pages 161–186.
- Jenniskens P. (1997). "Meteor stream activity. IV. Meteor outbursts and the reflex motion of the Sun". *Astronomy & Astrophysics*, **317**, 953–961.
- Jenniskens P., Betlem H., de Lignie M., and Langbroek M. (1997). "The detection of a dust trail in the orbit of an Earth-threatening long-period comet". *The Astrophysical Journal*, **479**, 441–447.
- Jenniskens P., Nénon Q., Albers J., Gural P. S., Haberman B., Holman D., Morales R., Grigsby B. J., Samuels D., and Johannink C. (2016). "The established meteor showers as observed by CAMS". *Icarus*, **266**, 331–354.
- Krizhevsky A., Sutskever I., and Hinton G. E. (2012). "ImageNet classification with deep convolutional neural networks". In Pereira F., Burges C. J. C., Bottou L., and Weinberger K. Q., editors, *Advances in Neural Information Processing Systems 25*. Curran Associates, Inc., pp. 1097–1105.
- Lyytinen E. and Jenniskens P. (2003). "Meteor outbursts from long-period comet dust trails". *Icarus*, **162**, 443–452.

# Meteor film recording with digital film cameras with large CMOS sensors

Peter C. Slansky

Hochschule für Fernsehen und Film, Munich, Germany

<http://www.peter-slansky.de/astronomie/meteore/>

[slansky@mnet-online.de](mailto:slansky@mnet-online.de)

Professional digital film cameras with high sensitivity are still quite unusual in meteor observation. This may have one reason in their high costs. In the meantime, however, consumer photo cameras with film mode and very high sensitivity came to the market for about 2000 EUR. The special possibilities of digital film cameras with large CMOS sensors—including photo cameras with film recording function—for meteor recording were presented by the author using three examples: a 2014 Camelopardalid, shot with a Canon EOS C 300, an 2014 exploding Aurigid, shot with a Sony  $\alpha$ 7S, and the 2016 Perseids, shot with a Canon ME20F-SH. All three cameras use large CMOS (Complementary Metal Oxide Semi-conductor) sensors; “large” meaning Super-35 mm, the classic 35 mm film format ( $24 \times 13.5$  mm, similar to APS-C size), or full format ( $36 \times 24$  mm), the classic 135 photo camera format. Comparisons were made to the widely used cameras with small CCD (Charge-Coupled Device) sensors, such as Mintron or Watec; “small” meaning  $1/2''$  ( $6.4 \times 4.8$  mm) or less. Additionally, special photographic image processing of meteor film recordings were presented. Also, the results of a practical comparison of the stellar limiting magnitude between the Sony  $\alpha$ 7S and a Watec with the same lens were shown. This presentation goes back to an article with the same title in WGN (Slansky, 2016). Here, the emphasis is on the topics not covered in that article.

## 1 Introduction

A classic still photograph with an exposure time of some seconds, minutes, or hours shows a meteor as a streak. All information of the background sky is summed up over the integration time; all information about the meteor is summed up over the time and space of its angular movement over the sky. So, in a single photograph, a lot of information from the meteor is lost, namely with respect to the angular velocity of the meteor head and the temporal development of brightness and color of the meteor head, trains, and wakes.

To provide this information, video cameras are widely in use. Many of them are still based on analog technology with small monochrome CCD sensors in “Standard Definition” with 575 TV lines, resulting in a digital resolution of  $720 \times 576$  pixels. However, this was technology introduced in the late 1980s. Instead, television has stepped further to “High Definition” with  $1920 \times 1080$  pixels (“Full HD”). Today “Ultra-High Definition” is on the rise and becoming available, with  $3840 \times 2160$  pixels (“UHD”). Obviously, this technological progress is interesting for meteor film recording.

## 2 Camera technology

Digital film cameras and digital photo cameras with film function have in common that film recording is done with a significant oversampling: Most of those cameras use sensors with 1.5 to 2 times more pixels horizontally and vertically than samples in the signal. Oversampling does not mean binning: the real time downscaling

of oversampling is done by complex algorithms, and the scaling ratio is not limited to integer numbers such as 2:1 or 3:1. The oversampling is also a mean to compensate the loss of resolution of a color sensor, compared to a monochrome sensor, caused by the Bayer mask: in a color sensor with a Bayer mask, half of the sensor pixels are filtered in Green, a quarter in Red and another quarter in Blue. To reconstruct all three primaries for every sample of the signal, the native signal from the sensor has to be “de-bayered”. For this, the information of two green-filtered sensor pixels, one red-, and one blue-filtered sensor pixel are combined. This causes an average loss of resolution of the sampled signal compared to the native sensor resolution of about  $0.63\times$ , horizontally and vertically. This loss can be compensated by an oversampling with 1.5 times more pixels horizontally and vertically. So, oversampling gives digital film cameras a smooth image without artifacts like aliasing or color aliasing. The oversampling ratio has to be taken for width *and* height, so a 2:1 oversampling means four times more native pixels on the sensor than recorded samples in the signal.

The Canon EOS C 300<sup>1</sup> has a color CMOS sensor with a Bayer mask with a native resolution of  $3840 \times 2160$  pixels. The native signal from the sensor is de-bayered and downsampled in real time, resulting in a full HD signal with  $1920 \times 1080$  samples being recorded. That means an overall number of 8 300 000 pixels on the sensor, but 2 070 000 samples per image. Compared to still photography cameras with up to 30 Megapixels this may sound mediocre, but full HD resolution is five times

<sup>1</sup><http://www.canon.com>.

the pixel count of standard definition video (SD) with 440 000 pixels per image, being provided by cameras like Mintron or Watec (that do not use oversampling).

Professional digital film cameras and consumer photo cameras with film mode offer another valuable advantage over conventional video cameras: a significantly wider contrast range. A video camera is always linked to a television standard that also specifies the gamma curve. In Europe, these standards are CCIR 601 for SD video cameras, respectively, ITU Rec. 709 for HD video cameras, both with a gamma of 0.45, with only a limited scale of variation. In digital film cameras, the contrast transfer function can be adjusted manually or via a set of different gamma presets such as “cine gamma” or “S-Log” (Sony) or “C-Log” (Canon). These gamma curves provide a very flat contrast distribution characteristic and a significantly higher contrast range before low lights and high lights get clipped. It has to be noted that this advantage will only pay off when the signal is quantized with 10 bit or more. Unfortunately, there are still recent missing links in the workflows for meteor imaging with 10 bit and more. And, unfortunately, most consumer photo cameras, including the Sony<sup>2</sup>  $\alpha$ 7S, are limited to 8 bit when using the internal film recording function. Consumer cameras do not have a RAW recording in film mode.

### 3 Video cameras versus film cameras

Digital film cameras with large CMOS color sensors have the following advantages for meteor recording:

- fully digital signal processing with no digitization artefacts by a frame grabber such as jitter;
- resolution is a factor 2.2 higher for HD against SD, respectively, 5 times as many pixels;
- comparable star limiting magnitude at a much larger field;
- at same image field of view better optical efficiency due to longer focal length and proportionally larger entry pupil;
- higher contrast rendition via various flat gamma curves up to 14 F-stops versus standardized video contrast rendition curve limited to about 7 F-stops;
- color image.

There are also the following disadvantages:

- 5–6 times the data rate and the data amount;
- spectral sensitivity limited to visual 400–640 nm (this can be avoided by removal of the UV-/IR blocking filter—some digital film cameras have a removable filter such as the Canon ME20F-SH);

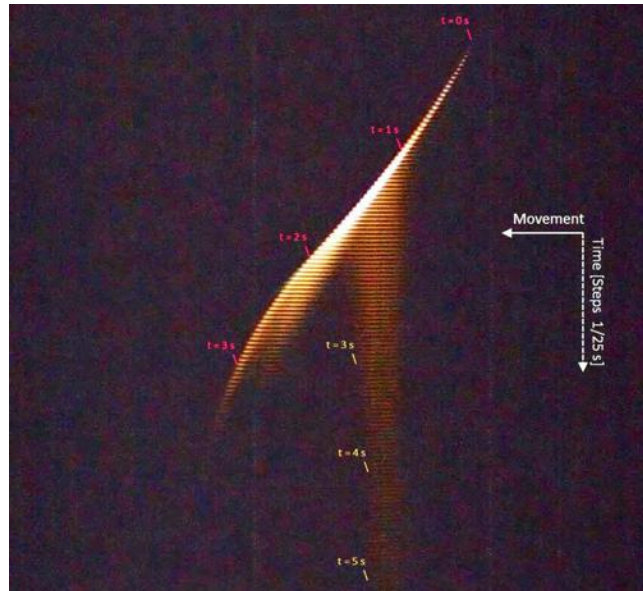


Figure 1 – Still image sequence from film recording of a Camelopardalid on May 24, 2014, at  $1^{\text{h}}58^{\text{m}}08^{\text{s}}$  UT from Munich city center, shot with a Canon EOS C 300 at ISO 20 000, 25 fps and 1/25 s with Zeiss Superspeed Cine Distagon 1.2/18 mm at  $F = 1.2$ .

- proprietary professional/consumer camera technology;
- complicated operation compared to video cameras;
- consumer photo cameras have an internal recording limited to 30 minutes due to custom’s and taxation laws;
- higher price.

Another major problem is a lack of interoperability between the existing softwares for HD film post-production and astronomical image processing.

The cameras used by the author are summarized in Table 1.

### Camelopardalids 2014

The Camelopardalids (e.g., Jenniskens<sup>3</sup>, 2014) could be observed for the very first time on May 24, 2014. That was my first film recording of a meteor. I borrowed a Canon C 300 with a Zeiss Superspeed Cine Distagon from my University and pointed it to the zenith on my rooftop terrace in the Munich city center, with Polaris and Vega in the picture. With ISO 20 000, 25 fps and  $F = 1.2$ , a stellar limiting magnitude of +5.2 was achieved.

For Figure 1, 145 film frames were cropped to stripes and composed one under another. So, the temporal development of the meteor from right to left, including movement, brightness, and color, can be studied in steps

<sup>2</sup><http://www.sony.com>.

<sup>3</sup><http://meteor.seti.org>.

Table 1 – Cameras used by the author.

Camera	Canon EOS C 300	Sony $\alpha$ 7S	Canon ME20F-SH
			
Year of introduction	2012	2014	2015
Camera Type	Professional digital film camera	Consumer photo camera with film mode	Ultra-high sensitivity professional digital film camera
Cooling	Active, controlled	Passive, uncontrolled	Active, controlled
Sensor type	Bayer color CMOS	Bayer color CMOS	Bayer color CMOS
Sensor size	22.5 × 12.7 mm	35.6 × 23, 8 mm	35.6 × 20.0 mm
Native sensor resolution	3840 × 2160 pixels	4240 × 2832 pixels	1920 × 1080 pixels
Native pixel size	6.25 × 6.25 $\mu$ m	8.4 × 8.4 $\mu$ m	19 × 19 $\mu$ m
Resolution in film mode	1920 × 1080 samples	1920 × 1080 samples 3840 × 2160 samples (external recording)	1920 × 1080 samples
Sample size	12.5 × 12.5 $\mu$ m	19 × 19 $\mu$ m	19 × 19 $\mu$ m
Oversampling	2×	2.2×	–
Maximum Sensitivity	ISO 20 000 (later ISO 80 000)	ISO 400 000	ISO 4 000 000
Maximum frame rate	60 fps	60 fps (1920 × 1080 samples) 120 fps (1280 × 720 samples)	60 fps
Internal recording codec	MPEG-2 8 bit	XAVC S 8 bit	External recording only via HD-SDI or HDMI, 8–12 bit
Maximum data rate	50 Mbit/s (internal)	50 Mbit/s (internal)	Depends on recorder
Lens mount	Canon EOS or PL	Sony E	Canon EOS
Price (body only)	ca. 13 000 EUR	ca. 2 000 EUR	ca. 19 000 EUR

of 1/25 s from top to bottom. Changes in the angular speed can be seen from the S-shape of the figure of the meteor head. Also note the development of the orange persisting train.

#### 4 Perseids 2016

For the 2016 Perseids observing campaign the author and Bernd Gährken, also from Munich, drove to Emberger Alm in the southern Austrian Alps at 1740 m above sea level. The 2016 Perseids turned out to have two maxima over two nights.

Canon Germany Ltd., Krefeld, equipped the author with two Canon ME20F-SH cameras with Canon USM II 1.4/35 mm photo lenses. Together with two Sony  $\alpha$ 7S with 2.8/35 mm Zeiss lenses all cameras were mounted on an equatorial mounting. Two film data recorders Ambient PIX 240i were connected to the Canon cameras. All cameras were pointed to Polaris for covering the same sky area simultaneously. The sensitivity was set up differently from camera to camera via ISO number and F-stop. This setup was chosen to compare the cameras on the same motive and for a direct measurement of the population index. The latter experiment failed, but the recordings of the cameras were remarkable.

The Canon ME20F-SH was introduced by Canon in 2015 as an ultra-high sensitive professional film camera with a maximum sensitivity of ISO 4 000 000, ten times of the sensitivity of the Sony  $\alpha$ 7S. It has no internal recording nor a viewfinder nor a display, all needs to be



Figure 2 – The 45 brightest Perseids of August 12, 2016. This composite image was gained with the maximum function. The star in the image center is Polaris; Ursa Minor is left. The film sequence was shot with a Canon ME20F-SH running at 25 fps,  $t = 1/25$  s and ISO 1 400 000, equipped with a Canon USM II 1.4/35 mm photo lens at  $F = 2.0$ .

attached externally. The ME20 has a full format CMOS sensor with a native resolution of Full HD (1920 × 1080 pixels), resulting in a pixel size of 19 × 19  $\mu$ m, the largest native pixel size on the market right now. Together with an advanced noise reduction system this is the key to the extraordinary sensitivity. For this goal the manufacturer sacrificed smoothing of the image by oversampling. Unfortunately, the Canon ME20F-SH is out of reach for most amateur astronomers by its price of 19 000 EUR (body only). The need for an external recorder, a display and a separate power supply does not make the handling very comfortable. But with the settings as in Figure 2 at 25 fps and with a field of view of 54° × 38°, the Canon ME 20F-SH reached a limiting stellar magnitude of +8.6.

During the first night, August 11 to 12, 2016, the cameras ran for 2<sup>h</sup>52<sup>m</sup> without interruption, during the second night, August 12 to 13, 2016, for 3<sup>h</sup>43<sup>m</sup>, resulting in an overall recording time of 6<sup>h</sup>35<sup>m</sup> hours.

Back at home, the numbers of the meteors in the field of the camera were detected by three different methods. First, the author watched the 6<sup>h</sup>35<sup>m</sup> of film recordings “simply” in real time on a Full HD computer monitor under controlled surrounding lighting conditions. By this “Visual HD method”, 513 meteors were detected in total: 387 Perseids and 126 others.

Secondly, the video files should be analyzed with METREC (Molau, 1999). Unfortunately, the METREC software only works with an analog real time SD video signal. So, all 6<sup>h</sup>35<sup>m</sup> of film recordings were downscaled and converted to a SD video file with DVD compression. This video was analyzed in real time with METREC by Sirko Molau. Reducing the resolution from Full HD to SD should result in a significant loss in meteor detection. By the “METREC SD method”, 499 meteors were detected: 343 Perseids and 157 others. (Due to some technical problems interpolation had to be made for a small part of the video.) There were many matches between the two methods, but also missed hits by one of the methods.

Thirdly, the negative effect of downscaling the original Full HD film files should be avoided. So, they were segmented into  $3 \times 2 = 6$  pixel-top-pixel crops of  $720 \times 576$  pixels (with overlapping) and exported to H.264 files. These were stored on a small hard disk drive media player and played back in real time. This led to “Sirko’s titanic struggle” with 40 hours of SD video files. Doubles and overlappings of meteors from segment to segment had to be eliminated by hand. Further challenges were the settings of the detection threshold related to the image noise and the correction of the perspective because of the optical axis not being in the image center after the cropping.

By this “METREC HD method”, 916 meteors were detected over all: 557 Perseids and 359 others. At last, the author consolidated all meteors detected by the three different methods, resulting in an overall number of 947 meteor detections: 561 Perseids and 386 others. For a single camera with a field of view of  $54^\circ \times 38^\circ$ —approximately 1/14th of the sky—this is quite remarkable.

## 5 Perseids 2017

The cover of WGN, the Journal of the IMO, vol. 44, no. 6, December 2016, shows a sequence from an exploding Aurigid. By the high angular velocity and the exposure time of 1/25 s, the meteor head appears as a streak with a length of about 20 pixels. To enhance the temporal resolution, the frame rate of the camera must be increased. The Sony  $\alpha$ 7S has a maximum frame rate of 120 fps. This was tested on the 2017 Perseids. Unfortunately, there were many clouds on the observing

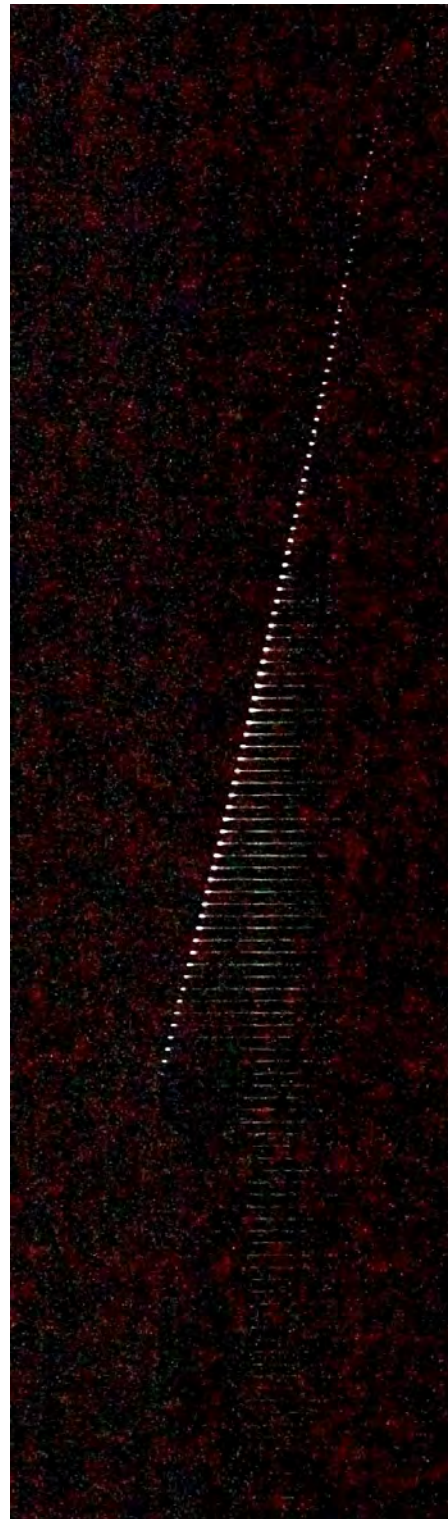


Figure 3 – Perseid, shot on August 12, 2017, at 22<sup>h</sup>46<sup>m</sup>09<sup>s</sup> UT, at Zetttersfeld, Austria, 1800 m above sea level with Sony  $\alpha$ 7S at ISO 400 000 and 120 fps,  $t = 1/125$  s, with Zeiss/Contax Distagon 2.8/35 mm at  $F = 2.8$ .

location of the author at Zetttersfeld, north of Lienz, Austria, 1800 m above sea level. Although all Perseids that were recorded had an unspectacular temporal development, the advantage of the higher frame rate can be seen in Figure 3.

The Perseid in Figure 3 appeared approximately  $40^\circ$  from the radiant. In the image the meteor head shows

hardly any motion blur. For larger angles from the radiant, faster meteor cameras with even higher frame rates than 120 fps must be used. In the future the author will try to realize this.

## 6 Sensitivity: a comparative test

The experiences from the 2016 Perseids campaign had proved that the effective meteor detection efficiency is influenced by a vast number of parameters, of which the nominal camera sensitivity, represented by the ISO setting, is only one. This gets even more complicated when two cameras with different sensor types and sensor sizes are compared. In the context of the 2017 Lyrids campaign and, again, in collaboration with Bernd Gährken, the author realized a practical comparative test for the stellar limiting magnitude between the Sony  $\alpha$ 7S with full format color CMOS sensor and a Watec 120N+ with 1/2" monochrome CCD sensor.

The test was done with the same lens to provide exactly the same optical output onto the pixels. A Canon FD 1.4/50 mm photo lens was chosen. Both cameras were set onto an equatorial mounting and pointed to the Vega region, the lens was changed quickly. Due to the fixed focal length of 50 mm the sky region was reproduced to a constant region on the sensors. In postproduction the image of the Sony was cropped to the image field of the image of the Watec. The whole image processing was done with a consistent workflow: 100 film frames were combined with the median function and a constant contrast rendition. The pixels of the cameras have nearly exactly the same size, but in film mode the Sony operates with a  $2.2\times$  downscaling. So, for the comparison the image of the Sony first had to be upscaled by the factor 2.2 and then cropped. By this, at an identical field of view the resolution of the Sony image is only  $0.45\times$  of the resolution of the Watec. This can be seen in Figure 4 by the larger diameter of the stars, in particular, Vega.

The stellar limiting magnitude was determined by star counting in the image field compared to a star chart from a planetary program.

As can be seen from Figure 4, the Sony  $\alpha$ 7S reveals a slightly higher stellar limiting magnitude with the same lens as the Watec 120N+. Interestingly, this is independent from the usage of the UV-/IR-blocking filter—even though the image of the Sony shows significantly more noise. At the same time, the field of the Sony is 5 times larger than that of the Watec.

## Conclusions

Film cameras and photo cameras with film function with large CMOS sensors offer new possibilities for meteor observation. Further research should be made with higher sensitivity, higher frame rate, higher contrast

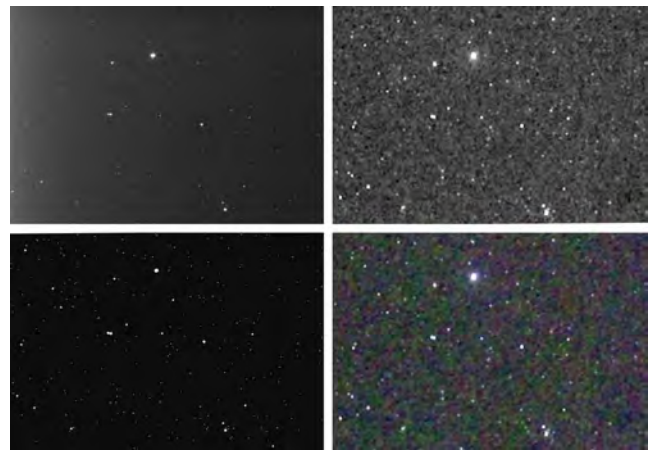


Figure 4 – Camera comparison of the resulting stellar limiting magnitude with the same lens used. *Bottom left*, star chart with stellar limiting magnitude +9.0; *top left*, Watec 120N+ with stellar limiting magnitude +8.3; *top right*, Sony  $\alpha$ 7S without UV/IR-blocking filter in color mode with stellar limiting magnitude +8.6; *bottom right*, Sony  $\alpha$ 7S with UV/IR-blocking filter in black-and-white mode with stellar limiting magnitude +8.6.

range and higher color rendition. Very important is the development of resolution independent meteor detection software that can operate the original data from film cameras and that is interoperable with common film postproduction software and astronomical image processing software.

## Acknowledgements

The author wants to thank Daniel Fischer and Peter Jenniskens for “setting him on the track”, Canon Germany Ltd. for providing him with two ME20F-SH for the 2016 Perseids campaign, Bernd Gährken for his support, and Sirko Molau for his titanic struggle with more than 46 hours of film meteor data.

## Bibliography

- Jenniskens P. (2014). Camelopardalids (IAU#451) from Comet 209P/LINEAR. *WGN, Journal of the IMO*, **42**, 98–105.
- Molau S., (1999). “The meteor detection software Met-Rec”. In Baggaley W. J. and Porubčan V., editors, *Proceedings of Meteoroids*, Tatranská Lomnica, Slovakia, 17–21 August 1998, pages 131–134.
- Molau S., Kac J., Crivello S., Stomeo E., Barentsen G., Goncalves R., and Igaz A. (2014). “Results of the IMO Video Meteor Network—March 2014”. *WGN, Journal of the IMO*, **42**, 120–124.
- Rendtel J. (2002). *Handbook for Photographic Meteor Observations*, IMO Monograph No. 3.
- Rendtel J. and Arlt R. (2012). *Meteore. Eine Einführung für Hobby-Astronomen*, Oculum-Verlag.
- Slansky P. C., Möllering D. (1993). *Handbuch der Professionellen Videoaufnahme*, Edition Filmwerkstatt, Essen.

# Kolonica-Modra: the new system for forward-scatter radio meteor observations

Pavel Zigo

Dept. of Astronomy, Physics of the Earth, and Meteorology, FMPI, Comenius University,  
SK-8248 Bratislava, Slovakia  
zigo@fmph.uniba.sk

A new transmitter dedicated to radio forward-scatter meteor observations was installed in the east of Slovakia at the Vihorlat Observatory and Astronomical Observatory on Kolonica Saddle. The transmitter of the system was built at Modra Observatory. The first experiences and results from this system are presented.

## 1 Introduction

A transmitter as a source of radio waves is the key component of a forward scatter radio system. In Europe, plenty of transmitters suitable for radio meteor observations exist, each of them having their own pros and cons. The main groups of such transmitters are summarized in this paper.

The best solution for accurate data processing, however, is building a dedicated transmitter with known parameters. A new transmitter of this kind was recently installed at the Vihorlat Observatory and Astronomical Observatory on Kolonica Saddle. The instrumental setup and first experiences are described in the last part of this paper.

## 2 Important transmitter parameters

According to the classical theory of forward scattering of radio waves off meteor trails (Wislez, 1996),  $P_T$  (transmitter power, Watt),  $G_T$  (transmitter gain), and  $\lambda$  (wavelength of transmitted radio wave, meter) are the main technical parameters of a transmitter. The  $G_T$  parameter is a directional characteristic which is given by the transmitter antenna radiation pattern. It is important to notice that in the relevant equations a factor  $\lambda^3$  occurs, which means that amplitudes and durations of received echoes strongly depend on wavelength. Besides these three parameters, it is also necessary to know the position of the transmitter and of the receiver in order to calculate the Observability Function (Verbeeck, 1997).

## 3 Suitable transmitters

In this section, we describe temporary European transmitters suitable for forward scatter observations.

### 3.1 Terrestrial analog TV transmitters

As a consequence of the EU decision to cease analog TV transmissions after 2012 and to switch any terrestrial

TV broadcasting to digital mode, many of the radio meteor observers started to look for other radio sources. There are still some suitable transmitters in eastern Europe (Ukraine, Belarus, Russia).

Their main advantages are a strong signal, a suitable frequency (45–70 MHz), and the relatively low cost of the system. On the other side, their operation is often not continuous, they generate a modulated signal, and their parameters are often unknown.

### 3.2 FM radio broadcast transmitters

The very dense network of FM transmitters is very rarely used for meteor observations, due to their relatively high frequency (80–100 MHz) and very unstable operations.

### 3.3 GRAVES radar

According to the RMOB database, most of the European observers use this transmitter today. (For example, at 12 September 2017 in the meteor live observatory page<sup>1</sup>, 30 European observers out of 39 used the GRAVES transmitter).

Pros of this system are a very strong signal and continuous operation. The high frequency with  $\lambda \approx 2$  m, and the antenna beam directed to south consisting of four switching elements represent important cons of this transmitter.

### 3.4 Dedicated transmitters

The most important advantage of a set-up with transmitters dedicated to forward scatter meteor observing is complete knowledge of, and control over, all parameters of the system. Unfortunately, this solution is relatively expensive due to installation costs, charges for electricity, maintenance, etc.

In the recent past the system Bologna-Lecce-Modra, or BLM for short (Hajduk et al., 1995) was in the operation. Now, the VVS Beacon (Steyaert, 2006) and BRAMS (Lamy et al., 2014) are active.

<sup>1</sup><http://www.rmob.org/livedata/main.php>.

### 4 Kolonica-Modra system

Taken into account the position of the Modra observatory and of the other stations of the SVMN (Toth et al., 2012) a transmitter dedicated for forward scatter observing was built at the Vihorlat Observatory and at Astronomical Observatory on Kolonica Saddle.

As can be seen in Figure 1, the transmitter-receiver (TR) stretches across the entire territory of Slovakia. The hilly profile of the TR path is shown in Figure 2.



Figure 1 – Google map of the transmitter-receiver (TR) baseline. The transmitter is located at the Kolonica Observatory and the receiver at Modra Observatory.

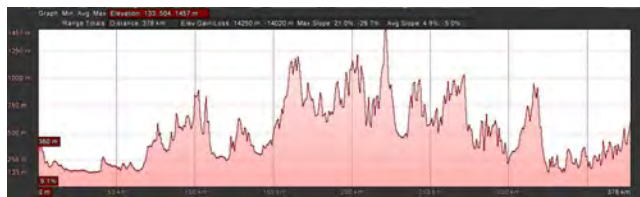


Figure 2 – The height profile of the TR baseline, with a maximum height around 1400 m.

The main parameters of the transmitter are as follows:

- frequency—49.97 MHz;
- power—90 W;
- TR azimuth—282°;
- waveform—CW;
- polarization—horizontal;
- transmitter antenna—5-element Yagi.

The antenna diagram is shown in Figure 3.

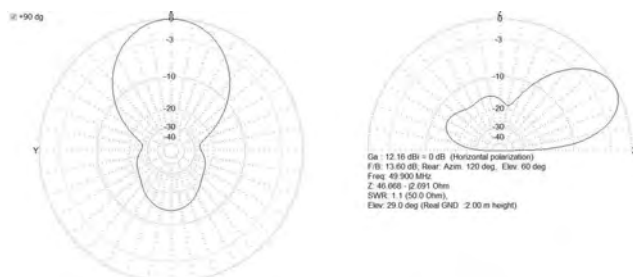


Figure 3 – Modeled horizontal and vertical radiation pattern of the transmitter antenna.

### 5 First experiences

The system has been in experimental operation since January 2017. The antenna mast and building of the transmitter are shown in Figure 4. On the receiver side, an analog (AOR 8600) and a SDR (Funcube Dongle) receiver has been tested. The first experiences can be summarized as follows:

- the echoes are very similar to the former BLM system echoes;
- there are no echoes from airplanes nor “exotic” (epsilon shape) echoes as from GRAVES,
- during sporadic-E (mainly in June and July) periods, the signal interferes with some TV transmitters localized in the east (Ukraine?).



Figure 4 – Five-element Yagi transmitting antenna at Kolonica Observatory.

### Acknowledgements

The author wishes to thank Dr. Igor Kudzej, CSc., and other colleagues of Kolonica Observatory for their effort provided during the installation and operation of the transmitter. This work was supported by the Slovak Research and Development Agency under the contract nos. APVV-16-0148, APVV-0517-12, and by the Slovak Grant Agency for Science grant no. VEGA 1/0225/14.

### References

Hajduk A., Hajdukova M., Gajdos S., Kostecky P., Zigo P., Cevolani G., Grassi G., and Trivellone G. (1995). “The Bologna-Modra forward-scatter radar experiment: reflection properties of meteor trains”. *Planetary Space Science*, **43**, 747–749.

Lamy H., Ranvier S., Martinez Picar A., Gamby E., Calders S., Anciaux M., and De Keyser J. (2014). “BRAMS—the Belgian RAdio Meteor Stations”. In Muinonen K., Penttilä A., Granvik M., Virkki A., Fedorets G., Wilkman O., and Kohout T., editors, *Asteroids, Comets, Meteors 2014*.

- Steyaert C. (2006). “The VVS meteor beacon”. In Bastiaens L., Verbert J., Wislez J.-M., and Verbeeck C., eds., *Proc. IMC*, Oostmalle, Belgium, 15–18 Sep. 2005. IMO, pp. 25–33.
- Tóth J., Kornoš L., Piff R., Koukal J., Gajdoš Š., Popek M., Majchrovič I., Zima M., Világi J., Kalmančok D., Vereš P., and Zigo P. (2012). “Slovak Video Meteor Network—status and results: Lyrids 2009, Geminids 2010, Quadrantids 2011”. In Gyssens M. and Roggemans P., eds., *Proc. IMO*, Sibiu, Romania, 15–18 Sep. 2011. IMO, pp. 82–84.
- Verbeeck C. (1997). “Calculating the Sensitivity of a forward Scatter Setup for Underdense Shower Meteors”. In Knöfel A. and Roggemans P., editors, *Proceedings of the International Meteor Organization*, Apeldoorn, the Netherlands, 19–22 September 1996. IMO, pages 122–132.
- Wislez J.-M. (1996). “Forward scattering of radio waves off meteor trails”. In Roggemans P. and Knöfel A., editors, *Proceedings of the International Meteor Organization*, Brandenburg, Germany, 14–17 September 1995. IMO, pages 99–117.

# Novel injection moulded gratings for video meteor spectroscopy.

William Ward, Paul Reynolds, Rachel Love, and Nikolaj Gadegaard

School of Engineering, University of Glasgow,  
Rankine Building, Oakfield Avenue, Glasgow, G12 8LT, United Kingdom  
william.ward@glasgow.ac.uk, paul.reynolds@glasgow.ac.uk, rachel.love@glasgow.ac.uk, and  
nikolaj.gadegaard@glasgow.ac.uk

Due to the random appearance of meteors on the sky, conventional transmission gratings can produce images with severely tilted spectra. This is caused by the meteor motion being at a shallow angle with respect to the dispersion axis of the grating. To alleviate this, it is useful to have a grating that can disperse in two perpendicular axes simultaneously. This can be achieved by using a grating with a grid construction. This paper describes the design, production and use of such a grating.

## 1 Introduction

Meteor spectroscopy normally utilizes grooved optical transmission gratings mounted in front of the camera lens as shown in Figure 1. In laboratory applications the single dispersion direction is not normally problematic. However with meteor spectroscopy the meteors often fall in such a manner as to produce a spectrum that is not optimal. This is caused by the angle of motion of the meteor with respect to the dispersion axis leading to a tilted spectrum. Such spectra are difficult to process resulting in a loss of resolution at best and may ultimately be un-useable.

One possible solution is to design a grating such that the light is dispersed in multiple directions simultaneously thus increasing the chances of obtaining a useable spectrum.



Figure 1 – Usual configuration for video meteor spectroscopy.

## 2 Grating design

In gratings, the diffraction is achieved by passing the light through a structure consisting of a series of narrow grooves cut into a suitable substrate. Modern gratings also include polymer and holographic replica gratings

which are copies of a master ruled grating. These gratings give a single axis of dispersion. Diffraction is a complex process and the reader is referred to a suitable text book covering the issue for more details, e.g., Hecht (2005).

With the appearance of the meteor being random, this single dispersion axis' direction can place limitations on the ultimate resolution due to the possibility of the spectrum being tilted. When the meteor is such that it is at a shallow angle to the dispersion axis, the quality of the reduced spectrum can be poor. Examples of this are shown in spectra captured during the 2015 Quadrantid meteor shower (Ward, 2015).

A solution to this is to design a grating such that two (or more) axes of dispersion are possible. This can be achieved by using a grid structure as the grating elements. This can be thought of as the convolution of two sets of grooves perpendicular to each other. Thus no matter the fall of the meteor it will always be less than 45 degrees from either perpendicular dispersion axis. This greatly enhances the chances of obtaining a recoverable spectrum from any given meteor bright enough to be captured.

The configuration of the grid defines the characteristics of the diffraction pattern in the same way for grooves in a conventional grating. Hence, four dispersion axes are produced in the design presented here.

The initial design is shown in Figure 2. It is a repeating structure spaced such that the mould will have 600 structures/mm in the horizontal and vertical directions. In discussion with Dr. Paul Reynolds, it was suggested that a simple aspect ratio of 1:1 was adopted for manufacturing purposes.

## 3 Grating manufacture

Electron beam lithography was used to define the diffraction grating pattern in a resist layer on silicon, followed by etching of the pattern into the silicon substrate. A nano-imprint process was then used to transfer the pattern onto a polymer master material for use

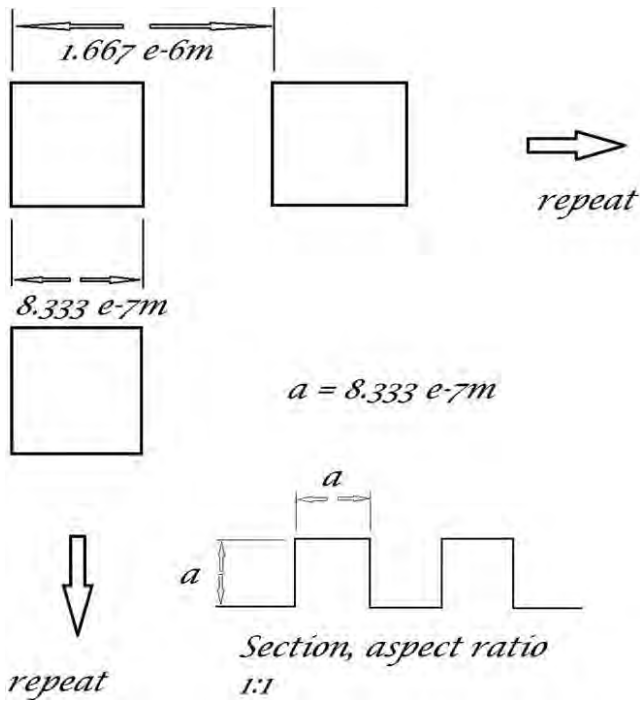


Figure 2 – Pattern used in the design of the polycarbonate grating.

as a die in a polymer injection moulding process. The gratings were produced on a Engel Victory 28 injection moulder (Figure 3) and the parts were moulded in polycarbonate (Macrolon OD2015). The lithography, masks and moulds were made by Dr. Paul Reynolds and the production and inspection processes were carried out by Miss Rachel Love.



Figure 3 – Victory 28 injection moulding machine.

## 4 Testing

Tests of the grating were done in the laboratory using a helium-neon (HeNe) laser. This has a red beam at a wavelength of 633 nm with an output power of 0.800 mW. The grating was mounted in front of the HeNe laser and the power in the zero order and pattern of first order images was measured. Power measurements were made with an Anritsu ML910B optical power meter with a MA9802A silicon photodiode sensor calibrated for 633 nm.

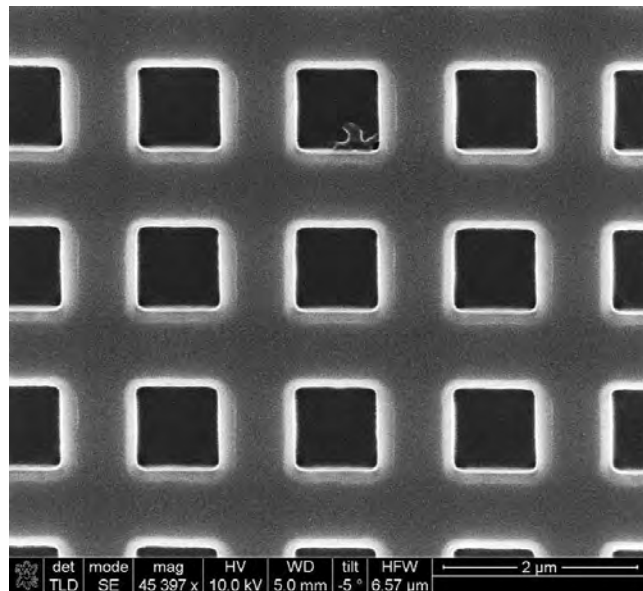


Figure 4 – Electron micrograph of grating surface.

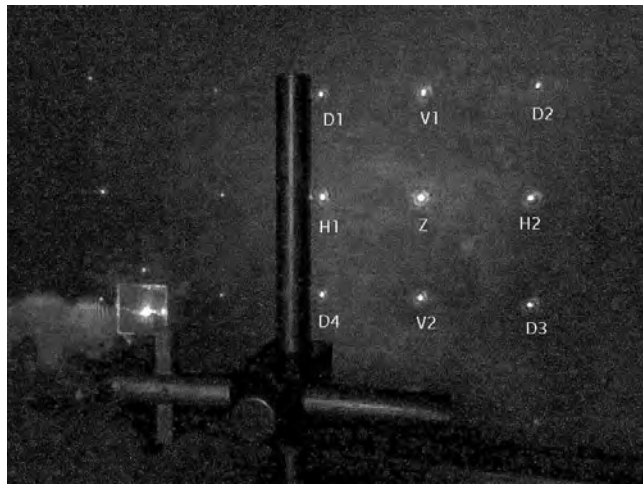


Figure 5 – Diffraction pattern of test grating using a HeNe laser (633 nm) with reference names used in power measurements.

Table 1 – Optical power measured in diffraction pattern spots of multi-axes polycarbonate grating.

Reference ID	Optical Power
Z	0.233 mW
H1	0.068 mW
H2	0.069 mW
V1	0.066 mW
V2	0.065 mW
D1	0.030 mW
D2	0.029 mW
D3	0.030 mW
D4	0.029 mW
Total	0.619 mW

The zero order image (Reference Z in Figure 5) was measured at 0.233 mW. Table 1 shows the power measurements.

Figures 4 and 5 show that 29% of the incident beam is transmitted in the zero order, whilst less than 9% goes into H1. For comparison, the test was repeated using

Table 2 – Optical power measured in diffraction pattern spots of 600 grooves/mm educational grating.

Reference ID	Optical Power
Z	0.388 mW
H1	0.184 mW
H2	0.073 mW
Total	0.645 mW

the same laser and measurement configuration but with a conventional Paton Hawksley educational blazed grating with 600 grooves/mm. Being a conventional grating only one set of images are produced. The equivalent “H1” and “H2” positions spots were measured. Table 2 shows the results of the comparison measurements.

In this case, 49% of the incident beam is transmitted but a much higher percentage, 29%, is concentrated into the first-order image. This indicates that the “diffraction efficiency” of the grid-based grating is lower compared to conventional grating by a factor of approximately 3. In practical terms the result is that, for any given observing situation, a brighter meteor is required to record a similar spectrum using a multi-axes grating compared to the same system using a conventional grating:

$$\Delta m = -2.5 \log \left( \frac{b_2}{b_1} \right), \quad (1)$$

where  $b_1$  refers to the brightness of the spot (H1) as measured through the polycarbonate grating and  $b_2$  is the brightness of the equivalent spot through the conventional grating. Considering the relative optical powers of the first order power measurements and using Equation (1), the magnitude penalty is approximately 1.1 magnitudes between the polycarbonate grating and the comparison blazed grating.

## 5 Conclusions

Using injection moulding techniques, a polycarbonate grating with a grid structure was designed and manufactured.

During the Perseids, two WATEC 910 HX/RC cameras carrying 12 mm  $f/1.2$  lenses were fitted with the polycarbonate pillar gratings. Initial testing captured an early Perseid meteor. This is shown in Figure 6. This image demonstrates the validity of the optical principle. A highly tilted spectrum can be seen to the left of the zero order image and a much better presented spectrum can be seen below the zero order image. The faintness of this well presented spectrum for such a bright meteor illustrates the limitations in performance. The

meteor image was saturated in the original video. By visual inspection and comparison to the known stars in the image ( $\alpha$  And and  $\beta$  Peg), a negative magnitude is probable.



Figure 6 – A Perseid meteor with a highly tilted spectrum to the left of the main meteor image. Below is a spectrum with much better dispersion geometry. It is however considerably fainter.

The particular design of the pillar structure results in a non-blazed diffraction pattern having 4 dispersion axes. This results from the profile of the grid structure. A significant percentage of light is dispersed into many high orders which are individually faint. Whilst the principle of ensuring that a good dispersion geometry is always available has been shown, the magnitude penalty limits the utility of this style of grating to brighter meteors and fireballs only.

## Acknowledgements

The author wishes to thank Dr. Paul Reynold and Ms. Rachel Love for their generous help and support with this experiment. Thanks go also to the *Bioelectronics Interface Group* leader, Dr. Nikolaž Gadegaard, for the use of the injection moulding machine facilities. Finally, we thank Mr. Alex Pratt for his assistance in reviewing the original manuscript.

## References

- Hecht E. (1989). *Optics*. Second ed. Addison Wesley.
- Ward W. (2015). “Meteor spectroscopy during the 2015 quadrants”. *WGN, Journal of the IMO*, **43**, 102–105.

# How the received radio meteor signal determines the final spectrogram

Tom Roelandts

Impulse Response, Beerse, Belgium

tom@impulseresponse.eu

Radio meteors are typically visualized using spectrograms, although the properties of the meteor trail are simply encoded in the varying signal power of the received signal. In this paper, we discuss some aspects of how the properties of the received signal determine the shape of the reflections in the final spectrogram. Simulated radio meteors are used for illustration.

## 1 Introduction

Radio meteors are typically visualized using spectrograms. Since there is sometimes confusion on how the shape of the reflections in the spectrogram follows from the actually received signal, this paper illustrates some of these effects.

In Roelandts (2016), we have provided an overview of the complete signal path, starting from the radio signal that is transmitted, and ending with the final spectrogram that is typically used to visualize the received signal. However, in that paper we did not go into detail on how the received signal gets translated into the shape of the meteor reflection in the spectrogram. In the current paper, we show how the reflection profile, the Doppler shift of the received signal, and the combination with the directly received carrier, are translated into the final reflection image of the meteor in the spectrogram.

## 2 Effect of Doppler shift and directly received carrier

All the illustrations in the current paper were generated through simulations. The sampling rate of the simulations was 5512 Hz. The simulated underdense meteors consist of a fast linear rise followed by an exponential decay. For comparability with typical results from, e.g., the BRAMS network (Calders and Lamy, 2011; Ranvier et al., 2015), the results were then upconverted to a carrier frequency of 1000 Hz.

Figure 1 shows five different simulated meteor reflections. The first four are *underdense* reflections, with a Doppler offset of 25 Hz, 0 Hz, -50 Hz, and 25 Hz, respectively. Additionally, the fourth one lacks a directly received carrier. It is important to notice that the shape of the actual reflection is not at all influenced by the Doppler offset or by the directly received signal. The *only* visible effect of the Doppler is that the reflection is shifted up or down in frequency.

To show the effect of the Doppler shift in combination with the directly received carrier, we have to look at the combined signal that is the input of the receiver.

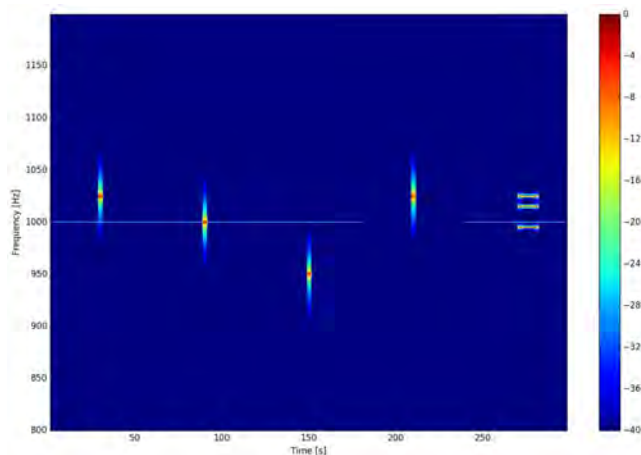


Figure 1 – Spectrogram with five simulated reflections.

The first reflection from Figure 1 has a Doppler shift in the received signal of 25 Hz, combined with a directly received carrier at a power level of 1% of the meteor signal (Figure 2). For clarity, we mention that the signal is colored solid blue inside its envelope because of the high frequency oscillations, with respect to the time scale shown, of the 1000 Hz carrier.

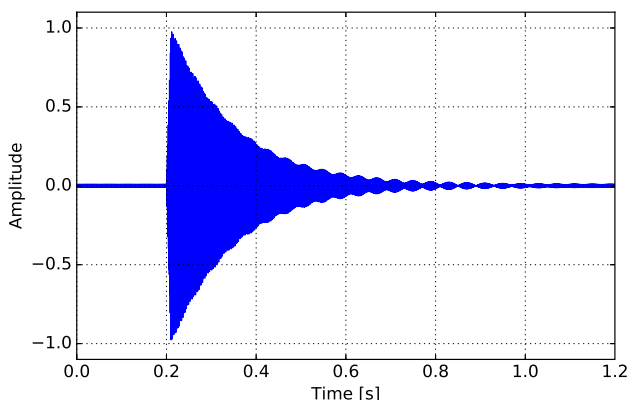


Figure 2 – Underdense meteor profile with a 25 Hz Doppler shift and a directly received carrier at 1% of the power of the meteor signal.

The oscillations in the envelope of the signal are so-called *beats*. These are amplitude variations that are caused by two signals that are close together in frequency, so that they show a pattern of alternating constructive and destructive interference.

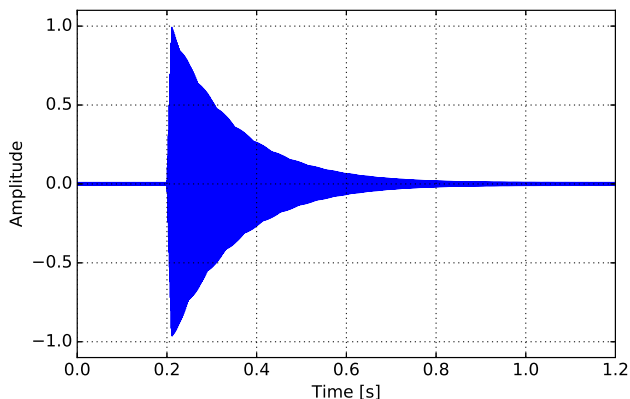


Figure 3 – Underdense meteor profile with a 0 Hz Doppler shift and a directly received carrier at 1% of the power of the meteor signal.

The second reflection from Figure 1 has a Doppler shift in the received signal of 0 Hz (i.e., no Doppler shift), combined with a directly received carrier at a power level of 1% of the meteor signal (Figure 3). The beats have disappeared. However, there is still some influence from the combination of a modulated signal (reflected off the meteor) with an unmodulated one (the directly received carrier). Also compare with Figure 5, where there is no directly received carrier.

The third reflection from Figure 1 has a Doppler shift in the received signal of  $-50$  Hz, combined with a directly received carrier at a power level of 1% of the meteor signal (Figure 4). The frequency of the beats is higher than in Figure 2, because the frequencies of the two signals are now further apart, so that the cycles of constructive and destructive interference follow each other more closely.

The fourth reflection from Figure 1 has a Doppler shift in the received signal of 25 Hz, and no directly received carrier (Figure 5). The beats have disappeared.

The fifth, and last, reflection from Figure 1 is entirely different from the previous four. It shows the combination of three long-lived reflection points (active for 10 s) with Doppler shifts of 25 Hz, 15 Hz, and  $-5$  Hz, respectively, and a directly received carrier at 1% of the power of the meteor signal (Figure 6).

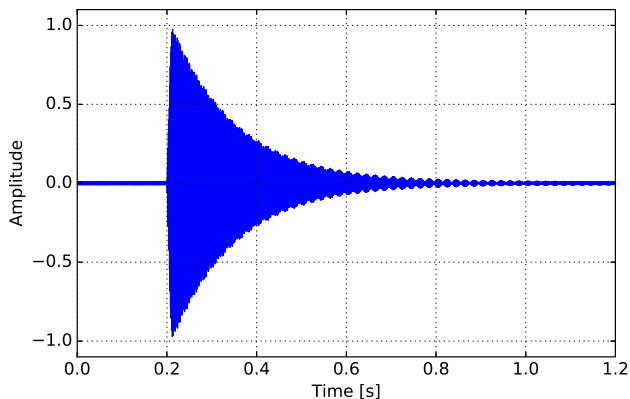


Figure 4 – Underdense meteor profile with a  $-50$  Hz Doppler shift and a directly received carrier at 1% of the power of the meteor signal.

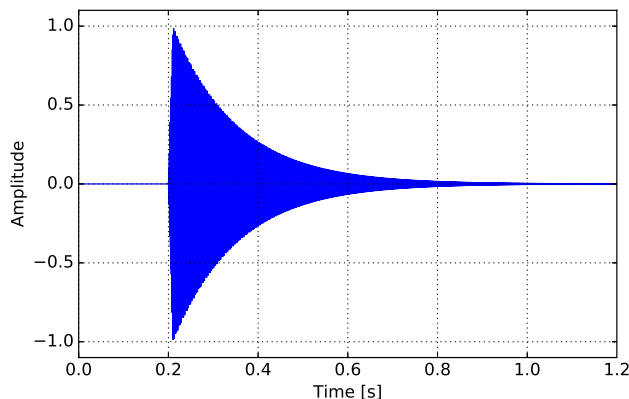


Figure 5 – Underdense meteor profile with a 25 Hz Doppler shift and a no directly received carrier.

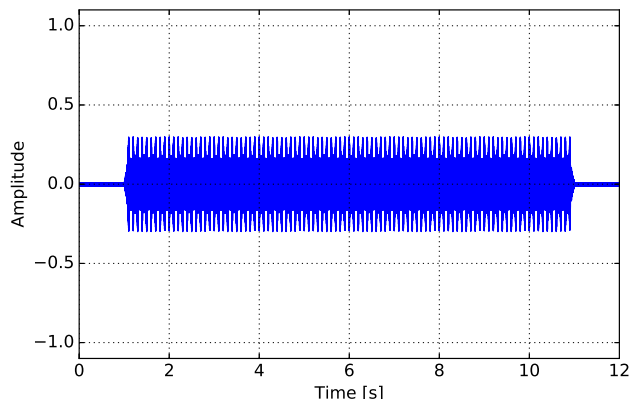


Figure 6 – Combination of three individual long-lived reflection points, with Doppler shifts of 25 Hz, 15 Hz, and  $-5$  Hz, respectively, and a directly received carrier at 1% of the power of the meteor signal.

We have included this 10 s reflection in the spectrogram (Figure 1) to show that a longer signal can be completely different from underdense reflections, especially with respect to the width of its spectrum. In the case of meteor reflections, this is mainly because the underdense meteors are *short*, while the three reflection points from the fifth reflection are *long*.

This is the crucial point that we want to emphasize in this paper: the underdense meteors have a relative broad spectrum, i.e., they are tall in the spectrogram, because of the properties of the received signal, and not because of an effect of the receiver, sampling, etc.

It is a general rule of thumb in signal processing that a short signal needs a large bandwidth. A very basic signal that can be used to illustrate this, is a rectangular pulse. Figure 7 shows both a short and a long pulse. Figure 8 illustrates nicely that the spectrum of the long pulse is much narrower than the spectrum of the short pulse.

### 3 Conclusions

Through several simulated radio meteors, we have illustrated how the received signal determines the shape of the reflections in the spectrogram. We have shown

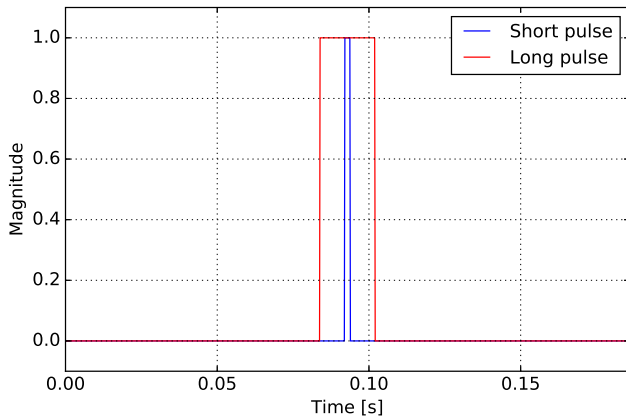


Figure 7 – A short and long rectangular pulse.

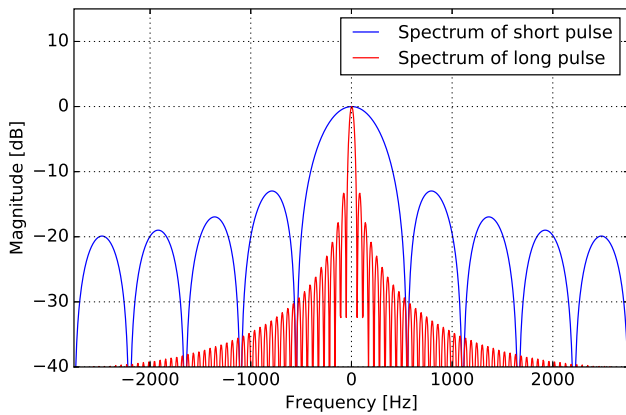


Figure 8 – Spectra of the short and the long rectangular pulse of Figure 7.

that the shape of the reflections is not influenced by the Doppler shift or the directly received carrier. Underdense meteors have a wide frequency range because they are short, and single reflection points that stay active for a long time can result in a much smaller frequency range.

## References

- Calders S. and Lamy H. (2011). “BRAMS: status of the network and preliminary results”. In Gyssens M. and Roggemans P., *Proceedings of the International Meteor Conference*, Sibiu, Romania, 15–18 September 2011. IMO, pages 73–76.
- Ranvier S., Lamy H., Anciaux M., Calders S., Gamby E., and De Keyser J. (2015). “Instrumentation of the Belgian RAdio Meteor Stations (BRAMS)”. In *Proceedings International Conference on Electromagnetics in Advanced Applications (ICEAA)*, Turin, Italy, 7–11 September 2015. IEEE, pages 1345–1348.
- Roelandts T. (2016). “The radio meteor signal path from transmitter to spectrogram: an overview”. In Roggemans A. and Roggemans P., editors, *Proceedings of the International Meteor Conference*, Egmond, the Netherlands, 2–5 June 2016. IMO, pages 250–253.

# Using a small phased array for meteor observations

Antonio Martínez Picar and Christophe Marqué

Solar-Terrestrial Center of Excellence, Royal Observatory of Belgium  
 Av. Circulaire 3, 1180 Brussels, Belgium  
 antonio.martinez@observatory.be

A prototype of a phased array of 8 elements is being built at the Humain Radio-Astronomy Station by the Royal Observatory of Belgium. The main goal of this instrument is monitoring the solar activity in the band of 20–80 MHz using Software Defined Radio receivers and employing beam-forming techniques to track the Sun. However, because the operation frequency of the BRAMS forward-scatter system lies within the frequency range of such an array, an appealing window of opportunity opens for meteor science as well. In this paper we explore the possibility of using the expected capabilities of the Small Phased Array Demonstrator to register radio meteor echoes.

## 1 Introduction

In order to deliver warnings and alerts about solar events that can potentially influence life on Earth, the Solar Influences Data analysis Center (SIDC) of the Royal Observatory of Belgium (ROB) observe and study the Sun using different instruments located on-board space probes and also on ground-based facilities.

The Humain Radio-Astronomy Station (HuRAS), located approximately 100 km south-east of Brussels, currently harbors three solar radio observation instruments: CALLISTO, ARCAS, and HSRS. Additionally, the Radio Working Group of the SIDC is developing two extra instruments to extend the total frequency range of the observations: ANT34 (solar flux monitoring system) and the Small Phased Array Demonstrator (SPADE). Figure 1 shows the frequency ranges of the instruments.

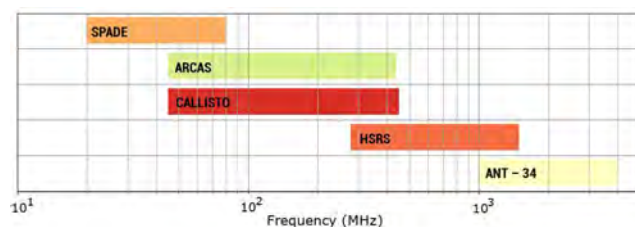


Figure 1 – Frequency chart of current and future radio instruments in HuRAS.

Because the frequency range planned for SPADE includes the frequency of the pure sine signal emitted by the beacon of the Belgian Radio Meteor Stations (BRAMS) network (Calders and Lamy, 2012) registering radio meteor echoes is, in principle, feasible.

## 2 SPADE proposal

The project, founded by the Belgian Science Policy Office (BELSPO), started on January 2016 with the objective to demonstrate that,

- the technology of Software Defined Radio (SDR) receivers, beam-forming methods, and phased arrays can be combined in functional radio astronomy instruments; and

- such an instrument can be built at a modest cost, within reach of institutional bodies such as universities or observatories.

SPADE's intended frequency range is 20–80 MHz. It will consist of 8 fixed antennas. High availability is expected from this instrument because SPADE will not include any moving parts, a usual source of incidents.

A phased array works similarly to an interferometer, but summing instead of multiplying the received signals. Choosing an appropriate set of complex weights to be applied to the received signals allows for steering the main beam, manipulate the beam shape, and direct the placement of nulls. A *beamformer* may, appropriately, be considered a spatial filter.

Some benefits of this technique includes interference avoidance and rejection, and higher signal-to-noise ratio (SNR), while the use of SDRs and digital post-processing procedures allows the generation of simultaneous beams pointing in different areas of the sky.

## 3 Design of the instrument

SPADE requires wide-band and "wide field-of-view" for the elements of the array. A *tied-fork dipole* antenna shows the best performance-to-costs ratio (Figure 2) A plastic box on top of the antenna contains the *Front-End Electronics* (FEE) which includes—among other components—a Low Noise Amplifier which adds 12 dB of gain to handle cable losses without affecting noise performance (Hicks et al., 2012).

The FEE circuit board design offers direct feed points connections in 90° for each polarization. A metallic grid deployed underneath the antenna reduces the ground losses and variable soil conditions.

Generally speaking, it is desirable that the layout of the array provides a symmetric beam with low side lobe levels. For designs with low antenna count, as in the case of SPADE, an irregular distribution of the antennas does not represent an advantage.



Figure 2 – Wide-band antenna selected as SPADE array element installed at the Royal Observatory of Belgium during a testing period.

In order to define the final outlay of the array, different distributions of the elements were simulated using NEC2++<sup>1</sup> (Molteni, 2014). A circular distributed array with central antenna element shows a good balance in total gain and reduced side lobes levels (Figure 3), even in steering mode simulations.



Figure 3 – 3D visualization of SPADE array pattern simulation in 50 MHz for a circular distribution of antennas around a central one.

The radio frequency signal coming from each antenna of the array is digitalized by an SDR, which in turn sends the resulting digital data stream to a main processing

<sup>1</sup>The simulations were carried out using loaded elements (aluminum) and including *real ground* (HuRAS soil conductivity and permittivity).

computer. In this server, each of the digitally represented signals is appropriately weighted and summed in order to *shape* and point the radio-telescope beam towards the direction of interest, without moving mechanically any part of the telescope. A reference clock signal is also included in order to keep all the SDRs synchronized. Figure 4 shows a general diagram of the different signals involved in SPADE operation.

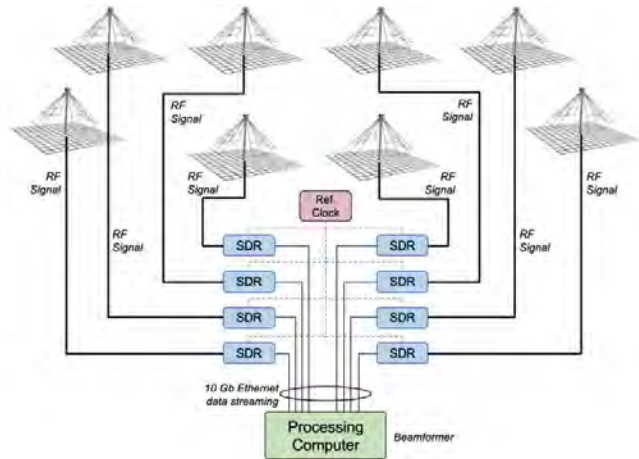


Figure 4 – General diagram of the different SPADE signal paths.

## 4 Building SPADE

The instrument is still in construction phase. However, it is interesting to mention some advances made in the effort of having its *first light* before the end of 2017.

In order to achieve beam patterns that are as similar as possible to the design, the area of the array field should be as planar as possible. The Ruze formula modified for a Phase Array (D'Addario, 2008) gives a requirement of an accuracy of  $\lambda/25$ , i.e., 15 cm at a frequency 80 MHz. This number is *root mean square* (rms) for random deviation. However, the systematic error should be much smaller. Therefore, an accuracy of about 6 cm was requested.

In order to improve even more the total gain and the general behavior of the array, the initial design using individual wire-meshes beneath each antenna was replaced by a single  $20\text{ m} \times 20\text{ m}$  ground plane. We chose a  $15\text{ m} \times 15\text{ m}$  galvanized welded wire mesh material that is structurally sound and inexpensive, made with a wire diameter of 6 mm. The different pieces of this material were galvanically connected with one-another.

The location of each element was determined using a Differential GPS (D-GPS) unit. The final measured error corresponds to a precision of approximately 80 mm.

Pipes to conducting the RF cables (RG-213 type) from each antenna to the cabin—which will harbor the receivers and the processing PC—were placed before the flattening of the terrain. Figure 5 shows a general view of the current status of SPADE works at HuRAS.



Figure 5 – General view of SPADE array field in HuRAS. Behind the SPADE antennas, the 6 m-dish and its piggy-backing log-periodic antennas (used by the HSRs, ARCAS, and CALLISTO instruments) can be seen.

## 5 Observing meteors with SPADE

Although SPADE was initially intended to carry out solar observations, it will be a radio-telescope with some remarkable features. Helmboldt et al. (2014), using a similar radio-telescope (with more antennas), reported that they had registered meteor echoes successfully employing a 55.25 MHz signal from analog TV transmissions.

Moreover, HuRAS is located in a radio-frequency-protected area, which ensures low noise levels affecting the radio observations. Meteor echoes have been registered for many years now by the BRAMS equipment located at HuRAS (Lamy et al. 2015), which is an encouraging fact in the pursuit of observing radio echoes with SPADE.

SPADE’s digital beam-former allows performing simultaneous observations. A parallel pipeline must be set-up in order to process the meteor observations without affecting the solar measurements. To implement this parallel pipeline, the GNU Radio free and open libraries<sup>2</sup> will be used.

## Acknowledgements

The authors wish to thank Marc De Knijf and the rest of the ROB’s Technical Services Department for their prompt and effective implementation of all tasks necessary to complete this mission successfully.

We also wish to mention the very helpful advices given by Dr. Christophe Craeye (Université Catholique de Louvain) which has led our design efforts in the right direction.

## References

- Calders S. and Lamy H. (2012). “BRAMS: status of the network and preliminary results”. In Gyssens M. and Roggemans P., editors, *Proceedings of the International Meteor Conference*, Sibiu, Romania, 15–18 September 2011. IMO, pages 73–76.
- D’Addario L. R. (2008). “Combining loss of a transmitting array due to phase errors”. *Interplanetary Network Progress Report*, **175**, 1–7.
- Helmboldt J. F., Ellingson S. W., Hartman J. M., Lazio T. J. W., Taylor G. B., Wilson T. L., and Wolfe C. N. (2014). “All-sky imaging of meteor trails at 55.25 MHz with the first station of the Long Wavelength Array”. *Radio Sci.*, **49**, 157–180.
- Hicks B. C., Paravastu-Dalal N., Stewart K. P., Erickson W. C., Ray P. S., Kassim N. E., Burns S., Clarke T., Schmitt H., Craig J., Hartman J., and Weiler K. W. (2012). “A wide-band, active antenna system for long wavelength radio astronomy”. *Publications of the Astronomical Society of the Pacific*, **124**, 1090–1104.
- Lamy H., Anciaux M., Ranvier S., Calders S., Gamby E., Martinez Picar A., and Verbeeck C. (2015). “Recent advances in the BRAMS network”. In Rault J.-L. and Roggemans P., editors, *Proceedings of the International Meteor Conference*, Mistelbach, Austria, 27–30 August 2015. IMO, pages 171–175.
- Molteno T. C. A. (2014). “NEC2++: An NEC-2 compatible Numerical Electromagnetics Code”. Technical Report 2014-3, University of Otago, Dunedin, New Zealand.

<sup>2</sup><https://www.gnuradio.org/>.

# Twenty years of IMO Video Commission: a retrospective

Sirko Molau

Abenstalstraße 13b, 84072 Seysdorf, Germany  
sirko@molau.de

At the occasion of the 20th anniversary of the IMO Video Commission, we analyze the goals and projects that were defined upon the foundation of the Commission, to what extent they have been achieved over the past 20 years, and which meteor projects we will see in the near future. We conclude that video observations have been a major success story over the last 20 years, not least thanks to the IMO and its Video Commission.

## 1 Introduction

The IMO Video Commission was proposed by Council Member Marc Gyssens in 1996. It was founded one year later at the 1997 IMC in Petnica. Now that the IMC has returned to Petnica in 2017, we want to give a retrospective of what happened during the twenty years between those two events.

The status of video observation in 1997 and our plans were laid down by Molau et al. (1997). The paper proposed three key projects and some supplementary projects for video observers. It also defined the key tasks for a Video Commission within the IMO, and, hence, serves as perfect basis to answer following questions:

- Where did we start from?
- Which plans did we have?
- What did we achieve (and what not)?
- Where are we standing today?
- What will we see in the (near) future?

## 2 Status of video observations in 1997

### 2.1 Video systems

By 1997, about 40 video systems were operated by amateur astronomers world-wide (about 15 in Japan, 10 in Germany, 5 in the Netherlands and the rest elsewhere). Video systems were highly individual. A first series of 5 identical video cameras was just introduced in Germany. All systems were image-intensified using first- or second-generation tubes—Mintron and Watec cameras were not yet available.

Observations were stored on video cassettes. Because of this limitation, video systems were only used for selected major showers like the Quadrantids, Perseids, Orionids, or Geminids. There was no continuous night-sky monitoring by video.

### 2.2 Hardware and software

PC hardware was based on 486 and Pentium I PCs with a few hundred MHz clock rate running DOS or Windows 95. USB 1.0 and Firewire were just introduced, and the first USB devices became available, so video was always handled as analog signal. Framegrabbers were slowly emerging on the consumer market.

The first software packages supported the measurement of video meteors, but automated meteor detection was still under development and automated systems seemed impossible.

### 2.3 Meteor science

Most of our knowledge from meteor showers was based on visual observations, which had been standardized 15 years earlier. The dust trail theory (see, e.g., Asher and McNaught, 1999) was not yet developed and published, so outbursts like the Leonid returns at the end of the century were predicted based on the position of the parent comet and subsequently rather inaccurate.

## 3 Key projects

### 3.1 Minor meteor showers

*Minor meteor showers were regarded as key target in 1997, because video observations would combine the advantages of visual observations (high sensitivity) and photographic observations (high accuracy). So they suit perfectly to study minor and detect new meteor showers.*

In fact, automated meteor detection and observation became available much earlier and the degree of automation was much higher than anticipated. A first video camera started continuous observation in March 1999 and marked the starting point of the IMO Video Meteor Network.

Further large video networks were established subsequently in several countries, e.g., Poland (PFN, 2004), Japan (SonotaCo, 2004), Croatia (CMN, 2007), USA (CAMS, 2010), Benelux (CAMS Benelux, 2012).

Results from a first automated meteor shower search based on IMO Network video data was presented at the IMC 2006. The analysis revealed about 50 meteor

showers. Further analyses based on up to a million single station meteors in 2013 increased that figure to over a hundred meteor showers. Similar automated meteor shower surveys (though based on double station data) were carried out by SonotaCo network (2009), CAMS (2012), CMN (2013) and others.

The northern hemisphere was soon densely covered by video systems, but over time video observations were also carried out in the southern hemisphere, e.g., in Australia (IMO Network, 2003), Brazil (BRAMON and EXOSS, 2014), and New Zealand (CAMS NZ, 2014).

Later, new algorithms such as clustering and orbit linking techniques were applied, e.g., by CMN to detect showers of very low activity and with large radiation areas. The reporting and handling of (new) meteor showers was standardized by the IAU Meteor Data Center (MDC). At this time, the MDC list contains 726 meteor shower entries, among which 112 established showers.

Recent work has suggested that we should be more critical in the hunt for new meteor showers. Meteoroid stream modeling has shown that one parent body may produce several radiant, and the same radiant may be produced by several parent bodies. Neslušan and Hajduková (2017) analyzed all major orbital catalogs available and found that only about 100+ showers can be detected with statistical significance.

*We may conclude that the original goal of this key project was fully achieved.*

### 3.2 Meteoroid orbits

*By 1997, only a few hundred precise meteoroid orbits were available, mainly based on double-station photographic work. We proposed to use video cameras to increase this number by orders of magnitude thanks to their high sensitivity. It would require double- and multi-station video observations.*

The SonotaCo network started in 2004 in Japan and evolved soon into a dense network (130 cameras at 31 stations in 2008) with significant overlap. They provided a catalog of soon over 100 000 precise orbits and the first all-sky radiant maps.

In 2010, CAMS started in the US with a different approach: they operated only 3 stations in California, but each of these was equipped with a battery of 20 cameras. CAMS provided soon a similar output as the SonotaCo network. They added the dynamic aspect to the radiant maps, i.e., how the map changes during the year.

The EDMOND database (established in 2012) follows yet another approach. It combines data from the IMO Network and a number of national video networks in Europe using different detection software (METREC and UFOCAPTURE). In this combined data set, double-station recordings are searched, orbits computed, and analyses conducted.

Today all three major databases (SonotaCo, CAMS, and EDMOND) have about the same size and in com-

binations provide data from a million meteoroid orbits. Smaller national networks provide additional orbital data. Meteor shower search in these databases is more reliable than from single-station data, but notwithstanding it is similarly challenging to find reliable clusters in the six-dimensional space of orbital elements.

*In summary, we may say that the original goal of this key project was fully achieved.*

### 3.3 Flux densities

*By 1997, shower activity profiles were solely based on visual observations. Video observations were supposed to be more objective and to be able to study a wider range of particle populations (meteoroid sizes). Since individual meteors would not have to be analyzed in detail, it was argued that “flux analysis could be done almost automatically”.*

In the first ten year of the IMO Network, however, only relative activity profiles were obtained by comparing the meteor counts from different showers and years. With automated meteor shower searches, average shower profiles were provided starting from 2006. Later, geometric corrections (observability function) were applied to these profiles.

With the introduction of limiting magnitude determination and the calculation of the effective collection area of a video camera, we were able to calculate absolute flux densities in the IMO Network starting from 2011. In the same year, we obtained first real-time flux data from the Draconid outburst.

The NASA All-Sky Network team has been working on flux densities obtained with their cameras since 2012.

*Overall, we must admit that the original goal has been only partially achieved so far.*

Systematic errors in the limiting magnitude calculation (e.g., from Moon) are not fully understood and corrected at this time. Real-time flux monitoring was only conducted once as proof of concept, but did not make it to regular operation up to now, and currently only the IMO and NASA All-Sky Network are collecting flux density data.

## 4 Supplementary projects

### 4.1 Very faint meteors

*In 1997, we stated that video observations open the window to meteor down to magnitude +9, which had not been observed in the optical domain before.*

Indeed, since then a number of observers operated cameras with medium-sized fields of view (10°–30° in diameter) capable of recording meteor of magnitudes +7 to +8 on a regular basis. Some cameras like ESCIMO and the UWO Deep Gen II further pushed these boundaries.

However, the small field of view of such cameras brings “standard” meteor detection software to its limits, because meteors pass the field of view within only a few video frames and leave long shutter breaks. Meteor detectors using line-based algorithms (e.g., Hough transform) seem to be more appropriate. We shall also note that the fraction of sporadic meteors increases with the limiting magnitude.

*Overall, we must admit that the original goal has been only partially achieved so far.*

Very faint meteors are still an interesting topic of research:

- telescopic observations have ceased, so there are no other optical observations in that magnitude range;
- well-known meteor showers (e.g., the Lyrids) seem to disappear at these faint magnitudes, and other showers may show up;
- video observations of very faint meteors close the gap between optical and radar observations;
- modern high-resolution cameras are sufficiently sensitive to work at higher frame rates which allow the use of standard detection algorithms.

## 4.2 Observations of outbursts

*In 1997, it was suggested that video systems would allow objective observations, even under meteor-storm-like conditions.*

The Leonid outbursts between 1998 and 2002 were indeed well covered by video, and triggered extended research activities. The dust trail model (see, e.g., Asher and McNaught, 1999) was ultimately confirmed and features like short-term rate oscillations detected. Even airborne missions by NASA and ESA were conducted.

A number of further outburst were detected or observed by video, e.g., from the October Draconids (1998, 2011), September  $\epsilon$  Perseids (2008, 2013),  $\eta$  Aquariids (2013),  $\kappa$  Cygnids (2014),  $\kappa$  Cancrids (2015),  $\gamma$  Draconids (2016), and Perseids (2016 and other). However, video could also prove the absence of predicted outbursts on several occasions.

*Without any doubt, the original goal of this project was fully achieved.*

## 4.3 Fireball patrol

*In our 1997 paper, we suggested that “almost autonomous” all-sky video systems would be able to collect valuable fireball data and fill the gap to continuous working photographic networks like the European Fireball Network. Robust (i.e., non-intensified) cameras would be required, and the sensitivity of these cameras would not be the main concern anymore.*

Thanks to the high degree of automation, video systems were soon used as fireball cameras. However, since accuracy is more important than sensitivity for this purpose, video systems were inferior to photography or still-imaging with high-resolution CCD cameras. For this reason, they were often used in combination with other systems.

Dedicated fireball cameras and networks were installed among others in Canada (ASGARD, 2004), Slovakia (AMOS, 2007), and the USA (NASA MEO, 2010).

A different approach was followed by the French FRIPON network starting in 2014. They are increasing the accuracy of impact area predictions by a dense network of low-cost all-sky cameras which will ensure multiple detections of the same event.

*We conclude that the original goal has been achieved only partially so far.*

Further results may be expected from FRIPON, which is still in the roll-out phase. High-resolution video cameras are more competitive compared to photography and still imaging, by providing better accuracy and a greater dynamic range.

## 4.4 Specific meteor characteristics

*It was suggested in 1997 that video observations may be used to study details like wakes, persistent trains, light curves, and other meteor characteristics.*

In fact, databases of millions of meteor recordings with sum image and/or video footage have been collected by now. There have been some recent studies on light curves (e.g., EDMOND 2015, Petnica Meteor Group 2016). Specialized guided systems like CAMO (UWO 2007, based on the AIM-IT system of 2004) are used to study the meteoric phenomena at high resolution. However, other phenomena were not yet in focus.

*In summary, the original goal has been achieved at this time to a small extent only.*

## 4.5 Meteor spectra

*In 1997, we proposed that video observations can record spectra of much fainter meteors than photography, and increase the spectra database significantly.*

In the following years, many low-resolution meteor spectra have been obtained by video systems, and temporal aspects (i.e., different appearance and disappearance time of spectral lines) could be studied too. Spectra were automatically collected by camera networks on the Canary Islands (CILBO, 2010), in the US (CAMSS, 2013), and at other locations. However, there was only a limited gain in knowledge due to the low resolution. A quantum leap was achieved by the use of high-definition color video cameras, e.g., by observers in Japan (NMS, 2015).

The analysis of spectral data remains demanding, because what we observe is not the meteoroid itself but rather the excited atmosphere around it, so most of the spectral lines and bands we see are of atmospheric origin. There is also no clear correlation between the strength of spectral lines and the abundancy of the corresponding chemical elements.

*In summary, we have achieved the original goal only partially so far.*

#### 4.6 Calibration of other techniques

*In 1997, we noted that video observations are useful to calibrate visual and radio observations, and to train visual observers.*

These days, IMO video and visual observations are regularly combined to confirm each other (e.g., in case of unusual shower activity). Other groups like UWO (Canada) and UKMON (UK) conduct radio and video observations in parallel, and correlate the results.

There have also been attempts to compare video and radio data (e.g., to compare meteor shower surveys obtained by radar and video, or the Daytime Arietids and Sexantids project), but this instrumental overlap was not yet comprehensively studied.

*In summary, we have achieved the original goal only partially so far.*

### 5 Overall goals

Besides observational projects, a number of tasks for the IMO Video Commission were defined at its foundation:

- coordination of activities and the encouragement of more observers to apply this still rarely used observation method;
- coordination between video observers, and fruitful cooperation with other techniques like photographic, visual, and telescopic observation;
- providing information on the “how” and “why” of video observations, technical hints, construction plans for video cameras, suggestions for observational targets, and support for data analysis;
- Maintenance of a video database and providing free access to the stored meteor data;
- providing a contact address for everybody who has specific video-related questions or problems.

*These goals were all fully achieved by the IMO Video Commission over the past 20 years.*

## 6 Conclusions

By now, video has become the most frequently adopted observing technique for meteors with over a thousand camera systems operated world-wide. Video observations do not require promotion by an IMO Commission anymore, but the other Commission tasks are not outdated.

Some of the original projects are still attractive (e.g., real-time flux calculations and meteor characteristics) and a number of promising new projects and technologies are emerging. Here are a few examples:

- high-precision orbits by improved velocity determination (CABERNET, CHIPOLA);
- HDTV video without digital-analog-digital signal conversion;
- dense networks of low-cost video systems;
- high frame rate video and millisecond light curves;
- Virtual Meteor Observatory and big data analyses;
- neural networks and machine-learning techniques;
- improved meteoroid stream modeling based on existing data.

*Beyond any doubt, video observation of meteors is an ongoing success story, and we have good reasons to celebrate the 20th anniversary of the IMO Video Commission!*

## References

- Asher D. J and McNaught R. H. (1999). “Leonid dust trails and meteor storms”. *WGN, Journal of the IMO*, **27**, 85–102.
- Molau S., Nitschke M., de Lignie M., Hawkes R. L., and Rendtel J. (1997). “Video observations of meteors: history, current status, and future prospects”. *WGN, Journal of the IMO*, **25**, 15–20.
- Neslušan L. and Hajdukova M., Jr. (2017). “The separation and confirmation of showers”. *Astron. & Astrophys.*, **598** A40.

# Orbital uncertainties in radar meteor head echoes

Daniel Kastinen<sup>1,2</sup> and Johan Kero<sup>1</sup>

<sup>1</sup> Swedish Institute of Space Physics (IRF), Box 812, 98128 Kiruna, Sweden  
daniel.kastinen@irf.se

<sup>2</sup> Umeå University, Department of Physics, 90187 Umeå

We present the general methodology for finding uncertainties in measurement systems and associated data analysis algorithms. We then apply these ideas on MU radar meteor head echo observations. The method is based on Monte-Carlo simulations, statistical estimator theory, and fundamentally known—yet stochastic—uncertainties. The end results are multidimensional and non-Gaussian probability distributions in the orbital elements for every meteor event. We also discuss how these new uncertainties should be utilized when the data is used for further research.

## 1 Introduction

In spite of the underlying orbital dynamics being well understood, it is still an open question how much extraterrestrial material enters the Earth's atmosphere (Plane, 2012). Meteoroids and dust entering the atmosphere take part in physical and chemical processes important for a wide range of phenomena, such as the formation of clouds at 15–25 km altitude responsible for ozone destruction in the polar regions and mid-latitude ice clouds at 75–85 km which are possible tracers of global climate change (Plane, 2003). Characterization of dust trails and meteoroid streams is also highly relevant for models like the European Space Agency (ESA) Interplanetary Meteoroid Environment for eXploration (IMEX) project (Soja et al., 2015) to assess the dust impact hazard to spacecrafts.

Numerical simulations of cometary dust trails and the dynamics of meteoroid streams is an active research area. In 2005, Vaubaillon et al. (2005a; 2005b) presented the first approach to combine a physical model of a comet nucleus and a dynamical model of individual meteoroid particles using large computer processing resources. Recently, we have also seen an advance towards statistical simulations of meteoroid streams (Kastinen and Kero, 2017). This opens up the door for a whole new way to use measurements and to systematically make predictions and compare with events.

Output from numerical simulations does by itself not necessarily constitute valuable scientific material. Simulation data need context to be useful, and one very common way to provide this context is to try to emulate reality and compare with observations. However, the quality of the context that these comparisons or calibrations provide cannot be evaluated without an understanding of the quality of both the simulation and the measurement. In these comparisons and calibrations, it is vital to have an accurate understanding of the associated errors, biases, and uncertainty distributions to properly link the simulations to the measurements.

The goal of this paper is to thoroughly examine the errors that are associated with a High-Power Large-Aperture (HPLA) radar meteor head echo observation

pipeline (Kero et al., 2012). We will outline in a pedagogical manner some basic principles associated with statistical analysis of algorithms, error estimations in measurement systems, and associated work. We will also discuss some of the principles of using the additional information provided by these uncertainties and probability distributions.

## 2 Measurement uncertainty example

### 2.1 Theory

Consider an algorithm, here described as a function  $F$ , that takes a measurement  $x$  as input during circumstances  $C$  and produce an output  $y$ . We can treat the problem of finding the probability distribution of the algorithm in two ways. First, let us consider the algorithm stability itself. We can find the accuracy of the algorithm as a probability distribution if we have a model for the input as a function of the circumstances and the output parameter  $y$ , which we denote by

$$G(C, y_0) = x, \quad (1)$$

where  $y_0$  is known and picked beforehand. These variables are not restricted to numbers. For example, if  $x$  is a sinusoidal signal of frequency  $F$ , and  $y$  and  $C$  are the sampling frequency and sampling number, we can simulate the signal and generate simulated algorithm inputs. The accuracy of the algorithm can be determined by passing the simulated variable  $x$  through our algorithm

$$F(x, C) = y, \quad (2)$$

and calculate the accuracy with the known parameter  $y_0$  as  $\Delta y = y - y_0$ . Let us consider that, if

$$F(G(C, y_0), C) = Y, \quad (3)$$

then

$$Y \sim \mathcal{H}_{y_0}. \quad (4)$$

If the algorithm  $F$  and the model  $G$  does not contain any stochastic processes or unstable/chaotic algorithms, the distribution  $\mathcal{H}_{y_0}$  will be a Dirac delta function. This

is most often not the case, as, e.g., white noise is a stochastic process that should be included in  $G$ . Here, the notation  $\mathcal{H}_{y_0}$  indicates that, for each  $y_0$ , we will have a different distribution function that  $Y$  is distributed according to. We are interested in the probability

$$P(y = y_0 \mid F(x_m, C) = y_m) = \Gamma(y), \quad (5)$$

where  $y$  is a variable,  $\Gamma(y)$  a distribution function,  $y_0$  is the true parameter value,  $x_m$  is a measurement of the  $x$  variable and  $y_m$  is the output from our algorithm for the given measurement. In other words, we want to know the probability distribution for the true value of the parameter  $y_0$  given our algorithm output  $y_m$ . If the algorithm contains systematic errors, the maximum probability may not be located at  $y_m$ .

Through  $G$  we can assume that all  $\mathcal{H}_{y_0}(y)$  are known. We can reformulate Equation (5) by asking instead, “from which  $\mathcal{H}_{y_0}(y)$  is it most probable that  $y_m$  was drawn, where  $y_m$  is a sample of the stochastic variable  $Y$ ?” or

$$P(Y \sim \mathcal{H}_y) = \Gamma(y). \quad (6)$$

We have introduced the stochastic variable  $Y$  of which  $y_m$  is a sample. It has an unknown distribution, but we know it is one of the calculated  $\mathcal{H}_{y_0}$ . Thus we look for the probability distribution  $\Gamma(y)$  describing the probability that  $Y$  is distributed according to  $\mathcal{H}_y$ . To find  $\Gamma$ , we first state that, given  $\mathcal{H}_{y_0}$ , there is a  $\mathcal{H}_{y_0}(y)$  probability to draw  $y$ . Thus the probability that  $y_m$  was drawn from  $\mathcal{H}_{y_0}$  is  $\mathcal{H}_{y_0}(y_m)$ , and so we know that

$$\Gamma(y) = \frac{\mathcal{H}_y(y_m)}{\int_M \mathcal{H}_y(y_m) dy}, \quad (7)$$

where  $y \in M$ . A simple case is where the shape of the distribution function does not change but is merely displaced, i.e.,

$$\mathcal{H}_{y_0}(y) = \mathcal{H}(y - y_0). \quad (8)$$

Then the distribution for the true parameter value given a measurement is simply

$$\Gamma(y) = \frac{\mathcal{H}(y_m - y)}{\int_M \mathcal{H}(y_m - y) dy} = \mathcal{H}(y_m - y). \quad (9)$$

Although not in the scope of this paper, we highly recommend reading some standard literature on estimator statistics such as bootstrapping (Efron, 1982).

## 2.2 Example

As a practical example, let us consider the set of leaf length measurements shown in Figure 1. The Figure shows comparisons of this data with two different models for the population distribution. Let us assume that the leaves were measured by a technician, for simplicity hereafter referred to as Bob. Before trying to answer the question which of models 1 and 2 (or none of them) best describe the true distribution of leaves, we need to characterize uncertainties and biases in Bob’s measurement method. One way to proceed doing so would be

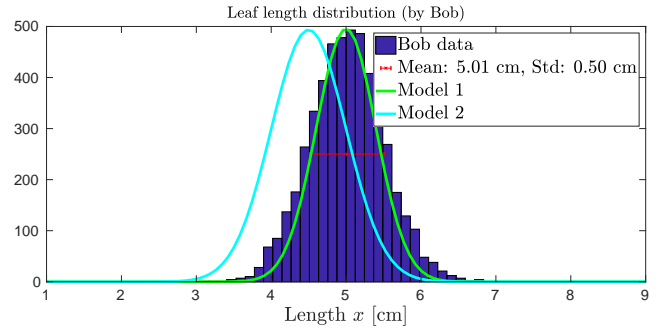


Figure 1 – Set of leaf length measurements collected by Bob and scaled distribution models.

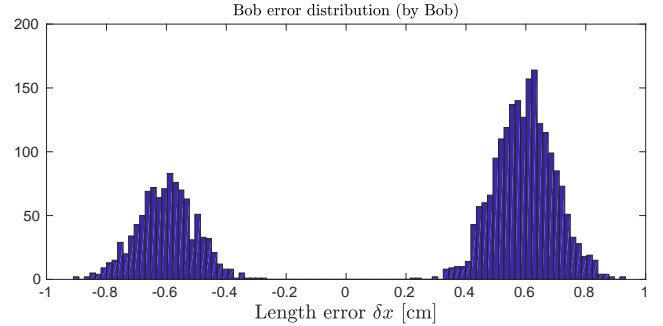


Figure 2 – Error distribution  $H_{y_0}(y - y_0)$  of Bob’s leaf measurements.

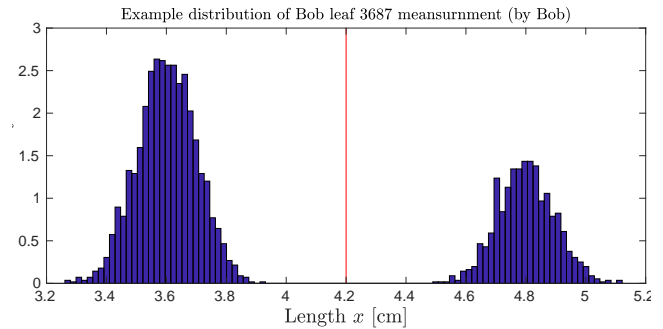


Figure 3 –  $\Gamma$  distribution for leaf 3687 where the histogram is the probability distribution for the true length and the red line is the originally reported length  $y_m$ .

to give Bob a set of 3D-printed leaves that we know the exact length of.

Let us in this practical example assume that Bob’s measurement method by some reason contains systematic errors resulting in the distribution described in Equation (8). We now plot the error distribution of the reference measurements in Figure 2 and assume that this is the distribution  $\mathcal{H}$ . We can then apply Equation (9) to a specific measurement, e.g., leaf 3687 that was recorded to have a length of  $y_m = 4.2$  cm, to find the probability distribution  $\Gamma$  of the true leaf length, plotted in Figure 3. Now, we can use this information to split the length measurement of this leaf over the bins used in the analysis produced in Figure 1. Doing so, we arrive at a partition for this particular measurement shown in Figure 4. Doing the same for all measurements that was originally presented in Figure 1, the distribution will converge towards the true distribution. The result of the procedure is given in Figure 5. Since we have corrected for the measurement errors, this new distribution

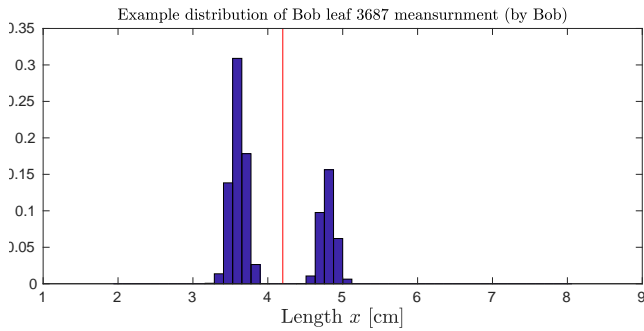


Figure 4 – Create a discrete version of a Kernel Density Estimation by splitting each leaf over the previous bins and summing. The vertical red line is the originally reported length  $y_m$ .

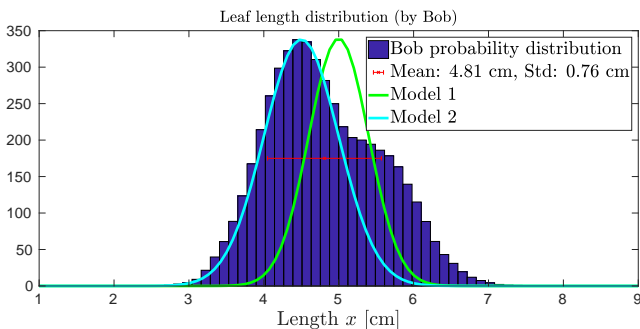


Figure 5 – The most probable leaf length distribution.

is the “most probable distribution given the measurements”. At high number statistics, this distribution gives a good representation of the true distribution.

Figure 5 shows that none of the models are able to reproduce the shape of the corrected distribution. The true distribution is somewhat bimodal, and it seems that model 2 describes rather well one of its two components only. Both models clearly lack capability to describe the true dynamics of leaf lengths.

Before trying to draw any conclusions about the lengths of the leaves in the trees that Bob sampled in his measurements, we should also note that the example this far has not included any debiasing procedure. For example, let us assume that Bob is short compared to the trees. If this is the case, he could only reach the lowest leaves of a tree and thus has a bias towards his measurements, unless he was climbing the trees. Thus we have only compared a measurement distribution to the model, only when the bias is known can we produce a population distribution.

This result raises the very important question: what value of  $y$  does one report? The direct output of the algorithm  $y_m$ , the maximum probability value, the mean probability value, as much information as possible or some other measure?

### 3 Measurement uncertainty application

The methodology presented above is very general and thus we encourage others to apply such techniques to other measurements systems.

After all of the above calculations were performed for the MU radar meteor head echo data observation pipeline (Kero et al., 2012), we arrive at a set of orbital elements equal to the number of Monte-Carlo iterations we performed. Here, we present results from performing the analysis on two meteor events detected by the MU radar. Each analysis set contained 10 000 Monte-Carlo clones, sampled using a white noise perturbation and estimator statistics to introduce the stochastic processes. In Figure 6, we show the Monte-Carlo clone distribution for the meteor with ID 1150440. Figure 8 shows the corresponding Probability Density Function (PDF). All the figures plot combinations of the familiar orbital elements, which are

- $a$ , semi-major axis;
- $e$ , eccentricity;
- $i$ , inclination;
- $\omega$ , argument of periapsis; and
- $\Omega$ , longitude of the ascending node.

To compare the analysis with a previous estimation of uncertainties, where a 95% Student- $t$  confidence limit was given for the orbital elements of these two events, we take the univariate histograms and calculate the interval that contains a 1-sigma equivalent number of clones. The 1-sigma threshold for a univariate normal distributions corresponds to 68.27% of the probability mass. However, these parameters are not representative of the true uncertainties.

Figure 6 clearly shows parameter correlations in the plane intersection plots. Thus, one must use more sophisticated representations to parametrize the distributions of the uncertainties in the data. Another example, pertaining to the meteor with ID 1150491, is given in Figure 7 and 6, respectively.

## 4 High level statistics

Now that we have obtained this additional information, we must apply it somehow to improve our methods. One straightforward way is to simply examine the distributions before using the data in analysis and to discuss the weight we assign to results based on such measurements.

However, if we intend to use the distributions as done in the example in Section 2.2, it can be done in exactly the same manner. This may be one of the easiest ways to compare simulations to measurements. The procedure is similar to a Kernel Density Estimation (KDE) where, instead of using the same kernel for all measurements, each point is given its own probability distribution. More examples follow below.

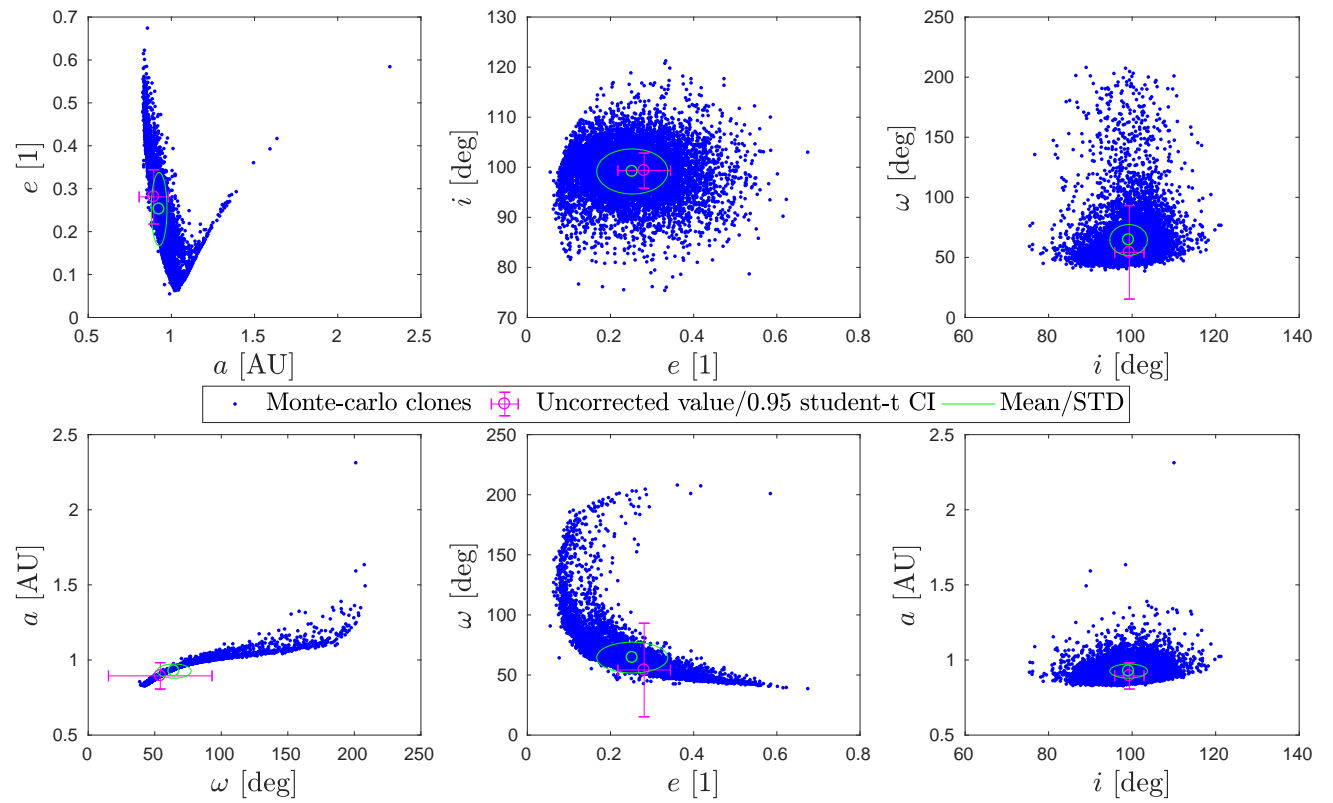


Figure 6 – Meteor ID 1150440 Monte-Carlo clone distribution in orbital element space. Plotted are only the coordinate plane projections on  $a$ ,  $e$ ,  $i$ , and  $\omega$ , as the uncertainty in  $\Omega$  is approximately 0.

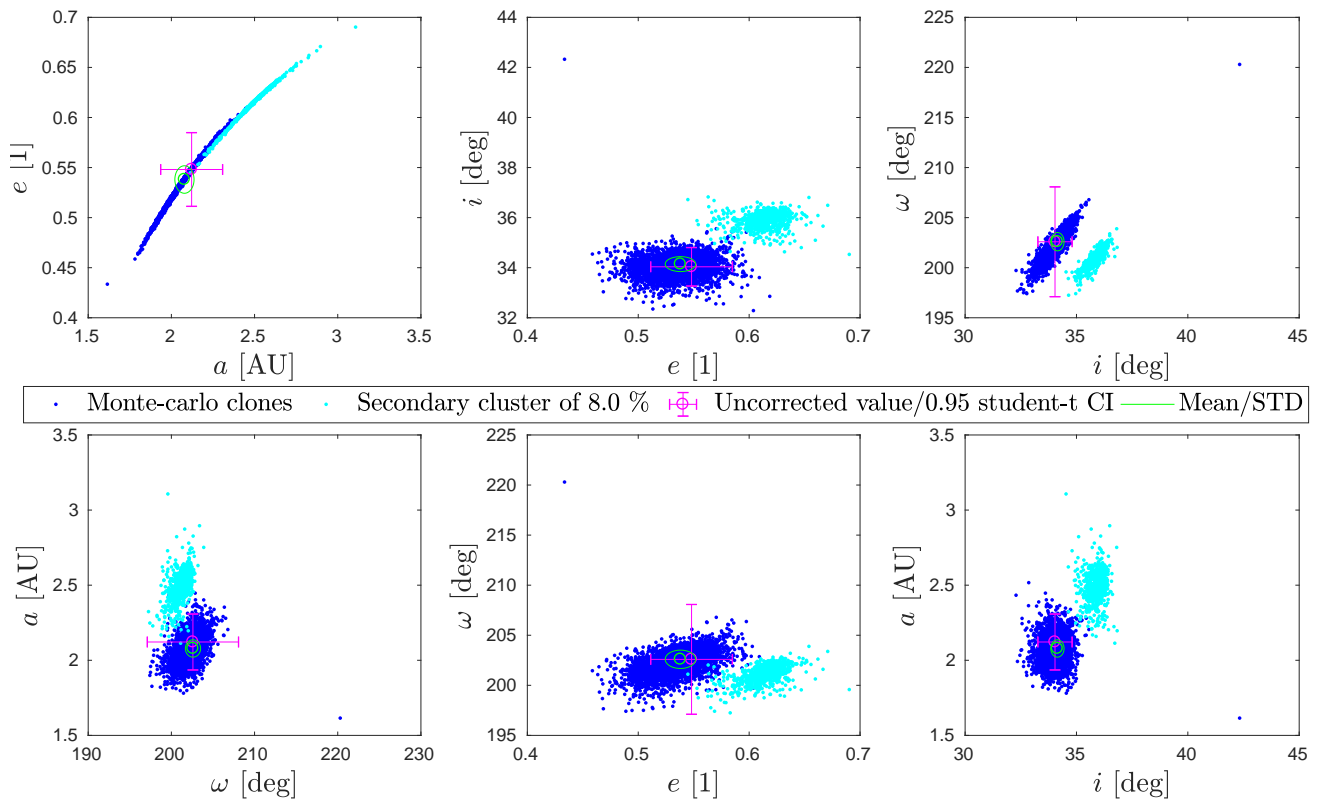


Figure 7 – Meteor ID 1150491 Monte-Carlo clone distribution in orbital element space. Plotted are only the coordinate plane projections on  $a$ ,  $e$ ,  $i$ , and  $\omega$ , as the uncertainty in  $\Omega$  is approximately 0.

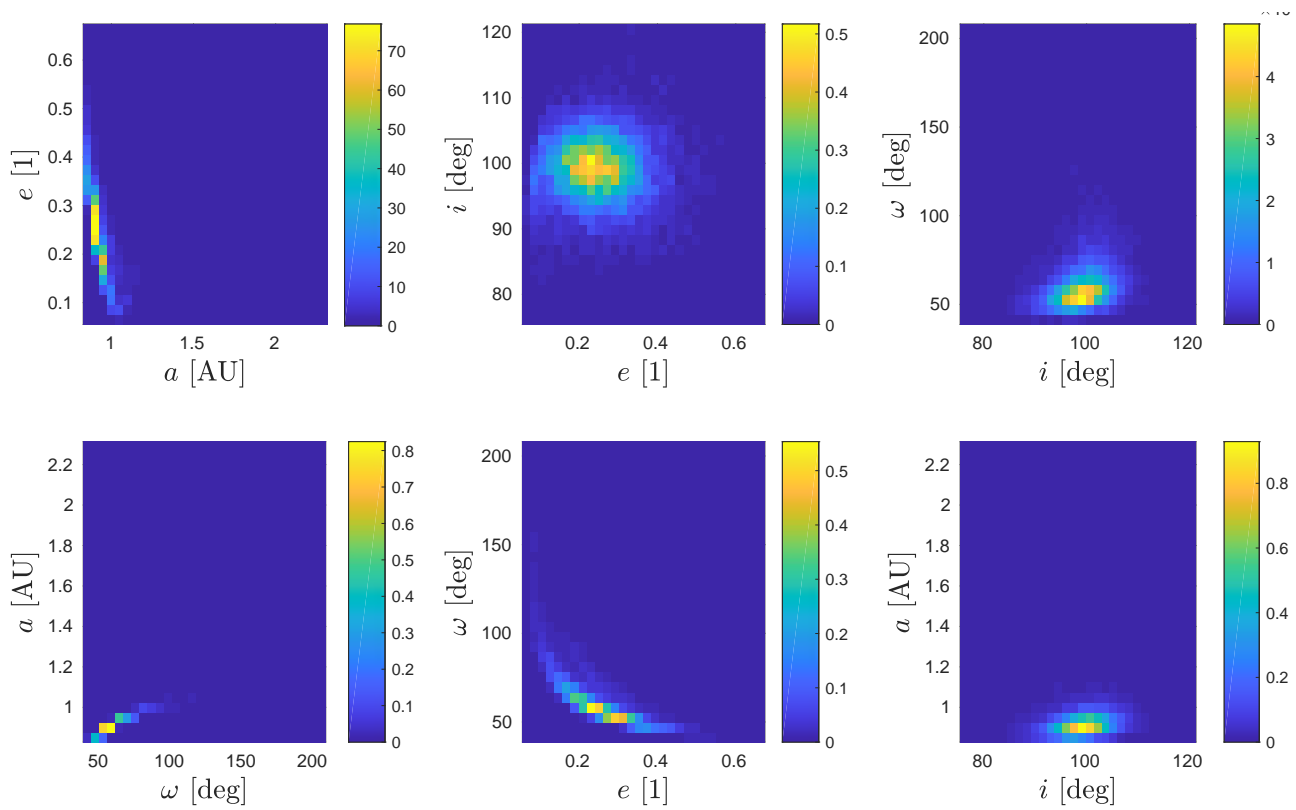


Figure 8 – Meteor ID 1150440 PDF in orbital element space. The PDF was calculated by taking a 4-dimensional histogram.

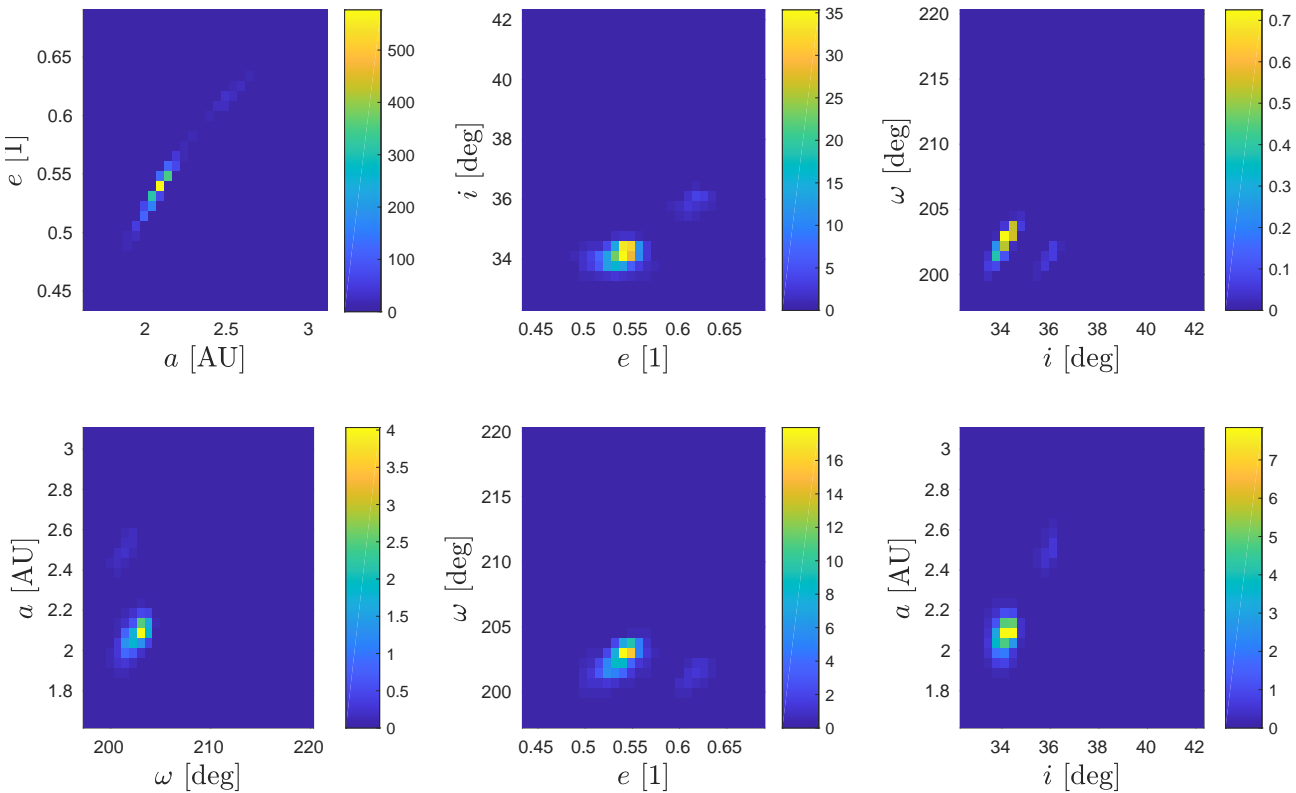


Figure 9 – Meteor ID 1150491 PDF in orbital element space. The PDF was calculated by taking a 4-dimensional histogram.

## 4.1 Example 1

Using a statistically large simulation, we can find a meteoroid flux density  $F_0(\mathbf{x})$  in orbital element space  $\mathbb{X}$  ( $\mathbf{x} \in \mathbb{X}$ ). We can then take our  $N$  measurements of meteoroid orbits  $\mathbf{y}_i \in \mathbb{X}$  with the corresponding probability distributions  $G_i(\mathbf{x})$ ,  $i = 1, \dots, N$ , and form a most probable density estimate  $G_0(\mathbf{x})$  as

$$G_0(\mathbf{x}) = \sum_{i=1}^N G_i(\mathbf{x}). \quad (10)$$

If we normalize the simulation and measurements to the same units, we can qualitatively compare the simulation output  $F_0(\mathbf{x})$  with the measurements. The comparison can be done either as distribution functions

$$F_{\text{simul.}}(\mathbf{x}) = \frac{F_0(\mathbf{x})}{\int_{\mathbb{X}} F_0(\mathbf{x}) d\mathbf{x}}; \quad (11)$$

$$F_{\text{meas.}}(\mathbf{x}) = \frac{1}{N} G_0(\mathbf{x}), \quad (12)$$

or as real fluxes

$$F_{\text{simul.}}(\mathbf{x}) = \frac{F_0(\mathbf{x})}{H_{\text{mass}}}; \quad (13)$$

$$F_{\text{meas.}}(\mathbf{x}) = \frac{G_0(\mathbf{x})}{H_{\text{bias}}(\mathbf{x})}, \quad (14)$$

where  $H_{\text{mass}}$  is the conversion from the simulation mass sampling to a real mass flux and  $H_{\text{bias}}$  is the bias function of the measurement system. One interesting aspect that we find here is that the simulated flux density  $F_0(\mathbf{x})$  could represent an arbitrary statistical measure: it could be the most probable flux, it could be the mean flux, it could be the stability-weighted mean flux, etc.

## 4.2 Example 2

If we would like to look into the origin of a certain meteoroid indexed  $i$ , we could simply use the probability distribution for the orbital elements  $G_i(\mathbf{x})$  and draw  $M$  random orbits from this distribution. Then, we would propagate these  $M$  orbits backwards in time and look at how the distribution evolves.

## 4.3 Example 3

Suppose we would like to select all October Draconids from a data set. Usually, a human would look at the data and adjust parameters for a clustering methods until the result looks like “it does not include sporadics” or simply select the ones that “look like they are Draconids”. This introduces a large uncertainty in the classification since there is no quantifiable science basis for the classification, except for intuition/experience. Instead, let us use the simulation data from Example 1,  $F_0(\mathbf{x})$ , and assume this represents the October Draconids. If we use these data to train a machine-learning algorithm, only the model assumptions and the algorithm efficiency will influence the selection process.

Then, we also give the algorithm of the distributions for the individual measurements  $G_i(\mathbf{x})$  so that the algorithm can provide an “October Draconid likelihood”, this time based solely on model restrictions and first-principle physics.

## 5 Conclusions

The investigation of uncertainties associated with a data reduction pipeline is important for the users of the final data product. We conclude that the easiest method is a Monte-Carlo type iteration of the pipeline where stochastic processes can be introduced in a variety of ways, e.g., through sensor response models, estimator statistics, fake events generation, or noise models.

We have demonstrated that such an analysis can drastically change results and also given some concrete examples on how to use the results in research applications. This opens a question that should be discussed within the community: what do you publish in an open database? The mean value, together with a variance? Coefficients from a distribution fitting process? All the Monte-Carlo clones? Pipeline output together with a number of statistical moments?

Whatever data are published together with the measurement results, it seems that the most important factor is ability to reproduce the probability density function (PDF). Thus, this should probably (pun intended) be the goal of any database: to provide a central value and enough data to accurately reproduce the measurement PDF while retaining simplicity.

## Acknowledgements

This work was supported by the Swedish Research Council Project Grant 2012-4074.

## References

- Efron B. (1982). The Jackknife, the Bootstrap and Other Resampling Plans. CBMS-NSF Regional Conference Series in Applied Mathematics, volume 38. SIAM.
- Kastinen D. and Kero J. (2017). “A Monte Carlo-type simulation toolbox for Solar System small body dynamics: Application to the October Draconids”. *Planetary and Space Science*, **143**, 53–66.
- Kero J., Szasz C., Nakamura T., Terasawa T., Miyamoto H., and Nishimura K. (2012). “A meteor head echo analysis algorithm for the lower VHF band”. *Ann. Geophys.*, **30**, 639–659.
- Plane J. M. C. (2003). “Atmospheric chemistry of meteoric metals”. *Chemical Reviews*, **103**, 4963–4984.
- Plane J. M. C. (2012). “Cosmic dust in the Earth’s atmosphere”. *Chem. Soc. Rev.*, **41**, 6507–6518.

- Soja R. H., Herzog J. T., Sommer M., Rodmann J., Vaubaillon J., Strub P., Albin T., Sterken V., Hornig A., Bausch L., Grün E., and Srama R. (2015). “Meteor storms and showers with the IMEX model”. In Rault J.-L. and Roggemans P., editors, *Proceedings of the IMC*, Mistelbach, Austria, 27–30 August 2015. IMO, pages 66–69.
- Vaubailon J., Colas F., and Jorda L. (2005). “A new method to predict meteor showers. I. Description of the model”. *Astron. Astrophys.*, **439**, 751–760.
- Vaubailon J., Colas F., and Jorda L. (2005). “A new method to predict meteor showers. II. Application to the Leonids”. *Astron. Astrophys.*, **439**, 761–770.

# Study of distinct meteor spectra populations

Pavol Matlovič<sup>1</sup>, Juraj Tóth<sup>1</sup>, Regina Rudawska<sup>2</sup>, and Leonard Kornoš<sup>1</sup>

<sup>1</sup> Faculty of Mathematics, Physics, and Informatics, Comenius University, Mlynská dolina, Bratislava, Slovakia

matlovic@fmph.uniba.sk

<sup>2</sup> ESA European Space Research and Technology Center, Noordwijk, the Netherlands

The AMOS-Spec program (Matlovič et al., 2017; Rudawska et al., 2016) is aimed to study spectra and physical properties of meteoroids in the magnitude range of  $-1$  to  $-10$  (corresponding to millimeter- to decimeter-sized objects). A preview of the updated results of the spectra survey performed during the first three years of the program is presented. Spectral classification of the samples shows chondritic ratios between the silicate, volatile, and metallic content for the majority of meteors, but also considerable contribution of various distinct spectral types suggesting more peculiar compositions. Furthermore, the first observations and the potential of the new higher-resolution AMOS-HSpec spectral systems operating on the Canary Islands and in Chile are described.

## 1 Introduction

Meteor spectroscopy has been gaining popularity among professional and amateur astronomers in recent years, due to the accessibility of simple video-based systems providing lower-resolution meteor spectra. The precision and high resolution of early photographic spectrographs (e.g., Borovička, 1993) cannot be achieved, but this is partially compensated by the sensitivity of the video systems. The intention of the AMOS-Spec (All-Sky Meteor Orbit System Spectrograph) and AMOS-HSpec (High-resolution Spectrograph) spectral program is to provide a balance between sufficient spectral resolution, astrometric precision, and the statistical advantage of the video detection sensitivity.

It has been shown that lower-resolution spectra can be used to study the composition of meteoroids based on the variations of relative intensities of the main meteor emission multiplets of Mg I-2 (representing the silicate content in meteoroids), Na I-1 (volatiles), and Fe I-15 (metals and silicates). This is the basis of the spectral classification of primarily smaller meteors introduced by Borovička et al. (2005). In addition, multi-station observations can be used to determine the trajectories, orbits, and light curves of the studied meteoroids, which can be further applied to deduce physical properties, such as material strength, dynamic pressure, or density. Obtaining such sets of parameters for a large number of observations provides us with complex view on the population of meteoroids in the Solar System. For known meteoroid streams, it also suggests implications for the structure and properties of their parent comets and asteroids.

## 2 Instrumentation

### 2.1 AMOS-Spec

AMOS-Spec is a semi-automatic remotely controlled video system for the detection of meteor spectra located at the Astronomical and Geophysical Observa-

tory (AGO) in Modra, Slovakia. The main device components are a 30 mm  $f/3.5$  fish-eye lens, an image intensifier (Mullard XX1332), a projection lens (Opticon 19 mm  $f/1.4$ ), and a digital camera (Imaging Source DMK 51AU02). This setup yields a  $100^\circ$  circular field of view (FOV) with a resolution of  $1600 \times 1200$  pixels and a frame rate of 12/s.

The incoming light is diffracted by a holographic grating with 1000 grooves/mm placed above the lens. The spectral resolution of the system varies due to the geometry of the all-sky lens with a mean value of 1.3 nm/pixel. The system covers the visual spectrum range of approximately 370–900 nm with a sensitivity level of 10% at 900 nm. The spectral response curve of the AMOS-Spec system was determined by measuring the known spectrum of Jupiter. The typical limiting magnitude of the system for meteors is approximately +4, while only meteors brighter than approximately magnitude 0 can be captured along with their spectrum. More details about the properties and capabilities of the AMOS systems can be found in Tóth et al. (2015).

Spectral events recorded by the AMOS-Spec are supplemented by network of four AMOS systems in Slovakia, which provide multi-station observations.

### 2.2 AMOS-HSpec

Since 2015, the AMOS network has been expanded into global scale by installation of two systems on the Canary Islands (Teide Observatory, Tenerife; Roche de los Muchachos Observatory, La Palma) and two in Chile (Space Obs, San Pedro de Atacama; Paniri Caur Observatory, San Francisco de Chiu Chiu). To obtain simultaneous spectral observations, new higher-resolution spectrographs were employed to accompany existing AMOS stations in Tenerife, La Palma, and San Pedro. The operation of the spectral camera in Tenerife was finalized in cooperation with the Valašské Meziříčí Observatory in the Czech Republic.

The display component of these spectrographs is based on a 6 mm  $f/3.5$  lens, a high-definition digital Point Grey camera providing a  $60^\circ \times 45^\circ$  FOV with a resolution of  $2048 \times 1536$  pixels and a frame ratio of 15/s. The applied 1000 gr/mm holographic diffraction grating results in a spectral resolution of 0.5 nm/pixel. The typical limiting magnitude of the system is approximately +3 for meteors and  $-1.5$  for meteor spectra.

### 3 Results

#### 3.1 Distinct meteor spectra populations

Here, we discuss the observations of the AMOS-Spec system collected since December 2013. While the first results (Rudawska et al., 2016) showed small variations on mostly normal-type meteor spectra, an increasing number of observations is beginning to uncover the real, much more diverse, structure of the spectral classification of the studied meteoroid population (millimeter- to decimeter range). The ternary diagram displaying the spectral classification of 198 meteors is shown in Figure 1.

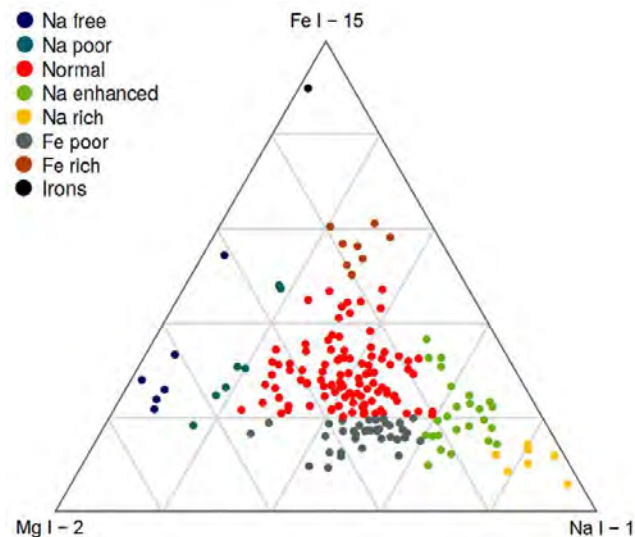


Figure 1 – Spectral classification of meteors observed by the AMOS-Spec based on relative intensities of main meteor emission multiplets of Mg I - 2, Na I - 1, and Fe I - 15. The displayed spectral classification is before correction for meteor speed.

Most of the meteoroids are defined as normal type with relative ratios of Mg I - 2, Na I - 1, and Fe I - 15 characteristic for ordinary chondrites. The division between normal and Fe-poor meteoroids is not precisely defined, as the lower intensity of Fe in these meteoroids is in most cases probably caused by the lower brightness of observed meteors. Besides the two mainstream classes comprising 73% of the entire sample, we also observed meteoroids belonging to various distinct spectral types. The following main task is to find out whether the observed spectral variations of main multiplets are caused by actual compositional differences in the studied meteoroids, or are only a result of different atmospheric flight conditions (meteor speed and size). For exam-

ple, increased intensity of Na in Na-rich meteors is often connected to low-velocity meteors with characteristically lower temperatures. The low excitation potential of sodium causes Na-line radiation to be dominant compared to other multiplets.

In general, the distribution of the determined spectral classes and their individual populations show different features when compared to similar surveys performed by Borovička et al. (2005) or Vojáček et al. (2015). We believe that these distinctions are mainly caused by different size distributions of observed meteoroids.

Smaller meteoroids observed by Borovička et al. (2005) result in fainter meteors, in which lower temperatures are achieved and self-absorption of spectral lines plays a less significant role. Furthermore, we expect to observe compositional differences between millimeter-sized particles on the one hand and centimeter- to decimeter-sized particles on the other hand, as a result of their formation process as well as the evolutionary influence of solar and cosmic radiations, that penetrate surface layers of meteoroids and particularly affect the presence of volatiles.

The complete analysis of the AMOS-Spec observations will be published in a separate paper, which is currently in preparation.

#### 3.2 Exceptional fireball spectra from the Canary Islands and Chile

The observing conditions at the Canary Islands and the Atacama Desert in Chile promised at least comparable number of spectral detections, even with smaller FOV and higher-resolution for the new systems compared to the wide-field AMOS-Spec. This can be confirmed after the first year of operation of AMOS-HSpec, in which 95 meteor spectra were observed by the two combined systems on the Canary Islands and 36 spectra by a single system in Chile.

The provided spectral resolution of 0.5 nm/pixel is sufficient to distinguish up to hundreds of lines of the main and high-temperature spectral components. In addition, the spectral sensitivity and high altitude of the observing stations provide more details into the near-UV part of the spectrum. The collected spectra could potentially be used for detailed modeling and for determination of the elemental abundances in meteoroids.

As an illustration, we provide spectral profiles of one of the brightest spectral events observed on the Canary Islands (Figure 2). This case is a potential meteorite dropper with saturation hindering large part of the spectrum and obstructing line intensity analysis for the most part of the meteor path. As a silver lining, many more details are provided in the 600–700 nm range of the spectrum, where spectral lines are too faint to be detected by standard video spectrographs. This area mostly consists of a mixture of Fe I, Ti I, Si II, and O I lines and molecular radiation of FeO and N<sub>2</sub>.



- meteoroids”. *Planetary and Space Science*, **143**, 104–115.
- Rudawska R., Tóth J., Kalmančok D., Zigo P., and Matlovič P. (2016). “Meteor spectra from AMOS video system”. *Planetary and Space Science*, **123**, 25–32.
- Tóth J., Kornoš L., Zigo P., Gajdoš S., Kalmančok D., Világi J., Šimon J., Vereš P., Šilha J. Buček M., Galád A., Rusňák P., Hrábek P., Ďuriš F., and Rudawska R. (2015). “All-sky Meteor Orbit System AMOS and preliminary analysis of three unusual meteor showers”. *Planetary and Space Science*, **118**, 102–106.
- Vojáček V., Borovička J., Koteš P., Spurný P., and Štork R. (2015). “Catalogue of representative meteor spectra”. *Astron. Astrophys.*, **580**, A67.

# Fine-scale observations of Doppler frequency shifts affecting meteor head radio echoes

Jean-Louis Rault<sup>1</sup>, Mirel Birlan<sup>2</sup>, Cyril Blanpain<sup>3</sup>, Sylvain Bouley<sup>4</sup>, Stéphane Caminade<sup>4</sup>, François Colas<sup>2</sup>, Jérôme Gattacceca<sup>5</sup>, Simon Jeanne<sup>2</sup>, Julien Lecubin<sup>3</sup>, Adrien Malgoyre<sup>3</sup>, Chiara Marmo<sup>4</sup>, Jérémie Vaubailon<sup>2</sup>, Pierre Vernazza<sup>6</sup>, and Brigitte Zanda<sup>7</sup>

<sup>1</sup>International Meteor Organization, Radio Commission, 91360 Épinay-sur-Orge, France  
f6agr@orange.fr

<sup>2</sup>Institut de Mécanique Céleste et de Calcul des Éphémérides, Observatoire de Paris, 75014 Paris, France

mirel.birlan@obspm.fr, francois.colas@obspm.fr, simon.jeanne@obspm.fr, and jeremie.vaubailon@obspm.fr

<sup>3</sup>OSU Pythéas, CNRS, Université d'Aix-Marseille, 13007 Marseille, France  
blanpain@osupytheas.fr, julien.lecubin@osupytheas.fr, and adrien.malgoyre@osupytheas.fr

<sup>4</sup>Géosciences Paris Sud, Université Paris Sud, CNRS, Université Paris-Saclay, 91405 Orsay, France

sylvain.bouley@gmail.com, stephane.caminade@ias.u-psud.fr and chiara.marmo@u-psud.fr

<sup>5</sup>Centre Européen de Recherche et d'Enseignement des Géosciences de l'Environnement, CNRS, Aix-en-Provence, France

gattacceca@cerege.fr

<sup>6</sup>Laboratoire d'Astrophysique de Marseille, Université d'Aix-Marseille, 13007 Marseille, France

pierre.vernazza@lam.fr

<sup>7</sup>Muséum National d'Histoire Naturelle, 75005 Paris, France

brigitte.zanda@mnhn.fr

The French FRIPON (Fireball Recovery and Interplanetary Observation Network) program relies on a video camera network associated to radio sensors running in a radar multistatic configuration to observe fireballs and to determine accurate meteoroids orbits and potential meteorites strewnfields. This paper focuses on some peculiar phenomena observed with radio means during the final phase of the meteors flight.

## 1 Introduction

The French FRIPON program plans to install a network composed of 100 video cameras and 25 radio receivers to observe fireballs in order to compute associated meteoroid orbits and to determine the possible meteorite strewnfields. Currently, 80 cameras and 13 receivers are already operational.

The orbit and atmospheric trajectory of a meteoroid is determined by means of optical triangulation on the bolide's apparent trajectory, and its accurate velocity is computed thanks to radio data.

The French Air Force GRAVES radar, the primary purpose of which is to detect and classify satellites, is used by FRIPON in a multistatic configuration running in forward and back scatter modes.

Although the main initial purpose of the radio observation system was the calculation of the accurate velocity of a meteoroid, it quickly became apparent that this system also enabled, as a result of its properties, the

detailed observation of the meteoroid's behavior during its atmospheric flight.

## 2 Observational method

A multistatic radar configuration has been chosen for the FRIPON experiment.

The GRAVES transmitter, located near Dijon, France, is a HPLA (High Power Large Aperture) radar-type. It is transmitting 24 hours a day a powerful permanent 143.050 MHz CW (Continuous Wave) carrier thanks to its 4-planar phased-array antennas. Each of the four antenna systems is scanning an azimuthal sector of 45° (from 90° to 270°) in the southern direction.

The FRIPON SDR (Software Defined Radios) receivers are located where some of the 100 video cameras are (see Figure 1), and they share the same local computer that is used to process and to transfer the video data to the FRIPON central server and database. Each radio set-up consists of a FunCube Pro +2 SDR receiver and a colinear vertical omnidirectional antenna.



Figure 1 – Location of the GRAVES transmitter and of the FRIPON radio receivers. In addition to the French receivers, some receivers are also installed in Austria, Spain, and Belgium (September 2017).

Each time an optical multi-detection occurs (i.e., a meteor is detected on several video camera stations), the related video and SDR I/Q (In phase/in Quadrature) radio data are automatically transferred through a VPN (Virtual Private Network) to the FRIPON central server. Furthermore, the I/Q radio data recorded 24 hours a day are stored for about one month on the local hard drive of each station and can thus be uploaded at any time for data processing, even if no optical event is associated.

### 3 Head echo observations

The radio waves radiated by a transmitter are scattered by the free electrons of the plasma surrounding the fast moving body of a meteoroid and by the free electrons of its ionized train, provided that the density of these electrons is high enough, depending on the frequency of the radio waves that is used. The plasma frequency at which a radio wave is reflected is given by

$$f_n = \sqrt{\frac{N_e e^2}{\pi m}}, \quad (1)$$

where  $m$  and  $e$  are respectively the mass and the electric charge of an electron,  $N_e$  the electron density, and  $f_n$  the frequency of the reflected wave.

A trail echo amplitude is very sensitive to the geometrical configuration of the incident radio waves. The Snell-Descartes Law fully applies to the quasi-cylindrical train mirror that produces a specular reflection. If a meteor train is not properly oriented (i.e., if it is not tangent to an ellipse which foci are the TX and RX locations), there will be no train echo at all.

On the other hand, a head echo has much less geometrical dependence, as a large part of the reflecting plasma surface surrounding the meteoroid is considered as almost spherical, as observed by Kero et al. (2008) and simulated by Dyrud et al. (2008). Therefore the RCS (Radar Cross Section) of a head echo look similar for different receivers located at distant places.

### 3.1 Velocity measurements

Knowing at any time the position of a meteoroid entering the atmosphere thanks to its trajectory determination by video means, its velocity is deduced from Equations (2) and (3):

$$f_{RX} = f_{TX} \frac{1 - \frac{1}{c} \frac{dR_T}{dt}}{1 + \frac{1}{c} \frac{dR_R}{dt}} \quad (2)$$

$$= f_{TX} \frac{1 + \frac{V_g}{c} \cos\left(\delta - \frac{\beta}{2}\right)}{1 - \frac{V_g}{c} \cos\left(\delta + \frac{\beta}{2}\right)}, \quad (3)$$

where  $V_g$  is the geocentric velocity of the target, TX the transmitter location, RX a receiver location,  $f_{TX}$  the transmitted frequency and  $f_{RX}$  the Doppler-shifted frequency measured at the receiver location. Other symbols are explained in Figure 2.

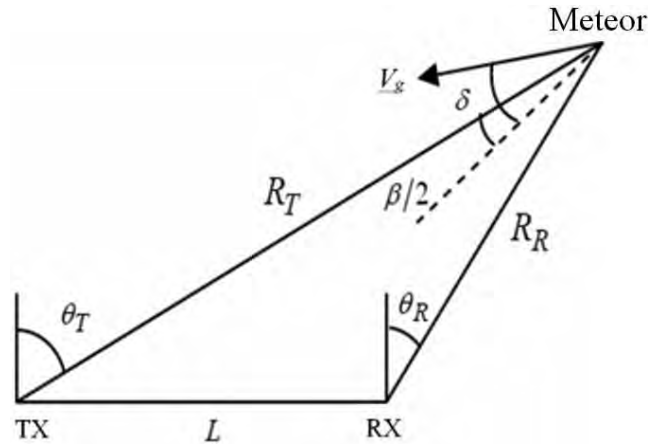


Figure 2 – Transmitter location TX, receiver location RX, and geocentric target velocity vector  $V_g$ . The diagram explains some of the symbols used in Equations (2) and (3).

Figure 3 shows an example of a meteor head echo used to compute the meteoroid's geocentric velocity.

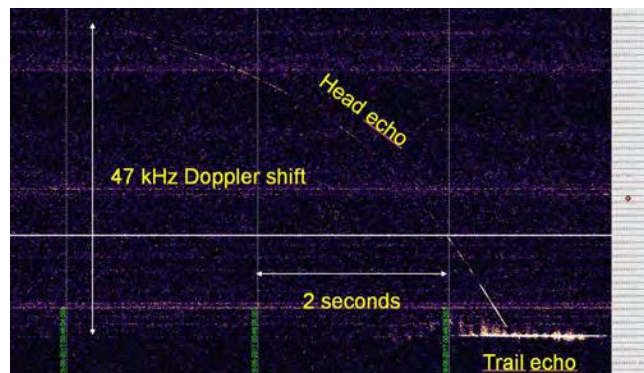


Figure 3 – Example of a fireball head echo detected on 19 June 2017 at 0<sup>h</sup>46<sup>m</sup>08<sup>s</sup> UTC at the FRIPON radio station in Toulouse.

We find that, on a large number of head echoes, the Doppler frequency drift results in a smooth curve. The

trajectory of the meteoroid shown in Figure 3, computed thanks to the video data from five FRIPON cameras, is displayed in Figure 4. Figure 5 shows the related measured magnitudes of the meteor along its path.



Figure 4 – Trajectory of the 19 June 2017, 0<sup>h</sup>46<sup>m</sup>08<sup>s</sup> UTC, bolide computed from video data of FRIPON camera stations located in Besançon, Chatillon, Pontarlier, Saint Lupicin and Troyes.

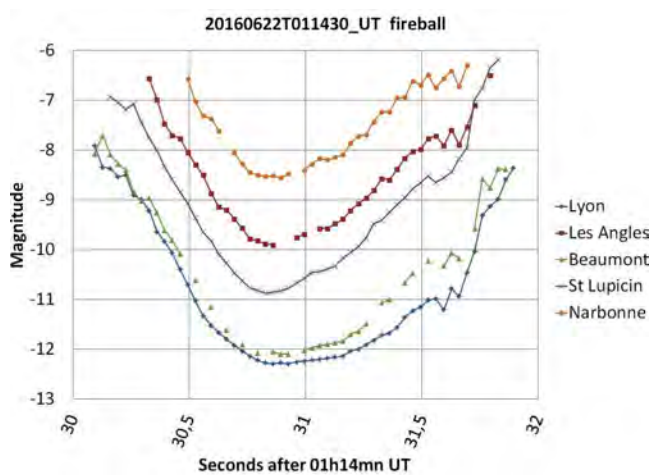


Figure 5 – Magnitudes graphs of the 19 June 2017 bolide as recorded by five different FRIPON cameras.

The main purpose of FRIPON radio observations is to determine as accurately as possible the meteoroid’s velocity. However, it appeared serendipitously that the HPLA configuration of the transmitter used by FRIPON, associated with its transmission of a pure CW VHF (Very High Frequency) carrier, allow to observe a variety of detailed meteor heads phenomena, such as fragmentation, spinning, and others.

### 3.2 Partial fragmentation of a bolide

Sometimes a meteoroid fragments partially during its atmospheric trajectory.

An example of such behavior can be seen in Figure 6, for a fireball recorded on 22 June 2016 at 1<sup>h</sup>14<sup>m</sup>30<sup>s</sup> UTC.

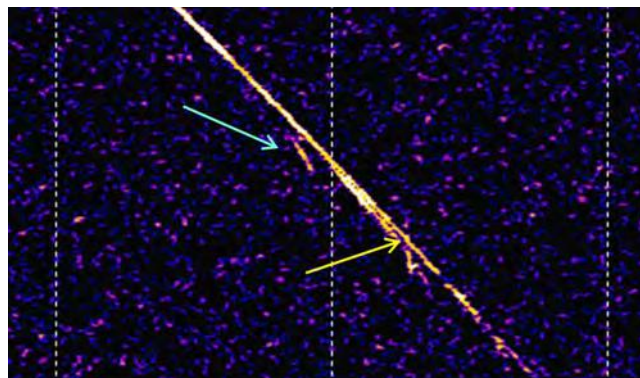


Figure 6 – The arrows show at least two distinct fragments decelerating faster than the main body observed on 22 June 2016 at 1<sup>h</sup>14<sup>m</sup>30<sup>s</sup> UTC.

### 3.3 Sudden changes in Doppler shifts

Smooth Doppler shifts curves indicate that the radial velocity measured by each radio station is varying regularly, according to the geometry of Figure 2. It happens, however, that large and sudden variations of Doppler shifts occur during the final phase of a fireball.

An example of such a behavior is shown on Figure 7.

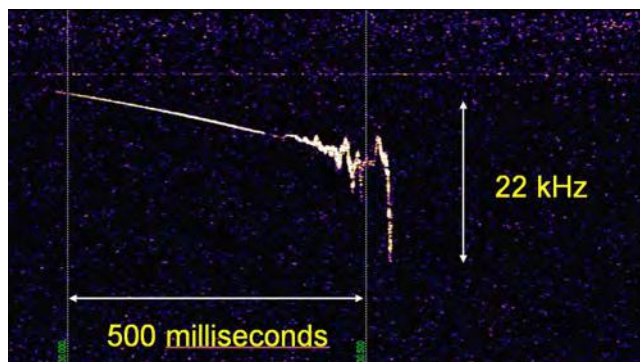


Figure 7 – Sudden Doppler shift variations on the bolide observed on 15 July 2017 at 2<sup>h</sup>01<sup>m</sup>30<sup>s</sup> UTC.

### 3.4 Periodic Doppler shift oscillations

It appears that meteor Doppler shift curves are sometimes affected by regular oscillations during the last phase of their trajectory, as a first example is shown on Figures 8 and 9.

Finally, a complex Doppler signature of a fireball observed on 16 December 2016 at 1<sup>h</sup>32<sup>m</sup>21<sup>s</sup> UTC is shown in Figure 10.

Such high-frequency periodic fluctuations of the Doppler frequency shifts are not observed in any case by the FRIPON cameras. The fact that their shooting rate is only 30 frames per second probably explains that the cameras do not see such fast magnitude variations.

## 4 Discussion

Meteor head plasma behavior simulations such as performed by Dyrud et al. (2008) and Silber et al. (2017) apply to meteor flying in a steady state. At the end

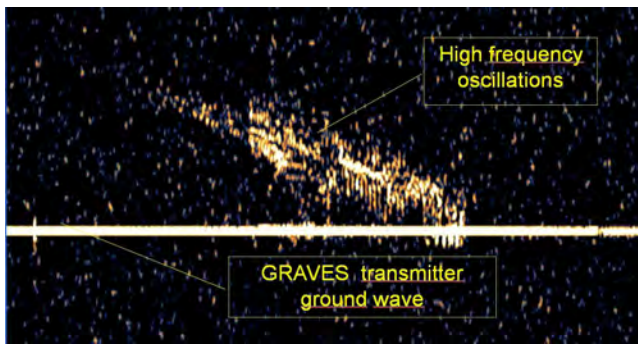


Figure 8 – High-frequency oscillations affecting the Doppler shift curves of the bolide detected on 4 August 2017 at 0<sup>h</sup>04<sup>m</sup>46<sup>s</sup> UTC, as recorded by the FRIPON radio station located in Suttrieu. The same phenomenon was also observed by the distant radio station of Toulouse.

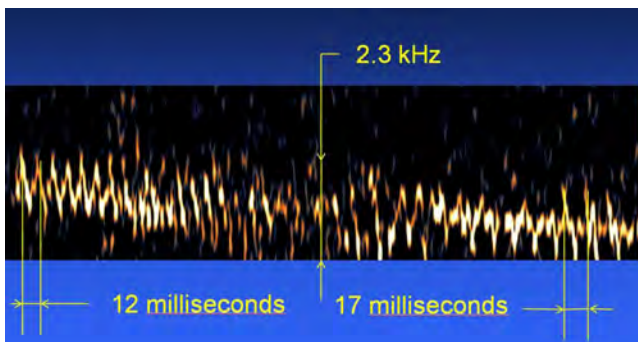


Figure 9 – Zoom on the Doppler shift oscillations shown in Figure 8.

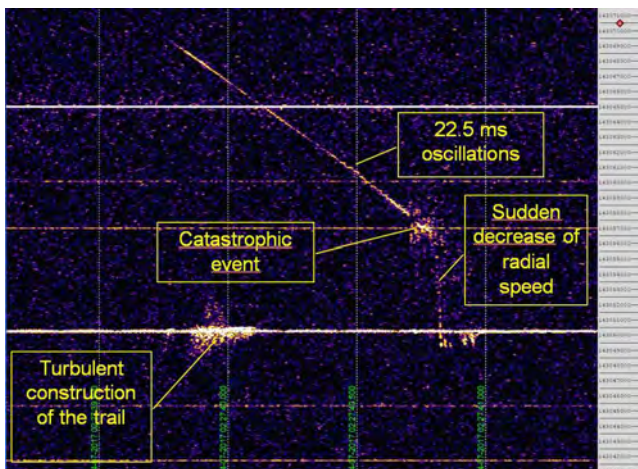


Figure 10 – Doppler signature of the bolide observed on 16 December 2016 at 1<sup>h</sup>32<sup>m</sup>21<sup>s</sup> UTC by the Orléans, Marseille, and Orsay FRIPON radio stations.

of their flight, bolides undergo very harsh stresses due to the important variation of the atmospheric pressure, stresses which deeply modify the behavior of the plasma surrounding the meteoroid. The sudden frequency variations in Doppler signatures observed with the FRIPON radio system, that employs a HPLA radar in multistatic mode, highlights large radial velocities and associated RCS fluctuations. In the case of the example shown in Figure 10, it appears that the sudden frequency variations are due to some changes in the apparent distance of the RCS, probably because the global volume and the shape of plasma surrounding the body changes during the final fragmentation.

The regular Doppler oscillations visible on Figures 8 and 9 can be explained, according to the current observational data, by the spinning of an asymmetric meteoroid. This hypothesis is supported by some meteor magnitude flickering already observed by Beech et al. (2003), and by the periodic RCS amplitude fluctuations detected by Kero et al. (2005).

## 5 Conclusions

An HPLA transmitter such as GRAVES, radiating a permanent pure carrier at a short wave length (about 2 m) proves to be a powerful tool to examine in detail the plasma surrounding the meteoroid. The automation of our data processing of radio records will allow the systematic analysis of all recorded head echoes.

The combination of radio data from different stations allowing a 3D view versus time of the observed phenomena is one of the next steps ahead for the FRIPON program that is planned to run for the next 10 years.

## Acknowledgements

FRIPON is funded by the ANR grant N.13-BS05-0009-03. FRIPON data are hosted at IDOV+C (Integrated Data and Operation Center). Support for IDOC is provided by CNRS and CNES.

Warm thanks go to Karl Antier for the attentive proof-reading of a previous version of this paper and for his pertinent remarks.

## References

- Beech M., Illingworth A., and Murray I.S. (2003). “Analysis of a ‘flickering’ Geminid fireball”. *Meteoritics and Planetary Science*, **38**, 1045–1051.
- Dyrud L., Wilson D., Boerve S., Trulsen J., Pecseli H. Close S., Chen C., and Lee Y. (2008). “Plasma and electromagnetic simulations of meteor head echo radar reflections”. *Earth, Moon, and Planets*, **102**, 383–394.
- Kero J., Szasz C., Pellinen-Wannberg A., and Wannberg G. (2005). “Power fluctuations in meteor echoes observed with the Eiscat VHF radar”. *Earth, Moon, and Planets*, **95**, 633–638.
- Kero J., Szasz C., Wannberg G., Pellinen-Wannberg A., and Westman A. (2008). “On the meteoric head echo radar cross section angular dependence”. *Geophysical Research Letters*, **35**, L07101.
- Silber E. A., Hocking W. K., Niculescu M. L., Gritsevich M., and Silber R. E. (2017). “On shock waves and the role of hyperthermal chemistry in the early diffusion of overdense meteor trains”. *Mon. Notices Royal Astron. Soc.*, **469**, 1869–1882.

# Meteors in the near-infrared as seen in the Ondřejov catalogue of representative meteor spectra

Damir Šegon<sup>1</sup>, Maria Vukić<sup>2</sup>, Marko Šegon<sup>2</sup>, Željko Andreić<sup>3</sup>, and Peter S. Gural<sup>4</sup>

<sup>1</sup> Astronomical Society “Istra” Pula, Pula, Croatia  
damir.segon@pu.t-com.hr

<sup>2</sup> Department of Physics, University of Rijeka, Rijeka, Croatia  
maria\_vukic@hotmail.com and segi120@gmail.com

<sup>3</sup> Faculty of Mining, Geology, and Petroleum Engineering, University of Zagreb, Zagreb, Croatia  
zeljko.andreic@obla.krgn.hr

<sup>4</sup> Gural Software Development, 351 Samantha Drive, Sterling, VA 20164, USA  
peter.s.gural@leidos.com

The discrepancy between visual and video meteor magnitudes has been discussed through recently published data on independently observed meteor spectra. The preliminary results show that there is a dependency between the percentage of the meteors radiation in the near infra-red part of the spectra and the meteors entrance velocity.

## 1 Introduction

The differences between visual and video meteor magnitudes have been initially mentioned by Shigeno and Toda (2008). Their results have shown that there is a significant difference between estimated visual magnitudes and calculated video magnitudes, but there were no conclusions on the possible relationship explaining those differences. Purely qualitative efforts in that sense were made by members of Croatian Meteor Network (Šegon et al., 2013). These previous studies were based on single-station observations, meaning there were no data on meteor trajectories or atmospheric velocities. Both groups of authors concluded that the amount of near-infrared (NIR) radiation from atmospheric lines contained in meteor spectra (invisible to the human eye or photographic emulsions, but well-detected by CCD sensors) is important and represents the reason for differences in visual and video meteor magnitudes.

An important step towards finding the relation between visual and video magnitude may be the work on video meteor spectra collected by Vojáček et al. (2015; 2016). Based on their published catalogue, we discuss the impact of radiation in the NIR part of a meteors spectrum on the estimation of video magnitudes.

## 2 Results and discussion

In our analysis we used calibrated spectra of video meteors of magnitudes between +2 to -3 as provided by Vojáček et al. (2015). In order to have the infrared part of the spectra covered by the analysis, only meteor spectra ranging up to at least 850 nm were used in this analysis. For each analyzed meteor spectrum, the overall intensity has been calculated as the area below the entire spectral curve, and a separate value calculated as the area below the spectral curve ranging from

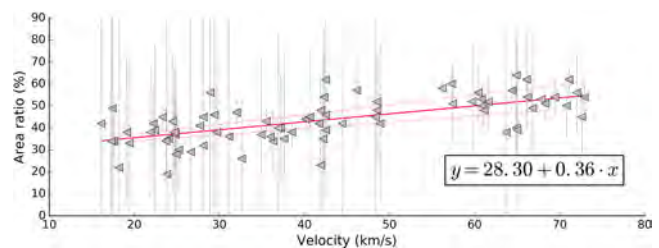


Figure 1 – Relationship between the ratio of the NIR to the fully integrated spectrum the meteors entrance velocity. The dependence of infrared light output of the meteor on its entrance velocity is clearly seen.

wavelengths of 700 nm and longer, representing the radiation in the NIR part of the spectrum. The ratio of the NIR to the fully integrated spectrum has been calculated and compared to the meteors entrance velocity.

The results of our analysis are summarized in Figure 1. The dependence of infrared light output of the meteor on its entrance velocity is clearly seen.

The scatter of data for meteors possessing the same entrance velocity is in some cases large, but a clear trend of increasing the infrared part of the meteor spectrum with increasing entrance velocity can be seen. The scatter may be explained by variability of meteoroid composition, and will be addressed in future work. The linear relation connecting the percentage of the meteors NIR radiation to the total meteors radiation (NIR%) can be expressed as

$$NIR\% = 28.3 + 0.36V_i,$$

where  $V_i$  stands for the meteors entrance velocity in km/s. The authors deem the consequences of this finding very important, since there is no way to calibrate the video meteor magnitudes in order to be comparable to visual or photographic work. The fastest meteors ra-

diate about half (or more) of their total radiation in the NIR part of their spectrum! Note that the relationships used for photometric mass estimation are based on visual or photographic magnitudes which are insensitive to the NIR part of the spectrum. Thus, video magnitudes cannot be used without being corrected for the effect exhibited above.

The detailed analysis of obtained results is in progress and will be published in a future full-length article in *WGN, Journal of the IMO*.

### 3 Conclusions

Initial results of the analysis of individual meteor spectra from the catalogue of representative meteor spectra (Vojáček et al., 2015; 2016) for the NIR-part of the spectrum, and the dependence on the meteor's entrance velocity have been presented. We have found that the part of the meteors radiation in the near infrared is directly proportional to the meteors entrance velocity.

### Acknowledgements

Željko Andreić was supported by the University of Zagreb (Mathematical Research in Geology II; head T.

Malvić) for 2017. This work has been partially supported by the Ministry of Science and Education of the Republic of Croatia, and the Association of Technical Culture of the Istrian County.

### References

- Šegon D., Andreić Ž., Vida D., Novoselnik F., and Korlević K. (2013). "Meteors in the near-infrared". In Gyssens M. and Roggemans P., editors, *Proceedings of the International Meteor Conference*, La Palma, Canary Islands, Spain, 20–23 September 2012. IMO, pages 111–114.
- Shigeno Y. and Toda M. (2008). "Comparison of TV magnitudes and visual magnitudes of meteors". *WGN, Journal of the IMO*, **36**, 79–82.
- Vojáček V., Borovička J., Koten P., Spurný P., and Štork R. (2015). "Catalogue of representative meteor spectra". *Astron. & Astrophys.*, **580**, A67.
- Vojáček V., Borovička J., Koten P., Spurný P., and Štork R. (2016). "Catalogue of representative meteor spectra". In Roggemans A. and Roggemans P., editors, *Proceedings of the International Meteor Conference*, Egmond, the Netherlands, 2–5 June 2016. IMO, page 333–337.

# Properties of faint meteors derived from video observations

Vlastimil Vojáček<sup>1,2</sup> and Jiří Borovička<sup>1</sup>

<sup>1</sup> Astron. Inst. of the Czech Academy of Sciences, Fričova 298, Ondřejov, 251 65, Czech Republic  
vojacek@asu.cas.cz and borovicka@asu.cas.cz

<sup>2</sup> Charles University, Faculty of Mathematics and Physics, Prague, Czech Republic

Properties of millimeter-sized meteoroids were studied using video technique. Direct cameras paired with spectral camera allowed us to study orbits, atmospheric trajectories, and spectra of 152 faint meteors of magnitudes between +3.5 and −5.5. The fragmentation model developed by Borovička et al. (2007) was used to derive physical properties of a selection of 94 meteoroids. Along with complex information about meteoroid trajectories and orbits, this approach helped to reveal new knowledge about the internal structure of millimeter-sized meteoroids. Furthermore, the size distribution of grains for Jupiter-family members was compared to results of the COSIMA instrument of the Rosetta mission. A dependence of the differential ablation on the grain sizes was revealed. Two phases of the fragmentation for one Geminid meteoroid were studied. Even millimeter- and centimeter-sized meteoroids can contain different materials within one single body.

## 1 Introduction

Video observations are used more and more for meteor observations by both professional and amateur astronomers. Also, spectral observations of meteors are becoming more common these days. Astronomers are interested in differences between individual meteors, in the structure of meteoroids, and in the abundances of individual chemical elements in meteor spectra. New models of meteoroid erosion are being developed.

Double-station video observations combined with spectroscopic video observations can be a very good way to study millimeter-sized meteoroids. Almost two decades of video observations of meteors at the Ondřejov Observatory using VHS cameras gave us a broad database to study large quantities of meteoroids.

The model of meteoroid fragmentation developed by Borovička et al. (2007) using observation of 9 Draconids can thus be tested with the study of a large number of sporadic meteoroids. We tried to use this complex information in conjunction with spectral data to reveal more about the still poorly known inner structure of small meteoroids.

## 2 Observations and equipment

The video observations performed by the Department of Interplanetary Matter of the Ondřejov Observatory were the source of the data for this work. We used observations that took place between 2004 and 2014, during the activity periods of major meteor showers. These data were kindly provided for this work. Most of the video observations were carried out in the Czech Republic, based on the Ondřejov and Kunžak Observatories. Data from the observation campaigns of the Leonids in Tajikistan in 2009 and the Draconids in Italy in 2011 were also used.

The S-VHS cameras used for observations (Panasonic NV-S88 and NV-SX50) were equipped with image intensifiers (until 2005, it was Dedal-41, from 2005 Mulard XX1332). The same cameras were used for spectral observations. A spectral grating Milton Roy with 600 grooves/mm blazed to 470 nm was used. The spectral sensitivity extends from 380 nm to 900 nm. Arsat 50 mm  $f/1.4$  lenses were used most of the time, but Jupiter 85 mm  $f/2$  and Flektogon 35 mm  $f/2.4$  lenses were used too.

Detailed description of the data reduction are given by Vojáček et al. (2015). All spectra were calibrated for the spectral sensitivity of the system.

The same source of data was used as in the work of Vojáček et al. (2015). The present work uses an extended database of observations and also uses data that were not selected for the catalogue of representative meteor spectra, but were adequate for our purpose. In addition, this work analyzes, compares, and connects the study of faint meteors spectra with the fragmentation process of meteoroids in the atmosphere.

## 3 Spectral classification

The wavelength reduction for all meteor spectra was done manually. The three meteor spectra components (the Planck continuum, the atmospheric lines, and the low-temperature meteoric lines) were also manually fitted. The three meteoric lines that we can work with in case of faint meteors are magnesium Mg I-2 at 518.2 nm, sodium Na I-1 at 589.2 nm and iron Fe I-15 at 526.9–544.9 nm.

The spectral classification for all 152 meteors was done according to relative intensities of Mg, Na, and Fe lines and was taken from work of Borovička et al. (2005).

The more volatile sodium line prevails thanks to the low temperature in slow meteors. Thus the correction of relative intensity Na/Mg for the speed of the meteoroid had to be considered. The ternary graph is shown in the Figure 1. The black line shows theoretical position of meteors with normal chondritic composition according to Borovička et al. (2005). The position depends on the speed of the meteor (marked in km/s above the line).

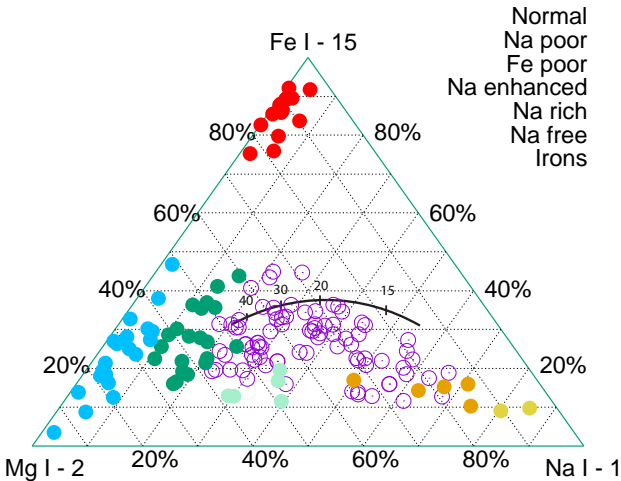


Figure 1 – Classification of meteor spectra. Each class is represented by a different symbol. The black line shows the theoretical position of meteors with normal chondritic composition according to Borovička et al. (2005) as a function of meteor speed (in km/s).

#### 4 Results of the fragmentation model

The fragmentation model developed by Borovička et al. (2007) was applied to 94 meteors. The model is using the dustball concept with quasi-continuous fragmentation. Grains are released during the flight of the meteoroid. After they are released they behave as one body. The equations of the meteor ablation and fragmentation are applied. The physical parameters in these equations are used as free parameters for best fit of the lightcurve and the deceleration curve. The deceleration curve shows the difference between the computed position of the meteoroid without deceleration and the actual measured position. If the meteoroid is slowing down, we can observe a typical lag: the deceleration curve. Parameters like the initial mass and the initial velocity, bulk density of the meteoroid  $\delta$ , ablation  $\sigma$  and erosion coefficient  $\eta$ , sizes (their limits) of grains and number of grains released, and energy received before the start of the erosion (per unit cross section)  $E_s$  can be derived. For more details about the model, see Borovička (2007). We assumed the grains to have a density of  $3000 \text{ kg/m}^3$  and a spherical shape. For iron meteoroids, we assumed the density of grains to be  $6000 \text{ kg/m}^3$ .

The results of the application of the fragmentation model reveal large differences in physical parameters. Some of the parameters are shown in Table 1. The mete-

oroids contained grains of very small sizes up to sizes of the same order as some meteoroids themselves. The total number of grains per meteoroid varied between  $10^2$  and  $10^8$ . It can be seen that some meteoroids did indeed contain a large number of grains. The two orders of magnitude range for the energy necessary to start the ablation implies that meteoroids may contain both strong and fragile material.

Table 1 – Some results from applying the fragmentation model developed by Borovička et al. (2007). Here,  $E_s$  is the energy necessary to start the erosion.

Parameter	Value
Grain sizes	$5 \mu\text{m} - 2.5 \text{ mm}$
Grain numbers	$10^2 - 10^8$
$E_s$	$10^5 - 10^7 \text{ J/m}^2$

The COSIMA instrument on the Rosetta spacecraft collected a number of cometary particles while orbiting around the Comet 67P/Churyumov-Gerasimenko. Horning et al. (2016) analysed these particles. They measured sizes of the captured grains. The particle sizes varied from  $15 \mu\text{m}$  up to approximately  $300 \mu\text{m}$ , and the total number of particles was 7524. The histogram of grain sizes was fitted by a power law function with exponent  $-3.3$ . Since Comet 67P/Churyumov-Gerasimenko is a member of the Jupiter-family comets, we tried to compare results of the COSIMA instrument with our sample of meteoroids on Jupiter-family orbits. The grain sizes derived from the modeling varied approximately from  $5 \mu\text{m}$  (mass of  $1 \times 10^{-10} \text{ g}$ ) up to  $2.5 \text{ mm}$  (mass of  $3 \times 10^{-2} \text{ g}$ ). The total number of grains for all meteoroids summed together was  $1.6 \times 10^{10}$ . The larger range of grain sizes was probably caused by the larger sample of our meteoroids. The distribution of grain sizes up to approximately  $300 \mu\text{m}$  was similar. The power law fit of our data was with exponent  $-3.4$ , in good agreement with the power law function of grain sizes from Comet 67P/Churyumov-Gerasimenko. The histogram of grain sizes up to  $450 \mu\text{m}$  is shown in Figure 2. The power law fit is showed as well as the power law fit with exponent  $-3.3$  taken from Horning (2016).

The fragmentation model was successfully applied to 94 of the total number of 152 meteors. The remaining 38% of all meteors could not be modeled. The model failed to work for cases where there was no or very little deceleration. The model also failed if there were not enough points for the fit, i.e., if the meteor observation was too short.

#### 5 Study of differential ablation

The spectral video observations allowed us to study monochromatic light curves. These light curves show the time evolution of intensities of individual spectral lines. The monochromatic light curves of three low-temperature meteoric lines of MgI, NaI, and FeI were studied.

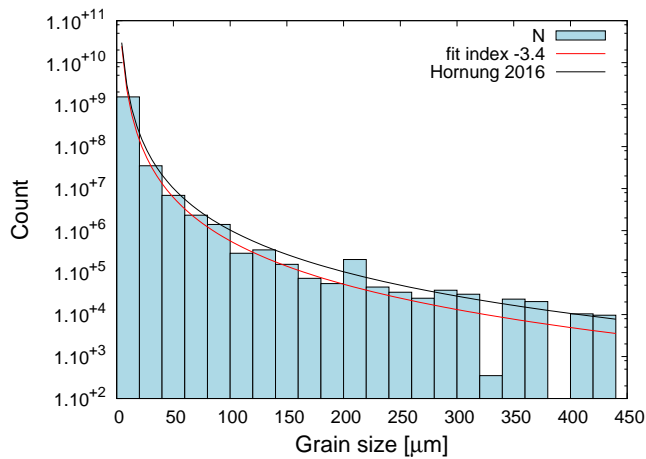


Figure 2 – Histogram of grain sizes of Jupiter-family meteoroids up to  $450 \mu\text{m}$ . Our power law fit with exponent  $-3.4$  is shown. The power law fit of grain sizes captured by Rosetta with exponent  $-3.3$  taken from Hornung (2016) is also shown.

There are obvious differences in intensity among individual lines for different spectral lines. But we could also observe differential ablation in some cases. We could see that the sodium line somewhat differed from the other two lines. We could observe meteors with early release of sodium, but also some cases showing a somewhat later release of sodium.

We tried to describe the shape of individual light curves using simple analysis. Despite the sometimes complicated shape of the monochromatic light curves, we used one quantity to describe the monochromatic light curve shape. We studied the height where half of the individual element was radiated out, instead of using the position of the maximum of the light curve (because of the complicated shape). This quantity was computed by integrating the monochromatic light curve along the trajectory. The height where the integral reaches half of its total value is the height where half of the element was radiated out. We focused on heights where half of the mass of sodium or magnesium was radiated out. Comparison of these heights can help us to better see if the sodium was released earlier or later than the magnesium.

The difference between the height where half of the sodium was radiated out and the height where half of the magnesium was radiated out is shown in Figure 3. This difference is indicated in kilometers. If the difference is 0, half of the magnesium and half of the sodium were radiated out at the same height. If the sodium was released earlier than the magnesium, the value of the difference is positive and if the sodium was released later than magnesium, the value of the difference is negative. The Na-free and iron meteoroids as well as the meteors with only atmospheric lines in their spectrum were excluded from Figure 3, since the determination of the Na-Mg half mass height difference is very inaccurate for these classes.

The dependence of the difference between these heights for Na and Mg on the grain sizes of the meteoroid was

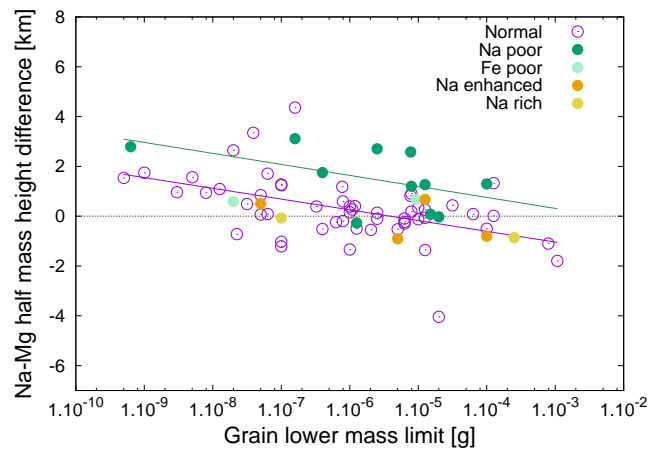


Figure 3 – The difference between the height where half of the mass of the sodium was radiated out and the height where half of the mass of magnesium was radiated out as a function of photometric mass and the upper mass limit of grains. The lower line is a fit for the normal class, and the upper line a fit for the Na-poor class.

revealed. As can be seen in Figure 3, the larger the lower mass limit is for grains, the later the release of the sodium occurs. As mentioned above, we were assuming the same shape and density for the grains. Mass and size of grains are thus proportional. This might suggest that meteoroids containing smaller grains have also a larger inner shape allowing faster release of volatile sodium. This hypothesis has to be further investigated in the future.

## 6 Sodium-depleted classes

Throughout this work, the Na-free and Na-poor classes differed from the other classes. There are two sources for both Na-free and Na-poor meteoroids: the Sun-approaching meteoroids and the meteoroids on cometary orbits. However, we did not observe much difference in physical properties between sodium-depleted meteoroids on Sun-approaching orbits and sodium-depleted meteoroids on cometary orbits.

The sodium-depleted material showed rather lower values of porosity and higher beginning heights for the meteors. They also require more energy to start the erosion. So, the sodium depletion is making the meteoroid material stronger. The Na-poor and Na-free meteoroids tend to have lower mass. According to limits of size for grains, the Na-poor and Na-free meteors usually do not contain very small grains based on the limits for grain size. The sizes of grains are otherwise comparable to sizes of most of the normal class. The study of meteor morphology revealed that Na-free and Na-poor meteors produced no or only faint wakes.

We can also see that for a given grain size the Na-poor members tend to release their sodium earlier. Knowing just one quantity (and not the whole shape of monochromatic light curves), one can assume that the lack of sodium for the Na-poor meteors is the cause of the early release of the sodium. In other words, the sodium runs

out faster. To confirm this presumption, we have to look at monochromatic light curves of Na-poor meteors. From a total number of 21 meteors classified as Na-poor, 11 of them were successfully modeled. We show some monochromatic light curves of Na-poor meteors in the Figure 4. The sodium light curve for Na-poor meteors usually does not start earlier than the magnesium line, but the sodium can end earlier than the magnesium. The initial brightening of Na and Mg suggests that the release rate for sodium and magnesium is more or less the same, but since there is less sodium in the meteoroid, this element simply “runs out”. Thus the shift of differential ablation is probably caused by the smaller amount of sodium in Na-poor meteoroids.

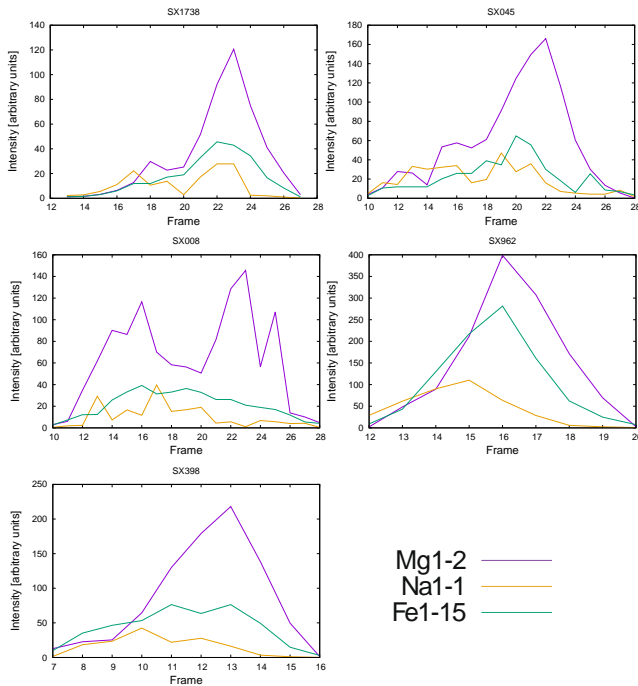


Figure 4 – Examples of monochromatic light curves of Na-poor-modeled meteors.

All these differences for Na-poor (and Na-free) meteoroids lead us to the conclusion that these classes might have a different structure. Figure 5 shows—schematically, but illustratively—an idea of this different structure of Na-poor and Na-free meteoroids: they do not contain grains larger than the other classes (in fact, some normal meteoroids contained larger grains than any other Na-poor member). Unlike other classes, however, they usually do not contain very small grains. The smallest grains were probably depleted in interplanetary space, during close approaches to the Sun or by exposure to cosmic rays. The Na-poor and Na-free classes do not produce long wakes, probably because they contain less grains, but the fragmentation model did not allow to prove this.

## 7 Geminid meteoroid

The meteoroid with the highest negative difference of half-mass heights of Na and Mg in Figure 3 is the Geminid SX336, on which we now focus in more detail.

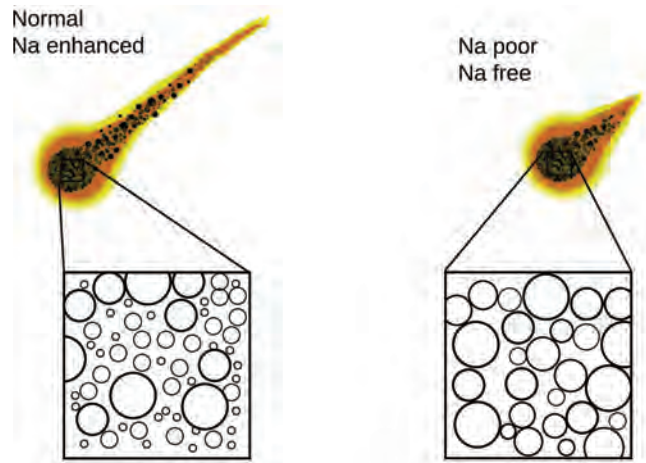


Figure 5 – Schematic representation of the differences in inner structure of on the one hand normal and Na-enhanced classes (left) and on the other hand Na-poor and Na-free classes (right).

As any Geminid, this meteoroid was on a Sun-approaching orbit. The spectrum was classified as normal. It is one of two meteoroids with a Sun-approaching orbit that were not classified as Na-poor or Na-free (the second one was an iron meteoroid). Although the relatively large lower mass limit predicts later release of sodium, this meteor differs a lot from the dependence shown in Figure 3.

The light curves in Figure 6 show that the shape of the magnesium and iron lines are similar, with a lower intensity for the iron line. They both show two maxima. The release of the magnesium was the quickest. The sodium increase was slower. The slope of the sodium line was almost the same during the flight until the maximum at the very end of the meteor. It only gets a little bit higher after the second stage of the fragmentation starts.

The light curve in white light shows two stages of fragmentation. When we observe two stages, we assume that there is a part of the material that was unaffected by the erosion until some point during the flight. After that point, the erosion of the second part starts. Thanks to the shape of the light curve, we are able to

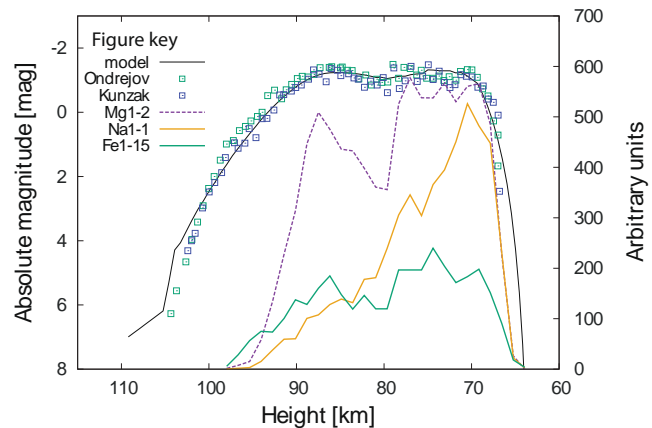


Figure 6 – The monochromatic light curves and integral light curve of the Geminid meteor SX336.

estimate the properties of this stronger part. The results from the fragmentation model for both stages of the erosion are shown in Table 2. The number of grains in the first stage was two orders higher. There were only larger (millimeter-sized) grains released during the second stage. In the first stage, about  $1.5 \times 10^3$  grains were released, and, in the second stage, only 19 grains were released.

The Geminids are well-known for the variations of the amount of sodium in their spectra. It was suggested by Čapek et al. (2009) that the sodium depletion is caused in interplanetary space during close approaches to the Sun. The sodium depletion does not depend on meteoroid sizes. The porosity and the grain sizes play a key role in the rate of this depletion. Meteoroids with smaller grains deplete the sodium faster during their passages around the Sun. The SX336 meteoroid contained large grains both in the first and in the second stage of the erosion. Moreover, in the first stage, there were also smaller grains. In the second stage of erosion there were only larger grains (over 1 mm in size). The part with the smaller grains fragmented first. Because of the faster depletion of sodium on the orbit for smaller grains, there was less sodium than what one would expect for a chondritic composition. The material in the second stage of erosion was different, however. Because of the larger grains, the depletion of the sodium in that stage was much slower or did not take place at all. When the stronger part of the meteoroid started to fragment, the relative intensity of the sodium line started to correspond to the chondritic composition. Because of the difference in inner structure, we observe a much later release of the sodium than what is typical for other meteoroids.

*Table 2* – Comparison between the first and second stages of the erosion for the Geminid meteor SX336 according to the fragmentation model developed by Borovička et al. (2007). Here,  $N$  is the number of grains in the meteoroid,  $E_s$  the energy necessary to start of the erosion,  $m$  the initial mass, and  $m\%$  the mass subject to the second stage of erosion expressed as a percentage of the initial mass.

First erosion			
Grain sizes (mm)	$N$	$E_s$ (J/m <sup>2</sup> )	$m$ (g)
0.23–2.16	$1.38 \times 10^3$	$1.2 \times 10^6$	$5.0 \times 10^1$
Second erosion			
Grain sizes (mm)	$N$	$E_s$ (J/m <sup>2</sup> )	$m\%$ (g)
1.46–2.32	19	$6.6 \times 10^7$	30

## 8 Conclusions and additional remarks

We reduced, measured, and analyzed a total number of 152 observations of faint sporadic and shower meteors. All these meteors were observed from at least two stations using video techniques. They were observed both in white light and by using a spectral grating. Observations were run mainly from the Czech Republic by

the scientific staff of the Ondřejov Observatory during the period 2004–2014. Using the double-station recordings, we obtained atmospheric trajectories and orbital parameters of the observed meteoroids.

The results of the fragmentation model showed a fairly wide range for some parameters among all meteoroids. The masses of grains ranged approximately from  $1 \times 10^{-10}$  g up to  $3 \times 10^{-2}$  g, corresponding to a size range from 5 μm up to 2.5 mm. Individual meteoroids contained approximately between  $10^2$  and  $10^8$  grains. We compared sizes of grains derived from modeling with results of measurements of cometary particles collected by the Rosetta spacecraft orbiting Comet 67P/Churyumov-Gerasimenko (Hornung et al., 2016). We found good agreement in the distribution of sizes for grains collected from this Jupiter-family comet with results of our modeling of Jupiter-family meteoroids.

Reduced meteor spectra were classified according to the classification of faint meteor spectra suggested by Borovička et al. (2005). The main goal of this work was the combination of results from the spectral and fragmentation analysis. We used the time evolution of three spectral lines, namely Na, Mg, and Fe (monochromatic light curves). The shapes of these monochromatic light curves varied for individual meteors. To describe the differences in the release of these three spectral elements, we used the height at which each element was radiated. Difference in this height for sodium and magnesium depended on the sizes of grains of meteoroids. The early release of sodium was typical for meteoroids with small grains. Bodies with large grains released the sodium at the same time as the magnesium, and in some cases even later than the magnesium.

A special case in our study was the Geminid meteor SX336, as the late release of Na was unusual for the given grain sizes. This meteoroid fragmented in two stages. We proposed that different degrees of sodium depletion in interplanetary space in the parts of the material eroded during these two stages was the reason for the later release of the sodium. Larger grains and thus probably lower depletion of the sodium in the second stage of fragmentation caused a later maximum for the Na line.

The Na-free and Na-poor groups differed from the others. The monochromatic light curves suggest that the early release of sodium is a consequence of Na depletion in interplanetary space. At some point during the flight in the atmosphere, the smaller amount of sodium “runs out”. Other physical properties suggest that there is a real difference in the structure between the sodium-depleted classes compared to other spectral classes.

## Acknowledgements

The authors wish to thank all observers. Without their countless sleepless nights, this work could not have been done.

This work was supported by the grants 16-00761S and P209/11/1382 of the Grant Agency of the Czech Republic.

## References

- Borovička J., Koten P., Spurný P., Boček J., and Štork R. (2005). “A survey of meteor spectra and orbits: evidence for three populations of Na-free meteoroids”. *Icarus*, **174**, 15–30.
- Borovička J., Spurný P., and Koten P. (2007). “Atmospheric deceleration and light curves of Draconid meteors and implication for the structure of cometary dust”. *Astron. Astrophys.*, **473**, 661–672.
- Čapek D. and Borovička J. (2009). “Quantitative model of the release of sodium from meteoroids in the vicinity of the Sun: Application to Geminids”. *Icarus*, **202**, 361–370.
- Hornung K., Merouane S., Hilchenbach M., Langevin Y., Mellado E. M., Della Corte V., Kissel J., Engrand C., Schulz R., Ryno J., Silen J., and COSIMA Team (2016). “A first assessment of the strength of cometary particles collected in-situ by the COSIMA instrument onboard ROSETTA”. *Planetary and Space Science*, **133**, 63–75.
- Vojáček V., Borovička J., Koten P., Spurný P., and Štork R. (2015). “Catalogue of representative meteor spectra”. *Astron. Astrophys.*, **580**, A67.

# Detectability of minor features in meteor shower activity profiles

Jürgen Rendtel

Leibniz Institut für Astrophysik, An der Sternwarte 16, 14482 Potsdam, Germany  
jrendtel@aip.de

International Meteor Organization, Eschenweg 16, 14476 Potsdam, Germany

Verification of activity variations or small outbursts based on model calculations requires a careful selection and analysis of observational data. Possibilities and limits of detection are shown using data from several events in 2016, covering the Perseid peak period (various dust trail encounters) and the  $\mu$ -Leporids end-March (no observational evidence). Data of the  $\varepsilon$ -Eridanids (September 12) and the  $\alpha$ -Monocerotids (November 21) show weak peaks at the predicted positions. Additional calibration using several data sets allowed us to determine a ZHR of the order of 5 for both events.

## 1 Introduction

The structure of meteoroid streams is affected by several effects starting at the moment of the ejection from the parent object until the observation of meteoroids encountering the Earth's atmosphere. Modeling dust trails has become quite successful over the years. The annual IMO Meteor Shower Calendar provides information about possible events, being it larger outbursts, trail encounters, or chances for very minor activity. For the events in 2016, we compiled a review of observational evidence (Rendtel et al., 2017) using visual, video, and radio (forward scatter) data. Here we have a look at the level of detectable variations and possibilities of calibration of various data samples.

## 2 Minor variations in a major shower

In 2016, the Perseids (007 PER) were expected to cross three dust trails of different age (Table 1). Additionally, the general activity level was assumed to be rather at a ZHR of 150 than the usual 100–120 due to Jupiter perturbations (Rendtel, 2015).

The analysis of visual data provides us with a smooth ZHR profile (Figure 1). The clearly visible peaks show the passages of the 4-revolution trail and the 2-revolution trail. This is very well confirmed by video flux data (Figure 2). In both profiles, the minor 1-revolution trail is not detectable. Contrary to the other peaks, the latter was expected to add a ZHR of about 10, i.e., an increase of the order of 5% just at the ascending branch of the first major peak. No obvious additional feature occurs. In the video flux profile, one may suspect a minor shoulder at  $\lambda_{\odot} = 139^{\circ}43\text{--}139^{\circ}44$ , but in view of some other variations, e.g., shortly before  $\lambda_{\odot} = 139^{\circ}55$ , an interpretation as a confirming signature of the 1-revolution trail encounter is questionable. At this point, the conclusion is that either the increase at the given time is too small (hidden within the error margins) or the timing was not correct. We have to conclude that we

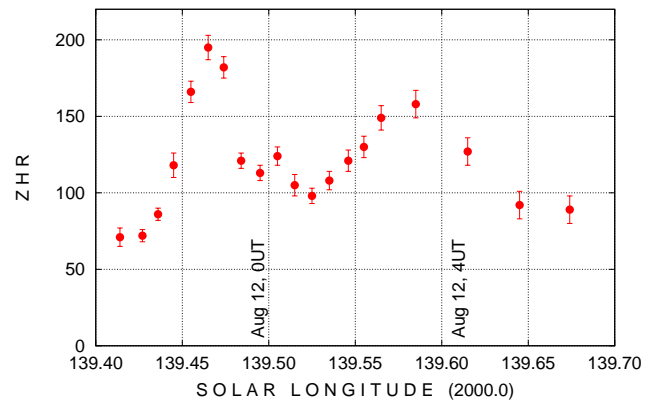


Figure 1 – ZHR profile of the 2016 Perseid maximum covering the trail encounter period, obtained from visual data.

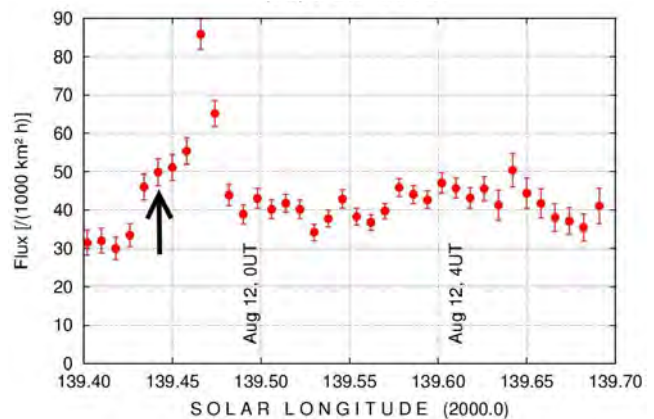


Figure 2 – Flux profile of the Perseid maximum as shown in Figure 1, obtained from video data. The arrow indicates a possible minor flux enhancement due to the 1-rev. trail.

cannot extract any significant information about the 1-revolution trail from both optical data sets. (The radio data are available only with lower temporal resolution.)

This gives an idea of the significance level we may expect for other events: variations which exceed 5% of the neighbouring values can be found and can be considered significant. This has also been shown in the Quadrantid (010 QUA) analysis of the 2016 return (Rendtel et al.,

Table 1 – Perseid dust trail encounters expected in 2016 (Rendtel, 2015).

Age of trail	Time (UT)	Expected additional rate	Author(s)
1-rev.	Aug 11, 22 <sup>h</sup> 34 <sup>m</sup>	10	Maslov, Lyytinen
4-rev.	Aug 11, 23 <sup>h</sup> 23 <sup>m</sup>	50	Maslov, Lyytinen
2-rev.	Aug 12, 0 <sup>h</sup> –4 <sup>h</sup>	bright meteors	Vaubailon

2017). For smaller peaks, the chance increases if the feature extends over several intervals so that several data points define a reliable profile.

### 3 Detectability of minor shower activity

#### 3.1 $\mu$ -Leporids end March

Apart from the Perseid peaks and the Quadrantid activity feature, the other events listed in the IMO Meteor Shower Calendar for 2016 (Rendtel, 2015) were expected to show rather low activity, perhaps close to the detection limit. Between March 28 and 30, a possible encounter with small meteoroids (i.e., faint meteors) from Comet 252P/LINEAR was calculated by Mikhail Maslov (see Rendtel, 2015). The most probable timing for a very minor activity was March 28, 11<sup>h</sup>–18<sup>h</sup> UT. The radiant was given as  $\alpha = 78^\circ$ ,  $\delta = -16^\circ$ , and the entry velocity was just 15.5 km/s.

The observing window for optical observations was quite narrow as the radiant in Lepus is above the horizon only in the early evening. Locations at tropical latitudes were best placed. Unfortunately, neither visual nor video observations cover the period appropriately. The most promising window was also too early for European longitudes. Radio forward scatter data seem to show two peaks. Both are based only on limited data points from regions where the radiant was low in the sky (and thus the correction factors were large; see Figure 3). Furthermore, the low velocity adds to the uncertainty, and one has to bear in mind that the ZHR calculation is based on the relation to the counts recorded in the preceding days (Ogawa et al., 2004).

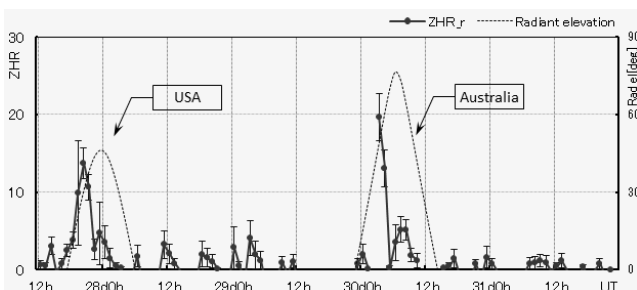


Figure 3 – Radio ZHR during end March 2016. The dotted lines give the radiant elevation of the  $\mu$ -Leporids for the contributing locations.

In this case, we have to conclude that there was no reliable signature of the shower. Peter Brown (2017) also confirmed that the Canadian CMOR radar did not record any activity around the given time.

#### 3.2 $\epsilon$ -Eridanids and $\alpha$ -Monocerotids

Vaubailon (see Rendtel, 2015) predicted possible activity of the  $\epsilon$ -Eridanids (209 EER) on September 12, at 17<sup>h</sup>30<sup>m</sup> UT (radiant  $\alpha = 57^\circ$ ,  $\delta = -15^\circ$ ). Sato (see Rendtel, 2015) noted that there is a chance of weak  $\alpha$ -Monocerotid (246 AMO) rates on November 21, at 18<sup>h</sup>30<sup>m</sup> UT. The exciting news is that any activity in 2016 at the given position would indicate a slightly higher rate in 2017 (November 21, 21<sup>h</sup>26<sup>m</sup> UT; still to come when this paper was written).

Both showers are lacking optical (visual and video) data. However, radio data give ZHRs of the order of 25, which is surprisingly high for both showers. In the case of the September event, the observations cover the well-known September  $\epsilon$ -Perseids (204 SPE) just a few days earlier (Figure 4). Meteors of the EER and the SPE have similar atmospheric entry velocities (64 km/s and 59 km/s, respectively). Except for the Antihelion source (lower velocity), there is no other significant meteor shower active, and the SPE showed neither rate enhancements nor magnitude peculiarities in 2016. Hence, we can use the data we obtained by visual and video observations, giving a ZHR around 6 (Figure 5), to calibrate the EER activity level. The (radio) ZHR of the SPE and the EER are essentially identical. Hence, we may use a calibration factor of 0.2 to determine the (optical) ZHR of the EER. With some confidence, we apply the same factor also to the AMO and conclude that both the EER and AMO showed significant and similar activity with ZHR  $\approx 6$  exactly at the calculated positions.

With this confirmation of the prediction for 2016 come the prospects for another observable return of the AMO in 2017—which needs to be confirmed. This interaction between prediction and observation is of great benefit for both modelers and observers.

### 4 Forthcoming events

The 2017 and 2018 IMO Meteor Shower Calendars include several events which are worth to be checked by all observational methods. Further data about possible encounters may be published at other times, so observers should also regularly check notes in WGN or at the various websites. Even a negative result is important information. In this sense, I urge that results from modeling are disseminated to the observers, despite the fact that there are several video camera networks covering essentially all periods. The chance of collecting independent data samples provides additional information, either in the confirmation of really minor features close to the detection limit or in more reliable flux or

Table 2 – Predicted meteor showers in 2017 and 2018 which require observational confirmation. (Check for later announcements notes in WGN or on the IMO webpages, and see the notes in the respective Meteor Shower Calendars.)

Shower	Date and time (UT)	Prediction	Author
246 AMO	2017 Nov 21, 21 <sup>h</sup> 26 <sup>m</sup>	Indication from activity observed in 2016	Sato
46P/Wirtanen	2017 Nov 30, ca. 0 <sup>h</sup> 6	Rad. $\alpha = 9^\circ$ , $\delta = +9^\circ$ , 15km/s	Maslov
015 URS	2017 Dec 22, 14 <sup>h</sup> 43 <sup>m</sup>	884 dust trail	Vaubailon
793 KCA	2018 Jan 09, 21 <sup>h</sup>	Observed 2015, 2016. Check recommended Rad. $\alpha = 138^\circ$ , $\delta = +9^\circ$ , 47km/s	
031 ETA	2018 May 05, 07 <sup>h</sup> 35 <sup>m</sup>	Resonant meteoroids	Kinsman

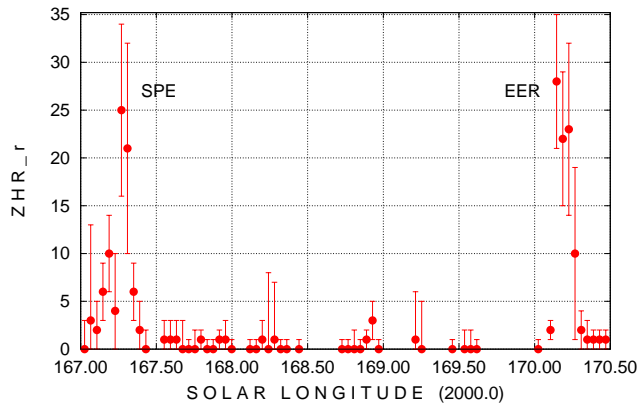


Figure 4 – Radio-ZHR profile of the period covering the SPE and EER activity. Using the optical (visual and video) data obtained for the SPE, we derive a calibration factor for the EER activity.

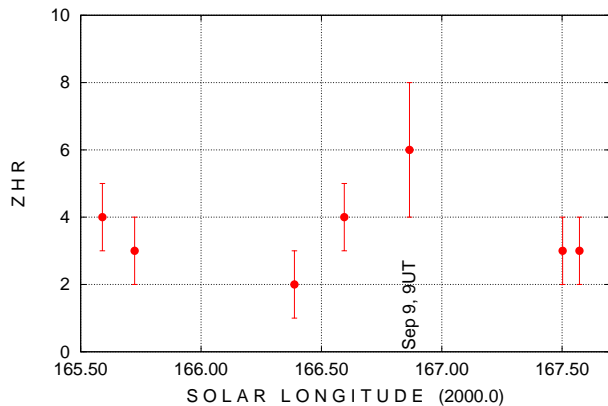


Figure 5 – ZHR of the September  $\epsilon$ -Perseids obtained from visual data giving a maximum ZHR of 6 close to  $\lambda_\odot = 267^\circ$ .

mass index data. Last but not least, observing around a possible unique meteor shower event is fun and may arouse curiosity to observe during periods of low activity.

### 5 Conclusions

Observational results may be used to adjust parameters used for the modeling possible encounters. This con-

cerns both the meteoroid stream number density (expressed as ZHR or flux) and the position of the peak (time of the event).

The findings may also help to find a minimum level of activity for the various techniques to provide reliable data on the timing and meteor rate or flux.

Combined data extend the mass range for which we may find results. and thus also allow us to derive information about the mass index  $s$  (population index  $r$ ), including mass sorting if the maxima of differing magnitude ranges are observed at different times as in the Quadrantids 2016. This can then be included into the model parameters as well.

### Acknowledgements

The review of meteor events in 2016 was compiled together with Hiroshi Ogawa and Hirofumi Sugimoto, using their analyses of radio forward scatter data collected worldwide.

### References

Brown P. (2017). Personal communication.

Ogawa H., Toyomasu S., Ohnishi K., Maegawa K., Amikura S., and Miyao K. (2004). “The international project for radio meteor observation 2001–2003”. In Čekada M. T. and C. T., editors, *Proceedings of the International Meteor Conference*, Bollmannsruh, Germany, September 19–21, 2003. IMO, pages 107–113.

Rendtel J., editor (2015). *2016 Meteor Shower Calendar*. IMO-INFO 3-15. IMO.

Rendtel J., Ogawa H., and Sugimoto H. (2017). “Meteor showers 2016: review of predictions and observations”. *WGN, Journal of the IMO*, **45**, 49–55.

# Radio observations of the 2016 daytime meteor showers

Giancarlo T. Tomezzoli

EurAstro Association, Zeppelinstraße 43, 81669, Munich, Germany

gt21949@gmx.de

To have a better understanding of the daytime meteor showers, the EurAstro Radio Station (EARS) observed the 2016 daytime showers by radio: Capricornids/Sagittarids (115 DCS),  $\chi$ -Capricornids (114 DXC), April Piscids (144 APS),  $\varepsilon$ -Arietids (154 DEA), Arietids (171 ARI),  $\zeta$ -Perseids (172 ZPE),  $\beta$ -Taurids (173 BTA),  $\gamma$ -Leonids (203 GLE), and Sextantids (221 DSX). The observed overdense rates around the expected maxima of said meteor showers in the EARS configuration were classified as *low* (maximum rate of up to 3 overdense echoes per hour), *medium* (maximum rate of up to 8–10 overdense echoes per hour), and *high* (maximum rate of up to 19–21 overdense echoes per hour). These manifested a certain agreement with the rates of said daytime meteor showers listed in Table 1 of the IMO Meteor Shower Calendar 2016. Combined radio observations with at least one other radio station on the other side of the Earth relative to EARS now appear the next step for the radio observations of the daytime meteor showers in 2017 and beyond.

## 1 Introduction

Two past articles (Tomezzoli and Verbeeck, 2015; Tomezzoli and Barbieri, 2016) presented the results of the radio observations of the Daytime Sextantids (221 DSX), made after the invitation by Jürgen Rendtel at the IMC 2014 in Giron, France, to observe 221 DSX with all possible means (Rendtel, 2014).

Tomezzoli and Verbeeck (2015) described radio observations of 221 DSX from EARS (EurAstro Radio Station) in Munich, Germany (48°07'58"0 N, 11°34'47"3 E) in the recording period from 2014 September 30, 7<sup>h</sup>00<sup>m</sup> UT, to 2014 October 5, 16<sup>h</sup>00<sup>m</sup> UT, and concluded that the 221 DSX radio meteor activity, if present at all, was at level much lower than that of the sporadic radio meteor activity.

Tomezzoli and Barbieri (2016) described combined radio observations of 221 DSX from EARS and RAMBO (*Radar Astrofilio Meteore BOlogna*) in Bologna, Italy (44°30'28"9 N, 11°21'12"0 E), respectively in the recording periods 2015 September 27, 8<sup>h</sup>15<sup>m</sup> UT, to 2015 October 3, 7<sup>h</sup>30<sup>m</sup> UT, and 2015 September 28, 0<sup>h</sup>00<sup>m</sup> UT, to 2015 October 4, 0<sup>h</sup>00<sup>m</sup> UT, and concluded that the radio observations of EARS and RAMBO were in mutual agreement confirming that, as in the year 2014, also in the year 2015 no evidence existed of a relevant radio meteor activity of 221 DSX.

To improve the knowledge of the radio meteor activity of the daytime meteor showers, EARS radio-observed the 2016 daytime showers listed in the IMO Meteor Shower Calendar 2016 (Rendtel, 2015).

## 2 EARS radio observations

EARS, based on the forward scattering principle, adopted the same configuration described in said two articles, i.e., radar GRAVES as radio beacon (emitter

at Broyes-lès-Pesmes, 47°20'51"72 N, 5°30'58"68 E, about 500 km from Munich), vertical antenna J-Pole 144, receiver ICOM 1500 (USB mode, 143.049 MHz), computer Pavillion dv6 (with processor Intel Core Duo T2500), and SpecLab V26 b10 as recording software. Meteor rates were derived by counting visually the radio echoes on the JPG images recorded every 5 minutes by SpecLab. Table 1 lists the targetted 2016 daytime meteor showers.

### 2.1 Capricornids/Sagittariids

EARS radio-observed the daytime Capricornids/Sagittariids (115 DCS) in the recording period 2016 January 29, 5<sup>h</sup>16<sup>m</sup> UT, to 2016 February 2, 18<sup>h</sup>05<sup>m</sup> UT. The radio observation ran smoothly without problems. Figure 1 shows the recorded meteor rates.

A remarkable overdense radio echo was recorded on 2016 January 29 at 8<sup>h</sup>55<sup>m</sup> UT (Figure 1).

The underdense rates revealed no meaningful maximum associated to the passage of 115 DCS. The overdense rates revealed maxima of 3 overdense echoes per hour on 2016 January 29 around 8<sup>h</sup>-10<sup>h</sup> UT, on 2016 January 30 around 5<sup>h</sup>-7<sup>h</sup> UT, on 2016 January 31 around 5<sup>h</sup>-10<sup>h</sup> UT, and on 2016 February 1 around 7<sup>h</sup>-9<sup>h</sup> UT.<sup>1</sup> Hence, we may associate to 115 DCS at the expected maximum the qualification “low overdense rates”.

### 2.2 $\chi$ -Capricornids

EARS observed the daytime  $\chi$ -Capricornids (114 DXC) in the recording period 2016 February 12, 5<sup>h</sup>21<sup>m</sup> UT, to

<sup>1</sup>We should also bear in mind that a maximum around the same time on every day may be an indication that the Observability Function is high near that time (which means that the forward scatter set-up is very sensitive to meteors from the radiant direction at that time). Also for the other daytime showers discussed in this paper, data were not corrected with the Observability Function.

Table 1 – The 2016 daytime meteor showers according to the IMO Meteor Shower Calendar 2016 (Rendtel, 2015).

Shower	Code	Activity	Max Date	$\lambda_{\odot}$ 2000	Radiant $\alpha$ $\delta$	Rate
Capricornids/Sagittariids	115 DCS	Jan 13–Feb 04	Feb 01	321°5	299° –15°	medium
$\chi$ -Capricornids	114 DXC	Jan 29–Feb 28	Feb 13	324°7	315° –24°	low
April Piscids	144 APS	Apr 20–Apr 26	Apr 22	32°5	9° +11°	low
$\varepsilon$ -Arietids	154 DEA	Apr 24–May 27	May 09	48°7	44° +21°	low
May Arietids	294 DMA	May 04–Jun 06	May 16	55°5	37° +18°	low
$\alpha$ -Cetids	293 DCE	May 05–Jun 02	May 20	59°3	28° –04°	medium
Ariets	171 ARI	May 14–Jun 24	Jun 07	76°5	42° +25°	high
$\zeta$ -Perseids	172 ZPE	May 20–Jul 05	Jun 09	78°6	62° +23°	high
$\beta$ -Taurids	173 BTA	Jun 05–Jul 17	Jun 28	96°7	86° +19°	medium
$\gamma$ -Leonids	203 GLE	Aug 14–Sep 12	Aug 25	152°2	155° +20°	low
Sextantids	221 DSX	Sep 09–Oct 09	Sep 27	184°3	152° 0°	medium

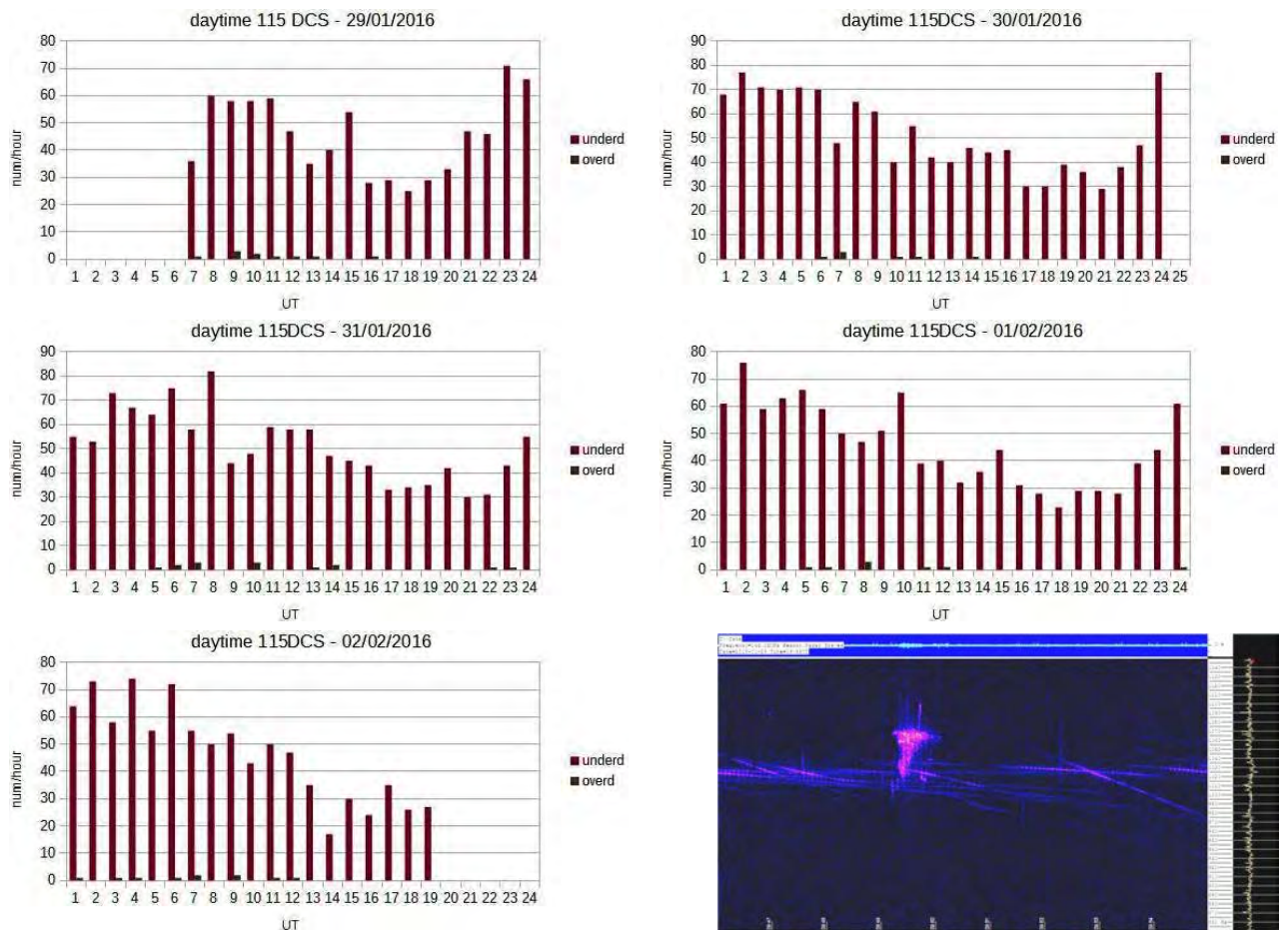


Figure 1 – Meteor rates for 115 DCS in the recording period 2016 January 29, 5<sup>h</sup>16<sup>m</sup> UT, to 2016 February 02, 18<sup>h</sup>05<sup>m</sup> UT, and an image of remarkable overdense radio echo on 2016 January 29 at 8<sup>h</sup>55<sup>m</sup> UT.

2016 February 14, 17<sup>h</sup>35<sup>m</sup> UT. The radio observation ran smoothly without problems. Figure 2 shows the recorded meteor rates.

A remarkable radio echo on 2016 February 12 around 19<sup>h</sup>34<sup>m</sup>–19<sup>h</sup>39<sup>m</sup> UT (Figure 2) was identified as radio interference generated in the building hosting EARS by analyzing the corresponding WAV file recorded by SpecLab.

The underdense rates revealed no meaningful maximum associated to the passage of 114 DXC. The overdense

rate revealed faint maxima of 3 overdense echoes per hour on 2016 February 12 around 7<sup>h</sup>–9<sup>h</sup> UT and on 2016 February 14 around 6<sup>h</sup>–8<sup>h</sup> UT. Hence, we may associate to 114 DCX at the expected maximum the qualification “low overdense rates”.

### 2.3 April Piscids

EARS radio-observed the April Piscids (144 APS) in the recording period 2016 April 21, 5<sup>h</sup>20<sup>m</sup> UT, to 2016 April 24, 17<sup>h</sup>25<sup>m</sup> UT. The radio observation ran smoothly

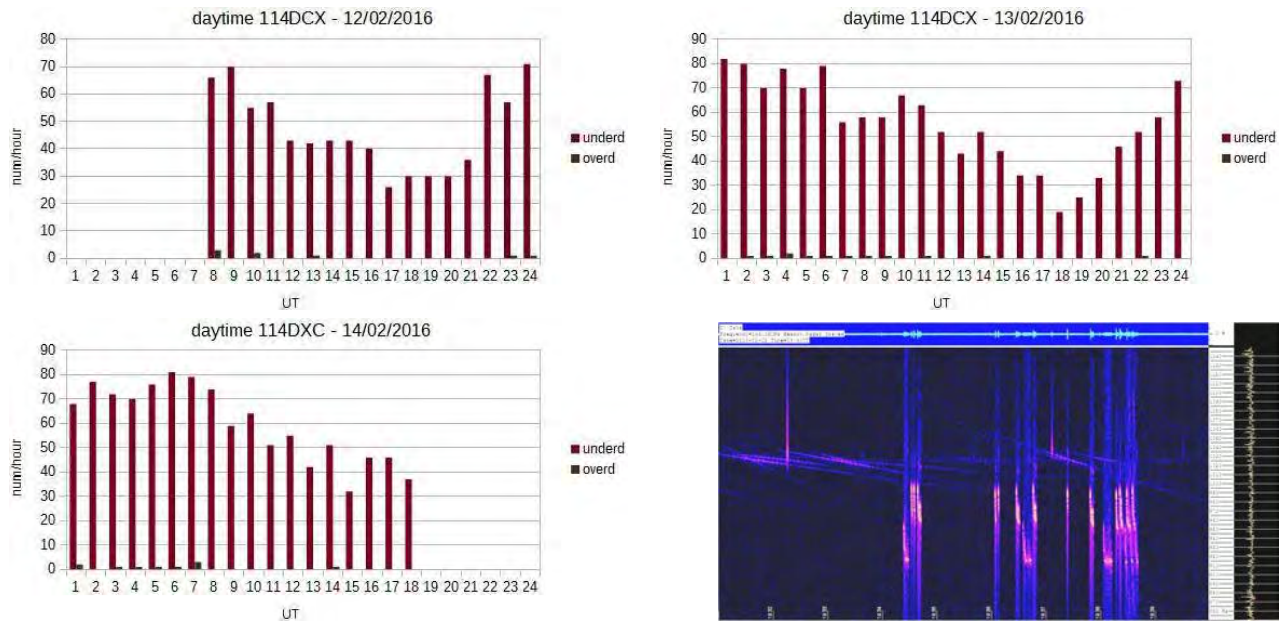


Figure 2 – Meteor rates of 114 DXC in the recording period 2016 February 12, 5<sup>h</sup>21<sup>m</sup> UT, to 2016 February 14, 17<sup>h</sup>35<sup>m</sup> UT, and an image of a remarkable radio echo on 2016 February 12 between 19<sup>h</sup>34<sup>m</sup> and 19<sup>h</sup>39<sup>m</sup> UT.

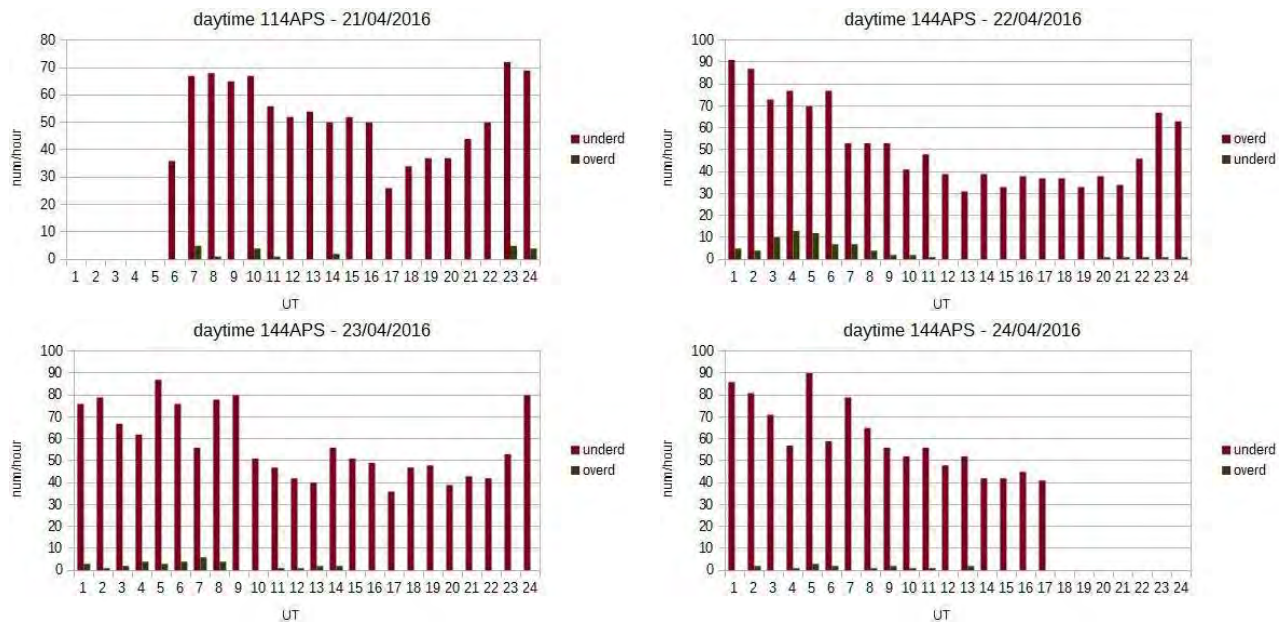


Figure 3 – Meteor rates of 144 APS in the recording period 2016 April 21, 5<sup>h</sup>20<sup>m</sup> UT, to 2016 April 24, 17<sup>h</sup>25<sup>m</sup> UT.

without problems. Figure 3 shows the recorded meteor rates.

The underdense rates revealed no meaningful maximum associated to the passage of 144 APS. The overdense rates showed an almost Gaussian maximum of 13 overdense echoes per hour on 2016 April 22 around 0<sup>h</sup>–11<sup>h</sup> UT. Hence, we may associate to 144 APS at the expected maximum the qualification “medium overdense rates”.

The much higher number of overdense echoes than for the previous two showers and the Gaussian-like maximum indicative either a shower maximum, or a high Observability Function, or both. The plots for the other observation days do not show a similar activity pattern.

## 2.4 ε-Arietids

EARS radio-observed the daytime ε-Arietids (154 DEA) in the recording period 2016 May 8, 14<sup>h</sup>32<sup>m</sup> UT, to 2016 May 11, 5<sup>h</sup>20<sup>m</sup> UT. The radio observation ran smoothly without problems. Figure 4 shows the recorded meteor rates.

The underdense rates revealed no meaningful maximum associated to the passage of 154 DEA. The overdense rate revealed two maxima of 6 overdense echoes per hour on 2016 May 9 around 4<sup>h</sup>–10<sup>h</sup> UT and 8 overdense echoes per hour on 2016 May 10 around 4<sup>h</sup>–7<sup>h</sup> UT. Hence, we may associate to 154 DEA at the expected maximum the qualification “medium overdense rates”.

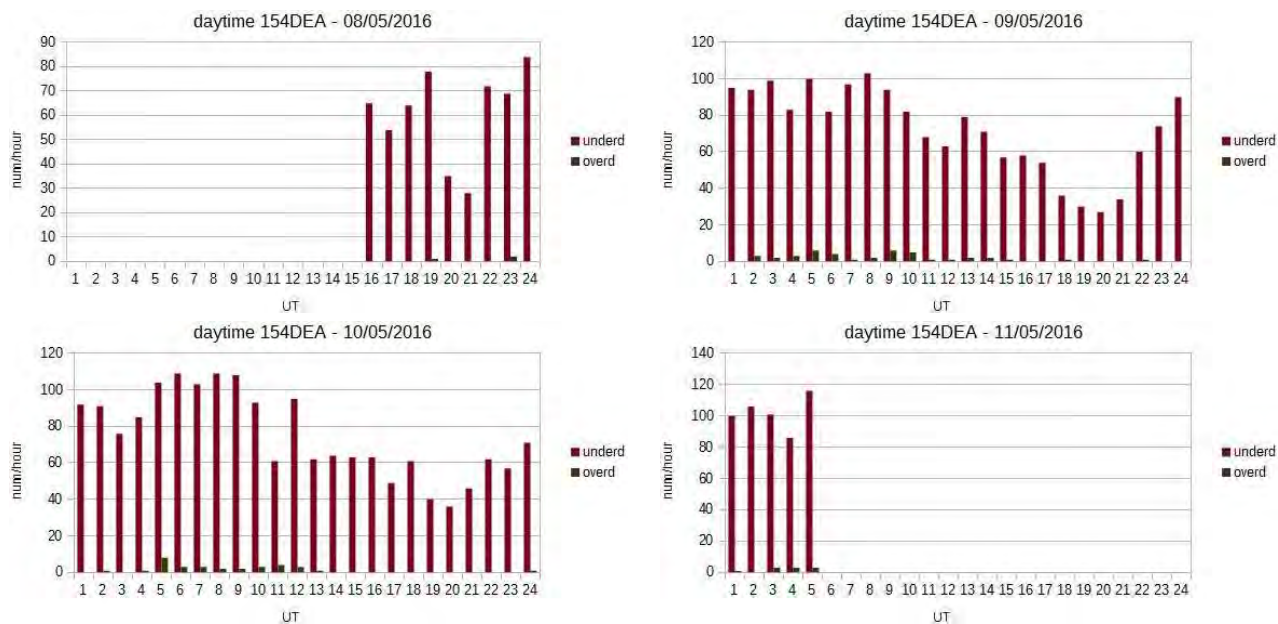


Figure 4 – Meteor rates of 144 APS in the recording period 2016 April 21, 5<sup>h</sup>20<sup>m</sup> UT, to 2016 April 24, 17<sup>h</sup>25<sup>m</sup> UT.

### 2.5 May Arietids and $\alpha$ -Cetids

Due to the IMC 2016 in Egmond, the Netherlands, EARS was not active during the May Arietids (294 DMA) and  $\alpha$ -Cetids (293 DCE) passages.

### 2.6 Arietids and $\zeta$ -Perseids

EARS radio observed the Arietids (171 ARI) and the  $\zeta$ -Perseids (172 ZPE) in the recording period 2016 June 6, 5<sup>h</sup>24<sup>m</sup> UT, to 2016 June 10, 5<sup>h</sup>30<sup>m</sup> UT. The radio observation ran smoothly without problems. Figure 5 shows the recorded meteor rates.

The underdense rates revealed no meaningful maximum associated to the passages of 171 ARI and 172 ZPE. The overdense rate revealed a maximum of 8 overdense echoes per hour on 2016 June 6 around 6<sup>h</sup>–12<sup>h</sup> UT, an almost Gaussian maximum of 19 overdense echoes per hour on 2016 June 7 around 4<sup>h</sup>–12<sup>h</sup> UT, a maximum of 21 overdense echoes per hour on 2016 June 8 around 6<sup>h</sup>–13<sup>h</sup> UT, and a maximum of 12 overdense echoes per hour on 2016 June 9 around 4<sup>h</sup>–12<sup>h</sup> UT. Hence, we may associate to both 171 ARI and 172 ZPE at their expected maxima the qualification “high overdense rates”.

Clearly, the Observability Function is high around 4<sup>h</sup>–12<sup>h</sup> UT. High shower activity was observed on June 7 and 8.

### 2.7 $\beta$ -Taurids

EARS radio-observed daytime  $\beta$ -Taurids (173 BTA) in the recording period 2016 June 27, 16<sup>h</sup>13<sup>m</sup> UT, to 2016 July 30, 16<sup>h</sup>30<sup>m</sup> UT. The radio observation ran smoothly without problems. Figure 6 shows the recorded meteor rates.

The underdense rates revealed no meaningful maximum associated to the passage of 173 BTA. The overdense rate revealed a maximum of 10 overdense echoes per hour on 2016 June 28 around 12<sup>h</sup>–15<sup>h</sup> UT, three maxima of, respectively, 10, 10, and 11 overdense echoes per hour on 2016 June 29 between 4<sup>h</sup> and 13<sup>h</sup> UT and a maximum of 10 overdense echoes per hour on 2016 June 30 around 3<sup>h</sup>–6<sup>h</sup> UT. Hence, we may associate to 183 BTA at the expected maximum the qualification “medium overdense rates”.

Maximum overdense rate of about 10 every day near the same time indicates a flat shower profile (clear shower activity, but without a defined maximum).

### 2.8 $\gamma$ -Leonids

5 EARS radio-observed the  $\gamma$ -Leonids (203 GLE) in the recording period 2016 August 23, 5<sup>h</sup>27<sup>m</sup> UT, to 2016 August 26, 5<sup>h</sup>15<sup>m</sup> UT. The radio observation in the recording period ran smoothly without problems. Figure 7 shows the recorded meteor rates.

The underdense rates revealed no meaningful maximum associated to the passage of 203 GLE. The overdense rate revealed a maximum of 8 overdense echoes per hour on both 2016 August 23 around 6<sup>h</sup>–12<sup>h</sup> UT and 2016 August 24 around 5<sup>h</sup>–9<sup>h</sup> UT. Hence, we may associate to 203 GLE at the expected maximum the qualification “medium overdense rates”.

No clear pattern can be observed here. During the other days, no similar activity was detected.

### 2.9 Sextantids

EARS radio-observed the daytime Sextantids (221 DSX) in the recording period 2016 September 25, 8<sup>h</sup>13<sup>m</sup> UT,

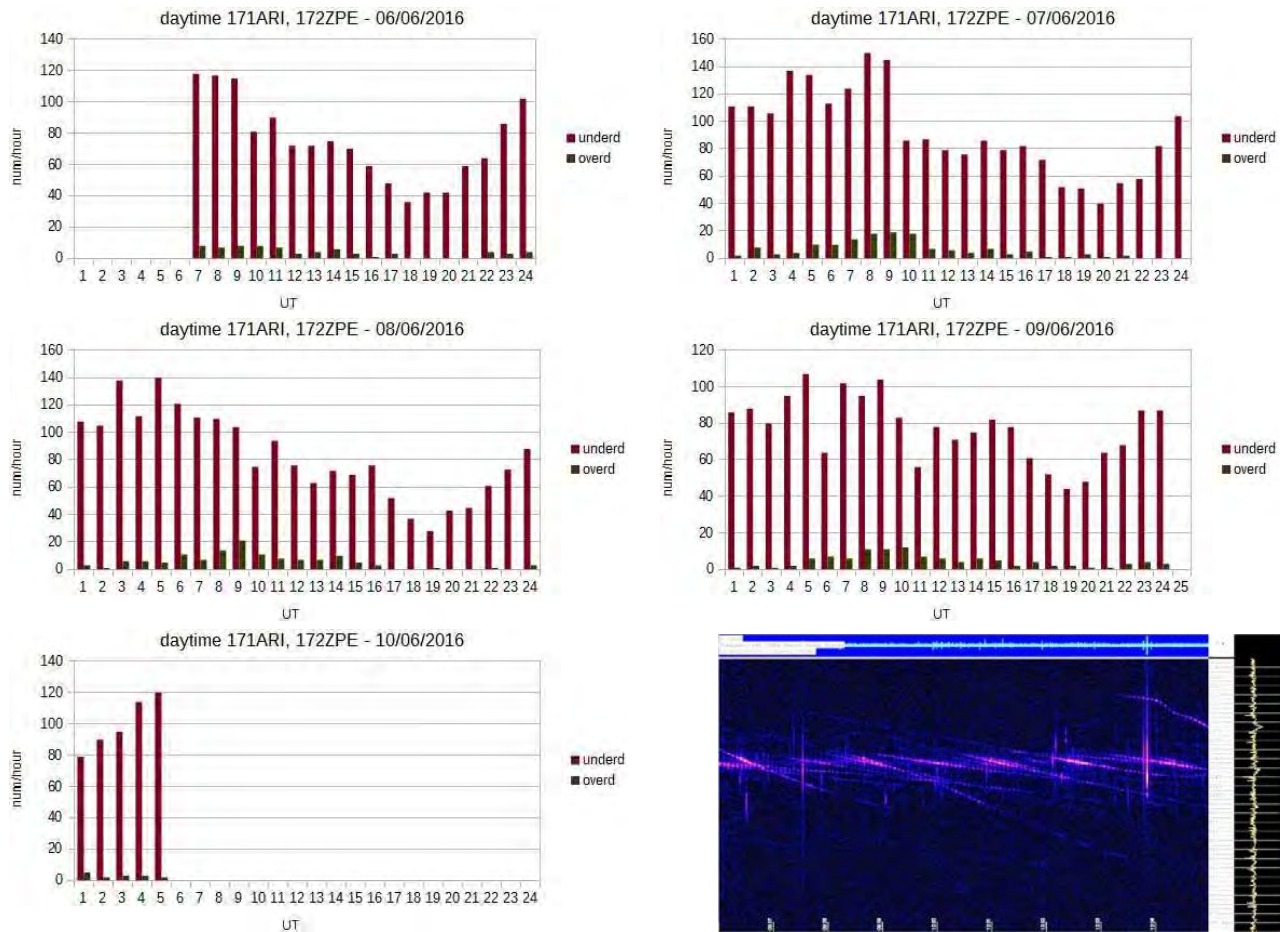


Figure 5 – Meteor rates of 171 ARI and 172 ZPE in the recording period 2016 June 6, 5<sup>h</sup>24<sup>m</sup> UT, to 2016 June 10, 5<sup>h</sup>30<sup>m</sup> UT, and image of radio echoes on 2016 June 7 between 7<sup>h</sup>56<sup>m</sup> and 8<sup>h</sup>05<sup>m</sup> UT.

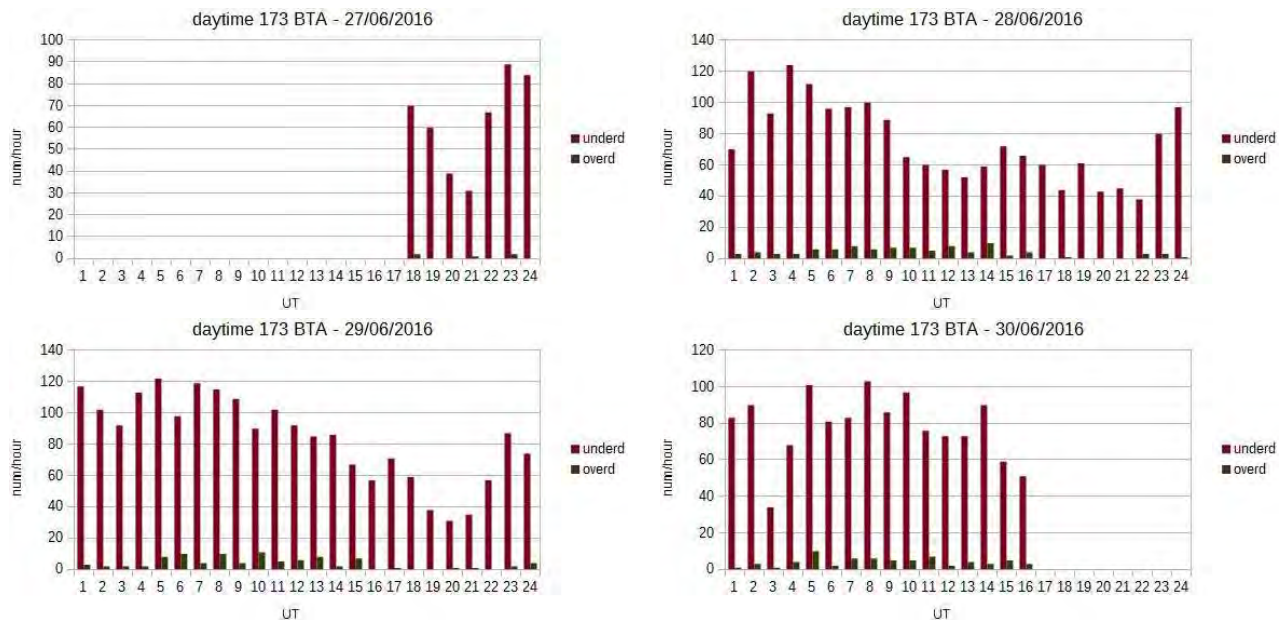


Figure 6 – Meteor rates of 173 BTA in the recording period 2016 June 27, 16<sup>h</sup>13<sup>m</sup> UT, to 2016 July 30, 16<sup>h</sup>30<sup>m</sup> UT.

to 2016 September 28, 17<sup>h</sup>35<sup>m</sup> UT. The radio observation in the recording period ran smoothly without problems. Figure 8 shows the recorded meteor rates.

The underdense rates revealed no meaningful maximum associated to the passage of 221 DSX. The overdense

rate revealed two maxima of, respectively, 8 and 10 overdense echoes per hour on 2016 September 27 around 1<sup>h</sup>–4<sup>h</sup> UT and 5<sup>h</sup>–8<sup>h</sup> UT.

Hence, we may associate to 221 DSX at the expected maximum the qualification “medium overdense rates”.

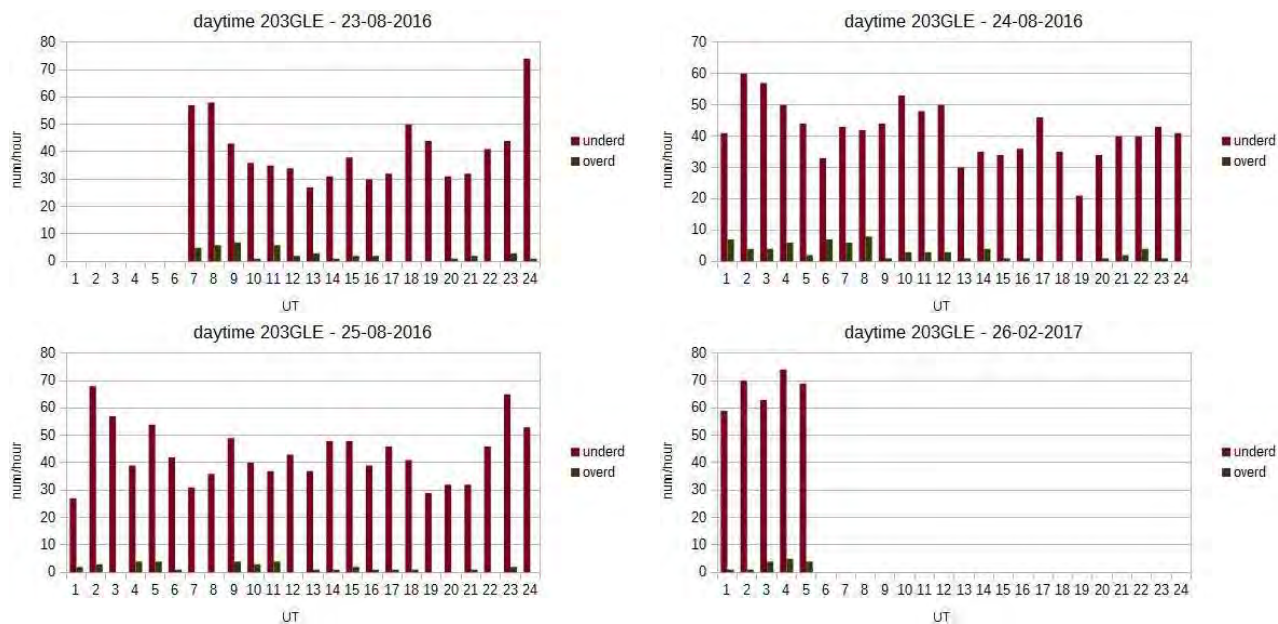


Figure 7 – Meteor rates of 173 BTA in the recording period 2016 June 27, 16<sup>h</sup>13<sup>m</sup> UT, to 2016 July 30, 16<sup>h</sup>30<sup>m</sup> UT.

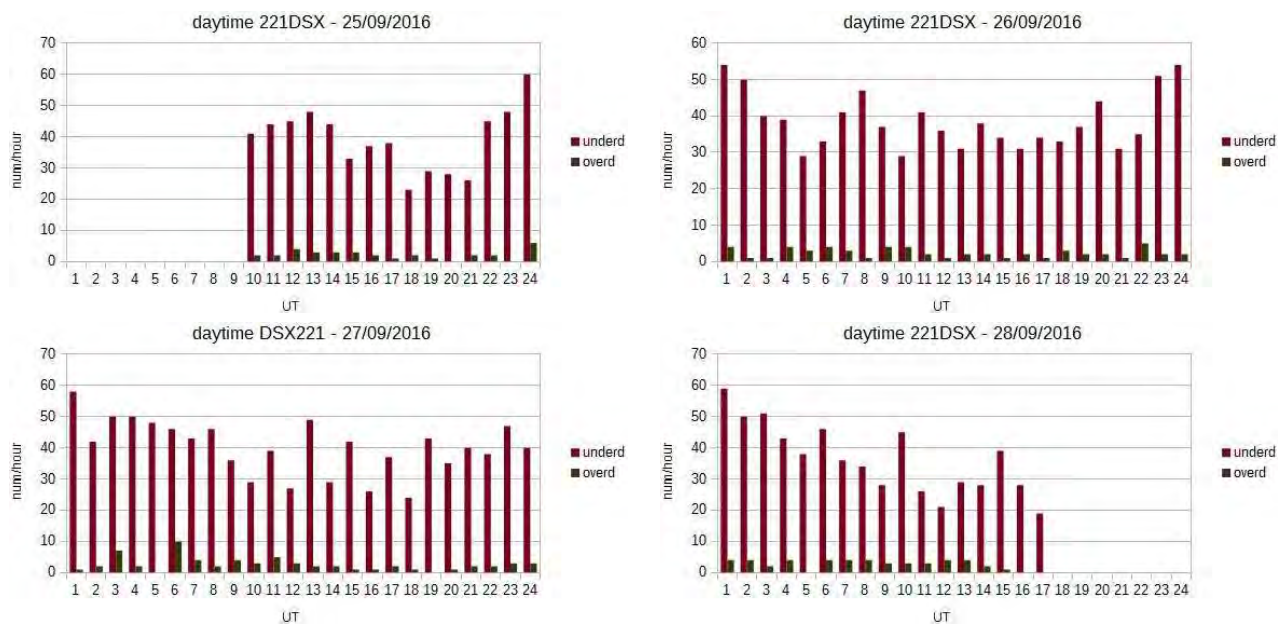


Figure 8 – Meteor rates of 221 DSX in the recording period 2016 September 25, 8<sup>h</sup>13<sup>m</sup> UT, to 2016 September 28, 17<sup>h</sup>35<sup>m</sup> UT.

The fact that the number of overdense meteors is significantly higher on September 27 at 2<sup>h</sup>–3<sup>h</sup> UT than on September 26 at the same time suggests that shower activity was higher on September 27 (since the Observability Function is the same on the same UT hours of neighboring days). The same is true for the number of overdense meteors at 5<sup>h</sup>–8<sup>h</sup> UT on both days, again suggesting the activity on September 27 was higher.

### 3 Discussion

The EARS radio observations did not allow to determine the total rates or underdense rates of the daytime meteor showers in 2016 at their expected maxima. How-

ever, they permitted to determine around said maxima and in the EARS configuration the associated overdense rates which can be classified as *low* (maximum rate of up to 3 overdense echoes per hour), *medium* (maximum rate of up to 8–10 overdense echoes per hour), and *high* (maximum rate of up to 19–21 overdense echoes per hour).

The associated overdense rates showed a certain agreement with the rates of Table 1 around the expected maximum. More specifically, 115 DCS had low overdense rates (“medium” in Table 1), 114 DCX had low overdense rates (“low” in Table 1), 144 APS had medium overdense rates (“low” in Table 1), 154 DEA had medium overdense rates (“low” in Table 1), 171 ARI and 172

ZPE had high overdense rates (“high” in Table 1), 173 BTA had medium overdense rates (“medium” in Table 1), 203 GLE had medium overdense rates (“low” in Table 1), and 221 DSX had medium overdense rates (“medium” in Table 1).

Of course, because of the Earth’s rotation, EARS could not observe daytime meteor showers, during the night, so that possible further radio echo maxima may have been lost. To avoid this and to further improve the knowledge of the radio meteor activity of the daytime meteor showers, combined radio observations with at least another radio station with opposite longitude relative to EARS would be very useful for producing uninterrupted radio observations of the daytime meteor showers.

## 4 Conclusions

The EARS configuration we adopted revealed itself to be reliable by providing uninterrupted radio observations in the recording periods around the expected maxima of the 2016 daytime meteor showers, improving in this way the knowledge of their radio meteor activity.

Combined radio observations with at least another radio station with opposite longitude now appears to be the next step for radio observations of the daytime meteor showers in 2017 and beyond.

## Acknowledgement

I am very grateful to Cis Verbeeck for his valuable comments and suggestions about the EARS observations and the presentation of this work at the IMC 2017. These are also incorporated into this article.

## References

- Rendtel J. (2014). “Daytime meteor showers”. In Rault J.-L. and Roggemans P., editors, *Proceedings of the International Meteor Conference*, Giron, France, 18–21 September 2014. IMO, pages 93–97.
- Rendtel J., editor (2015). *2016 Meteor Shower Calendar*. IMO-INFO 3-15. IMO.
- Tomezzoli G. and Verbeeck C. (2015). “No sign of the 2014 Daytime Sextantids and mass indexes determination from radio observations”. In Rault J.-L. and Roggemans P., editors, *Proceedings of the International Meteor Conference*, Mistelbach, Austria, 27–30 August 2015. IMO, pages 165–170.
- Tomezzoli G. and Barbieri L. (2016). “No sign of the 2015 Daytime Sextantids through combined radio observations”. In Roggermans A. and Roggemans P., editors, *Proceedings of the International Meteor Conference*, Egmond, the Netherlands, 2–5 June 2015. IMO, pages 291–293.

# Zeta Cassiopeiids—Twelve years of observations

Przemysław Żołądek<sup>1</sup> and Mariusz Wiśniewski<sup>1,2</sup>

<sup>1</sup> Comets and Meteors Workshop (PKiM), Bartycka 18, 00-716 Warszawa, Poland  
brahi@op.pl

<sup>2</sup> Central Office of Measures, Elektoralna 2, 00-139 Warszawa, Poland  
marand.w@gmail.com

The activity of the  $\zeta$ -Cassiopeiids has been analyzed using the new available video datasets. EDMOND and SonotaCo databases were used. Activity was confirmed every year from 2010 to 2015, starting at  $\lambda_{\odot} = 109^{\circ}$  and ending at  $\lambda_{\odot} = 118^{\circ}$ , with a maximum at  $\lambda_{\odot} = 113^{\circ}$ . Orbital elements of  $\zeta$ -Cassiopeiids are presented.

## 1 Introduction

The  $\zeta$ -Cassiopeiids form a minor meteor shower active in the middle of July, discovered independently in 2012 by the Polish Fireball Network (PFN, Żołądek and Wiśniewski, 2012) and by the Croatian Meteor Network (CMN, Šegon et al., 2012). This shower is currently known as Working List Shower 444 ZCS). The IAU Meteor Data Center (MDC) entry for this shower refers to three sets of shower data from, respectively, PFN, CMN, and CAMS (Jenniskens et al., 2016). According to these data, maximum activity occurs at  $\lambda_{\odot} = 113^{\circ}$  or at  $\lambda_{\odot} = 109^{\circ}$ , and the radiant is located close to  $\alpha_{\text{geo}} = 5^{\circ}$  and  $\delta_{\text{geo}} = 50^{\circ}$ . The geocentric velocity is just above 57 km/s. Orbits of  $\zeta$ -Cassiopeiids orbits are similar to orbits of Perseids, but the perihelion distance is larger (almost 1 AU).

The  $\zeta$ -Cassiopeiids were first observed during the night of July 14-15, 2005, when a small outburst was detected by PFN video cameras. Many bright ZCS meteors and fireball were observed that night, and according to an analysis of PKiM visual reports the ZHR was above 5.

Large sets of data were used for further analysis. We searched for  $\zeta$ -Cassiopeiids in the Sonotaco database using orbital similarity criteria and in the IMO Video Network database (single-station meteors). The  $\zeta$ -Cassiopeiids were active during every year from 2007 to 2011. The most important feature of the ZCS is their activity profile. Between  $\lambda_{\odot} = 110^{\circ}$  and  $\lambda_{\odot} = 116^{\circ}$ , the  $\zeta$ -Cassiopeiids are the most active meteor shower, with a clearly discernible maximum at  $\lambda_{\odot} = 113^{\circ}$ . The Perseids reach a similar activity level 9 days later, close to  $\lambda_{\odot} = 122^{\circ}$  (Figure 1).

## 2 Analysis

Large orbital datasets were used to investigate the existence of the ZCS meteor after 2011. The SonotaCo and EDMOND databases were merged into a single dataset with 483 406 meteoroid orbits. Only meteors observed at  $\lambda_{\odot} = 100^{\circ}$ – $130^{\circ}$  were used for calculations (32 077 orbits). Each meteor orbit in this selected subset was compared to every other meteor orbits; for each pair,

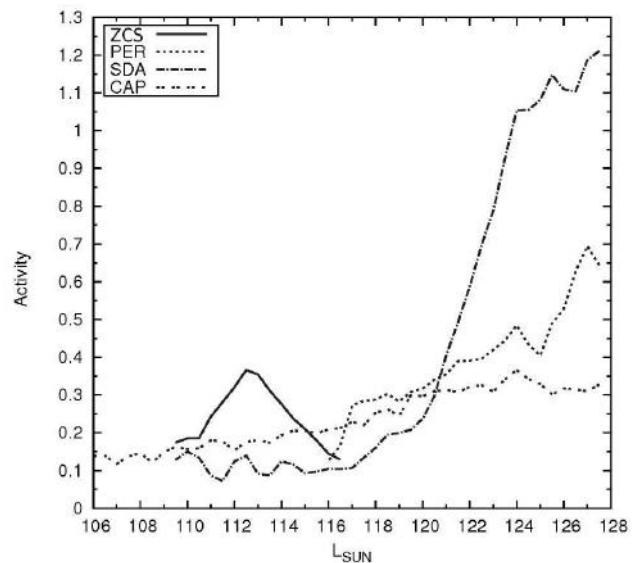


Figure 1 – Activity profile of the  $\zeta$ -Cassiopeiids calculated from IMO Video Network data

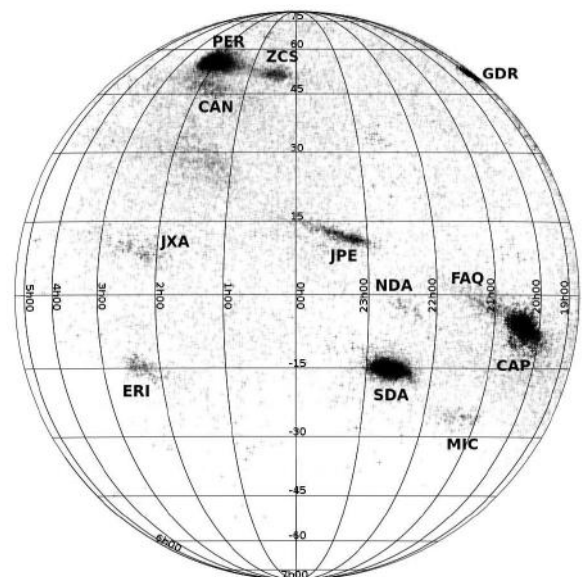


Figure 2 – The  $\zeta$ -Cassiopeiids among all meteor showers active between  $\lambda_{\odot} = 100^{\circ}$  and  $\lambda_{\odot} = 130^{\circ}$ .

orbital similarity was calculated using Drummond’s criterion. Pairs with a  $D'$  value above a certain threshold were rejected, and the others were retained. For every

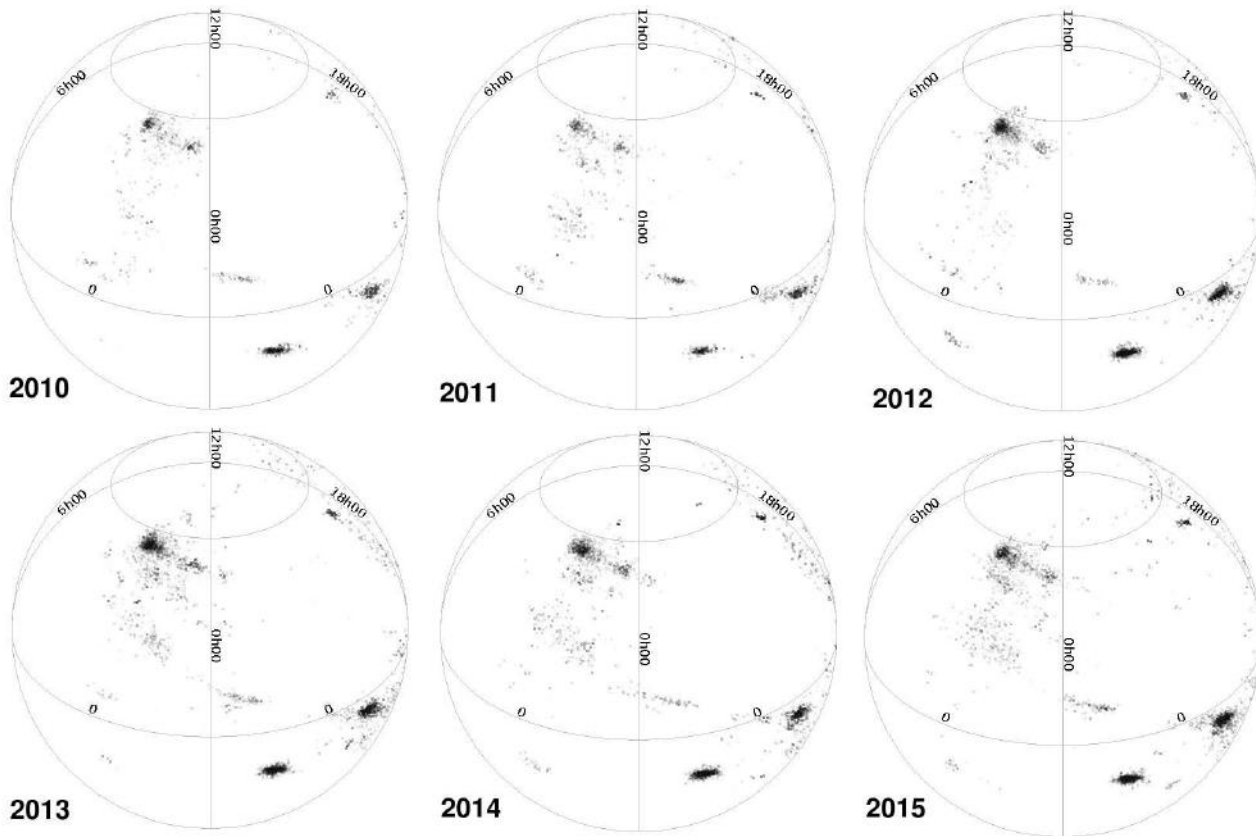


Figure 3 – Annual activity of the  $\zeta$ -Cassiopeiids.

orbit, the mean similarity with all other non-rejected orbits was calculated. By properly setting the rejection threshold, we could easily reject the sporadic background, while the more compact meteor showers became clearly discernible. The presence of the ZCS radiant was checked in the whole range of solar longitudes, in bins of one degree solar longitude and also separately year by year.

### 3 Results

The  $\zeta$ -Cassiopeiids radiant is clearly visible on the radiant map generated for the whole range of analyzed data; also 11 other meteor showers were identified in the solar longitude range  $\lambda_{\odot} = 100^{\circ}$ – $130^{\circ}$  (Figure 2).

The  $\zeta$ -Cassiopeiids activity was analyzed in bins of one degree in solar longitude. There is no trace of activity before  $\lambda_{\odot} = 109^{\circ}$ , but at  $\lambda_{\odot} = 110^{\circ}$   $\zeta$ -Cassiopeiids are clearly visible, and between  $\lambda_{\odot} = 112^{\circ}$  and  $\lambda_{\odot} = 114^{\circ}$  we observe quite strong activity. The radiant becomes weak after  $\lambda_{\odot} = 115^{\circ}$ , but some traces of activity are observed until  $\lambda_{\odot} = 118^{\circ}$ . At  $\lambda_{\odot} = 119^{\circ}$ , an activity increase is observed which is connected to the early Perseids. There is no clear gap between the ZCS and PER radiants, but activity profiles can be used to distinguish between these two (probably closely connected) meteor showers.

The  $\zeta$ -Cassiopeiids activity was checked year by year, for the range  $\lambda_{\odot} = 100^{\circ}$ – $130^{\circ}$  (Figure 3). The presence

of this meteor shower is clear in 2010 and 2011. In 2012, the radiant is a bit weaker, but between 2013 and 2015  $\zeta$ -Cassiopeiids are clearly visible again. There are not enough data in 2016 to detect the shower.

Largest numbers of  $\zeta$ -Cassiopeiids were observed for solar longitude  $\lambda_{\odot} = 113^{\circ}$ , which is consistent with the first analyses of this shower.

The orbital elements for the orbit with the best mean  $D'$  value (as the most representative for the shower) are the following:  $a = 21$  AU,  $q = 0.9938$  AU,  $e = 0.95358$ ,  $i = 107^{\circ}13'$ ,  $\omega = 162^{\circ}63'$ , and  $\Omega = 113^{\circ}176'$ . The corresponding geocentric radiant parameters are  $\alpha_{\text{geo}} = 6^{\circ}68'$ ,  $\delta_{\text{geo}} = 51^{\circ}24'$ , and  $V_{\text{geo}} = 57.16$  km/s. See also Table 1.

### 4 Conclusions

The current analysis of the Sonataco and EDMOND databases confirm activity of the  $\zeta$ -Cassiopeiids. This meteor shower is active annually in the period  $\lambda_{\odot} = 110^{\circ}$ – $118^{\circ}$ , with a maximum at  $\lambda_{\odot} = 113^{\circ}$ . The beginning of the activity is well defined, while the end of activity is unclear and seems to be connected with the beginning of the early Perseids. Both showers can be distinguished using activity profiles, as there is a significant activity dip between ZCS and the early Perseids. Nevertheless, a dynamical connection between the  $\zeta$ -Cassiopeiids and the Perseids is quite possible, and both showers may be closely connected.

Table 1 – Radiant positions, geocentric velocities, and orbital elements of the Zeta Cassiopeids.

Designation	$\lambda_{\odot}$ ( $^{\circ}$ )	$\alpha_{\text{geo}}$ ( $^{\circ}$ )	$\delta_{\text{geo}}$ ( $^{\circ}$ )	$V_{\text{geo}}$ (km/s)	$a$ (AU)	$q$ (AU)	$e$	$\omega$ ( $^{\circ}$ )	$\Omega$ ( $^{\circ}$ )	$i$ ( $^{\circ}$ )	Mean $D'$
_20140715_230530	113.176	6.68481	+51.2380	57.1638	21.4081	0.993772	0.953580	162.634	113.176	107.129	0.0679480200247
_20130714_214056	112.409	5.17808	+48.9153	58.5310	88.5351	1.00284	0.988673	166.669	112.409	110.039	0.0679633987666
_20140715_210944	113.099	4.64285	+51.9804	57.0304	171.156	0.999309	0.994161	165.081	113.099	105.636	0.0679651529655
_20130715_004713	112.532	4.36004	+50.4762	56.4849	11.1564	1.00276	0.910119	166.344	112.532	106.253	0.0679870056370
_20140716_212542	114.063	6.57075	+51.6779	57.2933	41.7638	0.997561	0.976114	164.279	114.063	106.851	0.0679984628783
_20130715_001410	112.510	6.34812	+49.0019	57.8987	16.4463	0.999464	0.939229	164.906	112.510	109.580	0.0680219756871
_20130714_013922	111.255	2.79872	+50.5083	57.4276	-49.5509	1.00320	1.02025	166.920	111.255	106.034	0.0680395914562
_20100716_015554	112.958	7.32322	+50.3343	58.1871	-71.2508	0.995218	1.01397	163.438	112.958	108.402	0.0680790879550
_20100715_220638	113.620	7.01311	+49.9137	58.3065	64.3769	0.998616	0.984488	164.724	113.620	109.515	0.0680830028885
_20130716_023624	113.558	6.98483	+51.5220	56.9202	21.6941	0.996459	0.954068	163.708	113.558	106.375	0.0680981241081
_20090716_023402	113.244	6.05770	+49.2141	58.0374	32.3097	1.00458	0.968908	167.513	113.244	109.116	0.0680999374613
_20140714_234634	112.249	4.22093	+49.7592	56.8871	11.3269	1.00317	0.911435	166.567	112.249	107.391	0.0681165250436
_20090716_015559	113.199	6.26712	+50.4718	56.9043	13.4019	0.998984	0.925460	164.647	113.199	107.075	0.0681270515224
_20140716_013713	113.276	8.06499	+49.8215	57.8452	20.1930	0.995343	0.950709	163.242	113.276	109.166	0.0681636140926
_20100715_231638	113.210	5.87005	+49.4426	57.8316	20.0676	1.00234	0.950052	166.297	113.210	109.038	0.0681878249815
_20110714_233706	111.668	3.12290	+50.0403	57.9385	-40.1939	1.00330	1.02496	166.995	111.668	107.392	0.0682695180591
_20100715_220638	112.868	3.68575	+51.2082	56.2045	12.3995	1.00271	0.919133	166.354	112.868	105.211	0.0682996042536
_20150714_230951	111.979	3.66584	+50.2018	57.9848	-37.3560	1.00337	1.02686	167.025	111.979	107.420	0.0682952328502
_20090716_234706	113.114	6.35370	+50.2817	58.2357	-17.6005	0.997894	1.01394	164.535	113.114	108.547	0.0683046849679
_20150715_232604	112.944	5.52864	+51.8433	56.2562	14.2469	0.996218	0.930075	163.466	112.944	105.123	0.0683349054525
_20140715_022639	112.236	4.57893	+50.1651	58.1821	-38.3156	1.00035	1.02611	165.643	112.236	108.067	0.0683428391710
_20130714_002155	111.561	4.26274	+48.7252	57.4953	12.5274	1.00336	0.919907	166.663	111.561	108.893	0.0683778075867
_20130716_024244	114.357	7.22923	+52.2280	56.9595	35.2887	0.995425	0.971792	163.387	114.357	106.025	0.0685082957135
_20140715_213253	113.114	5.28647	+49.1654	58.4176	61.6452	1.00458	0.983704	167.571	113.114	109.844	0.0685335837326
_071617MLA0014	113.961	6.69174	+51.1304	57.8255	-85.3103	0.999761	1.01172	165.350	113.961	107.426	0.0686059887440
_20090716_025054	113.235	5.59875	+52.2168	56.2209	21.6053	0.997903	0.953812	164.299	113.235	104.412	0.0687899286512
_071415MLA0023	112.331	4.52472	+51.9101	56.9128	-137.867	0.998826	1.00724	164.879	112.331	104.945	0.0687916343371
_20110716_202718	113.450	5.02169	+50.8763	58.1466	-55.9915	1.00179	1.01789	166.287	113.450	108.171	0.0688204402695
_071314MEA0007	111.511	2.15694	+50.3600	57.7004	-37.4619	1.00542	1.02684	168.100	111.511	106.633	0.0688354850370
_20140716_024008	112.960	5.22926	+50.7633	57.7878	-41.0385	1.00238	1.02443	166.593	112.960	106.962	0.0688522515835
_071617MLA0007	113.889	6.99467	+51.3544	56.9031	15.0410	0.995438	0.933818	163.201	113.889	106.905	0.0689766516156
_20120717_030135	114.416	8.70780	+51.1336	57.6647	58.3232	0.995415	0.982933	163.409	114.416	107.715	0.0690413911816
_20160716_032104	113.450	6.78049	+52.1093	56.1214	13.8801	0.995112	0.928307	163.034	113.450	104.834	0.0690567804617
_20100717_020929	113.921	8.73264	+50.4916	57.7797	29.4946	0.993589	0.966313	162.621	113.921	108.525	0.0690918046499
_20100717_023508	113.938	8.24356	+50.9842	57.2395	19.6372	0.994442	0.949359	162.874	113.938	107.416	0.0691303877073
_20130713_210221	111.429	1.59793	+50.6957	57.5382	-40.0038	1.00603	1.02515	168.419	111.429	106.198	0.0691459433560
_20130713_014923	110.665	3.10299	+49.6087	56.3915	9.66704	1.00191	0.896358	165.825	110.665	106.368	0.0691527971029
_20100715_195250	113.075	6.07652	+49.0924	58.2669	17.3887	1.00107	0.942430	165.655	113.075	110.547	0.0691855146092
_071617ZGR0015	113.932	6.90858	+51.7097	56.5819	13.6601	0.995419	0.927129	163.142	113.932	106.118	0.0692208045336
_20150716_005229	113.001	6.29904	+50.4673	56.6903	10.2071	0.997662	0.902258	163.944	113.001	107.083	0.0692248810958
_20090716_031934	113.254	6.16059	+51.0839	56.3043	10.6183	0.999058	0.905912	164.595	113.254	105.888	0.0692296026822
_20130716_005816	113.493	7.86159	+51.2425	56.9769	16.5034	0.991909	0.939897	161.858	113.493	106.958	0.0692306948023
_20090715_034642	112.318	7.86923	+50.3646	58.1806	-63.2333	0.991146	1.01567	161.912	112.318	108.403	0.0692353004920
_20130715_004713	112.532	5.78937	+51.5543	56.0603	10.6279	0.994262	0.906448	162.572	112.532	105.230	0.0692469953060
_20110716_221204	113.519	7.53154	+51.3195	57.5191	37.7173	0.990457	0.973740	161.488	113.519	107.647	0.0692546491117
_20120715_220934	113.626	5.41938	+51.6619	57.6655	-36.1778	1.00051	1.02766	165.718	113.626	106.508	0.0692839035787
_20120717_012602	114.711	8.08958	+51.4547	57.1624	21.3127	0.997913	0.953178	164.319	114.711	107.046	0.0692883825190
_071213RIB0005	110.676	2.61673	+49.7046	56.3190	9.91833	1.00051	0.898860	166.458	110.676	106.111	0.0692885875872
_20110717_215210	114.459	6.96977	+52.0055	57.5210	2683.32	0.996143	0.999629	163.786	114.459	106.901	0.0692941281946
_20090715_012044	112.222	4.00124	+48.8946	57.2018	11.4662	1.00598	0.912266	168.063	112.222	107.232	0.0692941281946
_20110717_012836	113.649	7.01634	+50.6148	56.8597	11.7578	0.997171	0.915191	163.825	113.649	107.270	0.0693138145284
_20140717_013653	114.230	8.76719	+51.0176	57.6886	39.3545	0.994307	0.974735	162.959	114.230	108.048	0.0693880550039
_20140714_224051	112.206	4.58332	+49.1174	57.2519	10.4779	1.00257	0.904316	166.234	112.206	108.649	0.0694528196651

References

Jenniskens P., Nénon Q., Gural P. S., Albers J., Haberman B., Johnson B., Holman D., Morales R., Grigsby B. J., Samuels D., and Johannink C. (2016). “CAMS confirmation of previously reported meteor showers”. *Icarus*, **266**, 355–370.

Šegon D., Andreić Ž., Korlević K., Gural P., Novoselnik F., Vida D., and Skokić I. (2012). “New shower in Cassiopeia”. *WGN, J. of the IMO*, **40**, 195–200.

Żołądek P. and Wiśniewski M. (2012). “The new July meteor shower”. *WGN, Journal of the IMO*, **40**, 189–194.

# The 2016 Gamma Draconids outburst

Christian Steyaert<sup>1</sup> and Jeffrey Brower

<sup>1</sup>Vereniging voor Sterrenkunde (VVS), Belgium  
steyaert@vvs.be and bcmeteors@gmail.com

The 2016  $\gamma$ -Draconids outburst observed by video is yet another outburst that was independently discovered by forward scatter radio observations. Thanks to the high declination of the radiant, it was recorded by many observers in the northern hemisphere. A detailed activity profile was also obtained.

## 1 Introduction

During the past few years, we have reported on forward scatter observations of predicted outbursts or enhanced activity of the following known streams:

- October 2011 Draconids (Steyaert, 2013);
- May 2013  $\eta$ -Aquariids (Steyaert, 2014a);
- May 2014 Camelopardalids, associated to Comet 209P/LINEAR (Steyaert, 2014b);
- February 2015  $\gamma$ -Lyrids (Steyaert, 2015). This outburst was confirmed by Brown (2016). There was a weak return in 2017 (Pellens, 2017).

This contribution is an update on our previous paper (Steyaert, 2015), and discusses a new and similar outburst.

## 2 Discovering outbursts

Figure 1 shows the hourly counts obtained by Felix Verbelen for 2014–2016. He has been monitoring the VVS beacon since the beginning of 2005 with the same receiver and antenna setup.

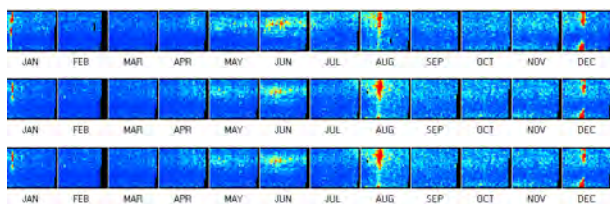


Figure 1 – Yearly overview of the counts of Verbelen obtained for the years 2014–2016.

The well-known annual streams are easily recognized: the Quadrantids on January 3–4, the Lyrids end April, the  $\eta$ -Aquariids early May, the long-lasting daytime streams in June, the Perseids in August, and the Geminids mid-December. The presence of the Orionids in October and the Leonids in November varies from year to year. There was also a strong return of the Ursids in 2016.

During February and March there are no known major streams, and the annual sporadic activity is the lowest

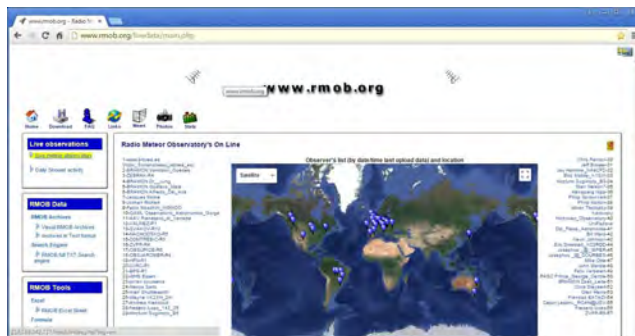


Figure 2 – Participating stations in RMOB (Radio Meteor Observatories On-line).

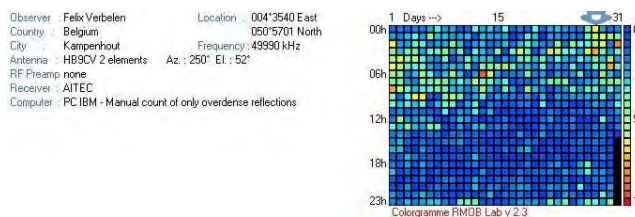


Figure 3 – Typical daily radio count pattern.

of the year. Hence, this is the period of the year (for the northern hemisphere) during which smaller streams can be more easily detected from the normally low counts. Along with the longer nights during these months, there is also a good chance of optically recording activity if the weather cooperates. Outside this period, the signal-to-noise ratio of a smaller stream is too low at nighttime.

For radio observers, unknown activity can also be more easily discovered when the sporadic activity is at its lowest, i.e., during local afternoon to midnight hours.

## 3 Observations

During July 2017, there were 57 submissions to RMOB (Radio Meteor Observatories On-Line, Figure 2).<sup>1</sup> Most of the observers employ automatic counting methods. Some of the stations are still in a testing phase. It should be noted that several new stations in Brazil have recently come on line, which creates the possibility of studying the southern hemisphere streams.

A typical monthly graph (Figure 3) shows the daily pattern with a maximum in the morning hours local

<sup>1</sup><http://www.rmob.org/livedata/main.php>.

time, and a minimum in the evening, with superimposed stream activity, like the daytime  $\beta$ -Taurids in early July.

## 4 Finding previously unknown activity

In checking the monthly submissions to RMOB, the following mail exchange between the authors took place:

```
Date: Tue, 02 Aug 2016 11:43:42 +0200
To: Jeffrey Brower <jbrower@meteorchaser.net>
From: Chris Steyaert <csteyaert@gmail.com>
Subject: Re: RMOB 2016 07 Brower
```

Hi Jeff,

Several observations recorded an outburst on July 28, 0h - 1h UT. I'll look into that one.

Seventeen reflections are seen in the 5-minutes Speclab waterfall spectrum (Figure 4), which is exceptional for that time of the day. An extrapolated rate of 200 per hour occurs only for the strongest streams.

An automatic counting script found only seven reflections, shown on the lower axis of Figure 4). It clearly needs more tuning.

In total, twelve RMOB observers recorded increased activity in the interval July 27, 23<sup>h</sup> UT–July 28, 2<sup>h</sup> UT, indicated with blue arrows in the various panels of Figure 5.

All types of transmitters are present:

- the 50 W VVS beacon (49.99 MHz);
- the Megawatts GRAVES radar (143.05 MHz) in France; and
- TV stations in North America and Japan.

Simply adding (without any scaling) the counts of these twelve observers for the two days around the outburst (Figure 6) confirms the higher activity for July 27, 23<sup>h</sup> UT, and July 28, 0<sup>h</sup> UT.

## 5 Optical observations

Contrary to the 2015 February 5 event, there was no need to try to locate the radiant of the stream based on the radio observations. Quoting from the *Central Bureau Electronic Telegram 4292*,<sup>2</sup>

JULY GAMMA DRACONID METEOR OUTBURST

P. Jenniskens, SETI Institute and NASA Ames Research Center, reports that stations of the CAMS meteor video camera network in the Netherlands detected unusually strong activity from the July gamma Draconids shower (IAU

<sup>2</sup><http://www.cbat.eps.harvard.edu/iau/cbet/004200/CBET004292.txt>.

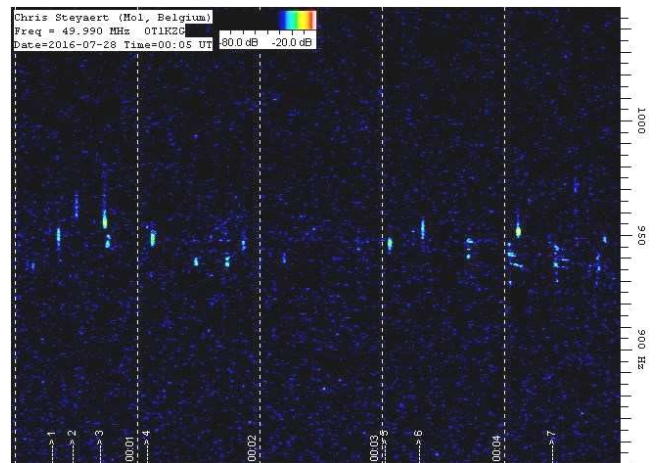


Figure 4 – Spectrum obtained by Steyaert in the interval July 28, 0<sup>h</sup>00<sup>m</sup>–0<sup>h</sup>05<sup>m</sup> UT.

shower number 184) between July 27d23h56m and 28d00h23m UT. According to the data analysis by M. Breukers (Hengelo, The Netherlands), about half of all 126 single-station-detected meteors in the partially clouded night (typically with brightness around magnitude +2) radiated from this shower's radiant, as did five out of nine multi-station meteors. The median geocentric radiant position was R.A. = 279.88 +/- 0.12 deg, Decl. = +50.12 +/- 0.46 deg (equinox J2000.0), with geocentric velocity 27.31 +/- 0.09 km/s, (equinox J2000.0).

Jeff records the counts in 10-minute intervals, which is a good compromise of time resolution versus number. The average number of reflections the day before and after the outburst in the interval 23<sup>h</sup>30<sup>m</sup>–0<sup>h</sup>30<sup>m</sup> UT is 4 to 7. It is significantly higher from July 27, 23<sup>h</sup>40<sup>m</sup>, to July 28, 0<sup>h</sup>30<sup>m</sup> (boxed in Figure 7). This is somewhat longer than the interval given by CAMS, most probably because it includes fainter meteors.

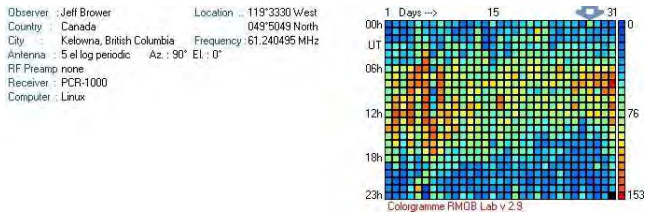
## 6 Radiant position

The radiant was rather high in the sky for Europe (Figure 8). This poses a problem for explaining the high number of underdense meteors in Figure 4.

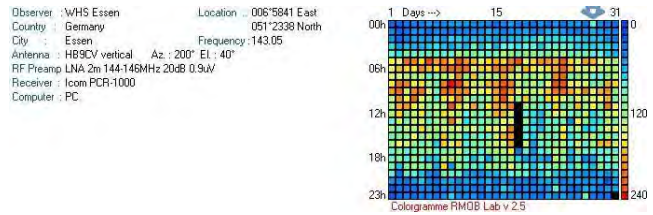
According to classical underdense specular reflection geometry, the reflections can only take place at a large distance, and consequently their number and intensity should be low. The same happens, e.g., at the Perseids culmination of the radiant, but this is from more overdense meteors at higher speed. This leads to the conclusion that the reflections in Figure 4 are short but non specular.

## 7 Conclusion

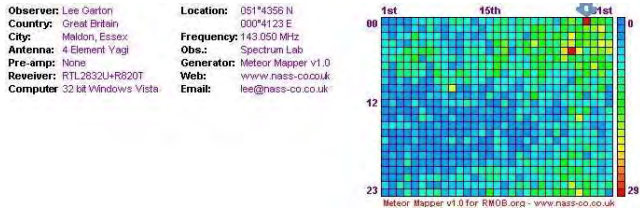
Beyond any doubt, moderately strong stream outburst can be identified in the heterogeneous forward scatter counts.



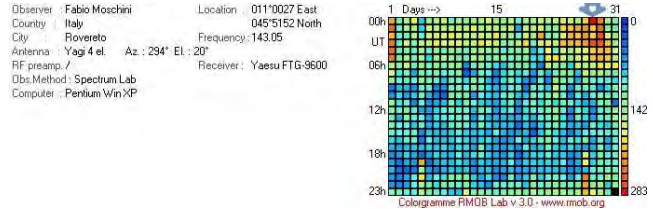
(a) Jeff Brower, Canada



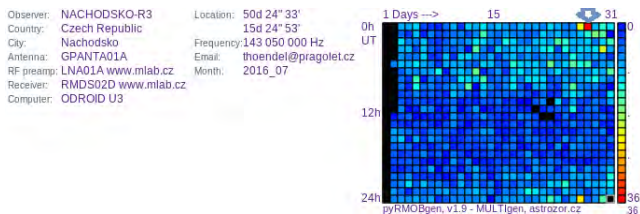
(b) Walter Hohmann Sternwarte, Germany



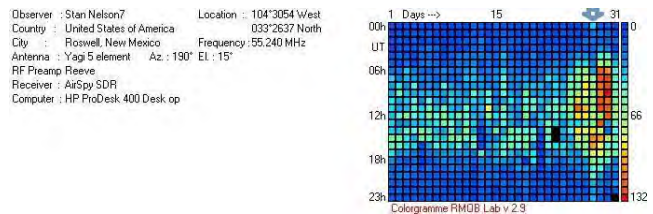
(c) Lee Garton, UK



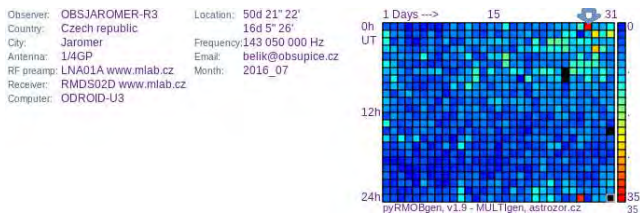
(d) Fabio Moschini, Italy



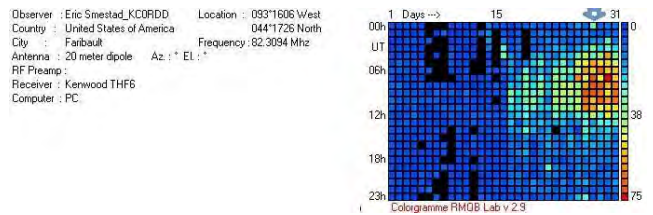
(e) NACHODSKO-R3, Czech Republic



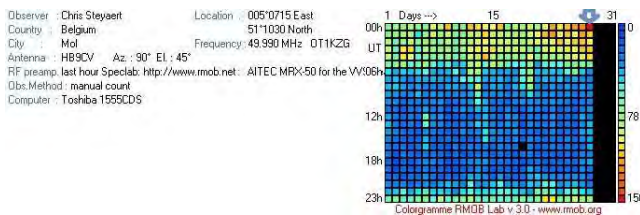
(f) Stan Nelson, USA



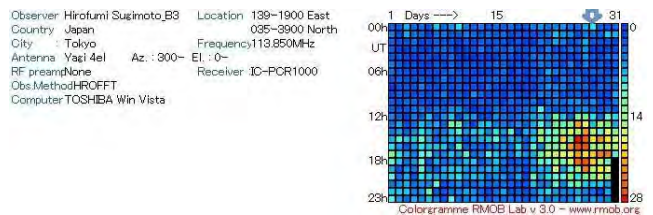
(g) OBSJAROMER-R3, Czech Republic



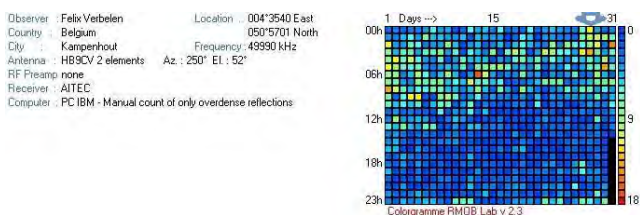
(h) Eric Smestad, USA



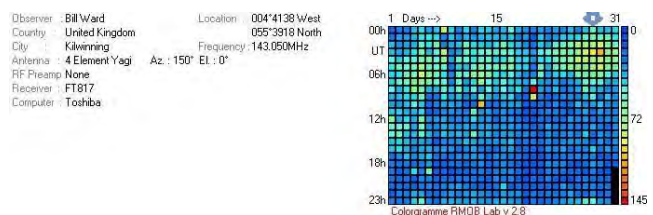
(i) Chris Steyaert, Belgium



(j) Hirofumi Sugimoto, Japan



(k) Felix Verbelen, Belgium



(l) Bill Ward, UK

Figure 5 – Twelve RMOB observations of increased activity in the interval July 27, 23<sup>h</sup> UT–July 28, 2<sup>h</sup> UT, indicated with blue arrows in panels (a)–(l).

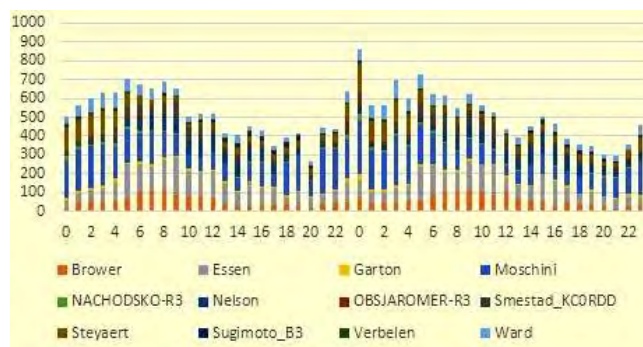


Figure 6 – Stack of all counts shown in Figure 5.

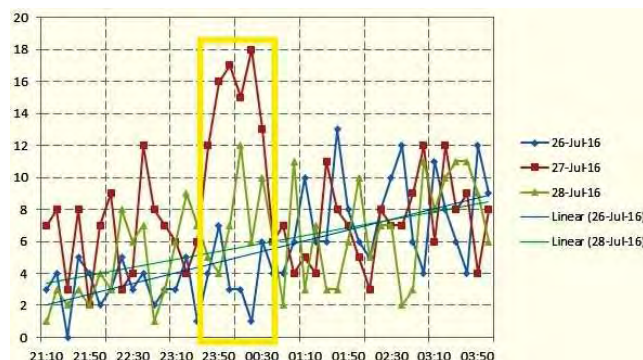


Figure 7 – Jeff Brower’s 10-minute counts around the time of the outburst.

### 8 Analysis opportunities

Currently, basic data in the Visual RMOB Archives<sup>3</sup>, which contains data since 2000, are not systematically scanned for unknown activity. Several more streams may await discovery in this database.

### Acknowledgement

The authors wish to thank the `rmob.org` contributors, the CAMS community, the IMO, and especially Pierre Terrier, who hosts `rmob.org` since 2001.

### References

Brown P. (2016). “Recent shower outbursts detected by the Canadian Meteor Orbit Radar (CMOR)”. In Roggemans A. and Roggemans P., editors, *Proceedings of the International Meteor Conference*, Egmond, the Netherlands, 2–5 June 2016. IMO, pages 42–45.



Figure 8 – Visible sky on July 28, 0<sup>h</sup> UT for  $\varphi = 51.2^\circ$  N and  $\lambda = 4.4^\circ$  E. The small green circle towards the center is the  $\gamma$ -Draconids radiant.

Pellens L. (2017). Personal communication.

Steyaert C. (2013). “Global radio Draconids 2011”. In Gyssens M. and Roggemans P., editors, *Proceedings of the International Meteor Conference*, La Palma, Canary Islands, Spain, 20–23 September 2012. IMO, pages 88–92.

Steyaert C. (2014a). “The global radio  $\eta$ -Aquariids 2013”. In Gyssens M., Roggemans P., and Źołądek P., editors, *Proceedings of the International Meteor Conference*, Poznań, Poland, 22–25 August 2013. IMO, pages 73–77.

Steyaert C. (2014b) “The global radio Camelopardalids 2014”. In Rault J.-L. and Roggemans P., editors, *Proceedings of the International Meteor Conference*, Giron, France, 18–21 September 2014. IMO, pages 190–193.

Steyaert C. (2015). “The 2015 February 5 event”. In Rault J.-L. and Roggemans P., editors, *Proceedings of the International Meteor Conference*, Mistelbach, Austria, 27–30 August 2015. IMO, pages 73–77.

<sup>3</sup><http://www.rmob.org/articles.php?lng=en&pg=28;>  
<http://rmob.org/visual/2017/>, and other years.

# First observations with the BRAMS radio interferometer

Hervé Lamy<sup>1</sup>, Cédric Tétard<sup>1</sup>, Michel Anciaux<sup>1</sup>, Sylvain Ranvier<sup>1</sup>,  
Antonio Martínez Picar<sup>2</sup>, Stijn Calders<sup>1</sup>, and Cis Verbeeck<sup>2</sup>

<sup>1</sup>Royal Belgian Institute for Space Aeronomy, Avenue Circulaire 3, 1180 Brussels, Belgium  
herve.lamy@aeronomie.be

<sup>2</sup>Royal Observatory of Belgium, Brussels, Belgium

The BRAMS radio interferometer located in Humain is presented. Contrary to the other traditional BRAMS receiving stations, it is able to retrieve the direction of the specular reflection point of meteor echoes. The interferometer is made of 5 antennas placed along 2 axes approximately aligned with the North-South and East-West directions, with a common central antenna. The principle of determining the direction of arrival from phase differences measurements following the method proposed by Jones et al. (1998) is presented and then applied to two examples of meteor echoes observed on December 5, 2016, one with a high signal-to-noise ratio and the other one much fainter. The results are discussed as well as the next steps needed to fully calibrate the radio interferometer.

## 1 Traditional BRAMS receiving station

BRAMS (Belgian RADio Meteor Stations) is a Belgian network of radio receiving stations aiming at detecting and studying meteoroids using forward scatter of radio waves off the meteor ionized trails. It consists of a dedicated transmitter emitting a pure sine wave at a frequency of 49.97 MHz and with a power of 150 W, and about 25 receiving stations covering the Belgian territory. A typical BRAMS receiving station consists of a 3-element Yagi antenna, a commercial ICOM-R75 receiver, a Behringer UCA222 external sound card (acting as the ADC), a BRAMS calibrator, and a GPS clock. The block diagram is shown in Figure 1. A signal coming from the BRAMS calibrator is added to the incoming signal from the antenna to ensure frequency and amplitude calibrations. Then, the receiver shifts the incoming signals received around 49.97 MHz to a frequency around 1 KHz that can be easily sampled by the external sound card at a frequency of 5512 Hz. The sound card also samples a signal coming from a GPS clock to ensure synchronization between all BRAMS receiving stations. Data are then stored on a local computer (see Lamy et al., 2015, for more details). The 3-element Yagi antenna has a very broad radiation pattern in order to cover a large portion of the sky where meteor trails are likely to appear. Therefore, when using data from a single BRAMS receiving station, the direction of the specular reflection point of a meteor echo is not known.

## 2 Radio interferometer in Humain

One station, located in the radio-astronomical site of Humain, in the South-East of Belgium, is a radio interferometer and is able to retrieve the direction of arrival of a meteor echo to an accuracy of the order of 1°. The general idea of an elementary radio interferometer is illustrated in Figure 2.

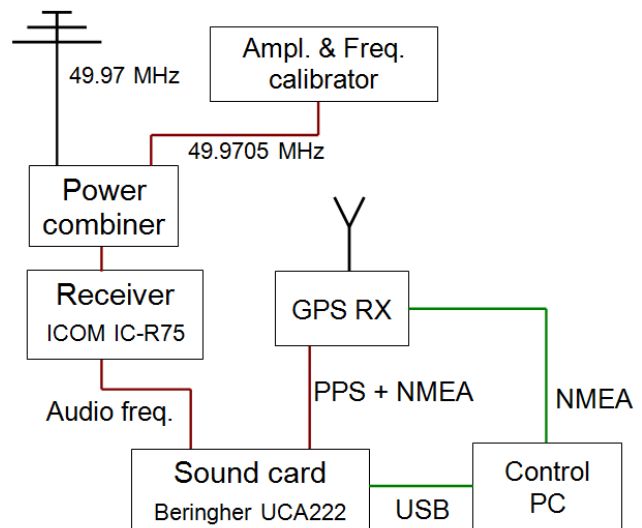


Figure 1 – Block diagram of a classic BRAMS receiving station.

Two antennas (called 0 and 1) are separated by a distance  $D$  (called the interferometer baseline). The radio wave reflected off the meteor trail is assumed to propagate in the plane containing the two antennas with an angle  $\zeta$  (measured from the vertical). Since the source of the (reflected) wave is located at more than 100 km, it is located in the so-called far-field of the antenna and the front wave can be assumed to be plane. The incoming signal reaches antenna 0 slightly earlier than antenna 1. The time delay is  $\tau = (D/c) \sin \zeta$ , where  $c$  is the speed of light. During this time, a phase difference measured between antennas 0 and 1 occurs due to the additional distance the incoming wave has to cover. We have

$$\phi_{10} = -\frac{2\pi}{\lambda} D \sin \zeta, \quad (1)$$

where  $\lambda$  is the wavelength in air of the incoming signal (approximately 6 meters for BRAMS).

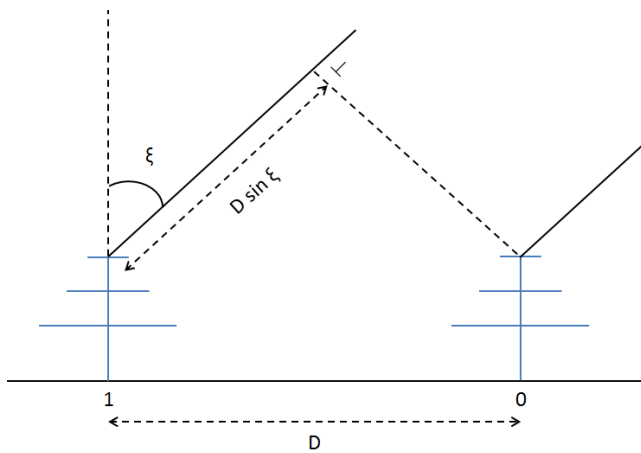


Figure 2 – Geometry of an elementary radio interferometer, where  $D$  is the interferometer baseline, and  $\zeta$  the angle of arrival of the incoming signal measured from the vertical.

In principle, the (planar) angle-of-arrival  $\zeta$  could then be measured using only two antennas. However, since  $\phi_{10}$  is measured within  $\pm\pi$ , Equation (1) admits one solution for  $\zeta$  in  $[-\pi/2, \pi/2]$  only if  $D \leq \lambda/2$ . Otherwise, there is an ambiguity due to the multiple solutions of the equation (their number being equal to the number of  $\lambda/2$ 's in  $D$ ). Unfortunately, if the two antennas are too close ( $D < \lambda/2$ ), they start to influence each other via mutual impedance effects and the phase measurements are not reliable anymore.

There are a number of ways to overcome this problem. Jones et al. (1998) proposed to use three co-aligned antennas instead of two (see Figure 3), and to measure phase differences with the central antenna acting as the phase reference. The trick is to use distances  $d_1$  and  $d_2$  between antennas at the extremities (1 and 2) and the central one (0) which differ by  $\lambda/2$ , e.g.,  $d_1 = 2.5\lambda$  and  $d_2 = 2\lambda$ .

Equation (1) can then be used for each pair of antennas:

$$\phi_{10} = -\frac{2\pi}{\lambda} d_1 \sin \zeta; \quad (2)$$

$$\phi_{20} = +\frac{2\pi}{\lambda} d_2 \sin \zeta. \quad (3)$$

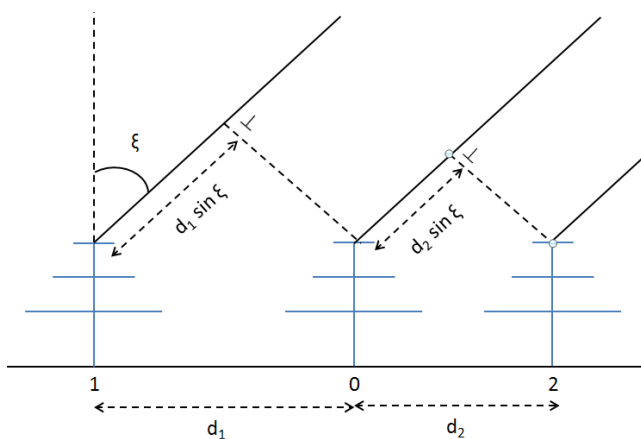


Figure 3 – A linear array of 3 antennas with the central antenna 0 being the phase reference.

Individually, both equations admit several possible solutions (respectively 5 and 4) but they can be either summed or subtracted to provide two estimates of  $\sin \zeta$ :

$$\sin \zeta = -\frac{\lambda}{2\pi} \frac{\phi_{10} - \phi_{20}}{d_1 + d_2} = -\frac{\phi_{10} - \phi_{20}}{9\pi}; \quad (4)$$

$$\sin \zeta = -\frac{\lambda}{2\pi} \frac{\phi_{10} + \phi_{20}}{d_1 - d_2} = -\frac{\phi_{10} + \phi_{20}}{\pi}. \quad (5)$$

Equation (4) admits 9 possible solutions while Equation (5) admits only one, as can be seen from Figure 4. Since the slope of the single branch of the bottom graph is not very steep, the solution is unique but inaccurate. On the other hand the slope of the nine branches of the top graph are very steep and, therefore, provide a very accurate estimate of the angle of arrival. For example, in Figure 1, it was assumed that the following values were measured:  $\phi_{10} = 100^\circ$  and  $\phi_{20} = -40^\circ$ . This gives respectively  $\phi_{10} + \phi_{20} = 60^\circ$  and  $\phi_{10} - \phi_{20} = 140^\circ$ . If we assume a phase uncertainty of  $\pm 10^\circ$ , we obtain the horizontal gray shaded areas. Using Equation (5) gives a value of  $\zeta$  between approximately  $-16^\circ 1$  and  $-22^\circ 9$ , and is therefore rather inaccurate. However, it allows to select the correct branch in the top graph, which provides a much more accurate solution for  $\zeta$  between approximately  $-17^\circ 6$  and  $-18^\circ 4$ . Therefore, by combining solutions from Equations (4) and (5), the angle of arrival can be estimated with an accuracy of less than  $1^\circ$ .

This provides the angle of arrival as if the meteor was in the plane of the three co-aligned antennas. In order to determine the zenith and azimuth angles of a meteor echo in the more general case, two linear and perpendicular axes of three antennas are used with the central antenna (used for phase reference) common to the two axes. The two axes are oriented along North-South (N-S) and East-West (E-W) directions. The method above then provides two angles  $\zeta_1$  (along N-S direction) and  $\zeta_2$  (along E-W direction) which are combined to compute the elevation angle  $\alpha$  (measured from N to E) and the azimuth angle  $\beta$  (measured from the ground up) of the meteor echo using the following formulas (see, e.g., Valentic et al., 1997; or Madkour et al., 2016):

$$\alpha = \arccos\left(\frac{\cos \zeta_2}{\cos \beta}\right) = \arccos\left(\frac{\cos \zeta_1}{\cos \beta}\right); \quad (6)$$

$$\beta = \arctan\left(\frac{\cos \zeta_2}{\cos \zeta_1}\right). \quad (7)$$

The BRAMS interferometer in Humain has been designed accordingly. The block diagram is shown in Figure 5. Six antennas are used since the central antenna is a crossed-Yagi antenna which will be useful for future radio polarisation measurements and study of meteor power profiles. In the following, the central antenna called “low” (L) will be used as reference for all phase measurements. The receivers are AR5001D, which allow the use of a 10 MHz reference provided by a GPS clock as a reference for the phase measurements. The ADC is the NI 9215 from National Instruments which samples simultaneously the signals coming from the six

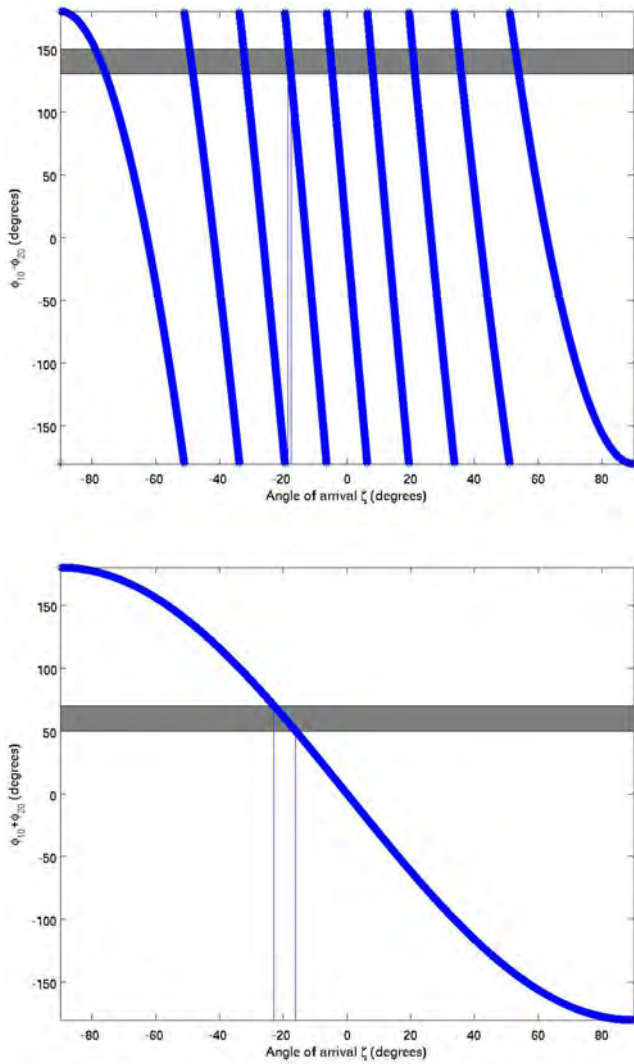


Figure 4 – Relationship between the sum and the difference of the phase differences,  $\phi_{10} + \phi_{20}$  and  $\phi_{10} - \phi_{20}$ , as a function of the angle of arrival  $\zeta$ . The gray shaded bands illustrate an uncertainty of  $\pm 10^\circ$ .

receivers and the PPS signal coming from another GPS clock. More technical details about the interferometer will be published elsewhere.

### 3 Determining radio meteor echo direction

In this section, we present a few examples where the techniques described in Section 2 are applied to radio meteor echoes observed with the BRAMS interferometer on December 5, 2016. Data are presented as spectrograms obtained using 16 384 samples of the raw time series and an overlap of 90% to compute the FFT. This provides a time resolution of the order of 0.3 s and a frequency resolution in the order of 0.33 Hz. These spectrograms were analyzed by users of the citizen science platform, the Radio Meteor Zoo (Calders et al., 2016; 2017) to manually detect meteor echoes and estimate the background to be subtracted from the activity curve observed during the Geminids (Verbeeck et al., 2018). The results of the aggregated inputs of the

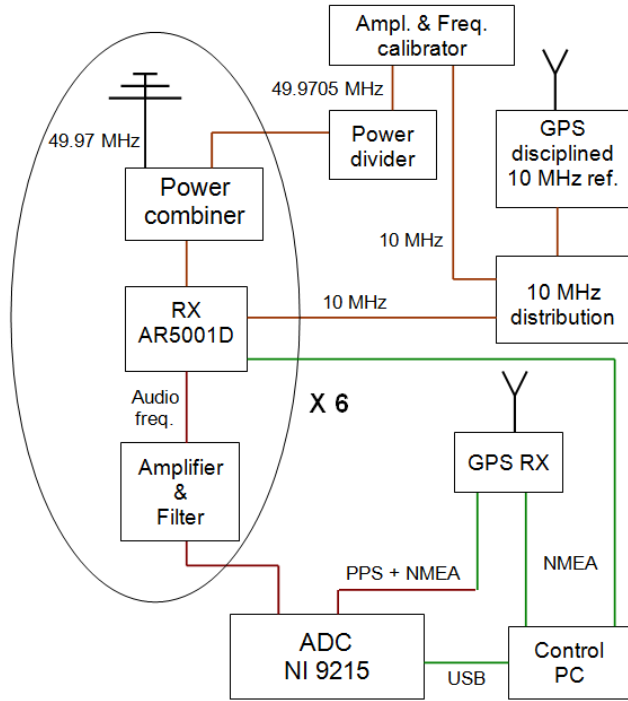


Figure 5 – Block diagram of the radio interferometer in Humain.

users are shown on the spectrograms as white rectangles. Figure 6 is the spectrogram obtained at 0<sup>h</sup>35<sup>m</sup> UT with seven detections (rectangles) from the RMZ users. Spectrograms are used here in order to determine the best frequency to use to calculate the phase. Since the phase of the meteor echo should not depend on frequency, the best procedure would consist in selecting the frequency bin in which the signal-to-noise (S/N) ratio is the highest.

First, let us consider the second rectangle from the left. A zoom on this region of the spectrogram is shown in Figure 7. It corresponds to a bright meteor echo that does not overlap in frequency with any other signal such as a reflection on an airplane or the direct signal coming from the transmitter.

To illustrate the method described in Section 2, 10 adjacent frequency bins centered on the upper bright “spot” of the meteor echo in Figure 7 are selected. The re-

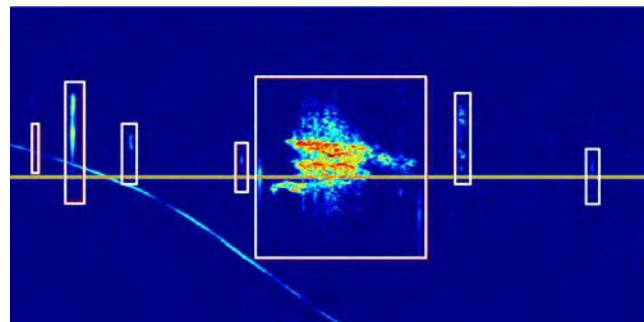


Figure 6 – Spectrogram obtained at Humain on December 5, 2016, 0<sup>h</sup>35<sup>m</sup> UT. Horizontal axis is time (5 minutes duration) and vertical axis is frequency (200 Hz centered on the direct signal from the beacon). Rectangles are aggregated results from individual contributions from RMZ users.

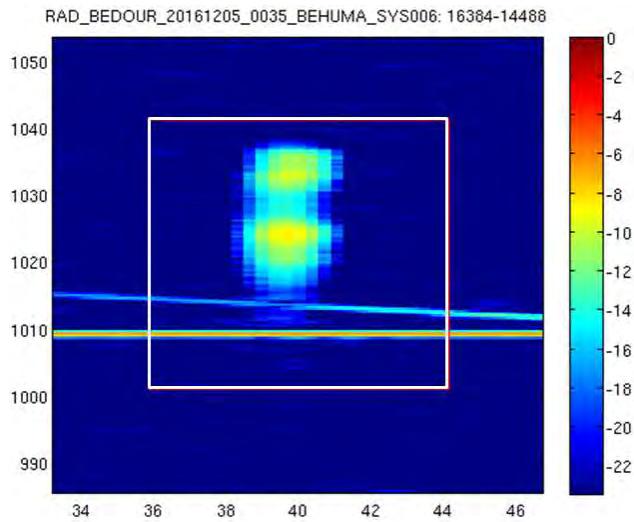


Figure 7 – Zoom around the second white rectangle of Figure 6.

sults for the phase differences between antenna pairs are shown in Figure 8. The phase differences are computed between the lower central antenna (called “L”) and any of the two other antennas along the North-South and East-West axes (respectively called “N” and “S”, and “E” and “W”). For example, phase N-L and phase S-L in Figure 8 correspond to  $\phi_{10}$  and  $\phi_{20}$  in Equations (4) and (5). For the selected frequencies, just before and after the meteor echo, only noise is recorded and, therefore, the phase differences vary completely randomly as expected. During the meteor echo, however, the phase differences become strongly coherent. As expected, the results do not depend on the frequency, the small variations observed being due to slightly different S/N ratios in the various frequency bins.

Figure 9 shows sum  $\phi_{10} + \phi_{20}$  and difference  $\phi_{10} - \phi_{20}$  of the phase differences along the two orthogonal axes.

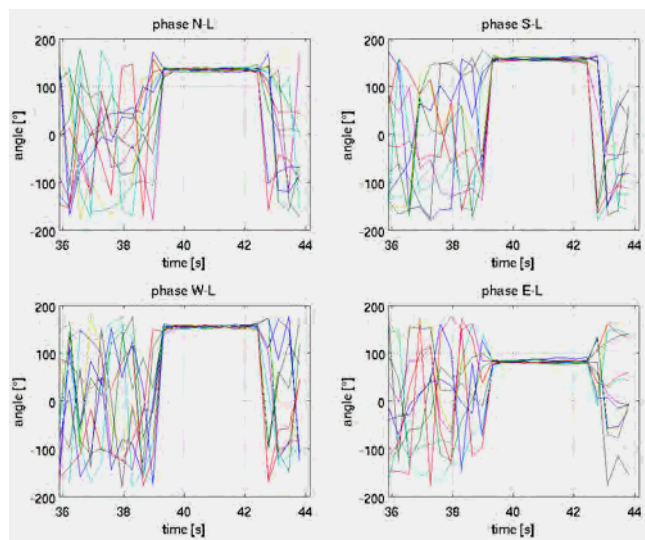


Figure 8 – Phase differences between the central antenna L and (top left) the North (N) antenna; (top right) the South (S) antenna; (bottom left) the East antenna; and (bottom right) the West antenna, for data from Figure 7. The 10 different curves correspond to adjacent frequency bins centered on the upper bright spot of the meteor echo shown in Figure 7.

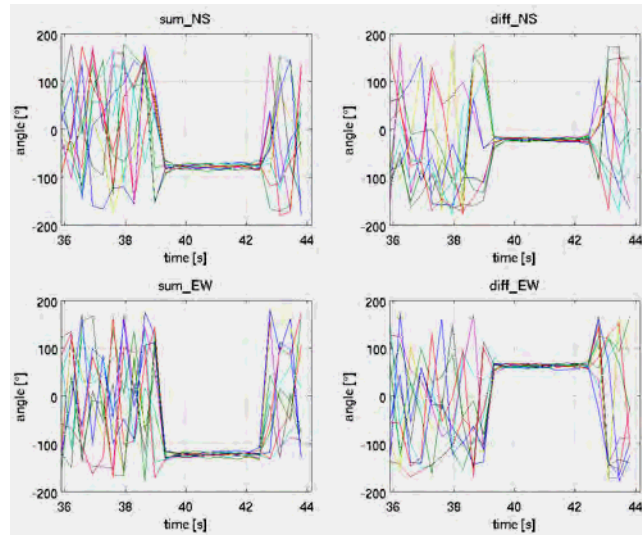


Figure 9 – Sum (left) and difference (right) of phase differences from Figure 8 for N-S axis (top) and E-W axis (bottom).

The Jones method is applied to these results to obtain the two angles of arrival  $\zeta_{N-S}$  and  $\zeta_{E-W}$  which are then combined to provide the elevation angle  $\alpha$  and the azimuth angle  $\beta$  of the meteor echo using Equations (6) and (7). (See Figure 10.) This procedure can be done for each selected frequency bin above. For clarity, only the results corresponding to the frequency bin with the highest S/N ratio (called “freqOfi”) are shown in Figure 10. The results at other adjacent frequencies are very similar. Again, the results are very stable during the meteor echo which gives confidence in the method. It has been checked that the same results are obtained when using frequencies corresponding to the lower bright “spot” of the meteor echo in Figure 7.

Let us now consider in Figure 11 a zoom on the sixth rectangle from Figure 6. It contains a much fainter meteor echo for which the S/N ratio varies strongly with frequency with values as low as 1 at some frequencies.

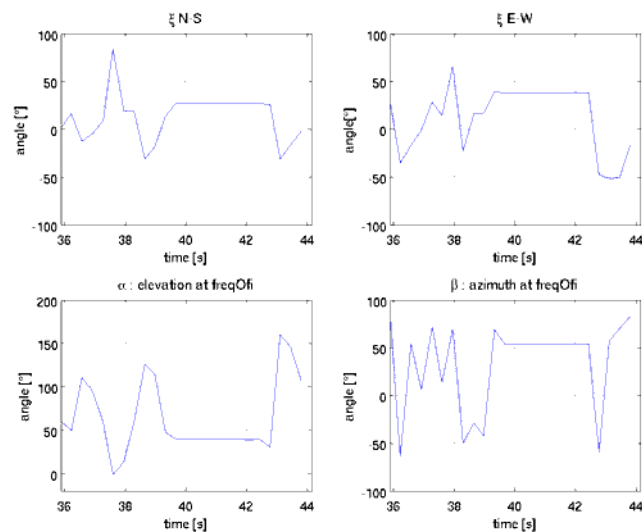


Figure 10 – Top: Angles of arrival,  $\zeta_{N-S}$  and  $\zeta_{E-W}$ , as a function of time for data from Figure 7. (Bottom: Corresponding elevation ( $\alpha$ ) and azimuth ( $\beta$ ) angles.

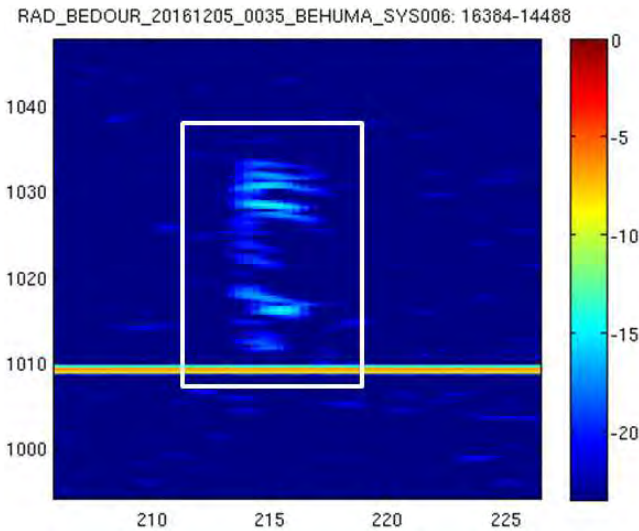


Figure 11 – Zoom around the sixth rectangle of Figure 6.

The meteor echo does not overlap with another signal either. We carry out the same procedure selecting 10 adjacent frequency bins centered on the one with the highest S/N ratio (at approximately 1027 Hz).

The phase differences between the central antenna and all of the four other antennas are shown in Figure 12. As expected, due to the lower S/N ratios, the results are much more scattered. However, the contrast between the coherency of the phase differences during the meteor echo and the randomness of the phase differences before and after the meteor echo remains very clear.

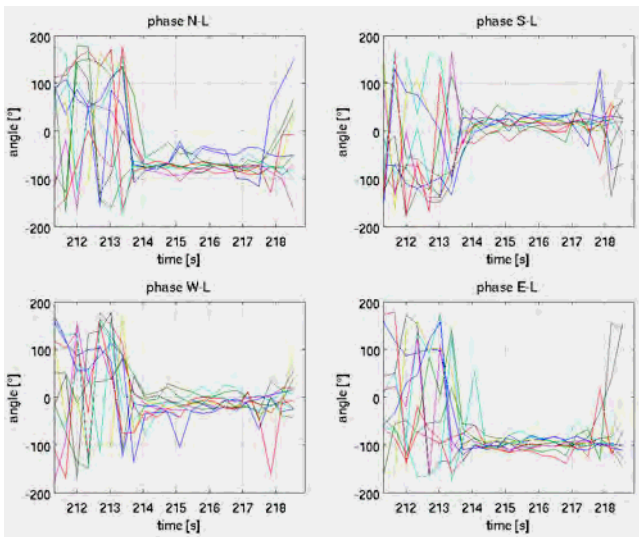


Figure 12 – Phase differences between the central antenna L and (top left) the North (N) antenna; (top right) the South (S) antenna; (bottom left) the East antenna; and (bottom right) the West antenna, for data from Figure 11. The 10 different curves correspond to adjacent frequency bins around 1027 Hz.

The directions of arrival in the N-S and E-W planes, and the azimuth and elevation angles for that particular meteor echo, are given in Figure 13. Again, only results for the frequency bin with the highest S/N ratio are shown. The results are still very stable over time during the meteor echo, emphasizing that the frequency bin with the highest S/N ratio should always be selected.

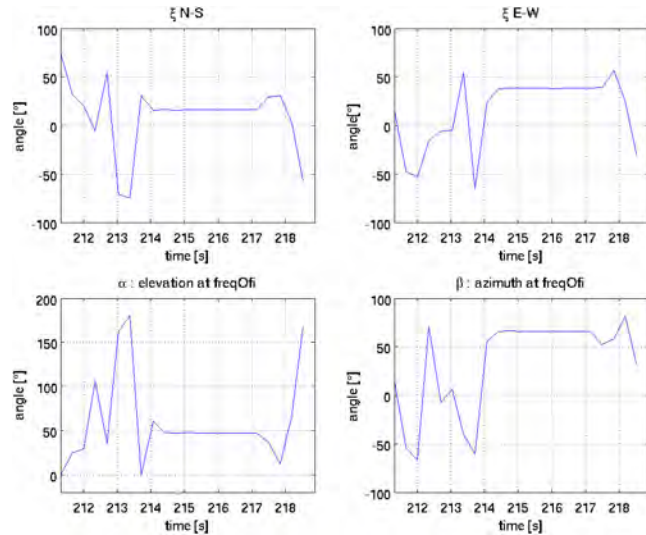


Figure 13 – Top: Angles of arrival,  $\zeta_{N-S}$  and  $\zeta_{E-W}$ , as a function of time for data from Figure 11. (Bottom: Corresponding elevation ( $\alpha$ ) and azimuth ( $\beta$ ) angles.

## 4 Discussion and conclusions

In Section 3, the method of Jones et al. (1998) was successfully applied to some data obtained with the interferometer in Humain on December 5, 2016. The phases were determined using the complex Fourier transform. The phase differences become coherent as soon as a meteor echo occurs and do not depend on the frequency, as expected. For bright meteor echoes, it was shown that using the frequency bin with the highest S/N ratio is more than enough to provide an accurate direction of arrival. However, for fainter meteor echoes, it might be needed to sum up the contributions of individual frequency bins present in the meteor echo to increase the S/N ratio. This should be done by adding the components of the Fourier transform in the complex plane before calculating the phases. Also, the examples presented in this study consist of “isolated” meteor echoes which do not overlap with any other spurious signal. In practice, an overlap occurs quite often. For these meteor echoes, an automated procedure should be developed in order to select a frequency bin that belongs to the meteor echo.

So far, the directions of arrival computed for the meteor echoes are not calibrated. There are a number of systematic errors that need to be taken into account and corrected for. This includes a possible difference in length between the cables going from antennas to receivers. A difference of 20 cm between two cables would produce a phase difference of  $18^\circ$  assuming a wavelength around 4 m in the cable (corresponding to a propagation speed around  $0.67c$ , provided by the seller). Also, the exact relative positions of the antennas must be measured. In the calculations above, it was assumed that  $d_1 = 15$  m and  $d_2 = 12$  m, and that antennas were perfectly aligned along the N-S and E-W directions. In practice, this is not the case. A precise determination of these systematic errors was carried out at the end of 2017, but were not yet implemented in the results presented in this study.

Once these systematic errors are taken onboard, the calibration itself can be performed with one of the following methods: (1) using the BRAMS calibrator (Lamy et al., 2015) as a transmitter and a calibrated antenna both attached to a drone flying in the far-field of the interferometer; (2) using the signal reflected from a plane whose position can be accurately determined (e.g., using websites such as Flight Tracker); or (3) using data from optical cameras located next to the interferometer. The first two methods are currently under investigation. The third one was used, e.g., by Madkour et al. (2016). The installation of a CAMS (e.g., Roggemans et al., 2016) camera in Humain is planned in early 2018 to test this method as well.

The results from the radio interferometer in Humain will be extremely important for the BRAMS network, in particular for the retrieval of individual meteoroid trajectories as only data from 3 additional traditional BRAMS receiving stations are then needed (see, e.g., Wislez, 2006).

## Acknowledgements

The BRAMS network is a project of the Royal Belgian Institute for Space Aeronomy (BISA) and funded by the Solar-Terrestrial Center of Excellence (STCE).

C. Tétard is funded by the Belgian Science Policy via the Brain-Be project BR/143/A2/METRO. The authors would also like to thank Ms. Margaux Stocq, student from the University of Brussels, who helped developing the MATLAB codes during her internship at BISA during the summer of 2017.

## References

- Calders S., Verbeeck C., Lamy H., and Martínez Picar A. (2016). “The Radio Meteor Zoo: A citizen science project”. In Roggemans A. and Roggemans P., editors, *Proceedings of the International Meteor Conference*, Egmond, the Netherlands, 2–5 June 2016. IMO, pages 46–49.
- Calders S., Lamy H., Martínez Picar A., Tétard C., Verbeeck C., and Gamby E. (2018). “The Radio Meteor Zoo: Involving citizen scientists in radio meteor research”. In Gyssens M. and Rault J.-L., editors, *Proceedings of the International Meteor Conference*, Petnica, Serbia, 21–24 September 2017. IMO, pages 13–15.
- Jones J., Webster A. R., and Hocking W. K. (1998). “An improved interferometer design for use with meteor radars”. *Radio Science*, **33**, 55–65.
- Lamy H., Anciaux M., Ranvier S., Calders S., Gamby E., Martínez Picar A., and Verbeeck C. (2015). “Recent advances in the BRAMS network”. In Rault J.-L. and Roggemans P., editors, *Proceedings of the International Meteor Conference*, Mistelbach, 27–30 August 2015. IMO, pages 171–175.
- Madkour W., Yamamoto M., Kakinami Y., and Mizumoto S. (2016). “A low cost meteor observation system using radio forward scattering and the interferometry technique”. *Experimental Astronomy*, **41**, 243–257.
- Roggemans P., Johannink C., and Breukers M. (2016). “Status of the CAMS-BeNeLux network”. In Roggemans A. and Roggemans P., editors, *Proceedings of the International Meteor Conference*, Egmond, the Netherlands, 2–5 June 2016. IMO, pages 254–260.
- Valentic T. A., Avery J. P., Avery S. K., and Livingston R. C. (1997). “Self-survey calibration of meteor radar antenna arrays”. *IEEE Transactions on Geoscience and Remote Sensing*, **35**, 524–531.
- Verbeeck C., Lamy H., Calders S., Tétard C., and Martínez Picar A. “Overview of major shower observations 2016–2017 by the BRAMS network”. In Gyssens M. and Rault J.-L., editors, *Proceedings of the International Meteor Conference*, Petnica, Serbia, 21–24 September 2017. IMO, pages 138–144.
- Wislez J.-M. (2006). “Meteor astronomy using a forward scatter set-up”. In Verbeeck C. and Wislez J.-M., editors, *Proceedings of the Radio Meteor School*, Oostmalle, 10–14 September 2005. IMO, pages 84–106.

# Overview of major shower observations 2016–2017 by the BRAMS network

Cis Verbeeck<sup>1</sup>, Hervé Lamy<sup>2</sup>, Stijn Calders<sup>2</sup>, Cédric Tétard<sup>2</sup>, and  
Antonio Martínez Picar<sup>1</sup>

<sup>1</sup>Royal Observatory of Belgium, Ringlaan 3, 1180 Brussels, Belgium  
cis.verbeeck@oma.be and antonio.martinez@oma.be

<sup>2</sup>Royal Belgian Institute of Space Aeronomy, Ringlaan 3, 1180 Brussels, Belgium  
herve.lamy@aeronomie.be, stijn.calders@aeronomie.be, and cedric.tetard@aeronomie.be

For the first time, meteor shower activity curves from BRAMS forward scatter observations are published here. The BRAMS team developed a technique to separate observations into the sporadic background and a shower component. This method is applied to the Perseids 2016 and 2017, the Geminids 2016, and the Quadrantids 2017.

## 1 Introduction

BRAMS (Belgian RAdio Meteor Stations) is a radio network located in Belgium using forward scatter measurements to detect and characterize meteoroids. It consists of one dedicated transmitter located in Dourbes in the south of Belgium and approximately 25 receiving stations spread all over the Belgian territory. The transmitter emits a circularly polarized continuous wave (CW) at a frequency of 49.97 MHz and with a power of 150 W. All receiving stations use the same material (including a 3 elements Yagi antenna) and are synchronized using GPS clocks. More details can be found in, e.g., Lamy et al. (2015).

Each BRAMS receiving station is recording continuously, producing each day 288 WAV files and detecting about 1500–2000 meteors. Though significant advances in automatic detection of meteor reflections in the BRAMS spectrograms have been made, the best detector stays the human eye. In August 2016, the Radio Meteor Zoo<sup>1</sup> was launched. This citizen science project, hosted on the Zooniverse platform (Lintott, 2008), exploits the (trained) human eye of many volunteers for classifying meteor reflections during certain observing campaigns. This enabled the BRAMS team to publish shower activity results for the first time here. More information about the Radio Meteor Zoo can be found in Calders et al. (2016; 2017).

In the current paper, we present meteor shower activity profiles from BRAMS observations. Section 2 describes the process of extracting the sporadic background during a meteor shower. Perseid near-maximum activity curves for 2016 and 2017 from BRAMS observations are presented in Sections 3 and 4, respectively, while Sections 5 and 6 provide the results for the Geminids 2016 and the Quadrantids 2017, respectively.

Finally, conclusions and future plans are outlined in Section 7.

<sup>1</sup><http://www.radiometeorzoo.org>.

## 2 Estimating the sporadic background

Since the current BRAMS observations were performed by basic forward scatter stations (i.e., without interferometer<sup>2</sup>), it is not possible to tell which individual meteor reflections are shower meteors. Hence, the only way to estimate shower activity is to estimate the sporadic background and subtract it from the total activity. We illustrate this process here in detail on the Perseids 2016 observations. The same method is applied in the activity analysis of any meteor shower.

Figure 1 shows an estimation of the sporadic background during the Perseids 2016 observations by the BRAMS receiving station Humain. The top left plot shows the hourly number of meteor reflections observed for each UT hour of the day, on individual days some time away from the Perseid maximum (August 17 in blue; August 19 in green; their average with standard deviations as error bars in black). It is assumed that there is no significant shower activity on those days, so the observations represent the sporadic background at that time. The sporadic background during the Perseid maximum is assumed to be the same.

The bottom left plot shows the average hourly number of meteor reflections for every UT hour of the day (average over August 17 and 19), with the standard deviations as error bars (in black). Since a sinusoidal diurnal variation is expected (Powell, 2017), a sine curve was fitted to these averages (both a weighted and unweighted fit). Figure 1 shows clearly that both fits are good approximations of the average hourly number of meteor reflections. The sporadic background during the Perseid observations will be modeled as the weighted sine fit.

The plots on the right in Figure 1 apply the same ideas, but on the hourly total duration (in seconds) of meteor reflections. Meteor shower maxima typically feature a

<sup>2</sup>Though there is an interferometer in the Humain receiving station, single-antenna data from Humain are employed in the present analysis. Shower analysis of interferometric data from Humain are foreseen in the near future.

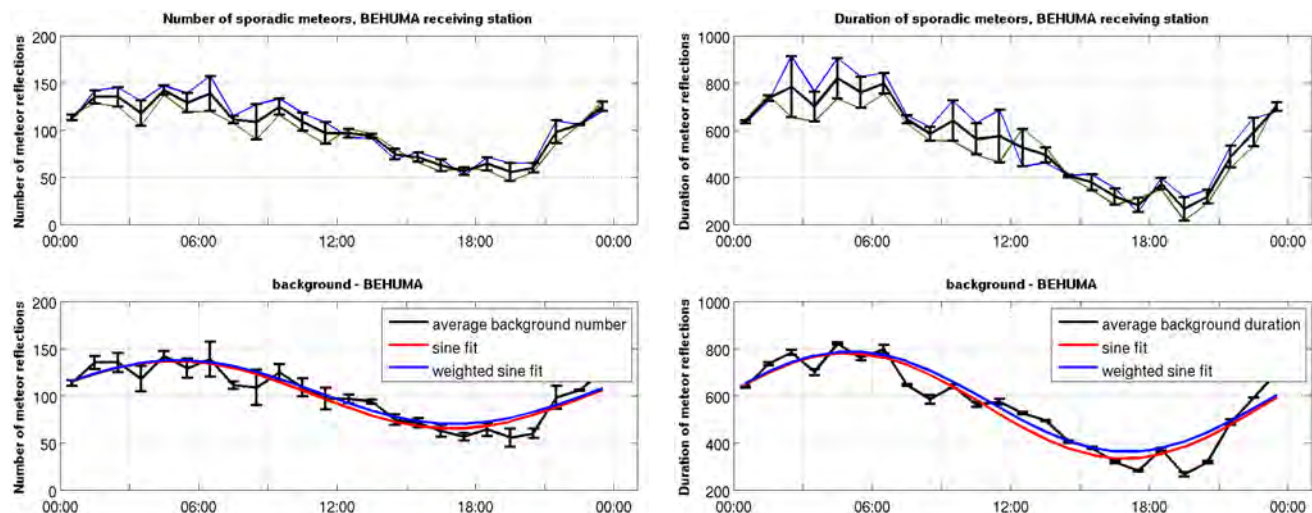


Figure 1 – Estimation of the diurnal variation of the sporadic background during the BRAMS Perseids 2016 campaign (receiving station: Humain). *Top left:* Hourly number of meteor reflections observed on individual days, some time away from the Perseid maximum (August 17 in blue; August 19 in green; average in black). *Bottom left:* Average and sine fits of the hourly number of meteor reflections. *Top right:* Hourly total duration (s) of meteor reflections observed on August 17 and 19, and their average. *Bottom right:* Average and sine fits of the hourly total duration of meteor reflections. Times are in UT.

lot of long-duration (overdense) reflections, which often overlap with shorter (underdense) reflections. As a result, counting the number of reflections can be a rather inaccurate measure of meteor activity. The hourly total duration of meteor reflections provides a more robust measure of meteor activity. The fitted sine curves shown in the bottom right plot of Figure 1 are a good representation of the average hourly total duration of meteor reflections. Hence, the hourly total duration of sporadic meteor reflections during the Perseid observations will be modeled as the weighted sine fit.

Similar results are obtained for other datasets.

### 3 Shower activity: Perseids 2016

The BRAMS station in Humain observed the 2016 Perseids from August 10, 0<sup>h</sup> UT until August 14, 0<sup>h</sup> UT. Figure 2 shows an estimation of the Perseids 2016 activity as observed from Humain during this period.

The hourly total number of meteor reflections is shown in the top left plot (red curve). As a proxy for the diurnal variation of the sporadic background, the average hourly number of meteors observed away from the shower maximum is plotted (black circles for the average and black sine curve for its weighted sine fit), as explained in Section 2. An estimate of the number of Perseid reflections per hour (blue curve) is obtained by subtracting the modeled sporadic background (the black weighted sine fit) from the hourly total number of reflections. The Perseid radiant elevation is featured in the bottom left plot. The plots on the right in Figure 2 show the same curves, but for the total duration rather than the number of meteor reflections.

It is clear that the number of Perseid reflections is much smaller than the large number of underdense sporadic

reflections (faint sporadic meteors) observed by Humain (top left plot in Figure 2). Hence, the scatter in the true sporadic rates (the difference between the real and modeled sporadic rates) hides the salient features in the Perseid rates. Since the proportion of Perseids to sporadics is a lot higher in the top right plot in Figure 2 (total duration of meteor reflections), the Perseid maximum on August 12 stands out better in that plot.

This is even more the case in Figure 3, which shows the same plots as Figure 2, but only taking into account the larger particles (meteor reflections lasting at least 10 seconds). Both in the number of reflections and the total duration of reflections, the Perseids clearly dominate the reflections lasting at least 10 seconds, and the Perseid maximum on August 12 stands out clearly.

A word of caution is in order. The shower meteor numbers in the present paper have not yet been corrected for the relative sensitivity of the forward scatter setup, which shows a large daily variation as the radiant crosses the sky. This daily variation is clearly seen in the plots (with a minimum near 18<sup>h</sup> UT for the Perseids), meaning it is pointless at this stage to determine at which exact time the shower maximum occurred. Using an analogy with visual data, the forward scatter data presented here are similar to raw visual rates rather than ZHRs. The relative sensitivity of the forward scatter setup is called the Observability Function and was modeled by Verbeeck (1997). The authors will incorporate the Observability Function into the analysis of the present data in a future paper.

### 4 Shower activity: Perseids 2017

The top left plot in Figure 4 shows the hourly number of meteor reflections (total observed, estimated sporadic, and estimated Perseids) for the Perseid observations by

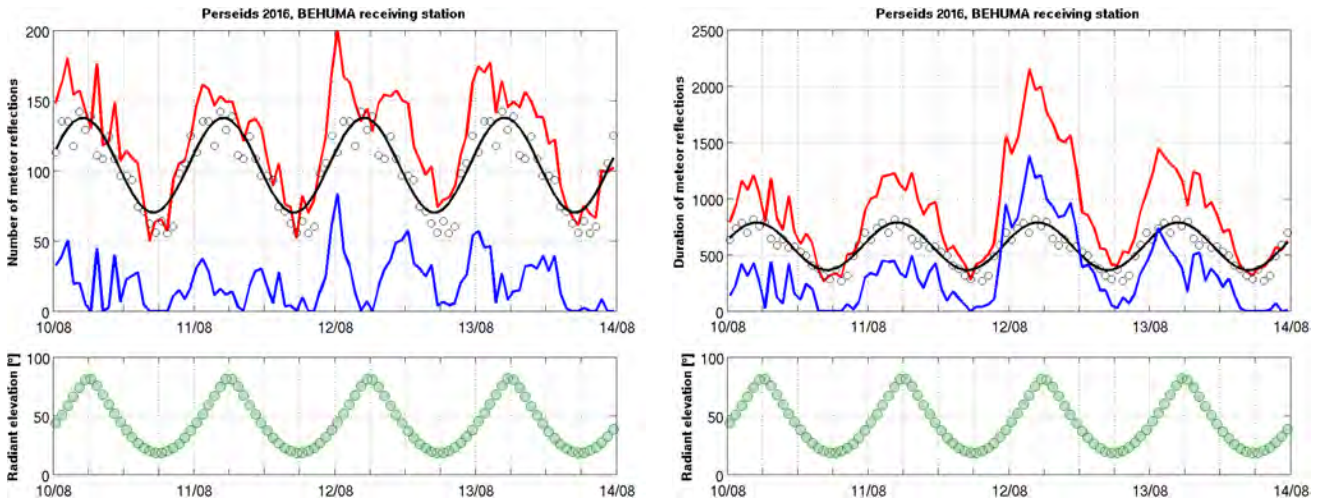


Figure 2 – Estimation of Perseids 2016 activity (BRAMS receiving station: Humain). *Top left*: Hourly number of meteor reflections (upper red curve: total observed; black circles and curve: estimation of diurnal variation of sporadic background and its weighted sine fit; lower blue curve: estimated hourly number of Perseid reflections). *Bottom left*: Radiant elevation. *Top right*: Hourly total duration (s) of meteor reflections (upper red curve: total observed; black circles and curve: estimation of diurnal variation of sporadic background and its weighted sine fit; lower blue curve: estimated hourly total duration of Perseid reflections). *Bottom right*: Radiant elevation. Times are in UT.

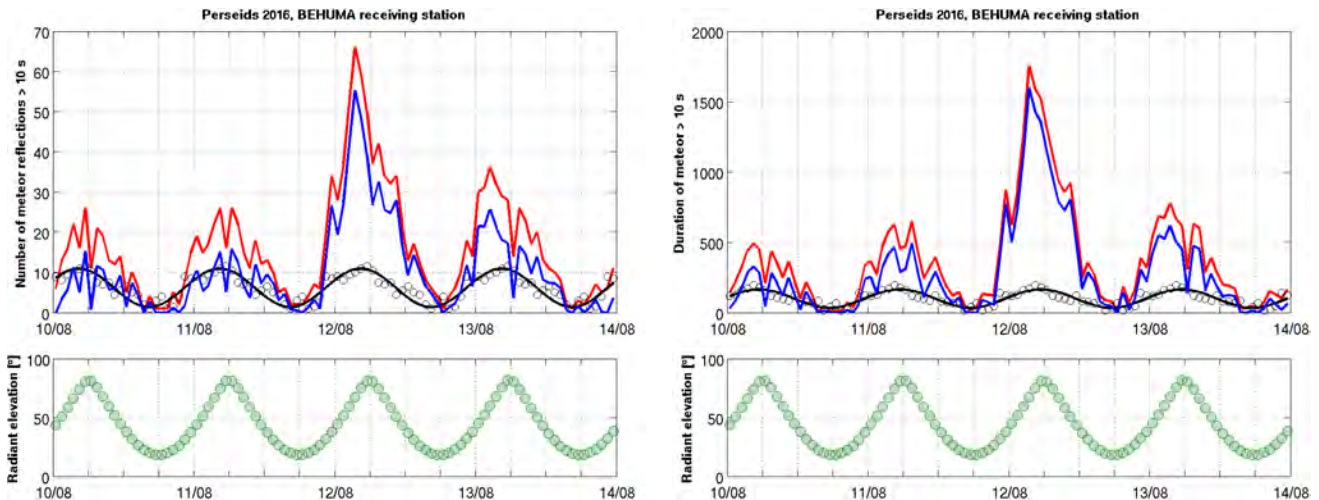


Figure 3 – Estimation of Perseids 2016 activity (BRAMS receiving station: Humain). *Top left*: Hourly number of meteor reflections lasting at least 10 seconds (upper red curve: total observed; black circles and curve: estimation of diurnal variation of sporadic background and its weighted sine fit; lower blue curve: estimated hourly number of Perseid reflections). *Bottom left*: Radiant elevation. *Top right*: Hourly total duration (s) of meteor reflections lasting at least 10 seconds (upper red curve: total observed; black circles and curve: estimation of diurnal variation of sporadic background and its weighted sine fit; lower blue curve: estimated hourly total duration of Perseid reflections). *Bottom right*: Radiant elevation. Times are in UT.

the BRAMS receiving station at Humain, from August 11, 0<sup>h</sup> UT until August 14, 0<sup>h</sup> UT.

The same features are observed as for the Perseids 2016, with comparable values for the sporadic background. The Perseids 2016 (Figures 2 and 3) show a distinctly higher activity on August 12 as compared to the neighboring days, while the Perseids 2017 (Figures 4 and 5) show a more even activity profile. All values for the Perseids observed on August 12, 2016, are a lot higher than all Perseid values observed in 2017. This is consistent with the increased Perseid activity in the late UT hours of August 11 and the early UT hours of August 12, 2016, as was observed by video (see Molau et al., 2017a), visual and radio techniques (see Rendtel et al., 2017).

The visual peak of the Perseids 2017 was observed in the late UT hours of August 12, when the radiant was very low in the sky. The relative sensitivity of the BRAMS system for Perseids at that time was too low to allow clear detection of the maximum.

## 5 Shower activity: Geminids 2016

The top left plot in Figure 6 shows the hourly number of meteor reflections (total observed, estimated sporadic, and estimated Geminids) for the Geminid observations by the BRAMS receiving station at Neufchâteau, from December 13, 0<sup>h</sup> UT until December 15, 0<sup>h</sup> UT, while the top right plot in Figure 6 gives similar information about the hourly total duration of meteor reflections.

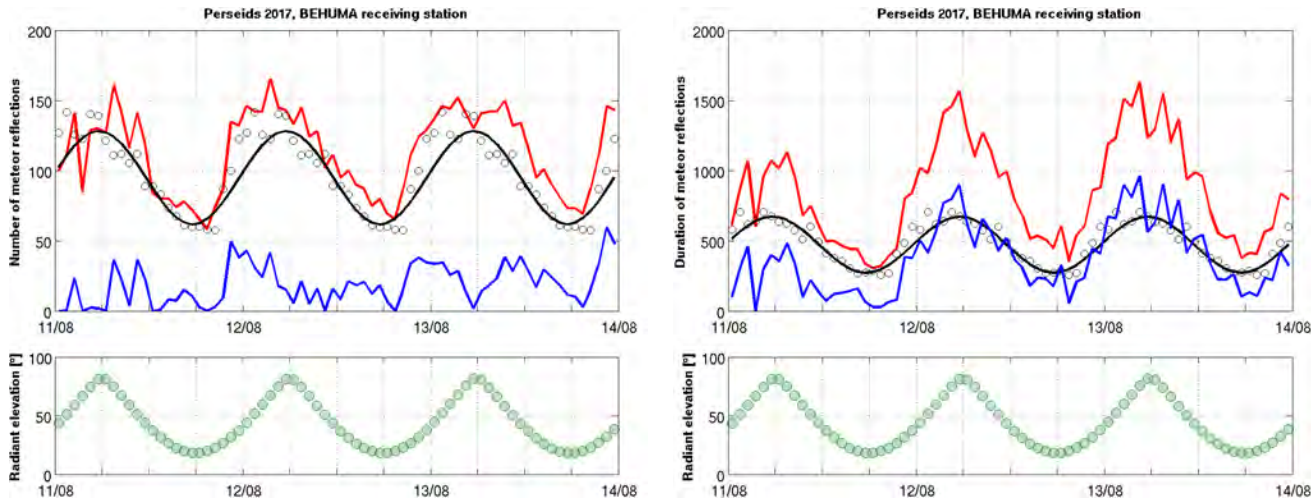


Figure 4 – Estimation of Perseids 2017 activity (BRAMS receiving station: Humain). *Top left*: Hourly number of meteor reflections (upper red curve: total observed; black circles and curve: estimation of diurnal variation of sporadic background and its weighted sine fit; lower blue curve: estimated hourly number of Perseid reflections). *Bottom left*: Radiant elevation. *Top right*: Hourly total duration (s) of meteor reflections (upper red curve: total observed; black circles and curve: estimation of diurnal variation of sporadic background and its weighted sine fit; lower blue curve: estimated hourly total duration of Perseid reflections). *Bottom right*: Radiant elevation. Times are in UT.

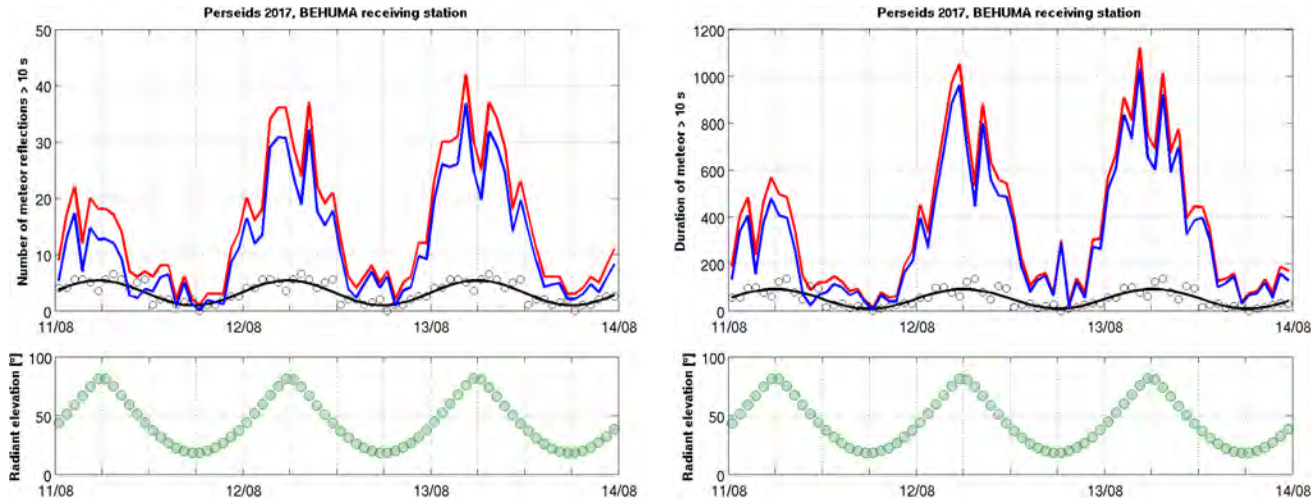


Figure 5 – Estimation of Perseids 2017 activity (BRAMS receiving station: Humain). *Top left*: Hourly number of meteor reflections lasting at least 10 seconds (upper red curve: total observed; black circles and curve: estimation of diurnal variation of sporadic background and its weighted sine fit; lower blue curve: estimated hourly number of Perseid reflections). *Bottom left*: Radiant elevation. *Top right*: Hourly total duration (s) of meteor reflections lasting at least 10 seconds (upper red curve: total observed; black circles and curve: estimation of diurnal variation of sporadic background and its weighted sine fit; lower blue curve: estimated hourly total duration of Perseid reflections). *Bottom right*: Radiant elevation. Times are in UT.

While the short observing interval of 48 hours does not allow to clearly identify the shower maximum from these plots, the corresponding plots in Figure 7 (only taking into account reflections lasting at least 10 seconds), clearly show an increased activity in the late UT hours of December 13 and the early UT hours of December 14, in line with the video observations reported by Molau et al. (2017b). Another peak is visible in the top right plot of Figure 7 around 15<sup>h</sup> UT on December 13, which is not seen in (Molau et al., 2017b), to be investigated further after correction by the Observability Function.

It should be pointed out that the sine fits for the sporadic background of reflections lasting at least 10 seconds (both for number of reflections and total dura-

tion) in Figure 7 is rather poor, with a maximum close to local midnight. However, due to the small amplitude of this sporadic background with respect to the shower component of reflections lasting at least 10 seconds, this does not affect the shower activity interpretations above.

## 6 Shower activity: Quadrantids 2017

The top left plot in Figure 8 shows the hourly number of meteor reflections (total observed, estimated sporadic, and estimated Quadrantids) for the Quadrantid observations by the BRAMS receiving station at Kampenhout, from January 2, 0<sup>h</sup> UT until January 5, 0<sup>h</sup> UT, while the top right plot in Figure 8 provides similar

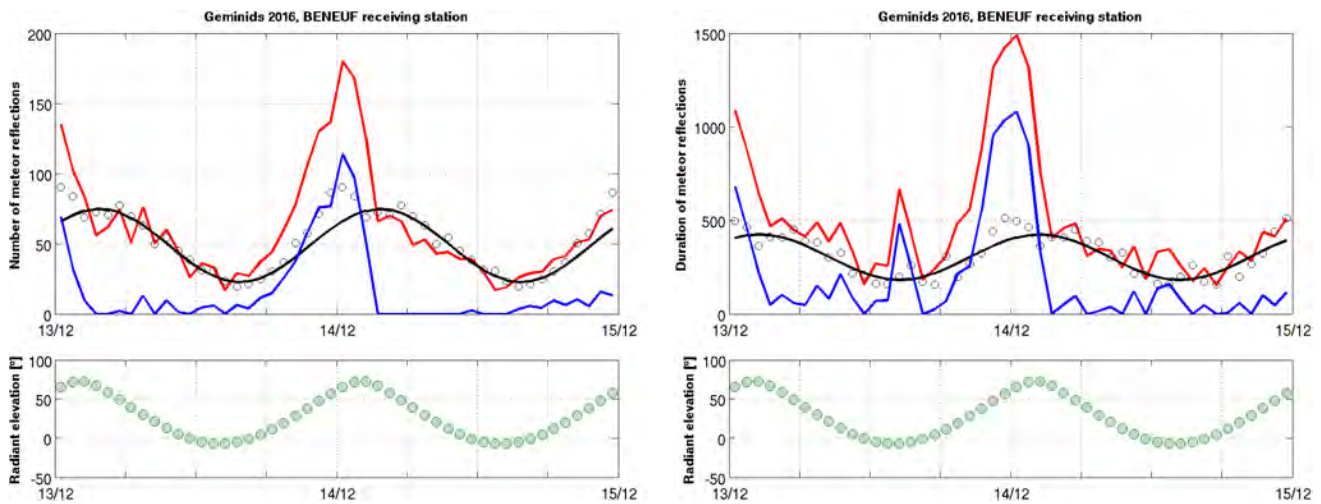


Figure 6 – Estimation of Geminids 2016 activity (BRAMS receiving station: Neufchâteau). *Top left*: Hourly number of meteor reflections (upper red curve: total observed; black circles and curve: estimation of diurnal variation of sporadic background and its weighted sine fit; lower blue curve: estimated hourly number of Geminid reflections). *Bottom left*: Radiant elevation. *Top right*: Hourly total duration (s) of meteor reflections (upper red curve: total observed; black circles and curve: estimation of diurnal variation of sporadic background and its weighted sine fit; lower blue curve: estimated hourly total duration of Geminid reflections). *Bottom right*: Radiant elevation. Times are in UT.

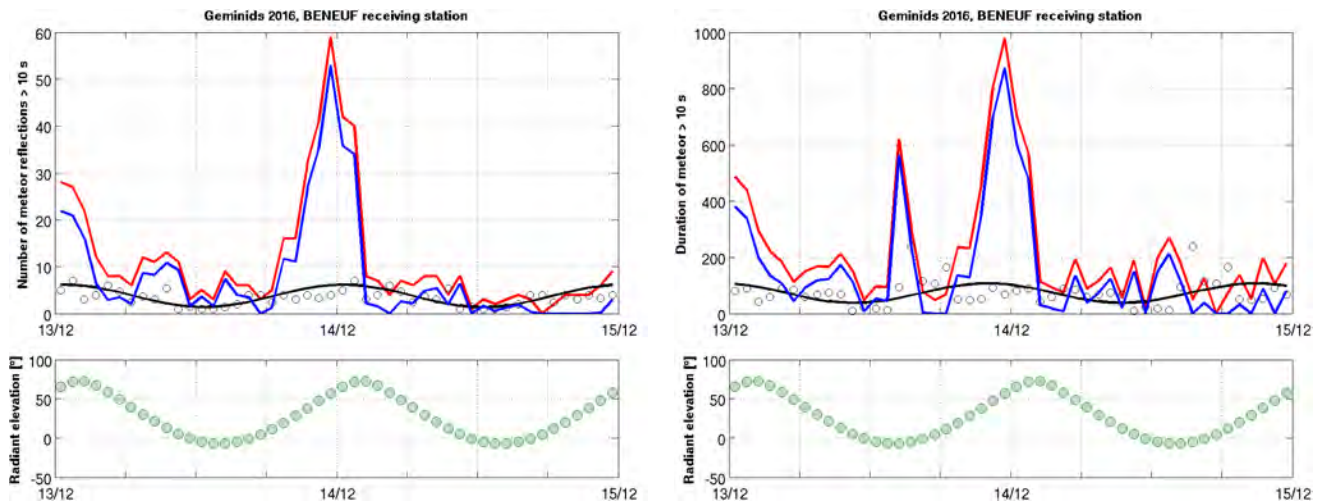


Figure 7 – Estimation of Geminids 2016 activity (BRAMS receiving station: Neufchâteau). *Top left*: Hourly number of meteor reflections lasting at least 10 seconds (upper red curve: total observed; black circles and curve: estimation of diurnal variation of sporadic background and its weighted sine fit; lower blue curve: estimated hourly number of Geminid reflections). *Bottom left*: Radiant elevation. *Top right*: Hourly total duration (s) of meteor reflections lasting at least 10 seconds (upper red curve: total observed; black circles and curve: estimation of diurnal variation of sporadic background and its weighted sine fit; lower blue curve: estimated hourly total duration of Geminid reflections). *Bottom right*: Radiant elevation. Times are in UT.

information about the hourly total duration of meteor reflections. Figure 8 provides the same information, but only taking into account reflections lasting at least 10 seconds.

All of these plots individually permit to deduce that the Quadrantid maximum took place on January 3, which is consistent with the video results reported by Molau et al. (2017c).

## 7 Conclusions and future outlook

The present study marks the first publication of meteor shower activity results of BRAMS, made possible by the citizen science contribution via the Radio Meteor Zoo.

Since most BRAMS stations do not include an interferometer, shower membership of individual meteor reflections cannot be decided. A method was developed to split the hourly number of meteor reflections in a sporadic background and a shower component. Comparing the results of the showers presented in this analysis (Perseids 2016 and 2017, Geminids 2016, and Quadrantids 2017) to the literature, this method seems to perform well.

Meteor shower maxima typically feature a lot of long-duration (overdense) reflections, which often overlap with shorter (underdense) reflections. As a result, indiscriminately counting the number of reflections can be a rather inaccurate measure of meteor activity. The hourly total duration of meteor reflections (total, spo-

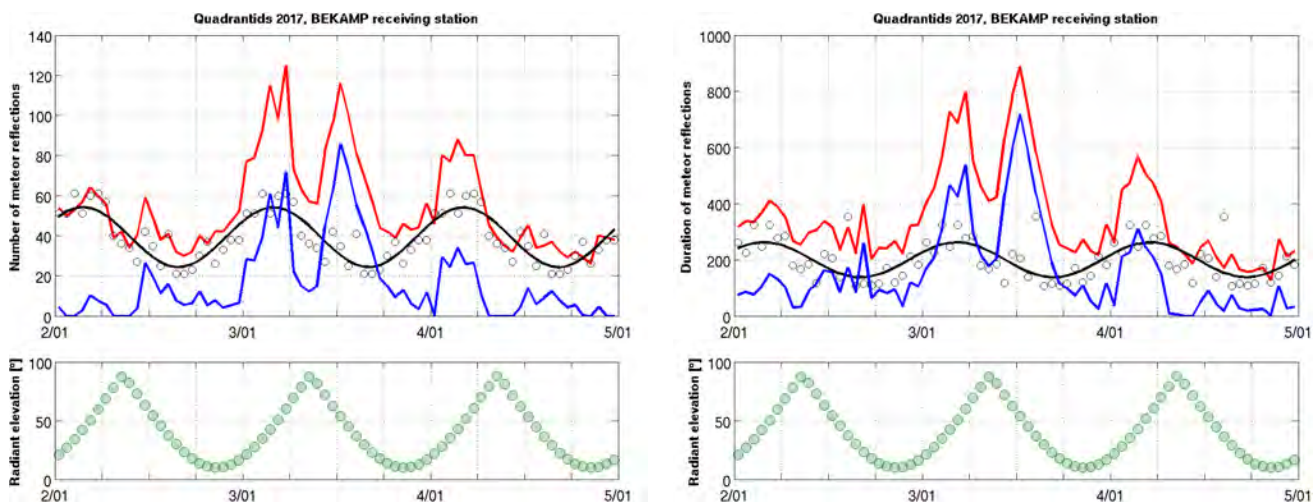


Figure 8 – Estimation of Quadrantids 2017 activity (BRAMS receiving station: Kampenhout). *Top left*: Hourly number of meteor reflections (upper red curve: total observed; black circles and curve: estimation of diurnal variation of sporadic background and its weighted sine fit; lower blue curve: estimated hourly number of Quadrantid reflections). *Bottom left*: Radiant elevation. *Top right*: Hourly total duration (s) of meteor reflections (upper red curve: total observed; black circles and curve: estimation of diurnal variation of sporadic background and its weighted sine fit; lower blue curve: estimated hourly total duration of Quadrantid reflections). *Bottom right*: Radiant elevation. Times are in UT.

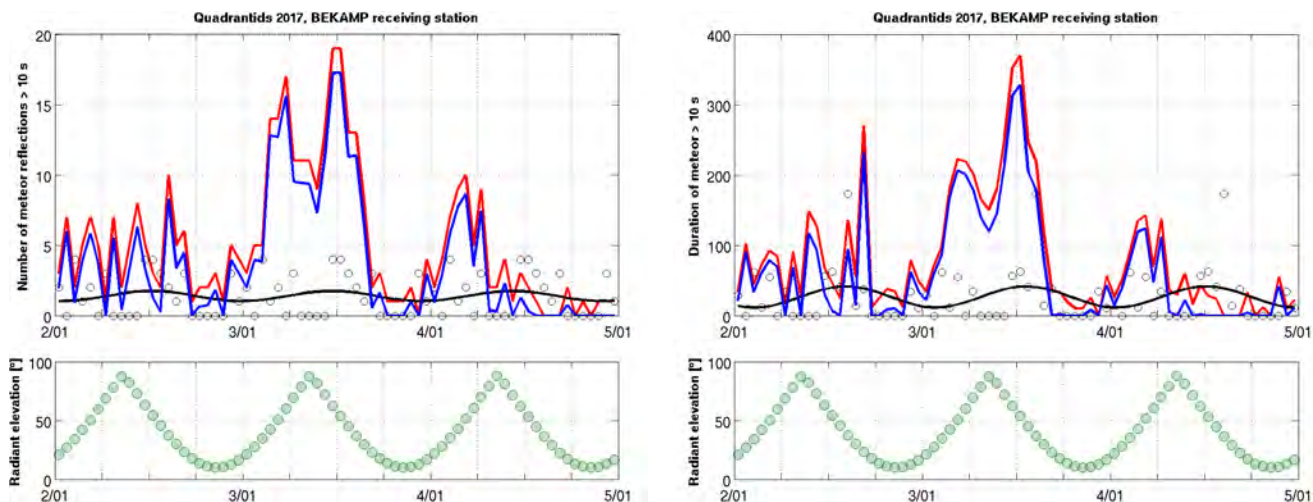


Figure 9 – Estimation of Quadrantids 2017 activity (BRAMS receiving station: Kampenhout). *Top left*: Hourly number of meteor reflections lasting at least 10 seconds (upper red curve: total observed; black circles and curve: estimation of diurnal variation of sporadic background and its weighted sine fit; lower blue curve: estimated hourly number of Quadrantid reflections). *Bottom left*: Radiant elevation. *Top right*: Hourly total duration (s) of meteor reflections lasting at least 10 seconds (upper red curve: total observed; black circles and curve: estimation of diurnal variation of sporadic background and its weighted sine fit; lower blue curve: estimated hourly total duration of Quadrantid reflections). *Bottom right*: Radiant elevation. Times are in UT.

radic background, and shower component) provides a more robust measure of meteor activity, and is always plotted alongside the hourly number of reflections. Forward scatter reflections from meteor streams with a small mass index (such as the Perseids) are outnumbered by the sporadic background. The shower activity profile can still be determined by only considering the reflections with a duration of at least 10 seconds, which correspond to larger particles.

Meteor numbers in this paper have not yet been corrected for the relative sensitivity of the forward scatter setup, which shows a large daily variation as the radiant crosses the sky. This daily variation is clearly seen in the plots, meaning it is pointless at this stage to determine

the exact times of the shower maxima. Using an analogy with visual data, the forward scatter data presented here are similar to raw visual rates rather than ZHRs. The relative sensitivity of the forward scatter setup is called the Observability Function and was modeled by Verbeek (1997). The authors will incorporate the Observability Function into the analysis of shower data in a future paper. It is expected that this will enable to determine the exact times of occurrence of shower maxima.

### Acknowledgements

The BRAMS network is a project from the Royal Belgian Institute for Space Aeronomy and funded by the

Solar-Terrestrial Center of Excellence (STCE). The authors thank all volunteers who helped us with the classification of the spectrograms. These volunteers make the success of the Radio Meteor Zoo. We also thank the Zooniverse team, who are hosting the Radio Meteor Zoo and who are always very enthusiastic in supporting us. Last but not least, there would be no observations without volunteers hosting the BRAMS receiving stations.

The authors are very grateful for their constant support of this project.

## References

- Calders S., Lamy H., Martínez Picar A., Tétard C., Verbeeck C., and Gamby E. (2017). “The Radio Meteor Zoo: Involving citizen scientists in radio meteor research”. In Gyssens M. and Rault J.-L., editors, *Proceedings of the International Meteor Conference*, Petnica, Serbia, 21–24 September 2017. IMO, pages 13–15.
- Calders S., Verbeeck C., Lamy H., and Martínez Picar A. (2016). “The Radio Meteor Zoo: A citizen science project”. In Roggemans A. and Roggemans P., editors, *Proceedings of the International Meteor Conference*, Egmond, the Netherlands, 2–5 June 2016. IMO, pages 46–49.
- Lamy H., Anciaux M., Ranvier S., Calders S., Gamby E., Martínez Picar A., and Verbeeck C. (2015). “Recent advances in the BRAMS network”. In Rault J.-L. and Roggemans P., editors, *Proceedings of the International Meteor Conference*, Mistelbach, Austria, 27–30 August 2015. IMO, pages 171–175.
- Lintott C. J., Schawinski K., Slosar A., Land K., Bamford S., Thomas D., Raddick M. J., Nichol R. C., Szalay A., Andreescu D., Murray P., and Vandenberg J. (2008). “Galaxy Zoo: Morphologies derived from visual inspection of galaxies from the Sloan Digital Sky Survey”. *Monthly Notices of the Royal Astronomical Society*, **389**, 1179–1189.
- Molau S., Crivello S., Goncalves R., Saraiva C., Stomeo E., and Kac J. (2017a). “Results of the IMO Video Meteor Network—August 2016”. *WGN, Journal of the IMO*, **45**, 13–17.
- Molau S., Crivello S., Goncalves R., Saraiva C., Stomeo E., and Kac J. (2017b). “Results of the IMO Video Meteor Network—December 2016”. *WGN, Journal of the IMO*, **45**, 56–62.
- Molau S., Crivello S., Goncalves R., Saraiva C., Stomeo E., and Kac J. (2017c). “Results of the IMO Video Meteor Network—January 2017”. *WGN, Journal of the IMO*, **45**, 63–66.
- Powell C. (2017). “Modelling & analysis of diurnal variation in meteor flux”. *WGN, Journal of the IMO*, **45**, 32–37.
- Rendtel J., Ogawa H., and Sugimoto H. (2017). “Meteor showers 2016: review of predictions and observations”. *WGN, Journal of the IMO*, **45**, 49–55.
- Verbeeck C. (1997). “Calculating the sensitivity of a forward scatter setup for underdense shower meteors”. In Knöfel A. and Roggemans P., editors, *Proceedings of the International Meteor Conference*, Apeldoorn, the Netherlands, 19–22 September 1996. IMO, pages 122–132.

# Meteorite detection with airborne support—a study case

Joe Zender<sup>1,4</sup>, Regina Rudawska<sup>1</sup>, Detlef Koschny<sup>1,2,4</sup>, Gerhard Drolshagen<sup>3</sup>,  
Gert-Jan Netjes<sup>4</sup>, Mirko Bosch<sup>5</sup>, Rik Bijl<sup>5,7</sup>, Rob Crevecoeur<sup>5</sup>, and  
Felix Bettonvil<sup>4,6</sup>

<sup>1</sup> ESA/ESTEC, 2200 AG Noordwijk, the Netherlands  
Joe.Zender@esa.int

<sup>2</sup> Chair of Astronautics, TU Munich, Germany

<sup>3</sup> Carl von Ossietzky University of Oldenburg, Oldenburg, Germany

<sup>4</sup> Werkgroep Meteoren, Amsterdam, the Netherlands

<sup>5</sup> Stichting Nationaal Modelvliegkamp, Maastricht, the Netherlands

<sup>6</sup> Sterrewacht Leiden, Universiteit Leiden, Leiden, the Netherlands

<sup>7</sup> Euro Drone Inspections bv, Maastricht, the Netherlands

The search for meteorites is a cumbersome and tough activity. After having instrumental evidence, i.e., the detection of fireballs in one of the existing fireball networks and the computation of the potential landing site area, a group of enthusiasts often spends days in the search for meteorites. This study analyses if the use of airborne cameras can support the meteorite search. A set of 11 test meteorites was distributed on two different kind of surface areas: a grass field and a harvested wheat field. A high-resolution camera mounted on a drone acquired images at 60 meters altitude. The images were post-processed to identify the meteorites. The algorithm detected at least half of the meteorites.

## 1 Introduction

The analysis of meteorites is scientifically important and provides information on the meteorite composition (Sitek et al., 2016; Erokhin et al., 2015; 2016; Spurný et al., 2014) and thus provides information on the parent body (Borovička et al., 2013; Sitek et al., 2016) and clues on evolution of our Solar System (Taylor, 2005). The detection of meteorites is rare. Often, they are found following an eyewitness report of the meteorite fall itself (Hankey and Perlerin, 2016). Borovička et al. (2015) provide an overview of the published meteorite findings after instrumental observations, limited to 22 cases until the end of 2013.

Other meteorite findings are reported after dedicated search campaigns in deserts (Ouazaa et al., 2008) or (ant)arctic regions (Haack et al., 2007; Karner et al., 2016).

To allow for a more systematic and geographical well-covered approach to the characterization of meteors, visual camera networks are operated on several continents. The observation of the meteor ablation phenomena in the atmosphere from at least two different observation points allows the computation of a potential landing ellipse—besides the computation of several physical meteor characteristics.

These networks are operated in several European countries, i.e., Slovakia (Porubčan et al., 2009), Croatia (Šegon et al., 2016), France (Colas, 2016), Italy (Gardioli et al., 2016), Germany/Czech Republic (Flohner et al.,

2012), Spain (Madieto et al., 2009), the Netherlands (Bettonvil, 2015), BeNeLux (Roggemans, 2016), and Poland (Wiśniewski et al., 2017), as well as in Australia (Day et al., 2016), Tajikistan (Kokhirova et al., 2015), the USA (Kenyon and Watson, 2005), Japan (Yamamoto, 2005), and Canada (Brown et al., 2010).

Once an event is reported within a camera network by several cameras, the potential landing ellipse is computed. If the landing area is suited for an on-ground search, a search team of enthusiastic meteor researchers is organized and a systematic search of the potential landing area is executed (Oberst et al., 2003; 2004; Tymński et al., 2015). The search typically requires days of concentrated walking in a well-organized and structured manner. Often the search is supported by hand-held metal detectors. All inspected areas must be recorded carefully to allow the continuation of the search campaign at a later time.

To improve or at least support the human-intensive search activity, we have experimented with an optical camera system mounted on a drone to detect meteorites placed on well-defined surface areas. The meteorites were provided by members of the IMO (see list of co-authors). The resulting airborne-images were analysed with an algorithm aiming at automatically detecting the meteorites. This article reports on the equipment, both the camera system and the drone (Section 2), the meteorite samples (Section 3), and provides an overview of the actual flight campaign (Section 4). Section 5 describes the data obtained and the analysis applied to them. The results are described in Section 6.

## 2 Instrumentation

An Altura Zenith drone, a commercial octocopter, was available for the test flights. It is a 3-axis stabilised drone of about 70 cm edge to edge, a weight of 2.5 kg, and a maximum take-off weight (MTOW) of 9.8 kg. The drone is powered by a 20000 mAh LiPo-battery allowing a flight time of up to 30 minutes. The Altura Zenith drone is equipped with a gimbal and can host a load of up to 5.5 kg. Although the drone was equipped with a GPS system and would have allowed an autonomous flight based on way-points, we used a standard 2.4 GHz remote control system to control the drone. The drone was equipped with a Sony Alpha 7R camera on the gimbal system, also controlled by another 2.4 GHz remote control system. The Sony camera has a backside-illuminated CMOS image sensor (Sony Exmor RS<sub>TM</sub>) of 35.9 mm × 24 mm with a theoretical pixel resolution of 7389 × 4926. The CMOS is based on a 1-inch stacked design obtaining RGBG each at 12 bit resolution, and has a maximum sensitivity at 610 nm, 530 nm, and 470 nm in the red, green, and blue bands, respectively. All bandpasses have a relatively high infrared contribution. We used a lens of 35 mm. The ground-based resolution is obtained by

$$r = \frac{fp}{dw}, \quad (1)$$

with  $r$  the resolution [pixel/m],  $f$  the focal length [m],  $p$  the number of pixels,  $d$  the camera distance to observable [m], and  $w$  the chip width [m]. We decided to fly at an altitude of 60 m, thus obtaining a theoretical resolution of slightly better than 1 cm × 1 cm. Figure 1, (a), shows the drone on the campaign day, just before the take-off. The camera is visible at the bottom of the drone, mounted on the gimbal and facing the observer.

## 3 Meteorite samples

A total of 11 meteorites were available as listed in Table 1. The meteorites were of different sizes, ranging from just above 1 cm to nearly 30 cm.

Figure 1, (b), shows all meteorites. On the campaign day, only the GDXX and GJNXX meteorites were available,

Table 1 – Some characteristics of the available meteorites.

Id.	Type	Size [cm]	Weight [kg]
GD01	Chondrite	18 × 16 × 8	2.374
GD02	Iron (Gibeon)	17 × 7 × 7	2.532
GD03	Iron (Can. Diablo)	5 × 3 × 2	0.183
GD04	Chondrite	2 × 2 × 2	
GD05	Chondrite	0.5 × 1 × 1	
GD06	Chondrite	8 × 6 × 4	0.411
GJN12	H4/5	4 × 3 × 2	0.03
GJN13	LL5	4 × 4 × 3	0.05
GJN14	Iron	9 × 5 × 4	
GJN15	Iron	17 × 8 × 7	
GJN16	Iron	24 × 10 × 11	

representing a reasonable mixture of ordinary chondrites and iron type meteorites of different sizes. The meteorites have been on loan from several co-authors of this article.

## 4 Flight campaign

The flight campaign was executed on a partly clouded summer day, 10 August 2016, at a model airplane flying field in Belgium at 11<sup>h</sup>00<sup>m</sup> local time. Due to the clouds, the light conditions were not stable. The wind was modest and not stronger than 3 Beaufort. The surface area to expose the meteorites was two-fold. First, all meteorites were laid down on a grass field at equal distances (2 meters); see Figure 2. The grass height was about 4 cm. After the first overflight, the meteorites were shifted by 4 meters onto a wheat field that was harvested about one week earlier. The drone and camera were operated by a pilot and a camera controller using two 2.4 GHz remote control devices. Images were obtained in regular intervals during the flight. Due to the large pixel size of the camera, most images contain all meteorite samples in a single exposure. The camera was operated at an altitude of 60 meters and delivered a sequence of several dozens of RGB-images in TIFF-format. These images were screened and 9 images were selected from the grass and the wheat field correspondingly.

## 5 Data analysis

As most aerial images show all meteorites in their scene, only one TIFF-image was selected for analysis. To begin with, the meteorites were identified visually and their image coordinates noted. Using these coordinates, a 80 × 80 pixel rectangle was cropped. The corresponding surface area represents 75 cm × 75 cm. The individual color planes RGB were analyzed by plotting line profiles along a center line intersecting the individual meteorites; see Figure 2 for the areas over the grass, and Figure 3 for the areas over the wheat field. The line profiles from the grass field analysis indicate that the meteorites have a low reflectance on all color planes, and that the reflectance profile changes showing a similar behavior.

The following algorithm, taking advantage on these observed reflectance behavior, was applied to the input scene:

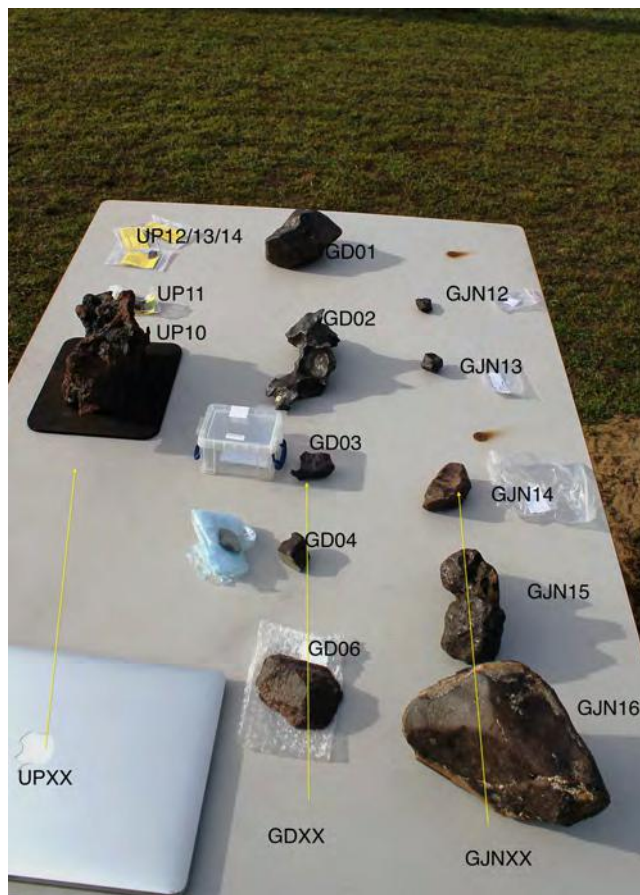
- Each individual color plane—indicated by R/G/B as red/green/blue, respectively, is rescaled from its original integer domain into floating point numbers in the range 0..1:

$$R_{a0:2^s-1} \mapsto R_{0:1},$$

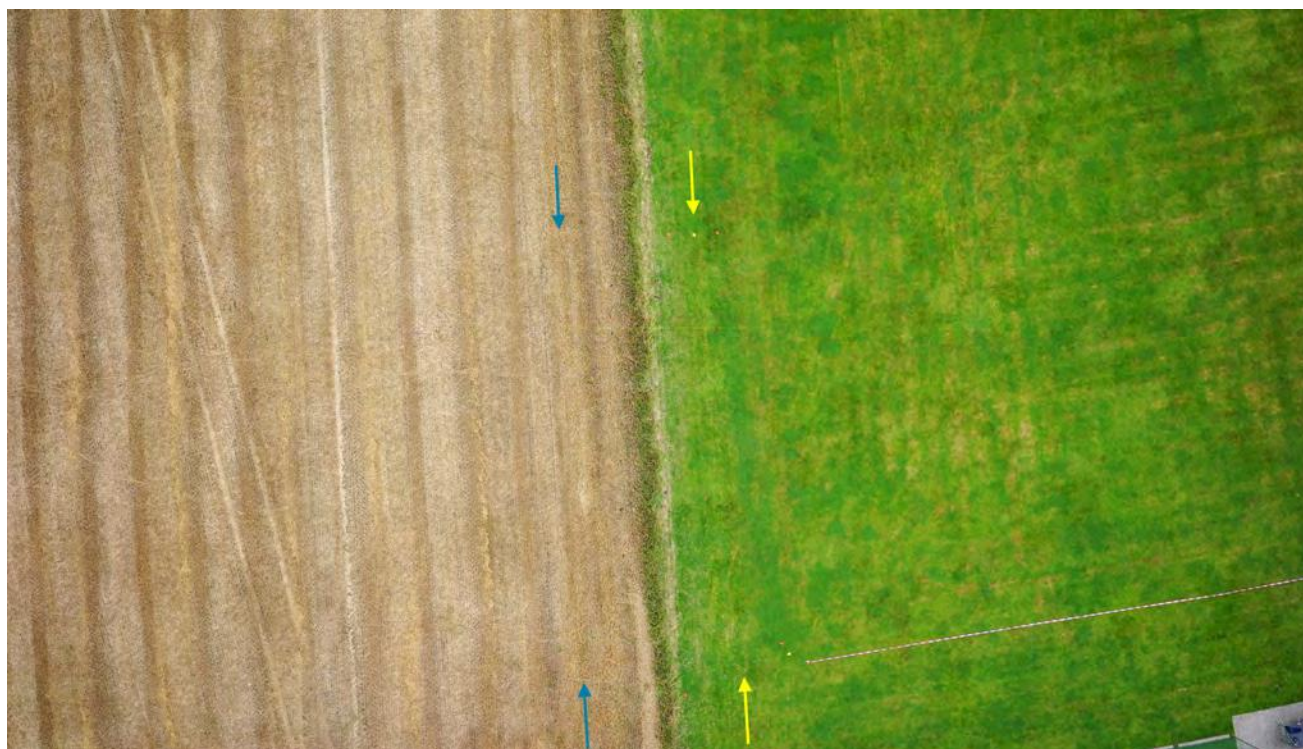
and the same, mutatis mutandis, for the G-plane and the B-plane.



(a) Drone



(b) Meteorites overview



(c) Campaign field

Figure 1 – (a) Drone with the mounted camera just before lift-off. (b) Meteorites before they were laid out in the field. (c) Aerial view of the campaign field. The meteorites were equally spaced, first in the area indicated by the yellow arrows, and later on in the area indicated by the blue arrows.

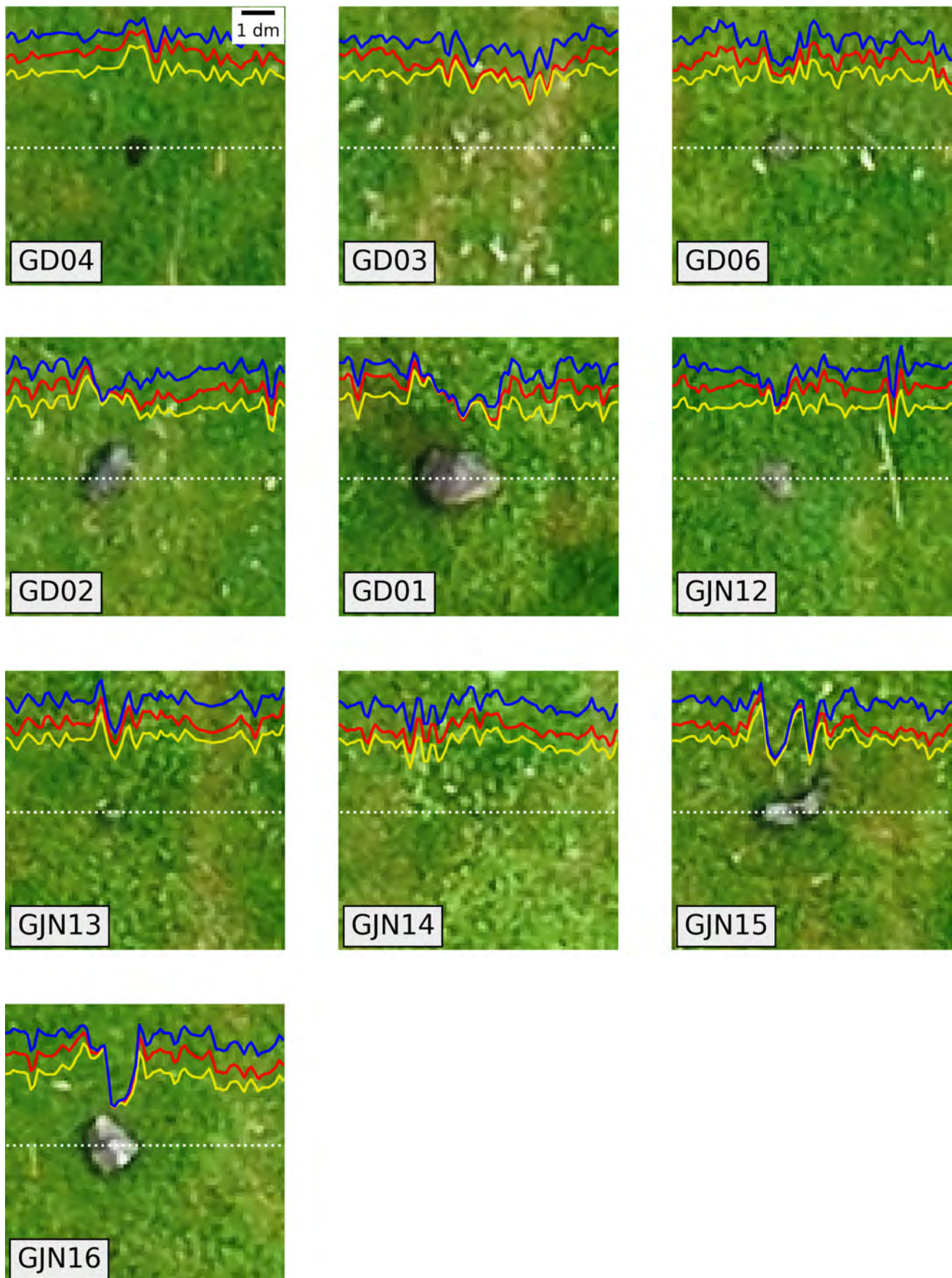


*Figure 2* – The inlet images show  $80 \times 80$  pixel rectangles cropped from the full frame aerial image with the meteorites in the image centers. The dotted lines indicate the meteorite positions. The colored line plots represent the profiles along the dotted line for each RGB color band, in red, yellow, and blue, respectively. The image was obtained over the grass field at a height of 60 meters.

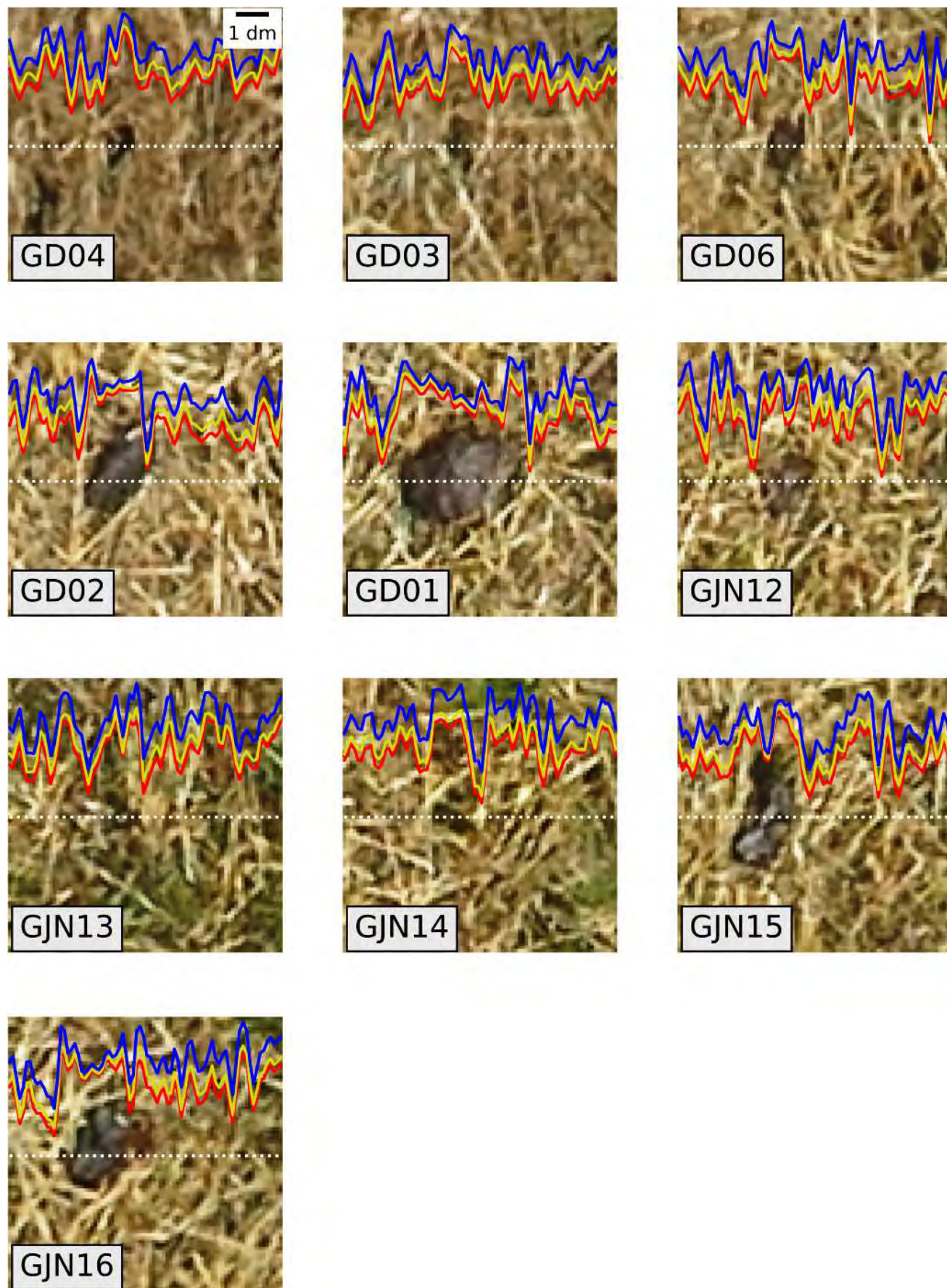
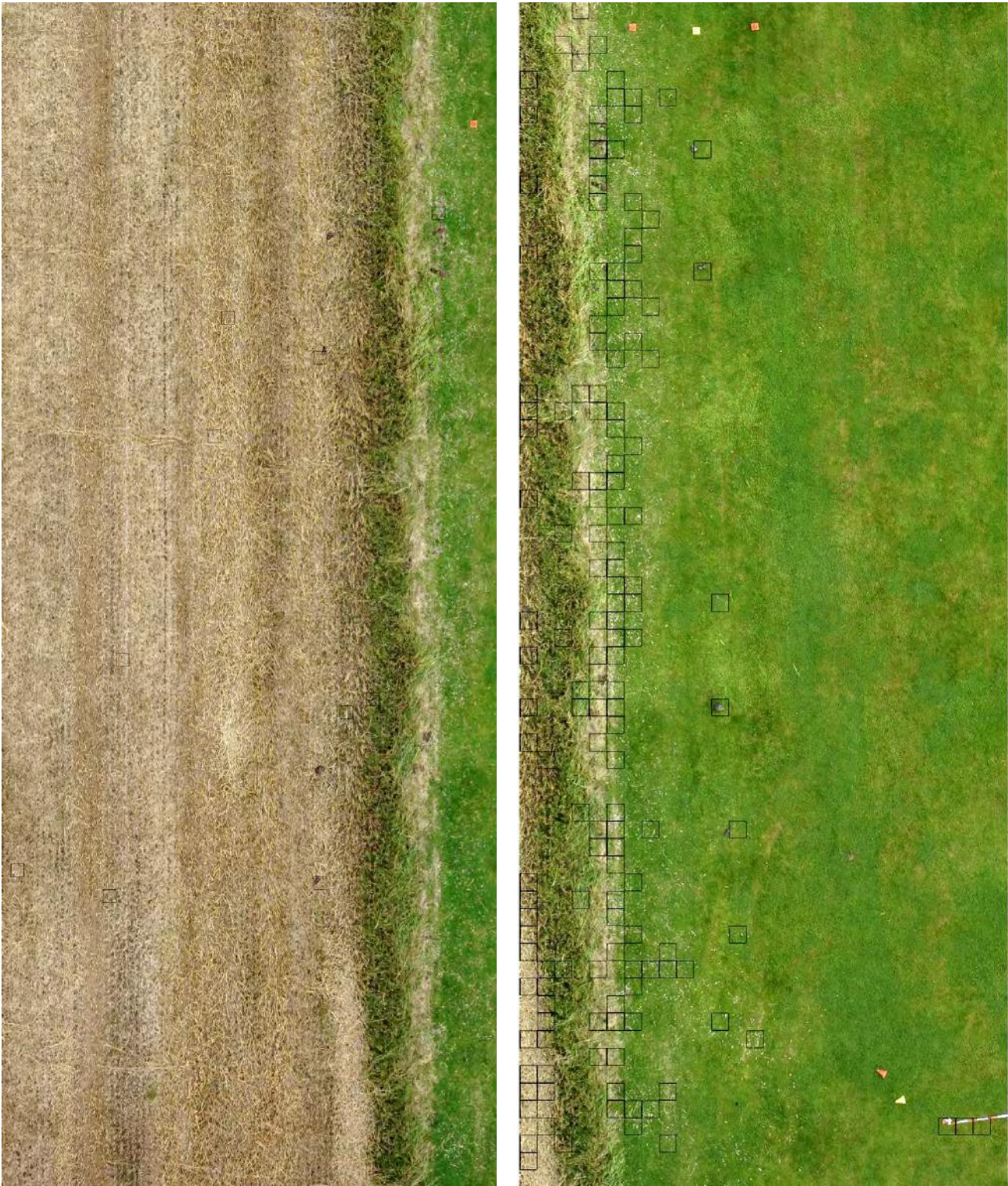


Figure 3 – Same as Figure 3, but over the wheat field.



(a) Wheat

(b) Grass

Figure 4 – The images show the (a) wheat and (b) grass fields with boxes drawn in the areas identified by the software algorithm as potential meteorite locations.

- Each color plane is inverted to avoid scaling problems caused by division by small numbers:

$$R_{0:1} \mapsto 1/R_{0:1} = \overline{R_{0:1}},$$

and the same, mutatis mutandis, for the G-plane and the B-plane.

- The pixel values of the individual color plane are

divided by each other:

$$D_{RG}(x, y) = \overline{R_{0:1}(x, y)} / \overline{G_{0:1}(x, y)};$$

$$D_{RB}(x, y) = \overline{R_{0:1}(x, y)} / \overline{B_{0:1}(x, y)};$$

$$D_{GB}(x, y) = \overline{G_{0:1}(x, y)} / \overline{B_{0:1}(x, y)}.$$

- The algorithm walks through the obtained arrays and checks if individual pixel values are lower than

a threshold:

```

threshold = 0.95;
if  $D_{RG}(x, y) < \text{threshold}$  and
 $D_{RB}(x, y) < \text{threshold}$  and
 $D_{GB}(x, y) < \text{threshold}$  and
then search pixel neighbors of  $(x, y)$  for
same condition.

```

- If more than 10 neighborhood pixels fulfill the above condition, the algorithm indicates a hit and thus a potential meteorite landing location.

In a first analysis, the threshold parameter used above and the number of neighborhood pixels was varied. The above values represent one of the sets used that resulted in the detection of half of the meteorites on the grass and the wheat field. The algorithm works well on the grass field and produces only a limited number of false detections, but, on the wheat field, the number of false detections is high. Figure 4 shows the scenes with boxes drawn for each meteorite detection by the algorithm.

## 6 Results and conclusions

This study tried to answer whether high-resolution camera images obtained from air could support future meteorite search campaigns. An airborne campaign was executed, and high-resolution images were obtained from 60 meter altitude and with 11 meteorites in the field of view. Two different surface areas, a grass field and a recently harvested wheat field, were available. The obtained images were analyzed using a simple algorithm. On both surface areas, half of the meteorites were detected by the algorithm.

This study is a first demonstration of the airborne meteorite support capabilities for future meteorite search campaigns. We conclude that meteorite search campaigns can be complemented by airborne cameras as described in this study.

Several aspects should however be considered:

- The pixel resolution determines the smallest detectable meteorite. The pixel resolution is driven by the flight altitude and thus determines again the region that is covered by a single exposure. In case of a potential search area of several square kilometers, one might have to analyze several thousands of single exposures. It is clear that the images obtained must be geo-referenced, and an algorithm must produce a list of potential meteorite locations with precise coordinates given.
- The algorithm applied takes into account dedicated meteorite reflectance characteristics. Detailed analysis is needed, and, with a better characterization, the algorithm might be improved.
- This study assumed that meteorites are lying on the surface. This assumption is wrong, however,

as the impact speed is typically sufficient to let the meteorites penetrate the surface, at least partially. More realistic cases need to be studied.

- Alternative instrument approaches could be studied to take advantage of other meteorite characteristics. One of the alternatives could be to take advantage of meteorite magnetism and fly a magnetometer-like instrument. Another approach would be to study dedicated meteorite reflections, e.g., in the ultraviolet wavelength regime (Wagner et al., 1980). With an active ultraviolet detector, the airborne campaign could then be executed during the night and allow the detection in a wide range of surfaces. Still another approach could involve to fly penetrating radars from the drones, which would be a technological improvement from the currently used hand-held metal detectors.

Finally, we would like to draw the attention to privacy and legal aspects: flying with an airplane or a drone requires following the national legislation for remote controlled airplanes, and the privacy of neighbors and landowners must be respected under all circumstances.

## References

- Bettonvil F. (2015). “HHEBBES! All-sky camera system: status update”. In Rault J.-L. and Roggemans P., editors, *Proceedings of the International Meteor Conference*, Mistelbach, Austria, 27–30 August 2015. IMO, pages 138–142.
- Borovička J., Spurný P., and Brown P. (2015). “Small near-Earth asteroids as a source of meteorites”. In Michel P., DeMeo F. E., and Bottke W. F., editors, *Asteroids IV*. Pages 257–280.
- Borovička J., Tóth J., Igaz A., Spurný P., Kalenda P., Haloda J., Svoreň J., Kornoš L., Silber E., Brown P., and Husárik M. “The Košice meteorite fall: atmospheric trajectory, fragmentation, and orbit” *Meteorit. Planet. Sci.*, **48**, 1757–1779.
- Brown P., Weryk R. J., Kohut S., Edwards W. N., and Krzeminski Z. (2010). “Development of an all-sky video meteor network in southern Ontario, Canada: the ASGARD system”. *WGN, Journal of the IMO*, **38**, 25–30.
- Colas F. (2016). “Official launching of FRIPON”. *eMeteorNews*, **1**, 67–68,
- Day B., Bland P., Al-Rajeh Y., and Schmidt G. (2016). “The Desert Fireball Network”. In *The Society for Astronomical Sciences 35th Annual Symposium on Telescope Science*. Pages 165–166.
- Erokhin Y. V., Koroteev V. A., Khiller V. V., Burlakov E. V., Ivanov K. S., and Kleimenov D. A. (2015). “The Kunashak meteorite: New data on mineralogy”. *Doklady Earth Sciences*, **464**, 1058–1061.

- Erokhin Y. V., Koroteev, V. A., Khiller V. V., Burlakov E. V., Ivanov K. S., and Kleimenov D. A. (2016). “The Ozeroye meteorite: New data on mineralogy”. *Doklady Earth Sciences*, **471**, 1273–1276.
- Flohner J., Oberst J., Heinlein D., and Grau T. (2012). “The European Fireball Network 2011—Status of cameras and observation results in Germany” In *Proceedings European Planetary Science Congress*, Madrid, Spain, 23–28 September 2012. Paper id. EPSC2012-441.
- Gardiol D., Cellino A., and Di Martino M. (2016). “PRISMA, Italian network for meteors and atmospheric studies”. In Roggemans A. and Roggemans P., editors, *Proceedings of the International Meteor Conference*, Egmond, the Netherlands, 2–5 June 2016. IMO, pages 76–79.
- Haack H., Schutt J., Meibom A., and Harvey R. (2007). “Results from the Greenland Search for Meteorites expedition”. *Meteorit. Planet. Sci.*, **42**, 1727–1733.
- Hankey M. and Perlerin V. (2016). “A tale of two fireballs”. In Roggemans A. and Roggemans P., editors, *Proceedings of the International Meteor Conference*, Egmond, the Netherlands, 2–5 June 2016. IMO, pages 111–112.
- Karner J. M., Harvey R. P., and Schutt J. (2016). “The Antarctic search for meteorites (ANSMET) in the Miller Range”. In *Proceedings 79th Annual Meeting of the Meteoritical Society*, Berlin, Germany, 7–12 August 2016, paper id 6551.
- Kenyon D. A. and Watson W. T. (2005). “The All Sky Camera Fireball Detector”. In *The Society for Astronomical Sciences 24th Annual Symposium on Telescope Science*, 24–25 May 2005. Pages 11–16.
- Kokhirova G. I., Babadzhyanov P. B., and Khamroev U. K. (2015). “Tajikistan Fireball Network and results of photographic observations”. *Solar System Research*, **49**, 275–283.
- Madiedo J. M., Trigo-Rodríguez J. M., Alonso J., Zamorano J., Ocaña F., Docobo J. A., Pujols P., and Lacruz J. (2009). “The Spanish Meteor Network (SPMN): full coverage of the Iberian Peninsula by means of high-sensitivity CCD video devices”. In *Proceedings European Planetary Science Congress*, Potsdam, Germany, 14–18 September 2009. Paper id. EPSC2009-560.
- Oberst J., Heinlein D., Köhler U., and Spurný P. (2004). “The multiple meteorite fall of Neuschwanstein: Circumstances of the event and meteorite search campaigns”. *Meteorit. Planet. Sci.*, **39**, 1627–1641.
- Oberst J., Heinlein D., Köhler U., Spurný P., and Neukum, G. (2003). “Photographic observations and successful recovery of the ‘Neuschwanstein’ meteorites”. *EOS Transactions*, **84**, 393–395.
- Ouazaa N., Perchiazzi N., Kassaa S., Zeoli A., Ghanmi M., and Folco L. (2008). “Meteorite finds from southern Tunisia”. *Meteorit. Planet. Sci. Suppl.*, **43**, 5090.
- Porubčan V., Svoreň J., Husárik M., and Kaňuchová Z. (2009). “Slovakian part of the European Fireball Network”. *Contributions of the Astronomical Observatory Skalnaté Pleso*, **39**, 101–108.
- Roggemans P., Johannink C., and Breukers M. (2016). “Status of the CAMS-BeNeLux network”. In Roggemans A. and Roggemans P., editors, *Proceedings of the International Meteor Conference*, Egmond, the Netherlands, 2–5 June 2016. IMO, pages 254–260.
- Šegon D., Vida D., Korlević K., and Andreić Ž. (2016). “Croatian Meteor Network: Ongoing work 2015–2016”. In Roggemans A. and Roggemans P., editors, *Proceedings of the International Meteor Conference*, Egmond, the Netherlands, 2–5 June 2016. IMO, pages 270–274.
- Sitek J., Dekan J., and Sedlačková K. (2016). “Analysis of Košice meteorite by Mössbauer spectroscopy”. *Journal of Electrical Engineering*, **67**, 307–310.
- Spurný P., Haloda J., Borovička J., Shrbený L., and Halodová P. (2014). “Reanalysis of the Benešov bolide and recovery of polymict breccia meteorites—old mystery solved after 20 years”. *Astron. Astrophys.*, **570**, A39.
- Taylor S. R. (2005). *Solar System Evolution. A New Perspective*. Second Edition. Cambridge University Press.
- Tymiński Z., Stolarz M., Żołądek P., Wiśniewski M., Olech A., Kubalczak T., Zaręba P., and Myszkiwicz M., Polakowski K., and Kosiński J. W. (2015). “Meteorite search campaigns of the Polish Fireball Network”. In Rault J.-L. and Roggemans P., editors, *Proceedings of the International Meteor Conference*, Mistelbach, Austria, 27–30 August 2015. IMO, pages 143–146.
- Wagner J. K., Cohen A. J., Hapke B. W., and Partlow W. D. (1980). “Vacuum ultraviolet reflectance spectra of group E chondrites and achondrites”. In *Lunar and Planetary Science Conference XI*. Pages 1193–1195.
- Wiśniewski M., Żołądek P., Olech A., Tymięski Z., Maciejewski M., Fietkiewicz K., Rudawska R., Gozdalski M., Gawroński M. P., Suchodolski T., Myszkiwicz M., Stolarz M., Polakowski K. (2017). “Current status of Polish Fireball Network”. *Planetary and Space Science*, **143**, 12–20.
- Yamamoto M. (2005). “Recent meteor observing activities in Japan”. In Triglav-Čekada M., Kac J., and McBeath A. editors, *Proceedings of the International Meteor Conference*, Varna, Bulgaria, 23–26 September 2004. IMO, pages 104–109.

# Time perception of a meteorite fall: first results

Auriane Egal<sup>1</sup>, Jérémie Vaubaillon<sup>1</sup>, Min-Kyung Kwon<sup>1</sup>, Vincent Perlerin<sup>2</sup>,  
Mike Hankey<sup>2</sup>, François Colas<sup>1</sup>, and William Thuillot<sup>1</sup>

<sup>1</sup>IMCCE, Observatoire de Paris, Paris, France  
auriane.egal@obspm.fr

<sup>2</sup>International Meteor Organization and American Meteor Society, USA

A study of the ability of human beings to correctly estimate and count the time in case of a meteorite fall is performed. A video showing a simulation of a bolide is shown to more than 500 people, who are asked to guess the duration of the phenomenon and provide an uncertainty. The people take each test twice: first without knowing what to expect nor what will be asked of them, and second knowing they have to estimate the duration of the phenomenon. The experiment is repeated for different populations, durations, and with or without fragmentation. The preliminary results of this study, which will be developed in a forthcoming publication, are presented.

## 1 Introduction

Thanks to the extension of meteors detection networks, it is rare for a meteorite fall in highly populated areas to be detected today only by human observers. However, the visual observation of fireballs remains the only source of information available in the case of meteorite falls having occurred in the past centuries (e.g., the Orgueil meteorite fall in 1864) or in regions not covered by detection networks. The exploitation of such observations sometimes led to a meteorite recovery shortly after their fall in Europe and over the American ground (Haack et al., 2012; Jenniskens et al., 2012; Fries et al., 2014; Hankey and Perlerin, 2016). In a lesser extent, visual observations of fireballs are also analyzed in order to determine the orbital origin of a meteorite (Gounelle et al., 2006). However, the accuracy of the computed orbits highly depends on the reliability of an eye-witness in estimating sensitive characteristics (trajectory, velocity) of an unexpected and impressive phenomenon. An accurate perception of the duration of a fireball is especially mandatory to valuably determine its orbital origin.

The purpose of this work is then to measure the ability of individuals to perceive a time duration, regardless of their knowledge about the science of meteors, in order to evaluate the usefulness of visual observations in determining the dynamic origin of meteorite falls.

## 2 Experiment

### 2.1 Methodology

In order to provide the same experiment conditions for all the witnesses tested, a reproducible simulation of a meteor in a night sky is created. The appearance duration of the meteor is thus precisely known. The animation is then presented to several people who are not expecting what to see. After a first viewing, a witness has to estimate the duration of the event. The

process is then repeated, warning the witness that the same question will be asked after watching exactly the same simulation. After the second viewing, the witness provides a second estimate of the phenomenon duration.

### 2.2 Simulations

For this experiment, three simulations inspired by the testimonials of the Orgueil meteorite fall were created. Simulations 1 and 2 represent a fragmenting fireball with respective durations of about 7 s and about 4 s. Simulation 3 represents a short fireball (lasting 3 s) without fragmentation. Several snapshots of Simulation 1 are shown in Figure 1.

### 2.3 Sampled population

Simulation 1 was widely used for the experiment and designed to compare the performances of witnesses with different degrees of knowledge in meteor science and observation. The animation was presented to observing specialists (scientists or amateurs regularly producing meteor observation reports), non-observing specialists (scientists or highly qualified amateurs working in the field of meteors), astronomy scientists not working in the field of meteors and to the general public. Simulation 1, 2, and 3 were presented to lay people with sufficient general interest in science to participate in the experiment. In total, 576 individuals took the test, personally interviewed and tested by Egal (83% of the total population) and Kwon (17%).

## 3 Results

### 3.1 Analysis

The data analysis relies on two main stages. The ability of the witness in counting the time is first evaluated by analyzing the accuracy of the duration estimated

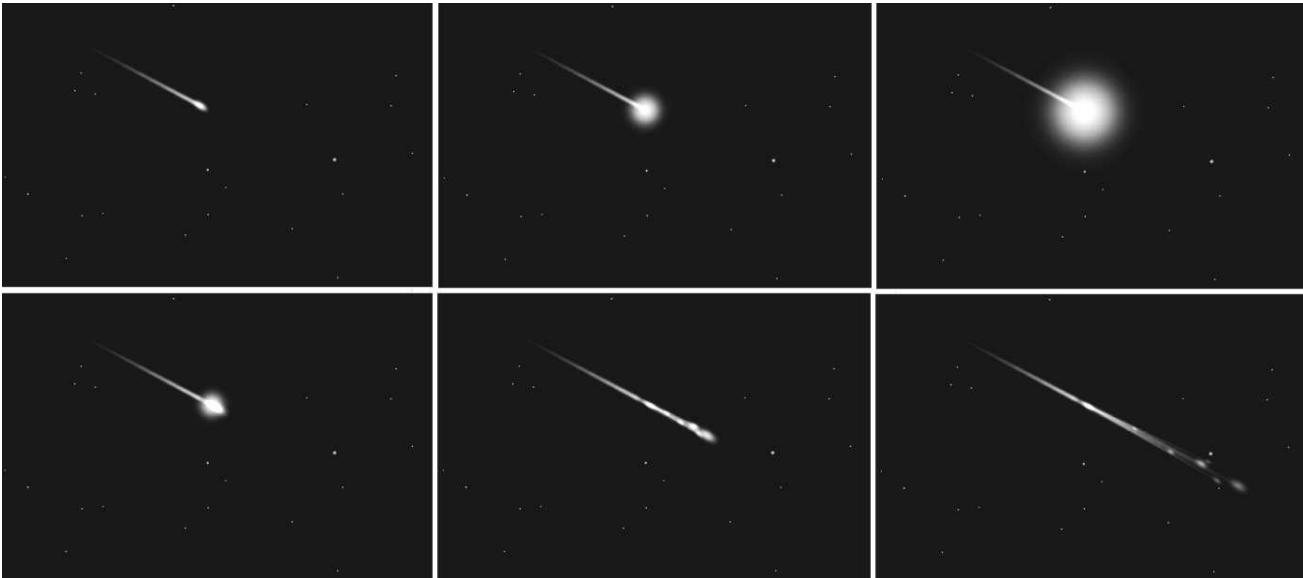


Figure 1 – Several snapshots of Simulation 1—fragmenting fireball.

during the second viewing. Depending on the reliability of the time perception of a witness, the accuracy of the duration estimated without expecting the question is then analyzed.

We now present the results for Simulations 1, 2, and 3.

### 3.2 Simulation 1

For a long simulation with fragmentation, less than one person in four was able to correctly count the real duration of the simulation during the second viewing.

The percentage of reliable witnesses providing a correct estimate of the duration of the fireball during the first viewing is below 5%.

### 3.3 Simulation 2

For a similar but shorter simulation (with fragmentation), twice as many people as in Simulation 1 were able to correctly count the time.

This time, 15% of reliable witnesses were able to accurately guess the fireball duration during the first viewing. However, the most probable estimate is mostly provided by people able to count the time, but whose first guess is at least 2 s below the real duration.

### 3.4 Simulation 3

For a short simulation (3 s) without fragmentation, the ability of the witnesses in counting the time of the second viewing is similar as in the case of Simulation 2.

In this case, the most probable guess is however provided by people able to correctly count the time and to guess the fireball duration during the first viewing with an accuracy of 1 s.

## 4 Conclusions

For a relatively long event (about 7 s) including fragmentation, the vast majority of witnesses was unable to correctly estimate the duration of the phenomenon within less than 2 s, either by crudely guessing or by counting the time. In the vast majority of cases, this error leads to underestimate the real duration of the fireball. The degree of knowledge of the topic did not clearly impact the above conclusions.

A shorter event leads to a greater number of people able to correctly estimate the total duration. The guess of the duration provided after the first viewing is however also generally smaller than the real duration in the case of a fragmenting fireball. This usual underestimation of the duration disappears in the case of a fireball without fragmentation. This difference is explained by the fact that a higher attention is paid to the time perception when the witnesses' concentration is not perturbed by distractive events such a fragmentation. Indeed, it has been shown (Gil, 2008) that time seems shorter when one does not focus on it. Fraisse (1979) confirmed that the less complex an observation is, the more attention a subject is able to give to the duration, resulting in a better time perception.

It is highly unlikely that a witness of a real meteorite fall would focus on counting the time. If the meteor does not first appear in the field of view of the observer, the first guess provides a result that underestimates the real duration even more, because of the time it takes for the witness to notice the phenomenon and carefully look at it. Unless it is possible to evaluate the reliability of a given witness, it is therefore impossible to discriminate between a correct estimate of the duration of a short event and a wrong guess of a long duration event. To consider a one-second uncertainty on the duration of a meteorite fall is far too optimistic, especially if it is a spectacular one. It is therefore necessary to consider the reliability of visual testimonies with great caution.

## 5 Discussion

The large number of candidates interviewed should suffice to deduce statistical results related to the perception of time. However, the reliability of these findings depends on the presence of bias in the sample of population tested. First of all, it should be checked that the samples chosen are sufficiently representative of a group of persons who would be likely to report the observation of a fireball to a scientific organization; but the composition of such a group is hard to pin down. By its nature, this type of event is potentially observable by a wide variety of individuals, regardless of their age, gender, or education level. Nowadays, the observing reports of fireballs can be written by any type of profile. For our experiment, we have then tried as much as possible to vary these parameters in the cases of the general public and the scientists. We questioned men, women, children, adults, and elders, speaking French, English, Spanish, Italian, or Portuguese. We made efforts to reach people interested enough in observational science to accept to be tested. Therefore, we hope not to have favored a certain type of profile for each category of the assessed population.

Because of the complexity of the topic, and considering that time perception depends strongly on psychological parameters of the witness, we do not claim here to provide robust results dealing with the accuracy of time duration guesses by a witness. This experiment, however, highlights general tendencies of time perception and the systematic lack of reliable duration guesses.

## Acknowledgement

We are grateful to Brigitte Zanda and Sophie-Eve Valentin Joly for helping us to gain access to the *Grande galerie de l'évolution* at the *Muséum National d'Histoire Naturelle* (MNHN, Paris) to conduct the tests with the public. This work was supported by grants from *Région Île-de-France* (DIM-ACAV).

## References

- Fraisse P. (1979). "Perception and estimation of time". *Annual Review of Psychology*, **35**, 1–37.
- Fries M., Le Corre L., Hankey M., Fries J., Matson R., Schaefer J., and Reddy V. (2014). "Detection

and rapid recovery of the Sutter's Mill meteorite fall as a model for future recoveries worldwide". *Meteoritics and Planetary Science*, **49**, 1989–1996.

- Gil S. (2008). "Perception du temps et émotions: étude de l'influence des expressions faciales émotionnelles chez l'enfant et l'adulte". Université Blaise Pascal-Clermont-Ferrand II, ED 0370, U.F.R. de Psychologie, Sciences Sociales et Sciences de l'Éducation.
- Gounelle M., Spurný P., and Bland P. A. (2006). "The orbit and atmospheric trajectory of the Orgueil meteorite from historical records". *Meteoritics and Planetary Science*, **41**, 135–150.
- Haack H., Grau T., Bischoff A., Horstmann M., Wasson J., Sorensen A., Laubenstein M., Ott U., Palme H., Gellissen M., Greenwood R. C., Pearson V. K., Franchi L. A., Gabelica Z., Schmitt-Kopplin P. (2012). "Maribo–A new CM fall from Denmark". *Meteoritics and Planetary Science*, **47**, 30–50.
- Hankey M. and Perlerin V. (2016). "A tale of two fireballs". In Roggemans A. and Roggemans P., editors, *Proceedings of the International Meteor Conference*, Egmond, the Netherlands, 2–5 June 2016. IMO, pages 111–112.
- Jenniskens P., Fries M. D., Yin, Q.-Z., Zolensky M., Krot A. N., Sandford S. A., Sears D., Beauford R., Ebel D. S., Friedrich J. M., Nagashima K., Wimpenny J., Yamakawa A., Nishiizumi K., Hamajima Y., Caffee M. W., Welten K. C., Laubenstein M., Davis A. M., Simon S. B., Heck P. R., Young E. D., Kohl I. E., Thiemens M. H., Nunn M. H., Mikouchi T., Hagiya K., Ohsumi K., Cahill T. A., Lawton J. A., Barnes D., Steele A., Rochette P., Verosub K. L., Gattacceca J., Cooper G., Glavin D. P., Burton A. S., Dworkin J. P., Elsila J. E., Pizzarello S., Oglione R., Schmitt-Kopplin P., Harir M., Hertkorn N., Verchovsky A., Nagao, K., Okazaki R., Takechi H., Hiroi T., Smith K., Silber E. A., Brown P. G., Albers J., Klotz D., Hankey M., Matson R., Fries J. A., Walker R. J., Puchtel I., Lee C.-T. A., Erdman M. E., Eppich G. R., Roeske S., Gabelica Z., Lerche M., and Nuevo, M., Girten B., and Worden S. P. (2012). "Radar-enabled recovery of the Sutter's Mill meteorite, a carbonaceous chondrite regolith breccia". *Science*, **338**, 1583–1587.

# Autonomous sensor network for detection and observation of meteors

Ana Vodopivec and Hakan Kayal

Dept. Aerospace Information Technology, University of Würzburg, Germany  
vodopivec@uni-wuerzburg.de and hakan.kayal@uni-wuerzburg.de

This paper describes the project ASMET for detection and observation of meteors and other transient sky phenomena (TSP), in particular with the application of some of the satellite technologies on Earth with respect to harsh environmental conditions (heating, cooling, power supply) and autonomy (portability, remote control, redundancy, sensors, network, reporting).

## 1 Introduction

The Space Technology Department as a part of the Chair for Aerospace Information Technology of the University of Würzburg is engaged in the development, construction, and operation of space systems, especially in the field of small satellites for scientific applications and higher autonomy as well as the search for extraterrestrial intelligence (SETI) and the exploration of Unidentified Aerospace Phenomena (UAP). Sky observations are reported by individuals who may not have a strong scientific or technical background or who lack the adequate equipment necessary to record an event in the sky just when and where it occurs. Since the location and time of a meteor is largely unknown, it is necessary to have as many small and particularly cost-effective systems as possible. At the University of Würzburg, an Experimental Sensor Platform (ESP) for this purpose was set up in 2008 and is continuously being improved (see Figure 1). Similar systems for the detection of the Transient Lunar Phenomena (TLP) are also developed within the group (Mohn et al., 2015).

Most of the meteors—caused by natural objects that dive into the Earth’s atmosphere at high speed, glow, and disintegrate—appear suddenly and unpredictably. Similarly to the UAPs and TSPs, neither the location nor the time of occurrence can be planned (except some

known meteor showers). An important challenge is to detect the meteor phenomenon at all. In many cases, there are no wide-area monitoring systems that could detect a meteor. Therefore, it is necessary that an autonomous network of sensors is established for detection and observation in inaccessible and uninhabited areas.

The primary goal of the project ASMET is to develop and test a system for autonomous detection and observation of meteors with the following system goals:

- continuous and reliable detection, observation, recognition, and recording of the phenomenon;
- real-time alarm function;
- low maintenance requirements due to autonomy;
- remote control capability;
- self-sufficiency;
- multiple data transmission and networking.

Since the system goals have a lot in common with space technology, especially with the development of autonomous satellites, the user requirements and functional requirements listed in Tables 1 and 2 are derived from the system goals according to space engineering standards.

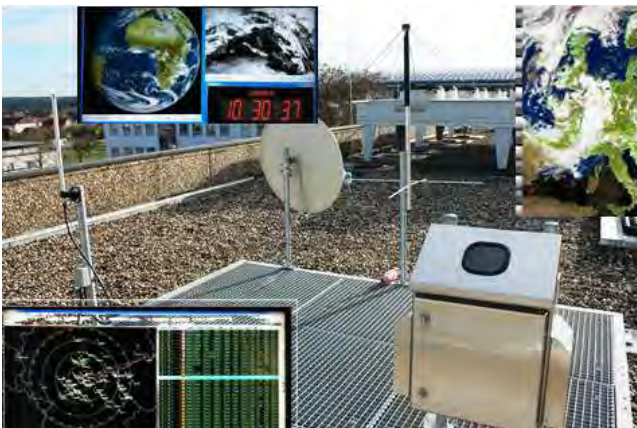


Figure 1 – Outdoor platform of the ESP and screenshots of received data from weather satellites and airplanes.

## 2 Project requirements

### 2.1 User and functional requirements

The specific functional requirements of the ASMET system are derived from the user requirements and from the meteor characteristics. For example, the functional requirement FR0600, “The system should be able to detect the meteors that persist for at least 2 seconds” is a detailed derivation from the user requirement UR0300, “The system should be able to autonomously recognize at least meteors from observed sky phenomena”. Some of the meteor phenomenon characteristics relevant for the project are categorized and highlighted in Table 3.

Table 1 – User requirements.

Nr.	Description	Priority	Fulfilled
UR0100	The system must detect short-term sky phenomena		yes
UR0200	Observation with the system must be possible day and night, 24/7		yes
UR0300	The system should be able to detect at least meteors from observed celestial phenomena autonomously	high	no
UR0400	The system should be able to detect at least as well as the healthy human eye	high	no
UR0500	The system should cover the entire sky of a location	high	yes
UR0600	There must be at least 2 systems at different locations		no
UR0700	The optical frame rate should be adjustable	med.	yes
UR0800	The system should be suitable for all weather conditions	med.	partly
UR0900	The system should be able to deal with light pollution and thus reduce false alarms	med.	no
UR1000	The system should be able to observe other short-term phenomena	med.	no
UR1100	The system can work in modes with different settings	med.	partly
UR1200	After detection, the system may lead another instrument in the direction of the phenomena	low	no
UR1300	The system must be able to send an alarm (short message) to the user upon detection		partly
UR1400	The system must be able to store the user data (images, videos, measured data, ...) redundantly and non-volatily		partly
UR1500	The detection metadata shall be available to the user no later than 3 minutes after detection	high	no
UR1550	The payload data should become available to the user at the latest after 24 hours of remote detection	med.	no
UR1600	The system should back up the detections of at least 7 past days in offline mode	high	no
UR1700	The system must remain capable of communicating throughout Europe under environmental conditions		
UR1750	The system should be able to detect reliably under environmental conditions throughout Europe	med.	no
UR1780	The system should remain capable of communicating worldwide under environmental conditions	low	no
UR1800	The system should be portable	med.	no
UR1900	The system should have a permanent, 24/7 self-sufficient energy supply	high	no
UR2000	The system is to be constructed modularly	low	yes
UR2500	The system should be expandable with additional sensors	low	yes
UR2900	The system design must remain within the budget		yes

Table 2 – Functional requirements.

Nr.	Description	Source	Priority
FR0100	The system must be able to detect TSPs in the wavelength range from 380 nm to 780 nm	UR0100 UR0400	
FR0200	The system should be able to record the TSPs for a period of at least 1 sec. to at least 2 min.	UR0100 UR0400	high
FR0300	The system should be able to detect the TSPs with a magnitude of at least +4	UR0100 UR0400	high
FR0400	The system should be able to detect the TSPs at night in min. 110 km height above ground	UR0200	high
FR0500	The system should be able to detect the TSPs during the day in min. 80 km height above ground	UR0200	high
FR0600	The system should be able to detect the meteors that persist for at least 2 sec.	UR0300	high
FR0700	The system is designed to provide a minimum sky coverage of $360^\circ \times 150^\circ$	UR0500	high
FR0800	The system should remain capable of communication between $36^\circ$ – $64^\circ$ N and $-30^\circ$ – $36^\circ$ E	UR1700 UR1750	high
FR0900	The system should remain communicative at temperatures between $-30^\circ$ C and $+60^\circ$ C	UR1700 FR0800	med.
FR1000	The system should have a max. of 8 kg weight and max. hand luggage dimensions for expeditions	UR1800	med.
FR1100	The system should be able to detect at least 8 meteors at the same time	UR0400 FR0200	med.

## 2.2 Meteor and system characteristics

There are many meteor characteristics (e.g., size, texture, brightness, origin, radiant, frequency). According to the latest IAU definition<sup>1</sup>, in the context of meteor observations, any object (original body) causing a meteor can be termed a meteoroid, irrespective of size.

ASMET system should be able to record meteors not fainter than magnitude +4 (FR0300) since most of the meteors detected are not fainter than +5 magnitudes (Campbell-Brown, 2016). The aim of the ASMET system is not only to perform meteor detection at night, but also to detect daylight meteors. Till now, daylight meteors have mostly been captured by radar observations since they are daytime- and weather-independent. However, nowadays much better cameras are available with higher dynamic range, higher sensitivity, and lower noise. With the benefit of integrated sensor data, reduction of false detections by a neural network, and appropriate dynamic calibration of the system that works seven days a week, twenty-four hours a day (UR0200) the daylight meteors detection must also be possible.

<sup>1</sup>[https://www.iau.org/static/science/scientific\\_bodies/commissions/f1/meteordefinitions\\_approved.pdf](https://www.iau.org/static/science/scientific_bodies/commissions/f1/meteordefinitions_approved.pdf).

## 2.3 Further properties and boundary conditions

There are many different measuring methods available to obtain the relevant meteor data. In this initial project, the ASMET system should mimic, and ideally surpass, the human eye's detection capabilities, as required by user requirement UR0400, "The system should be able to detect at least as well as the healthy human eye" (Table 1). Therefore, we should first analyze observation performance of the healthy human eye (spatial resolution, FOV, wavelength, light value, limiting magnitude, frames per second, size, distance, and frequency). Then we can derive from the user requirement, e.g., UR0400, the next functional requirement, e.g., FR0300, "The system should be able to detect the TSPs with a magnitude of at least +4", and so on, as listed in Table 2.

In the next projects, following project ASMET, some other rarely interlinked meteor characteristics, e.g., radiometric, acoustic, electrical, and astrometric will be simultaneously collected for the same meteor case to generate new knowledge and to reach secondary project goals (described in Section 4).

Table 3 – Meteor phenomenon categorization based on Sumners and Allen (2000), Beatty (2006), Hanslmeier (2007), and Brown et al. (2013).<sup>†</sup> The table entries most relevant to us are those referring to objects with an average diameter in the range of 30  $\mu\text{m}$  to 10 m.

Average Diameter (As big as)	Average Mass (Ablation)	Average Frequency	Name/Effect
< 30 $\mu\text{m}$	< 1 $\mu\text{g}$	100/second	Dust/Micrometeorite
30 $\mu\text{m}$ –1 mm	1 $\mu\text{g}$ –2 mg (all decay)	> 10/second (> 100 000/day)	Meteoroid/Telescopic meteor (> +5 m)
1 mm–1 cm (sand grain/pebble)	2 mg–2 g (all decay)	1/second (> 1000/day)	Visual meteor (–2+6 m.), > 1 g TNT
1 cm–50 cm (boulders/rock)	2 g–250 kg (mostly decayed)	1/hour (> 10/day)	Fireballs (< –2 m.), 1 kg–0.6 kT TNT
50 cm–1 m (microwave)	250 kg–1 T (mostly decayed)	1/day	Bolides (< –4 m.), 0.6 kT–1 kT TNT
1 m–10 m (car)	1 T–1.5 kT (icy/stony decay, iron not)	1/10 years	Asteroids/Superbolides (< –17 m.), > 0.6 kT TNT
10 m–50 m (house)	1.5 kT–200 kT	1/100 years	Local disaster, 1–600 MT TNT
50 m–100 m (soccer field)	200 kT–1.6 MT	1–2/1000 years	Regional disaster, 1 GT TNT
100 m–1 km (small village)	1.6 MT–1 GT	1/50–500 000 years	Continental disaster, > 1 GT TNT
1 km–10 km (small town)	1 GT–1.6 TT	1/10–100 million years	Mass extinction 1 TT–1 PT TNT
> 10 km	> 1.6 TT	< 1/billion years	Planet disaster

<sup>†</sup> See also Footnote 1 and <http://lexikon.astronomie.info/TNT/TNT.html>.

### 3 System concept

Meteor observations are mostly based on optic and radio methods. ASMET’s rough optical system concept consists of six basic functional groups (see Figure 2):

1. optical system (camera, heatable cover, and further sensors);
2. communication system (alarm, metadata, payload data, further stations);
3. computer system (board, data processing, archiving, distribution, and analysis);
4. thermal system (heating and cooling);

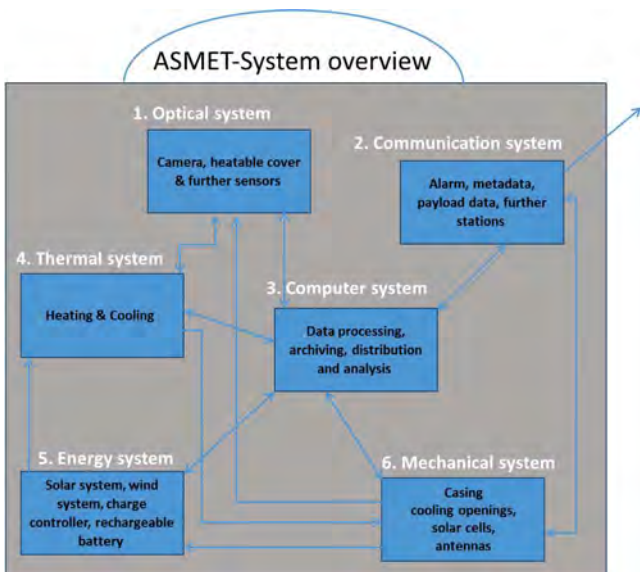


Figure 2 – ASMET system overview with relationships between functional groups.

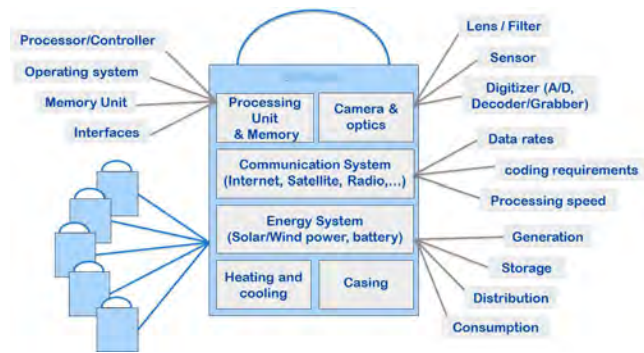


Figure 3 – ASMET functional groups with individual components and aspects.

5. energy system (solar and wind system, charge controller, rechargeable battery); and
6. mechanical system (casing, cooling openings, solar cells, antennas).

Optional additional sensors can also be added: rain sensor, wind gauge, seismic sensor, hygrometer, temperature measuring instruments, etc.

Based on the rough system concept, we develop a detailed top-down description of the individual components (Figure 3) for each of the six functional groups in the following subsections.

#### 3.1 Functional group “Optical system”

A typical optical system consists of the following components:

- external contactor (transparent glass dome, dome heating, temperature, rain, humidity sensor, O-ring, twilight switch module);

Table 4 – Optical and computer system concepts.

Concept A	Concept B	Concept C
Common products	Custom embedded	Futuristic technologies
Components off-the-shelf	Multi-sensor cams	Dynamic, neuron processing
Fisheye cam	Camera array	DAVIS sensor
Single Board (industrial) PC	Intelligent camera base unit	SNAP neuron processor
Prototype 1	Prototype 2	Next projects

- camera system (fisheye lens/lens, aperture, image intensifier, imaging lens/filter, (CCD or CMOS) sensor/camera, digitizer (A/D converter, decoder/grabber); and
- internal housing (lightweight, plastic) due to modularity (UR2000), adaptability, and easy interchangeability (with the opening for the supply of CPU hot air for drying the fish eye and dome and connected cables).

There exist basically three approaches to video observation of the entire sky: reflective (curved) mirrors, fish-eye lenses, and camera array. In the future, the development of Dynamic and Active-pixel VISION Sensors (DAVIS) could play an important role for high-speed vision applications (Tedaldi, 2016). We decided to study two system concepts (Table 4): Concept A with fish-eye lens Cam (MATRIX VISION mvBlueFOX3) and Concept B with four embedded 130° Cams (VRmagic VRmS-12/BW-COB M12 IR-Cut).

### 3.2 Functional group “Communication system”

In order to get a rough estimate of the communication needs, we use a simple (best guess) calculation of the frequency and usual duration of the meteor phenomenon. Furthermore, we want to distinguish, as with other M2M applications, between “control” and “monitoring”. The aspect of “system tracking” is not relevant to the ASMET project because the individual systems are stationary and do not move. “Control” requires a bidirectional low rate communication (telemetry data, such as Alarm-E-Mail with thumbnails, and telecommands, such as camera settings), and “monitoring” requires unidirectional high-rate transmission of event videos (e.g., meteors). Assuming that there are usually about 30 meteors per day (and night) with an average duration of 4 seconds, 120 seconds of transmitted payload data (video material) will be transmitted. Assuming an HD camera with at least 30 fps and a resolution of  $1920 \times 1080 = 2\,073\,600$  pixels results in 3600 (120 s  $\times$  30 fps) frames per day with 9.3 MB (12 bit  $\times$  3 color depth for RGB, CMOS  $\times$  resolution =  $12 \times 3 \times 2\,073\,600 = 74\,649\,600$  bit) per frame results in 33 GB/day and multiplied by 30 days requires 1 TB of non-volatile memory (SSD) per month. Each video

would add 10% overhead in meta-information (timestamp and possibly other sensor data) for internal communication and backup of all payload data. For external communication, however, only one event per day, of a length of 4 s, is sufficiently interesting (fireball, unrecognized event) to be uploaded to the server via satellite (push). Then, this takes 120 frames with each uncompressed frame of 9.3 MB, which results in at least 1.2 GB/day (including meta-information). In addition, the users could find a pair of thumbnails worth exploring and manually request further (uncompressed) videos (pull, via low rate communication). Such a video upload takes up to 30 minutes via commercial providers such as skyDSL2+ FLAT L Premium (upload 6 Mbit/s). In summary, there are four possible transfers to users:

- text-alarm only per e-mail;
- text-alarm per e-mail, with preview image attached;
- compressed video (system-AI decides to send);
- uncompressed video (user decides).

Communication channels and interactions with other observation stations will be developed in further work based on communication in satellite swarms.

### 3.3 Functional group “Computer system”

#### 3.3.1 Hardware-functional scenario

After we decided to install a single board (industry) PC in ASMET and to compare different models, we decided to use Axiomtek’s Pico-ITX Embedded Board<sup>2</sup> for the first prototype. We have compared the following criteria with regard to the fulfillment of primary objectives: CPU, graphic, data handling (operating system, SATA), communication channels (ethernet, USB, PCI), expandability and energy budget. Further prototypes are to be equipped with cheaper and more energy-efficient SBCs, such as LattePanda and Raspberry PI 3/Module. In Concept B, we use the D3 Intelligent Camera Platform<sup>3</sup>, which is available in combination with the four VRmagic Cams.

#### 3.3.2 Software-functional scenario

For meteor detection and analysis, it was decided to write our own custom software. There are countless examples of similar software (ASGARD, SANDIA, METEORSCAN, METREC, UFOCAPTURE, WSENTINEL, ASTRORECORD, ASTROVIDEO, LUCAM RECORDER, METEOR44, MOTION, CMN\_BINVIEWER, UFOID with cascade classifier, RECAP, and other OEM software and

<sup>2</sup><http://www.axiomtek.com/Default.aspx?MenuId=Products&FunctionId=ProductView&ItemId=8931&upcat=137>.

<sup>3</sup>[https://www.vrmagic.com/vrmagic-imaging/oem-solutions/camera-platforms/..](https://www.vrmagic.com/vrmagic-imaging/oem-solutions/camera-platforms/)

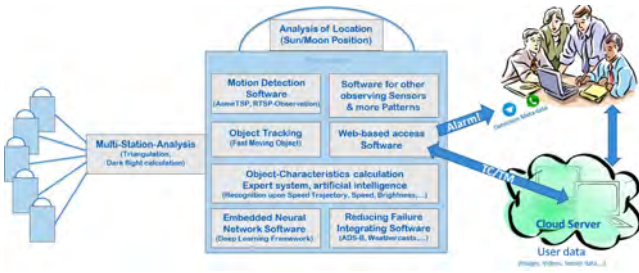


Figure 4 – ASMET Basic software concept.

detection algorithms), but we have decided to develop ASMETTSP software for university use for further customization and to improve existing ideas. Basic framework of the ASMETTSP software is a GUI programmed by students in C++ with QT-Cross-platform software development for embedded and desktop and OpenCV-Open Source Computer Vision Libraries for motion detection and analysis. This software is gradually being updated with sensor data and trained neural networks (Figure 4). We also use the common software UFO-CAPTURE as reference software.

### 3.3.3 Data storage, distribution and archiving

On the basis of user requirements (Table 1), the data concepts for storage, distribution, and archiving are worked out, e.g., the system should back up the detections of at least 7 past days in off-line mode, the detection metadata shall be available to the user no later than 3 minutes after detection, and the payload (full) data should become available to the user 24 hours after remote detection at the latest.

## 3.4 Functional group “Thermal system”

Regarding to a very harsh environment, heating and cooling aspects will be tested and gradually improved in the first prototype (Figure 5).



Figure 5 – First Prototype ASMET1.

## 3.5 Functional group “Energy system”

Power system with Sun module, rechargeable battery, solar controller, Webbox-LCD for online monitoring and long-term statistics, as well as fuses and lightning protection have been set up. In the next prototype, more attention has to be paid to include the full number of 3 solar panels and consider more low-power components, to evaluate the self-sufficient operation capabilities.

## 3.6 Functional group “Mechanical system”

A sketch of the housing for the first prototype (Concept A) was custom-made by us and commissioned to a company for production. Regarding Concept B, we will design the array mount for VRmagic cameras so that with 20° elevation and four overlapping fields of view, we can cover the entire sky

## 4 Conclusion and outlook

This paper is a description of the Project ASMET and its prototyping and testing phase. More detailed analyses and further prototypes are in preparation to integrate the “observation” and “analysis” of meteors and other transient celestial phenomena in better quality.

The task of the observation procedure is to set up and use autonomous observation systems with different kinds of sensors and algorithms to detect such transient phenomena as meteors are. The task of the analysis procedure is to analyze the meteor phenomenon itself but also all surrounding aspects like weather, air and space traffic, and astronomical situation, and to compare and combine these data with the results from other networked stations. This makes it necessary to have integrated and networked intelligent systems for observation, detection, and analysis with the specific time and location of the observation. By autonomous and synchronous observation of the same meteor from different locations with several different methods (e.g., optical and radio), including neural network analysis, more precise results can be extracted.

In addition to the primary project goals, the following secondary goals as next steps for future developments and subsequent projects are also considered:

- full autonomy;
- opening up of hard-to-reach, sparsely populated areas to the observation network;
- supplementation by additional instruments/sensors (e.g., environmental sensors);
- analysis and calculation of the trajectory and orbit;

- acquisition of comprehensive scientifically based data on so-called Unidentified Aeronautical Phenomena (UAPs) and their detection.

Long-term goals, in addition to education of university students, are to give students the opportunity to carry out interdisciplinary and practice-oriented research with their own prototypes resulting in diverse topics for final studies.

The currently available low-power single-board PCs and measuring instruments for sky observation have more performance and they are also more precise and lower-priced than before, which can be clearly seen, e.g., in the rapid development of the market for the commercial AllSky 360° HD 3D VR Cams with one or more lenses<sup>4</sup>. The open source software with countless libraries, databases and advances in autonomous driving and flying systems is also developing better and smarter than ever, e.g., the newest version of OpenCV supports deep neural networks (“createCaffeImporter”), as well as new and improved algorithms for important functions such as calibration, optical flow, image filtering, segmentation, and feature detection<sup>5</sup>. Novel end-to-end artificial intelligence products as system-on-chip (SOC) with dedicated Neural Compute Engine vision processing unit (VPU) and dedicated hardware accelerator for deep neural network inferences are appearing more and more on the market.

Area-wide, multistational observations will also allow orbital distributions to be determined. The atmosphere strongly reduces both the UV and IR range so that the best data in this range may come from cameras on small satellites<sup>6</sup> (meteors were also observed on other planets). Combining all of these aspects can help us to develop better methods to measure more accurate meteor characteristics optically and with all other methods.

## Acknowledgement

The project ASMET is funded by the European Regional Development Fund (ERDF) and with the support of the Bavarian Ministry of Education and Culture, Science, and Art and Government of Lower Franconia. We would also like to thank our project students,

partners, and consultants, as well as the University of Würzburg for providing the facilities for prototype installations and university Service Centre Research and Technology Transfer (SFT) for support.

## References

- Beatty K. (2006). *How Much Space Debris Falls into Earths Atmosphere Every Year?*. National Geographic Society.
- Brown P. G., Assink J. D., Astiz L., Blaauw R., Boslough M. B., Borovička J., Brachet N., Brown D., Campbell-Brown M., Ceranna L., Cooke W., de Groot-Hedlin C., Drob D. P., Edwards W., Evers L. G., Garces M., Gill J., Hedlin M., Kingery A., Laske G., Le Pichon A., Mialle P., Moser D. E., Saffer A., Silber E., Smets P., Spalding R. E., Spurný P., Tagliaferri E., Uren D., Weryk R. J., Whitaker R., Krzeminski Z. (2013). “A 500-kiloton airburst over Chelyabinsk and an enhanced hazard from small impactors.” *Nature*, **503**, 238–241.
- Campbell-Brown M. (2016). “Results from the Canadian Automated Meteor Observatory”. In Roggemans A. and Roggemans P., editors, *Proceedings of the International Meteor Conference*, Egmond, the Netherlands, 2–5 June 2016. IMO, pages 50–52.
- Hanslmeier A. (2007). *Einführung in die Astronomie und Astrophysik*. Second edition. Springer Spektrum.
- Mohn H., Balagurin O., Kayal H. (2015). “Autonome Beobachtung von Transient Lunar Phenomena”. In *Deutscher Luft- und Raumfahrtkongress 2015*. Document id. 370114.
- Summers C. and Allen C. (2000). *Cosmic Pinball: The Science of Comets, Meteors, and Asteroids*. McGraw-Hill.
- Tedaldi D., Gallego G., Mueggler E. and Scaramuzza D. (2016). “Feature detection and tracking with the Dynamic and Active-pixel Vision Sensor (DAVIS)”. In *Proceedings 2nd International Conference on Event-Based Control, Communication, and Signal Processing*, Krakow, Poland, 13–15 June 2016. IEEE.

<sup>4</sup><http://thewirecutter.com/reviews/best-360-degree-camera/>.

<sup>5</sup>[http://docs.opencv.org/3.3.0/d6/d0f/group\\_\\_dnn.html](http://docs.opencv.org/3.3.0/d6/d0f/group__dnn.html).

<sup>6</sup><http://www8.informatik.uni-wuerzburg.de/en/wissenschaftsforschung/sonate/>

# Brazilian video monitoring meteors network EXOSS: Status and first results—a citizen science project

Marcelo De Cicco<sup>1,2,3</sup>, Daniela Lazzaro<sup>1</sup>, Eduardo P. Santiago<sup>3</sup>, and EXOSS team<sup>3</sup>

<sup>1</sup>INMETRO, Divisão de Metrologia de Materiais,  
Av. Nossa Senhora das Graças 50, Duque de Caxias, 25250-020, Brazil.  
decicco10@gmail.com

<sup>2</sup>Observatório Nacional, Rua Gal. José Cristino 77, 20921-400, Brazil.  
lazzaro@on.br

<sup>3</sup>EXOSS.org, Brazil.  
eduardopsok@gmail.com

EXOSS—EXplOring the Southern Sky for new meteor radiants—is a citizen science project network aimed primarily to register meteors and fireballs or bolides using CCTVS low-cost cameras and meteor analysis suite software for video capturing and astrometry, evaluating (i) trajectories, (ii) velocities, (iii) radiants, (iv) orbits, and (v) light curves. The network is a social non-profit organization, constituted by amateurs scientists collaborating with professional astronomers. Currently, the network is composed of 66 stations, with 44 collaborators and 8 partners

## 1 Introduction

The EXOSS—EXplOring the Southern Sky for new meteors radiants—project is a citizen science project network that started its operations on May 2015. The aim of the project is primarily to register meteors and fireballs or bolides using CCTVS low-cost cameras and meteor analysis suite software for video capturing and astrometry (Molau and Gural, 2005), evaluating: (i) trajectories, (ii) velocities, (iii) radiants, (iv) orbits and (v) light curves (Ceplecha, 1987). The network is a social non-profit organization, constituted by non professional scientists collaborating with meteor science researchers.

### 1.1 Foundations

The initiative started on May 2015, with the union of a professional astronomer, Marcelo De Cicco, and nine amateurs, headed by Eduardo P. Santiago, Luciana Fontes, and Marco Mastria., committed to volunteer working and the development of the team as a whole, adopting the “Citizen Science” concept, that provides the opportunity to do scientific research to science enthusiasts or amateur scientists.

A year after founding EXOSS, a camera was set on OASI (Observatório Astronômico do Sertão de Itacuruba, in Pernambuco State, Brazil), creating our first partner network, called R-OASI (Rede OASI, Figure 1).

## 2 EXOSS network

The setup of EXOSS network is constituted by CCTVS for meteors video monitoring which are small CCD cameras, with 1/3" sensor, based on the Sony EXview HAD architecture, no IR-filter, and fast lens configurations  $f/0.9$  to  $f/1.2$ , near IR-corrected (aspherical lens), with

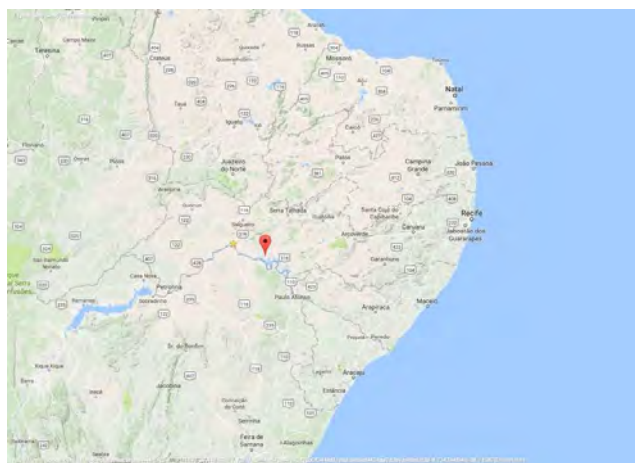


Figure 1 – Map showing northeastern Brazil. The red marker indicates the center of the R-OASI network

a field of view in the range of  $50^{\circ}$ – $80^{\circ}$ . In Figure 2, we show a typical EXOSS station.

Currently, the network consists of 66 working stations, with 44 collaborators and 8 partners covering 13 Brazilian states as shown in Figure 3.

Despite being essentially a network of volunteer people, the EXOSS project also has done many partnerships with several educational institutions, implementing more stations, for example, two cameras are operating on the campi of the Observatório Nacional and another one at the Observatório do Sertão de Itaparica (R-OASI). Another nine stations are being implemented in the Northeastern region of Brazil in order to increase the coverage, they are being installed on educational public institutions, as INSA (Instituto Nacional do Semi-Árido), on Campina Grande, Paraíba State and UFRPE (Universidade Rural de Pernambuco), on Recife, Pernambuco State.



Figure 2 – Four cameras setup of the EXOSS station in Itu, in São Paulo state.

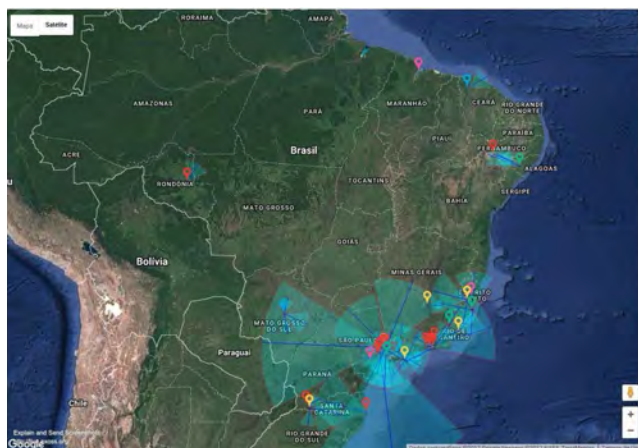


Figure 3 – Map of Brazil showing the EXOSS network.

Six cameras are already operating at OMCJN (Observatório Municipal de Campinas Jean Nicolini), one camera at UNIVAP (Universidade do Vale do Paraíba), one camera at UFES (Universidade Federal do Espírito Santo), one camera at UFRJ/OV (Universidade Federal do Rio de Janeiro-Observatório do Valongo), one camera at the public high school *Agostinho Neres Portela* in Sobral, Ceara State, and two cameras at UFMS (Universidade Federal do Mato Grosso do Sul).

## 2.1 Overview of the organization

The volunteers are the main source of EXOSS’s strength, as they keep operating the cameras, performing three basic tasks: (1) distinguishing captures from false positives, (2) astrometric analysis (using UFOANALYZER), and (3) synchronizing the final results with a specific database.

The EXOSS Database (DB) holds all files outputs from captures, analyses, and orbits, using a MYSQL formatting structure, so it is possible exploring data using SQL queries. In Figure 4, we show a “front end” after data extraction from DB.

Also, to maintain quality standards for our results from captures to final meteor orbits, the EXOSS project has developed training modules that allow newbies, leveled and all other volunteers updated with good practices that can be accessed through an on-line portal, as shown in Figure 5.

The network is managed by a Board of Coordinators. The Board consists of four members, Eduardo P. Santiago, Luciana Fontes, Marcelo De Cicco, and Marco Mastria dividing the various tasks among each other. The members of this Council are active in the following areas:

- Marcelo De Cicco: general coordinator, studies and data research, technical guidance, and representation of the EXOSS network;
- Eduardo P. Santiago: support and activation of the stations;
- Marco Mastria: software development and IT support;
- Luciana Fontes: administrative tasks, social media, and human resources.

At the base of the organization are the members who actively participate in the project, keeping the cameras operational, performing the elimination of false positives, conducting the pre-analysis, and synchronizing the results with the DB. For capturing, analyzing and orbits evaluation, the project adopts the UFO suite (Molau and Gural, 2005).

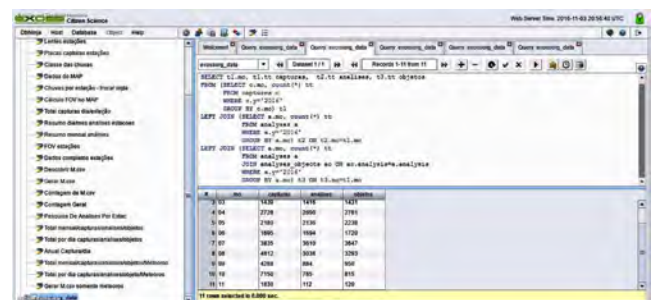


Figure 4 – DB front end, the upper right window contains a query template, and, at the bottom, the final result is shown that can be exported as .CSV, .XLS, .SQL and JSON/PHP.



Figure 5 – An image from the EXOSS support and training portal.

Besides meteor video monitoring, many others activities related to meteors studies are being conducted by EXOSS and its team, such as

- lunar impact monitoring<sup>1</sup>—two EXOSS members, Carlos Henrique Barreto and Tiago Torres, are periodically observing the Moon for impact detections;
- IMO fireball report—Eduardo P. Santiago disseminates the IMO fireball tool in Portuguese<sup>2</sup> and manages Latin-American reports;
- scientific outreach—videos about coming meteor showers on YouTube, news about fireballs and general information related to small bodies and planetary field published on the EXOSS webpage<sup>3</sup> and on many other social media like Facebook, Instagram, and Twitter.

### 3 First results

In the period May 2015–May 2017, a total of 28 000 single meteors were registered (using Q1 UFO quality), as shown in Figure 6. Of these totals, 1624 are multi-station meteors and 1276 orbits could be evaluated.

The above histogram shows an average of 690 meteors per station. Only four stations got more than 2000

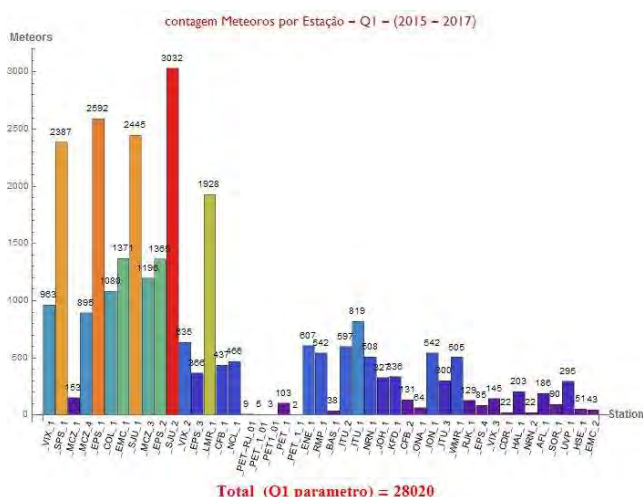


Figure 6 – Absolute frequency histogram of meteors per station.

meteors. Many factors contributed for those figures, such as camera calibration, operator experience, local weather, and starting date of the station's operation.

An efficiency of 6% was obtained in terms of the total number of orbits calculated from 28 000 meteors, 94% of which are double-station and the remaining 6% are three- or more multi-station captures.

### Acknowledgements

The EXOSS project is carried out with voluntary contribution by a large number of amateur astronomers to whom we are grateful for their continuous efforts. Our thanks are due to the people of the EXOSS team mentioned on the EXOSS website<sup>4</sup>

### References

- Ceplecha Z. (1987). “Geometric, dynamic, orbital and photometric data on meteoroids from photographic fireball networks”. *Bulletin of the Astronomical Institutes of Czechoslovakia*, **38**, 222–234.
- Molau S. and Gural P. S. (2005). “A review of video meteor detection and analysis software”. *WGN, Journal of the International Meteor Organization*, **33**, 15–20.

<sup>1</sup><http://press.exoss.org/projetos-2/impacto-lunar/>.

<sup>2</sup><http://bolido.exoss.org>.

<sup>3</sup><http://press.exoss.org>.

<sup>4</sup><http://press.exoss.org/associados/estacoes-associadas-a-exoss/>.

## FRIPON—Status of radio and optical network

F. Colas<sup>1</sup>, M. Birlan<sup>1,16</sup>, J.-L. Rault<sup>2</sup>, B. Zanda<sup>3</sup>, S. Bouley<sup>4</sup>, J. Gattacceca<sup>5</sup>, J. Vaubaillon<sup>1</sup>, P. Vernazza<sup>6</sup>, S. Jeanne<sup>1</sup>, L. Jorda<sup>6</sup>, C. Marmo<sup>4</sup>, A. Steinhauser<sup>3</sup>, K. Baillie<sup>1</sup>, A. Egal<sup>1</sup>, C. Blanpain<sup>7</sup>, J. Lecubin<sup>7</sup>, A. Malgoyre<sup>7</sup>, S. Caminade<sup>8</sup>, M. Marsset<sup>9</sup>, D. Gardiol<sup>10</sup>, A. Cellino<sup>10</sup>, M. Di Martino<sup>10</sup>, D. Koschny<sup>11</sup>, A. Toni<sup>11</sup>, R. Rudawska<sup>11</sup>, H. Lamy<sup>12</sup>, E. Jehin<sup>13</sup>, B. Poppe<sup>14</sup>, E. Drolshagen<sup>14</sup>, T. Ott<sup>14</sup>, G. Drolshagen<sup>14</sup>, S. Molau<sup>2</sup>, L. Ferrière<sup>15</sup>, A. Nedelcu<sup>1,16</sup>, and S. Ribas<sup>17</sup>

<sup>1</sup> Institut de Mécanique Céleste et de Calcul des Ephémérides, CNRS UMR 8028, Observatoire de Paris, PSL Research University, 77 av. Denfert Rochereau, 75014 Paris, France  
francois.colas@imcce.fr, mirel.birlan@imcce.fr, simon.jeanne@obspm.fr, jeremie.vaubaillon@obspm.fr, kevin.baillie@obspm.fr, and auriane.egal@obspm.fr

<sup>2</sup> International Meteor Organization  
f6agr@orange.fr

<sup>3</sup> Muséum National d'Histoire Naturelle, 75005 Paris, France  
brigitte.zanda@mnhn.fr and asma.steinhauser@mnhn.fr

<sup>4</sup> Géosciences Paris Sud, Université Paris Sud, Université Paris-Saclay, Orsay, France  
sylvain.bouley@gmail.com and chiara.marmo@u-psud.fr

<sup>5</sup> CEREGE, CNRS, Aix-en-Provence, France  
gattacceca@osupytheas.fr

<sup>6</sup> Laboratoire d'Astrophysique de Marseille, Université d'Aix-Marseille, 13007 Marseille, France  
pierre.vernazza@lam.fr and laurent.jorda@lam.fr

<sup>7</sup> OSU Pythéas, CNRS, Université d'Aix-Marseille, 13007 Marseille, France  
blanpain@osupytheas.fr, julien.lecubin@osupytheas.fr, and adrien.malgoyre@osupytheas.fr

<sup>8</sup> Institut d'Astrophysique Spatiale, Université Paris Sud, Université Paris-Saclay, Orsay, France  
stephane.caminade@ias.u-psud.fr

<sup>9</sup> Astrophysics Research Centre, Queens University, Belfast, BT7 1NN, Northern Ireland  
michael.marsset@qub.ac.uk

<sup>10</sup> INAF, Osservatorio Astrofisico di Torino, Torino, Italia  
gardiolo@oato.inaf.it

<sup>11</sup> European Space Agency, ESA/ESTEC, Keplerlaan 1, 2201 AZ Noordwijk, the Netherlands  
detlef.koschny@esa.int, andrea.toni@esa.int, and regina.rudawska@esa.int

<sup>12</sup> Royal Belgian Institute for Space Aeronomy, Brussels, Belgium  
herve.lamy@aeronomy.be

<sup>13</sup> Space Sciences, Technologies and Astrophysics Research Institute, Université de Liège, Belgium  
ejehin@uliege.be

<sup>14</sup> University of Oldenburg, Ammerländer Heerstraße 114, 26111 Oldenburg, Germany  
{theresa.ott, esther.drolshagen, bjoern.poppe, gerhard.drolshagen}@uni-oldenburg.de

<sup>15</sup> Natural History Museum, Vienna, Austria  
ludovic.ferriere@univie.ac.at

<sup>16</sup> Astronomical Institute of the Romanian Academy, Bucharest, Romania  
nedelcu@aira.astro.ro

<sup>17</sup> Parc Astronòmic Montsec, Àger, Lleida  
sjribas@montsec.cat

We present the evolution of FRIPON from its funding in 2015. As many projects, full operation mode took more time than planned, but we are now ready to detect any bright fireball over France and compute accurate orbits, trajectories, and, if we are lucky, strewn fields. Most of our delay was due to the installation of this huge network including 100 all-sky cameras and 20 radio receivers, but also to underestimating the complexity of the network itself. FRIPON is working now, and, furthermore, it is now easy to extend to Europe and to any country, as all our work will be released. Italy and northern Europe are currently installing FRIPON stations. With the GRAVES radar data, we are able to get an accuracy of a few tens of meters per second.

## 1 Introduction

FRIPON is the acronym of “Fireball Recovery and InterPlanetary Observation Network”. This project of network was founded by ANR, the French Research National Agency (Colas et al., 2014). The deployment of network started in 2015 and in 2017 approximately 90% of the network is active over France.

The aim of FRIPON is to answer questions that arise about the connections between meteorites and asteroids. It is easy to study a meteorite in a laboratory but we cannot tell where it came from. In fact, its orbit is most of the time difficult to compute.

We currently know more than 740 000 asteroids with their orbits, but only sparse or almost no physical information of this population. However, physical parameters are crucial for understanding the origin and evolution of the Solar System. Recent theories of Solar System formation and evolution (Walsh and Morbidelli, 2011) concluded that it is possible to find primitive objects in the inner part of the Main Belt of Asteroids. Some of them could hit the Earth due to some Yarkovsky non-gravitational force drifts and to the “express delivery” dynamical evolution toward the inner Solar System (Nedelcu et al., 2014). It is therefore essential to know the orbit of the observed meteors (and meteorites) and to find connections between them and their potential parent bodies.

The main goals of FRIPON are to recover fresh meteorites fallen in France and to compute accurate orbits of fireballs to identify possible new dynamical families.

The FRIPON objective is to detect and measure all the bright fireballs (negative magnitudes) over France in order to achieve the following:

- making accurate statistics on the impact flux of meteoroids hitting the Earth;
- searching for dynamical families and parent bodies of meteoroids;
- searching for meteorite falls;
- engaging in scientific outreach for meteors, meteorites, and, more globally, Solar System bodies.

The operative novelty of the FRIPON network is the required real-time operation mode from the meteors detection to the orbits and strewn field production. The final goal is to be able to trigger a field research campaign 24 hours after the detection of a meteor able to produce a meteorite. To be effective in researching the meteorite rapidly after its fall, the network Vigie-Ciel<sup>1</sup> based on a collaborative science program (Colas et al. 2015) was created in parallel to FRIPON. Such an organization allows to mobilize trained persons for quickly searching the meteorite inside the zone representing the

<sup>1</sup><http://www.vigie-ciel.org>.

ellipse of fall computed by the FRIPON automatic detection and calculus tools.

## 2 Network design

FRIPON is composed of an optical network for detection and measurement of bright fireballs. In order to get more accurate speed data, we also developed a radio network based on the military radar GRAVES (Rault et al., 2014). In order to be efficient, we used the same hardware for all the stations. All the acquisition PCs are connected on the same network (VPN, Virtual Private Network) to be easily managed. We have, e.g., a real-time evaluation of the network state (internet link, camera connection, storage space, etc.). Detections are made by the optical network.

### 2.1 Optical counterpart

The goal of the network is to detect bright meteors (presenting negative magnitudes). As these events occur not so often, the network covers the French territory (Figure 1). Theoretical estimates show that the recovery of one meteorite per year (Colas et al., 2012) is feasible by the network. Finally, in order to observe in good condition (high elevation) with several cameras, it is necessary to use a median spacing of 100 km, that is to say one hundred cameras for France. As we use digital cameras allowing short exposure time, it is possible to observe daytime events; at that time we do not use this mode as it produces too many false detections. The detection mode is triggered by Sun elevation ( $h < -6^\circ$ ).

### 2.2 Radio counterpart

An optical network is very efficient for measuring fireball geometry. For determining accurate velocities, the FRIPON network uses the GRAVES radar head echo Doppler effect that can be processed with the geometrical model obtained by the cameras. Optical speed measurement accuracy is about a few hundred meters per second; combined with radio data, we reach an accuracy of a few tens of meter per second. Speed measurement is essential for semi-axis determination and,



Figure 1 – FRIPON optical network. European extensions over Italy, BeNeLux, Germany, and Romania are also shown.



Figure 2 – GRAVES radio beacon and the position of radio antennas over France.

therefore, fundamental for pinpointing the origin of fireballs and their possible parent bodies. FRIPON records radar echoes of the French radar GRAVES used by the French Air Forces to track low-altitude artificial satellites (Rault et al., 2014). The radar is usable all over France, a 200 km spacing being sufficient for radio observatories, so only a quarter of the optical stations will have radio equipment (Figure 2).

### 3 Detection and data reduction: FreeTure and FRIPIPE

The FRIPON network developed its own software for detection of fireballs using all-sky cameras. **FreeTure** is an open source software available on the Github archive (Audureau et al., 2014). Consequently, the radio counterpart of the detection algorithm was conceived and developed (Rault et al., 2014).

Data reduction of optical and radio data were formalized into a pipeline called **FRIPIPE** (Vaubailon et al., 2018). The pipeline includes the astrometric calibration for all-sky cameras based on long-exposure images, the astrometry of each event, the computation of fireball trajectory, and the dark flight to finally get the strewn field in case of a meteorite fall.

### 4 State of the network

The network is up and running for about 90% of the detectors in optical domain. Fifteen radio stations are nominally running. To avoid false detections, we only download in our database events seen by at least two stations. We have an annual average of 2000 multiple detections. As we only observe bright events, we only detect the two bright meteor shower of the Perseids and the Geminids. Bright fireballs are most of the time disconnected from meteor showers. Several events were detected by more than 20 all-sky cameras. While four GRAVES radar beams are scanning the sky, and while the system is down from time to time for maintenance, and because of several geometry reasons, we do not have systematic radio and video coincidences, i.e., no radar

detection for a bright video event and many radio echoes of meteors unseen by cameras. An upgrade of GRAVES is planned, and we hope to get more flexibility on our regular observations.

Two campaigns of recovery of meteorite falls were organized during 2016 and 2017. Based on the computations done by FRIPIPE, the meteorite falls should have occurred near the town of Roanne (August 6, 2016) and in the forest of the Chambord Castle (March 27, 2017), both in France. A third search was also organized in Northern Italy by the Prisma network (Gardiol et al., 2016). Unfortunately, the recovery campaigns were unsuccessful into finding pieces of meteorites due to the difficulty of the terrain encountered (like big ferns in the Chambord forest). Nevertheless, they offer the opportunity to test and ameliorate the procedures of organizing such campaigns in the context of the VigieCiel and FRIPON networks.

### 5 Extension of the network

Even if the surface of France is large enough to get scientific results, it is clear that the efficiency of the network is directly proportional to its surface. It was clear that we had to extend over Europe as meteorites do not know borders! Our policy was to install FRIPON camera and computers in some countries in Europe to start collaborations. The main extension concern Italy with the Prism project (Gardiol et al., 2016). We are also extending over Northern Europe (Koschny et al., 2018) We can see the progress of the project on Figures 1 and 2 and on the FRIPON website<sup>2</sup>.

### 6 Conclusions

The FRIPON network is now operating. With our experience and feed-back we are reasonably optimistic that we can recover a meteorite in the near future. Moreover, with 2000 fireball orbits computed annually, we can start the statistical studies of possible fireball families. We suspect that these families in between meteor streams are mainly connected to comet and asteroid families. The project took more time to develop than anticipated, as we had to manage in real-time detection and data processing of one hundred cameras. The good thing, however, is that it is now easy to extend to other parts of Europe to get more results. As the entire project is open source, the extension can be done in several ways, from stand-alone stations to networks isolated from or connected to FRIPON.

### Acknowledgements

FRIPON is funded by the ANR grant N.13-BS05-0009-03. Vigie-Ciel is part of the *65 Millions d'Observateurs* project, from the *Muséum National d'Histoire Naturelle*,

<sup>2</sup><https://www.fripon.org>.

funded by the French *Investissements d’Avenir* program. FRIPON data are hosted at Integrated Data and Operation Center<sup>3</sup>. Support for IDOC is provided by CNRS and CNES. We want to thanks SIP (*Service d’Informatique Pytheas*) in Marseille for the difficult task of operating the network.

## References

- Audureau Y., Marmo C., Bouley S., Kwon M.-K., Colas F., Vaubaillon J., Birlan M., Zanda B., Vernazza P., Caminade S., Gattacceca J. (2014). “FreeTure: A Free software to capture meteors for FRIPON”. In Rault J.-L. and Roggemans P., editors, *Proceedings of the International Meteor Conference*, Giron, France, 18–21 September 2014. IMO, pages 39–41.
- Colas F., Zanda B., Bouley S., Lewin E., Vaubaillon J., Marmo C., Rotaru M., Labenne L., Julien J. F., Linares M., Steinhauser A., Rault J.-L., and Vernazza, P. (2015). “Vigie Ciel, a collaborative project to study fireballs and organise meteorite recoveries”. In *Proceedings European Planetary Science Congress*, Nantes, France, 27 September–2 October 2015. Paper id. EPSC2015-604.
- Colas F., Zanda B., Bouley S., Vaubaillon J., Vernazza P., Gattacceca J., Marmo C., Audureau Y., Kwon M.-K., Maquet L., Rault J.-L., Birlan M., Egal A., Rotaru M., Birnbaum C., Cochard F., and Thizy O. (2014). “The FRIPON and Vigie-Ciel networks”. In Rault J.-L. and Roggemans P., editors, *Proceedings of the International Meteor Conference*, Giron, France, 18–21 September 2014. IMO, pages 34–38.
- Colas F., Zanda B., Vernazza P., Vaubaillon J., Bouley S., Gattacceca J., Baratoux D., Birlan M., Cournede C., Fieni C., Hutzler A., Jambon A., Maquet L., Mousis O., Rochette P., Strajnic J., and Vachier, F. (2012). “(FRIPON) Fireball Recovery and InterPlanetary matter Observation Network”. *Proceedings ACM*, Niigata, Japan, May 16–20, 2012. Paper id. 6426.
- Gardiol D., Cellino A., and Di Martino M. (2016). “PRISMA, Italian network for meteors and atmospheric studies”. In Roggemans A. and Roggemans P., editors, *Proceedings of the International Meteor Conference*, Egmond, the Netherlands, 2–5 June 2016. IMO, pages 76–79.
- Koschny D., Rudawska R., Zender R., Colas F., Vaubaillon J. (2017). “FRIPON-NL—The first FRIPON camera in the Netherlands”. In Gyssens M. and Rault J.-L., editors, *Proceedings of the International Meteor Conference*, Petnica, Serbia, 21–24 September. IMO, pages 10–12.
- Nedelcu D. A., Birlan M., Popescu M., Bădescu O., and Pricopi D. (2014). “Evidence for a source of H chondrites in the outer main asteroid belt”. *Astron. Astrophys.*, **567**, L5.
- Rault J.-L., Colas F., and Vaubaillon J. (2014). “Radio set-up design for the FRIPON project”. In Rault J.-L. and Roggemans P., editors, *Proceedings of the International Meteor Conference*, Giron, France, 18–21 September 2014. IMO, pages 185–186.
- Vaubailon J., Egal A., Kwon M.-K., Marmo C., Birlan M., Jeanne S., Rault J.-L., Blanpain C., Lecubin J., Maltgoyre A., Colas F., Bouley S., Caminade S., Vernazza P., Gattacceca J., and Zanda B. (2018). “FRIPON: the FRIPON pipeline”. In Gyssens M. and Rault J.-L., editors, *Proceedings International Meteor Conference*, Petnica, Serbia, 21–24 September 2017. IMO, pages 53–55.
- Walsh K. J. and Morbidelli A. (2011). “The effect of an early planetesimal-driven migration of the giant planets on terrestrial planet formation”. *Astron. Astrophys.*, **526**, A126.

<sup>3</sup>IDOC, <https://idoc.ias.u-psud.fr>.

# Installation of the Mendocino College-Ukiah International Latitude Observatory meteor project

Timothy W. Beck<sup>1</sup>, Martin Bradley<sup>2</sup>, Daniel Hunchard<sup>1</sup>, Crystal Morataya<sup>1</sup>,  
Jeremy Ronco<sup>1</sup>, and Chatnaee Upton<sup>1</sup>

<sup>1</sup> Mendocino Community College, Ukiah, CA 95482, USA

<sup>2</sup> Ukiah International Latitude Observatory, Ukiah, CA 95482, USA

In autumn 2017, the Ukiah International Latitude Observatory has been preparing to take astronomical data for the first time since the International Earth Rotation and Reference Systems Service (IERS) ended visual observations in 1982 after 83 years. In conjunction with cameras to be installed at the Mendocino College North County campus, our project hopes to extend the CAMS network into the rural Redwood Empire of northern California. The collaborators seek to expand the role of the Observatory as an educational and interpretive center and create original research opportunities for scientific-minded students at the College. We present photos of our nascent project and solicit constructive input.

## 1 Mendocino College

Mendocino-Lake Community College District is a small community college located in a large rural area in northern California (see Figure 1). The district encompasses approximately 8300 km<sup>2</sup> and serves around 3000 full-time students. The college currently consists of a main campus in Ukiah; satellite campuses in Willits, Fort Bragg, and Lakeport (Lake County); as well as the Point Arena Field Research Station on the bluffs overlooking the Pacific Ocean.



Figure 1 – Location of Mendocino County in northern California.

## 2 Ukiah Latitude Observatory

In 1895, the International Geodetic Association (IGA) called for an unprecedented international effort to observe and measure the wandering of the Earth's pole and its resulting variation of latitude. The United States Coast and Geodetic Survey became involved, and, by 1899, the IGA had established six International Latitude Observatories at 39°08' N: three in the United States, and one each in Italy, Russia, and Japan. Only two of the United States latitude observatories survive today. The various stations continued to function until



Figure 2 – Sign showing the coordinates at Ukiah International Latitude Observatory.

advances in computer technology and satellite observations rendered them obsolete in 1982. The data collected by the observatories over the years still have use to scientists, and have been applied to studies of polar motion, the physical properties of the Earth, climatology, and satellite tracking and navigation.

The Ukiah International Latitude Observatory property was deeded to the City of Ukiah and currently serves as a public park. The observatory itself is used as an interpretive and educational center for the surrounding community. However, as of 2017, we are extending its mission to once again include astronomical observations.

## 3 The project

Our group has constructed two CAMS stations, each consisting of two cameras. One is currently installed at the observatory and is taking nightly data, which have been used to perform calibrations and optimize the camera settings in anticipation of the installation of the second station. While we initially intended for

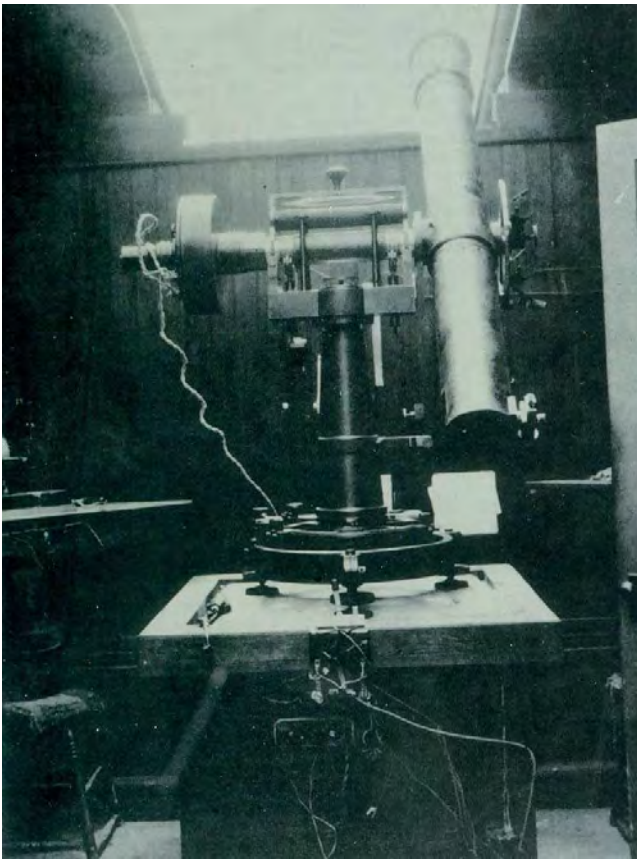


*Figure 3* – Zenith telescope used at Ukiah International Latitude Observatory.

the second station to be located at the North County Campus in Willits, we no longer believe this is optimal for calculating trajectories. We will install the second set of cameras 75 km south in Sonoma County, with the future possibility of relocating it or adding a third site at the Point Arena Field Station within the district.

#### 4 Goals

The collaboration between Mendocino College and the Ukiah International Latitude Observatory has been a



*Figure 4* – CAMS station used in the project.

goal unto itself, a union of the historical and present day hubs of scientific activity in our area. And while a significant component of our project is outreach to the scientifically minded youth of Mendocino County, we believe that our local viewing conditions will generate useful data in a presently neglected portion of the night sky. Once confident we are using our cameras successfully, we plan to upgrade each site to at least eight cameras. We ultimately hope to integrate our observations with the wider San Francisco Bay Area CAMS community located to the south.

#### Acknowledgements

We would like to thank the Mendocino College Foundation for providing primary funding to acquire our computers, cameras, and other apparatus. We would also like to thank the City of Ukiah for supporting our efforts to repurpose the historical observatory.

Finally, we would like to thank Damir Šegon and Peter Gural for all of their invaluable insight and advice in helping us get this project started.

# Brazilian Meteor Observation Network: History of creation and first developments

Leonardo S. Amaral<sup>1</sup>, Lauriston S. Trindade<sup>1</sup>, Carlos A. P. B. Bella<sup>1</sup>,  
 Marcelo L. P. V. Zurita<sup>1</sup>, Renato C. Poltronieri<sup>1</sup>, Gabriel G. Silva<sup>1,2</sup>,  
 Cristóvão J. L. Faria<sup>1,3</sup>, Carlos F. Jung<sup>1,4</sup>, and Jakub A. Koukal<sup>5,6</sup>

<sup>1</sup> BRAMON—Brazilian Meteor Observation Network, Nhandeara, Brazil  
 lsamaral\_ios@hotmail.com, lauristontrindade@yahoo.com.br, carlos.pbella@gmail.com,  
 marcelozurita@gmail.com, and rcpoltronieri@gmail.com

<sup>2</sup> Instituto de Química, Universidade de São Paulo, São Paulo, Brazil  
 gabrielg@iq.usp.br

<sup>3</sup> SONEAR—Southern Observatory for Near Earth Asteroids, Oliveira, Brazil  
 cjacqueslf@gmail.com

<sup>4</sup> Departamento de Engenharia de Produção, Faculdades Integradas de Taquara, Taquara, Brazil  
 carlosfernandojung@gmail.com

<sup>5</sup> Valašské Meziříčí Observatory, Valašské Meziříčí, Czech Republic

<sup>6</sup> SMPH—Society for Interplanetary Matter, Brno, Czech Republic  
 j.koukal@post.cz

One way to learn more about the space environment in the terrestrial neighborhood is studying the annual flow of meteors that reaches our planet. Long-lasting projects and surveys have been dedicated to observing the sky with the purpose of capturing meteors, and generating large databases that allow searching for patterns in the sporadic meteor background and the identification of meteors associated with large and minor meteor showers. Most of the projects, however, are located in the northern hemisphere, making it difficult to detect southern hemisphere meteor showers. Thus, in order to increase the representativeness of meteor observation in this area and to allow the search for new radiants, BRAMON—the Brazilian Meteor Observation Network—was created, aiming to be a meteor-monitoring network based in Brazil. This work presents the network and the development of its first data-mining tool, necessary for its operation and search for new meteor showers. Using algorithms dedicated to the search for, and validation of, new radiants, the developed software called ENCONTREITOR was able to find at least 108 possible new radiators so far in open access databases. In conclusion, it was shown that there is a willingness among the public to develop a collaborative meteor-monitoring network in the molds of citizen science, even in a country with a tradition in scientific research that is still in development. In addition, the created software proved to be a robust tool to search for new radiants. In this way, the network is preparing to present the new meteor showers obtained by ENCONTREITOR, validating the findings, to the Meteor Data Center. Meanwhile, there are plans in other research areas involving meteors and other atmospheric events like Transient Luminous Events.

## 1 Introduction

Meteors are common phenomena in which a meteoroid collides with the upper atmosphere of a planet. A meteoroid travels through the space following a path determined by its orbit and, at the moment it penetrates the atmosphere, the direction from where it seems to come from is called the radiant. Some events, like the passage of an active comet, can generate streams with a large number of particles that follow the same orbit. If Earth intercepts this stream, a high number of meteors can be detected seemingly radiating from a single area in the sky, in what is called a meteor shower. Any meteor detected that does not belong to any of the known meteor showers is called a sporadic meteor (Ceplecha et al., 1998).

Large and long-lasting radar surveys and optical observation projects have collected a great volume of data on both sporadic meteors and meteor showers. Using mathematical and statistical tools, it is possible to search through the databases of these projects, allowing the identification of minor showers not previously noted (e.g., Šegon et al., 2015). Most of these projects are located in the northern hemisphere, making infeasible the detection of a representative number of meteors in the higher latitudes of the southern hemisphere (Campbell-Brown and Jones, 2006). More recently, new projects dedicated to filling this gap have been proposed (Janches et al., 2015; Jenniskens et al., 2016).

To expand the coverage area of the meteor surveys and to provide more reliable meteor orbital data on the

southern hemisphere, the authors of this paper and many other collaborators have created the first Brazilian optical meteor detection network based on recording stations, namely BRAMON—the Brazilian Meteor Observation Network. To support the search for new meteor shower radiants, it was necessary to develop a robust tool capable of finding patterns of new showers in this growing database. The development of this tool required constant testing of the underlying algorithms on real data, so, major open-access databases were investigated, namely the SonotaCo and EDMOND databases. This paper describes briefly the creation and implementation of BRAMON and the initial development of the ENCONTREITOR software, dedicated to finding and validating new minor meteor showers. Already 108 possible new radiants of meteor showers were identified with it.

## 2 BRAMON

### 2.1 The network

The Brazilian Meteor Observation Network or BRAMON is a scientific organization whose mission is to develop, promote and disseminate science and technology, especially the study of meteors, their origins and nature, and the characterization of their orbits. It is a non-profit collaborative network maintained by volunteers, bringing together several meteor-monitoring operators with the prime purpose of producing scientific data and providing them to the community, and this by analyzing the records acquired by the monitoring stations. In addition to the traditional astrometric analyses performed for sporadic meteor and meteor shower research, other activities can be developed with the data acquired with the cameras: obtaining spectra of meteors and other atmospheric phenomena with the use of diffraction gratings coupled to the cameras; triangulation and calculation of the trajectory of bright meteors to estimate possible strewn fields of meteorites (Rendtel, 2017); detection of other interesting phenomena such as sprites, blue jets, and other TLEs—Transient Luminous Events (Campbell-Burns and Kacerek, 2014); and observation of satellites and other artificial objects' reentry or whose orbit determination is of interest.

To encourage the participation of all members, BRAMON is constantly updating its database of good and low-cost materials and equipment. This allows the constant construction of new stations and guarantees the quality of the data obtained by the group. In the same way, the team is dedicated to keep operators well informed and oriented so that the best pointing and triangulation solutions are achieved. In addition, through the ideal of citizen science (Socientize, 2013), we seek the commitment of the public in the activities promoted by the network, allowing everyone to be able to contribute actively to the accomplishment of scientific research. In this context, the network not only conducts meteor-monitoring activities, but also promotes public observations and transmissions of meteor showers with the help of social networks. It also disseminates



Figure 1 – Coverage of the BRAMON camera network as of end 2016.

meteoritics in schools, colleges, universities, astronomy clubs, and official entities of study within the country.

### 2.2 Brief history

The first meteor monitoring station was set up by Professor Alberto Silva Betzler, in the state of Bahia, in 2005. In 2006, a station was put in operation by Professor Maria Elizabeth Zucolotto, curator of the meteorite collection at the Museu Nacional (National Museum) in Rio de Janeiro. The goal was to develop a national network solely to watch for bright meteors with the potential of meteorite dropping, in order to allow the determination of a more precise trajectory for the bolide, improving and simplifying the processes of finding and recovering the fragments. The idea was presented during the 10<sup>th</sup> ENAST—Encontro Nacional de Astronomia (National Astronomy Meeting)—in 2007, and caught attention of people who wanted to create a national meteor observation network. In the following years, some new stations became active, but the all-sky project could not flourish as planned mainly because of technical difficulties and the high cost of equipment.

In 2013, there was a new attempt to create a meteor-monitoring network, this time led by the amateur astronomers André Moutinho, Carlos Augusto di Pietro Bella, Eduardo Plácido Santiago, and Renato Cássio Poltronieri. At the end of that year, Eduardo Santiago started to dialogue with meteor-monitoring networks in Europe, like UKMON and CEMeNt/EDMOND. Particularly valuable was the continuous support of Jakub Koukal to create a project better adapted to the situation of amateur astronomy in Brazil. This time, the stations were designed using primarily old security cameras equipped with common lenses, instead of the too expensive all-sky design. With this setup we were able to obtain a narrower field of view, allowing the detection of fainter meteors and retrieving more precise data. The first meteor image captured by this network was acquired by the station of Renato Poltronieri on January 9, 2014.

Shortly after the success of capturing the first meteors, the station owners created a group in a social media website aiming to gather people interested in joining

the network. The growing number of stations allowed some regions to be covered by more than one camera, making possible the first meteor triangulation of the network (and probably the first ever over Brazil). The simplicity and the low cost of the components selected for the BRAMON stations enabled the network to grow rapidly and to aspire national coverage, as planned since the beginning.

BRAMON begun operation in 2014 with 9 stations, and grew to 23 in 2015. At the end of 2016, the network of cameras covered 50% of the Brazilian territory, with 39 stations spread across 16 states, as can be seen in Figure 1. Most of the stations are located in the southeastern region of Brazil, the most populated area of the country. In the northeastern region, the stations are concentrated near the coast, as the interior of this area has a semi-arid climate and low population density. The number of stations in the southern region is growing, with the potential of an even greater contribution to the detection of southern hemisphere meteor showers. During this period of operation, the stations recorded 76 568 individual meteors, of which 15 381 were double- or multi-station observations, which allowed for the calculation of 8041 orbits.

### 3 Encontreitor software

A meteor detection network is formed by gathering a group of single or multiple stations that operate to register meteors via video or radio recording. Later, the set of registrations, also known as captures, is used to extract useful data like the orbital parameters of the meteors. All the information collected is then sent to a database and becomes available for public or private research. The ENCONTREITOR software was developed to meet a primary need of an automated search process for new radiants in the emerging open-access meteor orbit database of BRAMON. The software can receive as input a set of orbits extracted from software like UFOORBIT, and it returns a list of possible new radiants. Other meteor detection networks such as EDMOND and SonotaCo also have a policy of keeping their databases open-access, allowing anyone interested in meteor research to search through the data. To validate the ENCONTREITOR software, a large number of tests was executed using the information stored in these databases leading to the preliminary discovery of 108 meteor showers (23 already approved by the Meteor Data Center as *pro tempore*, 75 under current analysis, and 10 to be submitted). The software can perform a series of tasks to find the new radiants as described below.

#### 3.1 Clusters of similar orbits

The ENCONTREITOR software is based in the Density-Based Spatial Clustering of Applications with Noise or DBSCAN algorithm (Sugar et al., 2017) to search the orbits in the database. As output, it returns clusters of

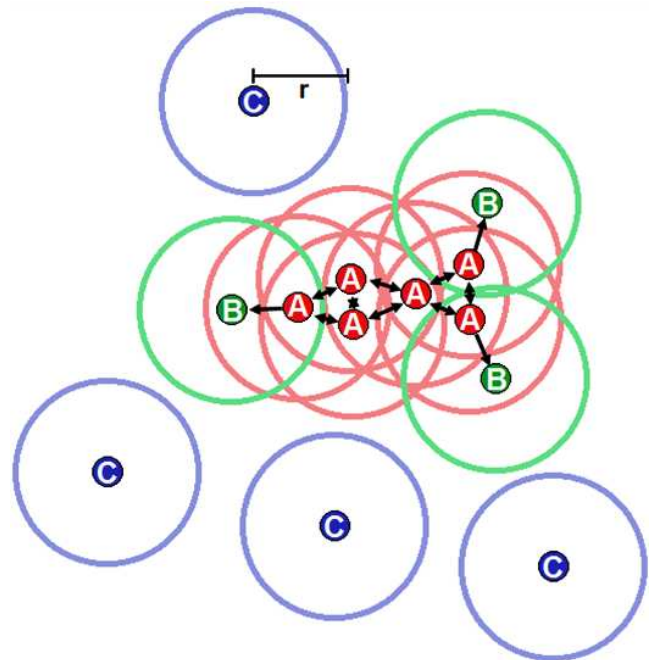


Figure 2 – Visualization of how the DBSCAN algorithm works. The minimum number of neighboring orbits for a point to be considered in the core is set to 4 in this illustration. The points A are core points, because the areas with radius  $r$  surrounding these points contain at least 4 points (including the central points themselves). The points B are reachable points, because the areas with radius  $r$  surrounding these points contain core points but less than four of them. The points C are noise, because they are neither core points nor reachable points.

similar orbits. The criterion for similarity used to compare the orbits is the  $D$ -criterion proposed by Drummond (Galligan, 2001; Jopek et al., 2002). This criterion compares the orbits giving a value of dissimilarity, that is, the smaller the number, the more similar are the orbits. The  $D$ -criterion uses the following orbital elements: eccentricity, distance of perihelion, longitude of perihelion, longitude of ascending node, and inclination. During the execution of the DBSCAN algorithm, a maximum value for the  $D$ -criterion must be given, along with the number of minimum neighboring orbits of a specific orbit for it to become considered as a core point, and the minimum number of orbits that defines a cluster, i.e., core orbits plus reachable orbits. A visual explanation is provided in Figure 2.

A cluster may not define a new meteor shower as it can contain zero, one, or many radiants. Clusters with more orbits than the parameter of maximum size of the cluster are divided into smaller ones and clusters with less orbits than minimum orbits for a radiant (usually 6 orbits) are discarded. The groups formed after this stage are tested to confirm if they may represent new radiants through a combinatorial analysis algorithm that tests the similarity of the orbital elements. An average orbit is calculated for each group, and the  $D$ -criterion is applied between each orbit of the group and its average orbit. If all the orbits in the group are similar to the average orbit, respecting the maximum value of the  $D$ -criterion accepted for this step, the group is regarded

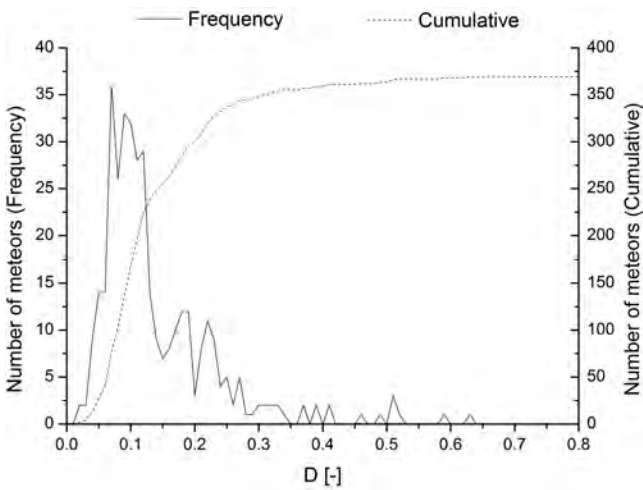


Figure 3 – Break-point method for the proposed September  $\varepsilon$ -Orionids radiant, showing the frequency and the cumulative series of meteors distributed per value of the similarity  $D$ -criterion (EDMOND and SonotaCo databases).

as a possible new radiant. Some of the approved groups may represent the same shower and share repeated orbits, so these groups are gathered in a single group and the repeated orbits are eliminated. The similarity of the average orbit of the possible new radiants is tested against the orbital elements of valid meteor showers in the IAU database. At this stage, the solar longitude is also taken into account to differentiate meteor showers whose orbits intersect the orbit of Earth at more than one point.

### 3.2 Validation mechanisms

After finishing the initial analysis of a given database, a list of possible new radiants is produced, which is then subjected to further validation using the break-point method and the Valideitor method. The break-point method (Welch, 2001; Neslušan et al., 2013) is a graphical analysis in which all the orbits of a possible new radiant are plotted according to their value of the  $D$ -criterion of similarity. In addition, in the same graph, the orbits are presented cumulatively with increasing value of  $D$ . The method requires the input of the values of the initial  $D$ , the final  $D$ , and the integration delta. An example of the method can be seen in Figure 4. In this example, the orbits plotted show a distribution that resembles a Gaussian at the left side of the graph (between  $D = 0$  and  $D = 0.2$ ), meaning that the orbits are concentrated near the orbital parameters of the radiant. In the cumulative series, the same region of the graph shows a fast growth, reaching an inflection point near  $D = 0.2$ .

To complement the break-point analysis, a method called Valideitor was proposed, in which the orbits of a possible new radiant are analyzed not only in function of  $D$ -criterion, but also as a function of time. It is expected that the temporal distribution of the meteors of a shower is Gaussian in the days near its peak. Using the method, it is possible to visualize the distribution

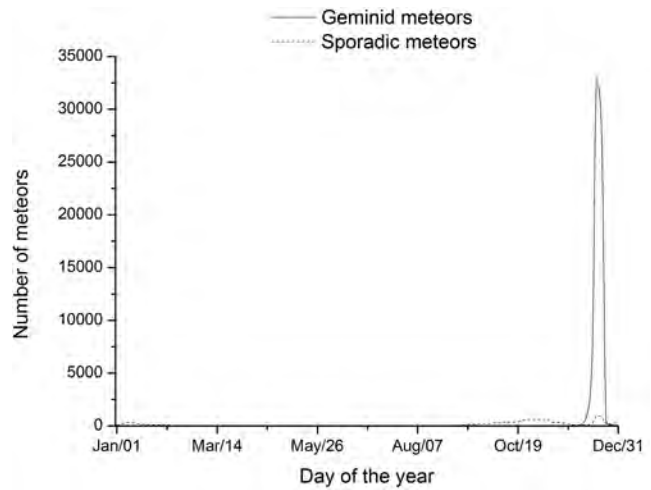


Figure 4 – Valideitor method of the Geminid radiant showing the number of meteors that are/are not associated to the shower inside a spherical area of radius  $10^\circ$  around the radiant center (EDMOND and SonotaCo databases).

of the orbits over time and how these orbits fit into the radiant. The method also makes it possible to understand how the orbits are distributed close to the radiant, providing a much greater understanding of the characteristics of the radiant and of its neighborhood. An example of an application of this method can be seen in Figure 4.

## 4 Conclusions

The implantation of a meteor-monitoring network like BRAMON in Brazil, a country with a still developing tradition in research in the meteor field, has shown that a good share of the population is interested in science. The number of people that appreciate astronomy has proved to be considerably high and, with the constant supply of information on good and cheap equipment, it is possible to bring these people together to contribute to a better understanding of the space environment in the terrestrial neighborhood, in a classical effort of citizen science. This endeavor has stimulated and encouraged the development of other useful solutions like the software ENCONTREITOR for the search of new meteor showers. The software facilitated the search through already established large databases, basing the analysis on the use of the  $D$ -criterion. It has also provided robust tools to validate the results using the break-point and the new Valideitor methods, increasing the confidence of the findings. The capacity of the algorithms was put to the test and they proved to be able to locate many new probable radiants. This development along with other ones made by BRAMON paves the way to a fully functional network with a high potential for discoveries in the field of meteor research in the southern hemisphere.

## 5 Future work

As a recently created meteor-monitoring network, BRAMON is still poorly known by the majority of the sci-

entific community dedicated to meteor studies. To increase its visibility, a presentation paper is already being written, in parallel with a more complete paper focusing on the creation and the development of the algorithms behind of the ENCONTREITOR software. With the aim of seeing the tentative new showers found by the software approved in the List of Established Showers of the Meteor Data Center, their analyzed data will also be published within the mandatory deadline. Meanwhile, the search for more radiants within the open access databases (including the new BRAMON database, now part of the EDMOND database) will continue. Lastly, a new research effort on Transient Luminous Event will be developed in partnership with the Institute of Astronomy, Geophysics, and Atmospheric Sciences of the São Paulo University (IAG/USP).

## Acknowledgements

The authors thank all the operators of the 39 BRAMON stations operational by 2016, all the new operators of the stations that started running since then, and all people who helped in the writing of this paper. They also thank the colleagues from the other meteor-monitoring networks that helped with the creation and development of BRAMON, making the dream become a reality, especially Roman Piffel from EDMOND and Richard Kacerek from UKMON.

## References

- Campbell-Brown M. D. and Jones J. (2006). “Annual variation of sporadic radar meteor rates”. *Monthly Notices of the Royal Astronomical Society*, **367**, 709–716.
- Campbell-Burns P. and Kacerek R. (2014). “The UK meteor observation network”. *WGN, Journal of the IMO*, **42**, 139–144.
- Cepelcha Z., Borovička J., Elford W. G., Revelle D. O., Hawkes R. L., Porubčan V., Šimek M. (1998). “Meteor phenomena and bodies”. *Space Science Reviews*, **84**, 327–471.
- Galligan, D. P. (2001). “Performance of the D-criteria in recovery of meteoroid stream orbits in a radar data set”. *Monthly Notices of the Royal Astronomical Society*, **327**, 623–628.
- Janches D., Close S., Hormaechea J. L., Swarnalingam N., Murphy A., O’Connor D., Vandepeer B., Fuller B., Fritts D. C., Brunini C. (2015). “The Southern Argentina Agile Meteor Radar Orbital System (SAAMER-OS): An initial sporadic meteoroid orbital survey in the southern sky”. *The Astrophysical Journal*, **809**, 36.
- Jenniskens P., Baggaley J., Crumpton I., Aldous P., Gural P. S., Samuels D., Albers J., Soja R. (2016). “A surprise southern hemisphere meteor shower on New-Year’s eve 2015: the Volantids (IAU#758, VOL)”. *WGN, Journal of the IMO*, **44**, 35–41.
- Jopek T. J., Valsecchi G. B., and Froeschlé C. (2002). “Asteroid meteoroid streams”. In Bottke Jr. W. F., Cellino A., Paolicchi P., and Binzel R. P., editors, *Asteroids III*. University of Arizona Press, Tucson, pages 645–652.
- Neslušan L., Svoreň J., and Porubčan V. (2013). “The method of selection of major-shower meteors revisited: the selection from the photographic, video, and radio databases”. *Earth, Moon, and Planets*, **110**, 41–66.
- Rendtel J. (2017). “Review of amateur meteor research”. *Planetary and Space Science*, **143**, 7–11.
- Šegon D., Gural P., Andreić Ž., Vida D., Skokić I., Novoselnik F. (2015). “Four possible new high-declination showers”. *WGN, Journal of the IMO*, **43**, 147–150.
- Socientize Consortium (2013). *Citizen science for Europe—Towards a better society of empowered citizens and enhanced research*. Green paper on citizen science.
- Sugar G., Moorhead A., Brown P., and Cooke W. (2017). “Meteor shower detection with density-based clustering”. *Meteoritics and Planetary Science*, **52**, 1048–1059.
- Welch, P. G. (2001). “A new search method for streams in meteor data bases and its application”. *Monthly Notices of the Royal Astronomical Society*, **328**, 101–111.

# Ten years of the Croatian Meteor Network

Damir Šegon<sup>1</sup>, Korado Korlević<sup>2</sup>, Željko Andreić<sup>3</sup>, Denis Vida<sup>4</sup>,  
Filip Novoselnik<sup>5,6</sup>, and Ivica Skokić<sup>5</sup>

<sup>1</sup> Astronomical Society “Istra” Pula, Pula, Croatia  
damir.segon@pu.t-com.hr

<sup>2</sup> Višnjan Science and Education Center, Istarska 5, 51463 Višnjan, Croatia  
korado@astro.hr

<sup>3</sup> Faculty of Mining, Geology, and Petroleum Engineering, University of Zagreb, Zagreb, Croatia  
zeljko.andreic@oblak.rgn.hr

<sup>4</sup> Dept. of Earth Sciences, University of Western Ontario, London, Ontario, N6A 5B7, Canada  
dvida@uwo.ca

<sup>5</sup> Astronomical Society “Anonymus”, B. Radića 34, 31550 Valpovo, Croatia  
novoselnikf@gmail.com, and ivica.skokic@gmail.com

<sup>6</sup> Fac. of Electrical Engineering, University of Osijek, Kneza Trpimira 2B, 31000 Osijek, Croatia

The Croatian Meteor Network (CMN) has been active since 2007, when more than a single camera started to capture meteors and the first CMN double-station meteor was captured. Since then, CMN has been active through lots of various activities, papers, and presentations. The chronological list of the most important achievements and results has been presented. The extensive paper on the anniversary will be published in *WGN, Journal of the International Meteor Organization*.

# American Meteor Society fireball camera

Mike Hankey and Vincent Perlerin

American Meteor Society and International Meteor Organization

mike.hankey@gmail.com and vperlerin@gmail.com

The American Meteor Society (AMS) has developed an open-source low-cost fireball camera system and back-end network to enable the deployment of a wide-area fireball network in the United States. This article presents both the hardware and software aspects of the project as well as the link between this camera network and the AMS Online Fireball Form used by thousands people around the world to share their fireball sightings with the scientific community since 2011.

## 1 Introduction

The AMS and the International Meteor Organization (IMO) collectively generate a comprehensive database of crowd-sourced visual observations that catalogs and characterizes over 300 confirmed fireball events each year since 2011 (Hankey and Perlerin, 2014). While sometimes the data gathered from the general public are sufficient for meteorite finding (Hankey et al., 2016), the witness reports alone do not provide accurate values needed to determine the meteoroids orbit. To compensate for this shortcoming, the AMS has developed hardware and software designed to capture scientifically calibrated recordings of fireball events. The goal of the camera network is to provide reasonably precise estimates for the trajectory, mass, and orbit calculated from video recordings. This data will be linked to events in the existing AMS/IMO fireball database and available to the public through the AMS and IMO websites. The AMS/IMO fireball database and API services have been enhanced to support machine to machine device registration, video, picture, and reduction data uploads and event monitoring and notification. An open data solutions pipeline is also planned pending the release of open source developments from other IMO members.

## 2 Hardware

The AMS Camera system has been developed using a combination of off-the-shelf and custom components. Devices are available as single-camera part-sky systems or as six-camera all-sky systems.

### 2.1 Single camera system

The single camera system was developed to appeal to beginners who might not have a large budget or a 360° view from their home. The system was designed for indoor use, eliminating many of the barriers people have with setting up sky cams (Figure 1). The device can be simply hung in a window. At its core, the system is comprised of a low-light, low cost CCTV IP project camera utilizing the Sony IMX290 CMOS chip, a Raspberry Pi 3 single board computer and a custom made PCB board

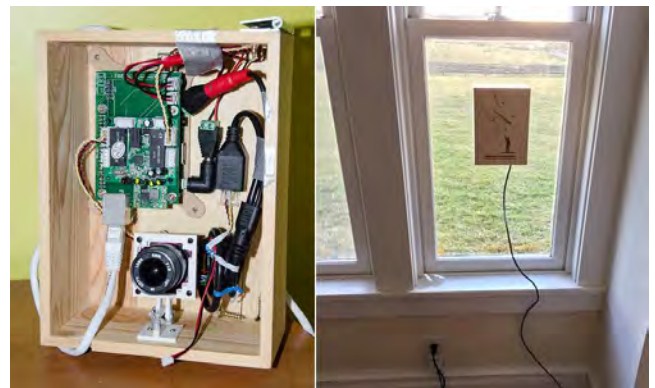


Figure 1 – Single camera device installation.

that supplies networking and power to the components. All elements are housed inside a small wooden box and connected with an Ethernet (POE) wire that provides 12 V power and Internet access. The components can be easily removed and placed inside an outdoor CCTV enclosure if this is the operators preference. The components used to build the device cost less than 200 USD.

### 2.2 All Sky 6 system

The All Sky 6 system (see Figure 2) is essentially 6 single camera systems packed into two enclosures. A 360° aluminum milled housing with an 11" acrylic dome holds the 6 cameras. Five of the cameras are spaced out 72° apart and the sixth is pointed straight up. A single Cat 6A cable supplies power and Ethernet to the cameras from a distance up to 100 meters. At its terminating end, the Cat 6A cable plugs into a 12 × 12 × 4 metal box that holds a power supply, network switches, and 6 Raspberry Pi computers. A single AC power cable and network cable into the cluster box provide power and networking to all 12 IP devices in the system. A low-end computer running Linux can also be used instead of the Pi cluster.

## 3 Software

Open source client side software has been developed to facilitate the capturing, detection, and communication



Figure 2 – Six-camera device.

of videos recorded by the devices. The code has been written primarily in Python using the OpenCV library for video capture and processing routines. The fireball device code accomplishes the functions described below.

### 3.1 Registration/authentication

New devices automatically register with the AMS site the first time they are turned on. The MAC address from the Raspberry PI provides a unique ID for the device. The operator claims the camera and associates it with his account by entering the MAC address inside a form on the AMS website. Once a device has been registered and claimed, it can freely communicate with all of the data APIs.

### 3.2 Capture program

A video capture program runs on the device 24 hours a day. The program holds the last 10 seconds of 25 frames per second video in a memory buffer and scans for any type of motion detection lasting more than 5 frames. Detections are saved to the SD card for later analysis and processing. A watchdog monitors the capture program and automatically restarts it in the event something caused it to crash or stop. This allows nearly fault-tolerant operations.

### 3.3 Auto settings

Since the camera operates 24 hours a day, the settings between night and day must also change. To complicate matters, light pollution created by city lights, the Moon, and reflecting clouds can also impact the ideal settings needed by the camera. For these reasons, a script was made that automatically adjusts the cameras brightness, contrast, and other settings throughout the day and night. Every 10 minutes, a series of frames is

taken from the camera, and the mean brightness is determined. The settings on the camera are then adjusted until the frames fall within an ideal brightness range.

### 3.4 Calibration

Calibration of the cameras field of view is achieved utilizing a long exposure mode built into the camera. While in this mode, the frame rate slows down to 7 FPS, but the sensitivity is greatly increased due to the integration of frames, essentially making a longer exposure. Stars as dim as magnitude +3 are visible in the frames. Ideally, at least two calibration frames are taken and saved each night. The images are then run through a local installation of `astrometry.net`. The images are plate solved, and a WCS (world coordinate system) file is saved and uploaded to the network site and associated with the camera. The WCS file maps the pixels  $x$  and  $y$  coordinates to right ascension ( $\alpha$ )/declination ( $\delta$ ) values. By virtue of knowing the cameras location and time of exposure, the  $\alpha/\delta$  values be can easily translated to the azimuth and elevation values needed to solve fireball captures.

### 3.5 Analysis

At this point, the data analysis portions of the program have not been written or implemented. The current goal is to develop the infrastructure and capture devices and get the network started. Once events are being saved and reduced, we will have the raw data to analyze and solve events. Ultimately from the network we hope to get solutions for the atmospheric trajectory, velocity, mass estimate, and orbit. When the time comes for this stage, we plan to leverage existing open source projects to solve and analyze events.

### 3.6 Data sharing

The fireball camera program is based on an open data concept where in all media reductions and solutions are saved in a central place and immediately available to the public through the AMS or IMO websites. The sharing is facilitated by the AMS fireball database back-end and FODE protocol APIs.



Figure 3 – Fireball capture by a 6 cameras device in November 2017 from Monkton, Maryland, USA.

### 3.7 Fireball alerts

Client-side software monitoring witness-reported events is used to find fireball captures on the client computers. An API that lists fireball reports within a certain distance of the camera provides a rough time frame and location for each event. Local files are then searched and compared with this time and if matches exist the files are uploaded to the backend. This system provides coincidental detection capabilities for single station captures.

### 3.8 User interface

A web based user interface resides on each Raspberry Pi device. The interface allows the camera operator to browse captures, change camera settings, and reboot the Pi if necessary. This interface simplifies the operation of the device so that end users do not need to use SSH or SFTP to monitor the system or access the files.

## 4 Network

The network has been developed to be open and support any type of device or camera. Video and photographic recordings of fireball events can be uploaded to the network through web forms or machine-to-machine APIs. To facilitate the uploading of media and transfer of data associated with these fireball observations, the AMS has developed the Fireball Observation Data Exchange Protocol (FODE). Standardized data object definitions, data exchange URLs, and sample client implementation code enable the protocol. The protocol is designed to ingest data from any type of camera network for the purposes of storing, analyzing, and sharing the data in a single place. All data uploaded through the APIs will be attached to witness reported fireball events in the database and if no event exists one will be created. The idea is to create a single media and data repository for all information about fireball events that occur in the world. This will enable the collection and sharing of fireball data across networks and devices providing a well-organized, easily shareable, single source for all information relating to an event.

Figure 4 shows the schema of the network.

### 4.1 Data object and API definitions

The FODE protocol is comprised of the following data objects. For each object, there are corresponding API URLs that enable creating, updating, and viewing data associated with the object.

#### 4.1.1 Device operator/API key

The device operator links to an AMS member login and exists by virtue of the existing AMS website. Device operators are given a secure API key through the AMS

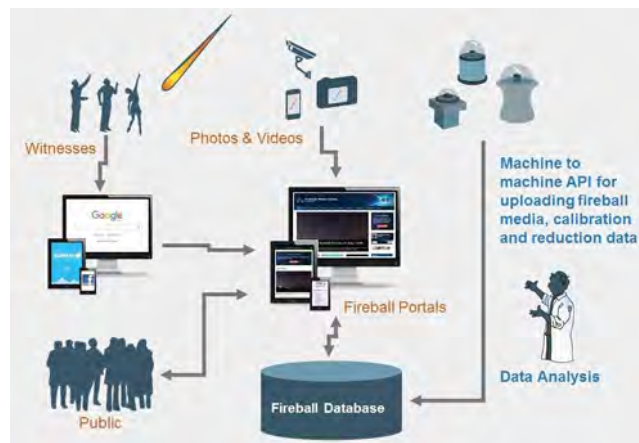


Figure 4 – Schema of the network.

website that enables communication with the machine-to-machine APIS. This key enables the system to identify all requests sent from the operators network.

#### 4.1.2 Device

The device represents a single camera inside an operators domain. The device is assigned with a uniquely identifiable AMS ID and must be registered and claimed to the operators profile before initiating data services. Longitude, latitude, altitude, and other details relating to the device are stored in the device record. Once the device is registered, the operator can upload media and data associated with the device by supplying the API key and the device ID. The device will also appear in the list of devices in the operators profile on the AMS website.

#### 4.1.3 Motion capture

A motion capture represents a device camera capture event that might be a fireball but has not been auto-detected. This function allows operators to upload a timestamp and single image (preferably a video stack) of the event. This allows operators without automatic detection to log event times and be notified of coincidental detections by other camera operators or eyewitness reports.

#### 4.1.4 Fireball capture

The fireball capture API allows operators to upload videos, still photos, or reduction data associated with fireball events. This API should be used only for events that have passed auto-detection or event-coincidence detection via witnesses or other motion capture logs.

#### 4.1.5 Heartbeat

The heartbeat is a simple API that allows the operator to log a recent capture frame from the camera. This enables a live view or latest view for all cameras in the network. The heartbeat also monitors the device

to make sure it is operational. If too many hours pass without a heartbeat, the camera operator is notified of a potential outage with the camera.

#### 4.1.6 Observation reduction

Fireball capture records can be amended with reduction data from the event. Multiple reduction records can be tied to each media file. For example, if two different reduction methods were applied on a video, both could be logged. Relevant reduction fields include the following: start  $x/y$ , end  $x/y$ , start  $\alpha/\delta$ , end  $\alpha/\delta$ . start azimuth/elevation, end azimuth/elevation, elapsed time, and peak magnitude. A free-form large-capacity notes field is also allowed to support the saving of more comprehensive reduction data sets.

#### 4.1.7 Trajectory and orbit solutions

Network operators can also upload event solutions associated with events. There is a one-to-many relationship between solutions and events allowing multiple solution providers or methods to be saved and associated with events. Trajectory solutions will incorporate the starting and ending longitude, latitude, and attitude; the starting, ending, and median velocity and the peak magnitude.

## 4.2 Web admin

Operators can view their devices, captures and other data through a web based admin on the AMS website.

All files and settings are also available for viewing and editing using a browser based app included with AMS fireball devices.

## 5 Conclusions and perspectives

Four All Sky 6 units have been in beta testing since July 2017, and, since that time, over 20 fireball events have been captured by the cameras. Much time and development has been put into the quick and cost-effective manufacturing of the devices. We estimate over 400 devices will be needed to complete the network across the country, so, for these reasons, much effort has been put into planning the production and marketing of the devices. As the network develops and multi-station captures become a possibility, we will implement solution computations. The main goal at this point is to make the devices available to the public and start building the network.

## References

- Hankey M., Fries, M., Matson R., Fries J. (2016). “AMSNEXRAD—Automated detection of meteorite strewnfields in Doppler weather radar”. *Planetary and Space Science*, **143**, 199–202.
- Hankey M. and Perlerin, V. (2014). “AMS fireball program, community website, mobile app, and all-sky camera”. In Gyssens M., Roggemans P., and Żołądek P., editors, *Proceedings of the International Meteor Conference*, Poznań, Poland, 22–25 August 2013. IMO, page 120.

# Observation of lunar impact flashes

Mert Acar<sup>1,2</sup>, Alper K. Ateş<sup>2</sup>, and Cenk Kayhan<sup>2</sup>

<sup>1</sup> Department of Astronomy and Space Sciences, University of Ege, Bornova, 35100, Izmir, Turkey  
mrtacarmerdo@gmail.com and mert.acar@istek.k12.tr

<sup>2</sup> ISTEK Belde Observatory, Uskudar, 34674, Istanbul, Turkey  
bilim.merkezi@istek.k12.tr

In this study, the results of 20 hours of observations to detect the lunar impact flashes from the ISTEK Belde Observatory are presented. Currently the ISTEK Belde Observatory is the only place working on lunar impact flash detection in Turkey. A 40 cm catadioptric telescope armed with a fast frame camera system is dedicated to this research. Several flashes have been detected with  $S/N > 5$ . In this manuscript, the probable causes of the detected flashes, such as impacts or iridium flashes, are discussed. An overview of the video recording observation technique and the number of validated flashes from the literature are given.

## 1 Introduction

Meteoroids are small natural bodies which are fragments from comets and asteroids traveling through the interplanetary medium of the Solar System. Sometimes, they strike planets or the Moon. If they reach the Earth we can see them as a meteor or fireball in the sky due to friction with the air molecules. Only a small fraction of the meteoroids make it to the surface. The Moon has no atmosphere like the Earth, so the falling objects do not create fireballs, yet the kinetic energy of the incoming object is converted into thermal energy which can be detected as an impact flash. Though the meteoroids can hit anywhere, flashes are easiest to detect on the night side of the lunar surface. Thanks to new sensitive fast-frame video cameras, many rapid and faint flashes can now be detected.

### 1.1 Time line lunar impact flash studies

A number of attempts have been made previously to observe and document lunar meteor impacts.

- First, Melosh et al. (1993) made a theoretical assessment of impact flash detection by using photometers. If the impactors are bigger than 1 meter, the impact flash can be detected by photometry technique by using a meter-class telescope.
- Ortiz et al. (1999) began to search for impact flashes with CCD cameras instead of photometers. They concluded that an impact flash can be detected using a 5–10 seconds exposure time with CCD cameras.
- During the 1999 Leonid meteor showers, two independent groups detected an impact flash on the Moon. This became the first confirmed observation of lunar impact flashes (Dunham et al., 2000; Ortiz et al., 2000).
- Bellot Rubio et al. (2000) observed the Moon with a 20-cm diameter telescope with a  $8' \times 6'$  video

camera. They pointed out that the luminous efficiency (the fraction of kinetic energy converted into radiation) of the collision processes can be determined.

- Chudnick et al. (2002) observed the 1999 and 2001 Leonids impacts and reported their positions on the Moon. Also, Ortiz et al. (2002) determined the mass distribution of 2001 Leonids impacts.
- The NASA MEO (Meteoroid Environment Office) started monitoring lunar impacts in 2006 and detected 399 impact flashes during 2005–2016.
- Yanagisawa et al. (2007) detected Geminids impacts and determined particle masses, duration of flashes, and impact angles.
- Suggs et al. (2014) determined the kinetic energy and mass distribution of 126 detected impacts by NASA ALaMO (Automated Lunar and Meteor Observatory) data.
- Larbi et al. (2015) observed the Moon with 35-cm and 20-cm diameter telescopes and detected two impact flashes.
- Kim et al. (2015) detected a flash during 2013–2014 with an educational telescope.
- The NELIOTA<sup>1</sup> project from Greece started monitoring the Moon for faint NEO impacts in 2017. They observe the Moon with a 1.2-m telescope and two video cameras. So far, they detected 27 impacts with Johnson-Cousins R and I filters.

## 2 Technique and observations

### 2.1 Technique

The observer does not need much equipment to start detecting impact flashes. A telescope with clean optics,

<sup>1</sup><https://neliota.astro.noa.gr/>.

a fast-frame camera, a computer with advanced capture software, and a high-resolution Moon map is what it takes for lunar impact studies. The observation procedure is rather simple: the telescope is pointed to the night side of the Moon, and the fast-frame camera is set to record consecutive video clips each lasting a few minutes. The recommended setup for visual observers is below:

- field of view wide enough to see the night side of the Moon (focal reducers are not advisable in view of signal loss);
- 1/30 fps or 1/60 fps for exposure times;
- LUNARSCAN software for automatic detection;
- REGISTAX and MAXIMDL software for data reduction.

## 2.2 Observations

The geographical coordinates of ISTEK Belde Observatory are  $41^{\circ}01'48''$  N latitude and  $29^{\circ}02'32''$  E longitude. Belde Observatory is the only place making lunar impact flashes observations in Turkey. The instruments used for this purpose are a Meade LX600 40 cm diameter Schmidt-Cassegrain  $f/8$  telescope and a Celestron Skyriiss ( $1600 \times 1200$ ) camera. The diameter of the telescope is large enough for detection of lunar impacts down to magnitude +9. Impact flashes can be detected at the night side of the Moon (dark side of lunar disk), so, for the lunar impact monitoring, observations should be carried out for a few nights during the waxing crescent and a few nights during the waning crescent.

The LUNARSCAN software is used for automatic detection of flashes in the field of view. Then, eliminating false detections is done manually. The REGISTAX software can then be used for the reduction of the data. After that, the IRAF or MAXIMDL software can be used for analysis purposes. We detected possible impact flashes during 20 hours of observing data. Most of them are false flashes caused by satellites flares or cosmic rays. After the reduction of our data, we have one impact flash candidate (Figure 1) and one micrometeorite or iridium flare (Figure 2).

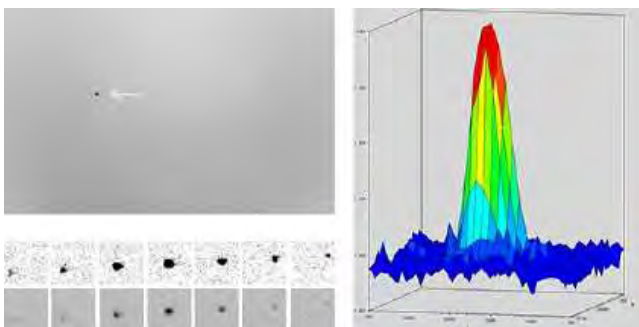


Figure 1 – Candidate impact flash image and line profile, JD 2457937.300579

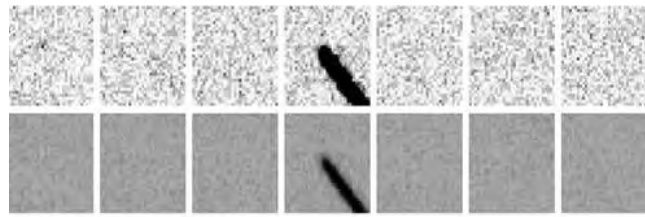


Figure 2 – The image obtained at JD 2457877.295718 is potentially an iridium flare or a micrometeorite. In 20 hours of observation, 6 such events have been recorded.

## 3 Conclusions

After the reduction of 20 hours of observing data, we have an impact flash candidate. Scientifically confirmed sightings require observations from two or more widely separated locations, or observations using two different filters at the same time. No other observer detected this event, unfortunately, so it is not possible to confirm that this is a real impact flash. We have just started monitoring the Moon for lunar impact flashes and we will continue to work on it. We would like to collaborate with anyone who is interested, or has expertise, in this field.

## Acknowledgements

We thank the ISTEK Foundation for financial support for this research project.

## References

- Ait Moulay Larbi M., Daassou A., Baratoux D., Bouley S., Benkhaldoun Z., Lazrek M., Garcia R., and Colas F. (2015). “First lunar flashes observed from Morocco (ILIAD network): implications for lunar seismology”. *Earth, Moon, and Planets*, **115**, 1–21.
- Bellot Rubio L. R., Ortiz J. L., and Sada P. V. (2000). “Luminous efficiency in hypervelocity impacts from the 1999 lunar Leonids”. *The Astrophysical Journal*, **542**, L65–L68.
- Cudnik B. M., Dunham D. W., Palmer D. M., Cook A. C., Venable R. J., and Gural P. S. (2002). “Ground-based observations of high velocity impacts on the Moon’s surface—the lunar Leonid

- phenomena of 1999 and 2001”. In *Lunar and Planetary Science Conference*, volume 33 of *Lunar and Planetary Inst. Technical Report*.
- Dunham D. W., Cudnik B., Palmer D. M., Sada P. V., Melosh J., Frankenberger M. B. R., Pellerin L., Venable R., Asher D., Sterner R., Gotwols B., Wun B., and Stockbauer D. (2000). “The first confirmed videorecordings of lunar meteor impacts”. In *Lunar and Planetary Science Conference*, volume 31 of *Lunar and Planetary Inst. Technical Report*.
- Kim E., Kim Y. H., Hong I.-S., Yu J., Lee E., and Kim K. (2015). “Detection of an impact flash candidate on the Moon with an educational telescope system”. *Journal of Astronomy and Space Sciences*, **32**, 121–125.
- Madiedo J. M., Ortiz J. L., Organero F., Ana-Hernández L., Fonseca F., Morales N., and Cabrera-Caño J. (2015). “Analysis of Moon impact flashes detected during the 2012 and 2013 Perseids”. *Astron. Astrophys.*, **577**, A118.
- Ortiz J. L., Aceituno F. J., and Aceituno J. (1999). “A search for meteoritic flashes on the Moon”. *Astron. Astrophys.*, **343**, L57–L60.
- Ortiz J. L., Sada P. V., Bellot Rubio L. R., Aceituno F. J., Aceituno J., Gutiérrez P. J., and Thiele U. (2000). “Optical detection of meteoroidal impacts on the Moon”. *Nature*, **405**, 921–923.
- Suggs R. M., Moser D. E., Cooke W. J., and Suggs R. J. (2014). “The flux of kilogram-sized meteoroids from lunar impact monitoring”. *Icarus*, **238**, 23–36.
- Yanagisawa M., Ikegami H., Ishida M., Karasaki H., Takahashi J., Kinoshita K., and Ohnishi K. (2008). “Lunar impact flashes by Geminid meteoroids in 2007”. *Meteoritics and Planetary Science Supplement*, **43**, 5169.

# Data management system of the Bolidozor network

Roman Dvořák<sup>1</sup>, Jan Štrobl<sup>2</sup>, and Jakub Kákona<sup>3</sup>

<sup>1</sup> Bolidozor, Czech Republic  
romandvorak@mlab.cz

<sup>2</sup> Astronomical Institute of the CAS, Czech Republic  
strobl@asu.cas.cz

<sup>3</sup> CTU in Prague, Czech Republic  
kakonjak@fel.cvut.cz

Stations of the Bolidozor radio meteor detection network produce every day a lot of data. In this paper, we present the way how are measured data stored in detection stations and how they are transferred to the common data storage server. All data are indexed to the database before transmission which provides a fast access and a simple search of the requested data according to several parameters (e.g., time, station, duration or length). The system provides a user-friendly web interface for accessing data and machine-readable outputs for external processing tools. Data management system is ready for use with multiple storage servers or extend to virtual-observatory standards.

## 1 Introduction

Bolidozor is a network of meteor radio detection stations (Figure 1), where each site produces a significant amount of data that must be stored on a shared storage for easy access and processing. We explain how measured data are managed and stored in Bolidozor.

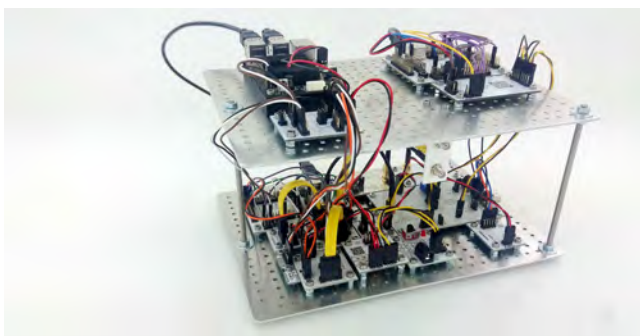


Figure 1 – RMDS02E (radio meteor detection station) assembled from MLAB modules.

## 2 Data outputs

Each station produces approximately 2 GB of data per day on average. For data recording stations, we use radio-observer software which provides several types of output data.

### 2.1 Metadata

CSV (comma-separated values) files contain information about each generated file. In case of the RAW file (meteor detection), it includes properties as duration, peak frequency, radio magnitude, or noise level of background.

### 2.2 Snapshots

A snapshot .FITS (flexible image transport system) image contains a continual spectrogram of one minute per



Figure 2 – Example of a snapshot. It is useful only for quick browsing by people.

file with a narrow frequency band around the GRAVES radar transmission frequency. In snapshots (see Figure 2), meteors are included that have not been detected. These files are used for determining the status of the station, because, in itself, it is possible to see, e.g., interference noise.

### 2.3 RAW files

When the radio-observer software detects some meteor, a RAW FITS file is created, the file contains unprocessed samples from an analog-digital converter. This file is intended for postprocessing.

In addition, a preview FITS image (spectrogram) of the RAW file is created.

See also Figure 3.

## 3 Data transmission

Measured data are immediately transferred to the central data storage server (`space.astro.cz`) with a data-uploader software which contains almost 7 TB of space for measured data. Because this is not enough for saving all historical data, old data are backed up on magnetic tapes of CESNET servers, and deleted from the `space.astro.cz` server.

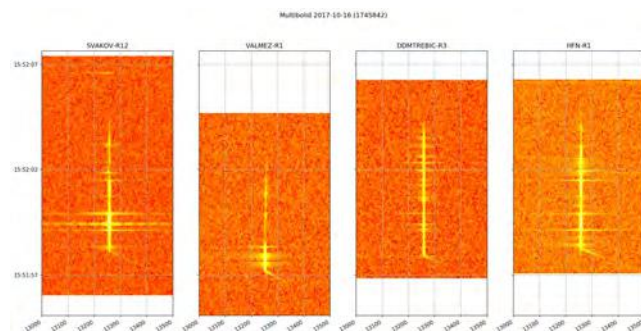


Figure 3 – Radio fireball with head echo captured by multiple stations. Graphs are precisely aligned by GPS time marks from RAW files.

## 4 Data streams

A station provides two types of UDP/IP data streams. These streams can be used with PySDR or Freya visualization software. The first data stream is uncompressed and contains all AD converter data. This stream is intended for debugging purposes. The second data stream includes compressed data and is suitable for visualization purposes. When a meteor is detected, the station makes a TCP/IP request with some fundamental properties of the event. This stream is used for real-time visualization on the map.

## 5 Standardized data access

Although the data are available from the central storage server via an `http` web page, this is not suitable for browsing and searching for required data programmatically. Moreover, old backed-up data are not accessible in real-time, and they must be requested from magnetic-tape storage. This can take several seconds or even minutes.

Therefore, stored data are indexed in the MLABvo database. MLABvo API provides us easy access to data based on parameters such as station, type of data (snapshot, meteor, multibolide), event time, and duration.

MLABvo can also obtain and provide backed-up data from magnetic tapes. It is based on the *jobs model* where the client sends a query for data and gets a *job-id*. The data required by the server are collected and prepared for fast access. When all the files are collected, the server creates a JSON containing links and information about each file (or event). Client download files from `http` links are obtained by *job-id*.

The MLABvo database is designed as a universal tool and is ready to manage data from other projects. Today, for example, it stores data from the Ionozor network which makes a radio ionosphere observation. The database is designed to be expanded with virtual-observatory standards by IVOA<sup>1</sup>.

<sup>1</sup>[http://www.ivoa.net/deployers/intro\\_to\\_vo\\_concepts.html](http://www.ivoa.net/deployers/intro_to_vo_concepts.html).

## 5.1 Python access

Since we have written most of the processing software in Python, we have prepared a Python library for easy access to the measured data on storage servers and MLABvo databases.

Several processing scripts are prepared in Python Jupyter notebooks.

## 6 Visualisation tools

Because viewing data in web index is not comfortable, and for some users very difficult, we have prepared some tools for easy browsing of measured data.

### 6.1 RTbolidozor

RTbolidozor (`rtbolidozor.astro.cz`, Real-Time Bolidozor) is the web interface for simple visualization of measured data. RTbolidozor provides several types of outputs.

#### 6.1.1 Multicount

Multicount is a graph which shows a detection count per period. It shows some detections per period from all stations in one chart. Each site has its own position within the rectangle. The position of the station is visualized by a gray square. Clicking on the station name displays the data for the selected station only.

See also Figure 4 for an example.

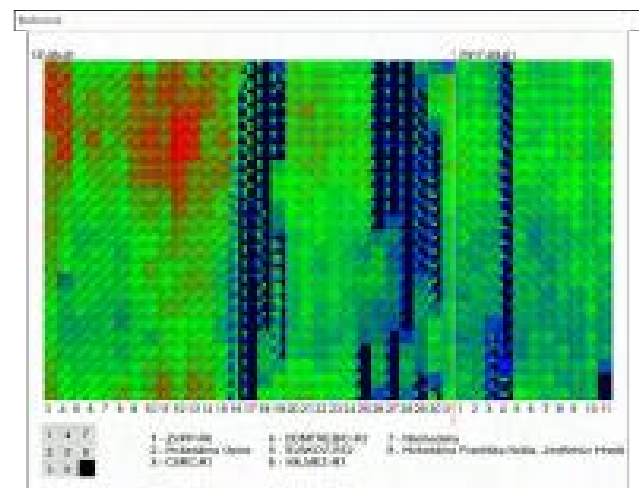


Figure 4 – Multicount.

#### 6.1.2 Real-time map

The real-time map show radio-meteor detections in real-time on the map of stations (Figure 5). When some meteor is detected, the source station blinks, and the sound is played. Next to the map, it is possible to see latest detected meteors.

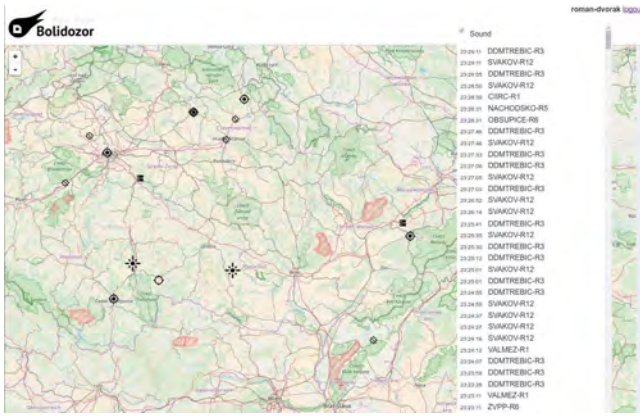


Figure 5 – Visualisation of meteor detections on the map of stations in real-time.

Date	Station	noise	freq	mag	duration	link
2017-09-06 10:18:30 Δ s	valmez	6.52916	26488.8	32.2215	8.87467	
2017-09-06 10:18:31 Δ s	svakov	1.22461	26494.6	2.72598	9.04533	
2017-09-06 10:18:32 Δ s	OBSUPICE	35.447	26502.0	79.8622	10.5613	
2017-09-06 10:18:26 Δ s	nachodsko	21.6012	26450.7	46.2349	4.096	
2017-09-06 10:18:31 Δ s	CIIRC	7.20452	26512.2	26.3519	9.04533	
2017-09-06 10:18:23 Δ s	HFN	5.3646	26507.8	19.0732	1.024	

Date	Station	noise	freq	mag	duration	link
2017-09-03 07:50:11 Δ s	CIIRC	25.9417	26532.7	119.395	12.9707	
2017-09-03 07:50:14 Δ s	svakov	1.14496	26500.5	5.12458	15.672	
2017-09-03 07:50:13 Δ s	OBSUPICE	38.3044	26523.9	76.9089	15.1893	
2017-09-03 07:50:07 Δ s	ZVPP	0.528096	26519.5	1.23582	3.92533	
2017-09-03 07:50:08 Δ s	valmez	12.4441	26526.9	38.964	6.99733	
2017-09-03 07:50:07 Δ s	domtrebic	5.36814	26525.4	12.6636	6.99733	

Figure 6 – List of multistation events

### 6.1.3 Multibolide

The multibolide part contains the list of multi-station bolides (Figure 6). The match is detected by the time of event and length of the record. Every multi-station event is marked by the unique id for easy access with MLABvo tools. It is useful for choosing interesting bolides for future processing. In the web interface are the links for easy access to the corresponding snapshots.

## 6.2 Server space.astro.cz

Data on primary storage server are browsable with a file index web page or with a Javascript JS9 fits viewer.

## 6.3 Bolidozor RMOBmultigen

RMOB histograms are generated centrally from data on the storage server (`space.astro.cz`) on the processing server `meteor1.astrozor`. It provides us with simple updates of the program and more efficient detecting of events.

## 6.4 PySDR

PySDR is Python software for live 2D waterfall display of measured data.

## 6.5 Freya

Freya is another Python 3D visualization software package (Figure 7). Besides the video representation, it generates sound in which it is possible to hear meteors as a whistle. Freya uses a reduced data stream, and is therefore suitable for permanent presentation (e.g., on observatories for visitors) or for streaming through the Internet.

The Freya software can be run under Linux as well as under Windows.

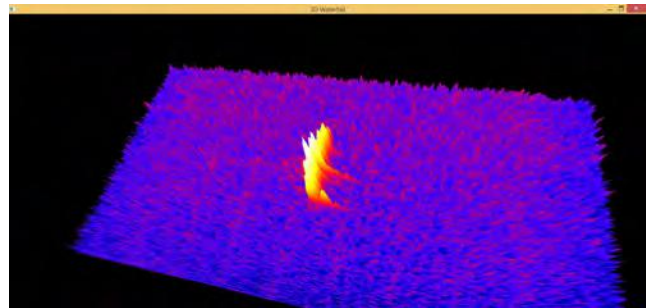


Figure 7 – Freya 3D waterfall.

## 7 Conclusions

The Bolidozor radio meteor detection network produces a large amount of data which are automatically transferred to a shared data server. Therefore, we are developing a set of programs that take care of data transmission, easy access to the data, and visualizations.

# Visual and photographic observations of meteors carried out by students of the Astronomical Observatory and Planetarium “Nicolaus Copernicus”

Ivanka Getsova-Momcheva, Ivaylo Belchev, Katerina Ruseva, Kalina Georgieva

Astronomical Observatory and Planetarium “Nicolaus Copernicus”, Varna, Bulgaria

igetsova@yahoo.com, ivailobelchev2000@gmail.com, katerina.ruseva100@gmail.com, and

kalina.v.georgieva@gmail.com

Our group attends astronomy courses at the National Astronomical Observatory and Planetarium “Nicolaus Copernicus” (NAOP) in Varna, Bulgaria. The age of the students ranges from 12 to 18 years. We often go to a village 28x201 km southeast from Varna to observe meteor showers and variable stars. During the last 7 years, we have collected data for thousands of meteors. In this paper, we briefly present our observations.

## 1 Introduction

We have observed many meteor showers listed in the IMO *Meteor Shower Calendar*, including the Quadrantids, June Bootids, Capricornids, Southern  $\delta$ -Aquariids, Piscis Austrinids, Perseids, Orionids, Leonids, and Geminids. We have obtained quite a few good results on part of these showers, and some of our findings are presented here. We used both IMO-approved methods—counting and plotting (Rendtel and Arlt, 2015).



Figure 1 – Observing site at Avren, 28 km southeast of Varna ( $\varphi = 43^{\circ}07'11''6$  N,  $h = 27^{\circ}40'09''5$  E,  $h = 299$  m)

In this paper, some results are presented in the form of graphs and photos for illustrative purposes. The Zenithal Hourly Rate is calculated on average for all observers for the mentioned showers. The radiants for Perseids, Orionids and Geminids were estimated using the VISDAT and RADIANT programs. The displayed meteor photographs have been captured by students at NAOP-Varna. Our aim is to contribute to the improvement of the statistics of the observed meteor showers, and to provide useful information for future observers.

## 2 Technical details

Our observations were initiated after adaptation to the darkness and once the radiant had risen at least  $20^{\circ}$  above the horizon.



Figure 2 – Students working with meteor plots on *Atlas Brno 2000.0* maps.

When we used the method of counting, usually during shower peaks, one of the observers would set up his or her alarm to go off every 10 or 15 minutes. The alarm rings were used as a time marker and were noted down by all participants. Most of us documented the data by writing with a pencil on small paper rolls fixed in place by a rubber band.

When the observer chose the method of plotting, however, he or she would attach star maps to a folder or a

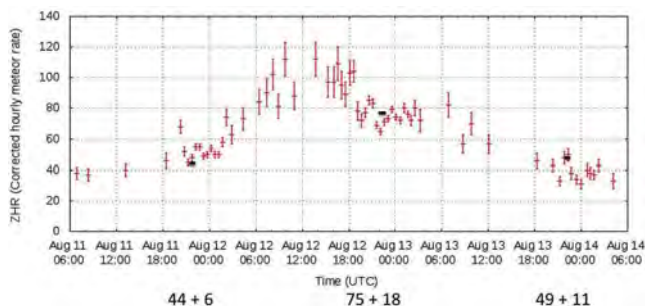


Figure 3 – ZHR profile for Perseids in 2013. Our average results are superimposed on the IMO graph.

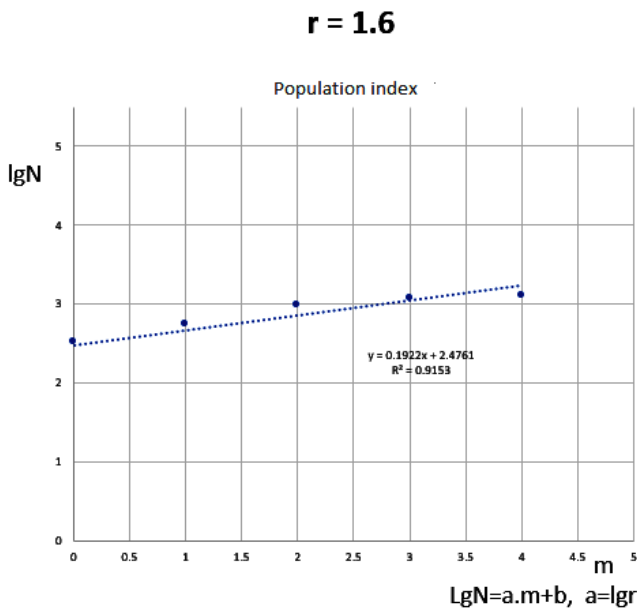


Figure 4 – Graphical determination of the population index for the Perseids based on 1300 meteors observed on August 12-13, 2015.

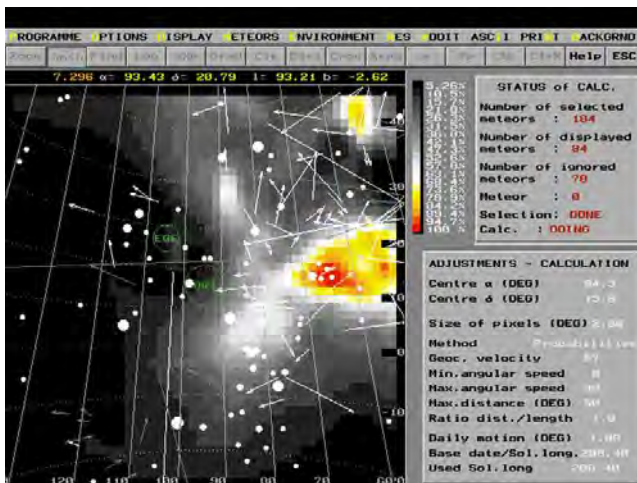


Figure 5 – Radiant position of the Orionids in 2011 based on all plotted meteors.

big piece of cardboard. Our star maps were taken from the *Atlas Brno 2000.0*. The paths of the meteors seen were drawn in a manner that unambiguously shows the beginning of the meteor and its trajectory. Trying to determine angular velocity is also very important. One of the applied methods was the so called F, M, or S method (fast, medium or slow). Another method involved approximately determining the angular velocity of the meteors, and calculating the fraction of the elevation of the meteors beginning point and the distance between the end point and the radiant. Plotting is more

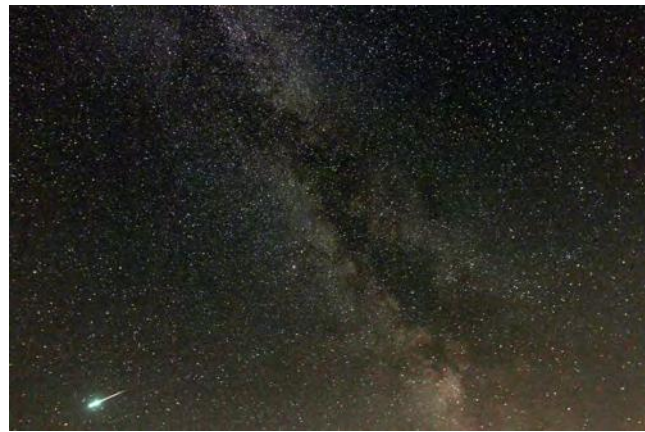


Figure 6 – Photo by Petar Petrov with a Canon EOS 7D  $f/2.8$  with an exposure of 25 s on ISO 1600 with a focal length of 16 mm of an  $\alpha$ -Capricornid meteor on 12 August 2013, at 19<sup>h</sup>24<sup>m</sup> UT.

suitable for minor showers or for beginners, because by using the maps they learn the constellations in-depth. Nonetheless, this method is also important for calculating the radiant area using ones own observations. We have registered the results obtained using both methods in the IMO's Visual Meteor Database.

### 3 Conclusions and future work

In conclusion, visual meteor observations can be difficult for beginners, but the end result is definitely rewarding. We are looking forward to performing new observations and presenting our future work to everyone interested in meteors.

### 4 Acknowledgements

The student authors would like to thank our teachers Ivanka Getsova-Momcheva and Eva Bojurova for teaching us the art of observing meteors and for all the time and energy they have invested in assisting us, not only by allowing us to gather knowledge via our courses, but also for creating this project. Special thanks go to Valentin Velkov for the moral and educational support during all our expeditions, and for introducing us to the legends of Avren.

### Reference

Rendtel J. and Arlt R., editors (2015). *Handbook for Meteor Observers*. IMO.

# New meteorite fall in the region of Igdi (Tata, Morocco)

Abderrahmane Ibhi<sup>1</sup>, Fouad Khiri<sup>1,2</sup>, and Lahcen Ouknine<sup>1</sup>

<sup>1</sup> Petrology, Metallogeny, and Meteorites Laboratory, University Ibn Zohr, Agadir, Morocco  
a.ibhi@uiz.ac.ma

<sup>2</sup> Regional Center of Trades of Education and Training, Inzegane, Agadir, Morocco  
fkhiri2009@gmail.com

On the evening of July 12, 2017, at 22<sup>h</sup>10<sup>m</sup> UT, a bright bolide was observed by thousands of eyewitnesses in an area 140 km south of the Tata town, in the rural commune of Ait Ouabelli, in southeast Morocco. Terminal fragmentation and sound phenomena were perceived near the end point of the trajectory. The bolide has traveled from north to south and has experienced several fragmentation events along its atmospheric trajectory. This extraordinary and rare event is extremely valuable to the scientific community, and it was the brightest and most comprehensively observed fireball in Morocco's astronomical history.

## 1 Introduction

Meteorite falls, also called observed falls, are meteorites collected after their fall was observed by people or automated devices. These meteorites are an important source of information about the history of the Solar System, and, therefore, their collection is important for scientific study. In particular, they offer fresh material (Khiri and Ibhi, 2015). However, on average, only five to six meteorites have been seen to fall annually throughout the world and recovered over the two last centuries (Graham et al., 1985; Ibhi, 2014). Some of these meteorites have great scientific and cultural value, such as the observed fall of the Martian Tissint meteorite (Chennaoui et al., 2012; Ibhi, 2013). According to the Meteorite Nomenclature Committee of the Meteoritical Society, 13 meteorite falls have been recorded to June 2017 in Morocco. Today, this number is expected to be up by a point since a new meteorite has fallen in the southeast of Morocco. Here, we try to describe the phenomena that have accompanied this fall and to share the results of our study on one of its fragments.

## 2 Collecting observations

Eyewitnesses in several localities (Agadir, Tafraout, Tata, Tirhirt, Foum El Hisn, Igdi, Boufalouss, Mofzou, Ait-Ouabelli, etc.) saw the bolide and heard three detonations a few minutes later. Mr. Rachid Benzakour, who is a journalist of the Moroccan radio channel *Radio Plus* and a resident of Ait Ouabelli, has testified that he and his family members saw a brilliant light which shot across the night sky. It seemed to be brighter than an electric welding light. The journalist reported that it was at first yellow, and then turned red-green before it split into three parts. Furthermore, the detonation energy has shaken the doors of the houses and the curtains of the garages. We thanked God that no big fragments had fallen in populated areas.

Immediately after the fireball event, the authorities of the area organized a field search to check for possible security problems. Hundreds of people moved to the site from surrounding douars, villages, and other cities (Erfoud, Laayoune, etc.) to search for meteorite fragments, despite the high temperature that has reached 50° C. The first fragments were recovered the following day between the Igdi, Ait Ouabelli, Boufalouss, and Mofzou douars (Figure 1). Most of the specimens found were quickly identified as meteorites because they exhibit a prominent fusion crust that covers a part of their surface. The majority of these fragments are composed of relatively small pieces, with the largest officially reported being 1 kg as of this publication. Observing this meteorite fall in this Saharan region and collecting its fragments on sand, during night-time, with a clear sky typical of July, was not too hard (Khiri et al., 2017). Moreover, Tata is a region where awareness activities in the domain of meteorites had significant impact, and contributed to the general understanding of these celestial rocks.

Indeed, subsequently a large number of eyewitness accounts were recorded and mapped by GPS. Now we are in a position to draw the distribution ellipse of the fall



Figure 1 – Many of the region's inhabitants converged to assist in recovering the fresh fragments before valuable information could be lost in bad weather conditions. Initial searches by nomads, based on the direction of the bolide, produced the first few fragments.

of the Igdi meteorite, which starts North of Igdi and continues in southern direction above the natural barrier of the “Jebel Bani”, which constitutes the border between Morocco and Algeria (Figure 2).

The strewnfield of Igdi is situated about 140 km south of the city of Tata in the region of Guelmim-Es Semara. The mapping of the locations where the fragments of the meteorite were found shows us that the fireball exploded into many fragments that are scattered over a field with a NNW to SSE direction about 25 km long, which is also the flight direction of the meteorite according to the observations of the nomads and which would be the direction of the strewn field (Figure2). The width of the ellipsoid is not yet well-defined due to lack of data.

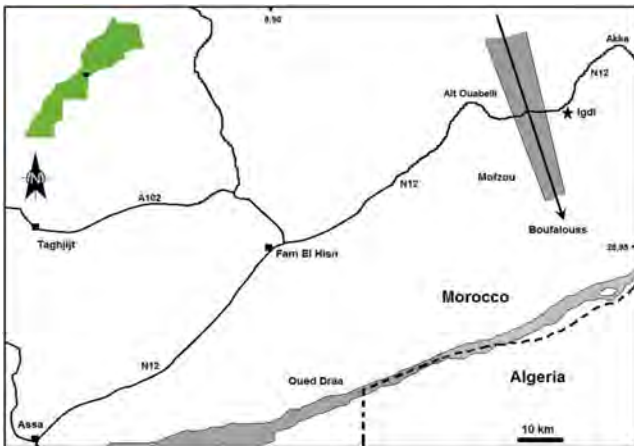


Figure 2 – Estimated flight path of the fireball that gave rise to the Igdi meteorite.

### 3 The Igdi 2 meteorite

The provisional name given to this meteorite is “Igdi 2”<sup>1</sup>. The fragment provided to researchers at the Ibn Zohr University in Agadir was approximately 20 mm in diameter and about 15 mm thick with a weight of 7.3 g (Figures 3–5). The measurement of the magnetic susceptibility on this fragment showed that  $\log \chi$  ( $10^{-9}$  m<sup>3</sup>/kg) is about 3.62 and the density is about 3.21. These values corresponds well to the confidence interval of the LL6-7 type ordinary chondrite meteorites in the alignment chart given by Folco et al. (2006), and reveal in this way that it is a meteorite that came from the main asteroid belt. Ordinary chondrites are the most common type of meteorites that fall to Earth, with a proportion around 86% (Bischoff and Geiger, 1995). Their study provides important clues for understanding the origin and the age of the Solar System.

Of course, we cannot predict when such falls occur nor judge the velocity at which they are falling and where they would impact. Fortunately, with the aid of nomads and rural people, interested in this spectacular phenomenon, who respect scientists and help them with

<sup>1</sup>The meteorite officially named “Igdi” was found in 2000 (no observed fall). For more details, see <https://www.lpi.usra.edu/meteor/metbull.php?code=12002>.



Figure 3 – Igdi meteorite fall fragment showing intact black fusion crust. Credit: A. Ibhi, Ibn Zohr University.

the collection of meteorites, we were able to carry out a preliminary study of this new fall. Additional material might be collected on the ground along the fireball track during the coming months. Then, we could have an idea about the total collected mass.

The study is intended to serve as a case example for post-event data recovery and trajectory reconstruction in these areas not covered by sky-camera networks and with limited scientific infrastructure. In addition, it presents the results of the provisional petrological study and the measurement of the magnetic susceptibility performed by the scientific team of the Ibn Zohr University on a fragment of this recovered meteorite fall (Figures 4 and 5). The study shows that the Igdi fall is an LL6-7 ordinary chondrite with shock stage S2-3 and a weathering grade of W0.

### References

- Bischoff, A. and Geiger T. (1995). “Meteorites for the Sahara: find locations, shock classification, degree of weathering and pairing.” *Meteoritics*, **30**, 113–122.
- Chennaoui H. A., Avicé G., Barrat, J.-A., Boudouma O., Chen G., Duke M. J. M., Franchi I. A., Gattacceca J., Grady M. M., Herd C. D. K., Hewins R., Jambon A., Marty B., Rochette P., Smith C. L.,



Figure 4 – A. Ibhi analyzing the Igdi fragment at the Ibn Zohr University.



Figure 5 – A. Ibhi measuring the magnetic susceptibility on a fragment of Igdi meteorite at the Ibn Zohr University.

- Sautter V., Verchovsky A., Weber P., and Zanda B. (2012). “Tissint Martian meteorite: A fresh look at the interior, surface, and atmosphere of Mars. *Science* **338** 785–788.
- Folco L., Rochette P., Gattacceca J., and Perchiazzi N. (2006). “In situ identification, pairing, and classification of meteorites from Antarctica through magnetic susceptibility measurements”. *Meteoritics and Planetary Science*, **41**, 343–353.
- Graham A. L., Bevan A. W. R., and Hutchison R. (1985). *The Catalogue of Meteorites*. Fourth edition. Trustees of the British Museum (National History), London.
- Ibhi A. (2013). “New Mars meteorite fall in Morocco: final strewn field”. *International Letters of Chemistry, Physics, and Astronomy*, **11**, 20–25.
- Ibhi A. (2014). “Tighert: A new Eucrite meteorite fall from Morocco”. In Rault J.-L. and Roggemans P., editors, *Proceedings International Meteor conference*, Giron, France, 18–21 September 2014. IMO, pages 173–175.
- Khiri F. and Ibhi A. (2015). “African meteorites falls: some statistics”. In *European Planetary Science Congress 2015*, Nantes, France, 27 September–2 October 2015. EPSC2015-80.
- Khiri F., Ibhi A., Saint-Gerant T., Medjkane M., and Ouknine L. (2017). “Meteorite falls in Africa”. *Journal of African Earth Sciences*, **134**, 644–657.

# Evaluation of cosmic effects and risks of small bodies in the Solar System at Konkoly Observatory

Antal Igaz, Gergely Csépany, Nándor Opitz,  
Krisztián Sárneczky, and László L. Kiss

Konkoly Observatory, Research Centre for Astronomy and Earth Sciences, Hungarian Academy of Sciences, H-1121 Budapest, Konkoly Thege Miklós út 15-17, Hungary  
igaz.antal@csfk.mta.hu and csepany.gergely@csfk.mta.hu

Our project deals with observational studies of small bodies in the Solar System that approach the Earth and have the potential of impacting our planet. The observations combine a range of astronomical and geophysical techniques, among which a network of dedicated digital meteor cameras for measuring accurate orbits of bright fireballs, and the most advanced digital ionosonde techniques to complement optical meteor observations with radar measurements. We also intend to build the most sensitive system for detecting lunar impacts, with which we can characterize the impactor population.

## 1 Introduction

The Konkoly Observatory of Budapest was founded in 1899, when Miklós Konkoly Thege donated his private observatory to the state. Konkoly observed many comets and meteor showers visually and spectroscopically as well and concluded there was a close correlation between comets and meteors according to their chemical composition. He was the discoverer of two famous meteor showers, the  $\kappa$ -Cygnids and the  $\alpha$ -Capricornids.

In the 1930s and 1940s, G. Kulin carried out a photographic survey program to search for asteroids using the 0.60 m telescope and discovered several dozen asteroids and a comet. At the Piszkestető Mountain station of Konkoly Observatory, photographic observations were carried out mainly by M. Lovas with the 0.60 m Schmidt-telescope in the context of a supernova survey program. He also discovered 2 unusual asteroids and 5 comets between the early 1960s and the 1980s. At the end of the 1980s and the beginning of the 1990s, I. Toth made photoelectric photometric observations on Main Belt asteroids.

In 1997, we started an extensive asteroid search program with the Schmidt-telescope, and during this work we discovered more than 2000 main-belters and 7 NEOs.

In late 2016, we got 3.1 million EUR funding from the Hungarian National Research, Development, and Innovation Office, for the 4-year long project “GINOP-2.3.2-15-2016-00003 Kozmikus hatások és kockázatok” (Cosmic effects and risks)<sup>1</sup>. This grant has allowed the observatory to introduce a significant number of new positions in research and technical support, along with major upgrades to the instrumentation for various fields.

## 2 Aims

The “Cosmic effects and risks” project deals with observational studies of small bodies in the Solar System that approach the Earth and may have the potential of impacting our planet. The investigations combine a range of astronomical and geophysical techniques. The aims can be grouped into four areas:

1. to discover, confirm, and characterize near-Earth asteroids utilizing the 0.60 m Schmidt and 1.02 m Ritchey-Chrétien telescopes of the Piszkestető Mountain Station of Konkoly Observatory, and other worldwide telescopes (Müller et al., 2017);
2. to develop and build a network of dedicated meteor cameras for measuring the accurate orbits of bright fireballs, and detecting the fast light flashes during this events;
3. to use the most advanced digital ionosonde techniques to complement optical meteor observations with radar measurements; and
4. to build the most sensitive system for detecting lunar impacts to characterize the impactor population (Kereszturi and Steinmann, 2017).

The main result of the project will be a better understanding of the cosmic risks from meteoroid impacts on Earth and in the near-Earth space.

In the following, we will discuss the Konkoly Meteor Observing Network (KoMON) in detail.

## 3 KoMON

The Konkoly Meteor Observing Network aims to record the brightest fireballs while having high spatial resolution and high temporal resolution at the same time and

<sup>1</sup><http://nkfih.gov.hu/palyazatok/palyazatok-kfi-szakpolitikai-velemenyezese/ginop-2-3-2-15>.

operating also at night as a regular meteor observing system. We aim to observe the fragmentation processes in high resolution to support meteorite recovery and give insights in the fragmentation process itself. We will also record the sound if the conditions allow.

The meteor detector station will be composed of five boxes that cover about 90° of the sky (four looking at the horizon and one at the zenith as shown in Figure 1), which will use Nikon D5500 cameras with LCD shutters and a NET GigE video camera. Both the camera and the video camera will be equipped with wide-field lenses to achieve the 90° field of view. Each station will also have a fast-reaction pan-tilt security camera oriented upwards which we will configure to observe the fragmentation of the meteors.

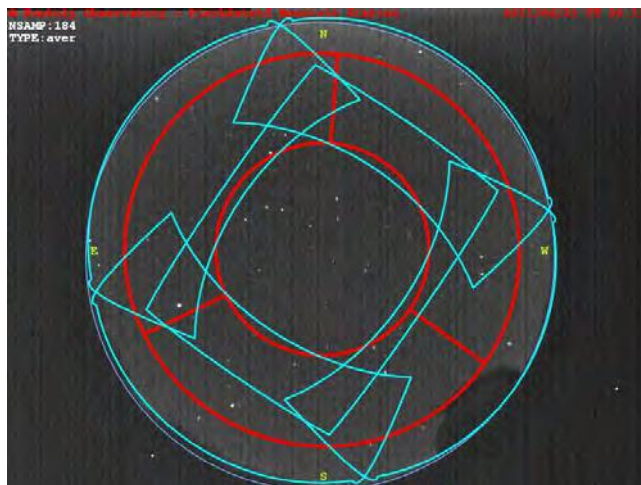


Figure 1 – Planned field of view (cyan squares) of the optical units using an example sky view from the Piskéztető Mountain Station. The red circles correspond with elevations of 30° and 60° above horizon.

The KoMON will operate at four sites in the beginning: Piskéztető Mountain Station, national parks with dark skies, and geodesic or GSM towers in rural areas, far away from the light pollution of the cities. Figure 2 shows the planned placement of the four stations.

#### 4 Milestones

In late 2017, we plan to build the first optical unit with the final parts in the final box that will also include the environmental regulatory system to heat and cool the box. We plan to benchmark and tune the software to detect meteorites in the coming months with this first box of the final size.

In early 2018, we plan to assemble the first station with five optical units and the fast reaction unit at Piskéztető. The final step will be to assemble and install all the four stations nationwide by the end of 2018. We plan to enter in the scientific mode of operation in early 2019.

After the KoMON has entered continuous operation, we want to supplement the four stations with some all-sky cameras at regions where the coverage is moder-

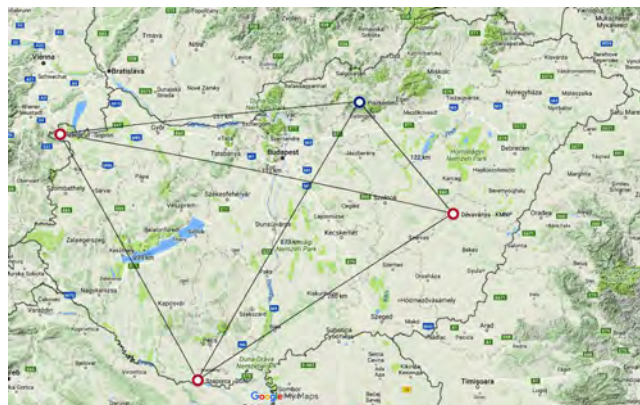


Figure 2 – Planned locations for the KoMON stations: Piskéztető Observatory, a geodesic tower near Sopron, and two national parks.

ate to obtain as much information about the meteors over Hungary as possible. These extra all-sky cameras can also help to track meteors in cloudy weather as the cloud coverage usually varies over Hungary, and the more cameras we have, the higher is the chance to observe the meteors, albeit at lower precisions than on clear nights.

#### 5 Conclusions

The Konkoly Observatory is carrying out a medium-term research project titled “Cosmic effects and risks” which aims to observe small bodies in the Solar System that approach the Earth and may have the potential of impacting our planet. The project aims to observe near-Earth asteroids, bright fireballs, and meteors, record meteor fragmentation, alleviate meteorite recovery, add ionosonde measurements to meteor detections, and detect lunar impacts. The KoMON network will use optical modes of observation to characterize meteors and meteorites over the sky in Hungary using four stations along the country.

#### Acknowledgements

This project has been supported by the GINOP-2.3.2-15-2016-00003 grant of the National Research, Development and Innovation Office (NKFIH, Hungary) and by the Hungarian Academy of Sciences.

#### References

Kereszturi A. and Steinmann V. (2017). “Characteristics of small young lunar impact craters focusing on current production and degradation on the Moon”. *Planetary and Space Science*, **148**, 12–27.

Müller T. G., Marciniak A., Butkiewicz-Bak M., Duffard R., Oszkiewicz D., Käuffel H. U., Szakáts R., Santana-Ros T., Kiss C., and Santos-Sanz P. (2017). “Large Halloween asteroid at lunar distance”. *Astron. Astrophys.*, **598**, A63.

# Atmospheric phenomena radio localization system

Jakub Kákona<sup>1</sup>, Roman Dvořák<sup>2</sup>, Martin Kákona<sup>3</sup>, and Jan Mikeš<sup>1</sup>

<sup>1</sup> CTU in Prague, Czech Republic  
kakonjak@fel.cvut.cz

<sup>2</sup> Bolidozor, Czech Republic  
romandvorak@mlab.cz

<sup>3</sup> Nuclear Physics Institute, Czech Republic  
kakl@astro.cz

Recent radio systems have significant capabilities to detect the presence of meteor trails. There is noticeable progress in the localization of these trails. Unfortunately, the current localization methods have important requirements, which limits their practical use. One example is the necessity of a correct model initialization, but the initial lack of position estimates results in a bad estimation performance. Therefore, we present a new receiver and signal processing system which could obtain better data to initialize the trajectory estimation model. As a bonus, the proposed system can also be used to detect other atmospheric phenomena than meteor trails.

## 1 Introduction

Recent radio systems have significant capabilities to detect the presence of meteor trails (Vallejo, 2016). There is noticeable progress in the localization of these pathways. Unfortunately, the current localization methods have important requirements which limit their practical use. One example is the necessity of a correct model initialization, but the initial lack of position estimates results in a bad estimation performance. Therefore, we present a new receiver and signal processing system which could obtain a better data to initialize the trajectory estimation model. As a bonus, the proposed method can also be used to detect more atmospheric phenomena than meteor trails only.

To obtain the initial position estimate, the information about the direction of the signal source is needed. Such data can be collected by radio direction finding methods. The most promising method is antenna array direction finding which allows simultaneous processing of the signal from multiple or complex signal sources.

## 2 Station hardware

Antenna array direction finding systems are complex systems for which no commercial solutions are available; therefore, the reception system must be developed.

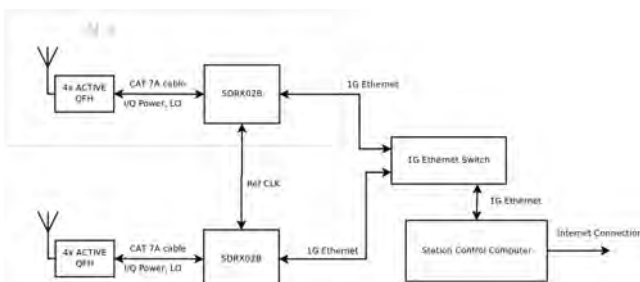


Figure 1 – Proposed radio reception station setup with multiple antenna arrays.

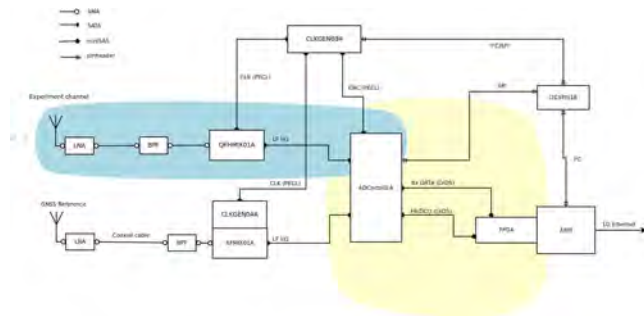


Figure 2 – Single receiver block. Full expansion of the SDRX02B part from Figure 1.

Therefore the new receiver hardware architecture is introduced to cover as many scientific use cases of antenna array receiver as possible.

Figures 1 and 2 show the overall schema of a receiver station connected to the network. This single location consists of multiple blocks each containing four antenna elements. The antenna block is visualized in Figure 3.

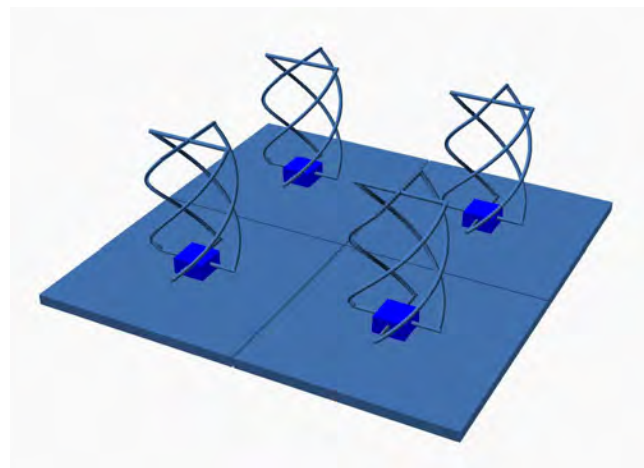


Figure 3 – Antenna array block, consisting of 4 active Quadri-filar Helix antennae with LNA, band-pass filters, and mixers.

The antenna blocks could be used multiple times per station. Therefore, they could potentially form a scalable antenna array optimized for application and/or project budget. System phasing is maintained by using a single oscillator between multiple antenna blocks. It is accomplished by using fiber optics cables with digital modulators from LVDS (Low Voltage Differential Signaling) signal output based on the central oscillator.

### 3 Time and frequency reference

Although all array elements have a frequency source based on the low-noise central oscillator, the overall precision of oscillator needs to be corrected by system design. In Figure 2, one can notice a GNSS (Global Navigation Satellite System) reference antenna. This antenna is the time and frequency signal source, because the received GNSS signal could be mixed to a receiver signal channel and processed in the software. Then, the software could output a station position, frequency shift of local oscillator, and relative phase of the signal. This information is precious for system oscillator correction and calibration.

### 4 Station software

Each station has multiple computation units. The antenna blocks are equipped with Xilinx Zynq FPGA containing ARM which allows running LINUX and GNURADIO. It allows basic processing antenna block signal and extracting GNSS reference data. The complete signal flow is displayed in Figure 4.

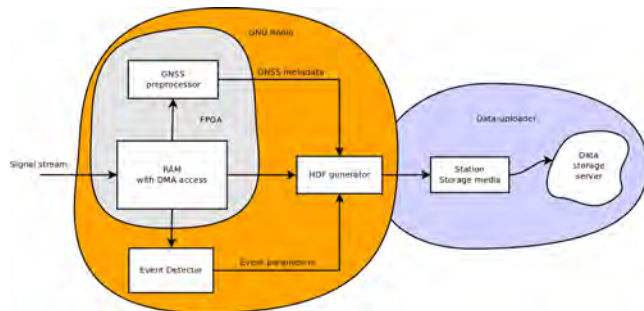


Figure 4 – Station signal processing diagram.

The data stream is cached in RAM, accessible to multiple processes. The event detector process detects signal features corresponding to observed phenomena. The GNSS preprocessor takes signal samples containing the GNSS received message and extracts information useful for station calibration and system verification.

### 5 Network deployment

It is our intention to replace the suitable existing Bolidozor network stations by a new receiver hardware allowing directional finding of atmospheric phenomena. This upgrade is not possible for all stations, however, because the antenna array needs a specific environment

to work correctly. The array must have a flat and conductive surface with minimal obstacles to avoid distortion of antenna radiation patterns. Therefore, the most suitable locations are observatories with large flat roofs covered with metal sheets. The current map of Bolidozor stations is shown in Figure 5.

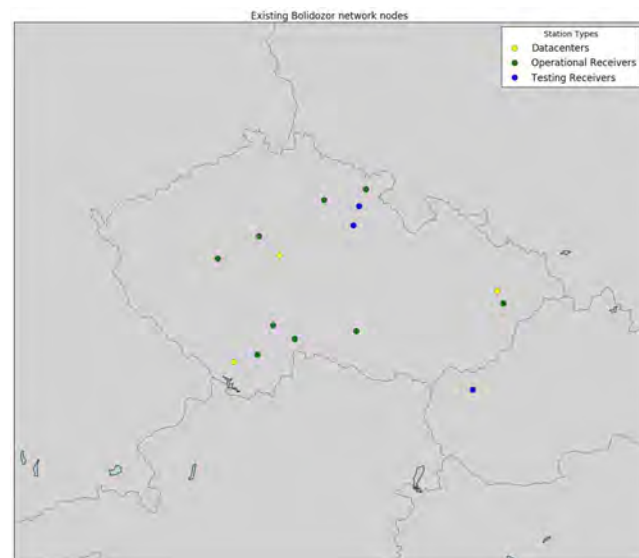


Figure 5 – Map of Bolidozor network nodes.

### 6 Network architecture

The data obtained by a station network with the antenna array receivers produce a significant amount of data. These data need to be processed to reduce the amount of data in storage. The overall architecture of the data processing system is shown in Figure 6.

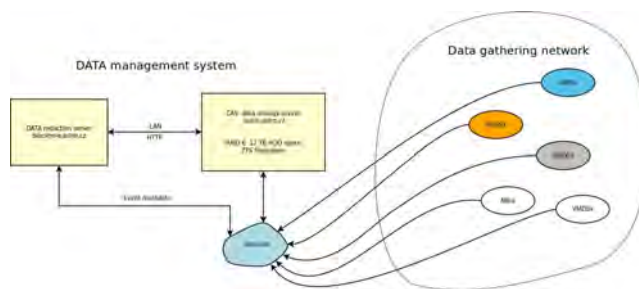


Figure 6 – System architecture of data processing.

A more detailed description of the current data storage and processing system can be found in Dvořák et al. (2017).

### 7 Conclusions

The proposed system has sufficient parameters to detect and collect data about multiple scientific research targets. It can be used for radio detection and localization of meteor trails, lightning mapping, or for reception of satellite telemetry. This is possible, because the receiving radio band is limited mostly by the antenna design. Therefore, the reception band could be changed by us-

ing differently sized antenna elements, or the station could be equipped with multiple antenna blocks, each suitable for a different scientific project. The proposed architecture allows the creation of software-defined radio reception campaigns triggered over a distributed and redundant receiver network.

### Acknowledgement

This work was supported by the European Regional Development Fund, Project CRREAT, with reference number CZ.02.1.01/0.0/0.0/15\_003/0000481.

### References

- Dvořák R., Štrobl J., and Kákona J. (2017). “Data management system of the Bolidozor network”. In Gyssens M. and Rault J.-L., editors, *Proceedings of the International Meteor Conference*, Petnica, Serbia, 21–24 September 2017. IMO, pages 184–186.
- Vallejo M. A. (2016). “Determining the radiant of a meteor using Graves radar”. In the blog [http://ea4eoz.blogspot.sk/2016/04/determining-radiant-of-meteor-using\\_10.html](http://ea4eoz.blogspot.sk/2016/04/determining-radiant-of-meteor-using_10.html).

# Nineteen years of meteor astronomy in Israel

Anna Levin, Tamira Tchenak, Ella Ratz, Shlomi Eini, Yaron Eini, and Shy Halatzi

## Meteor Section of the Israeli Astronomical Association

An overview of the activities of the Meteor Section of the Israeli Astronomical Association (IAA) is presented.

The IAA is a non-profit amateur and scientific organization dedicated to general astronomy.



Figure 1 – The IAA Meteor Section observing team, ready for the Perseids 2015 in the Arava Desert. (Photo Yaron Eini—<http://www.yaroneini.com>.)

The purpose of its Meteor Section is to observe and report meteoric activities to the International Meteor Organization (IMO) and to promote awareness of science, and of astronomy in particular, among the Israeli public. Our activities are published mainly in Hebrew.



Figure 4 – Team that went observing the Perseids 2014 in Be'er Menuha. (Photo Tamara Tchenak.)



Figure 2 – Arava Desert observing camp for the Perseids 2015. (Photo Yaron Eini—<http://www.yaroneini.com>.)



Figure 5 – Preparing to observe the Perseids 2014 in Be'er Menuha. (Photo Tamara Tchenak.)

The Meteor Section is the most significant organization for meteor observation and documentation in Israel. It includes about ten observers, led since 1998 by Anna



Figure 3 – Observing the Perseids 2015 from the Arava Desert. (Photo Yaron Eini—<http://www.yaroneini.com>.)



Figure 6 – Leonids in 1998 at Wise Observatory. (Photo Ofer Gabzo.)



# Meteorite-producing fireball streams

Alexandra Terentjeva and Sergey Barabanov

Institute of Astronomy of the Russian Academy of Sciences, Moscow, Russia  
 ater@inasan.ru and sbarabanov@inasan.ru

Meteorite-producing streams (mainly of asteroidal origin) may contain large bodies which are capable of causing great damage in the case of their fall on the Earth. Therefore, the problem of meteorite-producing streams is part of a general multi-faceted space hazard problem. Analysis of the catalogue of 78 fireball streams (Terentjeva, 1990) has revealed the streams which contain meteorite-producing bodies among their individual members. We found 11 such fireball streams, and 6 of them (54%) are related to meteoroid streams. As these meteorite-producing streams are an object of special interest, the attention of observers and meteor researchers is called to this problem.

## 1 Introduction

A first service for registration of near-Earth (potentially hazardous) asteroids and comets (Space Watch) has been working since 1985. Now, there are more than ten such services. Potentially hazardous asteroids or comets, as a rule, form associations and families, which may enter in meteoroid and fireball streams with meteoroids, having diameters of 1–10 m. It is currently believed that bodies with sizes in the order of 10 m may bring local-scale hazards. Those bodies can only be revealed occasionally, as they are very faint at a distance of 0.1 AU and almost always move with significant angular velocities. However, statistics of fireball and meteor showers, especially, related to asteroids and comets, can indicate which orbits and orbit families along with their theoretical radiants can be sources of hazardous bodies. They should be given preference for effective monitoring by observers, with given theoretical directions of motion and calculated angular velocities.

The meteorite-producing streams (mainly of asteroidal origin) may contain large bodies which are able to produce substantial destructions, when falling on Earth. Therefore, the problem of meteorite-producing streams is part of a more general problem of space hazards.

## 2 Research results

Having analyzed 78 fireball streams (Terentjeva, 1989a; 1990), we identified streams containing meteorite-producing bodies among their individual members. There are 11 such fireball streams. Orbital elements of these streams are presented in Table 1, and their orbits are shown in Figure 1. In the last column of Table 1, the number (by corresponding source) of meteorite-producing fireballs in the stream is indicated. Since in the work of Ceplecha (1978) the numbering is missing in the table of 44 European Network fireballs, we introduced such numbers which are given in the last column of Table 1.

From the 11 meteorite-producing streams considered, two streams are especially remarkable. The first is the  $\mu$ -Orionids (Table 1, No. 1) which has produced the

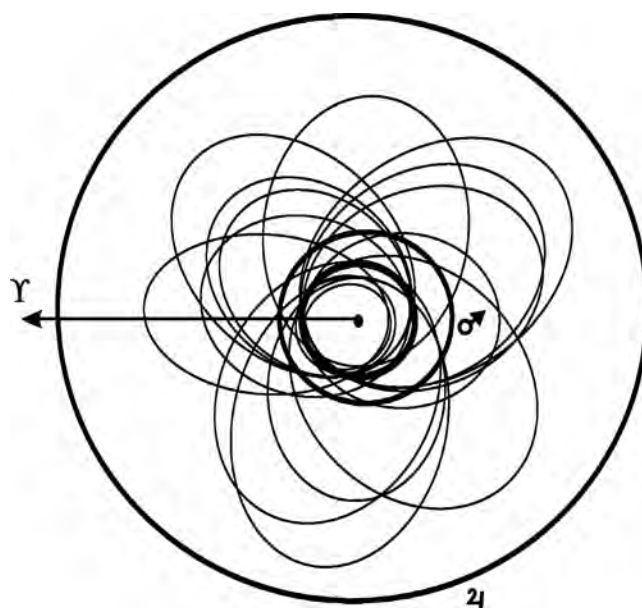


Figure 1 – Orbits of the 11 meteorite-producing fireball streams in Table 1.

Tagish Lake meteorite—or, more precisely, meteorite shower (Terentjeva and Barabanov, 2004). The possible range of initial mass seems to be 50–180 tons (Brown et al., 2001). The second is the  $\alpha$ -Coma Berenicids (Table 1, No. 21A), which has produced the Příbram meteorite, the initial mass of which was 21 500 kg (Ceplecha, 1978). The meteorite belongs to bodies of group I with greatest structural strength. The average density of bodies of group I is 3.7 g/cm<sup>3</sup>. The Lost City and Innisfree meteorites also belong to this group. Group I corresponds to ordinary chondrites. The meteorite-producing fireball from the  $\eta$ -Serpentids (Table 1, No. 38) is chondritic, too. The  $\zeta$ -Taurids (Table 1, No. 72) had 3 meteorite-producing fireballs with initial masses  $M_\infty$  of 17 000 kg, 240 kg, and 100 000 kg, respectively. In the 8 remaining streams,  $M_\infty$  ranges from 47 kg to 340 kg, with the exception of the  $\tau$ -Cetids (Table 1, No. 50), which includes a fireball with  $M_\infty = 35 000$  kg.

Among the 11 orbits of meteorite producing streams, 5 have their aphelion located within the Main Belt of asteroids, and 5 have their aphelion located outside

Table 1 – Meteorite producing fireball streams (Equinox 1950.0).

No. [1]	Fireball stream	Period	Corr. geoc. radiant $\alpha$ $\delta$	$V_\infty$ (km/s)	$a$ (AU)	$e$	$q$ (AU)	$i$	$\omega$	$\Omega$	$\pi$	Sources
1	$\mu$ -Orids	I 01–II 04	88° +12°	16.4	1.866	0.524	0.854	4° 1'	51° 7'	112° 5'	164° 2'	Tagish Lake
20 <sup>1</sup>	$\chi$ -Virids	III 22–IV 28	183° –11°	19.6	1.983	0.614	0.742	3° 8'	71° 3'	197° 0'	268° 3'	31 E
21A <sup>2</sup>	$\alpha$ -Comds	IV 07–10	196° +21°	21.6	2.66	0.70	0.782	13° 3'	241° 9'	18° 3'	260° 2'	Příbram, 8 E
26	$\eta$ -UMads	IV 25–V 25	203° +51°	16.6	2.404	0.578	0.995	15° 6'	194° 0'	53° 3'	247° 3'	240 F
37	$\mu$ -Serds	VII 03–31	232° –04°	14.1	2.447	0.594	0.992	3° 3'	197° 3'	114° 3'	311° 6'	405 F
38 <sup>1</sup>	$\eta$ -Serds	VIII 14–30	286° –03°	13.5	1.73	0.439	0.968	4° 5'	210° 5'	150° 2'	0° 7'	38 E
44	$\delta$ -Equ- $\epsilon$ -Gruds	(N)	319° +09°	18.3	2.629	0.659	0.868	9° 3'	228° 5'	169° 2'	37° 7'	–
		(Q)	321° –13°	16.3	2.294	0.607	0.898	2° 8'	39° 7'	355° 5'	35° 2'	151 F
		(S)	342° –52°	18.0	2.205	0.589	0.907	14° 9'	43° 1'	344° 8'	27° 9'	–
50	$\tau$ -Cetds	IX 28–XI 26	18° –19°	20.4	2.442	0.667	0.791	11° 6'	58° 4'	27° 4'	85° 8'	503 F
64	Cam- Lepds	(N)	115° +70°	14.6	0.794	0.287	0.566	16° 1'	337° 0'	228° 9'	205° 9'	–
		(S)	91° –14°	14.8	0.898	0.266	0.658	12° 7'	127° 8'	66° 4'	194° 2'	275 F
70	$\delta$ -Arids	(N)	53° +29°	18.4	1.826	0.560	0.766	4° 2'	247° 3'	251° 1'	138° 4'	–
		(Q)	55° +18°	19.4	2.440	0.671	0.786	1° 2'	59° 7'	75° 0'	134° 7'	219 I
		(S)	61° +07°	18.6	1.982	0.591	0.788	5° 8'	62° 8'	75° 4'	138° 2'	–
72 <sup>1</sup>	$\zeta$ -Tauds	XII 01–27	82° +23°	26.2	2.164	0.756	0.518	3° 8'	275° 7'	260° 0'	175° 7'	40 E, 470 F, 223 I

Notes: [1]—Terentjeva (1989a; 1990).

<sup>1</sup> Mean values of orbital elements recalculated due to addition of new stream members.

<sup>2</sup> Fireball stream identified after publication of catalogue [1].

Sources: F—McCrosky et al., *Prairie network fireball data 1963–75*, IAU Meteor Data Center, Lund, Sweden

(McCrosky et al., 1976); I—Halliday et al., *MORP network fireball data 1971–84*, IAU Meteor Data Center, Lund, Sweden;

E—Ceplecha (1978).

the Main Belt, in the neighborhood of the orbits of Hilda-type asteroids (with a distance from Sun of about 3.95 AU). Only one stream (Table 1, No. 64), with an aphelion distance  $Q \approx 1$  AU, belongs to the Earth group.

Upon considering the link between meteorite-producing streams and meteoroid streams, we found that 6 out of the 11 streams (54%) are related to meteoroid streams (Table 2). Thus, all meteoroid streams related to these specific fireball streams are also meteorite-producing streams.

Table 2 – Meteorite producing fireball streams related to meteoroid streams.

Meteorite-producing fireball stream [1]	Meteoroid stream [2]
1	2
20	41, 45
26	75
50	131, 132, 133
70	145
72	148

Notes: [1]—Terentjeva (1989a, 1990).

[2]—Terentjeva (1966).

It is necessary to add two more streams to the 11 meteorite-producing fireball streams we found.

The first is the meteoroid stream  $\iota$ -Piscids (Terentjeva, 1966, No. 131), because a very bright fireball was caused by this stream. The fireball flew over the Czech Republic and Poland on 2003 September 29 and produced a meteorite with a mass of 400 g (Spurný, 2003). A report on this subject was presented by us (Terentjeva and Barabanov, 2015).

The second is the meteoroid stream which produced the

Chelyabinsk fireball on 2013 February 15. We called this stream the Daytime Pegasid-Aquarids (Terentjeva and Bakanas, 2013). The large fireball produced the Chelyabinsk meteorite. The mass of the largest fragment of this meteorite is 570 kg or more (Popova et al., 2013).

Other researchers may extend our list of meteorite-producing streams considerably. We identified 15 fireball streams which do not have a meteorite-producing component, but have massive meteoroid bodies with initial mass  $M_\infty$  of about 50 kg or more (Table 3, Figure 2). The streams in this set have a wider variety of orbits. For example, one stream has an aphelion distance  $Q = 7.4$  AU, which is between the orbits of Jupiter and Saturn. Orbital inclinations  $i$  for three of the streams are 18°, 28°, and 30°, respectively (meteorite-producing streams have inclinations  $i \leq 16^\circ$ , see Table 1). A smaller proportion of aphelions (6 out of 15, that is 40%) is located in the Main Belt of asteroids. The remaining streams have typical Apollo orbits with aphelion distances between the outer Main Belt border and the Jupiter orbit, i.e.,  $3.8 \text{ AU} \leq Q \leq 4.8 \text{ AU}$ , except of course for the stream mentioned above with  $Q = 7.4 \text{ AU}$ .

In four of the streams, fireballs are detected which belong to groups II and IIIB in the Ceplecha and McCrosky classification. Bodies of group II have densities in the order of  $2.1 \text{ g/cm}^3$ , and are possibly linked to carbonaceous chondrites (Ceplecha, 1978). The bodies of group IIIB have density in the order of  $0.2 \text{ g/cm}^3$ . Many fireballs consist mostly of porous comet matter and have such a low density.

Note that entry velocities of meteoroid bodies in the atmosphere (for 11 streams out of 15) are within the range  $V_\infty = 14\text{--}26 \text{ km/s}$ , and thus do not exceed presently

Table 3 – Fireball streams with initial mass  $M_\infty$  of about 50 kg or more, and their relation to meteoroid streams

Fireball stream [1]	$M_\infty$ (kg)	Meteoroid stream
3	60	–
4	3200	–
6 (a)		8, 21 [2]
(b)	81	
(c)		
9	51	–
18	48	28, 42 [2]
22 (N)		38 [2]
(S)	5000	
33	1000	84 [2], 215 [3], 82 [4]
35	410	93 [2]
40	810	–
42 (a)		
(b)	4000	[5], [6], 122 [7]
45	270	237 [3]
51 (a)		–
(b)	47	
52 (N)	57	–
(S)		
76	68	–
77	59	–

- [1]—Terentjeva (1989a; 1990).
- [2]—Terentjeva (1966).
- [3]—Terentjeva (1968).
- [4]—Terentjeva (1967).
- [5]—Terentjeva (1965).
- [6]—Cook (1973).
- [7]—Lindblad (1971).

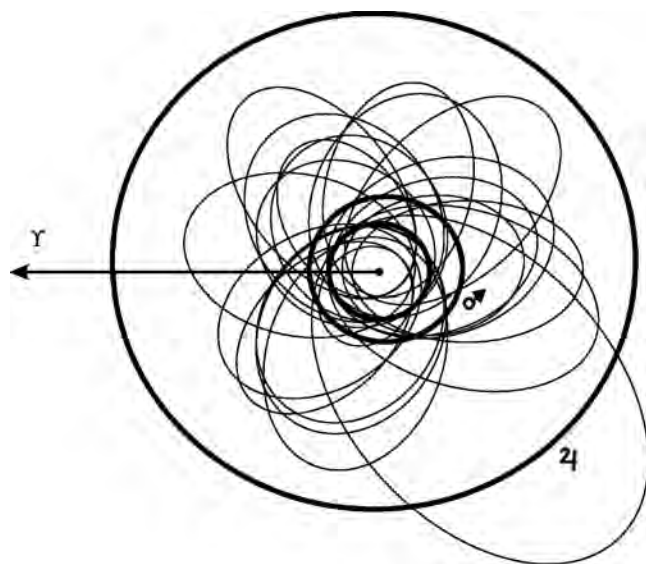


Figure 2 – Orbits of the 15 fireball streams in Table 3.

adopted upper limits for the entry velocity of meteorite-producing bodies in the atmosphere (Terentjeva, 1989b). Also, massive meteoroid bodies with large initial mass  $M_\infty$  do not “penetrate” the Earth’s atmosphere. Of course, in reality different kinds of dependences work which are much more complex than generally consid-

ered, as Ceplecha already noted (1978). However, apparently, we can assume that in a group of 15 fireball streams with massive bodies we deal with porous comet matter. Seven out of the 15 fireball streams of this group (47%) are related to meteoroid streams (Table 3).

### 3 Conclusions

Since meteorite-producing streams are of special interest, observers and researchers of meteors need to pay attention to the following:

1. One should compare the new extensive series of fireball observations, available now, with the meteorite-producing streams described above, hereby expanding our knowledge about those fireball streams.
2. To complement these streams with new data about the presence of meteorite-producing component in these streams, and to find new meteorite-producing streams.
3. It would be reasonable to organize an effective monitoring of meteorite-producing streams.

Minor meteor showers seem unattractive for some meteor observers due to their weak activity. There were many cases, however, where those “weak” showers produced unexpected fireworks of bright meteors and fireballs, and even created a surprise in the form of meteorite shower. It happened, for example, with the fireball stream  $\mu$ -Orionids, which produced the Tagish Lake meteorite (see above).

Thus meteorite producing streams should always be in the zone of high attention of meteor researchers.

### Acknowledgements

This work was supported by Program No. 7 of the RAS Presidium “Experimental and theoretical research of the objects of the Solar System and planetary systems of stars. Transient and explosive processes in astrophysics” and was also partially supported by the President RF grant NSh9951.2016.2.

### References

Brown P., ReVelle D., and Hildebrand A. (2001). “The Tagish Lake meteorite fall: interpretation of fireball physical characteristics”. In Warmbein B., editor, *Proceedings of the Meteoroids 2001 Conference*, Kiruna, Sweden, 6–10 August 2001. ESA SP-495, pages 497–505.

Ceplecha Z. (1978). “Fireballs of the European network”. *Meteoritika*, **37**, 60–68. In Russian.

- Cook A. F. (1973). “A working list of meteor streams”. In Hemenway C.L., Millman P.M., Cook A.F., editors, *Evolutionary and Physical Properties of Meteoroids*, NASA SP-319, pages 183–191.
- Lindblad B. A. (1971). “1. A stream search among 865 precise photographic orbits; 2. A computerized stream search among 2401 photographic orbits”. *Smithson. Contr. Astrophys.*, No. 12, 1–24.
- McCrosky R. E., Shao C.-Y., and Posen A. (1976). “Prairie network fireball data. I. Summary and orbits”. *Preprint Series*, No. 665. Center for Astrophysics, Cambridge, MA, USA.
- Popova O. P., Jenniskens P., Emel’yanenko V., Kartashova A., Biryukov E., Khaibrakhmanov S., Shuvalov V., Rybnov Y., Dudorov A., Grokhovsky V. I., Badyukov D. D., Yin Q. Z., Gural P. S., Albers J., Granvik M., Evers L. G., Kuiper J., Kharlamov V., Solovyov A., Rusakov Y. S., Korotkiy S., Serdyuk I., Korochantsev A. V., Larionov M. Y., Glazachev D., Mayer A. E., Gisler G., Gladkovsky S. V., Wimpenny J., Sanborn M. E., Yamakawa A., Verosub K. L., Rowland D. J., Roeske S., Botto N. W., Friedrich J. M., Zolensky M. E., Le L., Ross D., Ziegler K., Nakamura T., Ahn I., Lee J. I., Zhou Q., Li X. H., Li Q. L., Liu Y., Tang G. Q., Hiroi T., Sears D., Weinstein I. A., Vokhmintsev A. S., Ishchenko A. V., Schmitt-Kopplin P., Hertkorn N., Nagao K., Haba M. K., Komatsu M., Mikouchi T., Chelyabinsk Airburst Consortium. (2013). “Chelyabinsk airburst, damage assessment, meteorite recovery, and characterization”. *Science*, **342**, 1069–1073.
- Spurný P. (2003). “Atmospheric trajectory and heliocentric orbit of the EN290903 Ošwiecim fireball from photographic records”. *WGN, Journal of the IMO*, **31**, 171–173.
- Terentjeva A. K. (1965). “Investigation of the  $\delta$ -Aquarid meteor stream”. *Bull. Komissii po kometam i meteoram AN SSSR*, No. 11, 17–32. In Russian.
- Terentjeva A. K. (1966). “Minor meteor streams”. *Rezult. Issled. MGP, Issled. Meteorov*, No. 1, 62–132. In Russian.
- Terentjeva A. K. (1967). “Orbits of minor meteor streams”. *Astron. Circular of the Academy of Sciences of the USSR*, **423**, 1–7. In Russian.
- Terentjeva A. K. (1968). “Investigation of minor meteor streams”. In Kresák L. and Millman P. M., editors, *Physics and dynamics of meteors*, Dordrecht-Holland, pages 408–427.
- Terentjeva A. K. (1989a). “Fireball streams”. *WGN, Journal of the IMO*, **17**, 242–245.
- Terentjeva A. K. (1989b). “Minor bodies of the Solar System: meteorite orbits, interrelation, ‘mirror symmetry’ in C-distribution”. *Pisma v Astron. Zhurnal*, **15**, 258–269. In Russian.
- Terentjeva A. K. (1990). “Fireball streams”. In Lagerkvist C.-I., Rickman H., Lindblad B.A., and Lindgren M., editors, *Asteroids, Comets, Meteors III*. Uppsala University, pages 579–584.
- Terentjeva A. and Bakanas E. (2013). “Meteor stream of the large Chelyabinsk fireball”. *WGN, Journal of the IMO*, **41**, 39.
- Terentjeva A. and Barabanov S. (2004). “The fireball stream of the Tagish Lake meteorite”. *WGN, Journal of the IMO*, **32**, 60–62.
- Terentjeva A. K. and Barabanov S. I. (2015). “Meteorite producing stream of large meteor bodies”. In *NearEarth Astronomy. IX International conference. Abstract book*. Terskol, Russia 31 August–5 September 2015. Page 64.

# Calendar of meteor activity based on IMO video observations 2006–2015

Filip Fabris<sup>1</sup>, Marija Kosić<sup>1</sup>, Snježana Štefanić Hoefel<sup>1</sup>,  
Damir Šegon<sup>2</sup>, and Mateja Dumbović<sup>3</sup>

<sup>1</sup> High School “Zvanje Črnje, Rovinj, Croatia

filip1fabris@gmail.com, marijakosic099@gmail.com, and stefanic.snjezana@gmail.com

<sup>2</sup> Astronomical Society “Istra” Pula, Pula, Croatia

damir.segon@pu.t-com.hr

<sup>3</sup> Institute of Physics, University of Graz, Graz, Austria

mateja.dumbovic@uni-graz.at

The IMO data of detected video meteors were used to calculate the average and maximum meteor activity throughout the year. This resulted in a very practical calendar of meteor activity, which can be a helpful tool for not only amateur astronomers but also for children and the general public—all those who wish to observe meteors.

## 1 Introduction

Meteor showers are phenomena of many meteors visible as light trails in the sky radiating from one point direction, in a time interval spanning from several hours to several days. These phenomena can be observed throughout the year and are mostly caused by small-scale particles named meteoroids, which represent residue of mostly cometary material as the Earth passes through. Meteors enter the atmosphere of the Earth at great speeds and leave a light trail which may be observed visually or by other techniques, from which the most popular one is by video cameras.

Data from video observations collected by the International Meteor Organization (IMO) were used to compile a calendar which would represent averaged and maximal meteor activity for each day of the year.

## 2 Method

In order to calculate the average daily meteor activity, data from video observations provided on the IMO web pages were taken from the period from 2006 to 2015. Daily observations are relatively balanced on an annual basis, and there are not too many data gaps. The IMO data are given as reports listing the number of observed meteors and the effective observing time. Dividing the two, we get the meteor rate expressed in meteors/hour. Therefore, using IMO data, the daily meteor rate for each year in the chosen time period was obtained. These were then used to calculate the maximum and average daily meteor rate for each day of the year (1–365), where leap years were included but without their “leap day”, February 29th (activities for that date were recalculated for previous and the day to follow). As a result, a time series was obtained which represents the average and maximum expected meteor activity throughout the year.

## 3 Results

The average and maximum expected meteor activity throughout the year calculated from IMO data are presented in Figure 1.

The calendar has been built as a polar diagram containing data on averaged activity for each day of the year (blue line). Since the range of averaged data used covers 10 years, the differences in solar longitudes from day to day may be considered irrelevant, bearing in mind the particular purpose of the present calendar. Besides the averaged data, the maximal value on a given date is presented as a separate curve (red line) which might be found useful as a pointer to a date when an observer may expect some higher activity than the one stated on the calendar.

The most important meteor showers may be identified on the calendar, labeled with their respective abbreviations according to the IAU Meteor Shower Database. There are obvious peaks on dates which are not usually found as maximum of the activity for some showers, which can be seen in the case of the Orionids and  $\eta$ -Aquariids, corresponding to activity caused by separate trails observed during the processed period.

The number of actual meteors seen (or observed by other means) will most certainly be different from the one read from the calendar for most of visual observers or video cameras, due to varying sensitivities and observers skills, but the ratio of meteors seen or detected from night to night would most probably be proportional to the values obtained from the calendar.

## 4 Conclusions

The IMO data of video meteors were used to calculate the average and maximum expected meteor activity throughout the year.

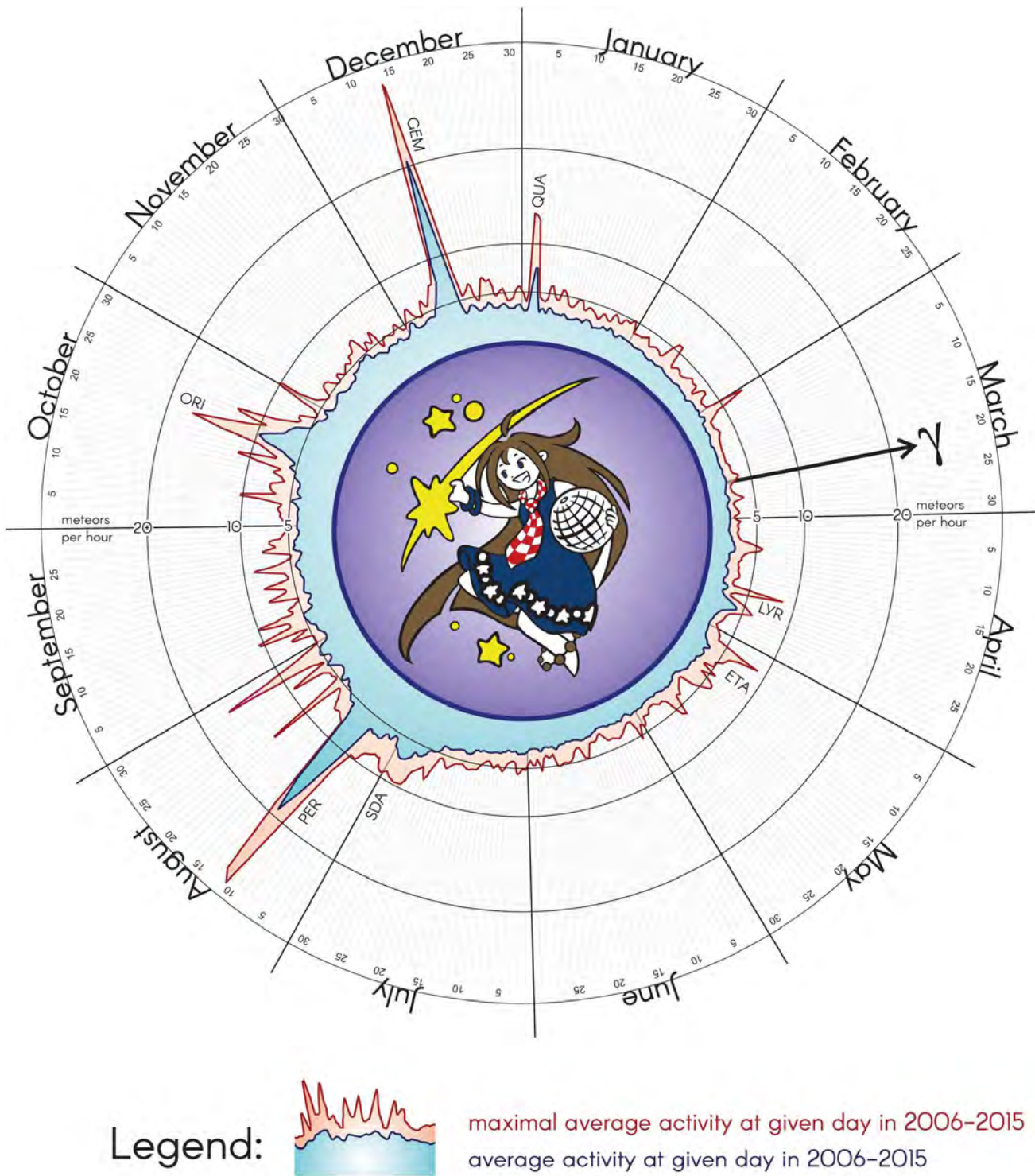


Figure 1 – Meteor activity calendar.

This resulted in a very practical calendar of meteor activity. The calendar shows when we may expect to see increased meteor activity, to which meteor shower this increased activity corresponds to, how many meteors we may expect to observe on average in one hour time, and what the maximum number of meteors is we may hope to observe in one hour time.

Therefore, the calendar of meteor activity can be a helpful tool for not only amateur astronomers but also for children and the general public—all those who wish to observe meteors and meteor showers.

## Acknowledgements

Filip Fabris wishes to thank his teacher and supervisor, Snježana Štefanič Hoefel, as well as Damir Šegon, for their patience and help in making this student project possible. Many thanks go also to Edin Velič for the help in visualizing the calendar of meteor activity.

This work has been partially supported by the Ministry of Science and Education of the Republic of Croatia, and the Association of Technical Culture of the Istrian Region.

## Bibliography

- Akademsko astronomsko društvo Rijeka. (Feb 21, 2017). [http://www.aad.hr/lista/6/almanah/8/me-te-or-ski\\_potoci.html](http://www.aad.hr/lista/6/almanah/8/me-te-or-ski_potoci.html).
- Biliškov N. (2009). *Meteori golim okom*. Sveučilišna knjižara.
- EarthSky's meteor. (Feb 18, 2017). <http://earth-sky.org/astronomyessentials/earthskymeteorshowerguide>.
- Eškola meteorski potoci. (March 10, 2017). <http://eskola.zvezdarnica.hr/osnoveastronomije/suncevsustav/meteori/>.
- Geminid meteors. (Feb 13, 2017). <http://www.space.com/34921geminidmeteorshowerguide.html>.
- International Meteor Organization. (Jan 2006–Dec 2015). <http://www.imonet.org/reports/>.
- Meteorski potok. (March 12, 2017). [https://hr.wikipedia.org/wiki/Meteorski\\_potok](https://hr.wikipedia.org/wiki/Meteorski_potok).

# Dark flight integrator in action: 2015 Easter bolide recalculated

Tibor Hegedüs<sup>1</sup>, Zoltán Jäger<sup>1</sup>, Zoltán Jäger, Jr.<sup>1</sup>, Szilárd Csizmadia<sup>2</sup>,  
Zsolt Kereszty<sup>3</sup>, and Zoltán Zelkó<sup>4</sup>

<sup>1</sup>Baja Observatory of the University of Szeged, Hungary  
hege@electra.bajaobs.hu

<sup>2</sup>Institute of Planetary Research, German Aerospace Center, Berlin, Germany

<sup>3</sup>Corona Borealis Observatory, Győr, Hungary, IMCA, Meteoritical Society

<sup>4</sup>Vega Astronomical Association, Zalaegerszeg, Hungary

As an extension of our previous meteor atmospheric trajectory calculator code, a new dark flight integrator has been developed by us. Here, we discuss the accepted atmospheric model, and the relevance of the wide-range behavior of the drag coefficient. As a trivial test, we compare our result with the analytic solution of free fall and step by step go to the more realistic cases. The first real application we made was the re-calculation of the so-called “Easter bolide” which flew over Hungary on 6 April 2015 at 17<sup>h</sup>31<sup>m</sup>01<sup>s</sup> UTC. The strewn field has been derived for different-sized stone pieces, and the probable effect of disintegration has also been considered by Monte Carlo simulation of the wide range of the characteristic speed of the final explosion. There was only one mini-expedition to the site for trying to recover some pieces—without success yet. The work will be continued.

## 1 Introduction and motivation

The need for a better understanding of the meteor flight in the atmosphere, and the determination of more reasonable search areas for possible meteorite falls associated to exploding bolides observed previously over Hungary has motivated us to build our own integrator code for solving the “dark flight” part of the meteor phenomena. Here, we present the basics of our model, and discuss some few test runs. In addition, we show its very first real application, to the so-called “Easter Bolid” which flew over Hungary on 6 April 2015 at 17<sup>h</sup>31<sup>m</sup>01<sup>s</sup> UTC. The field search already started in the resulting strewn fields areas, but no meteorite was found yet.

For the sake of a clearer overview (and better understanding) of the kinematics of the meteoroid body in the atmosphere, we first chose a flat Earth model with plan-parallel atmosphere. The selected Cartesian coordinates system and the initial configuration can be seen in Figure 1. Later, this restriction can be easily lifted and the coordinates system changed to an Earth-centered spherical coordinates system. The results do not much differ.

The meteoroid body is described as an homogeneous sphere with a radius  $r$  and a density  $\rho$ . The direction of the initial velocity vector is given by two angles:  $\alpha$ , the angle with the  $z$  axis (zenithal distance), and  $Az$ , the azimuth angle (considered in the usual sense, as in spherical astronomy). The components of the initial velocity vector are now

$$\begin{aligned} v_{x,0} &= -v_0 \sin \alpha \sin Az; \\ v_{y,0} &= -v_0 \sin \alpha \cos Az; \\ v_{z,0} &= -v_0 \cos \alpha, \end{aligned} \quad (1)$$

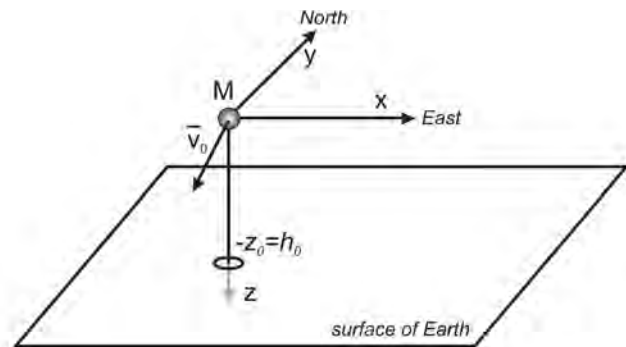


Figure 1 – Flat Earth-model with plan-parallel atmosphere and associated Cartesian coordinate system.

while the only component of the initial acceleration is  $a_{z,0} = g(h_0)$ . The value of the gravitational acceleration  $g(h)$  at any given height  $h$  is given by the well-known formula

$$g(h) = g(0) \frac{1}{(1 + h/R_E)^2}, \quad (2)$$

where  $R_E = 6371$  km, the mean radius of the Earth, and  $g(0) = 9.80665$  m/s<sup>2</sup>, the value of gravitational acceleration at sea level near 45° N geographical latitude.

## 2 Challenges related to the drag law

The meteoroid body is flying through a plan-parallel atmosphere in our model. Air density is a function of the height. In our approximation, the atmosphere is chemically homogeneous. Since the gas exhibits some kind of resistance against the moving bodies, the meteoroid will drag. This will cause a change of the velocity of the moving body, which can be calculated by introduc-

ing the related “drag force”. Under general conditions, it can be written as

$$F_d = -\frac{1}{2} K A \rho_a v_{\text{rel}}^2, \quad (3)$$

where  $K$  is the drag coefficient,  $A$  the cross-sectional area,  $\rho_a$  the density of the surrounding atmosphere, and  $v_{\text{rel}}$  the speed relative to the surrounding atmosphere. This scalar equation is seemingly very simple. As it is well known, the minus sign indicates that this force is always reacting *opposite* to the temporary direction of the moving body, while the “rel” index emphasizes that the force is proportional to the *relative* speed of the body, i.e., relative to the surrounding medium. In a real atmosphere, we must have at least a realistic estimate of the wind speeds at different heights. There are public databases containing some information about this, with a rough time and spatial distribution. The air density at the given point,  $\rho_a = \rho_a(h)$ , with  $h$  being the altitude, is a very important part in our problem. One can take it from real measurements (and interpolate between the known data), or one can use some one-dimensional or two-dimensional approximative calculations. The most generally used formula is the so-called “barometric approximation”, which can nevertheless deviate significantly from real in-situ measurements made by high-altitude balloons (the main reason being that this approximation assumes that the atmosphere is isothermal):

$$\rho(h) \approx \rho(0) e^{-\frac{g(h)M}{R_0 T_0} h}, \quad (4)$$

with  $g(h)$  the gravitational acceleration,  $M$  the molar mass of the Earth’s atmosphere,  $R_0$  the universal gas constant, and  $T_0$  the standard temperature. At low and very high altitudes, there are only minor discrepancies between the different models and interpolated real measurements. However, at medium altitudes (between 20–80 km, the interval that is the most important for a meteor flight), the discrepancies are large. In Figure 2, we have plotted the air density against altitude for barometric and power formulae and the ISA1975 standard atmospheric model, compared to real measurements of in-situ balloons at the nearest geographical node and time (considered for the Easter Bolide), for altitudes below 25 km. Seemingly, the power model approximates the real atmosphere the best, but for higher altitudes, it deviates much more from the ECMWF measurements, while ISA1975 gives the best values there.

The  $K$  factor (the so-called “drag coefficient”) in Equation (3) introduces further uncertainty. Although some efforts have been made to derive its value theoretically, its tabulated values are most often based on laboratory experiments. Unfortunately, these experiments cannot cover the typical high speeds of real meteor flights. In many previous dark flight calculations, one has simply substituted for  $K$  a constant value around 0.4–0.5 (considering a spherical or conical meteoroid body, since  $K$  also depends on the shape of the moving body, explaining why it is often referred to as the “form factor”). However, it is well-known nowadays that  $K$  depends

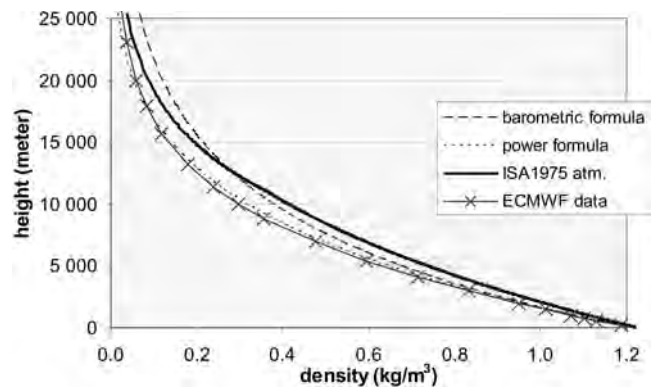


Figure 2 – Comparison between air density values according to various atmospheric models and measured air densities.

strongly on the relative speed and on the Reynolds number (which characterizes the motion in the given medium). Some authors apply a simple dependency based only on the Mach number (and, what is also a problem, on a rather narrow interval compared to the real one) or only on the Reynolds number. In reality,  $K$  depends on both combined factors. During the dark flight, meteoroid motion can exhibit big changes in the Mach and Reynolds numbers, as is illustrated in Figure 3 for the 2015 Easter Bolide. The  $K$  values were obtained using the so-called Henderson-formulae, taken from Vinnikov et al. (2016).

### 3 Integration and test runs

The integration is performed by the following simple and well-known method: at the  $i$ th step, we take the  $(i - 1)$ th vector of the velocity, and calculate the components of the drag force using the drag law described in Equation 3. After this, we can calculate the components of the acceleration. In our approximation, the temporary change of the meteoroid mass (and, thus, the change of the cross-sectional area of its body) is not yet taken into account, or the possible fragmentation over time. We consider the body as a spherical object having a constant mass and radius:

$$\begin{aligned} a_x &= -\frac{3}{8} K \frac{1}{r} \frac{\rho_a}{\rho_m} v_{\text{rel}} v_{\text{rel},x}; \\ a_y &= -\frac{3}{8} K \frac{1}{r} \frac{\rho_a}{\rho_m} v_{\text{rel}} v_{\text{rel},y}; \\ a_z &= g - \frac{3}{8} K \frac{1}{r} \frac{\rho_a}{\rho_m} v_{\text{rel}} v_{\text{rel},z}, \end{aligned} \quad (5)$$

where  $g$  is the gravitational acceleration at the actual height and  $\rho_m$  the density of the meteoroid. (For stony meteoroids, we took 3.4 g/cm<sup>3</sup>). With these values, we determine changes in velocity and spatial motion of the body during the applied  $\Delta t$  step. The density of the air  $\rho_a$  is recalculated at each integration step. The temperature (which is needed for calculating the kinematic viscosity and the Reynolds number) is taken from worldwide meteorological databases for the given date and closest node. The calculation is automatically stopped when the  $z$  coordinate reaches 0. Of course, we are especially interested in the final  $(x, y)$  coordinates, since they indicate the most probable fall location. The total time elapsed until the fall is also an interesting parameter.

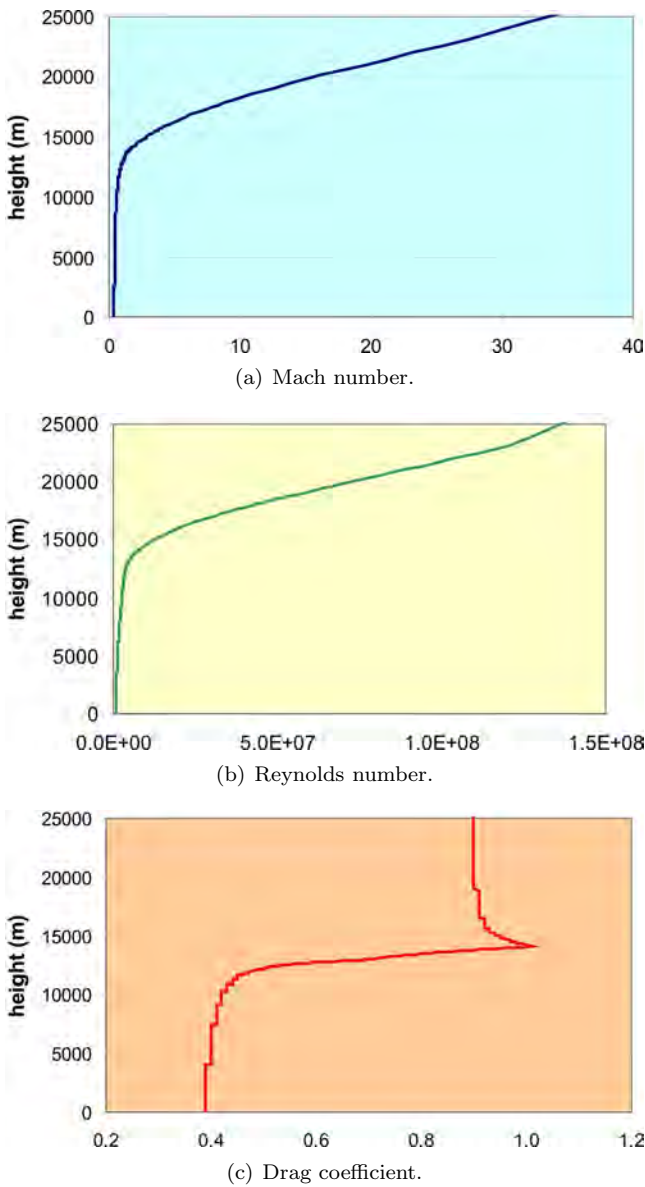


Figure 3 – Changes in Mach number, Reynolds number, and drag coefficient during the dark flight of the Easter Bolide, assuming a spherical shape and using the ISA1975 model.

Later we added an automatic change of the initial size of the meteoroid body, and for “simulating” the possible blow-up, the code can add also occasional side-speed components to the initial velocity vector. Thus, we can study the most probable strewn fields and support field searches for real events.

The very first tests included verification with the analytically solvable “free fall” case, in a homogeneous atmosphere. Moreover, an existing similar software was also available for comparison with our detailed results (Csizmadia, 2016). A comparison between both can be found in Figure 4. Our code runs were carried out with two different determinations for the value of the drag coefficient  $K$ .

After some successful tests, the first real application of our new code concerned the so-called Easter Bolide of 2015, observed over Hungary on 6 April 2015, at 17<sup>h</sup>31<sup>m</sup> UTC (Hegedüs et al., 2015). The final step towards a

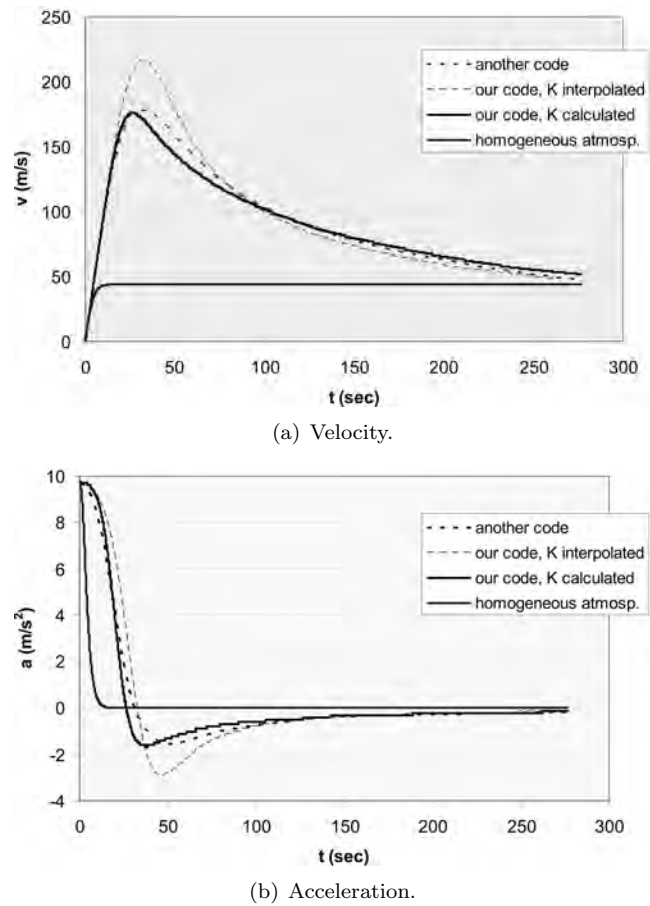


Figure 4 – Changes in velocity and acceleration for a spherical free-falling meteoroid body ( $r = 0.01$  m,  $\rho_m = 3400$  kg/m<sup>3</sup>,  $h_0 = 25\,143$  m, and  $v_0 = 0$  m/s).

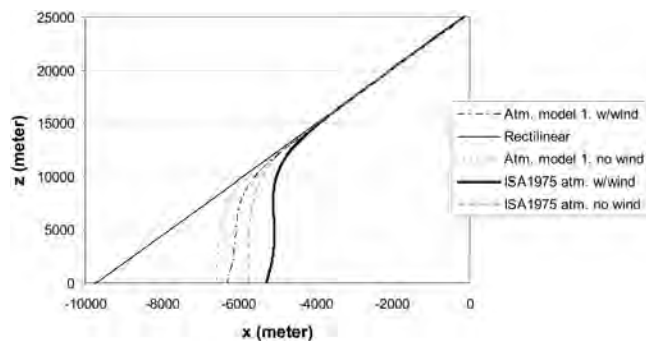
more realistic modeling was taking into account horizontal wind speeds (which modify the  $x$  and  $y$  components of  $v_{rel}$ ). There are a few sources containing such data, with a given time and spatial resolution. We used the archival ECMWF profiles.

#### 4 Effect of wind and initial parameters

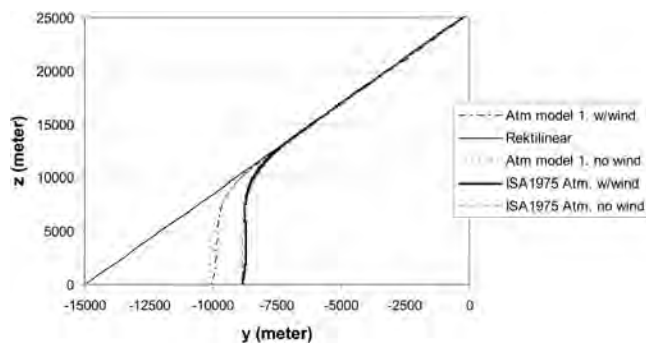
It is an interesting question to look at the effect of some initial parameters, as well as the real winds, on the final touchdown location. For this purpose, we show some of our results, namely the dark flight paths in the  $xz$  and  $yz$  planes, for two atmospheric models (see Figure 5). All other data are referring to the “Easter Bolide”, which was considered hypothetically to be a spherical body with a diameter of 10 cm in these graphs.

The S-shaped paths are wind-disturbed tracks of the falling body, while the other, nearly parabolic, ones are the non-wind disturbed tracks. The effect of the atmospheric structure results in some considerable differences in the  $x$  and  $y$  coordinates of the fall site. Figure 6 also shows the effect of different masses on the fall site (without any scattering by occasional differences in the input parameters).

In Figure 6, we presented the final results in the  $xy$  plane, converted to geographical coordinates. Since our



(a) Projection on the  $xz$  plane.



(b) Projection on the  $yz$  plane.

Figure 5 – Dark flight simulation of the 2015 Easter Bolide  $D = 0.1$  m,  $h_0 = 25\,425$  m, and  $v_0 = 10\,311$  m/s, with and without winds.

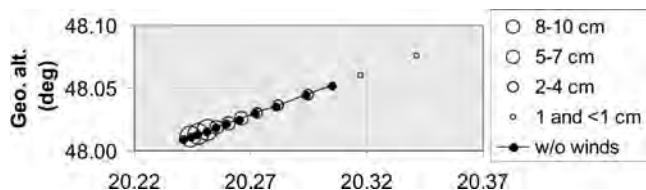


Figure 6 – Possible fall sites for differently sized pieces of the 2015 Easter Bolide over Hungary.

dark-flight calculation, there was only one mini-expedition to the site, searching for possible specimens on the field (Figure 7). No pieces were found yet. Some parts of the probable fall area are easy to search, like the open field on Figure 7, but some woody parts with



Figure 7 – Part of the probable fall area of the 2015 Easter Bolide.

dense undergrowth vegetation are extremely bad—see in the background of Figure 7.

### Acknowledgment

We are very grateful to Dr. Gy. Horváth, the Head of the Atmospheric Research Institute of OMSz, for supplying us with the archival ECMWF profiles.

### References

Csizmadia S. (2016). Private communication.

Hegedüs T., Csizmadia S., Zelkó Z., Kereszty Z., and Bró, Z. (2015). “2015 Easter bolide over North Hungary”. In Rault J.-L. and Roggemans P., editors, *Proceedings of the International Meteor Conference*, Mistelbach, Austria, 27–30 August 2015. IMO, pages 130–132.

Vinnikov V. V., Gritsevich M. I. and Turchak L. I. (2016). “Mathematical model for estimation of meteoroid dark flight trajectory”. In *AIP Conference Proceedings*. AIP, volume 1773, id. 110016.

# SCAMP, a new UK bolide network

Jim Rowe

jamesrowe999@gmail.com

SCAMP (the System for Capture of Asteroid and Meteorite Paths) is a new network of all-sky digital cameras based in the UK. At the moment, three cameras are operating.

## 1 Introduction

SCAMP (the System for Capture of Asteroid and Meteorite Paths) is a new network of all-sky digital cameras based in the UK. SCAMP records bright fireballs so that the location of any resulting meteorite can be calculated using triangulation and dark flight analysis. Any meteorites recovered using SCAMP will be donated to UK museums or universities, along with all images and data recorded.

The cameras are identical to those used in the French FRIPON network and run the same software. It is intended that observations from the SCAMP networks will be shared with FRIPON<sup>1</sup>. SCAMP is associated with the UK Meteor Observation Network<sup>2</sup>.

## 2 Current SCAMP network

At the moment, there are three cameras in the SCAMP network (Figure 1). When all three are operating, they provide coverage of the Midlands and most of Wales, with double-camera coverage of East Anglia, Western Wales, and the Home Counties.



Figure 1 – Current SCAMP network.

## 3 Individual camera locations

The three current locations are as follows.

<sup>1</sup><https://www.fripin.org/?lang=en>.

<sup>2</sup><https://ukmeteornetwork.co.uk/SCAMP>.

## 3.1 Camera 1—N. Lockyer Observatory

This camera was donated by the FRIPON project to Norman Locker Observatory, and is involved in SCAMP until such time as FRIPON wishes to extend to the UK. The camera has a clear view of the (smiling) Connaught dome and is mounted between the observatory's two UKMON cameras, as shown in Figure 2.



Figure 2 – Camera 1 at the Norman Lockyer Observatory, Sidmouth.

## 3.2 Camera 2—East Barnet, London

Installed in October 2016, Camera 2 is mounted on the disused chimney of a private house (belonging to the author) in East Barnet, North London (Figure 3). From this vantage point it can catch events over the Channel, the North Sea, the Midlands, and Wales.

## 3.3 Camera 3—Central Manchester

Installed in June 2017, Camera 3 is high on the roof of an academic building in the center of Manchester (Figure 4). The academic institution has an interest in SCAMP but is not formally aligned in any way, so is not named here.

## 4 Plans and problems

During 2017 and 2018, the authors would like to increase the number of SCAMP cameras to ten or more, adding cameras in Scotland, Wales, Ireland, and the English regions. The intention is to provide full coverage of the UK and Ireland.



Figure 3 – Camera 2 on a house in East Barnet, North London.

The authors do not have the software or skillsets to analyze data gathered. The objective is therefore just to extend the physical footprint of the FRIPON network to cover Britain in order to maximize the likelihood of recovering incoming meteorites, along with capturing a useful electronic record of the fall.

If a significant event is recorded, the authors will of course have the problem of what to do with the data. The data will be made available freely to anyone whose motivations are academic and not commercial, and to those who can assist with trajectory and dark flight analysis.

The authors have been unable to install a Debian-based version of the FREETURE software, so are running version 1.0 of the Windows software. This does not seem to function as well as the Linux-based software and does not produce results comparable to those produced by cameras in the FRIPON network, and so it is not clear whether full or useful datasets can yet be captured by SCAMP.



Figure 4 – Camera 3, high over the Manchester city center.

## 5 Conclusions

The SCAMP network has been set up with a focus on what the founders can do at the moment, rather than what we cannot do. We can install (and so have installed) a network of cameras across the UK, and we can run the Windows FREETURE software, so we have done both of those things. Soon, we hope to determine whether the data captured by SCAMP is actually useful and will assist with meteorite recovery. Ultimately we are aiming for full coverage of the UK and Ireland and integration with other networks using the same technology, such as FRIPON and PRISMA<sup>3</sup>.

<sup>3</sup>Prima Rete per la Sorveglianza sistematica di Meteore e Atmosfera—see <http://www.prisma.inaf.it/>.

# Shock waves generated by overdense meteors in the mesosphere-lower thermosphere

Elizabeth A. Silber<sup>1</sup>, Wayne K. Hocking<sup>2</sup>, and Reynold E. Silber<sup>3</sup>

<sup>1</sup>Department of Earth, Environmental and Planetary Sciences, Brown University, Providence, RI 02912, USA  
elizabeth\_silber@brown.edu

<sup>2</sup>Department of Physics and Astronomy, The University of Western Ontario, London, Ontario, N6A 3K7, Canada  
whocking@uwo.ca

<sup>3</sup>Department of Earth Sciences, The University of Western Ontario, London, Ontario, N6A 3B7, Canada  
reynold.silber@uwo.ca

Overdense meteors are in the size regime of the meteoroids capable of generating shock waves during the lower transitional flow regimes and prior to their terminal stage in the mesosphere-lower thermosphere region of the atmosphere. This paper presents an overview of the small scale physico-chemical processes occurring in, and on the boundary of, the extreme environment of the high temperature adiabatically formed meteor trail in the initial stages of the expansion. Additionally, we suggest that the observation and statistical treatment of VHF radar-detectable overdense meteor head echo (MHE) radar cross section (RCS) at corresponding heights and related parameters, correlated with simultaneously captured specular radio echo observations of the same events from geographically separate locations (at frequencies at or below 50 MHz) can be used as a reasonably accurate indicator of the meteor shock wave formation altitudes.

## 1 Introduction

The Earth is constantly bombarded with extraterrestrial particles of various sizes, also known as meteoroids (Brownlee, 1985) impacting at hypersonic velocities of 11.5 km/s to 72.5 km/s (Baggaley, 2002). When a meteoroid enters the Earth's atmosphere, the collisions with atmospheric particles lead to frictional heating, sputtering, evaporation, ablation and even fragmentation. The resulting luminous phenomenon is called a meteor. The hypervelocity flow refers to the flow of atmospheric gas over the meteoroid with the Mach number,  $M_\infty$  (defined as the ratio of the flow velocity to the local speed of sound). The value of  $M_\infty$  is typically between 35 and 270 (e.g., Boyd, 1998). The dynamics of meteoroid motion in the atmosphere and the related chemical processes between the ablationally formed thermalized meteor train and the ambient atmosphere have been subject of numerous studies (e.g., Boyd, 1998; Popova et al., 1998; Plane 2012).

### 1.1 Meteor-generated shock waves and physico-chemical processes

A largely neglected aspect of meteoroid's interaction with the atmosphere involves cause and effects of meteor-generated shock waves, and the small-scale physico-chemical processes occurring in, and on the boundary of, the extreme environment of the high-temperature adiabatically formed meteor trail in the initial stages of the expansion ( $t \leq 0.1$  s). For illustrative purposes,

the schematics of the meteor shock wave is shown in Figure 1 (adapted from Silber et al., 2017a). The meteoroid is approximated as a spherical body propagating at hypersonic velocity. For further discussion on shock wave formation, the reader is referred to Silber et al. (2017b). Overdense meteors (electron line density,  $10^{16} \leq q \leq 10^{19}$  electrons/m, and diameters  $d \geq 4$  mm up to small fireballs) are in the size regime of the meteoroids capable of generating shockwaves during the lower transitional flow regimes and prior to their terminal stage in the MLT (Mesosphere-Lower Thermosphere) region of the atmosphere, at altitudes between 75 and 100 km (Bronshten, 1983). Short-lasting high-temperature-driven reactions that take place on the boundaries of the postadiabatically expanding meteor train within the first 0.1 s after its formation and subsequent rapid and intense electron removal remain poorly understood. A comprehensive background on the topic can be found in Silber et al. (2017a). Section 2 contains an overview of the combined physico-chemical effects of meteor-generated cylindrical shock waves on the ambient atmosphere in the MLT region, as well as the subsequent hyperthermal chemistry on the boundaries of overdense meteor trains to address the physico-chemical processes accompanying the initial evolution of the high temperature meteor train.

### 1.2 Onset of shock waves

The strength of the meteor-generated shock waves depends on meteoroid atmospheric velocities and the val-

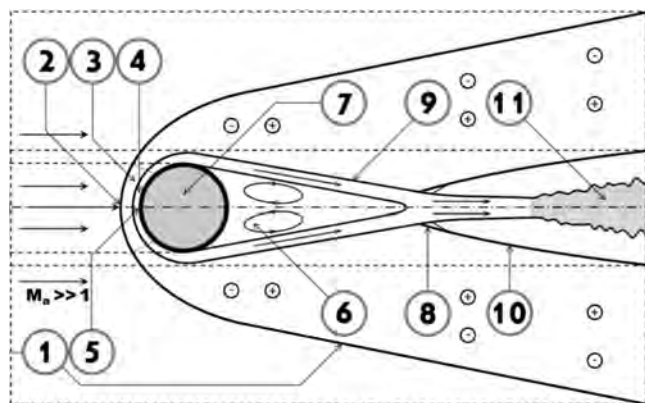


Figure 1 – Schematics of the meteor shock wave: (1) bow (cylindrical) shock wave front; (2) “ballistic” shock front; (3) sonic region; (4) boundary layer; (5) stagnation point; (6) turbulent region (in some older literature, this is referred as the dead-water region); (7) meteoroid; (8) neck and recompression region; (9) “free” shear layer; (10) recompression vapor (or a true cylindrical) shock wave front; (11) region of turbulent vapor flow and adiabatic expansion. Small circles with positive and negative signs indicate regions affected by the presence of ions and electrons, respectively. The diagram is only for the illustrative purpose and is not to scale. Adapted from Silber et al. (2017a).

ues of the Knudsen number in a given region. Most meteoroids ablate in the region of the atmosphere between 70 km and 120 km. In this region, the mean free path of the ambient atmosphere varies by up to  $\pm 2$  orders of magnitude relative to the meteoroid dimensions.

The inclusion of the specific flow regime in the analysis of the meteoroid interaction with the atmosphere is of critical importance as it will affect the analytical and computational treatment of ablation and mass loss, ionization (Campbell-Brown and Koschny, 2004), shock waves, and other relevant physical parameters (see Bronshten, 1983; Popova et al., 1998). However, practical detection and determination of the altitude of formation of meteor-generated shock waves (especially overdense meteors) have not been possible to date because of their rapid spatial and temporal attenuation in rarefied atmosphere, as well as the presence of radiative phenomena that extend to the meteor wake.

Additional uncertainty is introduced by the presence of ablation-amplified hydrodynamic shielding and its over-

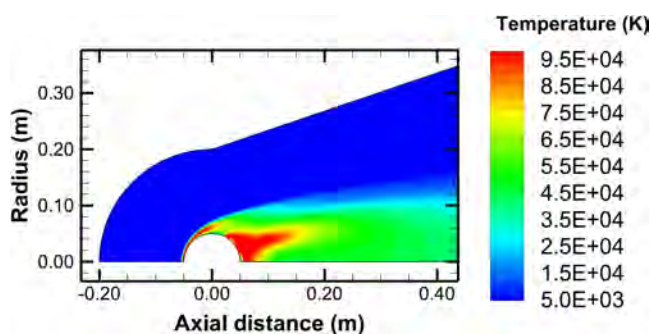


Figure 2 – The temperature distribution versus axial distance for a 10-cm meteoroid. The color bar represents the temperature scale.

all dimensions (Rajchl, 1969; Popova, 2001), which subsequently alter the considerations of the flow regime. Moreover, good estimates of shockwave dependence on the relevant meteoroid parameters (such as velocity, shape, bulk density, composition, and size), and the altitudes at which shock waves are generated, remain elusive. In Section 3, we will discuss the theoretical and statistical treatment of VHF radar-detectable overdense meteor head echoes (MHE) radar cross section (RCS) heights, and related parameters. We suggest that MHE RCS, correlated with simultaneously captured specular radio echo observations of the same events from geographically separate locations (at frequencies at or below 50 MHz), can be used as a reasonably accurate indicator of the meteor shock wave formation altitudes.

## 2 Overdense meteor-generated shock waves: implications for short-lasting physico-chemical processes

A theoretical study undertaken by Silber et al. (2017a) investigated the link between shockwaves generated by overdense meteors, and the short lasting hyperthermal chemistry during the initial evolution of the meteor train. This study was motivated by recent observational evidence (Jenniskens et al., 1998) that suggests slower thermalization times of the postadiabatically formed meteor trains which is conducive for hyperthermal chemistry. Silber et al. (2017a) investigated the combined role of meteor-generated shock waves and short-lasting thermally driven chemistry, which indeed play a significant role in the early removal of electrons from a postadiabatically expanding meteor train boundary. Electrons on the boundary region of the meteor train are consumed through the mechanism of post-hyperthermal dissociative recombination (Silber et al., 2017a).

A theoretical approach can be used to approximate the temperature of the ambient atmosphere near the meteor train, which is heated by the passage of the overdense meteor cylindrical shock wave. This is accomplished by considering the meteor velocity and energy deposition, and evaluating the pressure ratios between the ablation-amplified shock front and the ambient atmosphere.

The detailed description of this treatment is presented by Silber et al. (2017a). They modeled the hypersonic meteor flow in the MLT region using a simplified model without ablation, incorporated into the computational fluid dynamics (CFD) software package ANSYS Fluent. The details on the governing equations and rate parameters implemented in the model are given by Niculescu et al. (2016). The computation was performed using  $O_2$  and  $N_2$  as the only major species, at an altitude of 80 km. A spherically shaped meteoroid was assumed to have velocity of 35 km/s ( $M_{80\text{ km}} = 124.6$ ). Silber et al. (2017a) modeled two meteoroid sizes,  $d = 2.5$  cm and  $d = 10$  cm. However, the results for only one simulation are shown here ( $d = 10$  cm), in Figures 2–4. For further details about the model, see Silber et al. (2017a).

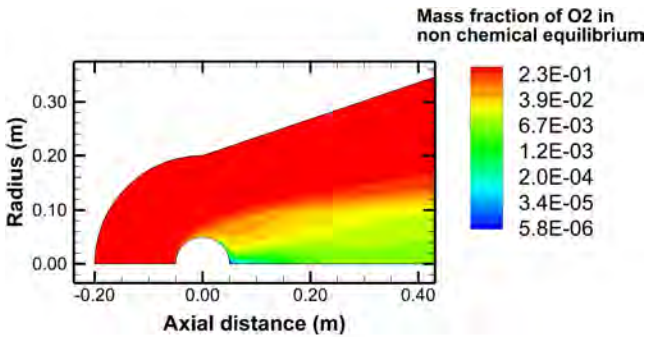


Figure 3 – The mass fraction of O<sub>2</sub> versus axial distance for a 10-cm meteoroid. The color bar represents the temperature scale. It is in log scale for better visualization.

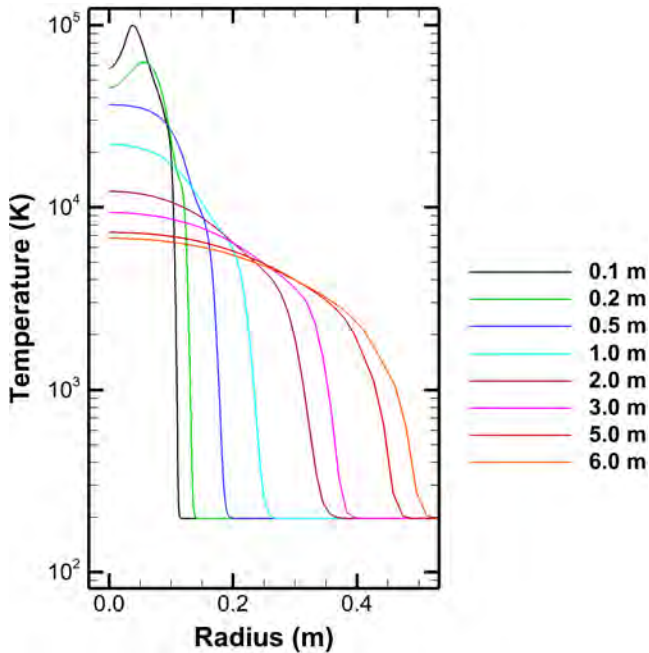


Figure 4 – The radial temperature distribution versus radial distance from the propagation axis of the modeled meteoroid. The colored lines shown in the legend represent the temperature distribution along the propagation axis.

### 3 Meteor head echoes: a theoretical approach

To resolve shockwave dependence on the relevant meteoroid parameters (such as velocity, shape, bulk density, composition and size), and the altitudes at which shock waves are generated, we consider VHF radar detectable Doppler shifted meteor head echoes (MHE) as a direct indicator of the formation of overdense meteor shockwaves. The formation of MHEs coincides with the sputtering regime in the free molecular flow, where the colliding atmospheric molecules directly impact the meteoroid surface and cause a large number of collisionally evaporated meteoric atoms to be ejected—some along the axis of meteor propagation with speeds of up to  $1.5v_{\text{met}}$  (Rajchl, 1969). The second- and third-order ionizing collisions of ejected meteoric atoms form fast scattering high energy electrons, some distance ahead of and around the meteor. Despite the retarding electrostatic barrier resulting from the initial charge separation between ions and electrons, the low plasma density (at

higher altitudes) causes the Coulombic forces to be ineffective in controlling the wide departure rate of high energy ballistic electrons. This mechanism can be considered to initiate the formation of MHEs, depending on the rate of sputtering and evaporation.

The observed MHE strongly depends on the observing radar frequency and associated biases (Westman et al., 2004). We propose that the altitude of specific overdense meteor shock waves formation can be established by determining the heights where the VHF radar observed MHE radar cross section (RCS) (with assumed Gaussian electron distribution) corresponds to the size of the initial overdense meteor ablation-amplified flow fields and the bow shock envelope (Silber et al., 2017b; 2017c). The ablation-amplified flow fields and shock envelope are estimated to be about 1–2 orders of magnitude greater than the initial characteristic meteoroid dimensions (Boyd, 1998; Jenniskens et al., 1998; Popova et al., 2001; Silber et al., 2017a). The size of MHE RCS depends upon altitude (Marshall et al., 2016), and it scales with the atmospheric mean free path and meteoroid velocity.

Thus, MHE RCS, at altitudes where it becomes compatible to the dimensions of the cm-sized meteor flow fields, and the bow shock envelope (Boyd, 1998; Jenniskens et al., 1998; Silber et al., 2017a) may be used to reliably determine the shock wave formation heights and constrain additional meteoroid parameters such as ablatational efficiency and composition that affect the formation of the shock envelope around a meteor. Moreover, the altitudes where MHE RCSs are compatible to the ablationally augmented flow fields around a meteor signify the existence of strongly stratified density gradients in the plasma layer in front of and around the meteoroid (as a direct precursor to the shock wave formation), where Coulombic forces are sufficiently strong as to prevent the large-scale electron scattering associated with MHEs at higher altitudes.

### 4 Conclusions

The cylindrical shock waves produced by overdense meteors are strong enough to heat the ambient atmosphere to temperatures around 6000 K in the near field and subsequently dissociate oxygen and minor species such as O<sub>3</sub>, but insufficient to dissociate N<sub>2</sub>. This substantially alters the considerations of the chemical processes taking place at the meteor train boundary. Silber et al. (2017a) demonstrated that the reduced quantities of ambient O<sub>2</sub> which survive the cylindrical shockwave, along with small quantities of O<sub>2</sub> that originates from the shock dissociation of O<sub>3</sub>, participate primarily in high temperature oxidation of meteoric metal ions, forming metal ion oxide.

For the case of overdense meteor trains, the subsequently formed meteoric metal oxide ions are predominantly responsible for the initial intense and short-lasting electron removal from the boundary of the expanding me-

teor train, through a process of fast temperature independent dissociative recombination. This altitude dependent process is typically completed within 0.1–0.3 s, which in good agreement with the results suggesting substantially slower cooling of meteor wakes (Jenniskens et al., 2004). The rate of this process is also strongly dependent on the second Damköhler number. The full scope of implications of this work is presented by Silber et al. (2017a).

We suggest that the observation and statistical treatment of VHF radar-detectable overdense MHE RCS heights and related parameters, correlated with simultaneously captured specular radio echo (or even high-resolution optical) observations of the same events from geographically separate locations (at frequencies at or below 50 MHz), can be used as a reasonably accurate indicator of the meteor shock wave formation altitudes.

## References

- Baggaley W. J. (2002). “Radar observations”. In *Meteors in the Earths Atmosphere: Meteoroids and Cosmic Dust and Their Interactions with the Earth’s Upper Atmosphere*. Pages 123–148.
- Boyd I. D. (1998). “Computation of atmospheric entry flow about a leonid meteoroid”. *Earth, Moon, and Planets*, **82**, 93–108.
- Bronshthen V. A. (1983). *Physics of meteoric phenomena*. Dordrecht, D. Reidel.
- Brownlee D. E. (1985). “Cosmic dust: Collection and research”. *Annual Review of Earth and Planetary Sciences*, **13**, 147–173.
- Campbell-Brown M. and Koschny D. (2004). “Model of the ablation of faint meteors”. *Astron. Astrophys.*, **418**, 751–758.
- Jenniskens P., Laux C. O., Wilson M. A., and Schaller E. L. (2004). “The mass and speed dependence of meteor air plasma temperatures”. *Astrobiology*, **4**, 81–94.
- Jenniskens P., Wilson M. A., Packan D., Laux C. O., Krüger C. H., Boyd I. D., Popova O. P., and Fonda M. (1998). “Meteors: A delivery mechanism of organic matter to the early Earth”. *Earth, Moon, and Planets*, **82**, 57–70.
- Marshall R., Close S., Brown P., and Dimant Y. (2016). “Effects of meteor head plasma distribution on radar cross sections and derived meteoroid masses”. In Roggemans A. and Roggemans P., editors, *International Meteor Conference*, Egmond, the Netherlands, 2–5 June 2016. IMO, pages 171–174.
- Niculescu M. L., Fadgyas M. C., Cojocaru M. G., Pricop M. V., Stoican M. G., and Pepelea D. (2016). “Computational hypersonic aerodynamics with emphasis on earth reentry capsules”. *INCAS Bulletin*, **8**, pages 55–64.
- Plane J. M. (2012). “Cosmic dust in the earth’s atmosphere”. *Chemical Society Reviews*, **41**, 6507–6518.
- Popova O., Sidneva S., Strelkov A., and Shuvalov V. (2001). “Formation of disturbed area around fast meteor body”. In *Meteoroids 2001 Conference*, volume 495. pages 237–245.
- Popova O. P., Sidneva S. N., Shuvalov V. V., and Strelkov A. S. (1998). “Screening of meteoroids by ablation vapor in high-velocity meteors”. *Earth, Moon, and Planets*, **82**, 109–128.
- Rajchl J. (1969). “On the interaction layer in front of a meteor body”. *Bulletin of the Astronomical Institutes of Czechoslovakia*, **20**, pages 363–372.
- Silber E. A., Hocking W. K., Niculescu M. L., Gritsevich M., and Silber R. E. (2017a). “On shock waves and the role of hyperthermal chemistry in the early diffusion of overdense meteor trains”. *Mon. Notices Royal Astron. Soc.*, **469**, 1869–1882.
- Silber R. E., Hocking W. K., Silber E. A., and Gritsevich M. (2017b). “On the possibility of constraining bright meteor shock wave forming altitudes—theoretical consideration of relationship to radar observed meteor head echo termination heights in MLT”. In *CAP Congress*, Kingston, Ontario, Canada, May 28–June 2, 2017. Abstract id. 1578.
- Silber R. E., Hocking W. K., Silber E. A., Gritsevich M., and Niculescu M. L. (2017c). “Detection and characterization of meteor shockwaves using radar observed meteor head echo/height correlation”. In *32nd URSI GASS*, Montréal, Québec, Canada, 19–26 August 2017, Montreal, Quebec, Canada.
- Westman A., Wannberg G., and Pellinen-Wannberg A. (2004). “Meteor head echo height distributions and the meteor impact mechanism observed with the EISCAT HPLA UHF and VHF radars”. *Ann. Geophys.*, **22**, 1575–1584.

# Past, present, and future of beacon signal transmissions for meteor radio observations in Japan

Kimio Maegawa<sup>1</sup> and Sumio Nakane<sup>2,3,4,5</sup>

<sup>1</sup> National Institute of Technology, Fukui College  
ja9boh@jar1.com

<sup>2</sup> Radio Amateur Satellite Corporation (AMSAT)

<sup>3</sup> Tucson Amateur Packet Radio (TAPR)

<sup>4</sup> Nippon Meteor Society (NMS)

<sup>5</sup> International Meteor Organization (IMO)  
snakane@nisiq.net

First, a historical overview is given of HAM radio beacon transmissions for meteor radio observations in Japan. Then, an outlook is given for amateur radio meteor observing in the future. We give our view on the road ahead for amateur radio meteor observing.

## 1 History

Beacon waves for meteor radio observation have been transmitted from the National Institute of Technology, Fukui College Amateur Radio Club, JA9YDB, since 1996. It has been on for over 20 years now, and are still being transmitted.

Amateur meteor radio observation using broadcast radio waves and meteor scatter communication by amateur radio were performed in the 1970s, but it was not done much after that. At Kyoto University's Open Lecture in September 1995, an amateur meteor observer, two amateur satellite experimenters, and a researcher of the middle- and upper-layer atmosphere had the opportunity to have lunch together and exchange ideas. After that, about 20 people interested in radio meteor observation had the opportunity to meet in the Shigaraki Siga Prefecture in Japan (MU Radar site) in December 1995 to get acquainted with Dr. Nakamura's way of thinking.

A test transmission was done by Mr. Kimio Maegawa, JA9BOH, in April 1996, and continuous beacon transmission at 53.750 MHz from JA9YDB started in August 1996. This has been ongoing for over 20 years, now, till the present (Figure 1).

In the early stages of observation, we used FFTDSP written by Mr. Mike Cook (AF9Y). After that, we used HROFFT written by Mr. Kazuhiko Okawa.

In the latter half of the 1990s, our group regularly held a meeting to read some chapters of the reference book by McKinley (1961)<sup>1</sup> Additionally, a radio meteor observation meeting was held annually around February from mid-1990s to 2009 (Figure 2). After that, the meeting has not been held anymore.



Figure 1 – JA9YDB beacon antenna.



Figure 2 – Participants to the Radio Meteor Observation Meeting 2009 held in Osaka, Japan.

Our group printed 500 copies of the report, and we distributed it in 2001.

In 2002, our group was able to publish the *Meteor Radio Observation Guidebook* (Nakamura, 2002) from CQ publishing, a prominent publisher of amateur radio literature in Japan (Figure 3).

<sup>1</sup>In particular, Chapter 8, "Radio echo theory", and Chapter 9, "Forward-scatter from meteor trails".



Figure 3 – Meteor Radio Observation Guidebook.

## 2 Outlook

Meteor observing by video cameras has become very prominent, lately. Although radio observing is now done at an extremely small scale in Japan, JA9YDB continues to transmit and allows meteor observations under the same conditions as in the past before. A few observers continue to perform radio observations.

Furthermore, transmission from the Fukui Prefectural Amateur Meteor Radio Observation Research Society, JH9YYA, has also started to transmit at 53.755 MHz since December 2016. The transmitter was down in mid June 2017 and stopped temporarily, but resumed on October 9. The mutual distances between JA9YDB and JH9YYA are about 20 km and we would like to use it to experiment with a new observation method.

## 3 What is the road ahead?

It has been over 20 years since HAM Radio Observation (HRO) began in Japan. In the past two decades, radio frequency technology, signal processing technology, and processor capacity knew dramatical progress. Unfortunately, and despite the technological progress, the observing method did not improve very much in Japanese amateur radio meteor observing.

In the field of amateur radio, meteor burst communication is popular, particularly in Europe. We refer to the DUBUS magazine<sup>2</sup> for more details on the topic.

<sup>2</sup><http://www.dubus.org>.

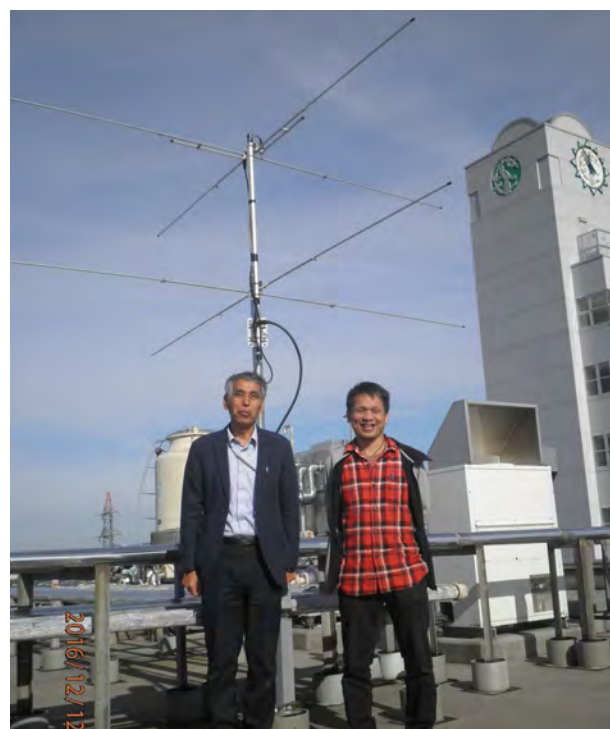


Figure 4 – JH9YYA beacon antenna with Mr. Kimio Mae-gawa (left) and Dr. Tadas Nakamura (right).

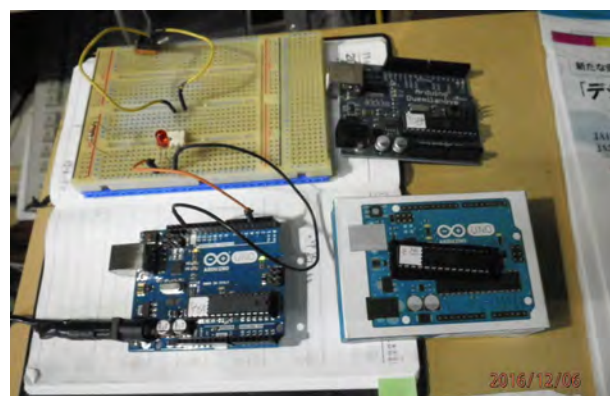


Figure 5 – Call sign sending equipment.

Along with waveforms such as FSK441, PSK2K, and MSK144, used for meteor scatter communication, we would like to try to use a coherent signal (multiple frequencies in a rationality ratio), take advantage of differences due to polarization, use a multi-point installation with multiple receivers, and so on, as new experiments. We would like to acquire knowledge and experience in meteor radio observation using new technologies becoming available to amateurs.

## References

McKinley D. W. R. (1961). *Meteor Science and Engineering*. McGraw-Hill.

Nakamura T. (editor) (2002). *Radio meteor observation guidebook*. RMO Editing Committee, CQ Publishing Co., Ltd. (In Japanese).

# Large Taurids detected by U.S. Government sensors

Przemysław Żołądek<sup>1</sup>, Arkadiusz Olech<sup>3</sup>, Mariusz Wiśniewski<sup>1,2</sup>,  
Zbigniew Tymiński<sup>4</sup>, and Marcin Stolarz<sup>1</sup>

<sup>1</sup> Comets and Meteors Workshop, Bartycka 18, 00-716 Warsaw, Poland  
brahi@op.pl

<sup>2</sup> Central Office of Measures, Elektoralna 2, 00-139 Warsaw, Poland  
marand.w@gmail.com

<sup>3</sup> N. Copernicus Astron. Center, Polish Acad. of Sciences, Bartycka 18, 00-716 Warsaw, Poland  
olech@camk.edu.pl

<sup>4</sup> NCBJ, Ośrodek Radioizotopów POLATOM, Sołtana 7, 05-400 Otwock, Poland  
zbyszek.tyminski@gmail.com

Possible large Taurids were found among the fireballs detected by US Government sensors. Four fireballs were detected over the Pacific Ocean and China, with a total energy between 0.11 and 0.37 kiloton TNT equivalent.

## 1 Introduction

The Taurids are active every year during the autumn months. Usually, it is a low-activity meteoroid stream with zenithal hourly rates less than 10. The Taurids, together with numerous small ecliptic showers, create the Taurid Complex, examined recently by various authors (Porubčan et al. 2006; Kaňuchová and Svoreň, 2014). An interesting feature of the Taurids stream is enhanced activity during some particular years (so-called swarm years). During such enhanced maxima, the mass index seems to be much higher, and numerous bright fireballs are observed. Such activity is caused by meteoroids involved in a 7:2 mean resonance with Jupiter (Asher and Clube, 1993). It has been observed in 2005 and 2015, exactly as predicted.

During the 2015 maximum, the Polish Fireball Network observed two Taurids much brighter than the Full Moon, and dozens of fireballs brighter than magnitude  $-4$ . Moreover, some NEO asteroids inside the Taurid stream have been found (Olech et al., 2016; 2017). These are probably the largest bodies of the 7:2 resonant stream. The presence of large bodies implies that Taurids are capable of producing large fireballs or even superbolides, detectable by U.S. Government satellites. Information provided on the JPL webpage includes the exact time of the fireball, the total impact energy, the height of the brightest point and, in some cases, velocity components.

## 2 Possible Taurids

Below, we discuss four possible Taurids captured by U.S. Government sensors.

### 2.1 No. 1: 25 May 1999, 6<sup>h</sup>27<sup>m</sup>41<sup>s</sup> UT

This fireball may be connected with the  $\beta$ -Taurids, observed during the Earth's second encounter with the Taurid stream. It was observed 800 km northwest of

Harbin City in Manchuria, China. Maximal magnitude was reached at 69 km, and its total energy was 0.37 kiloton TNT equivalent. The  $\beta$ -Taurid radiant was high above the horizon. Its possible absolute magnitude was  $-18.5 \pm 1.0$ .

### 2.2 No. 2: 2 Nov 2005, 5<sup>h</sup>16<sup>m</sup>47<sup>s</sup> UT

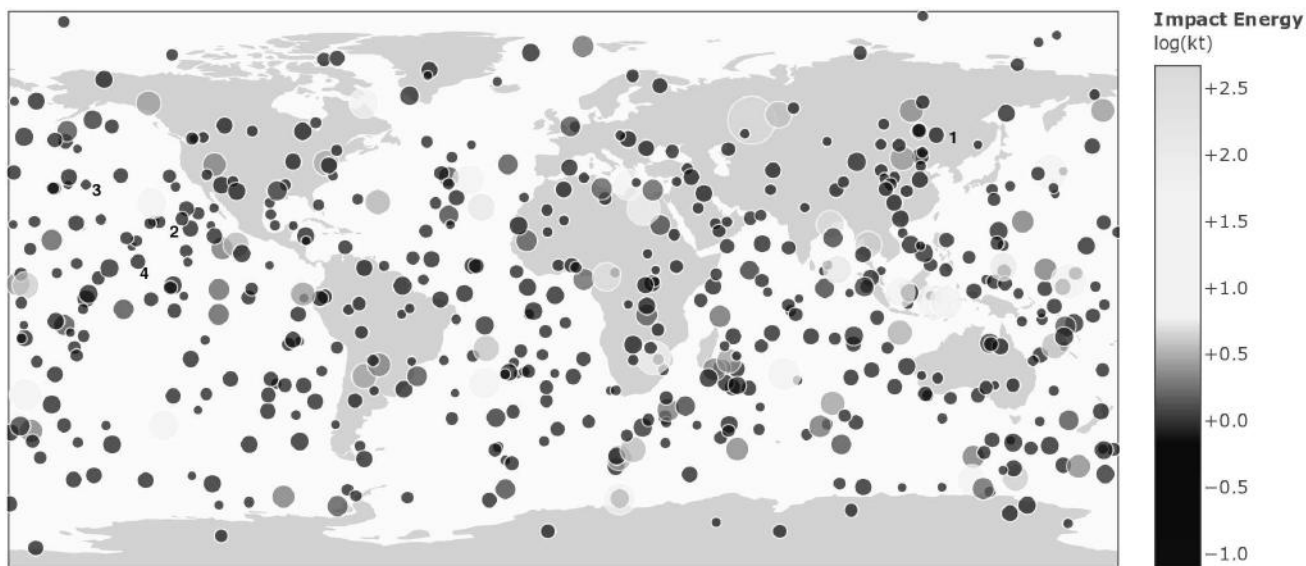
This fireball exhibited maximum brightness at an altitude of 74 km. The date of the fireball occurrence corresponds to the above-mentioned enhanced maximum of the Taurids in 2005. The fireball was observed over the Pacific Ocean, roughly 1200 km to the west of the Californian Peninsula. Its total energy equals 0.21 kiloton TNT equivalent. The Taurid radiant was  $25^\circ$  above the horizon at that time. The possible maximum absolute magnitude was  $-18 \pm 1$ .

### 2.3 No. 3: 2 Nov 2005, 7<sup>h</sup>04<sup>m</sup>32<sup>s</sup> UT

Just two hours after the previous fireball, a second large body entered the Earth's atmosphere, also over Pacific Ocean, 2500 km west of Los Angeles and 1500 km north of Honolulu. The height of maximum brightness was 68.5 km, and total energy 0.11 kiloton TNT equivalent. The Taurid radiant was  $20^\circ$  above the horizon. The possible maximum absolute magnitude was  $-17 \pm 1$ .

### 2.4 No. 5: 10 Oct 2015, 11<sup>h</sup>34<sup>m</sup>30<sup>s</sup> UT

This fireball was recorded during the 2015 Taurids maximum, 7 hours before a very bright Southern Taurid fireball was detected over Poland. It was observed over the Pacific Ocean, 2500 km southeast of Hawaii. The height of maximum magnitude was 71 km, and its total energy 0.29 kiloton TNT equivalent. The Taurid radiant was close to the local zenith. The possible maximum absolute magnitude was  $-18$ .



<https://cneos.jpl.nasa.gov/fireballs/>

Alan B. Chamberlin (JPL/Caltech)

Figure 1 – Large fireballs detected by U.S. Government sensors (notably, DoD—Department of Defense—satellites) between 15 April 1988 and 5 September 2005. Numbers 1–4 added to the image corresponds to Taurids fireballs described in the text. Image is courtesy of NASA/JPL-Caltech.

### 3 Detected height

For most fireballs detected by U.S. Government sensors, the altitude of maximum brightness is available. For most fireballs, maximum brightness was observed at heights of 20–50 km (Figure 2), which may correspond to their cosmic origin. High-altitude fireballs comprise only a small fraction of the examined data.

Interestingly, almost all fireballs with maximum brightness observed higher than 68 km occurred during the 2005 and 2015 Taurid encounters or during the 1999  $\beta$ -Taurid daylight encounter. Such heights are typical for large Taurid fireballs as observed by the Polish Fireball Network during the 2015 maximum (Olech et al., 2017). The observed energies are less than 0.5 kiloton TNT equivalent, which corresponds to magnitudes in the range of  $-16$  to  $-18$ .

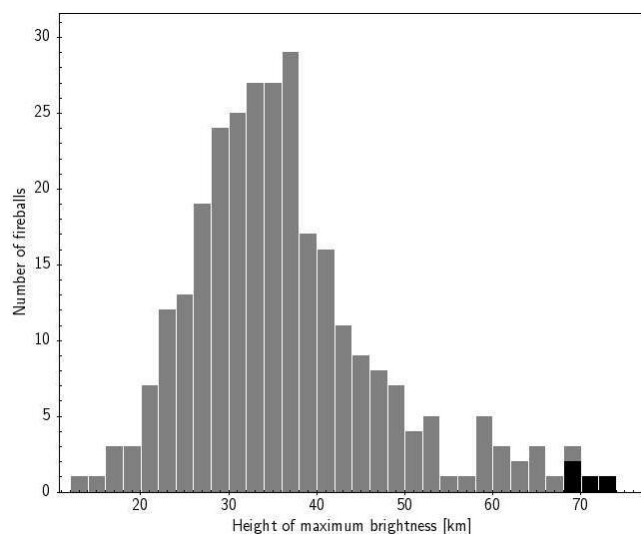


Figure 2 – Altitude of maximum brightness. Possible Taurids are marked by black bars.

### Acknowledgements

This work was supported by the NCN grant number 2013/09/B/ST9/02168.

### References

Asher D. J. and Clube S. V. M. (1993). “An extraterrestrial influence during the current glacial-interglacial”. *Quarterly J. Royal Astron. Soc.*, **34**, 481–511.

Kaňuchová Z. and Svoreň J. (2014). “Southern Taurids in the IAU MDC Database. Taurid complex.”. *Contrib. Astron. Obs. Skalnaté Pleso*, **44**, 109–118.

Olech A., Źołądek P., Wiśniewski M., Rudawska R., Bęben M., Krzyżanowski T., Myszkiewicz M., Stolarz M., Gawroński M., Gozdalski M., Suchodolski T., Węgrzyk W., and Tyimiński Z. (2016). “2015 Southern Taurid fireballs and asteroids 2005 UR and 2005 TF50”. *Mon. Notices Royal Astron. Soc.*, **461**, 674–683.

Olech A., Źołądek P., Wiśniewski M., Tyimiński Z., Stolarz M., Bęben M., Dorosz D., Fajfer T., Fietkiewicz K., Gawroński M., Gozdalski M., Kałużny M., Krasnowski M., Krygiel H., Krzyżanowski T., Kwinta M., Łojek T., Maciejewski M., Miernicki S., Myszkiewicz M., Nowak P., Polak K., Polakowski K., Laskowski J., Szlagor M., Tissler G., Suchodolski T., Węgrzyk W., Woźniak P., and Zaręba P. (2017). “Enhanced activity of the Southern Taurids in 2005 and 2015”. *Mon. Notices Royal Astron. Soc.*, **469**, 2077–2088.

Porubčan V., Kornoš L., and Williams I. P. (2006). “The Taurid complex meteor showers and asteroids”. *Contrib. Astron. Obs. Skalnaté Pleso*, **36**, 103–117.

# Statistical analysis of height and velocity distribution of the Perseids

Pei-Ying Wu<sup>1</sup>, I-Ching Yang<sup>1</sup>, and Chun-Nan Lin<sup>2</sup>

<sup>1</sup>Department of Applied Science, National Taitung University, Taitung, Taiwan  
tba1624@gmail.com and icyang61@gmail.com

<sup>2</sup>Department of Distribution Management, Shu-Te University, Kaohsiung, Taiwan  
cnlin@stu.edu.tw

Our study includes 14 805 Perseid meteors of the SonotaCo database from 2007 to 2016 in Japan. We obtain their height and velocity distributions. The kurtosis and skewness of the height distributions and velocity distributions are considered.

## 1 Introduction

Brown et al. (2002) presented multi-station electro-optical observations of the 1999 Leonid meteor storm, and obtained the distribution of beginning and end heights. Here, based on SonotaCo data (2009) between 2007 to 2016, we discuss the shape of the beginning and end height distributions and the geocentric and heliocentric velocity distributions of the Perseids.

## 2 Statistical analysis of height distribution

The beginning height distribution of the Perseids in 2007–2016 is shown in Figure 1. To describe the symmetry of the distribution curve, Figure 2 is shown. The kurtosis and skewness (Joanes and Gill, 1998) are calculated in Table 1 as measures of the tailedness and the asymmetry of the distribution.

Figures 3 and 4 and Table 2 are the analogues of Figures 1 and 2 and Table 1 for the end height distribution of the Perseids.

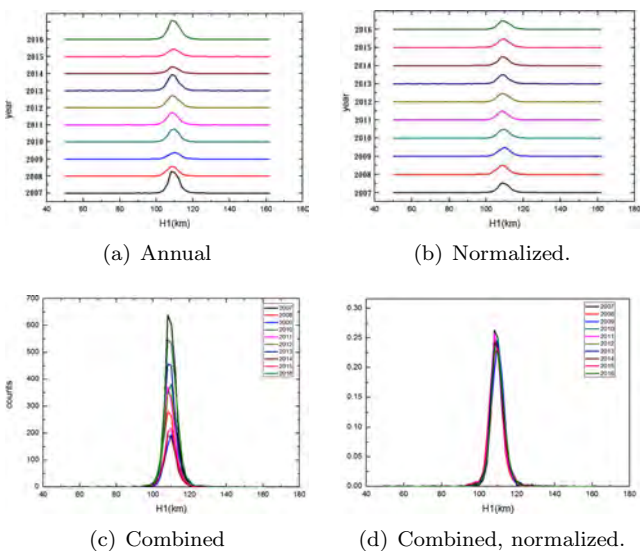


Figure 1 – Beginning height distributions.

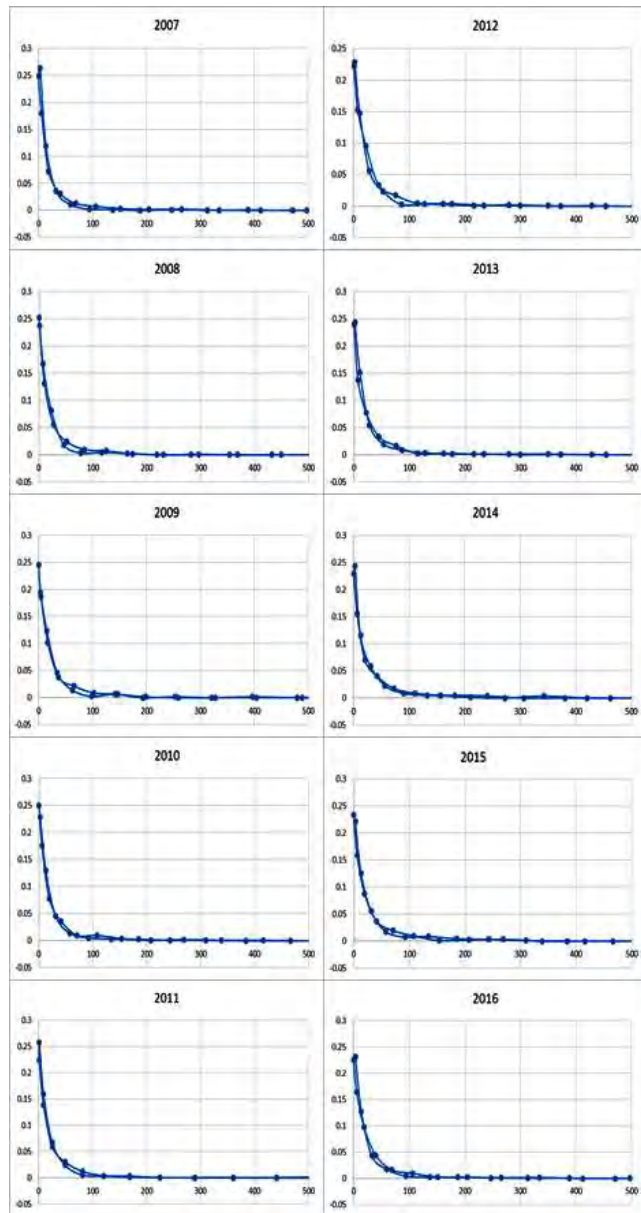


Figure 2 – Count vs.  $(H_1 - \bar{H}_1)^2$  plot of the right- and left-hand side of the curve in Figure 1, (d), where  $\bar{H}_1$  is the beginning height with the maximum count value.

Figures 1 and 2 show that the beginning height distribution is symmetric and leptokurtic, with zero skewness.

Table 1 – The Kurtosis and skewness of the annual beginning height distributions.

Year	Kurtosis	Skewness	Year	Kurtosis	Skewness
2007	40.22178	-2.93681	2012	3.650017	0.001340
2008	1.694996	0.353089	2013	31.99889	-0.65664
2009	1.996663	-0.00873	2014	5.638423	0.225124
2010	16.94567	-0.98926	2015	21.48264	1.618778
2011	10.23180	-0.79348	2016	9.441355	-0.25029

Table 2 – The Kurtosis and skewness of the annual end height distributions.

Year	Kurtosis	Skewness	Year	Kurtosis	Skewness
2007	6.258561	-1.50042	2012	1.135825	-0.73765
2008	0.925984	-0.80628	2013	5.416417	-1.10313
2009	0.471848	-0.52550	2014	2.586341	-0.91860
2010	2.539355	-0.98926	2015	1.385900	-0.45123
2011	1.434566	-0.79348	2016	2.204816	-1.00251

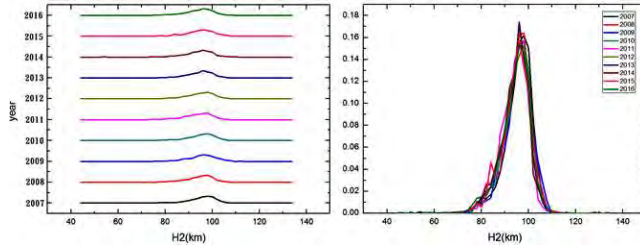


Figure 3 – Normalized end height distributions (annual and combined).

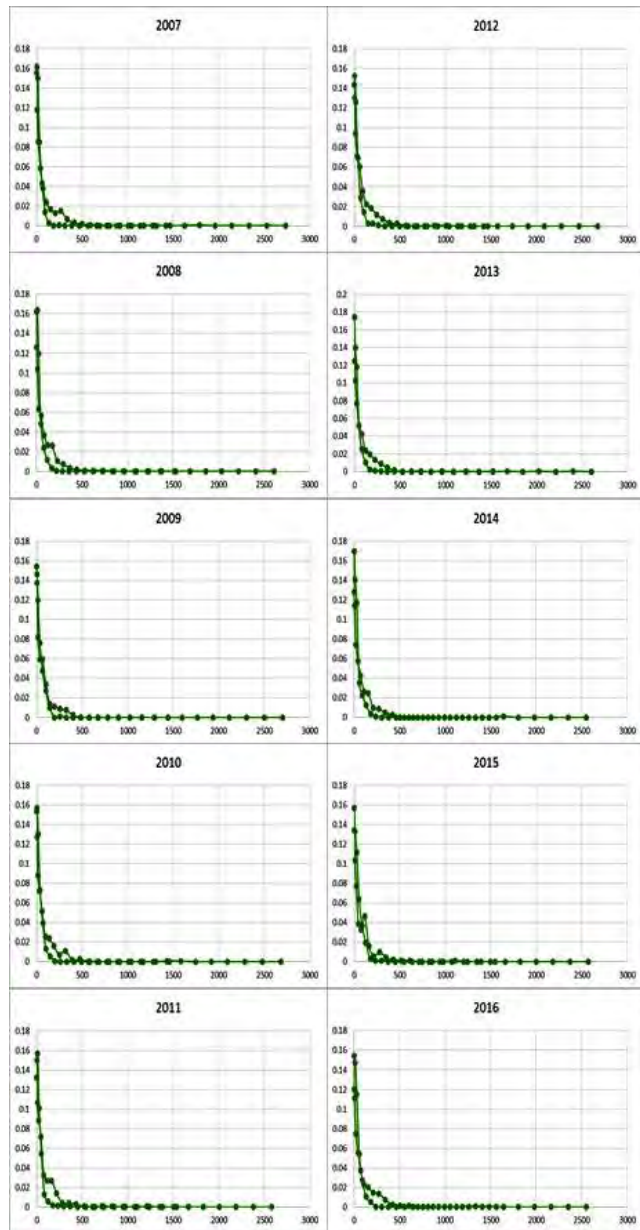


Figure 4 – Count vs.  $(H_2 - \overline{H}_2)^2$  plot of the right- and left-hand side of the curve in Figure 3, right, where  $\overline{H}_2$  is the end height with the maximum count value.

### 3 Statistical analysis of velocity distribution

The geocentric velocity distribution of the Perseids in 2007–2016 is shown in Figure 5. To describe the symmetry of the distribution curve, Figure 6 is shown. The kurtosis and skewness are calculated in Table 3 as measures of the tailedness and the asymmetry of the distribution.

Figures 7 and 8 and Table 4 are the analogues of Figures 5 and 6 and Table 3 for the heliocentric velocity distribution of the Perseids.

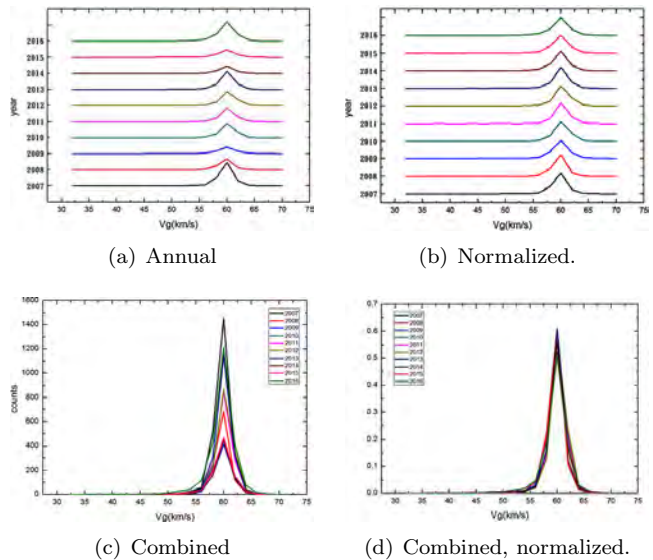


Figure 5 – Geocentric velocity distributions.

Table 3 – The Kurtosis and skewness of the annual geocentric velocity distributions.

Year	Kurtosis	Skewness	Year	Kurtosis	Skewness
2007	37.45115	-4.54430	2012	21.27527	-2.71751
2008	18.08323	-2.09244	2013	35.01786	-3.65819
2009	8.064054	-1.56145	2014	12.76156	-1.95245
2010	34.65781	-3.63871	2015	14.64384	-2.54844
2011	30.76895	-3.48506	2016	13.15525	-2.37531

### 4 Summary

Our two main results are that height distributions are symmetric, leptokurtic, and have zero skewness, and that velocity distributions are symmetric, leptokurtic, and have positive skewness.

### 5 Acknowledgements

I.-C. Yang and P.-Y. Wu thank the Ministry of Science and Technology (Taiwan) for financial support.

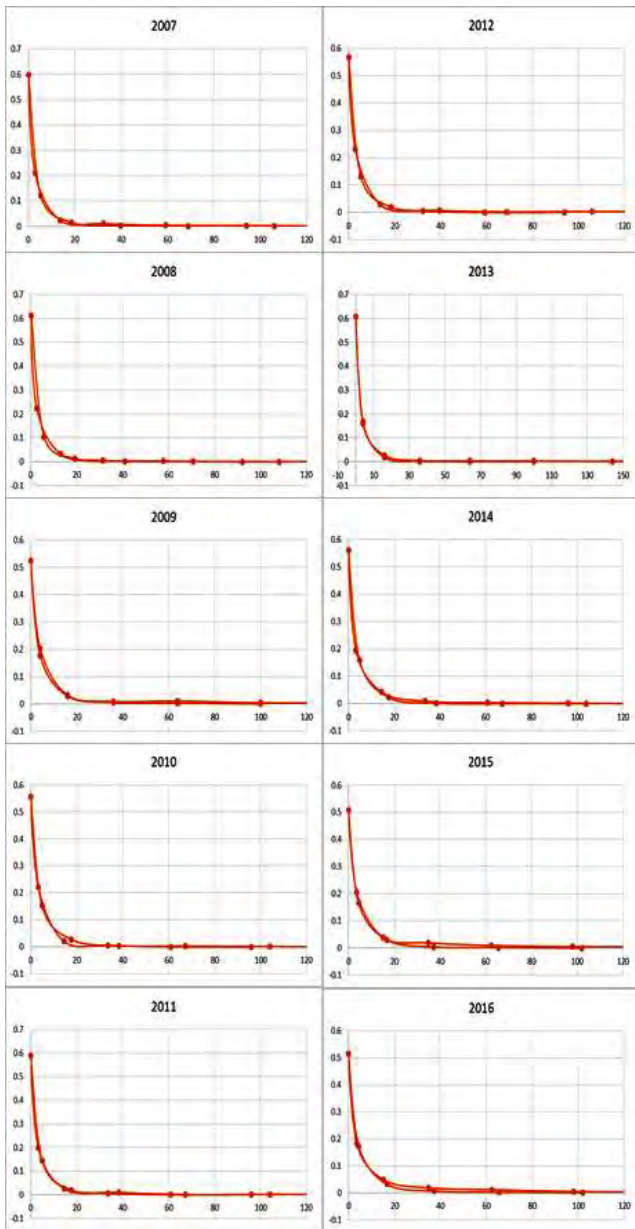


Figure 6 – Count vs.  $(V_g - \bar{V}_g)^2$  plot of the right- and left-hand side of the curve in Figure 5, (d), where  $\bar{V}_g$  is the geocentric velocity with the maximum count value.

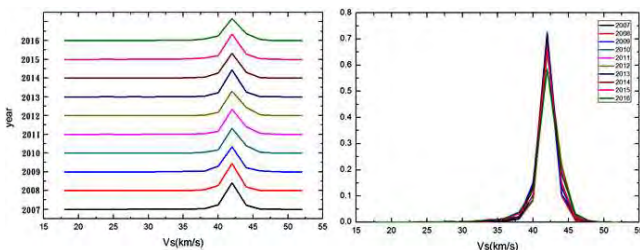


Figure 7 – Normalized heliocentric distributions (annual and combined).

References

Brown P., Campbell M. D., Hawkes R. L., Theijsmeijer C., and Jones J. (2002). “Multi-station electro-optical observations of the 1999 Leonid meteor storm”. *Planetary and Space Science*, **50**, 45–55.

Table 4 – The Kurtosis and skewness of the annual heliocentric velocity distributions.

Year	Kurtosis	Skewness	Year	Kurtosis	Skewness
2007	30.53541	−4.00529	2012	26.91166	−3.25684
2008	18.98717	−2.18475	2013	32.54614	−3.54314
2009	8.643117	−1.46666	2014	11.05086	−1.85638
2010	28.45243	−3.38084	2015	15.16172	−2.71522
2011	28.81138	−3.41411	2016	10.51124	−2.14398

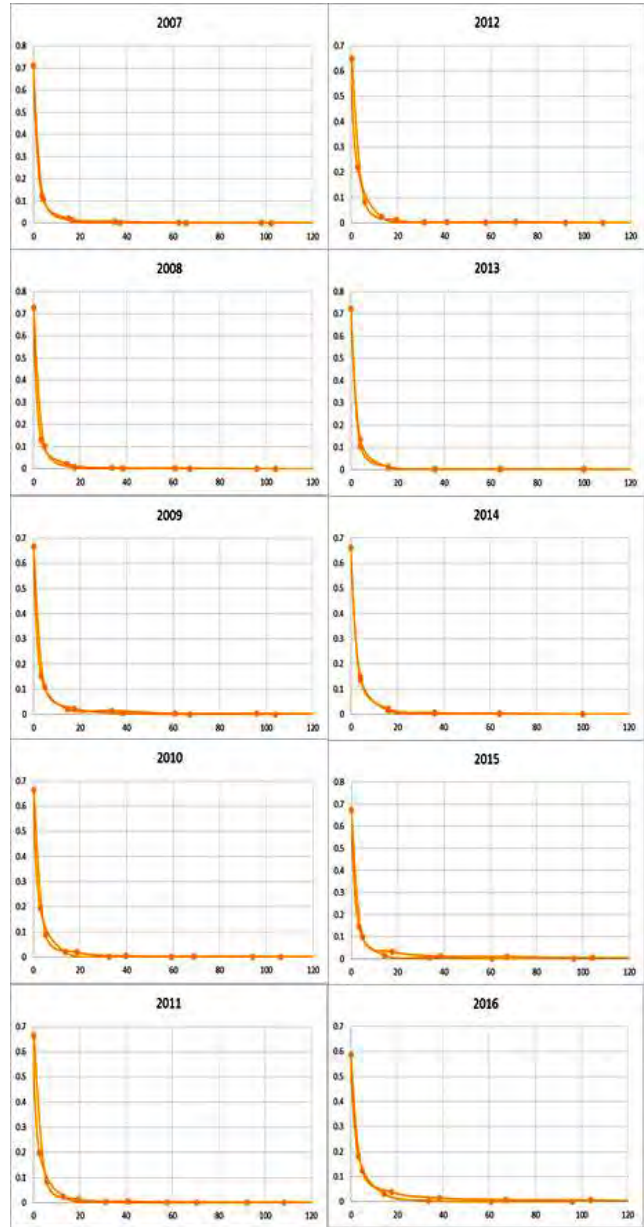


Figure 8 – Count vs.  $(V_s - \bar{V}_s)^2$  plot of the right- and left-hand side of the curve in Figure 7, right, where  $\bar{V}_s$  is the heliocentric velocity with the maximum count value.

SonotaCo (2009). “A meteor shower catalog based on video observations in 2007–2008”. *WGN, Journal of the IMO*, **37**, 55–62.

Joanes D. N. and Gill C. A. (1998). “Comparing measures of sample skewness and kurtosis”. *Journal of the Royal Statistical Society. Series D (The Statistician)*, **47**, 183–189.

# Some aspects of team visual observation analysis

Diana Sekulić, David Buzgo, and Sara Knežević

Petnica Meteor Group

Some of the first results of team visual observations during the Perseid shower 2017 campaign of the Petnica Meteor Group at Debelo Brdo (Valjevo, Serbia) are presented. The error in assessing meteor magnitude was analyzed, as well as the classification error for meteors and the dependence of the average magnitude value and the number of meteors seen on the limiting magnitude of the observers.

## 1 The idea

Where did the idea come from? Well, this year was a good occasion to test and measure typical observation errors. We had many new and inexperienced observers coming to the Perseid shower observations, and due to the Full Moon on the dates close to the maximum of Perseid activity, we thought it was a good idea to analyze our observations.

The main goal was to make a distinction between the perception of a meteor and the actual meteor event. In other words, the goal was to connect one meteor to all of the observers that saw it and to estimate the error made by each observer in a group and the overall quality of the observations.

## 2 Realization

The experiment was conducted by splitting observers into separate groups. In this case, observers were separated into three groups. Observers of the same group had roughly the same field of view. Each group consisted of three or more observers and one code-reader. The code-reader was the person who would read out loud the serial number of a meteor whenever someone requested one and the code-reader would write down the exact time when it happened. For more accuracy, an application was developed. The application automatically generated codes, which were read out loud by the code-reader, with timestamps, and saved them to a \*.txt file on an Android device.

Each observer wrote down his or her assessment of the associated shower and the magnitude, and wrote down the code for that meteor. That way, we were able to connect all the observers that saw the same meteor by comparing the codes. Afterwards, we linked the meteor events with the entries in our visual observation database, and calculated the different observation errors. The average assessed magnitude value was taken as the real value of the meteor magnitude. For each observer, we calculated the error in his or her assessment, and, finally, calculated the average error for one meteor.

The classification error was calculated as well. The concept of a classification error is that we can tell what percentage of observers in one group classified the me-

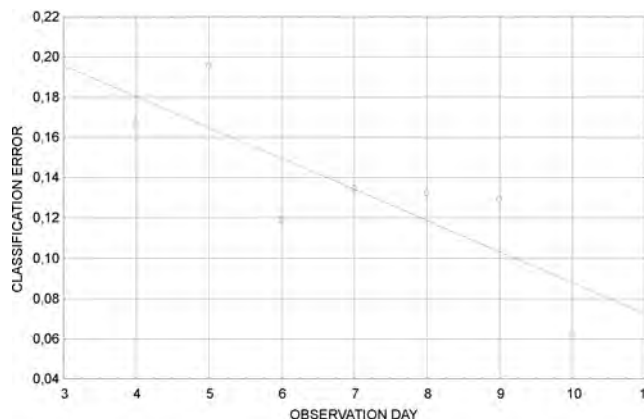


Figure 1 – Average classification error for four or more observers during a 7-day period.

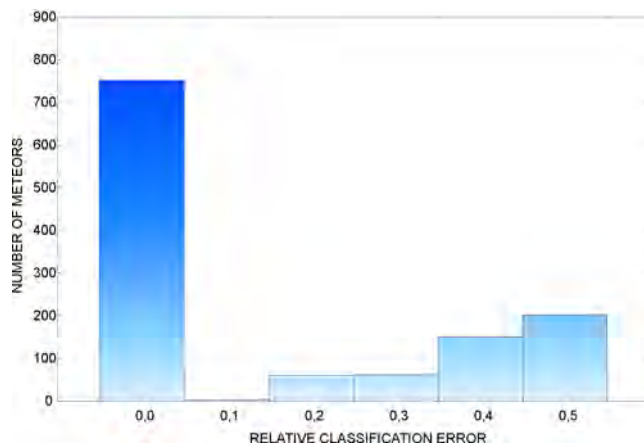


Figure 2 – Relative classification error for two or more observers.

eteor into the wrong shower. If, for example, five people saw the same meteor and four of them classified it as a Perseid and one as a non-Perseid, the classification error is 0.2 (1/5).

The relationship between the limiting magnitude of the observers and the number of meteors seen was also analyzed, as well as the limiting magnitude compared to the number of fainter meteors seen.

## 3 First results

We took the average assessed magnitude value as the real value of meteor magnitude. For each observer, we

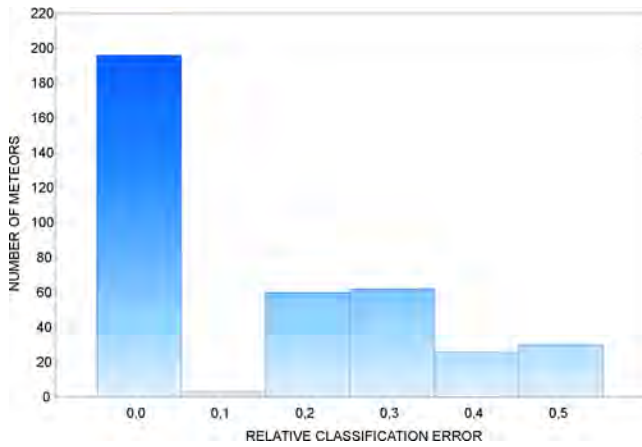


Figure 3 – Relative classification error for four or more observers.

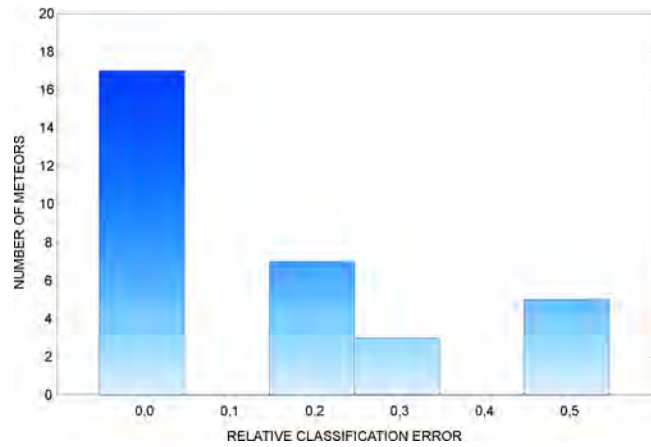


Figure 4 – Relative classification error for exactly seven observers.

calculated the error in their assessment, and, finally, calculated the average error for one meteor. The average error for one day is the average of all meteor magnitude errors. The idea of calculating standard deviations for one day is the same as the idea of calculating the average error for one day. The average error in magnitude perception is approximately 0.5 with the standard deviation of the error being approximately 0.5 as well.

In Figure 1, a temporal distribution of the average classification error is shown during the period when the number of new, inexperienced observers increased at the observations. Figures 2–4 show the classification error

for different numbers of observers who saw the same meteor. The classification error increases with the increase of the number of observers who saw the same meteor, which points out to the observers who do not classify meteors correctly.

The correlation between limiting magnitude and fainter meteors was 0.1, which is not that much, but nevertheless statistically significant ( $p < 0.05$ ). We expected that the observers with higher limiting magnitude would see more meteors, but our results do not show the correlation between the limiting magnitude and the number of meteors seen.

# Meteor video observations, $F$ and $T$ factor

Milica Rakić and Ana Nikolić

Petnica Meteor Group, Petnica Science Center, Valjevo, Serbia

inukki4@gmail.com and ana998nikolic@gmail.com

The  $F$  factor is a means of measuring the point on a light curve where most of the energy is released. In the process of analyzing light curves some information is lost. To preserve that information, we decided to introduce a new method, called  $T$  factor, which is determined by the center of mass of the light curve. The main intention of our project was to determine values of the  $F$  and  $T$  factors for four different meteor showers (Perseids, Geminids, Orionids, and Quadrantids) and to compare them. The results obtained by both methods were not matching previous research, where analyzed light curves were obtained with instruments of greater sensitivity. From our results, however, we can conclude that the  $T$  and the  $F$  factor are comparable classifiers for all four meteor showers, regardless of sample size, although the  $T$  factor seems to be a somewhat better classifier. In the future, we would like to test our program on meteors captured with cameras of much greater sensitivity and also to do the analysis for other meteor showers.

## 1 Introduction

Meteoroids are small bodies in the Solar System, originating from comets or asteroids. When interacting with the Earth's atmosphere, they ablate due to aerodynamic heating which we see as light phenomena called meteors. During that time they release a certain amount of energy that we correlate with the amount of light released, and then we use that to plot light curves (luminous intensity as a function of height). It is hard to study the physical structure and chemical composition of a meteoroid. Indeed, the brightness of the meteor changes during its trajectory through the atmosphere, and that light is directly dependent on the process of ablation. This is why we study the meteor light curves (i.e. the luminous intensity as a function of height). By studying these light curves, we may identify the structure and composition of meteoroids and also find the point where the most of energy was released.

There are two models that define the composition of a meteoroid: the single-body and the dustball model. According to the standard theory, meteoroids are single-body objects of uniform density and composition. Their maximum brightness is predicted to happen at the end of the trajectory, so light curves are asymmetrical. The theory formulated by For smaller and fainter meteors, however, Fleming et al. (1993) state that meteoroids are made of a lot of small particles connected with some kind of abrasive material. Their model predicts that maximum brightness occurs at the middle of the trajectories, so that light curves are nearly symmetrical.

## 2 Methods

The main method of describing light curves uses the  $F$  factor (Fleming et al., 1993). We used sets of  $F$  factors:

$$F_{\Delta M} = \frac{H_{B\Delta M} - H_{\max}}{H_{B\Delta M} - H_{E\Delta M}}, \quad (1)$$

with  $H_{\max}$  the height of maximum brightness,  $H_{B\Delta M}$  the beginning height, and  $H_{E\Delta M}$  the end height of the

meteor. We took the magnitude step  $\Delta M$  to be 0.25. The final  $F$  factor is an arithmetic mean of all partial factors. If the maximum brightness point is moved towards the end of the light curve, then  $F > 0.5$ , otherwise  $F < 0.5$ . Models of standard single-body theory produce light curves with  $F \approx 0.7$ , whereas the dustball model exhibit curves with  $F \approx 0.5$ . Larger  $F$  factors can indicate a more solid meteoroid body.

We had a problem of making a smooth curve without losing a lot of information within it, e.g., moving the point of the maximum and so changing its value and obtaining a false value for the  $F$  factor. This was especially a problem for short meteors with a small number of frames. So before doing any calculations, we first extended the number of frames and data using interpolation, adding five additional points between every set of two. Then, we made the light curves smoother using a method of moving average for every three points while maintaining the area below the light curve constant in the hope to conserving the energy.

The  $F$  factor exhibits the problem that during its calculation it does not keep all initial information, especially during the smoothening of the light curve. Also because we have low-sensitivity cameras and so incomplete light curves, we want to find the best and simplest method of classification. Therefore, we decided to introduce a new factor which we hoped will conserve more information: the  $T$  factor represents the center of mass of the light curve and the area beneath it as an equivalent to energy. The  $T$  factor is calculated by formula

$$T = \frac{H_T - H_B}{H_E - H_B}; \quad (2)$$

$$H_T = \frac{1}{A} \sum H_i \cdot A_i, \quad (3)$$

where  $H_T$  is the height of the center of mass of the light curve,  $H_B$  the beginning height,  $H_E$  the end height,  $A$  the area below the curve, and  $A_i$  and  $H_i$  respectively

the area and the height of the  $i$ -th part of the curve. We expected the  $T$  factor to have a value closer to the center of the light curve than the  $F$  factor.

We used the video data from the EDMOND database, captured by cameras with limiting sensitivity of about magnitude +4 (for stars) and frame rate of 25 fps, and video data from Serbian stations taken from the Petnica Meteor Group database. The video data were acquired and processed using UFOCAPTURE and UFOANALYZER software. Data were taken from four different stations: Padina (SRB), Debelo Brdo (SRB), Maruška (CZ), and Valašské Meziříčí or ValMez for short (CZ), and tested for four showers: Perseids, Geminids, Orionids, and Quadrantids. The number of samples exceeded 200 for all the meteor showers. The program for analyzing the light curves was written in the language PYTHON 3.

The original data were stored in XML files, obtained by analyzing video data with UFO software. Each frame in those files contains azimuth, elevation, time, and magnitude (among other data) of the meteor at that point. Using these data, we were able to calculate the height and distance from the camera to the meteor, for each frame. We also took table values of right ascension and declination for the radiant position of each meteor shower and translated those values to horizontal coordinates (elevation and azimuth). Those values were essential to analyze light curves and to calculate the parameters we needed. Having obtained these values, we were able to calculate the  $F$  and  $T$  factors.

### 3 Results

In order to take into account the influence of elevation of the radiant, i.e., the trajectory of the particle through the atmosphere, on the shape of light curves, we have divided our samples in two categories: meteors with higher radiant elevation and meteors with lower radiant elevation. Then, we ran our program to get the  $F$  and  $T$  factors. The results are shown in Table 1.

Table 1 – Comparison of the  $F$  and  $T$  factors for different meteor showers.  $N$  is the number of samples.

Show.	$F$ factor	$T$ factor	$N$
PER	$0.515 \pm 0.005$	$0.565 \pm 0.002$	533
GEM	$0.500 \pm 0.004$	$0.542 \pm 0.002$	449
ORI	$0.542 \pm 0.006$	$0.545 \pm 0.004$	339
QUA	$0.505 \pm 0.006$	$0.519 \pm 0.004$	233

We show in Table 1 some peculiar and unexpected results for the  $F$  factor of all the considered meteors showers. While we expected the  $F$  factor for the Geminids to have the highest value of all meteor showers, it turned out to be the smallest one. In Table 2, we exhibit a comparison of our results for the  $F$  factor with those of other relevant studies. From Table 2, we can see that none of results obtained by different papers were the same, or very close to each other. This can be explained by different approaches for processing the light

curves and potentially taking a dissimilar value for the magnitude step  $\Delta M$ .

On the other hand, we expected the  $T$  factor to have smaller values than the  $F$  factor, which with most showers turned out not to be the case. Values for the  $T$  factor of the Perseids compared to the Quadrantids are notably bigger. Also, the  $T$  factor may prove to be a better classifier, which is indicated by the standard error shown in Table 1.

Table 2 – Comparison of our results for the  $F$  factor with other studies: RaN (Rakić and Nikolić), Kel (Koten et al., 2004), and MaG (Grašić et al., 2016)

Show.	RaN	Kel	MaG
PER	$0.515 \pm 0.005$	$0.535 \pm 0.010$	–
GEM	$0.500 \pm 0.004$	$0.583 \pm 0.016$	$0.540 \pm 0.030$
RI	$0.542 \pm 0.006$	$0.545 \pm 0.012$	$0.561 \pm 0.006$

As for the comparison between the  $F$  and  $T$  factors, we can see that  $T$  tends to have higher values for most showers, except for the Orionids where both factors are almost balanced out. In Figures 1 and 2, we can see that the  $F$  and  $T$  factor do not seem to match, although their values are constrained between similar limits. Also, where the  $F$  factor seems to lose some information, the  $T$  factor is better at preserving it.

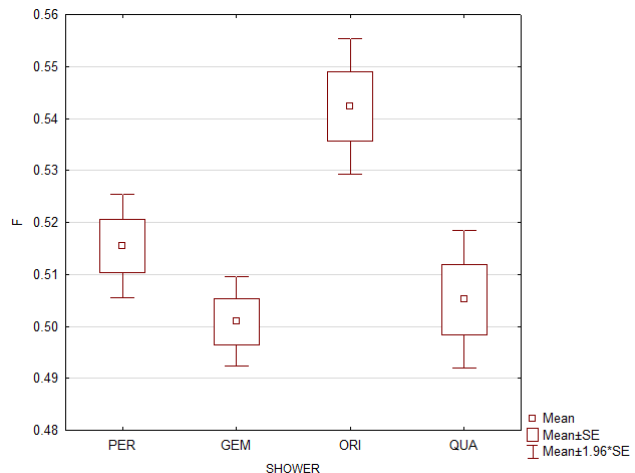


Figure 1 – Dependence of the  $F$  factor on different meteor showers.

In Figures 3 and 4, (a) denotes radiant elevations mostly above  $45^\circ$  and (b) denotes radiant elevations mostly below  $45^\circ$ . We can see that meteors whose radiants are higher up in the sky have bigger values for both  $F$  and  $T$ .

### 4 Conclusions

In conclusion, most showers are grouped in a certain range of values for  $F$  and  $T$ , except for the Orionids that tend to stand out regardless of which method we use to process the data. Considering that Geminids (and Quadrantids) are believed to be of asteroid origin and, because of that, more compact, the  $F$  factor is expected to be higher than for the other two showers. Contradictory to these expectations and regardless of

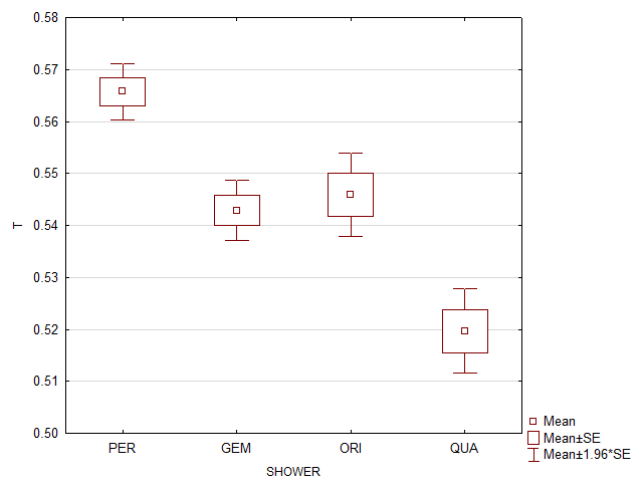


Figure 2 – Dependence of the  $T$  factor on different meteor showers.

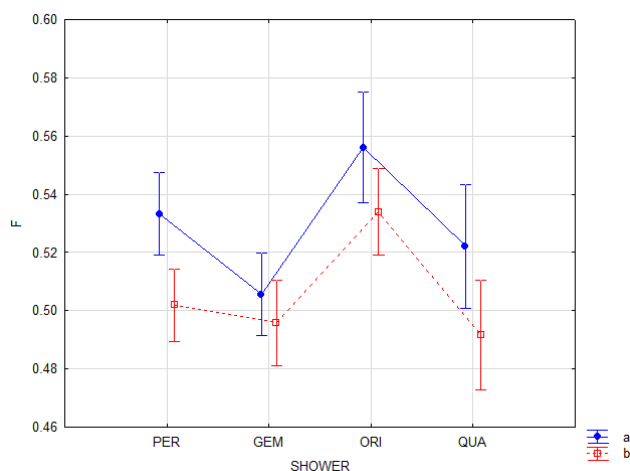


Figure 3 – The  $F$  factor difference depending on radiant elevation, where (a) are meteors with smaller radiant zenith distances, and (b) are meteors with larger radiant zenith distances. Vertical bars denote 0.95 confidence intervals.

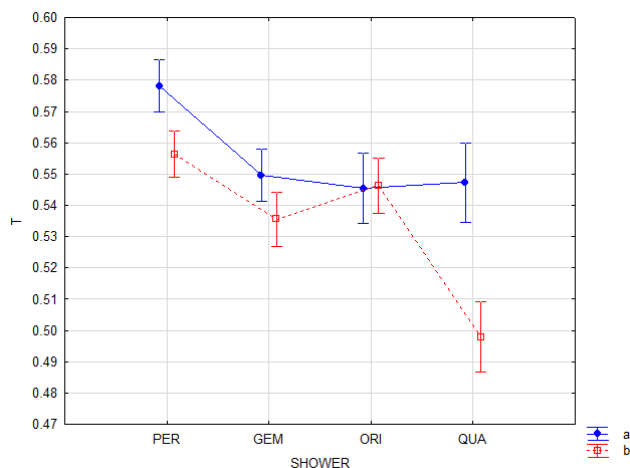


Figure 4 – The  $T$  factor difference depending on radiant elevation, where (a) are meteors with smaller radiant zenith distances, and (b) are meteors with larger radiant zenith distances. Vertical bars denote 0.95 confidence intervals.

the sample size, the Geminids have the lowest  $F$  factor and one of lowest  $T$  factor of all meteor showers. The  $F$  factor for Geminids reaches a mean value of 0.50 which does not match the result of Koten et al. (2004) whose

Geminids have a mean value of 0.58, the largest value among all showers. It is important though to state that their research was done with sensitive TV methods of detection, with which they could capture parts of light curves undetectable for standard video cameras. The size of the sample did not affect the result, however. In other words, with increasing sample size,  $T$  and  $F$  do not change within the error boundaries.

Also, there seemed to be a correlation between the elevation of radiant and the  $F$  and  $T$  factors. For all showers, meteors with smaller radiant zenith distances, or radiants that are higher up, have bigger  $F$  factors. From this, we can conclude that meteors that pass through less dense parts of atmosphere stay compact for longer amounts of time. From our results, we can conclude that both  $T$  and  $F$  factor are classifiers for all four meteor showers, regardless of sample size, although the  $T$  factor seems to be a somewhat better classifier.

As future research, it would be interesting to check these results on bigger samples and apply them to other meteor showers as well. Then, if it is proven that the classification really exists, it would be interesting to see what would be the physical reason for the differences detected and to explore in greater detail the influence of radiant elevation on these parameters. If possible, we would like to test these results for television meteors or videos from cameras with much higher sensitivity and to see the difference. Also, we would like to determine for larger numbers of meteors and specific showers their model starting heights.

### Acknowledgement

We thank Jakub Koukal from EDMOND for data from the Czech Republic.

### References

Fleming D. E. B., Hawkes R. L., and Jones J. “Light curves of faint television meteors”. In Štohl J. and Willams I. P., editors, *Meteoroids and their Parent Bodies*, Smolenice, Slovakia, 6–12 July 1992. Astronomical Institute, Slovak Academy of Sciences, pp. 261–264.

Gračić L., Milovanović N., and Pavlović D. (2016). “Video meteor light curve analysis of Orionids and Geminids and developing a method for obtaining the absolute light curves of shower meteors from the single station data”. In Roggemans A. and Roggemans P., editors, *Proceedings of the International Meteor Conference*, Egmond, the Netherlands, 2–5 June 2016. IMO, pp. 83–86.

Koten P., Borovička J., Spurný P., Betlem H., and Evans S. (2004). “Atmospheric Trajectories and Light Curves of Shower Meteors” *Astronomy & Astrophysics*, **428** (2), 683–690.

# Cloudiness estimation for video meteor observations

Vladimir Nikolić, Leander Schröder, and Aleksa Tešić

Petnica Science Center, Petnica, 14104 Valjevo, Serbia

vladimir.nik94@gmail.com, rleanderschroeder@gmail.com and aleksatesicsteske@gmail.com

We have developed a software package that can detect clouds in all sky camera images and give an estimate of how cloudy a particular area of the sky is. In practice, it can be used with a set of images to get an overview of cloudiness for the whole night(s). We use this software with an all sky camera that works in conjunction with a narrow field camera to give us relatively accurate cloudiness information for its field of view.

## 1 Introduction

The project started as a learning project during the Petnica Summer Institute Machine Learning 2017 Seminar. In an attempt to make something useful from the learning process, we contacted the Petnica Meteor Group to inquire about some of the problems they are having that could be solved with machine learning. The problem we were given was the following.

Petnica Meteor Group uses two cameras for meteor observation: a narrow field video camera that is triggered by meteors, and an all-sky camera used to estimate cloudiness for the video camera. The latter camera is necessary, as the former will not make any recordings during cloudy periods. This means that if they get no recordings at all, they do not know whether that is because it is cloudy or because the shower is not active.

## 2 Existing solutions

Before starting the project, we examined the existing solutions. There are, in fact, plenty that detect clouds in images, both day and night, however, each one of them had some problems:

- None of the solutions take into account clouds that are not obvious, such as those where you cannot see them, because the sky is just black. These clouds are high and can be detected by the lack of stars in that area of the sky;
- Most of them were fairly simple procedural solutions. They are prone to inaccuracies if the conditions change, such as lighting. A machine learning approach is able to take into account various situations and handle them properly, if given proper data;
- Less importantly, they did not estimate cloudiness for a given field of view, which is what we needed.

## 3 Our solution

To solve the problem, we attempted a machine learning approach. The idea is to create a neural network that

takes a night sky image as its input and have it output a cloud map. In this context, a cloud map would be a black and white image, where pixel intensity represents likelihood of that pixel belonging to a cloud. So, for example, a white pixel is definitely a cloud, a gray pixel is probably part of a cloud, and a black one is not. The output is intuitive, as white areas represent actual clouds, as seen in Figure 1.

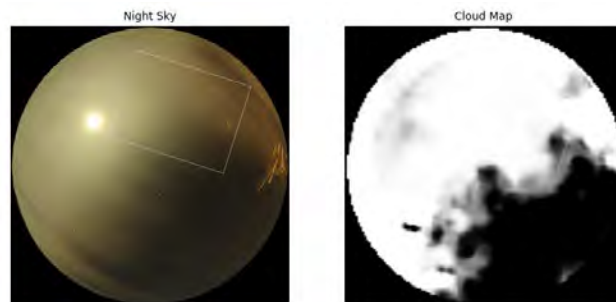


Figure 1 – Example of the neural network output, showing where the clouds are for the given input image.

### 3.1 Neural network

We used a Convolutional Neural Network (CNN<sup>1</sup>) which are standardly used when processing images. As a matter of fact, they process matrices (images in this case), so they can be applied to any problem where locality is relevant in given matrices. If the reader is not familiar with artificial neural networks, it is only important to know that they are very flexible and can be trained to output any kind of data as long as they are provided data to learn from. In this instance, we want to output a cloud image from a given sky image, so we need to give sky images and corresponding cloud images that we have labeled so that the network can learn to do the task by itself. Figure 2 shows an example of a CNN architecture, but they will not be explained in more detail as they are fairly complex and too long for this paper.

### 3.2 Data

The neural network needs data to learn from and that is, in our case, all sky images and their labels. As we

<sup>1</sup>[https://en.wikipedia.org/wiki/Convolutional\\_neural\\_network](https://en.wikipedia.org/wiki/Convolutional_neural_network)

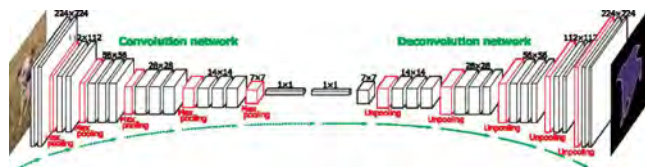


Figure 2 – Example of a Convolutional Neural Network.

have found no existing solution that solves this problem properly, we also could not find a fitting dataset, so we did the labeling ourselves. This process is slow, so only around 200 images have been labeled so far. An example of an image and its label can be seen in Figure 3. To mitigate this problem, we have synthesized data from our dataset. Data synthesis, in this context, means slightly altering existing data in such a way that we get new useful data. Concretely, because of the circular nature of all sky images, we are able to rotate the images and their labels several times, where each rotation would be a new data point, as seen in Figure 4.

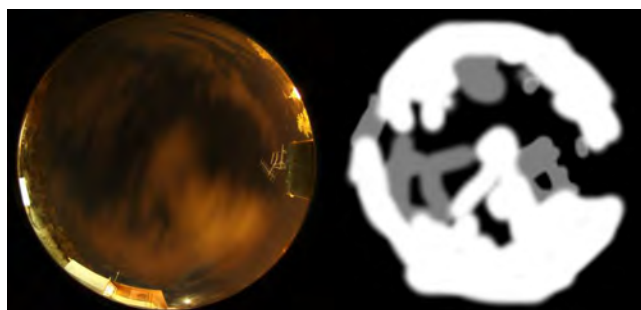


Figure 3 – Example image and its label.

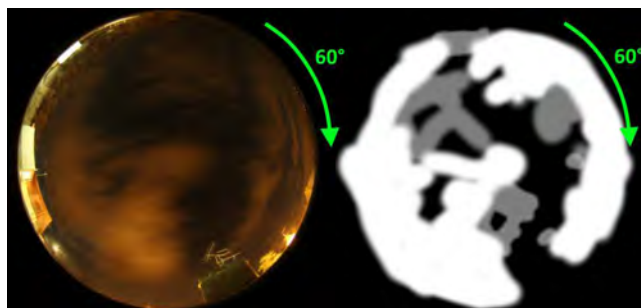


Figure 4 – Example of a rotation.

This method multiplies our data by the number of rotations we make to each image, but it is not perfect. The data we get is not qualitatively too different, so this only improves our network to some extent. Despite this, we have gotten fairly good results.

### 3.3 Field of view

The end goal is to get cloudiness percentage for a narrow field camera, so from a cloud map output, we need to extract the area of interest. The narrow field camera has the following parameters for its field of view: azimuth and elevation of the center, width of view, aspect ratio, and rotation from the horizon.

With these parameters, the program must calculate the vertices of the rectangle that forms the field of view. In

order to do that, we needed a method to convert coordinates between two systems—horizontal and cartesian. This means we need to be able to convert azimuth and elevation to pixel coordinates and vice versa.

Azimuth is easy to calculate, as the all sky images are circular and azimuth is just the angular offset on the image center. Elevation, however, is not as trivial, as all sky images are distorted; the elevation does not decrease linearly as you move away from the zenith. To get around this, we took several cloudless all sky images and catalogued the stars we found (Figure 5). Because we identified the stars, we knew their horizontal coordinates and we also knew their pixel coordinates, since we found them on actual images. With this catalogue, we could approximate the mapping between the horizontal and cartesian systems. Elevation, in the context of an image, is the distance from the center of the image, as that is where the zenith is. Given an elevation, we can determine how far it is from the center by finding two stars in the catalogue where our given elevation lies between the elevations of these two stars and linearly interpolate the distance.

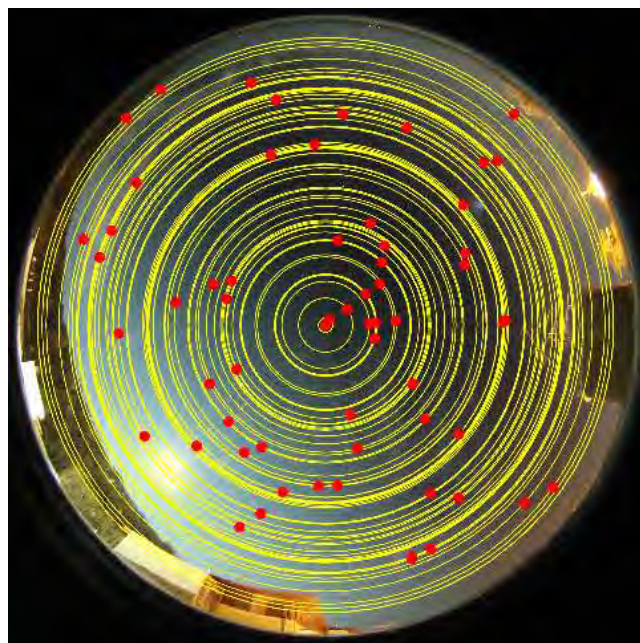


Figure 5 – The dots are the stars that we have catalogued and the concentric circles represent distances from the center with equal elevation. Each circle passes through a star of that elevation. The areas in between are linearly interpolated.

## 4 System in practice

The whole pipeline works like this. The user inputs all the necessary parameters, including field of view, date and time interval of interest, and night sky images. The user is then, optionally, presented with each individual sky image, its cloud map and cloudiness percentage for correctness check. After this finishes, a table with date/time and cloudiness columns is saved to a file as the end result. Figures 6 and 7 show the optional correctness check phase which displays the relevant parts

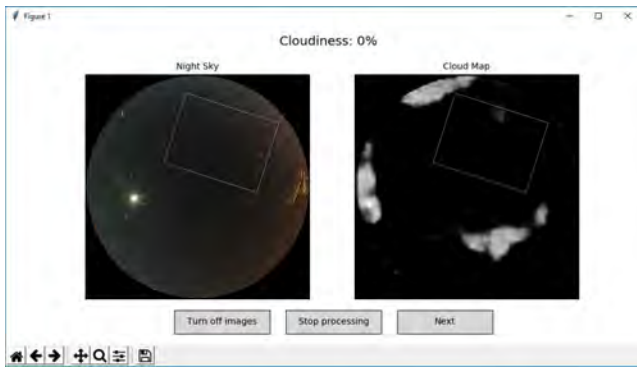


Figure 6 – System in the first practical example.

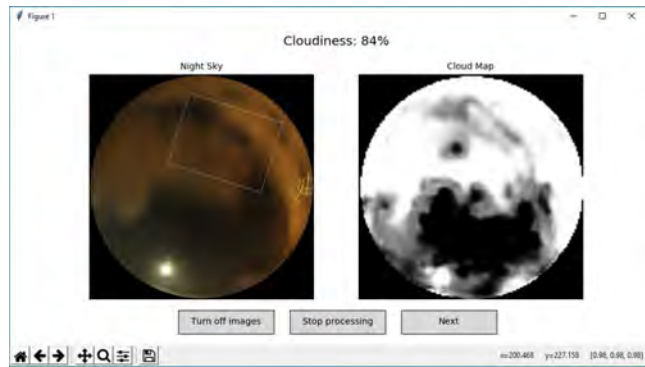


Figure 7 – System in the second practice example.

of the whole process. The source code for the project can be found online<sup>2</sup>.

## 5 Future work

The main point that needs to be addressed is the variability (or lack thereof) of accepted input images. Right now, the system only works well with all sky night images taken from the Petnica camera with its current settings. This is because the dataset the network was trained on only has these kinds of images. To improve the model, we need to label images taken with different cameras and settings such as brightness, sensitivity, exposure, etc. It is also possible to label daytime images to generalize cloud detection. All in all, the model im-

proves with every new labeled image that the network can learn from.

Another possible improvement is a different neural network architecture. The current one is not too complex, but works well on everyday computers. If a more accurate estimation is needed, a more complex architecture could be made, although, as is clear to anyone familiar with machine learning, a more complex network does not necessarily perform better due to overfitting.

## 6 Acknowledgements

We thank Branislav Savić from Petnica Meteor Group. He has provided us advice and answered all the questions related to the astronomy part of this project.

<sup>2</sup><https://github.com/schutzekatze/allsky-cloudiness-estimator>

## Author index

- Acar M., 181  
 Amaral L. S., 171  
 Anciaux M., 132  
 Andreić Ž., 107, 176  
 Ateş A., 181  
 Baillie K., 166  
 Baláž, 16  
 Barabanov S., 199  
 Baratoux D., 42  
 Beck T. W., 169  
 Belchev I., 187  
 Bella C. A. P. B., 171  
 Beriša S., 25  
 Bettonvil F., 145  
 Bijl R., 145  
 Birlan M., 53, 103, 166  
 Blanpain C., 53, 103, 166  
 Borovička J., 109  
 Bosch M., 145  
 Bouley S., 42, 53, 103, 166  
 Bradley M., 169  
 Brower J., 128  
 Brown P., 18  
 Buzgo D., 223  
 Calders S., 13, 132, 138  
 Caminade S., 53, 103, 166  
 Campbell-Brown M., 18  
 Cellino A., 166  
 Colas F., 10, 42, 53, 103, 153, 166  
 Collison J., 65  
 Crevecoeur R., 145  
 Csépany G., 50, 192  
 Csizmadia S., 206  
 Dauvergne J. L., 42  
 De Cicco M., 65, 162  
 Delcroix M., 42  
 Di Martino M., 166  
 Drolshagen E., 38, 166  
 Drolshagen G., 38, 145, 166  
 Dufke T., 25  
 Dumbović M., 203  
 Đuriš F., 16, 46  
 Dvořák R., 184, 194  
 Egal A., 53, 153, 166  
 Eini S., 197  
 Eini Y., 197  
 Erklev A. M., 25  
 Fabris F., 203  
 Faria C. J. L., 171  
 Ferrière L., 166  
 Fietkiewicz K., 29  
 Gadegaard N., 79  
 Gajdoš Š., 16  
 Galache J.-L., 65  
 Gamby E., 13  
 Ganju S., 65  
 Gardiol D., 166  
 Gattacceca J., 53, 103, 166  
 Gawroński M. P., 29  
 Georgieva K., 187  
 Getsova-Momcheva I., 187  
 Gozdalski M., 29  
 Guliyev A. S., 35  
 Gural P. S., 56, 65, 107  
 Gyssens M., 5  
 Halatzi S., 197  
 Hankey M., 153, 177  
 Hegedüs T., 206  
 Hocking W. K., 212  
 Huggins S., 18  
 Hunchard D., 169  
 Ibhi A., 189  
 Igaz A., 50, 192  
 Jäger Z., 206  
 Jäger Z., Jr., 206  
 Jeanne S., 53, 103, 166  
 Jehin E., 166  
 Jenniskens P., 65  
 Jorda L., 166  
 Jung C. F., 171  
 Kákona J., 184, 194  
 Kákona M., 194  
 Kalmančok D., 16  
 Kastinen D., 92  
 Kayal H., 156  
 Kayhan C., 181  
 Kereszty Z., 206  
 Kero J., 92  
 Khiri F., 189  
 Kiss L. L., 50, 192  
 Knežević S., 223  
 Korlević K., 176  
 Kornoš L., 16, 46, 99  
 Koschny D., 10, 32, 38, 145, 166  
 Kosić M., 203  
 Koukal J. A., 171  
 Kubritová A., 16  
 Kwon M.-K., 53, 153  
 Lamy H., 13, 132, 138, 166  
 Lazzaro D., 162  
 Lecubin J., 53, 103, 166  
 Levin A., 197  
 Lin C.-N., 220  
 Loehle S., 32  
 Love R., 79  
 Maciejewski M., 29  
 Maegawa K., 216  
 Malgoyre A., 53, 103, 166

- Marmo C., 53, 103, 166  
Marqué C., 85  
Marsset M., 166  
Martínez Picar A., 13, 85, 132, 138  
Matlovič P., 16, 99  
MBaye S., 42  
Mikeš J., 194  
Molau S., 88, 166  
Morataya C., 169  
Myszkiewicz M., 29  
Nakane S., 216  
Nedelcu A., 166  
Netjes G.-J., 145  
Nikolić A., 225  
Nikolić V., 228  
Nogami N., 34  
Novoselnik F., 176  
Olech A., 29, 218  
Opitz N., 50, 192  
Ordoñez A. J., 65  
Ott T., 38, 166  
Ouknine L., 189  
Perlerin V., 7, 153, 177  
Polakowski K., 29  
Polotronieri R. C., 171  
Poppe B., 38, 166  
Raj A., 29  
Rakić M., 225  
Ranvier S., 132  
Ratz E., 197  
Rault J.-L., 5, 6, 53, 103, 166  
Rendtel J., 7, 8, 115  
Reynolds P., 79  
Ribas S., 166  
Roelandts T., 82  
Ronco J., 169  
Rowe J., 210  
Rudawska R., 10, 32, 99, 145, 166  
Ruseva K., 187  
Santiago E. P., 162  
Sárneczky K., 50, 192  
Schröder L., 228  
Šegon D., 107, 176, 203  
Šegon M., 107  
Sekulić D., 223  
Silber E. A., 212  
Silber R. E., 212  
Silva G. G., 171  
Šimon J., 16  
Skokić I., 176  
Slansky P. C., 71  
Smolić I., 25  
Stapper A. P., 65  
Štefanić Hoefel S., 203  
Steinhauser A., 166  
Steyaert C., 128  
Stolarz M., 29, 218  
Štrobl J., 184  
Suchodolski T., 29  
Tchenak T., 197  
Terentjeva A., 199  
Tešić A., 228  
Tétard C., 13, 132, 138  
Thuillot W., 153  
Tomezzoli G. T., 118  
Toni A., 10, 166  
Tóth J., 16, 46, 99  
Trindade L. S., 171  
Tymiński Z., 29, 218  
Upton C., 169  
Uriarte Latorre I., 32  
Vaubailon J., 10, 53, 103, 153, 166  
Veljkovic K., 43  
Verbeeck C., 7, 13, 132, 138  
Vernazza P., 53, 103, 166  
Vida D., 18, 176  
Világi J., 16  
Vodopivec A., 156  
Vojáček V., 109  
Vojvodić N., 25  
Vukić M., 107  
Ward W., 79  
Wiśniewski M., 29, 125, 218  
Wu P.-Y., 220  
Yang I.-C., 220  
Zanda B., 53, 103, 166  
Zelkó Z., 206  
Zender J., 10, 32, 145  
Zigo P., 16, 76  
Zoghbi S., 65  
Żołądek P., 29, 125, 218  
Zurita M. L. P. V., 171



